



VNIVERSITAT
D VALÈNCIA

Tesis doctoral
2014

IRENE TADEO CERVERA
TESIS DOCTORAL

2014



VNIVERSITAT
D VALÈNCIA

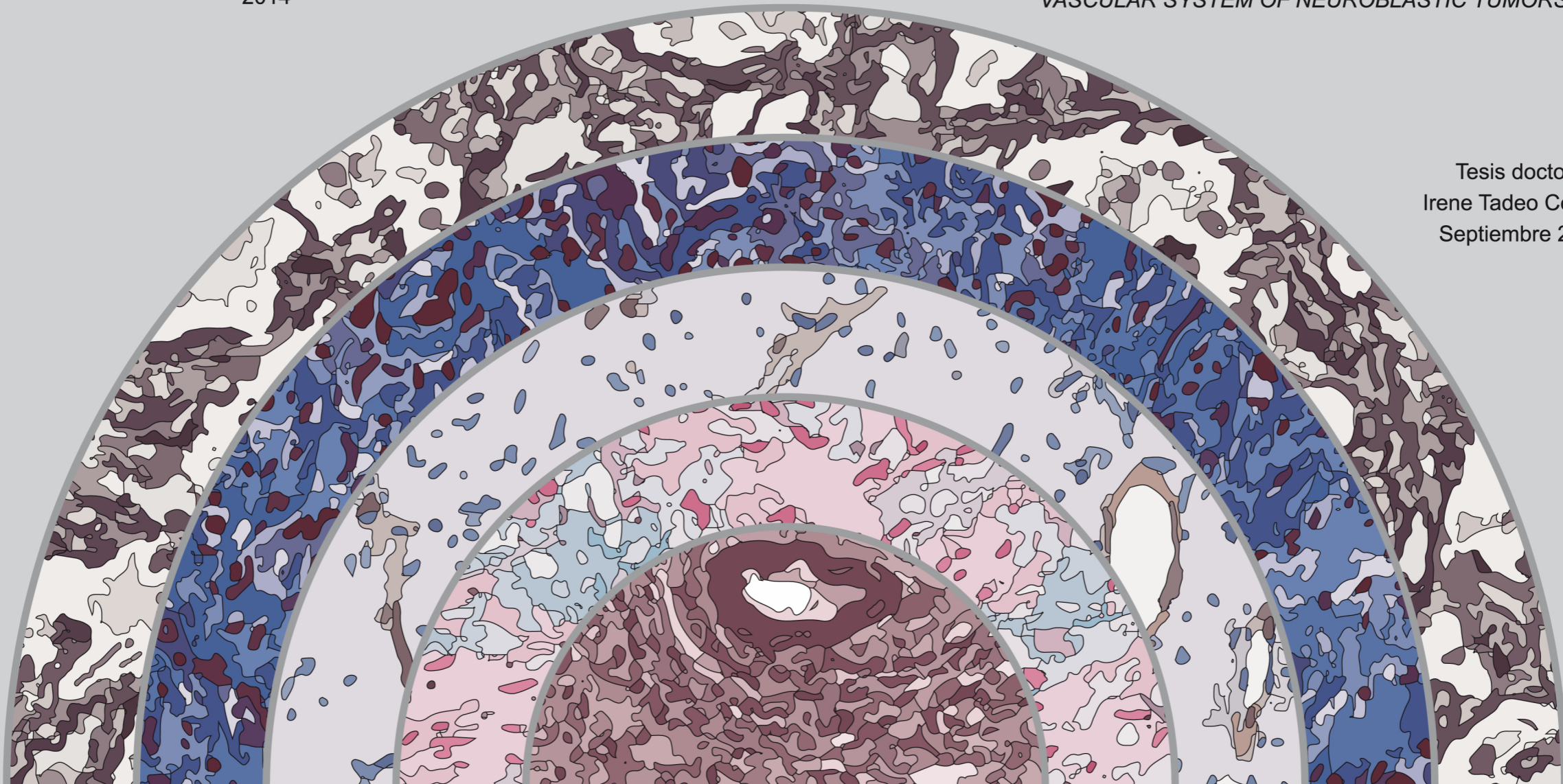


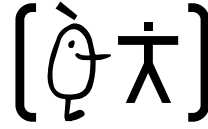
Facultat de Medicina i Odontologia
Departament de Patologia

ESTUDIO DEL ARMAZÓN ARQUITECTÓNICO Y DEL SISTEMA
VASCULAR DE LOS TUMORES NEUROBLÁSTICOS

*STUDY OF THE ARCHITECTURAL SCAFFOLDING AND THE
VASCULAR SYSTEM OF NEUROBLASTIC TUMORS*

Tesis doctoral
Irene Tadeo Cervera
Septiembre 2014





Facultat de **M**edicina i **O**dontologia
Departament de Patologia

ESTUDIO DEL ARMAZÓN ARQUITECTÓNICO Y DEL
SISTEMA VASCULAR DE LOS TUMORES NEUROBLÁSTICOS

*STUDY OF THE ARCHITECTURAL SCAFFOLDING AND THE
VASCULAR SYSTEM OF NEUROBLASTIC TUMORS*

Tesis doctoral presentada por Irene Tadeo Cervera, licenciada
en Biología, para optar al grado de Doctora con Mención Internacional
por la Universidad de Valencia.

Programa de Doctorado: 285-B Patología de los tumores humanos.

Directores de tesis: Dra. Rosa Noguera Salvá y Dr. Samuel Navarro Fos

Valencia, septiembre de 2014

Doña Rosa Noguera Salvá y Don Samuel Navarro Fos, doctores en Medicina y catedráticos de la Facultad de Medicina y Odontología,

CERTIFICAN:

Que Irene Tadeo Cervera, licenciada en Biología por la Universitat de València, ha realizado, bajo nuestra dirección, el trabajo que lleva por título:

Estudio del almacén arquitectónico y del sistema vascular de los tumores neuroblásticos.

El cual consideramos satisfactorio y apto para ser presentado como Tesis Doctoral en el Departamento de Patología de la Universidad de Valencia.

Y para que conste, expedimos este certificado en Valencia, a 11 de septiembre de 2014

Fdo.: Prof^a. Rosa Noguera Salvá
Prof^a. Catedrática de Histología

Fdo.: Prof. Samuel Navarro Fos
Prof. Catedrático de Anatomía
Patología

Agradecimientos:

Quiero reconocer el esfuerzo de los pacientes y sus familiares al permitir la investigación con sus muestras. Junto a ellos, gracias también a la Dra. Adela Cañete, Dra. Victoria Castel y Desirée Ramal, así como a todos los miembros de los servicios hospitalarios y a la Sociedad Española de Hematología y Oncología Pediátrica, que posibilitan que los estudios clínicos sigan adelante.

Quiero agradecer a los miembros del Servicio de Anatomía Patológica del Hospital Clínico de Valencia y, en especial, a Alejo Sempere, Cristina Monfort, María Ángeles Aucejo y Laura Martínez, su implicación en el procesado de las muestras recibidas. Asimismo, quiero mencionar a los miembros del Dpt. de Patología de la Facultat de Medicina de la Universitat de València, destacando a la Profesora Amparo Ruiz por haberme introducido en el análisis de imagen junto con Jose Benavent quien también quiero dar las gracias por su soporte técnico indispensable; así como al Profesor Robert Callaghan, por su soporte lingüístico.

Quiero dar las gracias a Prof. Yanuzs Wegrowsky y al Prof. Stéphane Brézillon por acogerme en Reims durante tres meses de mucho aprendizaje y enriquecimiento personal. También quiero hacer especial mención al Dr. Marcial García Rojo, cuya generosidad al abrirme las puertas de su laboratorio en el Servicio de Anatomía Patológica del Hospital General de Ciudad Real, durante casi cuatro meses ha sido clave para el desarrollo metodológico de esta tesis. También quiero destacar la implicación de la Prof^a. Gloria Bueno y Mila Fernández, del grupo VISILAB de la Escuela de Ingenieros de la Universidad de Castilla La Mancha; del Prof. Jose Vicente Manjón, Elies Fustery Jose Enrique Romero, del grupo ITACA de la Universidad Politécnica de Valencia; y de Luisma Escudero y Daniel Sanchez en el Instituto de Biomedicina de Sevilla (IBiS)/ Hospital Universitario Virgen del Rocío/CSIC/Universidad de Sevilla, que han colaborado en este trabajo. Finalmente, quiero agradecer el

soporte estadístico al Prof. Francisco Santonja y al Prof. Jose Bermudez, del Dpt. d'Estadística i Investigació Operativa de la Universitat de València.

Gracias a mis compañeros Ana Berbegall, Susana Martín, Maite Blanquer, Víctor Zúñiga y Elisa Alonso por hacer que cada día sea un gran día y por confiar en mí. No me olvido de Isidro Machado, de Eva Villamón y de Marta Piqueras, que me guiaron en los primeros momentos de mi travesía por el laboratorio y me enseñaron la dinámica de trabajo y de convivencia que tanto me gustaba. Gracias también a los alumnos que han pasado por nuestro laboratorio dejando su granito de arena: Jenny, Nuria, Andrea, Pablo, Silvia, etc...¡Qué tengáis un futuro lleno de felicidad!

Agradezco a mis directores de tesis las innumerables horas invertidas en mi formación y la perseverancia que han mostrado para que este trabajo saliera adelante. A Samuel: gracias por tu buen humor, tu paciencia y tu sabiduría. A Rosa: gracias por creer en mi y en este trabajo. Gracias también por tu inagotable energía.

Por último, pero no por ello menos importante, gracias a “mi gente”:

Gracias a mis amigos: Pilar, Elena, Aida, Marta y Diego por ser geniales durante todos estos años, y los que vendrán.

Gracias a Javi, por ser mi compañero de alegrías y de alguna que otra pena, por ser “le toi du moi”, mi mayor fan, mi fuente de energía y mi gran apoyo.

Gracias a mi familia: a mis tíos, primos, abuelos y, cómo no, ¡GRACIAS! a mi hermano y a mis padres. Gracias a vosotros me he convertido en quien soy hoy. Vosotros me habéis enseñado el valor del esfuerzo y a perseguir mis sueños, entre muchísimas otras cosas. Os doy las gracias por haber creído siempre en mí, por haberme ayudado en todo lo que habéis podido y por seguir ayudándome y guiándome aun ahora.

Trabajo financiado por: FAECC (369/2009), ISCIII & ERDF (RD06/0020/0102 y RD12/0036/0020), ISCIII (FIS PI10/00015 y FIS PI14/01008) y Conselleria d'Educació (ACOMP87/2012).

Summary

Neuroblastic tumor patients present an heterogeneous clinical evolution, from spontaneous regression to a high propensity for widespread metastatic dissemination. Although the application of a well-defined pre-treatment risk classification plays a central role in the improvement of survival during the last years, more efforts must be done to improve patient's survival in general and specifically in the subgroup of high risk patients. The morphological study of the tumoral tissue is contributing to such improvement. The histological category or the percentage of tumoral stroma, as well as the degree of differentiation of neuroblastic cells, evaluated by the pathologist with light microscopy, are factors that play a role in the diagnosis and prognosis of the patients. Given the role of tumoral extracellular matrix in biotensegrity and mechanotransduction, its architecture and the topology of its elements, as well as their interaction are being increasingly considered. Its quantification and characterization with microscopic image techniques start to be used.

We hypothesize that the destiny of a neuroblastic tumor cell is complex and, is in part directed by characteristics of a set of non-cellular extracellular matrix structural elements. Additionally, we think that the application of the patterns derived from the morphometric analysis of such elements and their association with the impact of the known prognostic factors, patient's survival will be improved. We aim to develop morphometric techniques to characterize different extracellular matrix scaffolding and vascular elements to find out potential uses as new prognostic markers for a better pre-treatment

stratification of the patients or as therapeutic targets to be able to remodel the aberrant elements of the tissue scaffolding, including microvascularization.

We constructed 19 tissue microarrays including more than 500 neuroblastomas which were stained with alcian blue pH 2.5, Gomori, Masson's trichrome, orcein and anti-CD31 for glycosaminoglycans, reticulin fibers, collagen type I fibers, elastic fibers and blood vessels, respectively. The slides were digitized with a whole-slide scanner and different image-analysis algorithms were designed or customized to specifically detect and characterize the amount, the size and the shape of the different extracellular matrix elements studied. These parameters were related to different neuroblastoma subgroups, taking into account several clinical, histopathological and genetic features.

The results obtained showed that reticulin fibers were the main components of the fibrous scaffolding and that microvasculature amount and architecture were relevant in the prognosis of neuroblastoma patients. A stiff and poorly porous extracellular matrix with irregularly-shaped vascular lumens was mainly detected in tumors belonging to patients with unfavorable prognosis. A subgroup of the high risk cohort with very poor survival could be defined by morphometric variables of reticulin fibers and blood vessels. Specifically, those samples with high stained areas occupied by reticulin fibers forming large, crosslinking, branching and disorganized networks and by blood vessels, as well as with irregularly-shaped capillaries and sinusoid-like vessels and dilated venules, presented a very unfavorable survival. In this cohort, cells with *MYCN* gene

amplification led to detectable topological changes regarding reticulin fibers and blood vessels.

We can conclude that it is possible and convenient to quantify the fundamental substance and characterize the architecture of the fibrous scaffolding and the vascular system of neuroblastic tumors by means of the morphometric analysis of microscopic images. Some of the morphometric features related to the different extracellular matrix elements studied could be used as a diagnostic support for the ultra-high risk group of patients, after studying a larger cohort. The obtained results suggest the need of developing multidisciplinary efforts for an international integration of these studies, and that the morphometric information of the elements of the extracellular matrix, including the vascular system, could be used for a therapy based on mechanotransduction.

Resumen

Los pacientes con tumores neuroblásticos presentan una evolución clínica heterogénea, desde la regresión espontánea hasta una alta propensión para la diseminación metastática generalizada. Aunque la aplicación de una clasificación de riesgo pre-tratamiento bien definida tiene un papel central en la mejora de la supervivencia durante los últimos años, han de llevarse a cabo más avances para mejorar la supervivencia de los pacientes en general y específicamente el subgrupo de pacientes de alto riesgo. El estudio morfológico del tejido tumoral está contribuyendo a dicha mejora. La categoría histológica o el porcentaje de estroma tumoral, así como el grado de diferenciación de las células neuroblásticas, determinadas por el patólogo con el microscopio óptico, son factores con un papel importante en el diagnóstico y el pronóstico de los pacientes. Actualmente, dada la relevancia de la matriz extracelular tumoral en la biotensegridad y la mecanotransducción, su arquitectura y la topología de sus elementos, así como su interacción están siendo cada vez más considerados. Su cuantificación y caracterización con técnicas de imagen microscópicas empiezan a ser utilizadas.

Nuestra hipótesis es que el destino de una célula tumoral neuroblástica es complejo y entre otros factores, está determinado por las características de un grupo de elementos estructurales no celulares de la matriz extracelular. Además pensamos que aplicando los patrones derivados del análisis morfométrico de estos elementos y asociándolos al impacto de los factores pronósticos conocidos, se mejorará la supervivencia de los pacientes. Nuestro objetivo es el desarrollo de

técnicas morfométricas para caracterizar distintos elementos del andamiaje de la matriz extracelular y de la vascularización con el fin de encontrar usos potenciales como nuevos marcadores con valor pronóstico para mejorar la estratificación de los pacientes, o como dianas terapéuticas para ser capaces de remodelar los elementos aberrantes del andamiaje tisular, incluyendo la microvascularización.

Hemos construido 19 micromatrices de tejido incluyendo más de 500 neuroblastomas, que fueron teñidos con azul alcian a pH 2,5, Gomori, tricómico de Masson, orceína y anti-CD31 para glicosaminoglicanos, fibras de reticulina, fibras de colágeno tipo I, fibras elásticas y vasos sanguíneos, respectivamente. Las laminillas fueron digitalizadas con un escáner de preparaciones y distintos algoritmos de análisis de imagen fueron diseñados o personalizados para detectar y caracterizar la cantidad, el tamaño y la forma de los distintos elementos estudiados de la matriz extracelular. Estos parámetros se relacionaron con los distintos subgrupos de neuroblastoma, teniendo en cuenta varias características clínicas, histopatológicas y genéticas.

Los resultados obtenidos mostraron que las fibras de reticulina eran los componentes mayoritarios del andamiaje fibroso y que la abundancia y arquitectura de la microvascularización era relevante para el pronóstico de los niños con neuroblastoma. Una matriz extracelular rígida y poco porosa con vasos sanguíneos con luces irregulares se detectó principalmente en tumores pertenecientes a pacientes con pronóstico desfavorable. Un subgrupo de la cohorte de alto riesgo con muy mala supervivencia pudo ser definido por variables morfométricas de las fibras de reticulina y de los vasos sanguíneos.

Concretamente, las muestras con un mayores áreas ocupadas tanto por fibras de reticulina formando grandes redes entrecruzadas, ramificadas y de organización compleja, como por vasos sanguíneos, junto con capilares y vasos tipo sinusoide de forma irregular y vénulas y arteriolas dilatadas, estaban asociadas a un pronóstico muy desfavorable. En esta cohorte, las células con amplificación del gen *MYCN* conllevaron cambios topológicos detectables en relación a las fibras de reticulina y los vasos sanguíneos.

Podemos concluir que es posible y conveniente cuantificar la sustancia fundamental, caracterizar el andamiaje fibroso y el sistema vascular de los tumores neuroblásticos gracias al análisis morfométrico de imágenes microscópicas. Algunas de las características morfométricas relacionadas con los distintos elementos de la matriz extracelular estudiados podrían ser usadas como ayuda diagnóstica del grupo de pacientes con riesgo ultra alto, tras estudiar una mayor cohorte. Los resultados obtenidos sugieren la necesidad de realizar trabajos multidisciplinarios para integrar de estos estudios a nivel internacional y que la información morfométrica de los elementos de la matriz extracelular, incluyendo el sistema vascular, pueda ser utilizada para una terapia basada en la mecanotransducción.

Abbreviations

?: Percentage

CS: Chondroitin sulfate

D: Deletion

d: differentiating

DS: Dermatan sulfate

ECM: Extracellular matrix

EFS: Event-free survival

FISH: Fluorescent *in situ* hybridization

G: Gain

GAGs: Glycosaminoglycans

GN: Ganglioneuroma

HA: Hyaluronan (hyaluronic acid)

HC: Histochemistry

HE: Hematoxylin –eosin

Hep: Heparin

Het: Heterogeneous

Hom: Homogeneous

HR: Hazard ratio

HS: Heparan sulfate

HSV: Hue, Saturation, Value

iGNB: Intermixed ganglioneuroblastoma

IHC: Immunohistochemistry

INPC: International Neuroblastoma Pathology Classification

INRG: International Neuroblastoma Risk Group

INRGSS: International Neuroblastoma Risk Group Staging System

IOD: Integrated optic density

KS: Keratan sulfate

LINES: Low and Intermediate Risk Neuroblastoma European Study

microRNA: miRNA

MLPA: Multiplex-ligand probe amplification

MNA: *MYCN* amplification

MNNA: *MYCN* non-amplified

n (GNB): nodular (ganglioneuroblastoma)

n: number

NB: Neuroblastoma

NCA: Numerical chromosome aberration

ncRNAs: non-coding RNA

ND: Non-deleted

NG: Non-gained

OS: Overall survival

pd: poorly differentiated

R, G, B: Red, Green, Blue

ROC: Receiver Operating Characteristic

SCA: Segmental chromosome aberration

SEHOP: Spanish Society of Pediatric Hematology and Oncology

SIOPEN: Society of Paediatric Oncology European Neuroblastoma
Network

SNP: Single nucleotide polymorphism

tEFS: Time of event-free survival

TMA: Tissue microarray

tOS: Time of overall survival

u: undifferentiated

Index

I. INTRODUCTION	1
1. General background of neuroblastoma	1
2. International neuroblastoma pre-treatment risk stratification.....	4
2.1. Clinical data	4
2.1.1. Stage.....	4
2.1.2. Age.....	4
2.2. Histological data	5
2.3. Genetic data	5
2.3.1. <i>MYCN</i>	5
2.3.2. 11q.....	6
2.3.3. Ploidy.....	6
3. Other genetic markers in neuroblastoma	6
4. Tumoral scaffolding.....	10
4.1. Glycosaminoglycans (GAGs)	15
4.2. Fibrous component	18
4.3. Vascular component.....	21
5. Role of computerized image analysis.....	23
II. HYPOTHESIS AND OBJECTIVES/ HIPÓTESIS Y OBJETIVOS	27
III. MATERIALS AND METHODS	33
1. Materials	35
1.1. Samples	35
1.2. Data relating to patients/samples.....	38
1.2.1. Clinical data	38
1.2.2. Histopathological data	40
1.2.3. Genetic data	41
1.2.4. Risk group.....	50
2. Methodology	51
2.1. Construction of tissue microarrays (TMAs).....	51
2.2. Cutting and staining of the sections.....	53
2.2.1. Staining of the fundamental substance: GAGs	54
2.2.2. Staining of the fibrous component	56
2.2.3. Staining of the vascular component	61
2.3. Digitization of the sections.....	62
2.4. Subjective assessment of the presence of ECM elements and histological observation	65
2.5. Design of algorithms and measurement procedures.....	66
2.5.1. Previous considerations	66

2.5.2. Algorithm for the fundamental substance: glycosaminoglycans.....	71
2.5.3. Algorithm for the fibrous component.....	74
2.5.4. Algorithm and measurement procedure for the vascular component.....	89
2.6. Statistical analysis.....	99
2.6.1. Validation of the morphometric technique.	100
2.6.2. Validation of the clinical and biological data.	101
2.6.3. Relationship between the quantity and the distribution of the ECM elements studied and the clinico-biological features of the tumors.	102
2.6.4. Survival analysis:.....	103
2.6.4. Study of ECM elements after treatment and in other samples	104
2.7. Topological integration of reticulin fibers and blood vessels regarding neuroblastic cells	105
IV. RESULTS.....	109
1. Morphometric measurements.....	111
2. Clinical and biological data.....	116
2.1 Description of the clinical, genetic and survival variables.	116
2.2. Univariate survival analysis	119
2.2.1. Clinical variables	120
2.2.2. Histopathology	122
2.2.3. Genetic variables.....	123
2.3. Multivariate survival analysis	127
3. Study of the GAGs.	128
3.1. Histological observation	128
3.2. Description of the variables.....	131
3.3. Favorable and unfavorable GAGs histological patterns ..	133
3.4. Survival analysis.....	136
3.4.1. Multivariate analysis	136
3.4.2. Study of the high risk group	136
3.5. GAGs after treatment and in other samples	136
4. Study of the fibrous component	138
4.1. Reticulin fibers.....	138
4.1.1. Histological observation.....	138
4.1.2. Description of the morphometric variables	142
4.1.3. Description of the spatial distribution	143
4.1.4. Favorable and unfavorable reticulin fibers histological patterns.....	146
4.1.5. Survival analysis.....	153

4.1.6. Reticulin fibers after treatment and in other samples	158
4.2. Collagen fibers	161
4.2.1. Histological observation	161
4.2.2. Description of the variables	164
4.2.3. Favorable and unfavorable collagen type I histological patterns	166
4.2.4. Survival analysis	168
4.1.5. Collagen type I fibers after treatment and in other samples	169
4.3. Elastic fibers	171
5. Study of the blood vessels	173
5.1. Generalities of vascularization	173
5.2. Histological observation	174
5.3. Total blood vascularization	179
5.3.1. Description of the variables	179
5.3.2. Favorable and unfavorable blood vessel histological patterns	181
5.3.3. Survival analysis	186
5.3.4. Blood vessels after treatment and in other samples	189
5.4. Capillaries (5-15 μ m)	191
5.4.1. Description of the variables	191
5.4.2. Favorable and unfavorable capillaries histological patterns	192
5.4.3. Survival analysis	198
5.5. Post-capillary venules and metarterioles (15-20 μ m)	200
5.5.1. Description of the variables	200
5.5.2. Favorable and unfavorable post-capillaries venules and metarterioles histological patterns	201
5.5.3. Survival analysis	206
5.6. Sinusoid-like blood vessels (20-50 μ m)	208
5.6.1. Description of the variables	208
5.6.2. Favorable and unfavorable sinusoid-like blood vessels histological patterns	209
5.6.3. Survival analysis	215
5.7. Venules and arterioles (50-200 μ m)	217
5.7.1. Description of the variables	217
5.7.2. Favorable and unfavorable venules and arterioles histological patterns	218
5.7.3. Survival analysis	222
5.8. Veins and arteries (>200 μ m)	227

5.8.1. Description of the variables	227
5.8.2. Favorable and unfavorable veins and arteries histological patterns.....	229
5.8.3. Survival analysis.....	233
6. Topological integration of reticulin fibers and blood vessels regarding neuroblastic cells	235
V. DISCUSSION	239
1. Morphometric techniques	241
2. Our clinical and biological data (INRG).....	245
3. ECM elements patterns, potential use as prognostic markers and treatment strategies.....	246
3.1. GAGs	246
3.2. Fibrous scaffolding.....	250
3.3. Blood vascularization.....	257
3.4. Topological, genetic and clinical integration.....	266
V. CONCLUSIONS/ CONCLUSIONES	269
VI. REFERENCES	278
VII. APPENDIX	301
VIII. COMUNICACIONES TO CONGRESSES AND PUBLICATIONS	308

I. INTRODUCTION

1. General background of neuroblastoma

Neuroblastoma (NB) is an extremely heterogeneous pediatric tumor accounting for 15% of the childhood deaths from cancer, although its survival has dramatically improved in the last years. NB can undergo spontaneous regression or maturation without cytotoxic therapy or, on the contrary, can have a high propensity for locally invasive growth and widespread metastatic dissemination despite aggressive treatment (1). It is the most common solid extra-cranial tumor in children and includes a very heterogeneous group of entities characterized by well-defined and delimited genetic, histopathological and clinical features (2).

Neuroblastoma is a disease of the sympathoadrenal lineage of the neural crest, and therefore tumors can develop anywhere in the sympathetic nervous system. Most primary tumors (65%) occur within the abdomen, with at least half of these arising in the adrenal medulla. Other common sites of disease include the neck, chest, and pelvis (3). The symptoms are usually diffuse and depend largely on the location of the primary tumor, as well as on the presence and location of metastatic disease. Patients with a local disease may suffer severe abdominal pain or may be free of local symptoms, in which case the tumor is incidentally discovered. Two major paraneoplastic syndromes (secretion of vasoactive intestinal peptide and opsoclonus-myoclonus) are more commonly seen in patients with localized tumors, suggesting that the syndrome itself might modify the malignant potential of the tumor (3). In contrast, patients with metastatic neuroblastoma typically present unspecific symptoms such as fever, pallor and anorexia. Metastatic site specific symptoms, such as bone pain, limping and

sometimes marrow failure, related to bone or bone marrow metastases are also common.

The median age at diagnosis for neuroblastoma patients is around 18 months. Approximately 40% of the patients are diagnosed by 1 year of age, 75% by 4 years of age and 98% by 10 years of age (4). In Spain, a mean of 71 children between 0 and 14 years of age have been diagnosed with neuroblastoma every year, during the years 1990 to 2009, accounting for 10% of the childhood malignancies, after leukemias (27%), tumors of the central nervous system (20%) and lymphomas (13%) (5). In the cohort of Spanish patients between 0-14 years, from 1983 to 2002, neuroblastoma has a rate of 11 cases per million (6).

The diagnosis of neuroblastoma is based on the presence of characteristic histopathological features of the tumor tissue or the presence of tumor cells in a bone marrow aspirate or biopsy, accompanied by raised concentrations of urinary catecholamines. High risk patients often have raised concentrations of serum lactate dehydrogenase, ferritin, or chromogranin, but these are relatively non-specific for the population as a whole and do not seem to be independently prognostic of outcome in the light of modern biological covariates. Enhanced sensitivity and specificity for detecting bone metastases as well as occult soft tissue disease is provided by metaiodobenzylguanidine scintigraphy (3).

Following the new staging system published by the International Neuroblastoma Risk Group (INRG) classification in 2009 (2), neuroblastoma patients are clinically classified in different groups

depending on their risk of relapse or event-free survival (EFS), based on clinical features, complex combinations of genetic aberrations, histopathology and DNA index (**figure 1**).

INRG Stage	Age (months)	Histologic Category	Grade of Tumor Differentiation	MYCN	11q Aberration	Ploidy	Pretreatment Risk Group
L1/L2		GN maturing; GNB intermixed					A Very low
L1		Any, except GN maturing or GNB intermixed		NA			B Very low
				Amp			K High
L2	< 18	Any, except GN maturing or GNB intermixed		NA	No		D Low
					Yes		G Intermediate
	≥ 18	GNB nodular; neuroblastoma	Differentiating	NA	No		E Low
					Yes		H Intermediate
			Poorly differentiated or undifferentiated	NA			
				Amp			N High
M	< 18			NA		Hyperdiploid	F Low
	< 12			NA		Diploid	I Intermediate
	12 to < 18			NA		Diploid	J Intermediate
	< 18			Amp			O High
	≥ 18						P High
MS	< 18			NA	No		C Very low
					Yes		Q High
					Amp		R High

Figure 1: INRG consensus pre-treatment classification schema. L: Localized tumor, M: metastatic, Ms: special metastatic, GN: ganglioneuroma, GNB: ganglioneuroblastoma, NA: Not amplified, Amp: Amplified. Very low risk: 5-year EFS >85%; Low risk: 5-year EFS >75% to ≤85%; Intermediate risk: 5-year EFS ≥50 to ≤75%; High risk: 5-year EFS <50%. EFS: Event-free survival. Reproduced from “The international Neuroblastoma Risk Group (INRG) classification system: an INRG Task Force report”, Cohn et al, J Clin Oncol 2009, 27(2):289-97(2).

Therapeutic approaches depend on the pre-treatment risk group and include surgery, chemotherapy, radiotherapy, and biotherapy, as well as observation alone in carefully selected circumstances (3). Currently, two European clinical trials attempt to enhance the treatment on patients with localized disease (Low and Intermediate Risk Neuroblastoma European Study, LINES 2009), as well as in patients with metastatic disease (High risk Neuroblastoma Study 1, 2012).

2. International neuroblastoma pre-treatment risk stratification

2.1. Clinical data

2.1.1. Stage

The new staging system includes two stages of localized disease, L1 and L2, which are dependent on up to 20 image-defined risk factors; and two stages of disseminated disease, M and Ms (2). These stages correlate to the former International Neuroblastoma Staging System (INSS) in such a way that previous stage 1 becomes now L1, stages 2 and 3 become L2, stage 4 becomes M and stage 4S becomes Ms (7, 8). L1 corresponds to localized tumors not involving vital structures, L2 are locoregional tumors with presence of one or more image-defined risk factors, M correspond to distant metastatic disease (except stage Ms) and Ms is defined as metastatic disease in children younger than 18 months with metastases confined to skin, liver and/or bone marrow (7).

2.1.2. Age

Age is a strong prognostic factor, independent of the validated staging system in use, given that outcome gradually worsens with increasing age. Previous findings indicate that the age cut-off should be set somewhere between 15 and 19 months and it has been established that 18 months of age is the optimal cut-off point (9), except for patients with diploid, stage M, *MYCN* non-amplified tumors, where the cut-off has been established at 12 months of age (10).

2.2. Histological data

Based upon previous classifications, the pathologists currently use the International Neuroblastoma Pathology Classification (INPC), a modification of the original Shimada's System (11-13). The INPC classifies four histological types: Neuroblastoma (NB) (Schwannian stroma-poor), intermixed Ganglioneuroblastoma (iGNB) (Schwannian stroma-rich), nodular Ganglioneuroblastoma (nGNB) (composite Schwannian stroma-rich/stroma-dominant and stroma-poor) and Ganglioneuroma (GN) (Schwannian stroma-dominant). There are three grades of neuroblastic differentiation: undifferentiated (u), poorly differentiated (pd) and differentiating (d). In localized stages, the INRG classification defines three prognosis-related categories: GN and iGNB with excellent prognosis regardless of the age, nGNB and dNB, and pd/uGNB and pd/uNB defining low/intermediate and intermediate/high pre-treatment risk groups, respectively, depending on the patient's age and the status of *MYCN* and 11q (13).

2.3. Genetic data

2.3.1. *MYCN*

MYCN amplification (MNA) (2p24) occurs in 20-25% of primary cases of NB and is strongly associated with unfavorable advanced stage disease, aggressive behavior and high risk of relapses (4). It was the first genetic marker included in risk stratification systems and patients with a MNA tumor are considered as high risk patients in all existing risk stratification systems. The use of fluorescent *in situ* hybridization

(FISH) is mandatory for the proper detection of *MYCN* status in European studies.

2.3.2. 11q

Rearrangements in chromosome 11q occur in approximately 20-30% of primary NB and are associated with poor outcome (13). 11q deletion (11qD) is also inversely related to MNA, indicating that these abnormalities represent distinct genetic subtypes of advanced stage NB (14-16). It has been related with decreased progression-free survival (16), although some exceptions have been described (17).

2.3.3. Ploidy

In children younger than 12-18 months of age with disseminated disease and normal *MYCN* copy number, DNA index has been found to have prognostic value (18-21). Tumors with a near diploid/tetraploid DNA content present a defect in genomic stability resulting in unbalanced chromosomal rearrangements which contribute to their unfavorable behavior (4).

3. Other genetic markers in neuroblastoma

Although prognosis has experienced a substantial improvement during the past years, there are still high risk subgroups doomed to therapeutic failure despite aggressive treatments. This calls for a need to investigate new therapeutic targets or elements that may improve the pre-treatment risk stratification.

Among these new elements, the INRG classification has recently considered that molecular data such as the presence or

absence of diverse segmental chromosomal aberrations (SCA) and other clinico-biological parameters enables the risk-based classification of the majority of these tumors (13).

Deletions of the short arm of chromosome 1 are identified in about 25-30% of the cases. They correlate with MNA and predict an increased risk of relapse in patients with localized tumors (3, 22). Most of the deletions involve the 1p36 region (22) where one or more suppressor genes have been described (23-25). 17q is often translocated to various chromosomal partners resulting in unbalanced translocations and 17q gain. 17q gain is associated with high risk disease features, such as advanced disease stage and age at diagnosis, MNA, 1p deletion, diploid or tetraploid chromosomal content and is an independent genetic parameter for outcome (26, 27).

Regarding specific genes, *ALK* gene, at 2p23.2, has been demonstrated to be constitutively activated by gene mutations, copy number variations and/or amplifications in familial and sporadic neuroblastomas (28, 29) and *PHOX2B* mutations are thought to predispose to neuroblastoma by increasing proliferation and promoting dedifferentiation of cells in the sympathoadrenal lineage (30). *ALK* and *PHOX2B* genetic alterations, as well as their overexpression have been related to poor prognosis of the disease (31, 32). These genes are therefore attractive targets for novel therapeutic strategies (31).

A segmental genomic profile, rather than the single genetic markers, adds prognostic information to the clinical variables age and stage in neuroblastoma patients without MNA, underlining the importance of pangenomic studies (10, 33-35). Pangenomic techniques

are acquiring a central diagnostic role at present, as the presence of one or more segmental chromosome aberrations has been related with tumor aggressiveness (33, 36, 37). Based on these observations, multilocus and pangenomic or array-based genetic profile with typical segmental chromosomal aberrations (deletion of 1p, 3p, 4p, 11q; and gain of 1q, 2p and 17) are taken into consideration in low risk patient therapy (37, 38). In the recently-opened Society of Paediatric Oncology European Neuroblastoma Network (SIOPEN) LINES study (European Low- and Intermediate-Risk Neuroblastoma) the genomic profile is taken into account for therapeutic stratification in such a way that it has been confirmed that SCA lead to a higher risk of relapse even in infants without MNA localised unresectable/disseminated neuroblastoma (39). More studies are necessary to determine the prognostic impact of the unusual group of tumors with no chromosome alterations (silent profile) (16, 37, 39) and other phenomena such as chromothripsis (40) or loss of heterozygosity (41).

Genetic association studies provide near-unbiased screens of common and rare variants with complex traits and highlight distinct loci in sets of genes among which to search for likely causal candidates. Complex trait-based exome chip analyses and exome sequencing studies highlight coding mutations within specific genes, but generally lack statistical power to establish significant associations. Therefore, association studies and rare variant analyses typically rely on downstream bioinformatics analysis to further reduce their shortlisted candidate genes to numbers that allow in depth experimental follow-up studies. Analyses of genetic variation data have been augmented by integration with complementary data sets, among others differential or

tissue-specific gene expression data, protein-protein interaction data or existing literature-based knowledge (42-47).

The majority of the genome is transcribed as non-coding RNA (ncRNAs), which directly control gene expression and influence the initiation and progression of several cancers. They can function as oncogenes or tumor suppressor genes. The expression patterns of a small-ncRNA family of miRNA (microRNA), define novel methods for stratification of neuroblastoma (48) and individual miRNAs have been linked to some known risk factors in neuroblastoma such as *MYCN*, 1p36 and 11q loss (49-53). Recently, a new prognostic 25-miRNA signature has been established, validated and tested in more than 500 neuroblastomas. This gene signature discriminates patients with respect to EFS and overall survival (OS), and has been shown to be an independent predictor of patient survival (54).

The aberrant demethylation or methylation of gene promoter regions is responsible for the deregulated expression of oncogenes or for the inactivation of tumor suppressor genes. Neuroblastoma can be clustered based on the methylation pattern of 10 genes, allowing the identification of several clinically-relevant groups of tumors (55). Global methylation studies have demonstrated that a methylator phenotype, characterized by the methylation of multiple regions, is a hallmark of neuroblastoma with poor prognosis (56). Several tumor suppressor genes have been shown to be silenced by aberrant hypermethylation of their promoters in neuroblastoma (55, 57-59) and the study of these genes has the potential to become a prognostic outcome predictor because it is associated with several clinical risk factors such as MNA, age at diagnosis and stage (60).

4. Tumoral scaffolding

Many processes relevant to neuroblastoma, such as stem cell differentiation, neuronal maturation, neurite extension, *MYCN* expression and the malignant potential and phenotype of tumor cells have all been shown to be influenced by extracellular matrix (ECM) stiffness (61). It has been demonstrated that cross-talks between Schwannian stroma and neuroblasts triggers tumor differentiation and inhibits angiogenesis (62). Other studies have demonstrated that neuroblastoma cells in culture respond to a 3D environment in a different manner from that found in a 2D environment. These studies suggest that the regulation of gene expression and morphology in neuroblastoma cultures is complex and depends on the geometry of the matrix as well as on its composition, structure, and mechanical properties (63).

In the general context of cancer, within the tumor ECM, a variety of support cells (fibroblasts, Schwann cells), tumor-associated immune cells and vascular (blood and lymph) endothelial cells are found, lying among a network of various reticulin, collagen and elastic fibers merged within the interstitial fluid (glycosaminoglycans, proteoglycans and glycoproteins) and gradients of several chemical species, which constantly interplay with cells and provide much of the structural support available to parenchymal cells in tissues, providing tensile strength and flexibility (64, 65).

Cells are linked to each other and to the ECM forming a mechanical biotensegral system which triggers a mechanical balance between compression and tension forces (ECM and cells forces,

respectively). Tensegrity is an architectural principle put forth by Buckminster Fuller in the 1960s (66, 67). According to the tensegrity principle, structures or tensegrity systems are stabilized by continuous tension with discontinuous compression (68). The principle of tensegrity applies at essentially every detectable size scale in the body, under the term of biotensegrity, from the musculoskeletal system to proteins or DNA (69, 70). As a tensegrity network, a single cell requires continuous tension (mediated by cytoskeleton elements as microfilaments and intermediate filaments) and local discontinuous compression (mediated by ECM and other cytoskeleton elements as microtubules). Several studies have demonstrated that cells can function as independent prestressed tensegrity structures through their cytoskeleton architecture (71-79). The individual prestressed cells are poised and ready to receive mechanical signals and convert them into biochemical changes (80).

ECM can be considered as a dynamic and multifunctional regulator which has its own biotensegrity system with reticulin and elastin fibers acting as tensional elements and fundamental substance and collagen fibers as resistant compressive elements. This tensegral network is considered to be a solid state regulatory system of all cell functions and is responsible for changes in cell shape and movement and for genetic and protein changes (64, 81, 82). As a result of the cell-ECM biotensegrity, substrate rigidity can therefore control nuclear function and hence cell function (83). Cells can use such substrate rigidity to exert traction forces on ECM and thus, cause its alteration. Indeed, in a state of reciprocal isometric mechanical tension, a dynamic mechanical balance exists between cell traction forces and resistance

points of the ECM. This dynamic biotensegral system enables our cells to mechanosense and to modify their microenvironment, thus promoting ECM remodeling in homeostasis and in tissue disorders. The manipulation of this mechanical balance could promote tissue regeneration. In fact, different elasticities of the ECM drive mesenchymal stem cell differentiation in a very specific way. Neurogenic, myogenic or osteogenic differentiations are induced in identical conditions of matrix serum and with variation of ECM softness, strength and stiffness, respectively (84). Furthermore, ECM stiffness guides cell migration. Fibroblasts prefer rigid substrates and when placed on flexible sheets of polyacrylamide, they migrate from the soft area to the stiff area (85).

Cancer can be understood as a disease of the developmental processes that govern how cells organize into tissues (86). Numerous studies have demonstrated that the tumor ECM not only responds to and supports carcinogenesis, but actively contributes to tumor initiation, progression and metastasis, and must not only be understood as a reactive neighboring, but also as an active contributor (87). In fact, it has been published that chronic growth stimulation, ECM remodeling, alteration of cell mechanics and disruption of tissue architecture are a non-genetic basis influencing cancer progression (88, 89). Given the complexity both within and outside the cancer cell, and the interactions between cancer cells and the surrounding stroma, it is not surprising that a single perturbation within a tumor can create a cascade of changes in multiple pathways and networks, some of which may have lethal repercussions (90).

Tumor malignancy is driven, among other factors, by the remodeling of contiguous stromal tissue to foster growth, metastasis and therapy resistance. Tumor cells alter the mechanical properties of the microenvironment to create favorable conditions for their proliferation and/or dissemination (91). They promote stiffening of their environment, which feeds back to increase malignant behaviors such as loss of tissue architecture and invasion (92). Matrix remodeling by tumor-associated stromal cells entails the assembly of a highly dense ECM, whose physicochemical attributes enhance malignancy through morphogenic deregulation, tumor cell proliferation, vascular recruitment, and stromal cell differentiation (93-95). Both tumor and stromal cells produce and assemble a matrix of collagens, proteoglycans, and other molecules such as cytokines that hinder the transport of macromolecules and stimulate the otherwise quiescent host cells to initiate a variety of processes, including desmoplasia and angiogenesis (96, 97). Mediated by increased deposition, unfolding and crosslinking of fibrillar adhesion proteins, stiffening increases cell contractility which, in turn, can directly and indirectly alter gene expression via altering transcription factor activity and the release of matrix-bound pro-tumorigenic growth factors (98-101). Similarly, changes in the microstructure, elasticity, distribution of pore sizes, chemical composition and fiber arrangement due to ECM remodeling can control aspects of tumor cell phenotype such as adhesion, mechanics and motility (102-106). The speed of malignant cells *in vitro* is also affected by the geometry of the ECM. Human glioma cells move faster through narrow channels than through wide channels or in non-stretched 2D surfaces. This is thought to be triggered by an increase in the polarity of the traction forces between cell and ECM (107). Recent

publications describe that not only neoplastic ECM stiffness, but also the firmness of tumor cells play a significant role in tumor progression. Steadiness of tumor cells, specially the metastatic cells, is lower than that of the normal cells of the same sample, and is currently caused by the loss of actin filaments and/or microtubules and the subsequent lower density of the scaffold (108, 109).

Furthermore, an elevated ECM stiffness progressively increases interstitial fluid pressure which thereafter interferes with effective spread of anti-cancer therapeutics within the solid tumor (11-13). The deregulation and disorganization of the tumor stroma alter the composition, structure, and stiffness of the ECM elements, leading to limited penetration and dissemination of therapeutic agents within solid tumors and enable the creation of niches within tissues and organs that offer sanctuary to tumors and activate therapy resistance programs (110, 111). Huge evidence has been provided that cancer therapeutic agents (chemotherapy and radiotherapy), which usually lack of total specificity, trigger collateral damage of tumor ECM mechanical properties and benign stromal cells, which were previously fighting the tumor, in such a way that cancer therapy resistance arises and relapse and metastasis are favored. This fact becomes evident while analyzing post-treatment biopsies that account for a high degree of fibrosis and calcification. Cancer therapeutics triggers DNA damage of tumor and stromal cells which results in the secretion of a spectrum of proteins, including the Wnt family members. The expression of Wnt by the prostate tumor microenvironment lymphocyte B cells attenuates the effects of cytotoxic chemotherapy *in vivo*, promoting tumor cell survival and disease progression (112, 113). Doxorubicin-

based chemotherapy of human breast carcinomas triggers overexpression of maspin which induces the accumulation of collagen fibers, thus causing disease progression (114). A novel Toll receptor-9-dependent mechanism that initiates tumor regrowth after local radiotherapy has also been reported (115).

4.1. Glycosaminoglycans (GAGs)

Since glycosaminoglycans (GAGs) have been recognized as essential players in critical biological processes regulating cellular properties, owing to their particular biofiltering, scaffolding and cell anchoring properties, they have been related to diverse malignancies and they are now understood as key players in cancer cell biology and novel therapeutical agents (116, 117).

GAGs are long, non-branched polymers of several disaccharides (up to 200 repeated saccharides), consisting of one uronic acid (almost always glucuronic acid and sometimes iduronic acid) and one hexosamine (glucosamine or galactosamine), presenting variable degrees of sulfation, and constitute the main components of the fundamental substance of the ECM (64). According to their chemical composition, GAGs can be divided in acid and sulfated: chondroitin sulfate (CS), dermatan sulfate (DS) and heparan sulfate or heparin (HS, Hep); acid and non-sulfated: hyaluronan (HA); and non-acid and sulfated: keratan sulfate (KS). GAGs can form proteoglycans by means of a linkage tetrasaccharyde, linking GAGs to a central protein (core protein) through a serine residue and catalyzed by four specific enzymes (**figure 2 A**). The formation of the linkage tetrasaccharyde is key for GAG synthesis to start in *GAGosomes* (118-120). Proteoglycans

can be located at the cell surface (syndecan, glypican), in the intracellular compartment (serglycin), secreted to the extracellular medium (small leucine-rich proteoglycans, hyalectans) or within the basement membrane (agrin, collagen XVIII, perlecan) (**figure 2 B**) (121, 122).

Diagnostic methods have typically centered on the analysis of GAG structure and concentration. HA has the capacity to bind large amounts of water to form viscous gels with special filtering properties and it is capable of forming polyvalent connections with other ECM proteins. This GAG, as well as the rest, has the capacity of modulating host-tumor interaction, lymphangiogenesis, angiogenesis and multidrug resistance. It can therefore be used as a drug carrier (123). HA accumulates in the stroma of various human tumors and modulates intracellular signaling pathways, cell proliferation, motility and invasive properties of malignant cells: a high stromal HA content is associated with poorly differentiated tumors and aggressive clinical behavior in human adenocarcinomas. On the contrary, squamous cell carcinomas and malignant melanomas tend to have a reduced HA content (123). When tumors produce HA, this fact is associated with invasion, host-tumor interactions, lymphangiogenesis/angiogenesis, epithelial-mesenchymal transition and with local and distant metastases in glioma, pancreatic adenocarcinoma, breast cancer and prostate cancer, respectively (123). Other studies have found a link between poor prognosis in prostate cancer and under-sulfation or overexpression of CS. Aggressive breast cancer tissue shows an increase of approximately 15% on GAG content with longer chains compared to non-lethal breast cancer tissue (124). The role of hyaluronan and its receptor CD44 has

been studied *in vitro* with different neuroblastoma cell lines. It has been demonstrated that CD44 and hyaluronan promote invasive growth into the brain, and that *MYCN* amplification down-regulates the expression of CD44, thus enhancing tumorigenic properties of neuroblastic cells (119, 125).

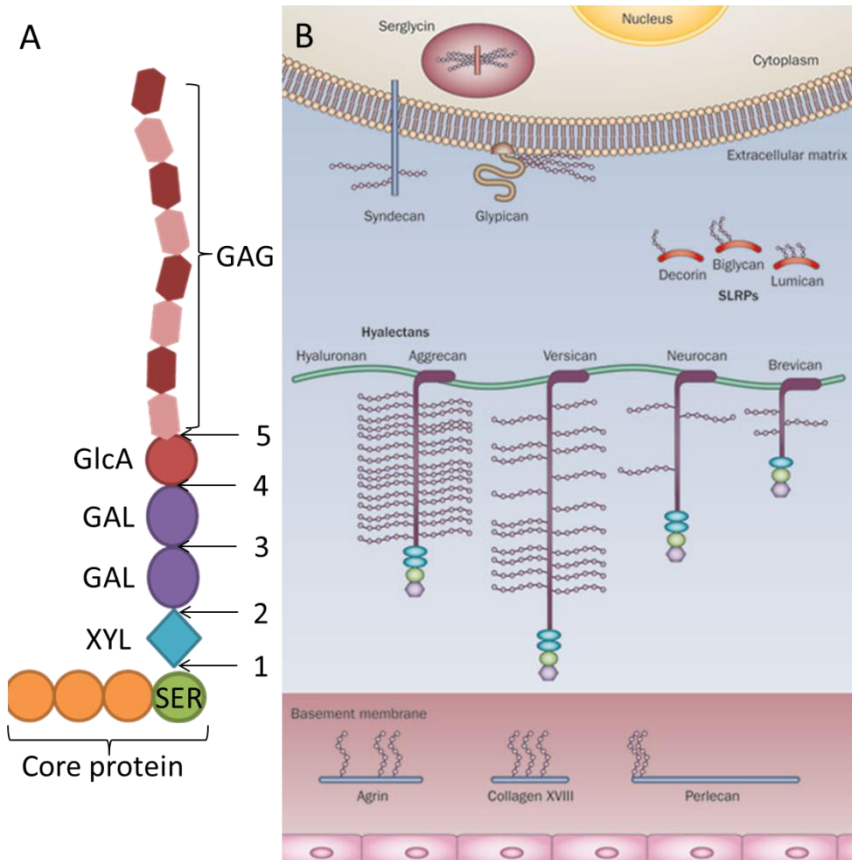


Figure 2: A) synthesis of GAGs after linkage of a linkage tetrasaccharide to a serine protein of a core protein, to form a proteoglycan. SER: serine, XYL: xylose; GAL: galactose; GlcA: Glucuronic acid. 1-5: enzymes for the synthesis of the linkage tetrasaccharide. 1: Xylosyltransferase, 2: β -4 galactosyltransferase, 3: β -3 galactosyltransferase, 4: β -3 glucuronosyltransferase, 5: N-acetylglucosaminyltransferase. **B)** Different proteoglycans depending on their location in the tissue. SLRPs: small-leucine-rich proteoglycans. B has been reproduced from “proteoglycans in prostate cancer”, Iris J. Edwards, Nature Reviews urology 9, 196-206, 2012 (122).

4.2. Fibrous component

The architectural role of the fibrous component of the ECM is clear and central for tissue homeostasis. In fact, scaffold architecture has been found to have a significant impact on cell growth (126).

Fibrous components of the extracellular matrix are classified in three groups, according to light microscopy findings (shape, staining properties and arrangement) and chemical properties: collagen, reticular and elastic fibers (127).

- Reticulin and collagen type I fibers

The primary proteins present in the ECM are the collagens. They are secreted by connective tissue cells, as well as by a variety of other cell types. As a major component of skin and bone, they are the most abundant proteins in mammals, constituting 25% of the total protein mass in these animals. A typical collagen molecule is extremely rich in proline and glycine, long, stiff and has a triple-stranded helical structure, in which three collagen polypeptide chains, called *α chains*, are wound around one another in a ropelike superhelix (128). Reticulin fibers, or type III collagen, are fine fibers forming an extensive branching network in certain organs. Their distribution is rather restricted: they are usually found mainly in the basement of epithelial tissues, the surface of adipose cells, muscle cells and Schwann cells, outside the endothelium of the hepatic sinusoids, and in the fibrous reticulum of lymphoid tissues. These fibers have a diameter of less than 2μm and support not only the physical structure of the cell but also various biological functions, largely through their ability to bind multiple interacting partners such as other ECM proteins, growth

factors, signal receptors and adhesion molecules (65, 127). Collagen type I fibers account for 90% of the body collagen and usually form thick bundles in bone, skin, tendons, ligaments, cornea and internal organs. These collagen strands can measure up to 100 μ m thick and usually follow a wavy course without branching in tissues.

It has been found that an aligned fiber matrix enhances differentiation of human neural crest stem cells towards the Schwann cell lineage (129) and evidence has pointed to collagen crosslinking as a significant contributor to the changes in cellular mechanical microenvironment that accompanies tumor progression (130).

Reticulin fibers are considered to play an important role in the adherence of cells and to constitute a skeletal framework suitable for individual cells and tissues (131). They are known to increase in amount and disorganize with aging and stress in physiological conditions (132). Desmoplasia (collagen type I and reticulin fibers accumulation) is associated with several malignancies. The deregulation and disorganization of the tumor stroma alter the composition, structure, and stiffness of the ECM, leading to the creation of niches within tissues and organs that offer a proper environment for tumors to successfully establish metastasis and activate therapy resistance programs (110, 111, 133). In primary breast tumors, collagen type I density is associated with breast cancer metastasis and may serve as an imaging biomarker of metastasis. The expression of COL11A1 gene continuously increases during ovarian cancer disease progression, with the highest expression in recurrent metastases. Knockdown of COL11A1 decreases in vitro cell migration and invasion and tumor progression in mice (134). The tumor-stromal interface of breast

primary tumors in 3D culture was studied with second harmonic generation, showing that randomly organized matrix realigned the collagen fibers allowing individual cells to migrate out along radially aligned fibers (135). The architecture of the collagen scaffolds in tumors is severely altered (100, 133).

- Elastic fibers

As basic structural elements, elastic fibers aberrations trigger severe pathologies such as Marfan's syndrome, emphysema, hypertension, actinic elastosis, and aortic aneurysms (136). Nevertheless, little evidence has been reported about its role in neoplastic processes.

Elastic fibers are generally twisted or straight strands of 0,2-1,5 μ m which sometimes branch to form a coarse network in loose connective tissue or form flattened sheets in dense elastic tissues such as the aorta (127).

It has been found that elastic fiber increase, together with a decrease in collagen fibers is associated with oral squamous cell carcinoma and lymph node metastasis (137). Elastin-rich lung ECM is largely remodeled during tumor invasion. The degradation of elastin produces peptides displaying a wide range of biological activities and increase invasive capacities of lung cancer cells by post-transcriptional regulation of metalloproteinase-2 (138). This mechanism has also been found to act in melanoma progression, another cancer associated with rich elastin microenvironment (139).

4.3. Vascular component

It is now widely accepted that angiogenesis is essential for tumor growth and metastasis (140, 141). Therefore, controlling tumor-associated angiogenesis is a promising strategy in limiting cancer progression.

Depending on their size and composition, blood vessels can be divided in capillaries (5-15 μ m), post-capillaries/metarterioles (15-20 μ m), sinusoid-like blood vessels (20-50 μ m), venules/ arterioles (50-200 μ m) and veins/ arteries (>200 μ m) (**figure 3**). In order to grow over the limit of oxygen and nutrients diffusion, tumors have developed different strategies to provide blood supply. These mechanisms are sprouting angiogenesis: the growth of new capillary vessels out of preexisting ones; intussusceptive angiogenesis: the division of preexisting vessels in two new vessels by the formation of transvascular tissue in the lumen of the vessels; recruitment of endothelial progenitor cells or angioblasts; vessel co-option: tumor cells can grow along existing vessels without evoking an angiogenic response; vasculogenic mimicry: tumor cells dedifferentiate to an endothelial phenotype and make tube-like structures, providing tumors with a secondary circulation system; mosaic vessels: both endothelial cells and tumor cells form the luminal surface of the vessels (142-144).

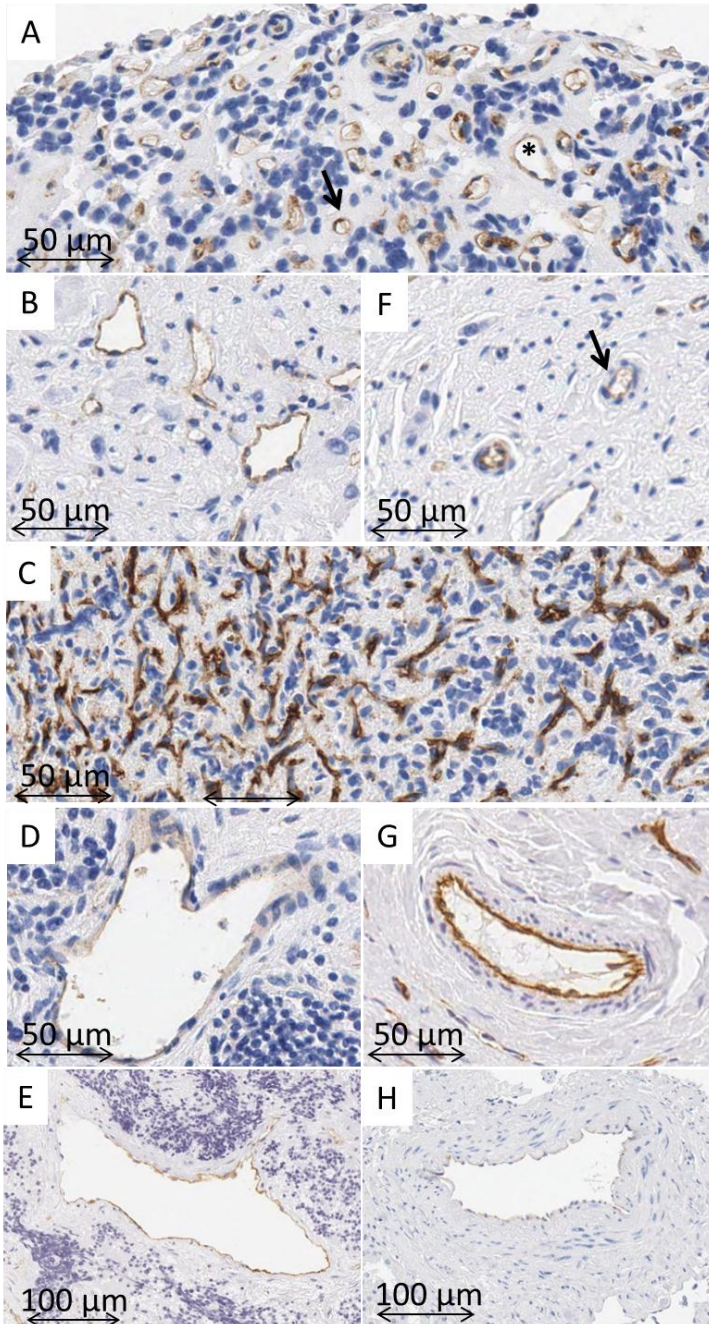


Figure 3: Types of blood vessels stained with IHC anti-CD31 in neuroblastic tumors. **A)** capillaries (5-15 μ m) and post-capillary venules (asterisk). **B)** post-capillary venules (15-20 μ m). **C)** Sinusoid-like blood vessels (20-50 μ m). **D)** venules (50-200 μ m). **E)** vein (>200 μ m). **F)** metarterioles (15-20 μ m). **G)** arterioles (50-200 μ m). **H)** artery (>200 μ m).

In many, aspects, tumor vessels are different from normal vessels. They are dilated, tortuous and poorly covered by pericytes (145, 146). The fact that tumor growth is dependent on angiogenesis has given rise to anti-angiogenic therapies targeting different pro-angiogenic molecules (147). The tumor microenvironment comprises numerous signaling molecules and pathways that influence the angiogenic response. Understanding how these components functionally interact as angiogenic stimuli or as repressors and how mechanisms of resistance arise is required for the identification of new therapeutic strategies (148).

In neuroblastoma, as well as in other malignancies, different studies have shown conflicting results, some indicating a prognostic value of angiogenesis and others rejecting such conclusions (149-154). This may arise from the fact that tissue vascularization has been quantified following different methods (151, 152), all based on the detection of the differential staining of the vessels with more or less specific immunostaining (against factor VIII, von Willebrand factor, CD34, CD31, caveolin or CD105) on image sections (154), hot spots (149), whole sections (151) or in tissue microarrays sections (153), thereby indicating the need for robust morphometric techniques which may standardize the measurement of angiogenesis.

5. Role of computerized image analysis

To effectively treat cancer, critical networks that are vital for the adaptive or compensatory mechanisms of cancer cells, but that are not required by normal cells, need to be identified and targeted, as a major limiting factor in successful treatment is the collateral damage to

normal tissue. Multimodality and multiparametric molecular and functional imaging provide unprecedented opportunities to image the ECM and the interactions between cancer cells and stromal cells (90). Imaging examinations have become essential as they allow repeated information to be recovered over time. The information obtained can be used to refine models and ultimately be applied to clinical practice (155). Innovative diagnostic methods that provide indications complementary to the conventional histopathology are under analysis. Morphometric techniques attempt to decrease human error, increase efficiency, assess large areas or huge amounts of tumor samples, create reproducible results, and help to standardize the measurements. The growing size and number of medical diagnostic images require the use of computer-automated segmentation algorithms for the delineation of ECM structures of interest, which play a vital role in the research of new biomedical-imaging markers (156). This is critical to analyzing whole sets of histochemical and immunohistochemical images to identify, describe and quantify tissue alterations of the ECM.

Despite sustained progress in our knowledge of biological signaling events regulating tumor malignancy, the clinical prognosis for many cancer types does not increase at the same rhythm. Increasing experimental evidence suggests that this discrepancy may be due in part to an under-appreciation of physical phenomena contributing to disease progression. As a result, cancer researchers are increasingly collaborating with mathematicians, chemists, physicists and engineers to study physicochemical characteristics of solid tumors and their role in modulating intracellular signaling (157). Some mathematical

concepts are therefore being investigated as tools to solve medical problems. For example, topological network analysis and the graph theory in combination with Voronoi tessellations (158) have recently been found to be useful in the diagnosis of muscular dystrophies and neurogenic atrophies, in the classification of neuromuscular disease or to model the progression of dementia (159-161). All the generated information is subject to capture relevant information about the organization of different tissue markers. Another novel approach to cancer research is the texture analysis of different tissue images and machine-learning methods to train automated algorithms which find different patterns in the tissue capable of discriminating between prognostic groups, among other variables, resulting in computer-aided diagnosis tools (162-165).

In this way, a computer-based grading system to support diagnosis for neuroblastoma that uses grades of differentiation and stromal development has been published (166, 167). Discrimination of stroma-poor and stroma-rich regions has also been reported using a mathematical model applied to digitized hematoxylin-eosin (HE) stained whole-sections with extraction of textural features (168). In addition, evidence has been provided that nuclear texture automated analysis can help to discriminate between different differentiated small round cell tumors (169). In an attempt to study the significance of new markers in neuroblastic tumors, the development of statistical modeling recently enabled our group to understand the prognostic value of new ECM and neuroblastic cell markers and to establish the degree of influence on neuroblastic tumors outcome (170).

II. HYPOTHESIS AND OBJECTIVES/ HIPÓTESIS Y OBJETIVOS

Our hypothesis generated after bibliographic revision are:

- 1- The destiny of a neuroblastic cell is not only directly decided by its genes but also by other cells and by the set of non-cellular extracellular matrix structural elements that converge in a cellular or tissular function.
- 2- In the same way than in healthy tissues, the composition and architecture of the extracellular matrix elements are related to histological subtypes of neuroblastic tumors with specific and quantifiable biological characteristics.
- 3- Extracellular matrix patterns derived from the architectural scaffolding could be morphologically and topologically characterized and could be related to patients prognosis (risk of relapse or death) and therefore:
 - a. May give rise to more accurate pre-treatment risk stratification. Specifically, we expect the study of these extracellular matrix markers to help defining a subgroup of patients with very poor survival, or ultra-high risk patients, which are the patients who may benefit the most from an enhanced stratification and/or novel therapies.
 - b. May be useful as new candidate elements for novel therapies.

To test these hypotheses, the following objectives were set:

- 1- Develop novel and accurate image analysis algorithms to be capable of characterizing glycosaminoglycans, reticulin fibers, collagen type I fibers, elastic fibers and blood vessels in neuroblastic tumors.
- 2- Perform statistical analysis to:
 - a. Correlate the extracellular matrix elements studied to clinical and biological features with known prognostic value (histopathology, age, stage, *MYCN* status, 11q status and genomic profile) in order to determine histological patterns with different degrees of malignancy.
 - b. Correlate the extracellular matrix elements analyzed with the risk of relapse or death, individually and in combination with other variables.
 - c. Deeper study the prognostic value of the morphometric variables in the high risk patient's subgroup.
- 3- Discuss the multipotentiality of features regarding glycosaminoglycans, reticulin fibers, collagen type I fibers, elastic fibers and blood vascularization.

Las hipótesis generadas tras la revisión bibliográfica son:

- 1- El destino de una célula neuroblástica no se decide únicamente y directamente por sus genes, sino también por otras células y un conjunto de elementos estructurales no celulares de la matriz extracelular que convergen en una función celular o tisular.
- 2- Del mismo modo que en tejidos sanos, la composición y arquitectura de los elementos de la matriz extracelular se relacionan con los subtipos histológicos de los tumores neuroblásticos con características específicas y cuantificables biológicas.
- 3- Los patrones de matriz extracelular derivados del andamiaje arquitectónico podrían ser caracterizados morfológicamente y topológicamente y podrían relacionarse con el pronóstico del paciente y, por lo tanto podrían:
 - a. Dar lugar a una estratificación de riesgo pre-tratamiento más ajustada. Específicamente, esperamos que el estudio de estos marcadores de la matriz extracelular ayude a definir un subgrupo de pacientes con muy baja supervivencia, o pacientes con ultra alto riesgo, que son aquellos que más podrían beneficiarse de una estratificación mejorada o de nuevas terapias.
 - b. Ser útiles como elementos candidatos para nuevas terapias.

Para comprobar estas hipótesis, se fijaron los siguientes objetivos:

- 1- Desarrollar algoritmos de análisis de imagen nuevos y precisos para ser capaces de caracterizar los glicosaminoglicanos, las fibras de reticulina, las fibras de colágeno tipo I, las fibras elásticas y los vasos sanguíneos en tumores neuroblásticos.
- 2- Llevar a cabo análisis estadísticos para:
 - a. Correlacionar los elementos de la matriz extracelular estudiados con las características clínicas y biológicas con valor pronóstico conocido (histopatología, edad, estadio, estatus de *MYCN*, estatus de 11q y perfil genómico) para distinguir patrones histológicos de con diferente grado de malignidad.
 - b. Correlacionar los elementos analizados de la matriz extracelular con el riesgo de recaída o muerte, individualmente y en combinación con otras variables.
 - c. Estudiar con más profundidad el valor pronóstico de las variables morfométricas en el subgrupo de pacientes de alto riesgo.
- 3- Discutir la multipotencialidad de elementos relacionados con los glicosaminoglicanos, las fibras de reticulina, las fibras de colágeno tipo I, las fibras elásticas y con la vascularización.

III. MATERIALS AND METHODS

1. Materials

1.1. Samples

We have analyzed 19 tissue microarrays (TMA) containing at least two representative cylinders of 1mm of 544 neuroblastic tumors including 458 primary tumors and 86 non-primary tumors from 499 patients, which were referred to the Spanish Reference Centre for NB Biological and Pathological studies (Department of Pathology, University of Valencia) from 1996 to 2007 (**table 1**), as well as control cylinders of different tissues including 24 different peritumoral tissue, tissue from 4 different other tumors and tissue from 29 different normal tissues/organs (**table 2**). Histologic and genetic studies were approved by the Spanish Society of Pediatric Hematology and Oncology (SEHOP) (file number: 59C18ABR2002) and European Committee (file number: 2010-021396-81), as well as by the Ethical Comitee of the University of Valencia. Participants or their family members/informants signed written informed consent forms for histological and genetic studies performed in our laboratory.

Most of the tumor samples were received frozen whereas a minority was received fresh in culture medium or paraffin embedded. The material was processed in the Pathology Service of the Hospital Clínico Universitario de Valencia. Following the diagnosis routine, the frozen and fresh samples were used to obtain several touch preparations, cell cultures (only for fresh samples) and frozen material for molecular techniques. A tumor sample was fixed in formalin and embedded in paraffin blocks for further histological and/or genetic tests in tissue sections. For histological research purposes, a fragment

of such material was included in TMAs. All received materials and the remainings after histopathological and genetic diagnosis were stored in the Healthcare Collection of Neuroblastic Tumors of the National Resgistry of Biobancs of the ISCIII (Reference: B0000339) at the Pathology Service of the Hospital Clínico de Valencia-INCLIVA. The steps followed are shown in **figure 4**.

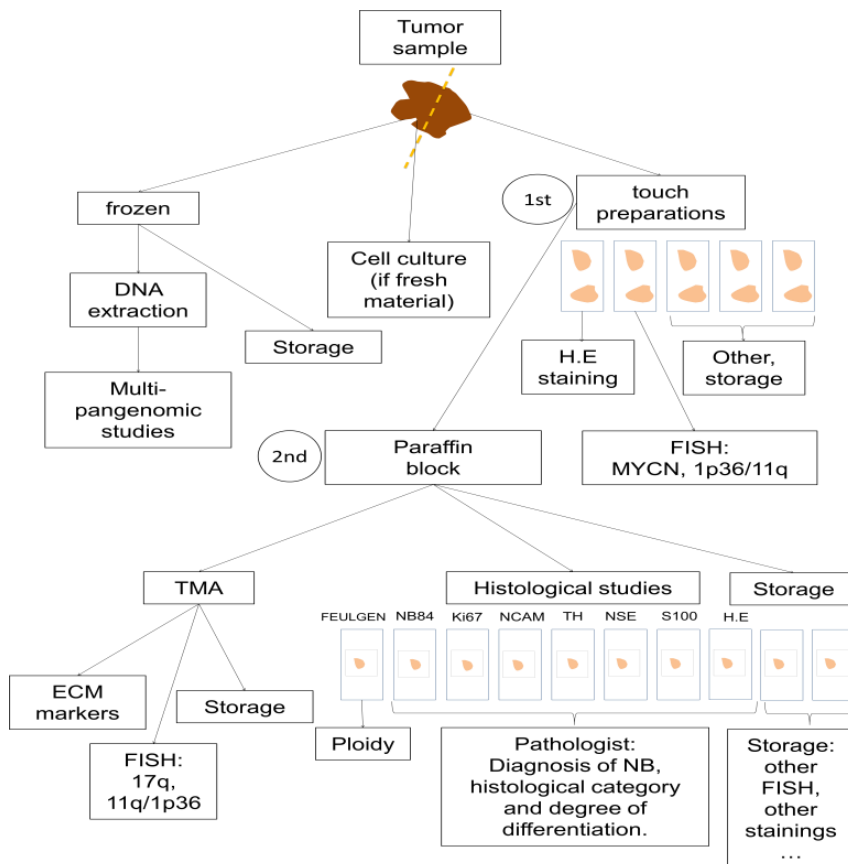


Figure 4: Pathway followed by a tumor sample received in the laboratory. The tumor is sectioned. One part is used for histological and genetic diagnosis on paraffin embedded tissue (or, exceptionally, on touch preparations) and the other section is frozen to be used for multilocus-pangenomic studies and storage. From the paraffin block, a cylinder can be extracted and introduced in a TMA, which is the case for the study of ECM. FISH: Fluorescent *in situ* hybridization, HE: Hematoxylin-eosin, ECM: Extracellular matrix.

Table 1: Description of the neuroblastic samples included in the TMAs.

Type of sample	Number (n)	Percentage (%)
Different biopsies	544 (499 ^a)	100 (91.5)
Primary tumors	458	84.2
Non-primary tumors	86	15.8

^abelong to different patients

Peritumoral tissues were obtained from paraffin blocks of tumors which include preserved organ/tissue where the tumor is located (liver, adrenal gland...). Normal tissues were obtained from paraffin blocks obtained from autopsies and tissue from other tumors was obtained from other malignancy's biopsies, stored at the Pathology Department. All non-neuroblastic samples included in the 19 TMAs are described below, in **table 2**.

As a consequence of this study, an image database including 5,725 images (544 tumoral samples x 2 cylinders + [24+4+29] control cylinders = 1,145 cylinders x [4 stainings + 1 HE]) was generated. Thirteen variables were calculated for the 1,145 cylinders stained for reticulin fibers, 1 variable was calculated for the cylinders stained for collagen fibers, 2 variables were calculated for the GAGs samples and 78 variables (13 x 6 subgroups) were calculated for the blood vessel study. A total of 105,340 data (1,145 cylinders x [13+1+2+76] variables) were generated.

Table 2: Type and quantity of peritumoral tissue and not neuroblastic samples.

Samples	Number of cylinders
Peritumoral tissue:	24
• Lymph node	1
• Adrenal gland	8
• Liver	2
• Striated muscle	1
• Pancreas	2
• Sympathetic ganglia and paraganglia, fat	10
Other tumors tissue (not NB):	4
• Lymphoma	1
• Olfactory estesiNB	1
• CC. sarcoma of the kidney	1
• Adrenocortical carcinoma	1
Non-tumoral tissue/organs:	29
• Kidney	14
• Liver	2
• Striated / Smooth muscle	5
• Spleen	1
• Placenta	5
• Salivary gland	2

1.2. Data relating to patients/samples

All data relating to patients, as well as biological findings, were filled and then exported from the self-designed database Neupat, in the Spanish Reference Centre for NB Biological and Pathological studies (Department of Pathology, University of Valencia) (171).

1.2.1. Clinical data

Age, stage and follow up information such as state of the disease, overall survival and event free survival were provided by the pediatric oncologists in charge or by the Reference center for NB clinical studies, directed by Dr. Victoria Castel and Dr. Adela Cañete, in Hospital La Fe of Valencia.

A. Age

The patient's age at diagnosis is indicated in months. It has been classified into different groups according to the INRG: less than 12 months, between 12 and 18 months and more than 18 months (**table 3**). The cohort studied ranged from 0 months (diagnosis at birth) to 223 months (18 years) with an average age at diagnosis of 26 months (2 years).

Table 3: Distribution of the patients according to INRGSS groups of age at diagnosis.

Age at diagnosis (months of age)	Primary biopsies		All samples	
	n	%	n	%
< 12	219	47.8	240	44.2
12-18	47	10.3	59	10.8
≥ 18	172	37.6	221	40.6
unknown	20	4.4	24	4.4
Total	458	100	544	100

B. Stage

Stage at diagnosis was also collected following the INSS, but was converted to the INRG Staging System (INRGSS) stages following the correlation described by Simon *et al*, and Monclair *et al* (7, 8). Therefore, the previous stage 1 becomes now L1, stages 2 and 3 become L2, stage 4 becomes M and stage 4S becomes Ms (7, 8). The stages of the studied cohort of patients are shown in **table 4**.

Table 4: Distribution of the samples according to INRGSS stage.

INSS stage	INRG Stage	Primary biopsies		All samples	
		n	%	n	%
1	L1	145	31.6	150	27.5
2	L2	48	10.7	59	11.0
3		95	20.7	124	22.8
4	M	112	24.4	146	26.8
4s	MS	32	6.9	36	6.6
	Unknown	26	5.7	29	5.3
Total		458	100	544	100

C. Event-free survival (EFS)

The EFS is the proportion of patients who have suffered no event, understanding relapse or *exitus* as an event. The EFS time (tEFS) is the period of time elapsed between the diagnosis of the disease and the first event, in case of relapse or death, or the last contact with the patient (last evaluation), in case of no event.

D. Overall survival (OS)

The OS is the percentage of patients who were alive when the study finished. The OS time (tOS) is the time elapsed between the diagnosis of the patient and the last evaluation or the death. All deaths were considered.

1.2.2. Histopathological data

Paraffin sections were stained with HE and immunohistochemical (IHC) techniques for NB84, TH, NSE, S100 and Ki67 (for the identification of neuroblastic cells, degree of differentiation, schwannian stroma and proliferation) and examined by a pathologist to evaluate the amount of neuroblastic cells, and histopathologically categorize them according to the INPC (12), into

neuroblastic tumors, including GN, iGNB, u/pd/d nGNB; and neuroblastomas: uNB, pdNB, dNB) (**table 5**). The pathologist also assessed the amount of neuroblastic cells in each biopsy (**table 6**).

Table 5: Distribution of the samples according to histopathology (category and degree of differentiation).

histopathology	Primary biopsies		All samples	
	n	%	n	%
GN	18	3.9	22	4.0
iGNB	29	6.3	40	7.3
u/pd nGNB	4	0.9	5	0.9
d nGNB	1	0.2	1	0.2
uNB	60	13.1	66	12.1
pdNB	270	59.0	301	55.2
dNB	35	7.6	55	10.1
NB NOS	41	9.0	54	10.1
Total	458	100	544	100

GN: ganglioneuroma, iGNB: intermixed ganglioneuroblastoma, u/pd/d nGNB: undifferentiated/ poorly differentiated/ differentiating nodular ganglioneuroblastoma, uNB: undifferentiated neuroblastoma, pdNB: poorly differentiated neuroblastoma, dNB: differentiating neuroblastoma, NOS: no otherwise specification neuroblastoma.

Table 6: Distribution of the samples according to the amount of neuroblasts.

Percent of neuroblasts	Primary biopsies		All samples	
	n	%	n	%
<10	6	1.3	7	1.3
10-50	129	28.2	166	30.5
51-60	55	12.0	67	12.3
>60	268	58.5	304	55.9
Total	458	100	544	100

1.2.3. Genetic data

The number and type of alterations detected in the tumors of the 19 TMAs is shown in **table 8**, presented as the combined results

arising from the different genetic techniques, including FISH and multilocus/pangenomic techniques.

A. Fluorescent *in situ* hybridization (FISH)

Touch preparations, paraffin sections and/or TMAs were used to study *MYCN* copy number and integrity of the chromosomal regions 1p36, 11q24 and 17q22. These were investigated with commercial probes: *MYCN* (2p24)/*LAF* (2q11); *MLL* (11q23) /*SE* 11; *MPO* (17q22) ISO 17q/*p53* (17p13), cocktail probes dual color direct labelled (Kreatech, Biotechnology) and 1p36 (*D1Z2*)/centromere Chromosome 1 (Qbiogene). Assessment and interpretation of FISH results were performed according to previously published European guidelines (172-174) (figure 5, table 7).

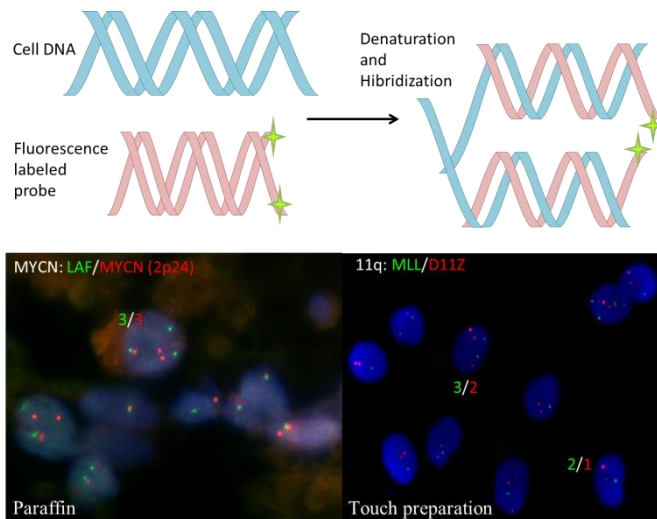


Figure 5: FISH technique. Cell and fluorescence labeled DNA probe, complementary to the region of interest are denatured and hybridized. *MYCN* gene (in red), 11q23 (in red) and the centromeres of chromosomes 2 and 11 (in green) are shown, with the counting of the proportion of signals.

A minimum of 100 nuclei for TMA or 200 nuclei for paraffin or touch preparations were scored for TMA cylinders and whole sections, respectively, taking into consideration the selection of non-overlapping nuclei and the analysis of multiple focal planes to ensure the detection of all signals (175).

Table 7: Recommendations for the terminology and definitions of the genetic results that have been formulated for neuroblastic tumors by the ENQUA group (172).

Marker	Status	Description
<i>MYCN</i>	no amplification	Same number of gene signals and control probe signals.
	gain	Number of gene signals is between 1 and 4 times higher than the number of control probe signals.
	amplification	Number of gene signals is 4 times higher than the number of control probe signals. *Homogeneous: amplified cells are found in combination with cells showing gain. *Heterogeneous: tumor amplified and non-amplified (not disomic) cells are found.
1p36, 11q	no deletion	Same number of the region signals and control probe signals.
	imbalance	Less signals (but minimum 2) of the region than control probe signals.
	deletion	One signal from the region with at least 2 control probe signals.
17q	no gain	Same number of region signals and control probe signals.
	gain	Number of region signals is between 1 and 4 times higher than the number of control probe signals.

B. Multilocus/pangenomic techniques

DNA from frozen tumors was extracted using phenol/chloroform/isoamyl alcohol extraction after proteinase K

treatment. More than one tumor piece was analyzed in some cases with heterogeneous tissue in order to extend the description of the tumor genotype. Given that only biopsies with more than 50% of tumor cells can be analyzed by multilocus-pangenomic techniques, several biopsies couldn't be analyzed by these techniques. In some cases, DNA was extracted from a set of 5 sections of 10 μ m from paraffin-embedded samples, following the same steps with minor modifications, after deparaffinization.

- Multiplex-ligand probe amplification (MLPA)

MLPA was used as a cost-effective first approach method in the detection of frequent SCAs in NB. The technique was performed using the SALSA MLPA Kit (A1-B1) P251/P252/P253 developed by MRC-Holland in co-operation with SIOPEN. The SALSA MLPA P251 (A1-B1 series) probemix contains probes for chromosomes 1, 3 and 11; P252 (A1-B1 series) probemix for chromosomes 2 and 17; and P253 (A1-B1 series) probemix for chromosomes 4, 7, 9, 12 and 14. Each panel includes control probes located in chromosome regions rarely altered numerically in NB. The technique is summarized in **figure 6**. The interpretation guidelines are described elsewhere (1, 176).

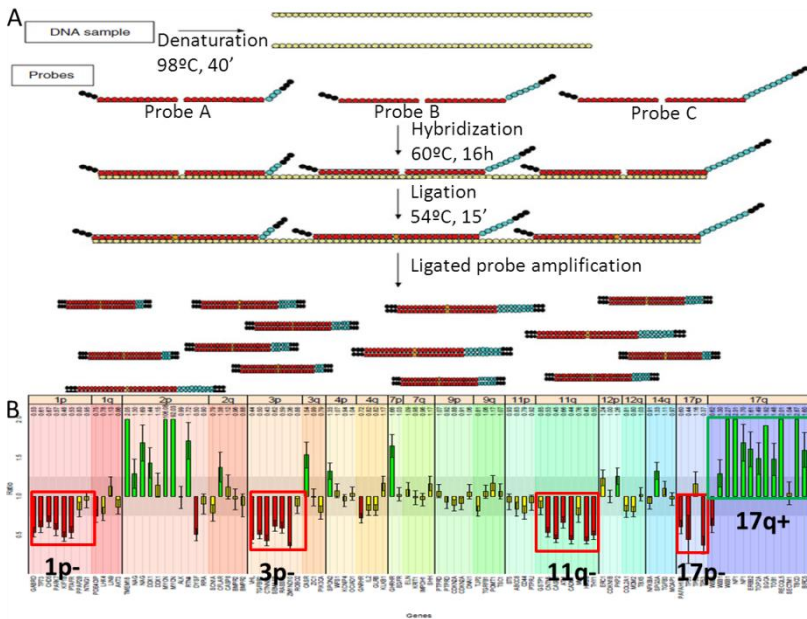


Figure 6: **A)** Explanation of the main steps of the MLPA process. **B)** Example of a tumor with several segmental aberrations processed by MLPA-Vizard software (Austrian Research Centers) and using SALSA MLPA Kit A1 NB P251/P252/P253. Image A reproduced from the book *Guidelines for Molecular Analysis in Archive Tissues*, by Stanta G. Ed. Springer, 2011. Chapter 33: Multiplex Ligation-dependent Probe Amplification (MLPA), Berbegall A.P. *et al*, pages 215-24 (177).

- Single Nucleotide Polymorphism array (SNPa)

For SNPa, two systems were used: Affymetrix® and Illumina®, excluding chromosome X from the study. A brief explanation of the techniques and examples of both methods are provided in **figure 7**.

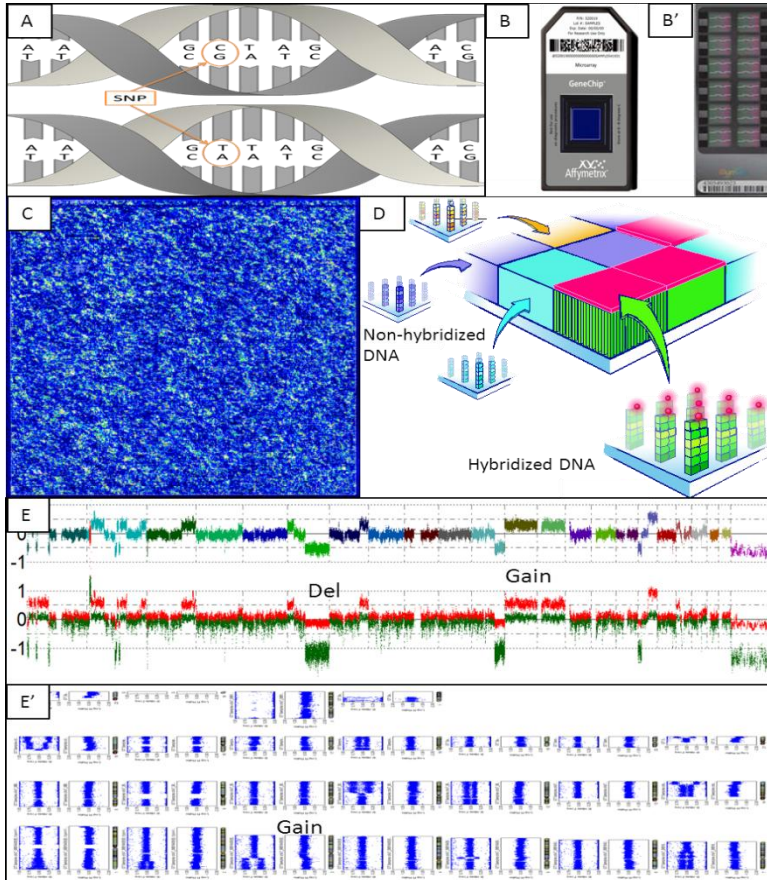


Figure 7: SNPa technique. **A)** Illustration of the SNP concept. **B)** microarray chip by Affimetrix® containing 262,256 probes. **B')** microarray chip by Illymina® containing 299,140 probes. **C)** Chip array output with each color indicating the status of the hybridization (example of Affimetrix®), **D)** Drawing of what occurs for each probe. **E)** Results of a tumor DNA with some genetic aberration (Affimetrix®). **E')** results of a tumor DNA with some genetic aberrations (Illumina®). Images B, C and D reproduced with courtesy of Affymetrix®.

Affymetrix® (Affymetrix, Inc., Santa Clara CA): GeneChip Human Mapping 250K arrays (262,256 SNPs) were used following the protocol provided by the supplier. The primary data analysis was made using GDAS software (Affymetrix), while genomic profiles were generated using CNAG (Copy Number Analyzer for Affymetrix GeneChip Mapping arrays) Version 3.0 with the AsCNAR (allele-specific copy-number

analysis using anonymous references) function (178). The UCSC genome browser, assembly February 2009, was used to visualize gene regions.

Illumina® (Illumina, Inc., San Diego, California, USA): the 12-sample HumanCytoSNP-12 BeadChip includes 299,140 markers. Genotypes were determined with the software Genome Studio c.2011.1 (Illumina, Inc., San Diego, California, USA) and the evaluation of the profiles was made with Karyostudio v.1.4 (Illumina, Inc., San Diego, California, USA).

- Combined results

FISH, MLPA and SNP_a results were combined into a single diagnosis for the different genetic regions with prognostic interest or found most frequently. As a result of this combination, and given that different results from two different techniques or two or more different tumor areas arise from the intratumor heterogeneity of these tumors, we can find heterogeneous aberrations for some chromosome regions. Specifically, *MYCN* gene, 2p, 17q, 11q and 1p were studied by different techniques and thus heterogeneity can be informed for most of them. 1q and 2p aberrations are mostly gains, whereas 3p and 4p are usually deletions. The data can be found in **table 8**.

Table 8: Distribution of the samples according to the status of different regions by FISH, MLPA and SNP_a techniques.

Region	Status	Primary biopsies		All samples	
		n	%	n	%
MYCN ^a	Hom MNA	63	13.7	80	14.7
	Het MNA ^c	14	3.1	18	3.3
	G	19	4.2	28	5.1
	Het G ^c	9	1.9	10	1.8
	MNNA	351	76.7	406	74.7
	NR	2	0.4	2	0.4
11q ^a	D	70	15.3	84	15.4
	ND	321	70.1	375	68.8
	Het D ^c	7	1.5	8	1.5
	NR	60	13.1	77	14.3
1p ^a	D	93	20.3	122	22.4
	ND	302	65.9	345	63.5
	Het D ^c	54	11.8	60	11.0
	NR	9	2.0	17	3.1
17q ^a	G	170	37.1	208	38.2
	NG	222	48.5	256	47.0
	Het G ^c	13	2.8	15	2.8
	NR	53	11.6	65	12.1
1q ^b	Aber.	24	5.2	28	5.1
	NAber.	259	56.6	292	53.6
	NR	175	38.2	224	41.3
3p ^b	Aber.	33	7.2	35	6.4
	NAber.	250	54.6	285	52.3
	NR	175	38.2	224	41.3
4p ^b	Aber.	15	3.3	17	3.1
	NAber.	268	58.5	303	55.6
	NR	175	38.2	224	41.3
2p ^a	G	53	11.5	69	12.7
	NAber.	370	80.8	429	78.9
	Het G ^c	12	2.8	16	2.9
	NR	22	4.8	30	5.5
Total		458	100	544	100

Hom: homogeneous, Het: heterogeneous, MNA: MYCN amplification, G: Gain, MNNA: MYCN Not amplified, NR: No results (unknown data or not evaluable result), D: deletion, ND: non-deleted, NG: non-gained, Aber: aberration; NAber: not aberration. ^aCombination of FISH, MLPA and SNP_a, ^bCombination of MLPA and SNP_a, ^cHeterogeneity arises from different results between FISH and Multi-pangenomic techniques (MLPA-SNP_a) and/or different tumor pieces.

The combination of all the genetic data defined an overall genomic profile, where the presence of at least one SCA (by FISH, MLPA or SNP_a) classified the sample as a SCA profile, and the absence of it by MLPA or SNP_a, classified the sample as a numerical chromosome aberration profile (NCA) (**table 9**). In the case of samples with only FISH for 2 to 4 chromosome regions status or MLPA with not evaluable chromosome profile or with non-informative profile for any chromosome, the sample was classified as unknown because we could not affirm the absence of any segmental aberration in those chromosomes not analyzed by FISH/MLPA techniques.

Table 9: Distribution of the samples according to MLPA/SNP_a results.

Multi-pangenomic results	Primary biopsies		All samples	
	n	%	n	%
SCA	223	48.7	280	17.8
NCA	95	20.7	97	51.4
NR/NE	140	30.6	167	30.8
Total	458	100	544	100

SCA: segmental chromosome aberrations, NCA: numerical chromosome aberrations, NR: no results, NE: not evaluable.

C. Ploidy

DNA content was analyzed by image cytometry to selectively study neuroblasts, excluding apoptotic or stromal cells from cytometric measurements (179), following the INRG recommendations. Feulgen stained paraffin sections images were captured at 50 magnifications (OLYMPUS BH-2 with ProgResTM c10Plus camera, JENOPTIK (JENA) and ProgRes CapturePro 2.1 software) and at least 500 to 600 alleatory and isolated neuroblasts nuclei and 25 to 50 lymphocytes serving as internal reference of diploidy were analyzed with the software ImagePro Plus, the median integrated optic density (IOD) values of

G0/G1-phase fractions of tumor cells and the median IOD values of G0/G1-phase fractions of diploid cell types (lymphocytes) were assessed. Median IOD of tumor cells divided per median IOD of diploid cells gave us an IOD value of the sample which is related to a ploidy following the intervals shown in **table 10**.

Table 10: Distribution of the biopsies according to their ploidy.

IOD value	Ploidy	Primary biopsies		All samples	
		n	%	n	%
1 - 1.19	Diploid	67	14.6	77	14.1
1.20 -1.25	Bord. diploid	3	0.7	3	0.6
1.26 - 1.74	Triploid	156	34.1	182	33.4
1.75 – 1.80	Bord. triploid	7	1.5	10	1.8
1.81 - 2.19	Tetraploid	20	4.4	25	4.6
2.20-2.26	Bord. tetraploid	1	0.2	1	0.2
> 2.26	Others	22	4.8	11	2.0
	Unknown	182	39.7	235	43.3
	Total	458	100	544	100

Bord: Borderline.

1.2.4. Risk group

The combination of all previous variables define a risk group, following **table 1**. How our data were grouped is shown in **table 11**:

Table 11: Distribution of the samples according to the risk group.

Risk group	Primary biopsies		All	
	n	%	n	%
Very low risk	184	40.4	196	36.1
Low risk (LR)	77	16.9	94	17.2
Intermediate risk (IR)	34	7.5	44	8.1
High risk	110	24.2	150	27.6
Unspecified LR or IR	24	5.3	29	5.3
Unknown	29	5.7	31	5.7
Total	458	100	544	100

2. Methodology

2.1. Construction of tissue microarrays (TMAs)

TMAs were constructed including all the evaluable cases described in the section “**1.1. samples**”. The samples were included chronologically in the corresponding TMA at least twice (two cylinders) to properly represent, if the case was given, different histologies of the sample and to have a higher chance to maintain at least one representative sample of each case after the processing of the TMA sections. The steps followed were (**figure 8**):

1. Select the samples to include: discard not evaluable samples, paraffin blocks with scarce material, etc...
2. Select two areas per sample in the HE section corresponding to the paraffin block as representative as possible of the tumor. This step was performed by the pathologist.
3. Design one grid per TMA where the order of every sample is indicated and taking into account that two control cylinders will be included to provide a proper orientation of the grid and the TMA when constructed, given that they are placed asymmetrically. In general, the TMAs were composed of 6 rows, 10 columns and two independent control samples in the lower left corner. The samples were assigned to the corresponding TMA following a chronologic order.
4. Construct an empty paraffin block which will be the receptor block.
5. Fix the receptor block in the fixed plate of the manual Beecher Instrument (Silver Springs, MD, USA) for TMA construction.

6. Perforate the receptor block using the perforator needle provided by the instrument with the smaller diameter.
7. Provisionally cover the plate with the receptor block with a mobile plate where the paraffin block containing the sample, called the donor block, is placed.
8. Compare the sample in the paraffin block with the HE section to identify the representative regions selected by the pathologist to be included in the TMA.
9. Perforate the donor block using the needle with 1mm diameter which keeps extracted sample section inside.
10. Move the mobile plate to expose the receptor block and introduce the extracted cylinder into it.
11. Move the plate with the receptor block 2 mm in the X axis, a distance between two cylinders which is enough to avoid contaminations.
12. Repeat steps 6 to 11 until the row is over.
13. Go back to the first cylinder of the row and move the plate with the receptor block 2mm in the Y axis to start a new row. Repeat steps 6 to 12.
14. When the process is over, following the designed grill, incubate the receptor block overnight at 37°C to assure the cohesion between the paraffin of the block and the paraffin of the introduced cylinders.

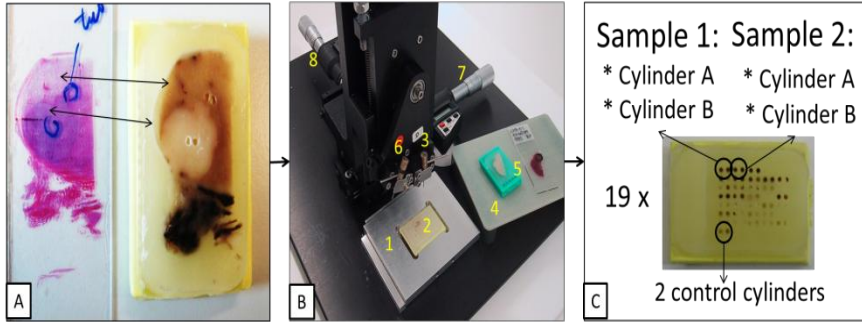


Figure 8: Steps followed to construct a TMA. **A)** HE of a sample with two representative areas selected and their corresponding location in the paraffin block (already perforated). **B)** Beecher Instrument (Silver Springs, MD) and the different parts composing it (1 and 2: fixed plate and receptor block; 3: small needle to perforate the receptor block; 4 and 5: mobile plate with one donor block and its HE to be able to locate the representative regions selected by the pathologist; 6: big needle to extract cylinders from donor blocks; 7: fingerwheel to move in the X axis; 8: fingerwheel to move in the Y axis. **C)** TMA obtained where each sample is represented by 2 cylinders and 2 control cylinders are placed asymmetrically.

2.2. Cutting and staining of the sections

The TMA paraffin blocks were cut routinely. Several serial sections of $3\mu\text{m}$ were made and stained histochemically (HC) for GAGs, reticulin fibers and collagen type I fibers and IHC anti-CD31 for blood vessels. The consecutive order of the slides that enables the histological correlation of the serial cuts is shown in **table 12**.

Table 12: Number of the slide stained with the different techniques for every TMA. Gomori: reticulin fibers, Masson's trichrome: Collagen type I fibers, Alcian blue: glycosaminoglycans, CD31: Blood vessels. Orcein technique was performed only in TMAs 1 and 2 with the slide numbers 29 and 50, respectively.

TMA nº	Gomori	Masson's Trichrome	Alcian Blue	CD31
TMA 1	27	28	26	14
TMA 2	46	48	47	11
TMA 3	10	11	12	8
TMA 4	25	26	28	24
TMA 5	27	28	29	26
TMA 6	26	27	28	30
TMA 7	24	27	28	30
TMA 8	28	29	24	23
TMA 9	27	29	30	26
TMA 10	27	28	29	32
TMA 11	10	11	13	8
TMA 12	7	8	9	4
TMA 13	3	5	6	4
TMA 14	3	5	6	20
TMA 15	4	5	6	9
TMA 16	16	15	18	-
TMA 17	5	4	6	9
TMA 18	7	8	9	10
TMA 19	4	5	6	8

-: unknown.

2.2.1. Staining of the fundamental substance: GAGs

One section of each TMA was stained with Alcian blue pH 2.5 Stain Kit (Artisan™, Dako). Acid GAGs (HS, CS, DS and HA), sulfomucins and sialomucins were stained in blue, the nucleus were stained in red and the cytoplasm in pale pink (**figure 9**). The staining proceeded as follows:

1. Deparaffinize and hydrate sections.
2. Rinse in distilled water.

3. Stain in Alcian blue pH 2.5 solution. (Alcian blue pH 2.5: Mix 1 g alcian blue with 100 ml 3% acetic acid and adjust pH to 2.5 using acetic acid). 10 mins.
4. Wash in running tap water. 2 minutes.
5. Rinse in distilled water.
6. Counterstain in 0.1% nuclear fast red solution. (0.1% fast red solution: Dissolve 5 g of aluminium sulfate in water. Add 0.1 g of nuclear fast red and slowly heat to boil and cool. 10 minutes.
7. Dehydrate.
8. Mount.

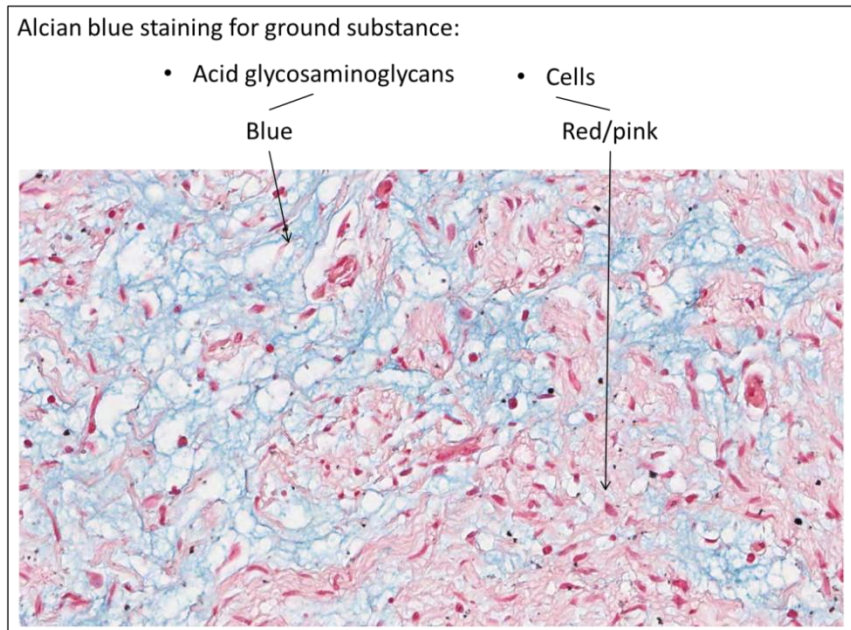


Figure 9: Alcian blue staining for fundamental substance. Acid glycosaminoglycans are stained in blue and nuclei and cytoplasm are stained in red and pink, respectively.

2.2.2. Staining of the fibrous component

- Staining of the reticulin fibers

Reticulin stains are silver stains based on the argyrophilic properties of reticulin fibers. Sections of the 19 TMAs were stained with a slightly modified Gomori which stains reticulin fibers in black (**figure 10**). The first step in the staining procedure consists of oxidation of the hexose sugars in reticulin fibers to yield aldehydes. The second step is called sensitization in which a metallic compound such as ammonium sulfate is deposited around the reticulin fibers, followed by silver impregnation in which an ammonical or diamine silver solution is reduced by the exposed aldehyde groups to metallic silver. Further reduction of the diamine silver is achieved by transferring the sections to formaldehyde; this step is called revealing. The last step consists of toning by gold chloride in which the silver is replaced by metallic gold and the color of the reticulin fibers changes from brown to black. The detailed protocol used was:

1. Deparaffinize and hydrate.
2. Rinse in distilled water.
3. Oxidize with 1% potassium permanganate. 1minute.
4. Rinse in distilled water.
5. Sensitize with 2% potassium metabisulfite. 1 minute.
6. Rinse in distilled water.
7. Silver impregnation in 2% ferric alum. 2 minutes.
8. Rinse in distilled water.
9. Treat with Wilder's reagent. 2 minutes.
10. Rinse in distilled water.

11. Reveal with formaldehyde. 5 minutes.
12. Rinse in distilled water.
13. Tone with 0.2% gold chloride. 2 minutes.
14. Rinse in distilled water.
15. Treat with 2% potassium metabisulfite. 2 minutes.
16. Rinse in distilled water.
17. Treat with 2% sodium thiosulfate.
18. Wash in running tap water. 5 minutes.
19. Dehydrate.
20. Mount.

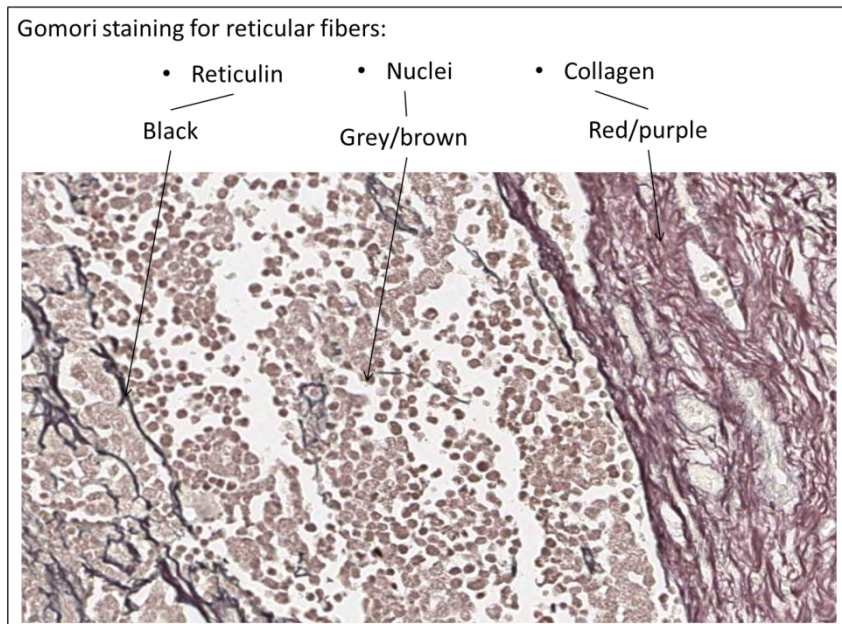


Figure 10: Gomori staining for reticular fibers. Reticulin is stained in black, nuclei in grey/brown and collagen fibers are unspecifically stained in red/purple.

- Staining of the collagen fibers

The quantification of the collagen fibers was performed on Masson's trichrome stained sections. Masson's trichrome stain consists

in the sequential staining with Harris hematoxylin which stains nuclei dark red, aniline blue which stains collagen and reticulin blue and molybdic orange G which stains erythrocytes dark orange. **Figure 11** shows the result of the technique. The protocol followed is detailed next:

1. Deparaffinize and hydrate.
2. Rinse in distilled water.
3. Stain with Harris hematoxylin. 5 minutes.
4. Wash in running tap water.
5. Bleach in chloridric alcohol followed by lithium carbonate. (Chloridric alcohol: 1% chloridric acid in 70º alcohol).
6. Wash in running tap water.
7. Rinse in 1% acetic water.
8. Stain with Ponceau fuchsin. (Ponceau fuchsin: Dissolve 0.15 g of acid fuchsin and 0.3 g of Ponceau xylydine in 0.9 ml of acetic acid and 450 ml of distilled water). 5 minutes.
9. Rinse in 1% acetic water.
10. Stain with molybdic orange G. (Molybdic orange G: Mix 8 g of orange G and 8 g of phosfomobdylic acid in 400 ml of water). 5 minutes.
11. Rinse in 1% acetic water.
12. Stain with aniline blue. (Aniline blue: Mix 0.8 g of aniline blue and 0.8 ml of acetic acid in 400 ml of distilled water). 5 minutes.
13. Rinse in 1% acetic water.
14. Rinse in distilled water.
15. Dehydrate.
16. Mount.

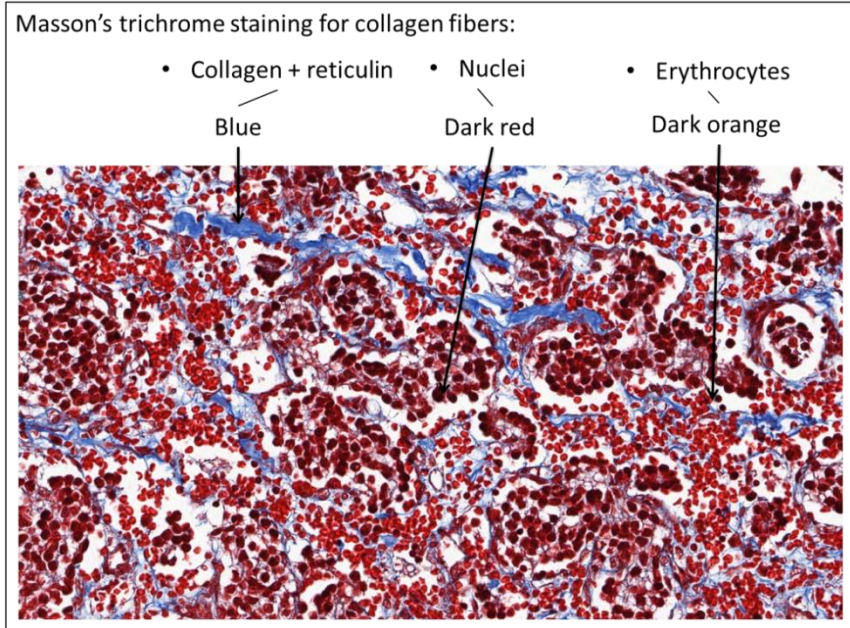


Figure 11: Masson's trichrome staining for collagen fibers. Collagen fibers (type I and reticular) are stained in blue, nuclei in dark red and erythrocytes are stained in dark orange.

- Staining of the elastic fibers

Orcein is a natural dye obtained from lichens which are found to stain elastic fibers dark brown (**figure 12**). The steps followed were:

1. Deparaffinize and hydrate.
2. Rinse in distilled water.
3. Oxidize with 1% potassium permanganate. 10 minutes.
4. Rinse in distilled water.
5. Bleach with 2.5% oxalic acid. 3 minutes.
6. Rinse in distilled water.
7. Rinse in 70° alcohol.
8. Incubate in orcein solution. (Orcein: dissolve 1 g of orcein in 98 ml of ethylic alcohol 70° and add 2 ml of concentrated chloridric acid). 3 hours.

9. Rinse in distilled water.
10. Differentiate with chloridric alcohol. (Chloridric alcohol: 1% chloridric acid in 70° alcohol). 2 minutes.
11. Wash in running tap water.
12. Rinse in distilled water.
13. Stain nuclei with Harris hematoxylin. 1 minute.
14. Wash in running tap water.
15. Rinse in distilled water.
16. Dehydrate.
17. Mount.

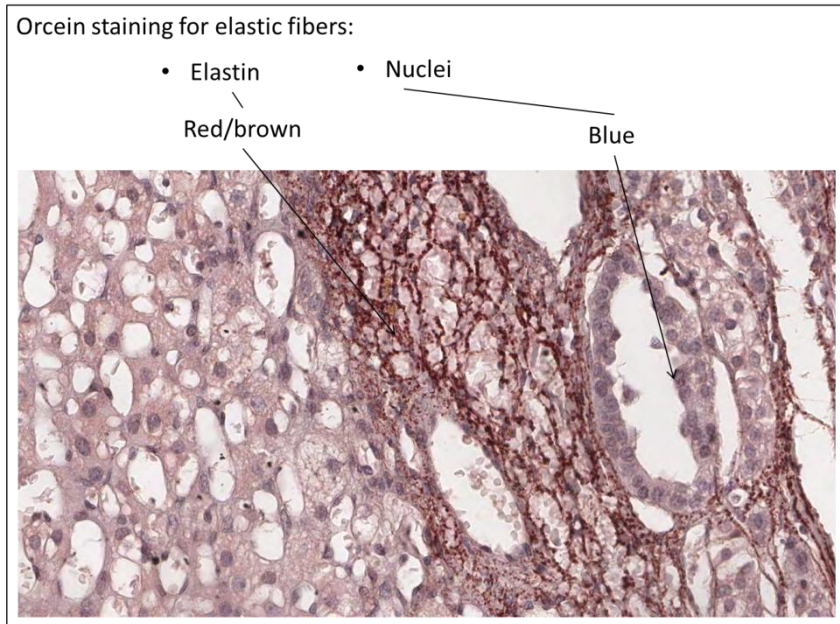


Figure 12: Orcein staining for elastic fibers. Elastin is stained in brown and nuclei in blue.

2.2.3. Staining of the vascular component

- Staining of the blood vessels

CD31 is a single chain type 1 transmembrane protein with a molecular mass of approximately 135 kDa, belonging to the immunoglobulin superfamily. CD34 was also applied to a subgroup of 96 samples but this marker was also staining cells other than endothelial (**congress nº 3**). CD31 is expressed on endothelial cells of epithelial origin (all continuous endothelia, including those of arteries, arterioles, venules, veins, and capillaries, but it is not completely expressed on discontinuous endothelium in, for example, splenic red pulp). In addition, CD31 is expressed diffusely on the surfaces of megakaryocytes, platelets, myeloid cells, natural killer cells, and some subsets of T cells, as well as on B-cell precursors. Cells labeled by the antibody predominantly display membrane staining, with weaker cytoplasmic staining (**figure 13**). The protocol used is detailed next:

1. Deparaffinize and hydrate.
2. Rinse in distilled water.
3. Epitope retrieval: Use high pH target retrieval solution (Dako) in autoclave at 1.5 atmospheres. 3 minutes.
1. Wash in running tap water.
2. Rinse in distilled water.
3. Block inner peroxide: Incubate in 3% H₂O₂. 5-10 minutes.
4. Rinse in distilled water.
5. Incubate in primary antibody: monoclonal mouse anti CD31 (Dako, clone JC70A) at 1/50 dilution. 30-45 minutes.

6. Rinse in distilled water.
7. Incubate in secondary antibody with EnVision FLEX/HRP visualization system (Dako). 30 minutes.
8. Rinse in distilled water.
9. Dehydrate.
10. Mount.

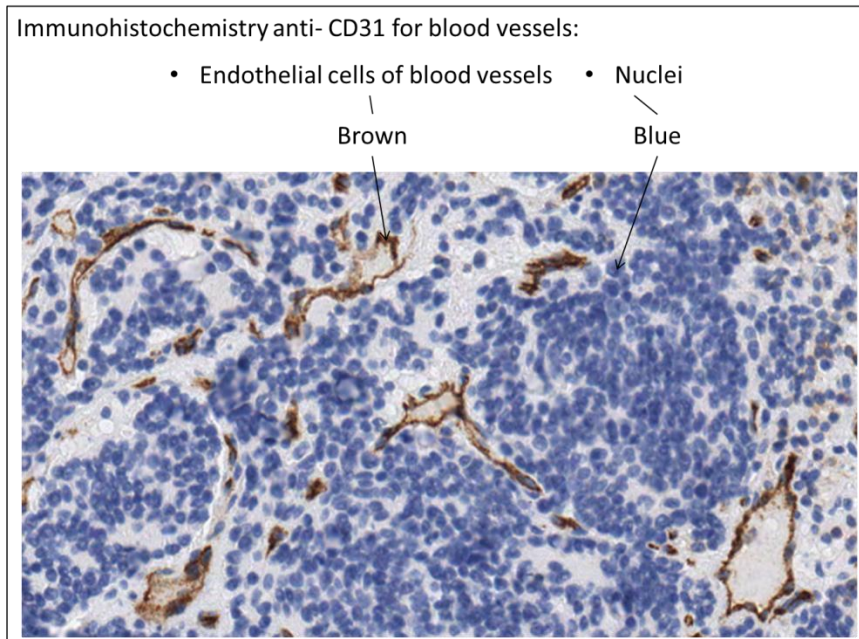


Figure 13: Immunohistochemistry anti-CD31 for blood vessels. Endothelial cells of blood vessels are stained in brown and nuclei in blue.

2.3. Digitization of the sections

A morphometric analysis of a huge amount of images necessitates digitization. A preliminary subset of 24 samples was digitized using the photomicroscope Leica DMD 108. 6 sequential photos were made at 20x magnifications and then carefully merged with Adobe Photoshop to reconstruct a single whole cylinder image (**figure 14**).

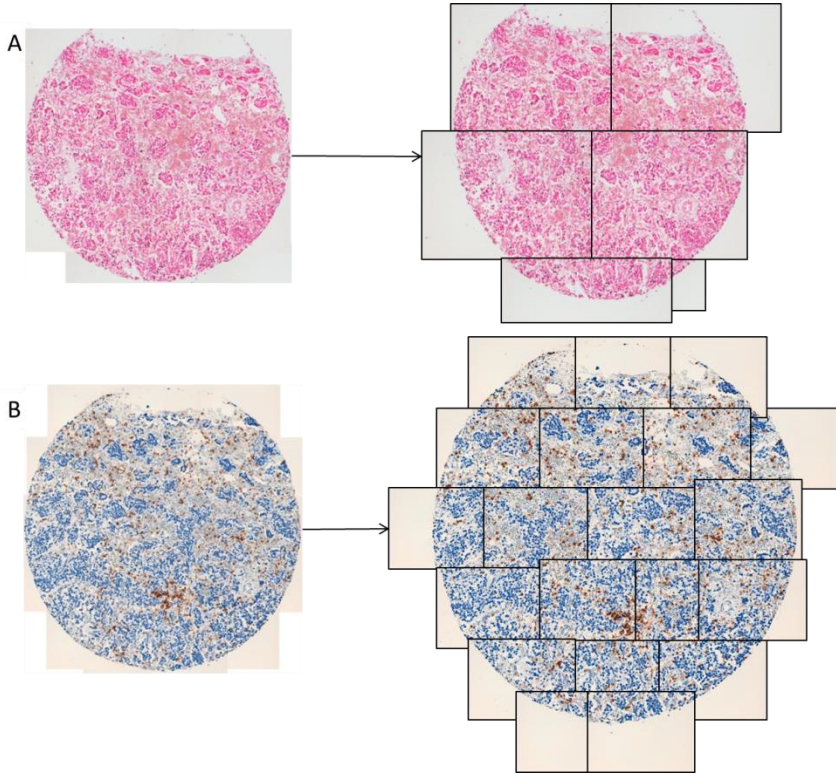


Figure 14: Process of HE and CD31 immunostaining image capture. **A)** At 20x magnification, 6 individual images of the cylinder must be captured to reconstruct the whole cylinder image. **B)** The whole 1mm cylinder image at 40x magnification must be reconstructed from 20 individual images.

Following our experience, this method needs approximately two weeks to digitize 30 samples (2 cylinders per sample) for a single staining at 20x magnification, or approximately 6 to 7 weeks at 40x magnification. In order to enhance the standardization of the image capture conditions and therefore, the quality of the measurements and to save time, a second method consisting of whole slide scanning was followed, as described next.

All the sections stained with the different methods were digitized with the ScanScope XT scanner, Aperio technologies. ScanScope XT scanner is a brightfield scanner that digitizes whole

sections at 20x and 40x magnification providing high resolution images in approximately 15 to 30 minutes per slide, depending on the magnification and the size of the tissue. 40x magnification was used, originating images with a resolution of 0.25 $\mu\text{m}/\text{pixel}$. Given to the enormous amount of pixels scanned, the images were compressed in JPEG2000 to 100-200 megabytes for the average size of a TMA, and saved to a proprietary TIFF format (SVS).

The sections were placed in a mobile plate one by one. An option for TMAs digitization provided by the scanner driver was used. This option recognizes the tissue cylinders and places several points per sample where the objective adjusts the focus to obtain clear and focused images. The mobile plate with the section moves in consecutive stripes until it sweeps the whole section while the objective scans. Individual scanned stripes are originated and stitched together automatically to reconstruct the whole image, which can be visualized up to 40x magnifications with the Image Scope viewer software (Aperio technologies). The process is briefly shown in **figure 15**.

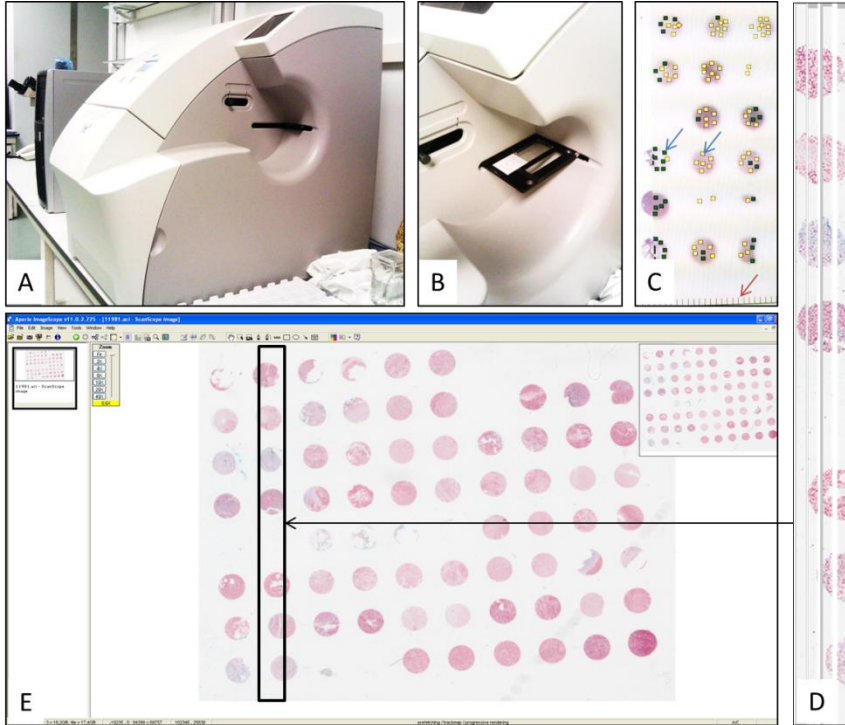


Figure 15: Digitization process. **A)** ScanScope XT, Aperio technologies. **B)** Mobile plate with one section on it. The plate is introduced in the scanner and placed under the objective to start the process. **C)** Preview of an area of the section. Blue arrows show the pre-set points where the scanner shall readjust the focus. Green points have already been properly focused and yellow points still have to be focused. The red arrow shows different marks corresponding to the different horizontal stripes which are going to be scanned individually and then stitched together. **D)** 4 single consecutive stripes are shown corresponding to the section in E. **E)** All the stripes are stitched to form a single image of the whole section. The image is opened in the free viewer ImageScope, Aperio technologies.

2.4. Subjective assessment of the presence of ECM elements and histological observation

A subgroup of 96 samples among all the studied, included in the TMAs was subjectively analyzed by a pathologist to assess the amount of each ECM element. The criteria used were:

- non-informative: artefact, scant material, lost cylinder.

- negative: no expression or <5% of stained area is detected.
- positive 1+: mild staining, 5-10% of the area.
- positive 2+: moderate staining, 10-50% of the area.
- positive 3+: strong staining, >50% of the area.

In addition to the subjective assessment, all the images of the four markers were observed by three researchers in order to find repeating patterns related to the organization of each ECM marker regarding neuroblastic cells, immune cells, blood vessels, etc...or any spetial recognizable organization.

2.5. Design of algorithms and measurement procedures

2.5.1. Previous considerations

Before describing the methods and the process for image analysis applied for each marker (**table 13**, **figure 16**), some considerations must be done:

A. Working images

The scanned section by Aperio ScanScope XT was automatically recorded in a proprietary format (SVS) consisting in JPEG2000 serial images put together and recorded in TIFF format. When working directly on the whole section, the image was used in TIFF format.

When working with other softwares, individual images of every cylinder had to be extracted. Images were extracted whether in TIFF format or in JPEG format. As a rule, given the enormous amount of

images stored, the chosen format was JPEG, compressed with the highest quality (quality 80), with an average weight of 60KB per image and an average size of 5500x5500 pixels. The compression of the images to JPEG, triggers a loss of some morphological properties, specifically in the roundness parameter. Nevertheless, the majority of the morphological measurements are not affected by compression (180-182).

In the particular case of blood vessels, a very good accuracy in the brown color of the stained pixels was required, and the images had to be stored in TIFF format, with an average weight of 80KB per image and an average size of 6500*6500 pixels.

Besides the image format, another important characteristic to take into account was the information contained in every pixel. The image was recorded in RGB color system, which comes from the combination of one intensity value for the Red, Green and Blue channels. Alternatively, this color configuration can be changed to better distinguish between different intensities and hues of the brown color. This was the case of the images used to measure blood vessels, which were switched from the RGB to the HSV color system, whose acronym comes from Hue, Saturation and Value of each pixel. In both cases and depending on the light intensity, pixels take a value which can range from 0 to 255 for each of the color channels, where 0 corresponds to the absence of light (black), and 255 corresponds to totally saturated (white) pixels.

B. Methods for image analysis

Depending on the staining to be measured and the availability of morphometric systems, different methods for image analysis were used:

- To use a commercial software for image analysis with established protocols which the user can adapt to the marker specific color. This was the case for GAGs. Aperio Image Scope, provided with an image analysis toolbox for positive pixel count was used on the whole scanned section (.svs format).
- To use a commercial software for image analysis which allows the user to configure personal image analysis protocols or *macros* capable of recognizing and describing the specific color and shape of the element of interest. Image Pro-plus v.6.0 was used to create *macros* to measure reticulin and collagen type I fibers.
- To design a personal application capable of solving commercial softwares lacks. In collaboration with the group VISILAB of the University of Castilla La Mancha, a specific software to measure lymph and blood vessels was developed (183) (**congress 5**).

C. Validation of the techniques

Artifacts such as calcifications, necrosis, non-tumor areas, fat, precipitates, etc... were excluded from the analysis. Structures

belonging to the tumor tissue, such as huge fibrous trabecules, big nerves, etc... were also excluded when substantially altering the measurements. The assessment of the robustness was done by:

- Subjectively validating, by at least two researchers, the results of the application of differentially customized algorithms, through the observation of the resulting segmented images.
- Performing a comparison between the results of the application of the algorithms on images coming from different methods of image capture: a photomicroscope and a slide-scanner. This test was only performed for reticulin fibers, given the higher complexity of this analysis compared to that of GAGs or Collagen type I (**congress 4**).
- Comparing the results of the application of the two customizations of the same algorithm on the same images. The algorithm was customized differently trying to be as accurate as possible by maintaining the size values and changing the RGB color ranges (**congress 4**).
- Comparing the hand-selected blood vessels and the AngioPath algorithm selection for the blood vessels on the same images, to calculate the sensibility and specificity of the algorithm.
- In all cases, the algorithms were validated using a preliminary pool (n=96 samples) of tumor and control tissue images and comparing the results with the subjective assesment of the cylinders by a pathologist. Non-tumoral samples were also used as controls of proper measurements (**table 13**).

- Validating, by three researchers, the adequacy of the results, once the algorithms were considered adequate and accurate and all the measurements were performed.

Table 13: Description of the different non-tumoral samples used as control samples.

Tissue	Scaffolding	Vascular system
Kidney	Loose. (more reticulin fibers for kidney; more GAGs for salivary gland)	Mostly capillaries* (+ arterioles, highly vascularized)
Placenta		
Salivary gland		
Muscle	Loose in endomysium; Dense in perimysium	
Liver	Reticular	Mostly sinusoids (+ venules and arterioles)
Spleen		

* Capillary networks are mainly terminal in the kidney and plexiform in the remaining structures

D. Summary of the methods and process of image analysis

The different methods used are summarized in **table 14**.

Table 14: Summary of the methodology used for the different components of the ECM.

Marker	Staining	Software	Algorithm
GAGs	Alcian blue HC	Image Scope	Positive Pixel Count
Reticulin fibers	Gomori HC	Image Pro-plus	Self-configured macros
Collagen type I fibers	Masson’s trichrome HC		
Elastic fibers	Orcein HC	-	-
Blood vessels	CD31 IHC	AngioPath	

HC: Histochemistry, IHC: Immunohistochemistry. All sections have been digitized with Aperio Scan Scope XT.

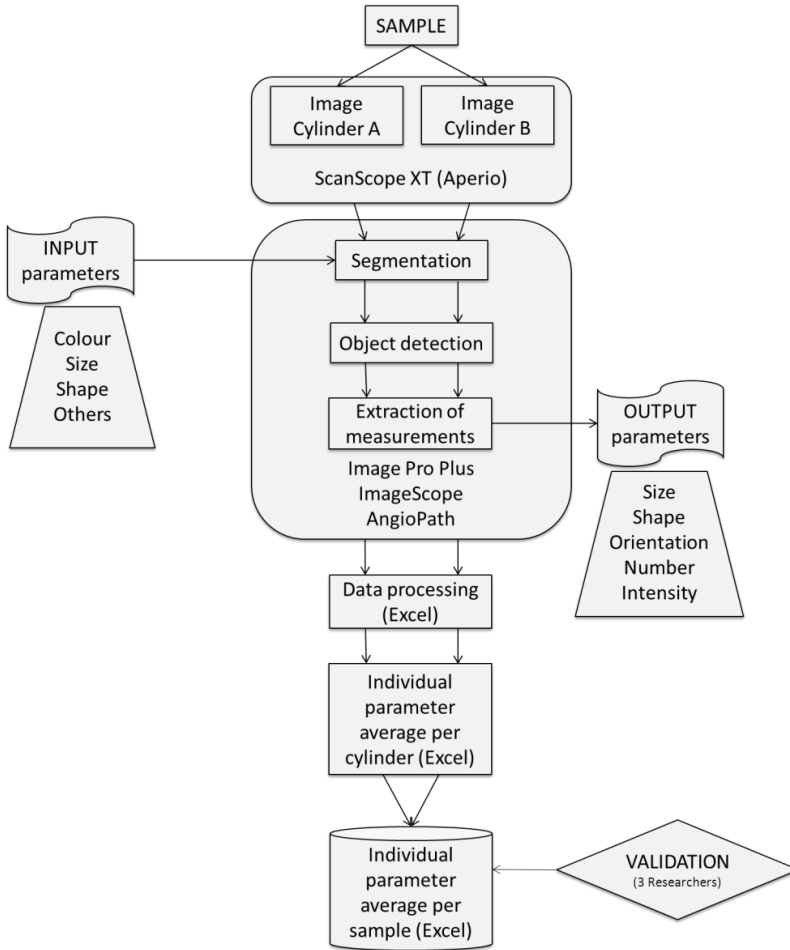


Figure 16: Flowchart showing the multi-resolution neuroblastoma image analysis system. Images belonging to different samples stained with different markers have been quantified by image analysis following a common process including segmentation (differential recognition of the staining) with specific input parameters for each marker and method and extraction of some given parameters. Adapted from Tadeo *et al.* (184).

2.5.2. Algorithm for the fundamental substance: GAGs

Each cylinder was analyzed individually with Aperio Positive Pixel Count algorithm on Aperio ScanScope software by selecting each cylinder outline in the whole section image. This algorithm was used

with the default parameters and counted the number of pixels belonging to a given staining intensity, being the intensity of each pixel the average between the values of red, green and blue (RGB) intensities. It recognizes Alcian blue stained pixels which have average intensities over 221. Nuclear fast red stained pixels were detected with weak, middle and strong intensities, painted in yellow, orange and brown following default parameters (**figure 17**). The remaining customizable parameters were set by default.

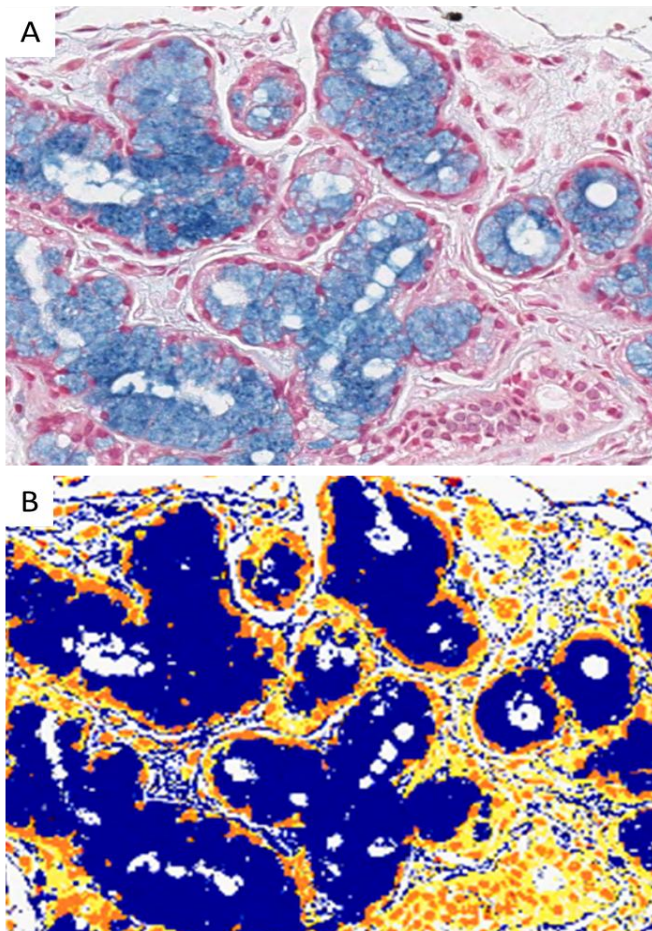


Figure 17: Segmentation obtained with the positive pixel count algorithm on a control tissue of a salivary gland. **A)** Original image. **B)** Mark-up image after segmentation. Alcian blue staining is marked in blue and nuclear fast red is marked in yellow, orange or maroon, depending on the intensity of staining.

Measurements obtained. The number of alcian blue stained pixels was multiplied by the area of a single pixel ($0.25 \times 0.25 \mu\text{m}/\text{pixel}$; see resolution of the image) to obtain the total alcian blue stained area per cylinder. Additionally, the outline of each cylinder was carefully selected to measure the area of analysis and then, the percentage (%) of alcian blue stained area per cylinder was calculated as area positive for alcian blue / total area of the cylinder $\times 100$. The % of GAGs per patient sample was calculated using the mean of the % of GAGs of all the cylinders belonging to the same case.

Assessment of the spatial distribution. The spatial distribution of the areas with GAGs was assessed subjectively by consensus of three researchers. Three patterns of distribution were recognized: homogeneous distribution when only one texture was recognized in the whole cylinder; diffuse heterogeneous when two intermixed textures were recognized; and focal heterogeneous when two textures were recognized but the positive area was zonal or focal (**figure 18**).

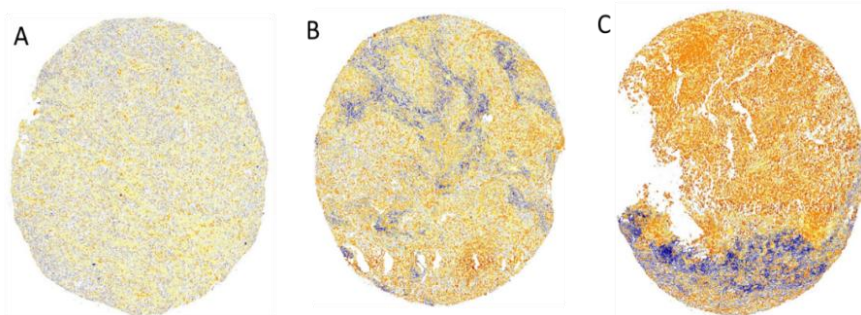


Figure 18: Different patterns recognized. In all cases, the marked-up image is shown, with the blue color being the alcian blue stained area and the yellow and orange areas being the cellular areas. **A)** Homogeneous distribution of the GAGs. **B)** Diffuse heterogeneous distribution of the GAG: two intermixed textures are recognized. **C)** Focal homogeneous distribution of the GAG: the cells area is homogeneously distributed and the GAG area is restricted to a focus at the lower part of the cylinder.

2.5.3. Algorithm for the fibrous component

Image Pro-Plus software (Media Cybernetics), which enables the design of specific algorithms, was used to analyze the fibrous component. An image of every cylinder was extracted in a separate JPEG-quality 80 image from the whole section scan.

A. Algorithm and measurement procedure of reticulin fibers

An algorithm capable of specifically detect the reticulin fibers and measure their amount, size and shape was customized. This algorithm proceeded as follows (**figure 19**):

1. Calibration of the image. The software recognizes the size of the pixels and converts the measurements in pixels to μm . The resolution of the scanned section is $0.25 \mu\text{m}$ per pixel.
2. Segmentation: detection of dark colored pixels with the red, green and blue ranges set at 0-119, 0-115 and 0-126 respectively.
3. Slight smoothing (3 points) of the selection and application of an 8-connect mode, where pixels that share only a corner are considered as a single object.
4. Small areas in nuclei were also stained in these ranges of color, as nuclear background, and are also detected. The ranges of some variables have been modified to discriminate the fibrous elements from the nuclear signal and generate a mask image or binary image, where the fibers are presented in white on a black background. For this purpose, small and round objects

have been excluded from the analysis (roundness under 3, area under $7.5 \mu\text{m}^2$, length under $8 \mu\text{m}$ and width under $1.5 \mu\text{m}$).

5. Once the fibers are properly recognized, the chosen parameters are measured and the information is incorporated to an excel file.
6. An image of the binary segmentation and a snapshot of the selected fibers marked-up in red on the real background image are also filed for further review.
7. The previous process gives us the total stained area. Then, we measure the tissue area to know the % of stained area. For this purpose the image is blurred to eliminate tissue nuances, a segmentation is carried out to differentiate the tissue signal from the background (absence of tissue) by selecting the red, green and blue ranges of 0-181, 0-178 and 0-172, respectively. Unspecific signals are eliminated by excluding small areas (under $5000 \mu\text{m}^2$), and the area of the cylinder is saved in an excel file.
8. A calculation is done to know the % of stained area corresponding to the reticulin fibers as total stained area*100/cylinder area.

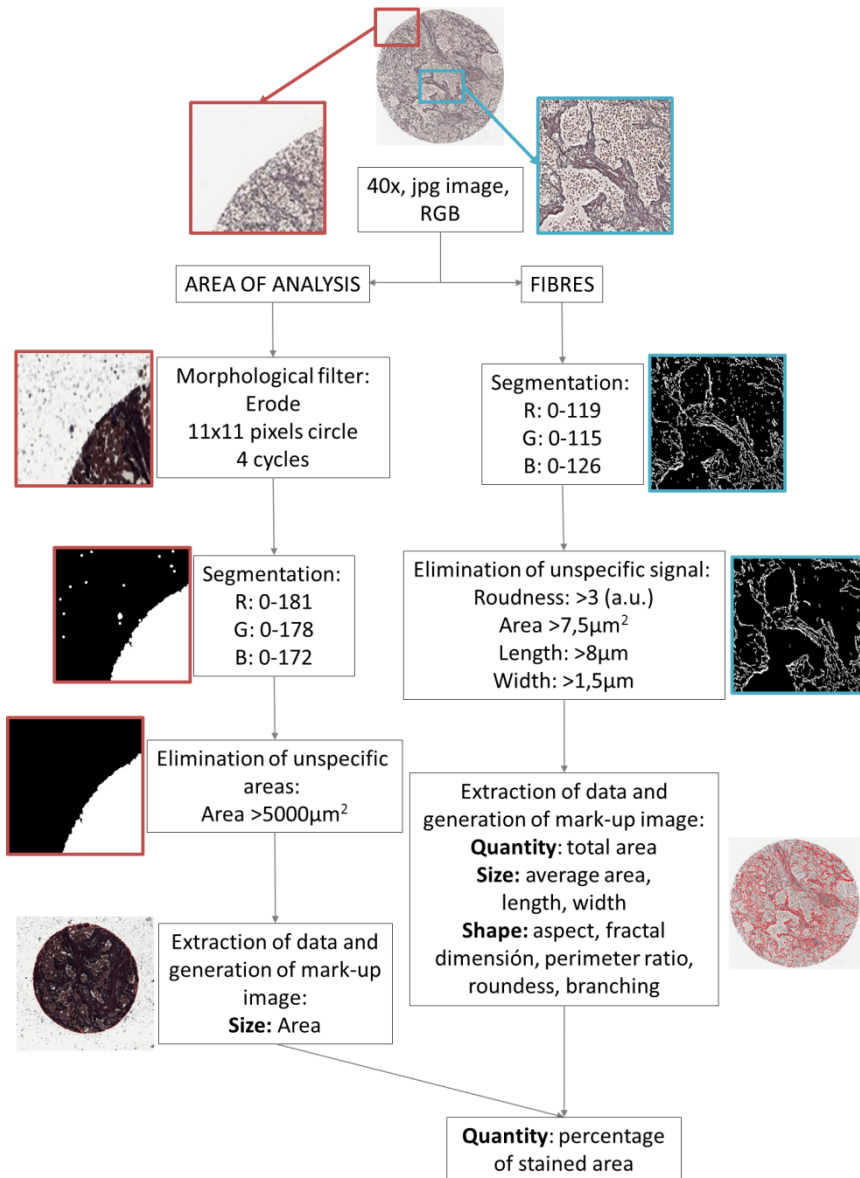


Figure 19: Criteria used for the segmentation and measurement of the reticulin fibers.

An example of the segmentation process in a control tissue (kidney) is provided by **figure 20**.

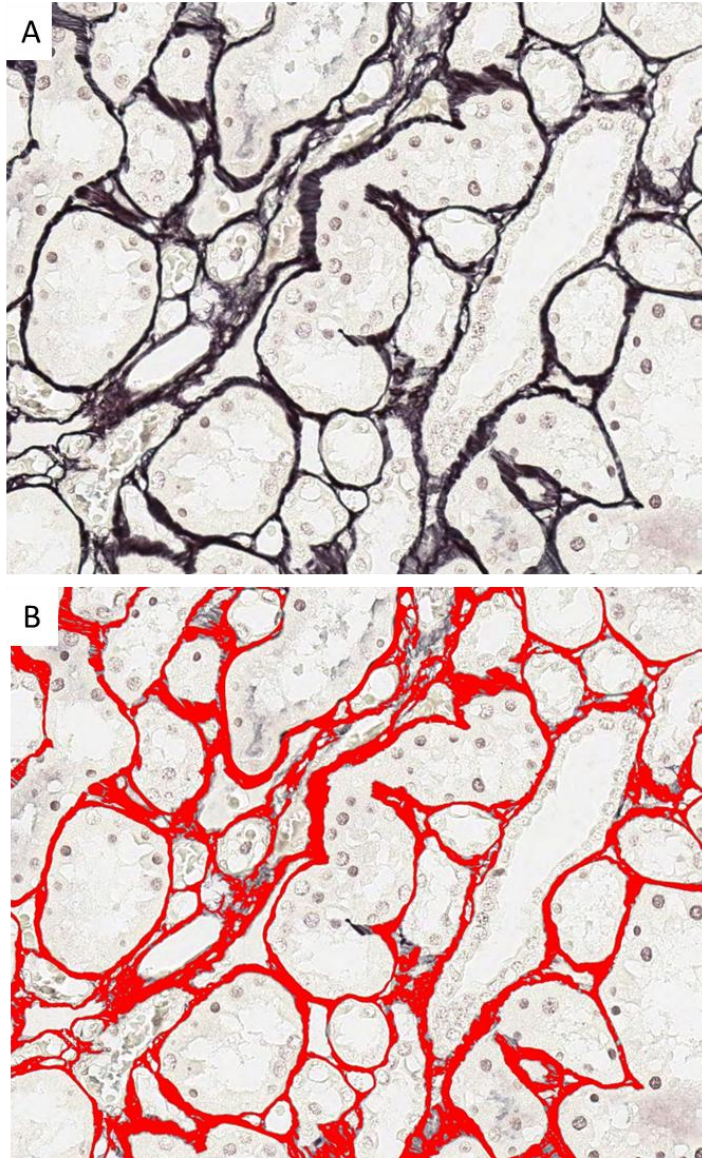


Figure 20: Segmentation process on a control cylinder containing kidney tissue. **A)** Original image. **B)** Image after segmentation. The reticulin fibers recognized by the algorithm are marked-up in red.

Measurements obtained. Eleven parameters were measured to be able to describe the quantity of the fibers as well as the size and the shape of every fiber.

- The quantity parameters measured were the density of reticulin fibers (number of fibers per mm^2) and the total area occupied by the fibers which was converted to % of stained area in combination with the cylinder area.
- The size parameters measured were:
 - width (μm): diameter along the minor axis of the object.
 - length (μm): diameter along the major axis of the object.
 - area (μm^2): area of the object.
- The shape parameters measured were (**guide for the interpretation of the reticulin fibers measurements, figure 21**):
 - aspect: ratio between the major axis and the minor axis of an ellipse equivalent to the object. It gives an idea of how ovoid the fibers networks are (length vs. width). A round object such as a wavy reticulin fiber network would have an aspect close to 1 whereas a straight line or an isolated reticulin fiber or a reticulin fiber network subject to tension would have a much higher aspect value. Aspect also provides information related to the predominance of isolated fibers or fiber networks. Moreover, a tissue where the majority of the fibers tend to be oriented in the same way, exerting greater strain, is related to a higher aspect value.
 - roundness: ($[\text{perimeter}^2] \div [4 \times \pi \times \text{area}]$). Empirically, roundness provides data regarding the degree of crosslinking of the fibers. It gives an idea of how deform or soft the fibers or fiber networks are. A less deform object (with low degree of crosslinking and deformity) would

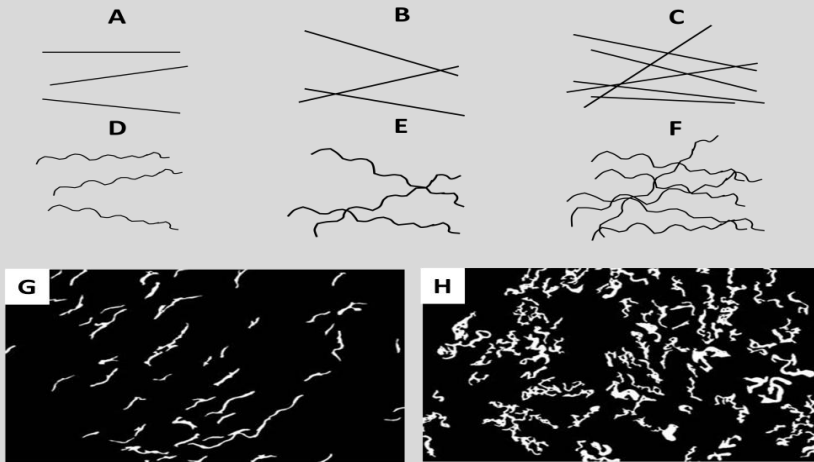
have a roundness close to 1 whereas, theoretically, a soft object (more subject to deformation) would have a higher roundness deviation.

- perimeter ratio: ratio of convex perimeter to real perimeter of the object, being convex perimeter the perimeter of the convex outline of each object. It reflects the irregularity of the fibers or fiber networks outline. The more the outline is irregular (wavy), the smaller the value is, varying from approximately 0.700 (irregular) to near 0.999 (regular). A value of 1 means a perfectly smooth outline.
- fractal dimension: the fractal dimension of the objects outline ranges from 1 to 2 and describes the amount of space and self-similarity of the structure. For example, a line exists in a single dimension and, therefore, has a fractal dimension of 1. On the other hand, a square exists in two dimensions and has a fractal dimension of 2. This parameter gives an idea about the disorganization or geometric complexity of the fibers networks: a fractal dimension of 2 represents the highest fiber mass and a value of 1 represents the most organized and porous ECM.
- branching: number of one-pixel-thick open branches. This parameter also gives an idea of the organization of the fibers forming scarce or extensive networks.

These parameters were measured for every fiber and then the average value was used to describe the characteristics of the fibers in a given cylinder. Finally, a second average value resulting from all the

cylinders representing the same sample was calculated to describe the general or final characteristics of the fibers in a given sample.

Guide for the interpretation of the reticulin fibers measurements:



Sample	Aspect	Roundness	Perimeter ratio	Fractal Dimension
A	21,0	7,2	0,998	1,07
B	2,5	15,4	0,990	1,10
C	2,1	14,1	0,974	1,21
D	12,6	8,1	0,973	1,12
E	2,1	21,4	0,965	1,16
F	1,9	16,2	0,938	1,26

Sample	Aspect	Roundness	Perimeter ratio	Fractal dimension	Branching
G	4,0	1,9	0,985	1,09	0,01
H	3,0	4,8	0,847	1,20	0,29

Figure 21: Examples of the shape parameters measurements. Two types of theoretical fibers outlines: **A-C)** straight or regular and **D-F)** wavy outline. Several degrees of crosslinking: **A, D)** No crosslinking, **B, D)** poor crosslinking and **C, F)** high crosslinking. Mark-up images (white represents the fibers) of reticulin fibers from tissue studied with **G)** regular outline without crosslinking and **H)** irregular and crosslinked fibers. Individual fibers of A and D are isolated and long and, therefore, their aspect (ovoid measurement) is very high. Fibers of figures B, C, E and F are counted as a single object which has similar width and length and, thus, their aspect decreases, being the most compacted and wavy networks more close to 1. Perimeter ratio, fractal dimension and roundness are closer to 1 when the fibers have smoother outlines, are more organized without or with scarce branching networks or there is less deformity and no crosslinking. The element with the highest deformity or the extensive fiber networks more irregular and messy (higher roundness, perimeter ratio and fractal dimension) is presumably the stiffest.

Assessment of the spatial distribution: Some characteristic patterns of distribution were recognized subjectively for the reticulin fibers (**figure 22**).

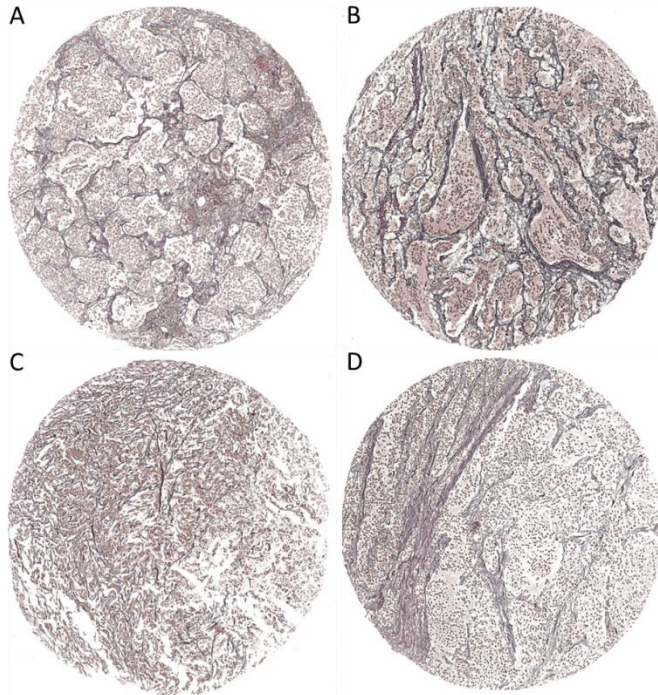


Figure 22: Representative samples of the four main subjective distribution patterns recognized for reticulin fibers. **A)** Organoid or glomerular pattern where the cells are grouped in roundish areas surrounded by fine reticulin fibers strands. **B)** Lobular or pear-like pattern where the cells are grouped in polygonal areas surrounded by thick strands of reticulin fibers. **C)** Reticular or network pattern where cells are arranged in an irregular manner forming rows and reticulin fibers form networks across them. **D)** Trabecular pattern where the cells are arranged forming regular and lineal areas flanked by more or less thick reticulin bundles.

The assessment of the distribution patterns which every cylinder exhibit became a very complicated task because of huge heterogeneity and subjective influence. Different approaches for the development of an algorithm to automatically classify the samples were performed in collaboration with the “Instituto de Aplicaciones de

las Tecnologías de la Información y de las Comunicaciones Avanzadas” (ITACA) of the Polytechnic University of Valencia which allowed the classification of every sample into the major different patterns of distribution recognized for the reticulin fibers. These approaches were:

1. Subjective assessment of the pattern of 96 different biopsies by three researchers. The pattern was assigned individually and then a consensus has been found.
2. Non-supervised classification or clustering of all the cylinders (n=1135): Supposing that the morphometric measurements characterizing the fibers are related to the patterns described, all the morphometric variables were combined, excluding the most influencing ones by principal component analysis (PCA). Euclidean distance and *Ward's* clustering method were used. The images of a specific cluster were validated by comparing them with the subjective assignation of the patterns (**congress 7**).
3. Automated classification of the images corresponding to the subjectively classified 96 samples, based on extracted image dictionaries following three steps: dictionary learning, classification method and performance test (**figure 23**) (**congress 8**).
 - Dictionary learning: A global dictionary was trained for all the images together. Then, a local dictionary was trained for every individual image. Both were trained using a KSVD algorithm. Finally, we obtained a signature for every image, comparing both dictionaries, which was associated to the subjective pattern previously assigned.

These signatures were reduced using a ReliefF algorithm to increase its discriminative power (uninformative characteristics were removed). We therefore obtained a reduced signature set with each signature associated to a reticulin fiber spatial distribution pattern.

- Classification method: To classify a given image, the previous steps were performed to obtain the image signature which was compared to the reduced signature set by calculating the Euclidean distance, giving rise to a series of distances associated to a potential class. We chose the three reduced signatures from the set of signatures more similar (smaller Euclidean distance) to the resulting signature of the image analyzed, each of the three being associated to a pattern. The major distribution pattern was assigned to the image, using the K-nearest neighbor algorithm.

- Performance test: The performance of the model was tested by a leave-one-out cross validation strategy.

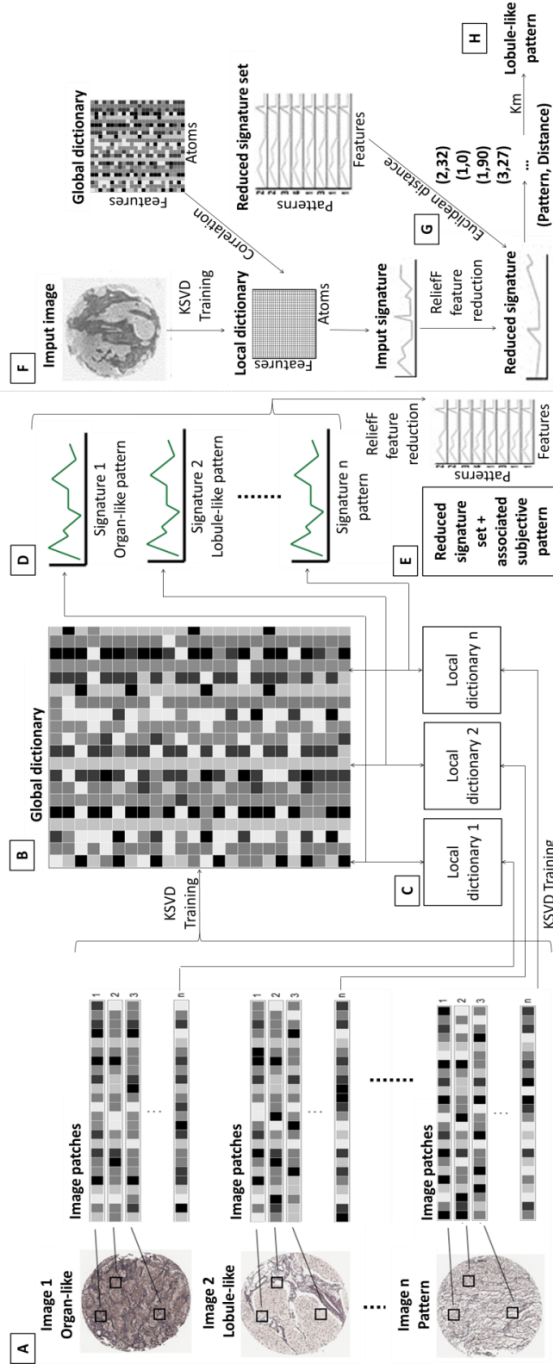


Figure 23: Automated classification of the reticulon fiber images depending on their distribution pattern based on dictionary training. **A)** Image pool with known subjective spatial distribution pattern where image patches have been extracted to form feature dictionaries. **B)** Global dictionary features extracted from the whole image pool. **C)** Local dictionaries corresponding to the individual images. **D)** Signatures extracted for each individual image by comparing both local and global dictionaries, which is associated to their known subjective pattern. **E)** The signatures are reduced with a Relief feature reduction algorithm to create a reduced signature set with associated subjective patterns. **F)** To classify a new image, a new local dictionary is extracted and compared with the global dictionary to obtain the input image signature, which is reduced. **G)** The reduced signature generated is compared to the reduced signature set associated to subjective distribution patterns and the similarities are calculated. The three most similar to the new reduced signature from the reduced signature set are found and the major distribution pattern is assigned to the new image.

B. Algorithm and measurement procedure of collagen fibers.

In the same way as for reticulin fibers, an image of every cylinder was extracted in a separate JPEG-quality 80 image from the whole section scan to be able to work with Image Pro-Plus software which was used to design an algorithm capable of specifically detect the bundles of collagen type I fibers. This algorithm proceeds as follow **(figure 24)**:

1. Calibration of the image. The software recognizes the size of the pixels and converts the measurements in pixels to μm . The resolution of the scanned section is $0.25 \mu\text{m}$ per pixel.
2. Color contrast enhancement to better distinguish different blue hues set at brightness 68, contrast 81 and gamma 10.
3. Detection of dark blue colored pixels with the red, green and blue ranges of 0-17, 0-90, 255-255, respectively.
4. Slight smoothing (3 points) of the selection and application of an 8-connect mode, where pixels that share only a corner are considered as a single object.
5. As Masson's trichrome not only stains type I collagen, but also reticulin fibers, and some unspecific elements, very restrictive characteristics of size and color must be applied. Following the reticulin fibers settings with a change in the width parameter, round objects (roundness under 2), small fibers area under $7.5 \mu\text{m}^2$, length under $8 \mu\text{m}$ and a width under $10 \mu\text{m}$ have been excluded. Only fibers forming big bundles are thus detected.

6. Once the fibers are properly recognized, the chosen parameters are measured and the information is extracted to an excel file.
7. An image of the binary segmentation or mask and a snapshot of the selected fibers marked-up in red on the real background image are also filed for further review.
8. The previous process gives us the total stained area but we need to measure the tissue area to know the % of stained area. For that purpose the image is blurred to eliminate tissue nuances, segmentation is carried out to differentiate the tissue signal from the background (absence of tissue) by selecting the red, green and blue ranges of 0-181, 0-178 and 0-172, respectively. Unspecific signal are eliminated by excluding small areas (under $5000 \mu\text{m}^2$) and the area of the cylinder is extracted and saved in an excel file.
9. A calculation is performed to know the % of stained area corresponding to the collagen type I bundles.

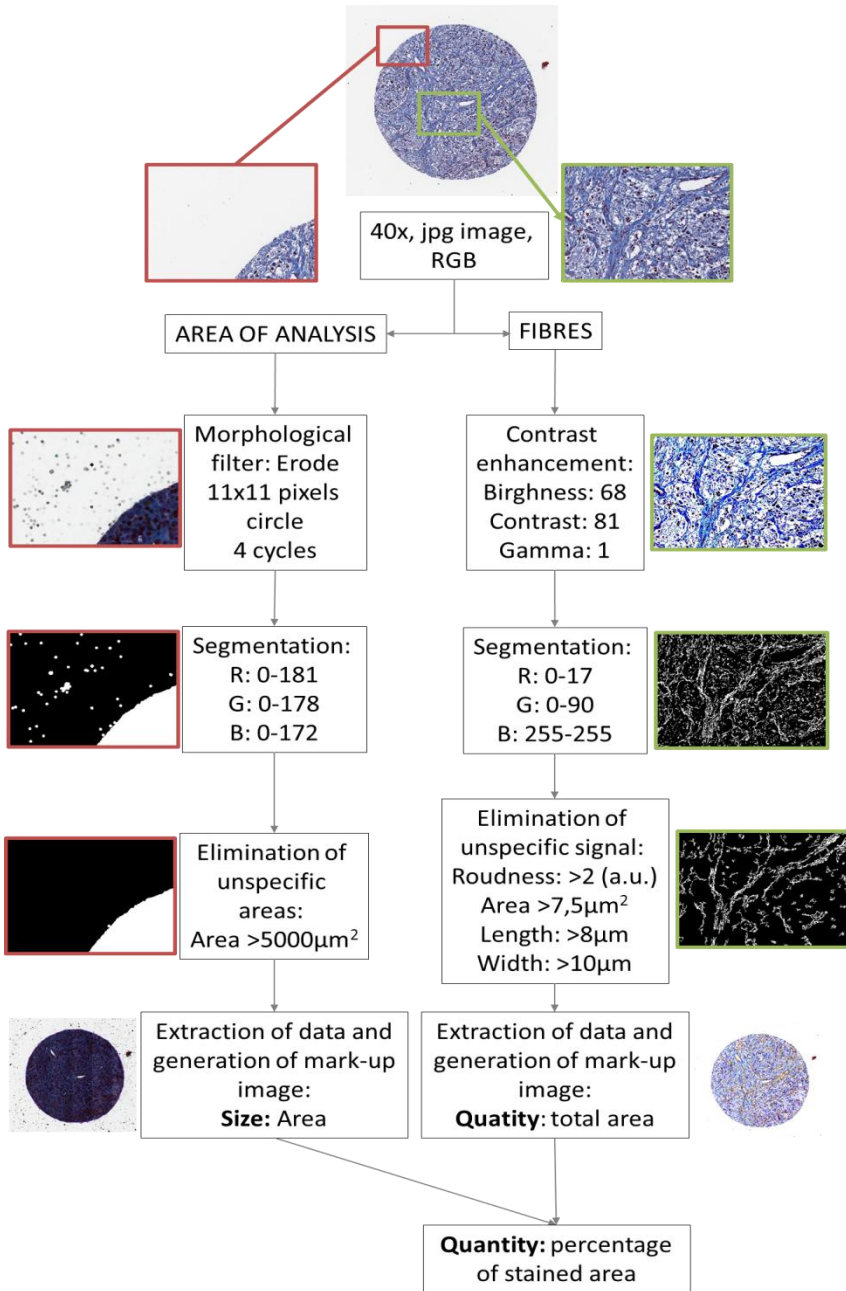


Figure 24: Criteria used for the segmentation and measurement of the collagen type I fibers.

An example of the segmentation process in a control tissue (striated muscle) is provided by **figure 25**.

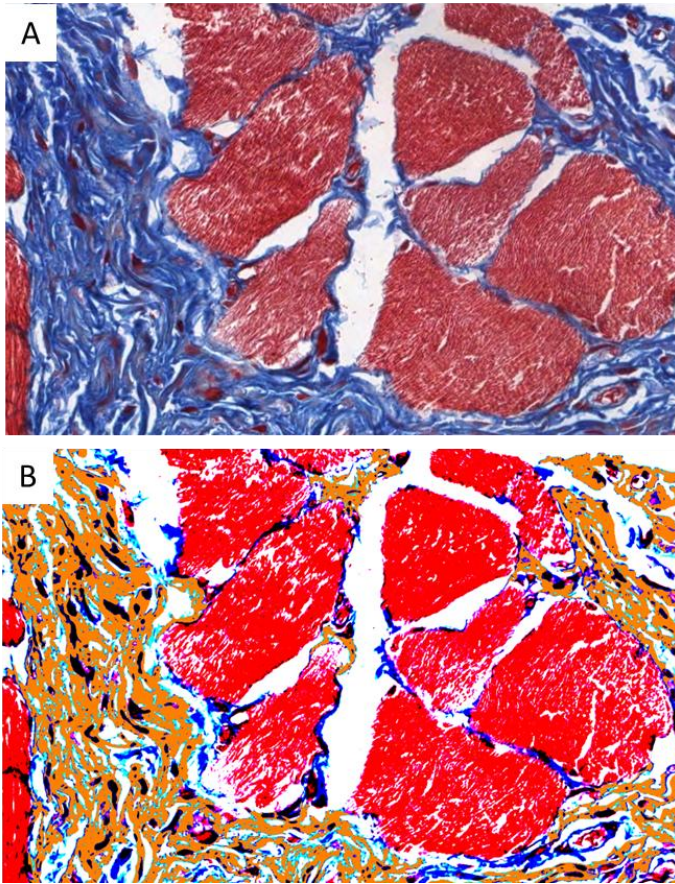


Figure 25: Segmentation process on a control cylinder containing striated muscle tissue. A: Original image. B: Image after segmentation. The collagen type I fibers recognized by the algorithm are marked-up in orange.

Measurements obtained. As the segmentation was done under strict conditions, the continuity of some fibers and thus the accuracy of the shape and size parameters was lost. Then, the parameter calculated for collagen type I fibers was the total area occupied by fibers which is translated to % of stained area in combination with the cylinder area.

C. Measurement procedure for elastic fibers

No algorithm was used. The amount of elastic fibers was observed by three investigators who subjectively assessed the % of stained area in 96 biopsies, following the score shown in **2.4. "Subjective assessment"**.

2.5.4. Algorithm and measurement procedure for the vascular component

The algorithm was developed in collaboration with the VISILAB group of the engineering school of the University of Castilla La Mancha. The steps are described hereafter but further information is provided in Fernandez-Carrobles MM. *et al*, 2013 (183, 185) (**congress 5**).

Images of the single cylinders were extracted in TIFF format, at 40x magnification, with a size varying between 6200 and 7300 pixels. Experiments were performed on a Dual Xeon 3.2 GHz and 2 GB RAM. The method has been implemented by the research group using C/C++ and IPP and OpenCV libraries for image processing. Also, the Intel TBB library has been used for parallelization of the algorithms. The algorithm developed for the segmentation of the blood vessels consists of two parts: segmentation based on HSV color model and a radial algorithm (**figure 26**).

- Segmentation based on HSV color model

Closed vessels with and/or without obvious lumen can be detected through their continuous brown color. The main aim of this

algorithm section is the brown color segmentation through an HSV color model. This part of the algorithm proceeds as follows:

1. Conversion of the cylinder RGB image to HSV color model. This conversion permits a more accurate segmentation of the brown color to extract the vessels contour.
2. Extraction of the S and H channel from HSV image. S channel stands out most brown shades and ground staining but this is not enough. For this reason H channel is also used.
3. Application of a binary inverted thresholding to S channel image and of a binary thresholding to H channel image. The values of the image pixels are compared to our brown (H and S) accepted threshold. The threshold applied to the H channel is always 20 but the inverted threshold applied to the S channel is 10 for weak stains, 20 for normal stains, and 30 for strong stains. Other values can be chosen for specific stains. We obtain a binary image or mask where the pixels of interest (under the threshold value) are marked in black on a white background.
4. Application of a logical OR and NOT operator to both binary images. The first segments brown color and erases the rest of the colors. The second is needed to highlight the contour vessels.
5. Elimination of small artifacts of the input image and joining close structures. Erode and dilate operations of 2 and 4 iterations respectively are performed in the image. Erosion, $E(x,y)$, is done by means of a convolution where the minimum value of the neighborhood pixels are selected, thus reducing the number of false positives. Dilation is the opposite operation of erosion.
6. Application of a contour finding operator. This algorithm is used to detect the vessel contour pixels that divide each segment of

the image, allowing their storage through sequences and in a way such that they can be later manipulated individually. This operator is applied to images created by a binary thresholding or a Canny operator.

7. Discard false positivities such as some macrophages, which could be detected as small vessels. To remove these false positivities only the vessels whose width is higher than 20 pixels (4.6 μm) were selected.

- Radial algorithm

This algorithm finds the vascular lumen and their brown endothelial surrounding cells and, then, the unconnected parts are joined together. Once the opened vessels are closed, the morphometric measurements are calculated. The algorithm proceeds as follow:

1. Extraction of the green channel from the RGB image. Green channel helps to better distinguish the different vascular lumens. Besides, the use of a single channel can reduce the computational time and also reduce the RAM memory used to process images.
2. Application of a binary thresholding to extract vascular lumens from the image. The threshold value was established at 236, after statistical analysis of the image histogram.
3. Application of a combination of erode (3 iterations) and dilate (2 iterations) operations to join large structures and remove the smaller structures from the previous binary image.

4. Filling of those closed contours having internal holes smaller than 400 pixels or 92 μm minimum size.
5. Performance of a second erosion of 1 iteration creating space between the vascular lumens and the vessel membrane.
6. Radial analysis consists of computing the normal direction for each vascular lumen point on the border with a possible vessel point. Then, the radial direction is used to check if there is any part of the membrane vessel nearby within a radio of 3 μm . To this end the endothelial cells detected in the previous algorithm are also used. Notice that a dilatation of 2 iterations is performed to the endothelial cells to avoid overlapping with the vascular lumen. A vessel is considered valid depending on the ratio of checked pixels that actually belong to the membrane vessel. The ratio is adjusted depending on the length of the vascular lumen contour, being equal to 60%, 50%, and 40% for small, medium, and big vessels, respectively. Small vessels are those with a vascular lumen contour length lower than 12.42 μm , medium vessels between 12.42 μm and 31.05 μm , and large vessels greater than 31.05 μm . **Figure 4** shows different vessels classified by size. Once a pixel is considered as a valid vessel a linear interpolation is done to close the open vessels.
7. Application of a contour finding operator to find the vessels contours of radial algorithm.
8. Removal of the small artifacts.

- Extraction of measurements

At this point, the algorithm provides two images composed of closed and open vessels. In the following steps both images are joined together and the morphometric measurements are calculated.

1. A binary thresholding is applied on the previous two images. This thresholding is performed in order to obtain a binary image with only the vessel contours; therefore the threshold value is 0.
2. Application of a logical AND and NOT operator to both images to combine into the same image those vessels segmented by the HSV color model and those obtained by the radial distribution analysis and to invert the image and highlight the contour vessels.
3. A contour finding algorithms applied to find the vessel contours of the final image. This procedure is similar to point (7) of the color-based segmentation algorithm and the radial analysis.
4. For each valid vessel, its position by means of its center pixel and twelve morphometric measurements are given. Morphometric measurements are also provided for each group of vessels according to their height.
5. All morphometric measurements are saved in an Excel format file and the final image with the vessel segmented and labeled is stored in a TIFF format file.

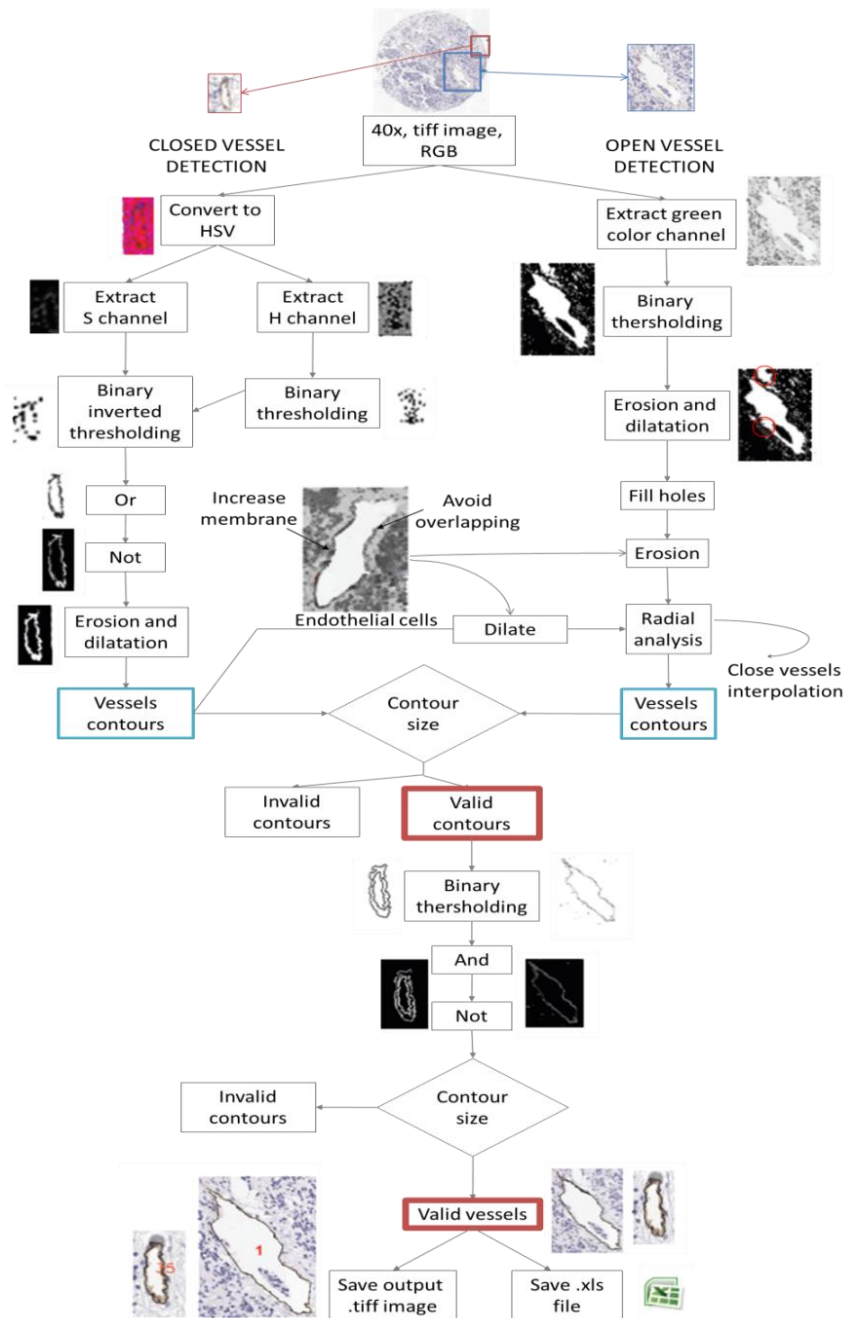


Figure 26: Vessel segmentation process. Division of the algorithm in two steps: the segmentation based on HSV color model (left) and then the radial algorithm for joining opened vessels (right).

An example of the segmentation process is provided in **figure 27**.

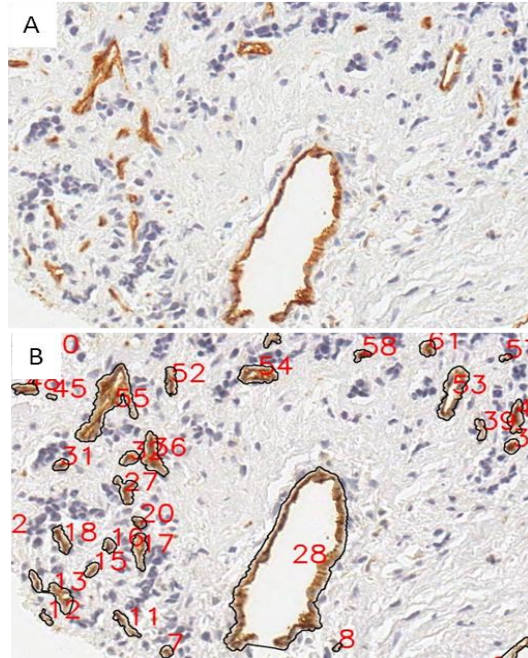


Figure 27: Segmentation process on a NB sample immunostained with CD31. **A)** Original image. **B)** Image after segmentation. Note that the big blood vessel with an interrupted staining of the endothelial cells surrounding the vascular lumen has been closed, thus providing morphometric measurements.

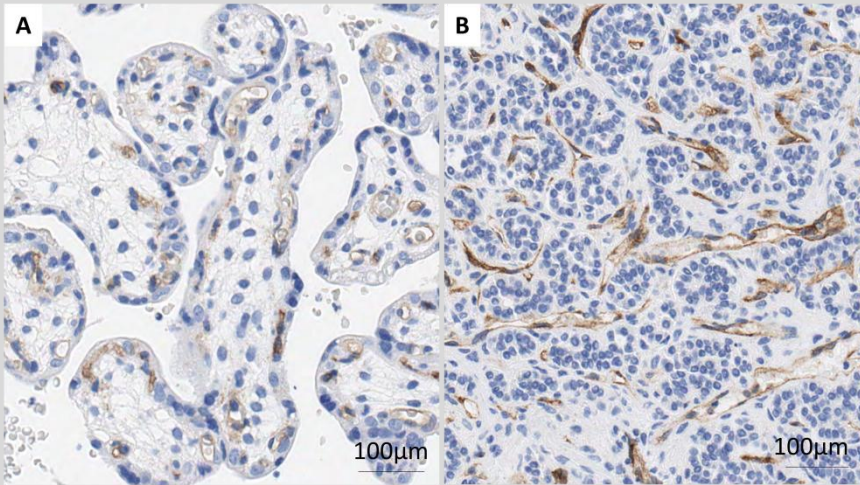
Measurements obtained. All the vascular vessels recognized are classified in 6 categories corresponding to different types of vessels, differentiated by their largest diameter or length: capillaries or vessels between 5-15 μ m; post-capillary venules and metarterioles with 15-20 μ m; sinusoid-like blood vessels, collecting venules and end arteries with 20-50 μ m; venules and arterioles with 50-200 μ m; veins and arteries with >200 μ m; and measurements corresponding to total vasculature. Note that the measurement used to distinguish between the different subgroups is the length instead of the width. Such decision was made to avoid misclassifications due to collapsed blood

vessels. For each of the categories, the next measurements were obtained (examples of the measurements in two different control tissues are provided in **guide for the interpretation of the blood vessels measurements, figure 28**):

- The localization of every vessel is provided as x and y coordinates, to be able to remove and locate any artifact or a given vessel measurement.
- The quantity parameters are:
 - Vessel density: number of vessels of each of the 6 categories (per mm^2 , in combination with the cylinder area).
 - Total area occupied by vessels which is converted to % of stained area in combination with the cylinder area.
 - For the different subgroups of blood vessels, the relative density and relative area of vascularization in a given subset with respect to the total vascularization is calculated as two new quantity parameters. Note that these values are obtained from the average of all the individual samples and therefore, the relative area or number of vessels distributed in the different size categories does not equal 100%.
- The size parameters measured were:
 - area (μm^2): area of the object
 - length (μm): diameter along the major axis of the object.
 - width (μm): diameter along the minor axis of the object.
 - perimeter (μm): perimeter of the object.
- The shape parameters measured were:

- aspect: ratio between the major axis and the minor axis of the best-fitting ellipse equivalent to the vessel contour. It gives an idea of how ovoid/flattened the vascular vessel is (length vs. width). A round object would have an aspect of 1 whereas an elongated vessel would have a much higher aspect.
- roundness: $([\text{perimeter}^2] \div [4 \times \pi \times \text{area}])$. It gives an idea of how deform the vascular vessel is. A round object would have a roundness of 1 whereas a deform object would have a higher roundness.
- perimeter ratio: ratio of convex perimeter to real perimeter of the object, being convex perimeter the perimeter of the convex outline of each object. It reflects the irregularity of the vessels outline.
- deformity (μm^2): $[\text{area of the convex outline of each vessel} - \text{area of the vessel}]$. The vessels with the highest irregular contour have the highest difference between the convex outline area and the vessel outline area and have the highest deformity value.
- shape factor: Its value is affected by the object's shape but independent of its dimensions. It represents the degree of deviation (value >1) from the circle shape (value = 1).
- Vertices or Branching: Calculates the approximate contour polygon with less distance between vertices using the Douglas-Peucker algorithm (186) and provides the number of vertices, which can be assimilated to the dregree of branching of the vessel.

Guide for the interpretation of the blood vessels measurements:



C	Total Vessels	Total Area (µm ²)	Rel. Area (%)	Area (µm ²)	Length (µm)	Width (µm)	Per. (µm)	Aspect	Round.	Per.Rat.	Deform.	Shape factor	Branch.
5_15	349	10875	41	31	9	5	27	2	2	0,867	107	0,3	2,4
15_20	46	3753	14	82	17	9	52	2,2	2,8	0,821	473	0,45	3,3
20_50	46	9160	34	199	28	14	98	2,4	4,1	0,732	1607	0,66	4
0_200	7	2771	10	396	66	15	190	5,3	7,5	0,751	4887	8,94	4,1
TOTAL	448	26559	100	59	13	7	39	2,1	2,4	0,847	374	0,49	2,7

D	Total Vessels	Total Area (µm ²)	Rel. Area (%)	Area (µm ²)	Length (µm)	Width (µm)	Per. (µm)	Aspect	Round.	Per.Rat.	Deform.	Shape factor	Branch.
5_15	370	14013	11	37	9	5	28	1,9	1,8	0,872	106	0,23	2,5
15_20	109	9683	8	88	17	8	51	2,3	2,5	0,825	380	0,34	3,2
20_50	214	47385	40	221	30	13	100	2,6	3,8	0,763	1711	1,28	3,9
0_200	51	45336	38	888	80	25	283	3,7	8,4	0,666	11995	15,92	5,3
TOTAL	745	118563	100	159	21	9	70	2,3	2,9	0,819	1500	1,63	3,2

Figure 28: Examples of vessels measurements in two control tissues. **A)** Placenta with abundant capillaries. **B)** Adrenal gland with sinusoid-like blood vessels. **C)** Data obtained from the placenta analysis. **D)** Data obtained from the adrenal gland analysis. When looking to the shape parameters, we can observe that all of them rise when changing the vessel group, except the perimeter ratio parameter which decreases. Bigger vessels are more irregular. Moreover, the total values of placenta vessels are smaller (more regular) than the total values of the adrenal gland vessels, which is coherent with the type of vessels found in both tissues. Placenta has the highest % of vessels (41%) in the capillary class (5-15µm), whereas adrenal gland has the majority of its vessels (40%) in the sinusoid-like class (20-50µm). Rel.: relative; per.: perimeter; round.: roundness; per. rat.: perimeter ratio; deform.: deformity; branch.: branching.

These parameters were measured for every vessel and then the average value was used to describe the vessels of different types in a given cylinder. Finally, a second average value resulting from all the cylinders representing the same sample was calculated to describe the vessels in a given sample.

2.6. Statistical analysis

All statistical analyses were performed using the software SPSS v. 22. In all cases, only p-values <0,05 were considered as statistically significant. We made a distinction for clinical and biological variables between the INRG groups and our groups, in such a way that, for example, although we have the information about *MYCN* states gain and heterogeneous amplification, these states are considered as MNNA according to the INRG classification. Following this argument, our data were grouped as follows:

- Stage INRG: This variable was not grouped and, thus, L1 vs. L2 vs. M vs. Ms were used.
- Age INRG: ≥ 18 months vs. <12 months + 12-18 months
- Histopathology INRG: GN + iGNB vs. (nGNB, NB) d vs. (nGNB, NB) u/ps vs. NB NOS.
- *MYCN* INRG: Hom MNA vs. Het MNA+G+Het G+MNNA
- 11q INRG: D + Het D vs. ND
- Ploidy INRG: Diploid + tetraploid (=diploid) vs others (=hyperdiploid).
- Risk group INRG: Very low risk + low risk + intermediate risk vs high risk.

2.6.1. Validation of the morphometric technique.

Different steps were followed for the assessment of the robustness:

- The comparison between the results of different methods of image capture and between the results of the application of the same algorithm customized differently was carried out for reticulin fibers. Bivariate correlation was used with the Pearson's correlation, with the following possible interpretations: $r=0.01$ to 0.19 : no or negligible relationship; 0.20 to 0.29 : weak positive relationship; 0.30 to 0.39 : moderate positive relationship; 0.40 to 0.69 : strong positive relationship; 0.70 or higher: very strong positive relationship.
- A Receiver Operating Characteristic (ROC) analysis was performed to test the sensibility and specificity of the blood vessels algorithm, comparing the hand-selected blood vessels and the algorithm selection on the same images. Sensitivity is the probability of detecting the marker when it is stained and specificity is the probability of not detecting the marker when it is not stained.
- The subjective categories assessed by a pathologist and the morphometric measurements were compared using non-parametric test for independent samples (Kruskal-Wallis or Mann-Whitney).

2.6.2. Validation of the clinical and biological data.

To validate our data with the previously described risk of relapse pre-treatment classification of the INRG (2), all variables taking part in the INRG risk classification were related with EFS and OS. Only the primary biopsies with complete information for all the variables and a minimum follow-up time of 3 months (263 cases out of 458) were considered. Given that in the INRG classification ploidy has only been found to be relevant in non-amplified neuroblastic tumors of patients with advanced disease under 18 months of age at diagnosis, and that this variable accounts for a relatively high number of unknown cases which would decrease the total number of cases analyzed, this feature was not taken into consideration for this first approach.

A. Description of the clinical, genetic and survival variables

The distribution of our data, grouped following the INRG pre-treatment risk stratification guidelines, was compared with the published one. Descriptive statistics such as mean, confidence interval and standard deviation were calculated for EFS and OS.

B. Univariate survival analysis

Survival analyses were performed with Kaplan-Meier estimator and Log-rank with EFS and OS.

C. Multivariate survival analysis

Those variables showing significant statistical relationships, with a significance level of 95%, underwent multivariate analysis using Cox regression analysis with the stepwise forward (Wald) method, to know which one of them was the most influencing.

2.6.3. Relationship between the quantity and the distribution of the ECM elements studied and the clinico-biological features of the tumors.

A. Description of the variables

The count, mean, median, standard deviation, minimum and maximum were provided, using the data base including all the patients biopsies (n=458). Categorical variables were compared with contingency tables and Kappa concordance index with the following possible interpretations: <0.20: negligible; 0.21-0.40: minimal; 0.41-0.60: moderate; 0.61-0.80: Good; 0.81-1.00: excellent.

B. Favorable and unfavorable ECM histologic patterns: univariate analysis with INRG clinical and biological variables

Given that our continuous numerical variables did not follow normal distributions, they were related to categorical variables using a non-parametric test for independent samples (Mann-Whitney for variables with two categories or Kruskal-Wallis for variables with more than two categories). Finally, categorical morphometric variables

(distribution patterns) were compared with categorical clinical and genetic variables using Chi-square test and contingency tables. The total database was also used.

2.6.4. Survival analysis:

To know whether the ECM elements morphometric variables affected survival or not, two approaches were made. First, we used multivariate analysis to know if they could help to improve the INRG pre-treatment risk stratification in combination or in addition to the parameters with known prognostic value. Second, we investigated inside the high risk patients group with known poor prognosis, if these new morphometric variables of the studied ECM elements could provide a new sub-classification of these patients who could benefit from novel therapeutic agents against these elements.

A. Multivariate analysis

The influence of the variables on OS and EFS was checked using Cox regression analysis with the stepwise forward (Wald) method. In it, Wald value and p-values indicate the strength of the relationship between the factor tested and survival. In addition, B value indicates the sense of the relationship (positive or negative). For this purpose, only the patients with complete information for all the variables (clinical, biological and morphometric) were used. New morphometric parameters were related to survival on their own and in combination with the INRG prognostic factors. The major value as prognosis factor will be assigned to those variables showing a statistically significant relationship with prognosis in combination with all INRG variables. Those variables showing a statistically significant relationship with

prognosis in combination with all INRG variables excluding stage will have a lower prognostic power than the previous. Finally, the morphometric variables related with prognosis when tested on their own can not be considered as having prognostic value.

B. Study of the high risk group

All morphometric variables were dichotomized using mainly the median value and, in some cases, the first or third quartile to perform survival analysis with Kaplan-Meier and log-rank test in the high risk patients group.

2.6.4. Study of ECM elements after treatment and in other samples

A. Description of the variables

The count, mean and standard deviation, using the total data base including all the primary and non-primary biopsies as well as peritumoral tissue, other tumors tissue and non-tumoral tissue, was provided. For this particular purpose and in order to simplify the analysis, only the amount of GAGs, fibers and blood vessels were taken into account (% of stained area for GAGs and fibers and density - number of vessels/mm²- for blood vessels).

B. Univariate analysis

Given that our continuous numerical variables did not follow normal distributions, they were related to categorical variables using a non-parametric test for independent samples (Mann-Whitney or Kruskal-Wallis). The total database was also used. As the number of

cases in some of the categories was low, the analysis was performed between the main groups.

2.7. Topological integration of reticulin fibers and blood vessels regarding neuroblastic cells

The correlative topology and organization of the ECM elements that have been studied can be determined through the Graph Theory mathematical analysis consisting in mathematical structures used to model pairwise relations between objects. For this purpose, a preliminary assay in collaboration with the Department of Cell Biology of the University of Sevilla and the Institute of Biomedicine of Sevilla was carried out with reticulin fibers and blood vessels, taking into account that at least 4 regions of interest (ROIs) have been extracted from each image to avoid tissue artifacts such as tissue breaks, precipitates or necrotic areas (**figure 29**). A subset of alleatory cases including samples from 10 high risk patients and 10 non-high risk patients; and 10 MNA plus 10 MNNA samples were selected. Following this method, we were able to compare different binary images obtained from the analysis of reticulin fibers and blood vessels which were assessed on serial thin sections with preserved histology. These overlapping images enabled both ECM markers to be considered at the same time and allow the co-location and study of the interaction between fibers and blood vessels taking the cell nuclei as a reference. The steps followed were:

- Overlap the binarized images corresponding to the different markers together with a binarized image representing the

neuroblastic cells in the same composite image to combine the positional information from the different structures.

- Convert the composite image in a graph. First, identify the centroid of the neuroblastic cells nuclear signals. Second, use the centroids as seeds to perform a Voronoi tessellation, forming a Voronoi diagram composed by Voronoi cells. These cells emerge from the different seeds and are characterized by the fact that all the points belonging to a given cell are closer to their corresponding seed than to any other seed.
- Establish a network of cellular contacts. In this network, the nuclei centroids are detected and converted in nodes and the whole graph is formed by joining the nuclei of adjacent Voronoi cells.
- Extract 146 features from the images with the binarized reticulin fibers, blood vessels and cells nuclei. 17 of them were related to geometrical features (position, area, or intensity of a marker) and the rest arised from the topologic networks. 3 networks were done: the first with all the nuclei, the second with the tesselations containing reticulin fibers and the third with the tesselations containing blood vessels.
- Perform statistical analyses to find differences between groups. We have performed preliminary comparisons based on the risk of relapse (high risk vs. non-high risk) and the status of MYCN (MNA vs. MNA) using the binarized images of reticulin fibers, blood vessels and neuroblastic cells nuclei as the reference features to provide the biological clues.

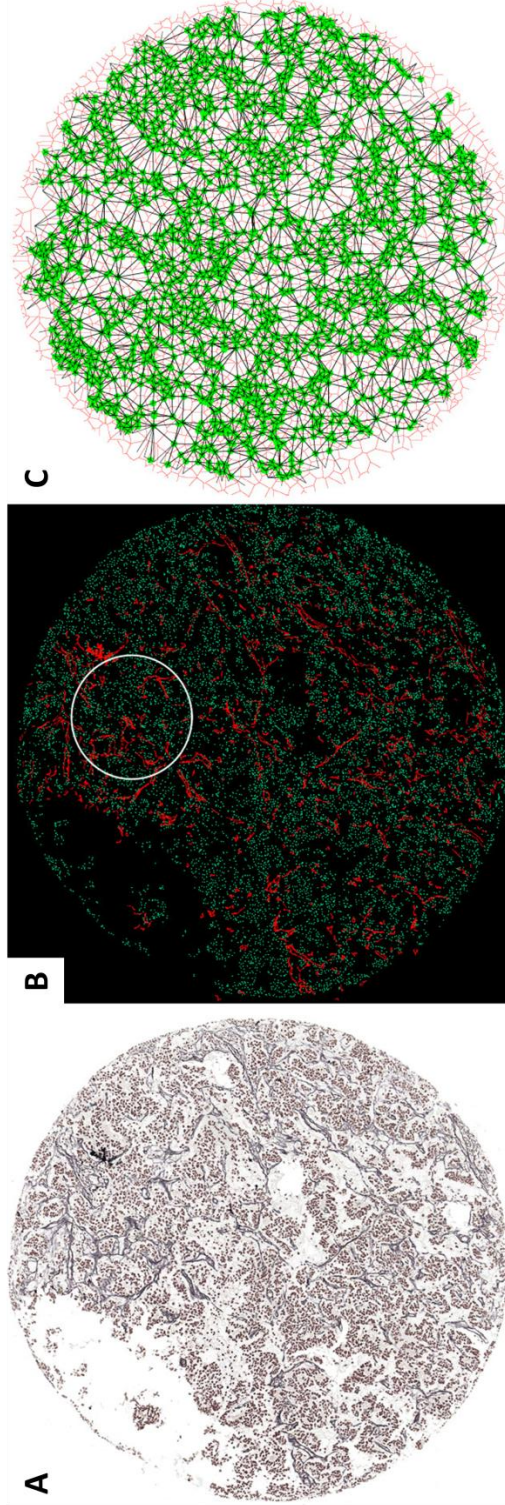


Figure 29: Construction of a network from a NB image. **A)** Stained slide to visualize reticulin fibers and cell nuclei. **B)** Processing of the previous image. Green represents the centroids of the cell nuclei and red represents the reticulin fibers. The white circle represents the region of interest (ROI) in C. **C)** Voronoi diagram (red) and overlapped contacts network (green) of a piece of the total image.

IV. RESULTS

Although the development of the algorithms and the interpretations of the results obtained after their application to characterize the different ECM elements (objective 1), are in fact part of the results of this research, they have been explained in the material and methods section. In the present section, we will:

- describe the results of the validation of the algorithms designed to characterize the architectural scaffolding and the vascular system of the neuroblastic tumors.
- show the results of the verification of the behavior of the clinical and biological INRG parameters in our studied cohort.
- present the data resulting from the morphometric analysis of the neuroblastic and control samples contained in TMAs, stained with the proper techniques to detect the different ECM elements studied and digitized.
- Expose the results of the statistical analysis relating the data coming from the morphometric analysis with the INRG prognostic clinical and biological variables and testing the prognostic value of the ECM elements studied.

1. Morphometric measurements

A. Subjective validation of the customization of the algorithms

At least two TMAs cylinders were used to validate the customization of the algorithms and to reassert the choice of the softwares and algorithms. Many trials were done for each algorithm to find the most balanced values for the RGB colors and size and shape parameters ranges to obtain faithful to reality measurements. **Figure**

30 shows examples of right and wrong softwares and customization of the algorithms.

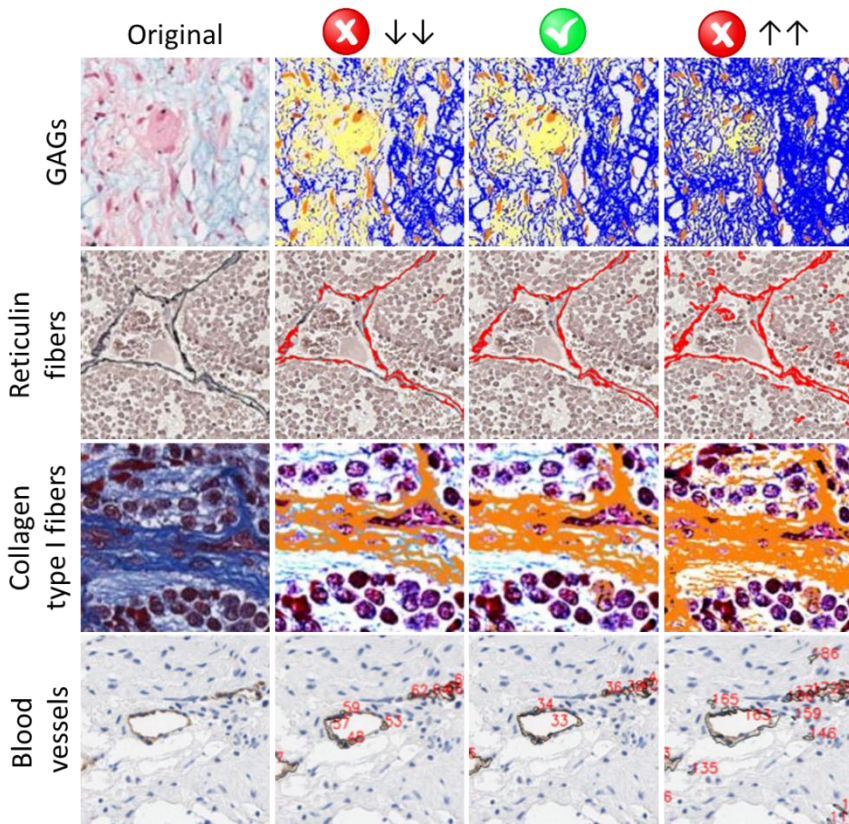


Figure 30: Example of the subjective validation process. Different ranges of the parameters were tested and the best-fitting result was chosen as the final calibration of the algorithms.

B. Comparison of images arising from two image capture methods

The first image capture method consisted of the photography of 6 consecutive 20x images with a photomicroscope (Leica DMD 108) and the reconstruction of the cylinder image. The second method was the digitization of the whole TMA with a slide scanner. Different light, color and resolution configurations were therefore considered. The

results of the comparison between two image capture methods in 24 samples are shown in **table 15**. For all the variables tested, a very good correlation, with Pearson's index >0.7 , was found.

Table 15: Results of the correlation between the morphometric data obtained after two intake techniques.

	Parameter	Pearson's correlation	p-value
Quantity	Number of fibers/mm ²	0.942	0.00
	% of stained area	0.935	0.00
Size	Area	0.955	0.00
	Length	0.952	0.00
	Width	0.952	0.00
Shape	Aspect	0.962	0.00
	Roundness	0.866	0.00
	Perimeter ratio	0.875	0.00

C. Comparison of the morphometric measurements arising from two different customizations of the same algorithm

The p-values resulting of the comparison between the morphometric measurements obtained after the analysis by two algorithms customized by the same researcher, at two different days, with different values for color and shape detection of the fibers but trying to be as accurate as possible, on the same images (n=97) are summarized in **table 16**. As can be observed, a very good correlation, with a Pearson's index >0.7 , was mostly found although some morphometric variables showed moderate and good correlations.

Table 16: Results of the correlation between the morphometric data obtained after two algorithm customization.

	Parameter	Pearson's correlation	p-value
Quantity	Number of fibers/mm ²	0.596	0.00
	% of stained area	0.807	0.00
Size	Area	0.550	0.00
	Length	0.710	0.00
	Width	0.770	0.00
Shape	Aspect	0.652	0.00
	Roundness	0.436	0.00
	Perimeter ratio	0.711	0.00
	Fractal dimension	0.728	0.00
	Branching	0.510	0.00

D. ROC test for the blood vessels algorithm

AngioPath tool was validated by means of a ROC analysis. An average of 97% sensitivity and 99% specificity was obtained. A comparison of a given cylinder where the blood vessels were selected by hand and automatically is shown in **figure 31**.

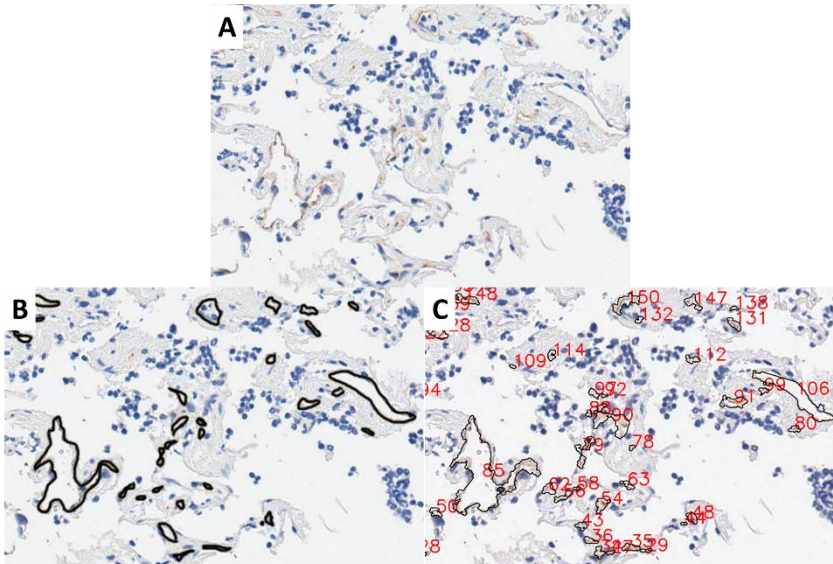


Figure 31: Example of an image used for the calculation of the sensitivity and the specificity. **A)** Original image. **B)** Blood vessels selected by hand with Photoshop. **C)** Blood vessels selection obtained from the automated analysis.

E. Consistency with the subjective assessment.

In all cases (n=96 biopsies and 148 cylinders), the comparison between the continuous variables indicating the % of stained area and the subjective assigned score results in p-values = 0.000. The increasing score assessed subjectively is associated to increasing objective amounts. Nevertheless, there is no correspondence between the value of subjective scoring and the objective quantification of the marker (**table 17**). In general, we can observe an overestimation of the amount of positive area in the subjective assessment.

Table 17: Correlation between the subjective scoring and the morphometric data.

Subjective score	GAGs	Reticulin fibers	Collagen type I fibers	Blood vessels
0 (<5%)	5.07±5.2	0.49±0.27	0.00±0.00	-
1+ (5-10%)	6.5±7.0	2.27±2.09	0.04±0.14	0.54±0.9
2+ (10-50%)	7±3.5	2.9±2.4	0.06±0.15	1.48±1.07
3+ (>50%)	14.7±6.9	7.17±6	1.01±2.06	3.08±2.77

The results of the measured non-tumoral samples were also compared to the known histological composition showing a good correspondence to reality (**table 18**).

Table 18: Measurements of the different non-tumoral samples used as control samples. The mean percentage of stained area is shown.

Tissue	GAGs	Reticulin fibers	Collagen type I fibers	Vascular system capillaries/sinusoids
Kidney	6.8±8.8	14.7±3.7	2.0±4.3	113±174/13±32
Placenta	3.2±1.9	10.2±2.3	1.5±1.8	431±123/69±18
Salivary gland	41.1	11.3	6.1	174/6.3
Muscle	6.3±4.0	10.8±7.1	4.4±2.1	140±112/11.4±6
Liver	0.8±0.09	8.2±9.7	0.02±0.03	0.0/0.0
Spleen	1.8	6.02	0.0	21/0.0

2. Clinical and biological data.

2.1 Description of the clinical, genetic and survival variables.

In our study, 36% of the patients (n=96) relapsed and 28% of the patients (n=74) died. The median EFS was of 92.5±4.1 months (IC 95%: 84.3-100.7) and the patients had a 5-year EFS of 63.1±3.1%. The median OS was of 114.5±4.2 months (IC 95%: 106.3-122.8) and the patients had a 5-year OS of 69.4±3.1%. The minimum, median and maximum follow up time were 3 months, 47±36.7 months, and 144 months for EFS/ 157 months for OS, respectively. **Tables 19 and 20** provide the information of the count, mean, confidence interval and standard deviation of tEFS, tOS and 5-year EFS and OS % depending on the stage, the age, the histopathology and the genetic features of the samples.

Table 19: Descriptors of the clinical and genetic data regarding EFS.

Factor	Count	tEFS			
		Mean	95% CI	5-year (%)	
Overall	263	92.5	84.3 - 100.7	63.1±3.1	
Stage	L1	71	131.1	125.8 - 136.4	97.0±2.1
	L2	85	99.9	86.3 - 113.5	65.9±5.4
	M	87	45.8	35.3 - 56.4	30.4±5.0
	Ms	20	92.5	77.6 - 107.4	90.0±6.7
Age (months)	<12	125	109.5	100.45 - 118.6	80.1±3.8
	12-<18	32	121.5	103.5 - 139.5	83.51±6.7
	<18	157	117.4	108.6 - 126.1	80.7±3.3
	≥18	106	60.3	48.8 - 71.8	38.4±4.9
Histopathology	GN+iGNB	9	110.3	90.8 - 123.8	100
	(nGNB/NB) d	17	83.8	56.4 - 111.2	62.1±12.3
	(nGNB/NB) pd, u	216	90.5	81.5 - 99.5	61.4±3.4
	NB NOS	21	94.0	70.9 - 117.2	68.6±10.7
MYCN	MNNA	214	103.4	94.6 - 112.1	71.3±3.3
	MNA	49	43.9	29.1 - 58.7	28.6±6.5
11q	ND	197	104.9	96.1 - 113.8	72.1±3.3
	D	66	57.2	44.7 - 70.2	38.2±6.1
Genetic profile	NCA	83	106.7	99.3 - 114.1	89.5±3.5
	SCA	180	78.6	69.0 - 88.2	52.2±3.8
Risk group	Non-high risk	176	123.6	116.1 - 131.0	84.7±2.9
	High risk	87	38.4	28.8 - 48.0	22.9±4.5

Table 20: Descriptors of the clinical and genetic data regarding OS.

Factor	Count	tOS			
		Mean	95% CI	5-year (%)	
Overall	263	114.5	106.3 - 122.8	69.4±3.1	
Stage	L1	71	133.2	129.6 - 136.7	98.5±1.5
	L2	85	116.1	104.3 - 127.9	77.4±4.9
	M	87	68.8	54.4 - 83.2	37.1±5.5
	Ms	20	104.7	96.6 - 112.9	94.7±5.1
Age (months)	<12	125	120.1	112.7 - 127.4	88.7±3.0
	12-<18	32	130.8	116.5 - 145.0	90.2±5.1
	<18	157	128.3	121.3 - 135.4	88.9±2.6
	≥18	106	80.7	67.3 - 94.1	42.8±5.2
Histopathology	GN+iGNB	9	68.5	41.1 - 96.0	100
	(nGNB/NB) d	17	44.9	28.9 - 61.0	81.1±9.9
	(nGNB/NB) pd, u	216	52.9	48.2 - 57.6	65.6±3.5
	NB NOS	21	58.3	41.8 - 74.9	90±6.7
MYCN	MNNA	214	129.6	121.7 - 137.6	79.1±3.1
	MNA	49	46.3	31.7 - 61.0	28.3±6.6
11q	ND	197	116.0	108.2 - 123.9	79.7±3.0
	D	66	85.2	68.4 - 102.0	42.9±6.8
Genetic profile	NCA	83	118.7	114.0 - 123.5	96.1±2.2
	SCA	180	100.3	90.0 - 110.7	72.5±3.4
Risk group	Non-high risk	176	134.9	129.7 - 140.1	93.4±2.0
	High risk	87	56.8	43.8 - 69.9	26.5±5.0

2.2. Univariate survival analysis

The p-values resulting of the Kaplan-Meier test comparing the INRG variables with EFS and OS in 263 patients with ≥ 3 months of follow-up information are shown in **table 21**. All the INRG variables were related to prognosis, except histopathology, which shows a tendency.

Table 21: p-values resulting of the Kaplan-Meier test comparing the INRG variables with EFS and OS.

Factor		EFS	OS
		p-value	p-value
Stage	L1	0.000	0.000
	L2		
	M		
	Ms		
Age (months)	<12	0.000	0.000
	12-<18		
	<18		
	≥ 18		
Histopathology	GN+iGNB (nGNB/NB) d (nGNB/NB) pd, u NB NOS	0.203	0.055
	GN+iGNB nGNB+NB	0.037	0.070
MYCN	MNNA	0.000	0.000
	MNA		
11q	ND	0.000	0.000
	D		
Genetic profile	NCA	0.000	0.000
	SCA		
Risk group	Non-high risk	0.000	0.000
	High risk		

The Kaplan-Meier survival probability curves are shown in **figures 30 to 35**.

2.2.1. Clinical variables

A. Stage

Patients with stages L1, L2 and Ms had a better survival compared to those with stage M (**figure 32**).

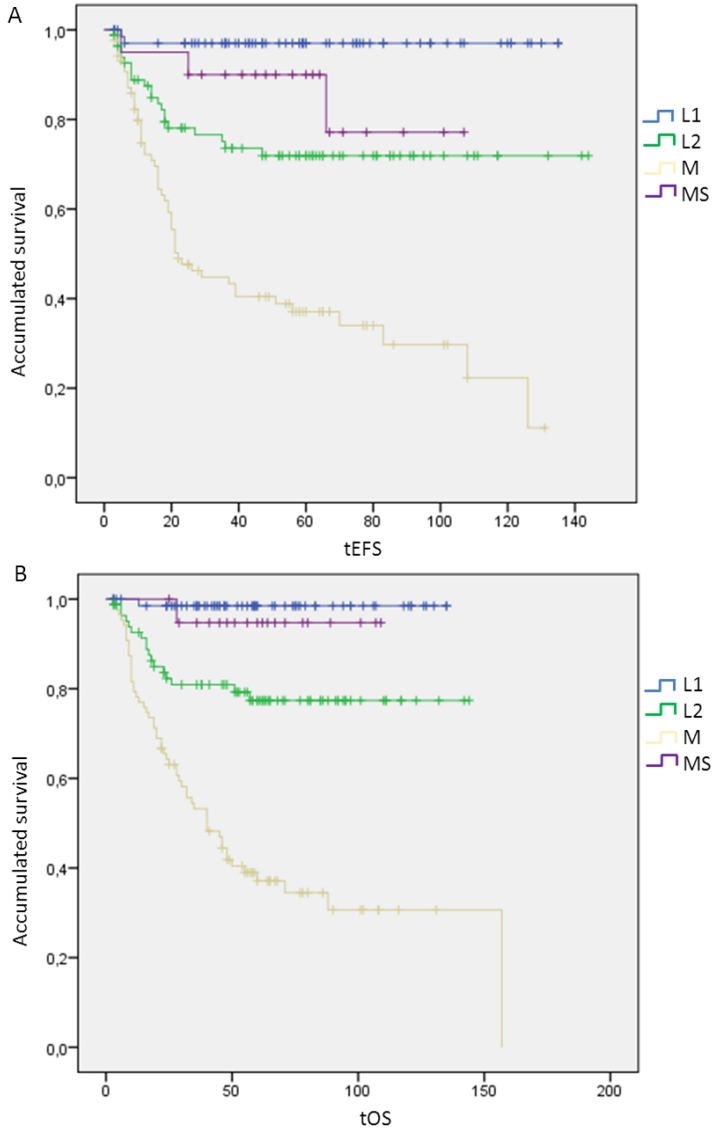


Figure 32: Kaplan-Meier survival curves showing the **A)** EFS and **B)** OS, depending on the stage ($p < 0.001$).

B. Age

Given the low % of patients with 12-18 months at diagnosis in our cohort, the differences were only found between $<$ and \geq 18 months (2), with the patients under 18 months of age presenting the best prognosis (**figure 33**).

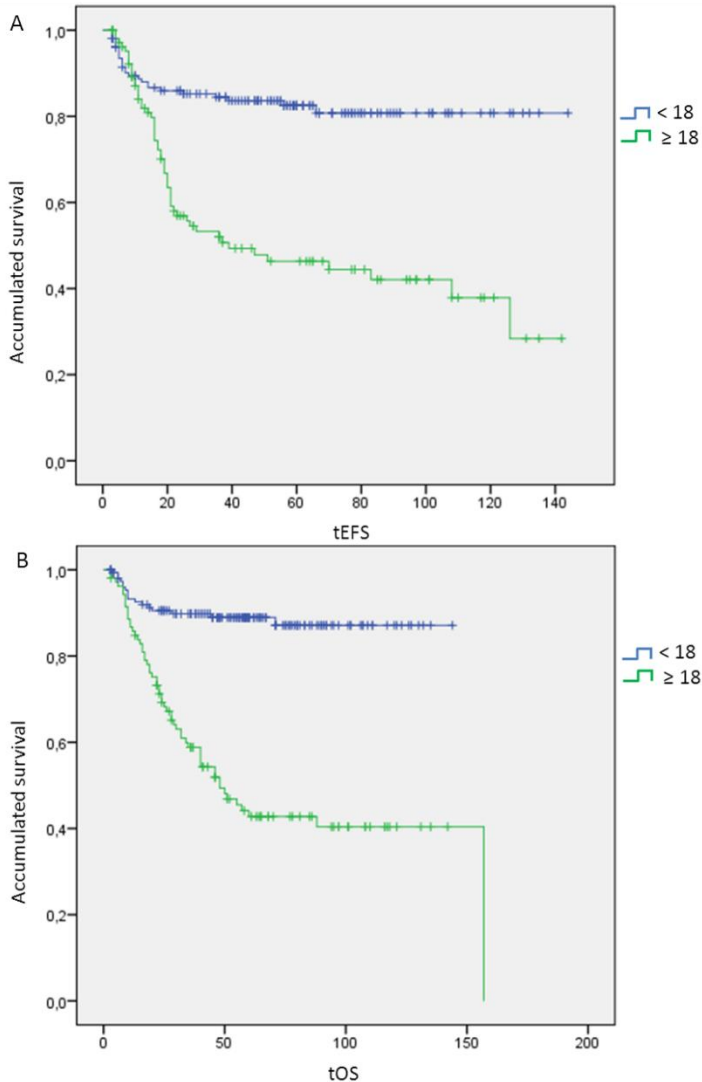


Figure 33: Kaplan-Meier survival curves showing the **A)** EFS and **B)** OS, depending on the age ($p < 0.001$).

2.2.2. Histopathology

Histological category as considered in the INRG did not show a statistical relationship with OS/EFS. Nevertheless, the p-value for OS was very near to 0.05 and the p-value for EFS when combining ganglioneuroma and intermixed ganglioneuroblastoma vs. nodular ganglioneuroblastoma and neuroblastoma was statistically significant. We can therefore assume that histological category shows a strong tendency towards risk of relapse or death, with differentiated histology indicating a better prognosis (**figure 34**).

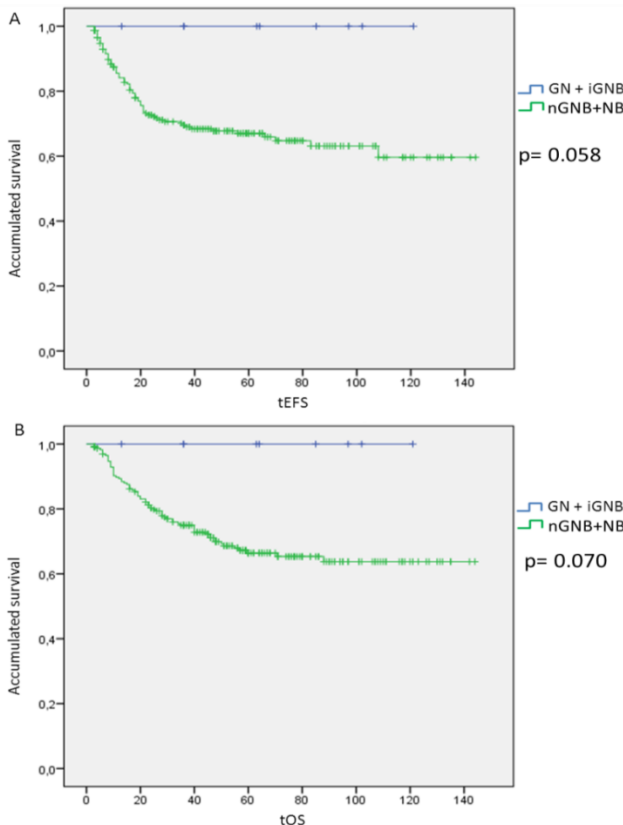


Figure 334 Kaplan-Meier survival curves showing the **A)** EFS and **B)** OS, depending on histopathology ($p > 0.05$). GN+iGNB: ganglioneuroma and intermixed ganglioneuroblastoma, nGNB+NB: nodular ganglioneuroblastoma and neuroblastoma.

2.2.3. Genetic variables

A. *MYCN* state

MYCN non-amplified tumors had a lower risk of relapse or death than *MYCN* amplified tumors (**figure 35**).

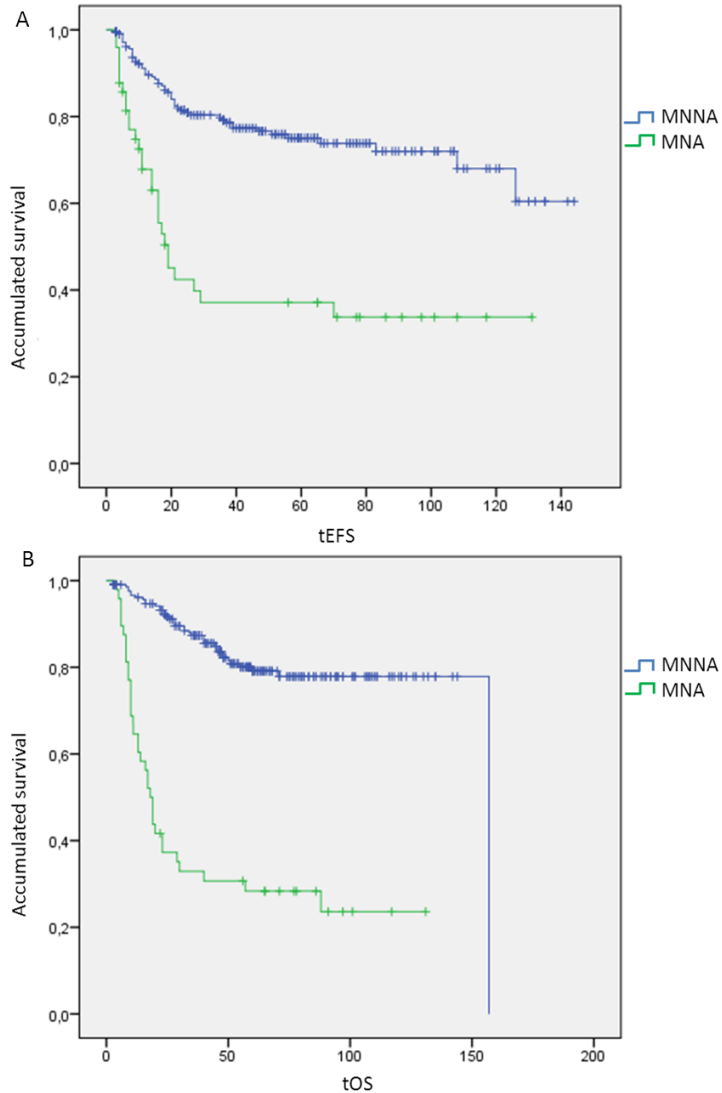


Figure 35: Kaplan-Meier survival curves showing the **A)** EFS and **B)** OS, depending on *MYCN* state ($p < 0.001$). MNNA: *MYCN* non-amplified, MNA: *MYCN* amplified.

B. 11q state

11q non-deleted tumors have a better prognosis than tumors with 11q deletion (**figure 36**).

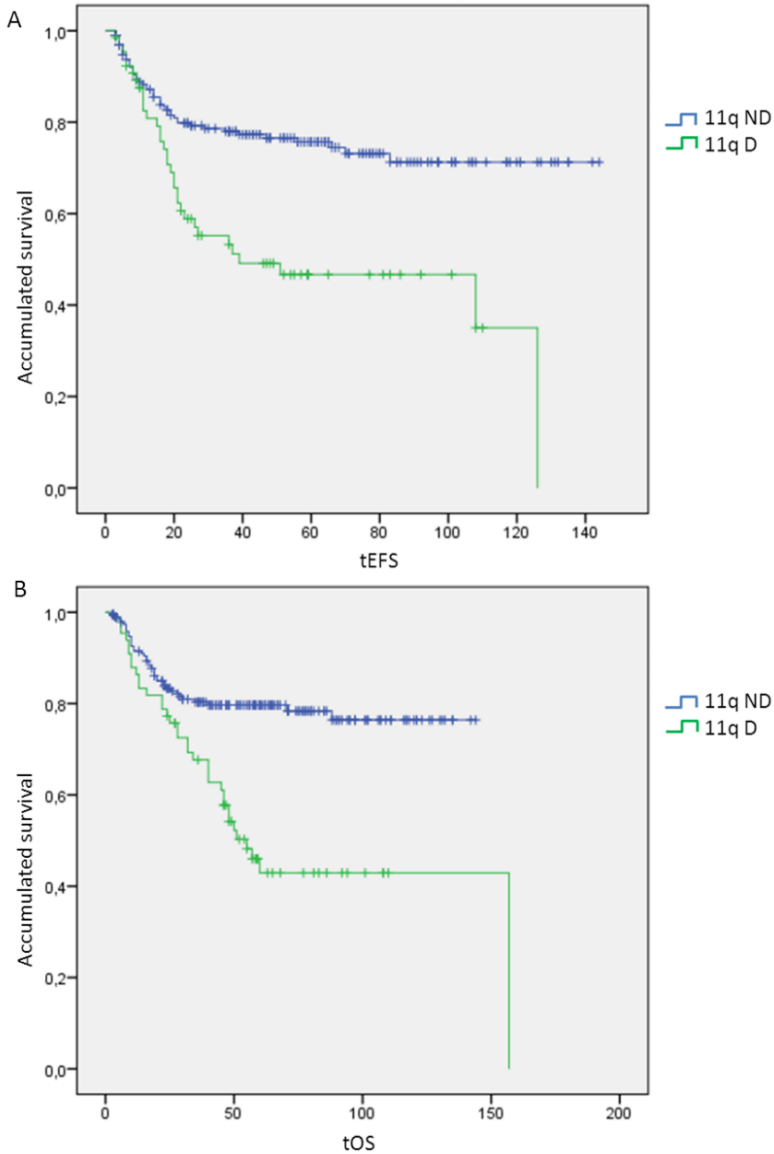


Figure 36: Kaplan-Meier survival curves showing the **A)** EFS and **B)** OS, depending on 11q state ($p < 0.001$). D: deleted, ND: non-deleted.

C. Genetic profile

Overall numerical chromosome aberration genetic profile is associated to a decreased risk of progression compared to tumors with segmental chromosome aberrations (**figure 37**).

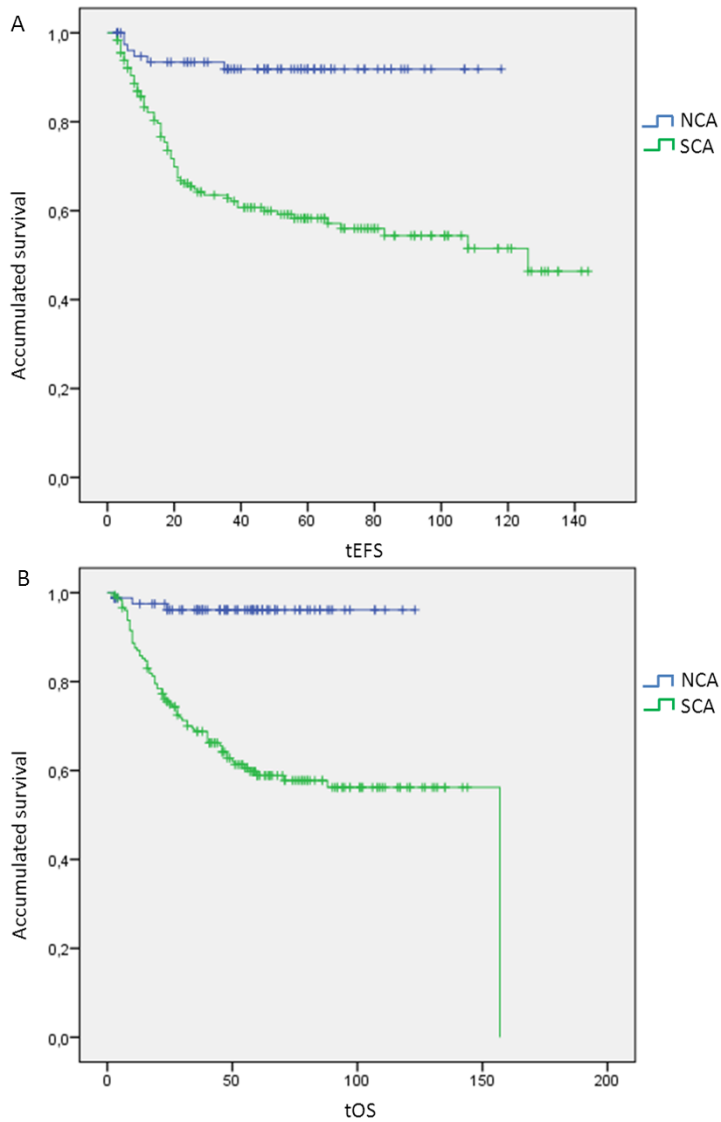


Figure 37: Kaplan-Meier survival curves showing the **A)** EFS and **B)** OS, depending on the genetic profile ($p < 0.001$). SCA: Segmental chromosome aberrations, NCA: Numerical chromosome aberrations.

D. Risk group

Non-high risk patients have a decreased risk of progression compared to high risk patients (**figure 38**).

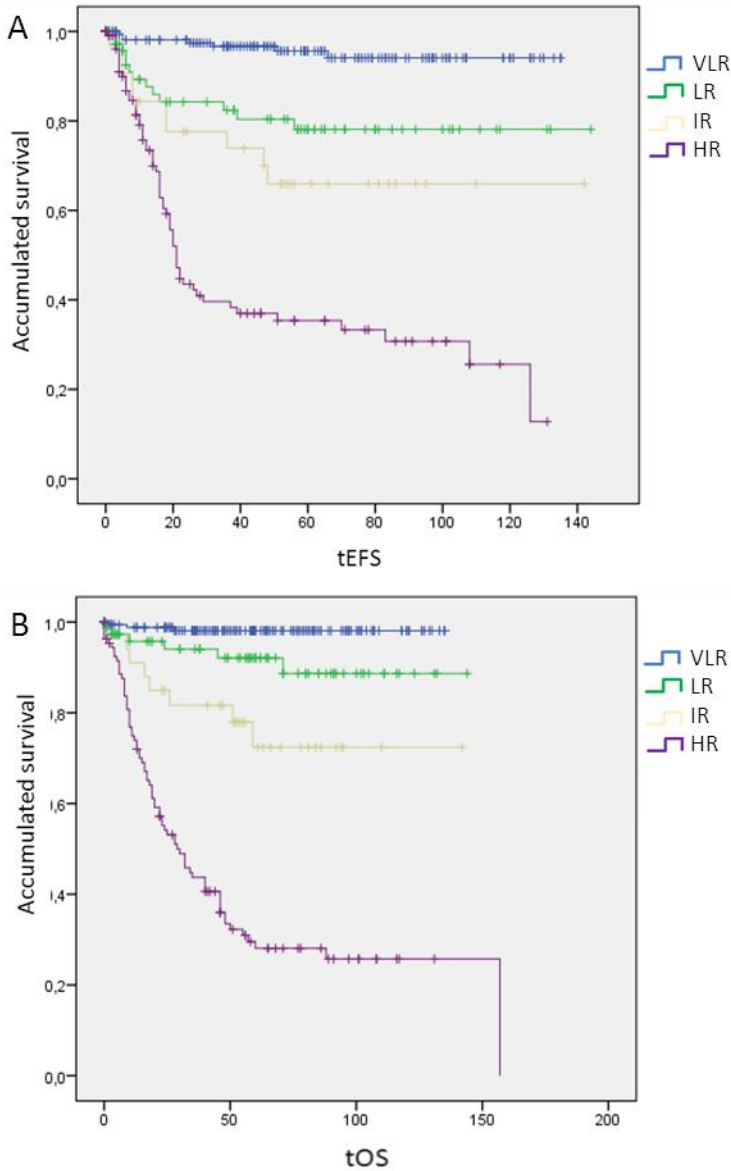


Figure 38: Kaplan-Meier survival curves showing the **A)** EFS and **B)** OS, depending on the risk group ($p < 0.001$). VLR: Very low risk, LR: Low risk, IR: Intermediate risk, HR: High risk.

2.3. Multivariate survival analysis

All the variables which showed significant relationship with tEFS plus histopathology (given the proximity to significance) underwent multivariate analysis using Cox regression (**table 22**).

According to it, the most influencing stage on the risk of relapse was stage M, followed by *MYCN* status with a HR of 1.7 (1.1-2.7), genomic profile with a HR of 2.4 (1.1-5.3) and, finally, histopathology, although the latest is associated with a p-value >0.05. Regarding OS, Cox regression includes *MYCN* status as the most influencing factor, followed by Stage and, finally, by 11q status.

Table 22: p-values resulting from relating the INRG variables to EFS and OS.

Variable	Wald	HR (95% CI)	p-value
EFS			
Stage	31.9		0.000
<i>MYCN</i>	6.2	1.7 (1.1-2.7)	0.013
Genetic profile	5.2	2.4 (1.1-5.3)	0.022
Histopathology	7.03		0.071
OS			
<i>MYCN</i>	34.3	4.5 (2.7-7.6)	0.000
Stage	20.1		0.000
11q	6.1	1.9 (1.1-3.2)	0.013

HR: Hazard ratio, CI: Confidence interval.

The very strong influence of stage on EFS masked the influence of other parameters with known prognostic value. Accordingly, a second Cox regression (**table 23**) was made, excluding the stage variable, to know the influence of the remaining factors. Cox regression results for EFS and OS without considering the stage, started with *MYCN* status and included the age variable but did not take into account the histopathology before 11q. The last influencing parameter was genomic profile.

Table 23: p-values resulting from relating the INRG variables to EFS and OS.

Variable	Wald	HR (95% CI)	p-value
EFS			
<i>MYCN</i>	16.7	2.7 (1.6-4.3)	0.000
Age	9.8	2.1 (1.3-3.5)	0.002
11q	9.2	2.0 (1.2-3.2)	0.002
Genetic profile	3.9	2.2 (1.0-5.0)	0.047
OS			
<i>MYCN</i>	30.2	4.3 (2.5-7.4)	0.000
Age	8.8	2.4 (1.3-4.4)	0.003
11q	8.04	2.1 (1.2-3.5)	0.005
Genetic profile	3.9	3.4 (1.0-11.9)	0.048

HR: Hazard ratio, CI: Confidence interval.

3. Study of the GAGs.

3.1. Histological observation

After the observation of alcian blue stained images, we could generalize patterns of GAGs accumulation regarding neuroblastic cells, leukocytes and blood vessels. Most frequently, undifferentiated and poorly differentiated neuroblastic cells areas did not present GAGs, which appeared restricted to stromal fibrous areas in more or less contact with neuroblastic cells clusters and, exceptionally, GAGs could accumulate within neuroblastic cells (**figure 39**). We also observed that GAGs accumulates were detectable in GN and iGNB ECMs, frequently coincident with the perineurium of nervous bundles, too (**figure 40**). Regarding the correlation of GAGs accumulation and leucocyte infiltrations, we could observe that leucocyte accumulations also lacked alcian blue positivity within the cells or around the clusters (**figure 41**). Finally, GAGs did not usually accumulate around blood vessels except in few samples (**figure 42**).

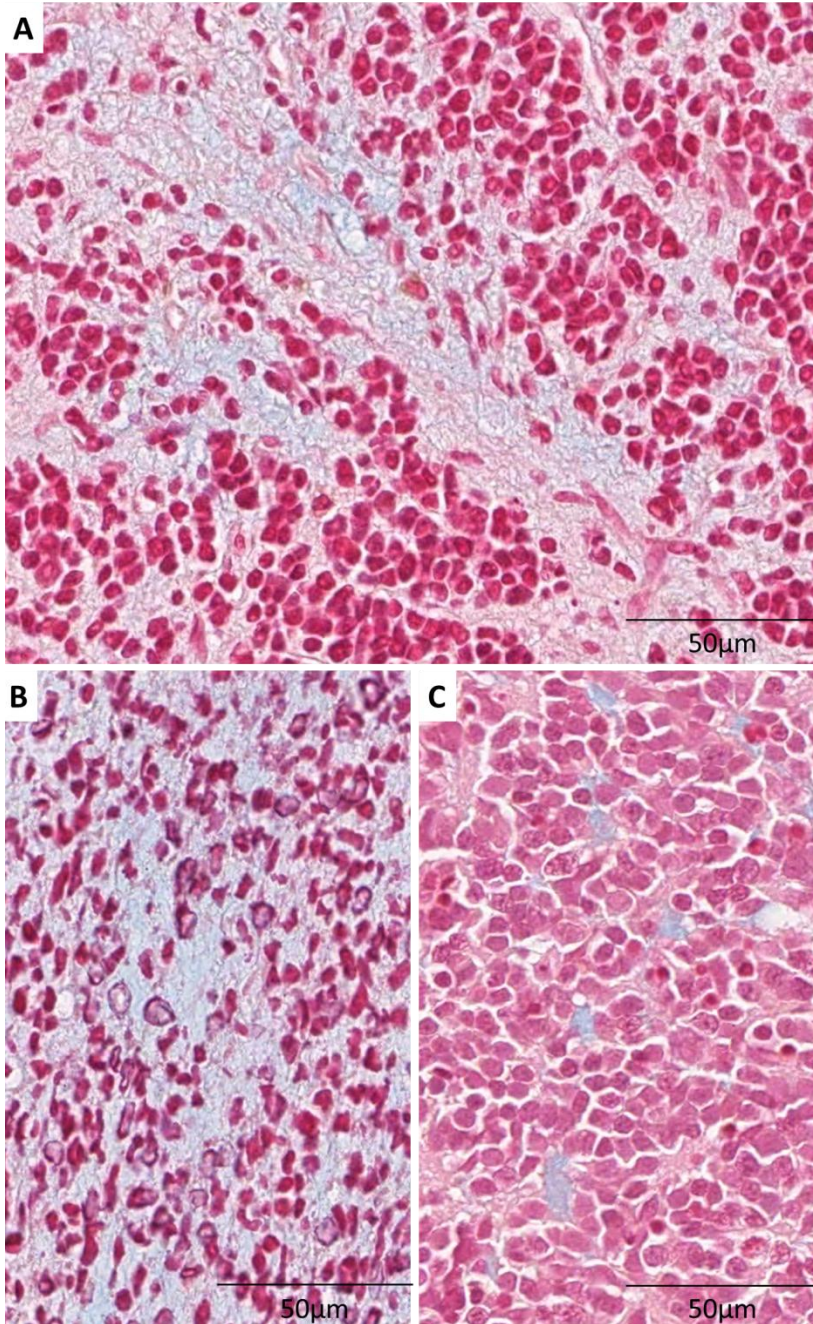


Figure 39: Example of one GAGs accumulation regarding neuroblastic cells. **A)** GAGs are mostly restricted to fibrous trabecules between neuroblastic cells clusters. **B)** Exceptionally, they can accumulate within neuroblastic cells or **C)** in small spaces between tumor cells.

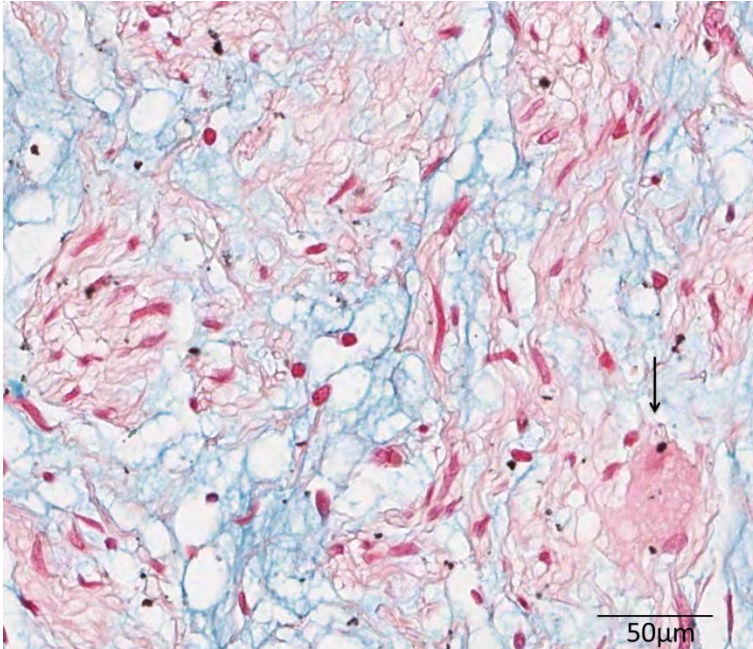


Figure 40: Ganglioneuroma showing an accumulation of GAGs in perineurium of nervous bundles. A ganglionic cell is signaled with an arrow.

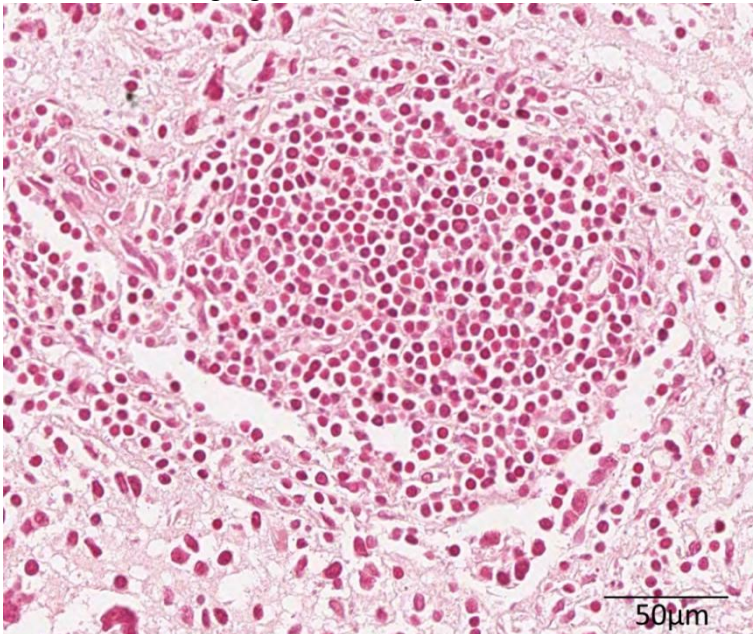


Figure 41: Tertiary lymph node with absent GAGs.

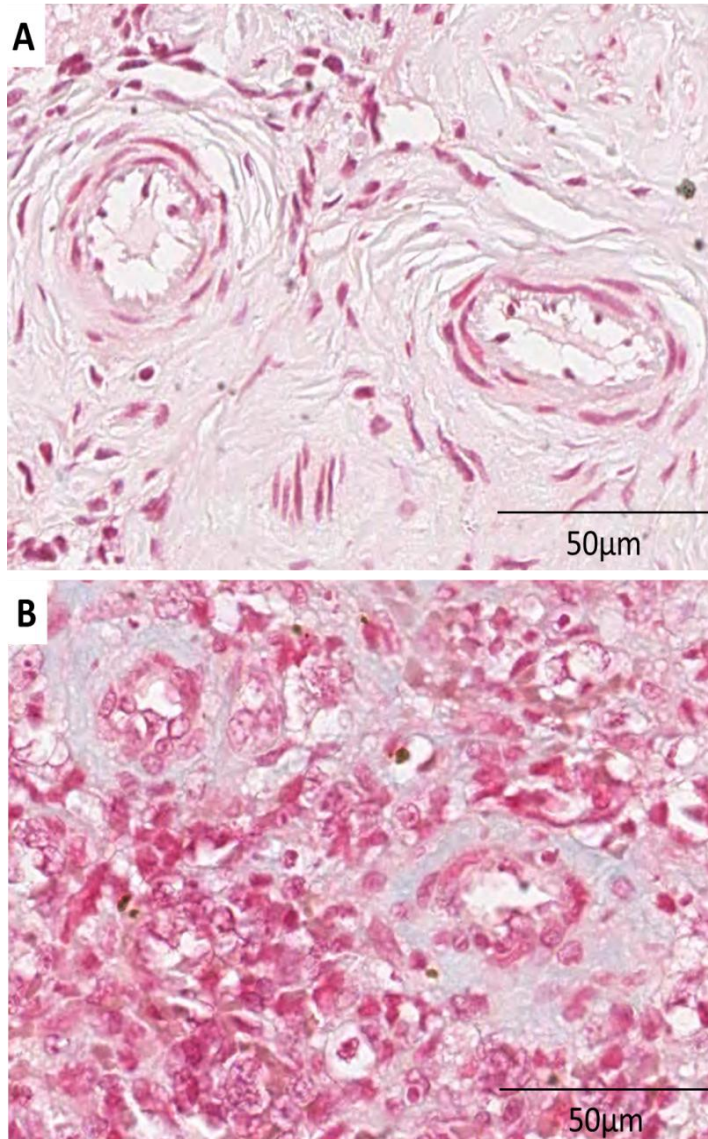


Figure 42: Arrangement of GAGs around blood vessels. **A)** Blood vessels are usually not surrounded by an accumulation of GAGs. **B)** Occasionally, blood vessels present a GAGs rich area around.

3.2. Description of the variables

Among the 458 patients, 71 were excluded from the GAGs study: 48 biopsies corresponded to lost cylinders and 23 were not

representative of neuroblastic tissue or presented some type of artefact.

The biopsies analyzed (n=387) had an average stained area of $4.11 \pm 4.37\%$ and a median of 2.82%. In general, neuroblastic tumors presented a scant amount of GAGs in their ECM, with the minimum value being 0.14% and the maximum amount found being 32.46% (**figure 43, table 24**).

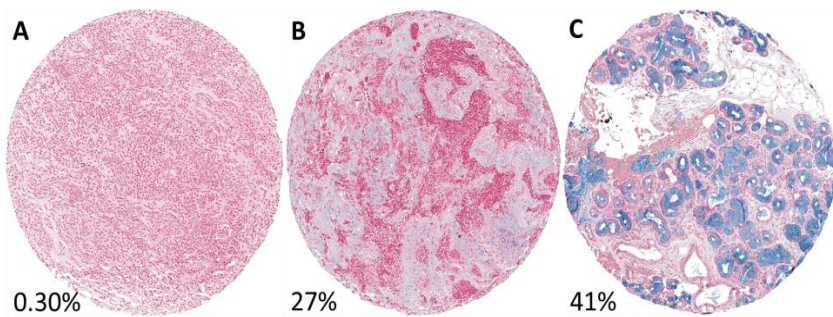


Figure 43: Different degrees of presence of GAGs. The % of stained area is shown. **A)** NB with scarce GAGs in its ECM. **B)** NB with high amount of GAGs. **C)** Salivary gland as positive control, with a very high % of area occupied by GAGs.

Table 24: Description of the morphometric measurements of the GAGs in a subset of 387 primary samples.

Parameter	Mean	Median	SD	Min.	Max.
% stained area	4.11	2.82	4.37	0.14	32.4

Most of the primary tumors (63%) presented an homogeneous distribution of the GAGs in their stroma. Nevertheless, a not negligible (36%) subset of biopsies had GAGs distributed heterogeneously in the ECM, with the heterogeneity being focal or diffuse in quite the same proportion. A different pattern between the different cylinders of the same biopsy was found in 16.5% of the samples (**table 25**).

Table 25: Description of the distribution pattern of the GAGs in a subset of 387 samples.

Spatial distribution	Count	%
Homogeneous	246	63.6
Heterogeneous:	141	36.4
• Focal heterogeneous	44	11.4
• Diffuse heterogeneous	33	8.5
• Combined both focal/diffuse	14	3.6
• Combined homogeneous/ heterogeneous	50	12.9

3.3. Favorable and unfavorable GAGs histological patterns

The results of the univariate non-parametric analysis comparing the GAGs abundance and distribution with the INRG variables with prognostic value are shown in **table 26**. The amount of ECM GAGs in primary tumors was related to the stage of the disease, the histopathology of the tumor and the risk group. A tendency was observed towards being related with the state of *MYCN* oncogene. The spatial distribution of such GAGs was not related to the INRG clinical and biologic characteristics.

Table 26: p-values resulting from relating the quantification of the GAGs and the clinical and genetic INRG variables.

INRG variable/Parameter	% stained area	Spatial distribution
Stage	0.041	-
Age	-	-
Histopathology	0.000	-
MYCN	0.060*	-
Genetic profile	-	-
11q	-	-
Ploidy	-	-
Risk group	0.002	-

-: not statistically significant, *: tendency.

How the % of stained area was distributed in the subcategories of the clinical and biological INRG variables is shown in **figure 44**. The tumors with differentiated histopathology (GN, iGNB), from patients with localized and non-high risk disease had a higher amount of GAGs in their ECM, compared to those with undifferentiated histopathology and from patients with metastatic and high risk disease. MYCN status was almost significantly related to the quantity of GAGs in such a way that MNNA samples would present a higher amount of GAGs than MNA samples.

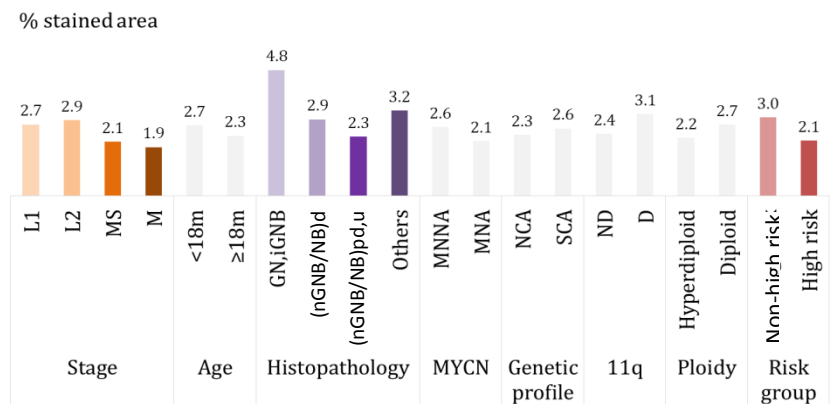


Figure 44: Distribution of the amount of GAGs depending on the INRG clinical and biological variables. Variables in grey mean no significant statistical relationship. Colored variables show significant statistical relationship (**table 12**). The median value is shown.

An image summarizing how different neuroblastic tumors subgroups were associated with different amounts of GAGs is presented in **figure 45**.

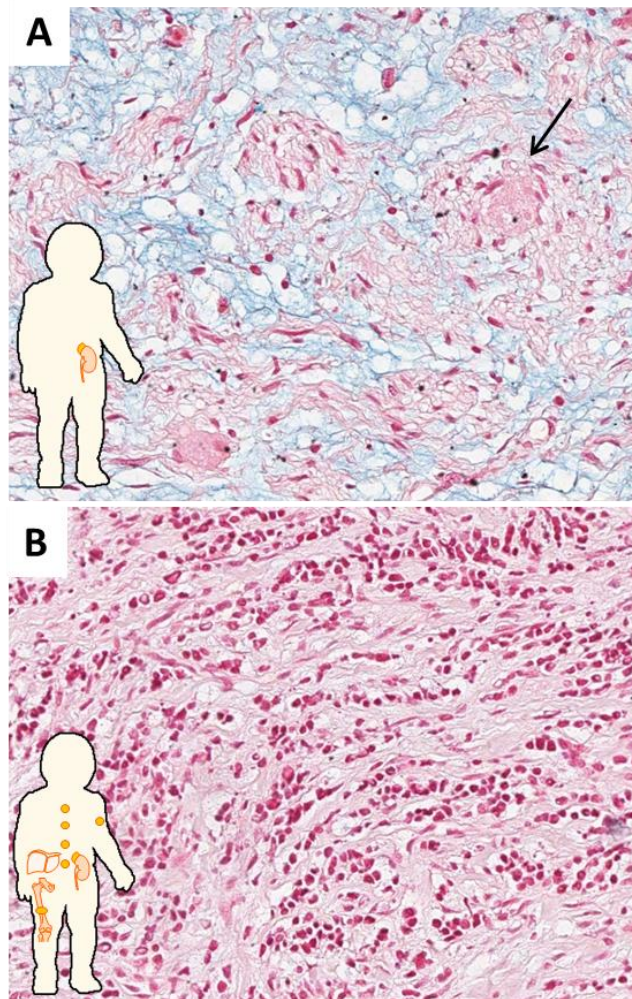


Figure 45: Summary of the associations between the INRG parameters and GAGs. **A)** Localized and non-high risk disease and differentiated histopathology (and MNNA) is related to high content of GAGs. A ganglionic cell is marked with an arrow. **B)** Metastatic and high risk disease and undifferentiated NB (with MNA) are related to poor amount of GAGs.

3.4. Survival analysis

The whole cohort, as well as the high risk patients subgroup who could potentially more beneficiate from an enhanced pre-treatment stratification or new therapeutic targets, were studied.

3.4.1. Multivariate analysis

When testing the GAGs variables on their own or in combination with the INRG variables, both the amount of GAGs and the pattern did not influence survival, whether including or excluding the stage. A table showing HR and p-values is therefore not provided.

3.4.2. Study of the high risk group

The dichotomized variables using the first quartile, the median and the third quartile did not show statistically significant differences of survival (OS, EFS) depending on the amount of GAGs. A Kaplan-Meier graph is therefore not shown.

3.5. GAGs after treatment and in other samples

The stained area of GAGs corresponding to the different samples of primary NB, non-primary NB, peritumoral tissue, other tumors tissue and non-tumoral tissue is shown in **table 27**. The results of the statistical analysis comparing the different groups of samples are presented in **table 28**.

In general, tumor samples (primary NB, non-primary NB and tissue other tumors) had a lower amount of GAGs in their ECM compared to the means of non-tumoral tissue (peritumoral and non-

tumoral tissue). Primary NB had an ECM with a statistically significant lower amount of GAGs compared to non-primary NB. Specifically, the amount of GAGs was the double in primary NB than in the adrenal gland, the major host organ for primary NB development. The sample containing the highest ECM GAGs amount was the salivary gland (41%), followed by sympathetic ganglia and paraganglia and fat (14%).

Table 27: % of stained area occupied by GAGs in the different control tissues studied.

Samples	GAGs	
	Mean	Median
Primary NB (n=387)	4.1±4.3	2.8
Non-primary NB (n=75)	5.3±4.9	3.7
Peritumoral tissue (n=23):	7.5±13.1	3.0
• Lymph node (n=1)	0.63	0.63
• Adrenal gland (n=7)	2.2±1.2	1.6
• Liver (n=2)	4.2±4.8	4.2
• Striated muscle (n=1)	1.9	1.9
• Pancreas (n=2)	1.7±1.0	1.7
• Sympathetic ganglia and paraganglia, fat (n=10)	14.1±18	7.0
Other tumors tissue (not NB) (n=4):	3.3±5.0	1.0
• Lymphoma (n=1)	0.4	0.4
• Olfactory estesion NB (n=1)	1.3	1.37
• CC. sarcoma of the kidney (n=1)	0.6	0.6
• Adrenocortical carcinoma (n=1)	10.9	10.9
Non-tumoral tissue/organs (n=25):	6.4±9.5	2.8
• Kidney (n=12)	6.8±8.8	2.5
• Liver (n=2)	0.8±0.09	0.8
• Striated / Smooth muscle (n=5)	6.3±4.0	5.1
• Spleen (n=1)	1.8	1.8
• Placenta (n=5/4/5)	3.2±1.9	2.9
• Salivary gland (n=1)	41.1	41.1

CC.: Clear cell.

Table 28: p-values arising from the comparison of ECM non-cellular parameters in different tissues.

Parameter	GAGs
Prim. NB vs Non-prim. NB	0.010
Prim. NB vs per. tissue	-
Prim. NB vs other tumors	-
Prim. NB vs non-tumoral	-
Non-prim. NB vs per. tissue	-
Non-prim. NB vs other tumors	-
Non-prim. NB vs non-tumoral	-
Per. Tissue vs other tumors	-
Per. Tissue vs non-tumoral	-
Other tumors vs non-tumoral	-

Prim. NB: primary NB, not-prim NB: non-primary NB, per.tissue: peritumoral tissue.

4. Study of the fibrous component

4.1. Reticulin fibers

4.1.1. Histological observation

The observation of the images alone enabled the identification of some specific arrangements in combination with the tumor cells, stromal cells and ECM elements. As explained in the previous section, some distribution patterns could be distinguished, meaning that some order exists in neuroblastic tumors regarding the distribution of the reticulin fibers. Reticulin fibers defined smaller or larger areas with more or less isolated cells or cell clusters (**figure 46**). The arrangement of the fibers regarding the immune cells (tertiary node-like structures or leucocyte infiltrates) was also peculiar in such a way that these cells were surrounded by the fibers or contained within a reticular network (**figure 47**). It is known that blood vessels are wrapped by reticulin

fibers. However, in some cases, the fibers were not restricted to the vessels outline, but formed an extended network in close relationship with the vessels (**figure 48**).

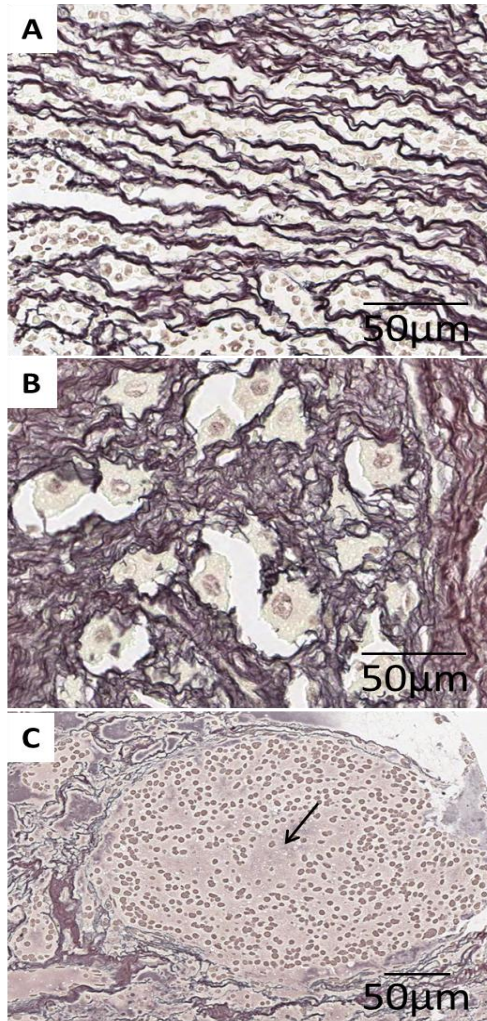


Figure 46: Special arrangements of the reticulin fibers around neuroblastic cells. Reticulin fibers are intermingled within neuroblastic and stromal cells. In some cases, the distribution seems to be arbitrary but, in most of the cases, the fibers tend to follow an organization. **A)** The fibers form lines in between the cells arranged in rows. In other cases, the cells seem to be trapped inside reticular fibrous structures which surround larger or smaller groups of cells. **B)** Ganglionic individual cells (or groups of two cells) of a ganglioneuroblastoma are separated from each other by a stiff fibrous ECM. **C)** A huge amount of neuroblastic cells are grouped inside a reticular septum, isolated from the rest

of the tumor cells and, in this particular case, a necrotic area can be appreciated (arrow) in the center.

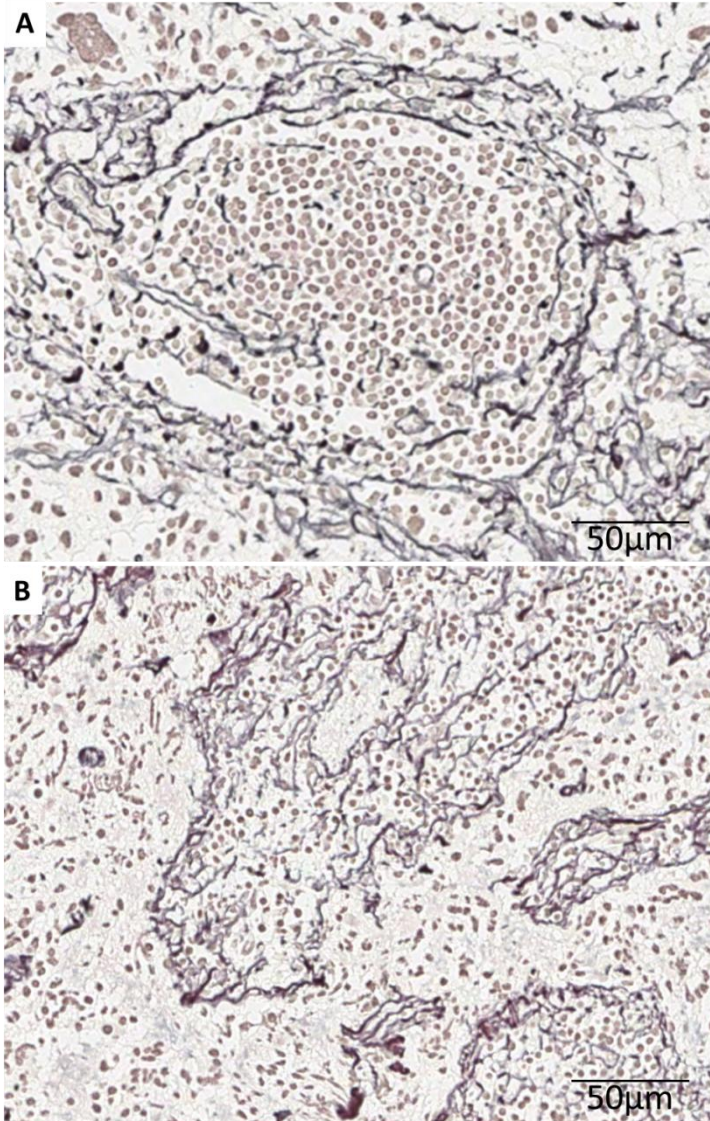


Figure 47: Special arrangement of the reticulin fibers around leucocytes. **A)** Structures very similar to tertiary lymph nodes in neuroblastic tumors are surrounded by a reticulin fiber scaffold with a scarce amount of fibers inside the nodule. **B)** A leucocytary infiltrate is accompanied by reticulin fibers. Note the absence of fibers related to the neuroblastic and other stromal cells.

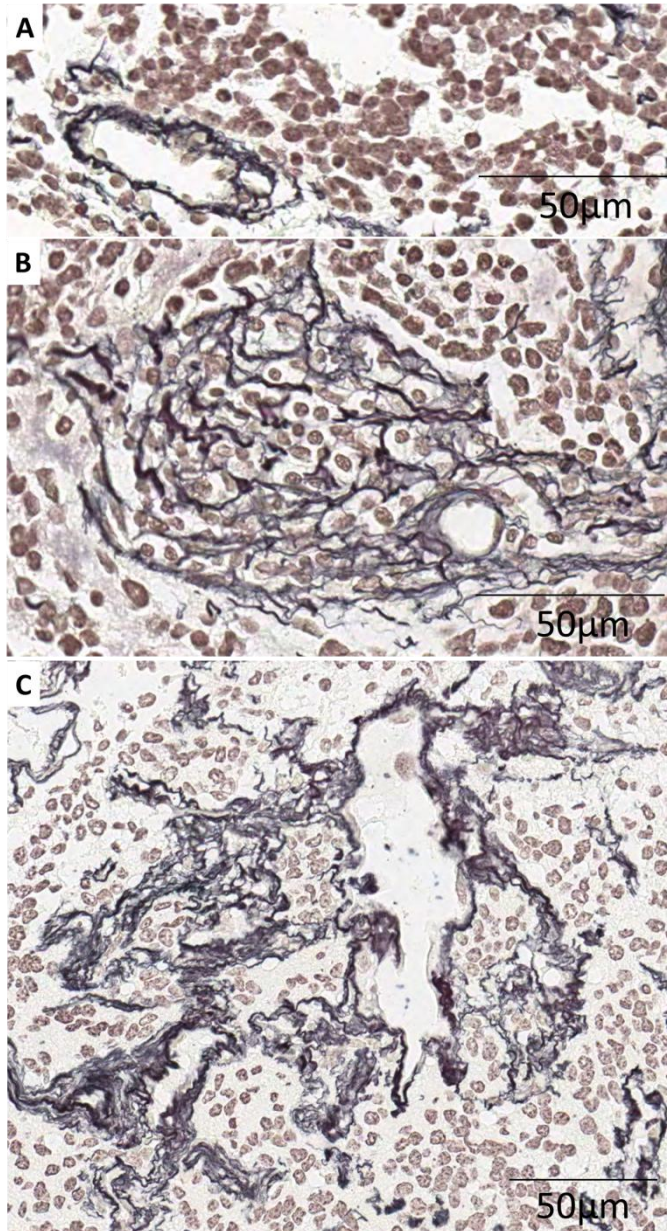


Figure 48: Special arrangement of the reticulin fibers around blood vessels. **A)** Vessels with reticulin fibers only around the lumen, concentric with the endothelial cells. **B, C)** Reticulin fibers can extend around the lumen in such a way that they support cells in close relationship with the vessels, which could be considered as perivascular niches. **B)** In this case the cells trapped in the reticulin fibers network are of leucocytary origin, whereas in **C)** the cells in the reticulin fibers network arising from the vessel are neuroblasts. Specific immunostainings are not shown.

4.1.2. Description of the morphometric variables

Among the 458 patients, 65 were excluded from the reticulin fibers study: 48 biopsies corresponded to lost cylinders and 17 were not representative of neuroblastic tissue or presented some kind of artefact. The biopsies analyzed (n=393) had a mean number of fibers per mm^2 of 895 ± 518 and an average stained area of $8.4 \pm 7.2\%$ (**figure 49**). In general, reticulin fibers of neuroblastic tumors formed networks with an average size of $115 \pm 179 \mu\text{m}^2$ of area, $21 \pm 5.4 \mu\text{m}$ length and $8 \pm 2.9 \mu\text{m}$ width. The average shape measurements were: aspect of 4 ± 0.8 (2.3 to 8.3), roundness of 7.4 ± 1.7 (4 to 13.5), perimeter ratio of 0.898 ± 0.04 (0.83 to 0.98), fractal dimension of 1.15 ± 0.1 (1.08 to 1.25) and branching of 0.15 ± 0.1 (0 to 0.6) (**table 29**).

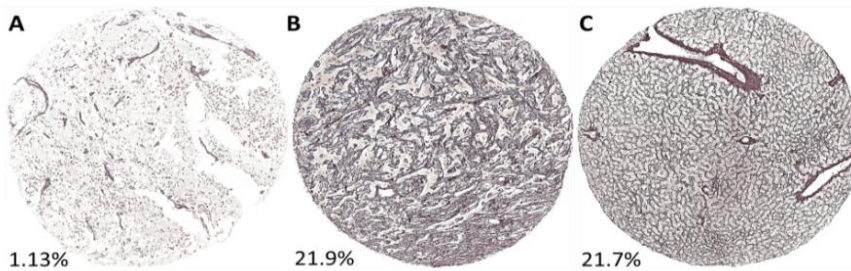


Figure 49: Different degrees of presence of reticulin fibers. The % of stained area is shown. **A)** NB with scarce reticulin fibers in its ECM. **B)** NB with high amount of reticulin fibers. **C)** Liver as positive control, with a very high % of area occupied by reticulin fibers.

Table 29: Description of the morphometric measurements of the reticulin fibers in a subset of 393 primary biopsies.

	Parameter	Mean	Median	SD	Min.	Max.
Quantity	Density	895.5	854.0	518.4	4.6	2685.9
	% stained area	8.4	6.6	7.2	0.01	46.7
Size	Average area	115.1	72.2	179.3	15.1	2224.3
	Length	21.7	21.0	5.4	11.7	46.9
	Width	8.4	8.2	2.9	2.6	21.7
Shape	Aspect	4.0	3.8	0.8	2.3	8.3
	Roundness	7.4	7.1	1.7	4.0	13.5
	Perimeter ratio	0.8984	0.9892	0.04	0.83	0.98
	Fractal dimension	1.15	1.16	0.1	1.08	1.25
	Branching	0.15	0.14	0.1	0.0	0.6

4.1.3. Description of the spatial distribution

A. Subjective assessment

Among the 96 biopsies studied (with at least two representative cylinders per biopsy), 22 were organoid, 17 were lobular, 12 were reticular and 25 were trabecular. 7 cases presented different distributions between the two cylinders, being one organoid/reticular, 3 of them heterogeneous lobular/reticular and 3 of them lobular/trabecular. 4 cases were not representative and 9 were lost. Given their similarity, organoid and lobular pattern were considered as a single class for statistical approaches. The assignment of the subjective distribution is shown in **table 30**.

Table 30: Distribution of the samples in different spatial organization patterns regarding reticulin fibers.

Spatial distribution	Count	%
Organoid	22	23
Lobular	17	17.7
Reticular	12	12.5
Trabecular	25	26
Heterogeneous	7	7.3
Unknown	13	13.5

B. Non-supervised clustering

All the images were grouped in three clusters with the most similar samples put together in a group or cluster (**figure 50**) which, according to **figure 51**, were not as well defined as they should (**congress 7**).

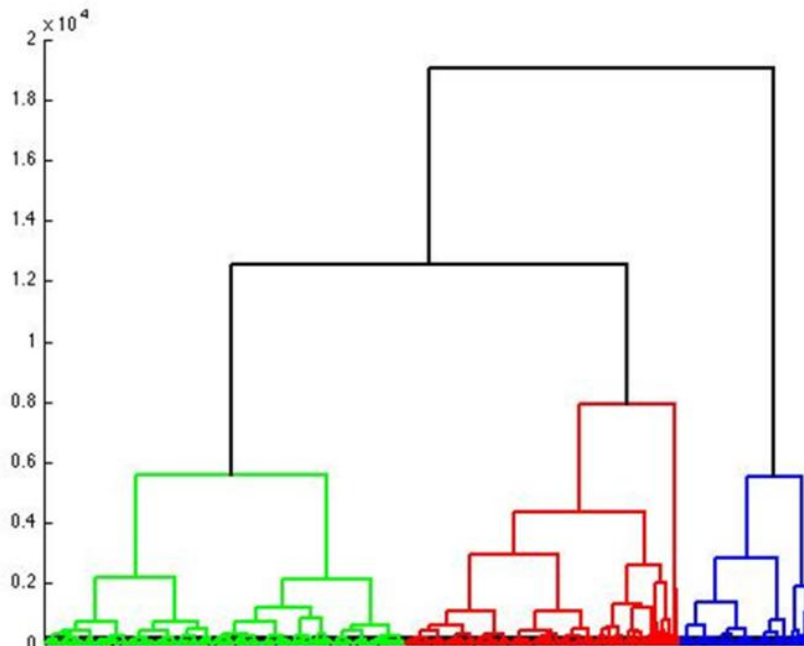


Figure 50: Dendrogram for the obtaining of the three clusters using all the available images. The different clusters are identified by different colors. Every signal in the horizontal axis represents a different image.

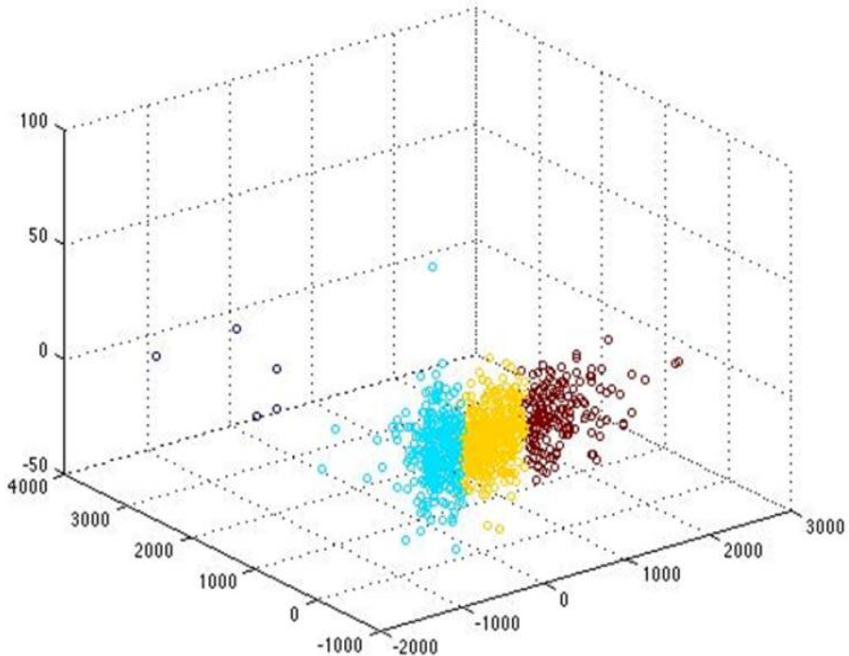


Figure 51: Results of the non-supervised classification from all the cylinders. The different clusters are identified by different colors. Each point in the graph represents a tumor cylinder in a three-dimension space defined by the three first principal components obtained from the variables extracted from the images. The three clusters, represented by three different colors should be separated from each other.

The comparison between the subjective spatial distribution patterns agreed by three investigators and the cluster assigned is shown in **table 31**. Kappa concordance index was of 0.149, which is <0.20 . This index corresponded to a negligible concordance, which means that this method was not accurate to classify our images automatically in the different distribution patterns.

Table 31: Comparison between the subjective distribution pattern and the clusters.

Count		Subjective distribution pattern					Total
		Org/ Lob	Ret	Trab	Het	Unknown	
Cluster	Org/Lob	15	2	19	2	0	38
	Ret	20	6	6	4	0	36
	Trab	1	4	0	0	0	5
	Het	3	0	0	1	0	4
	Unknow	0	0	0	0	13	13
Total		39	12	25	7	13	96

Org: organoid, Lob: lobular, Ret: Reticular, Trab: trabecular, Het: heterogeneous.

C. Classification based on image dictionaries

A 65% of correspondence with the subjective distribution patterns was achieved. Nevertheless, the majority of the cases were classified in a single class and, therefore, this method is not useful in its current state (**congress 8**).

4.1.4. Favorable and unfavorable reticulin fibers histological patterns

The results of the non-parametric analysis comparing the reticulin fibers features with the INRG variables with prognostic value are shown in **table 32**.

Reticulin fibers morphometric variables were related to the majority of the clinical and biological INRG variables. Specifically, patients age was associated with the % of stained area ($p=0.044$) and the shape of the fibers (0.047 for fractal dimension and 0.046 for branching). All morphometric parameters except branching were differentially distributed in neuroblastic tumors depending on the histopathology category and grade of differentiation ($p<0.05$ for the

number of fibers, the % of stained area and roundness, and $p \leq 0.01$ for the remaining parameters). The amount of fibers and the branching degree were also different depending on the state of *MYCN* ($p < 0.05$). The size and the shape of the fibers, as well as the stained area, were different between the two states of 11q ($p < 0.05$). Finally, whether the tumors were diploid or hyperdiploid also showed a difference in all morphometric measurements (except for the number of fibers) with p -values < 0.05 except for width, fractal dimension and branching, with $p \leq 0.01$. The distribution of the morphometric variables was not different with respect to stage and genetic profile. Regarding risk group, we could observe that the amount of reticulin fibers ($p = 0.031$), together with the aspect (0.047) and branching (0.004) shape variables were significantly related.

Table 32: p-values resulting from the relation of the morphometric characterization of the reticulin fibers and the clinical and genetic INRG variables.

Parameter	Stage	Age	Histopathology	MYCN	Genetic profile	11q	Ploidy	Risk group
Quantity	-	-	0.003	0.002	-	-	-	0.031
% stained area	-	0.044	0.011	-	-	0.012	0.020	-
Average area	-	-	0.000	-	-	-	0.005	-
Length	-	-	0.001	-	-	-	0.016	-
Width	-	-	0.000	-	-	0.039	0.001	-
Aspect	-	-	0.000	-	-	0.040	0.016	0.047
Roundness	-	-	0.017	-	-	-	0.002	-
Perimeter ratio	-	-	0.000	-	-	0.013	0.003	-
Fractal dimension	-	0.047	0.000	-	-	-	0.001	-
Branching	-	0.046	-	0.001	-	-	0.000	0.004

-: not statistically significant

How these parameters were distributed in the subcategories of the clinical and biological INRG variables is shown in **figures 52 to 54**. Only the parameters with at least one statistically significant relationship with the INRG variables are shown.

- Reticulin fibers quantity variables

GN and iGNB, MNNA tumors and tumors from non-high risk disease had a higher amount of reticulin fibers. For this histopathology category, as well as for tumors with 11q non-deleted, these fibers occupied a smaller area. Tumors from patients younger than 18 months of age and hyperdiploid tumors had more area occupied by reticulin fibers (**figure 52**).

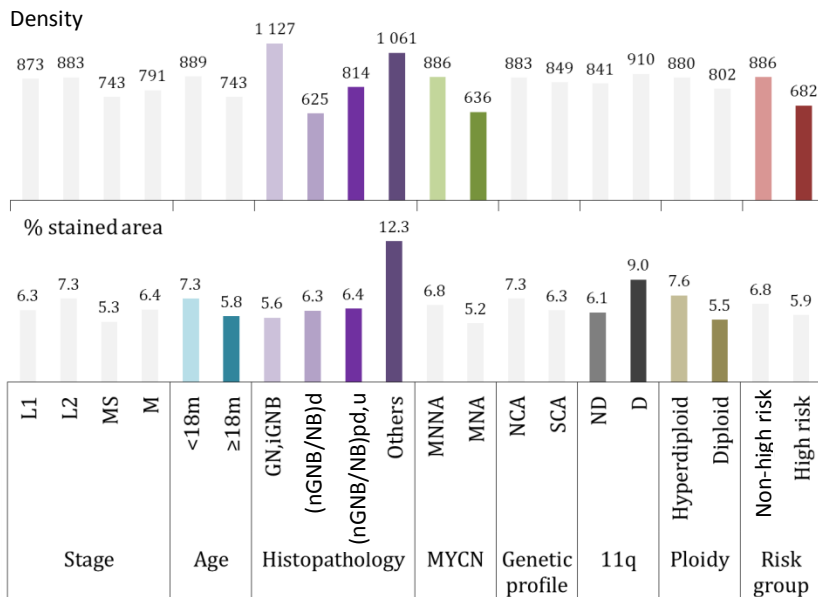


Figure 52: Distribution of the amount of reticulin fibers depending on the INRG clinical and biological variables. Variables in grey mean no significant statistical relationship. Colored variables show significant statistical relationship (**table 32**). The median values are shown.

- Reticulin fibers size variables

For tumors with favorable histopathology and 11q non-deleted, reticulin fibers networks showed a smaller length, width and, thus, average area, compared to their counterpart. Ploidy shows significant relationships in the opposite sense (**figure 53**).

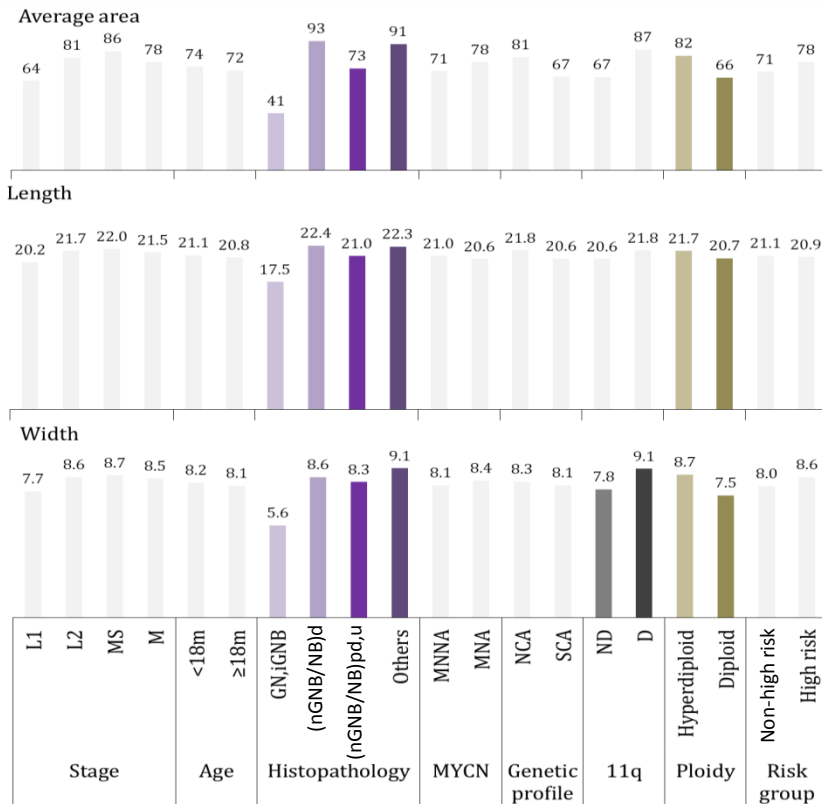


Figure 53: Distribution of the size variables depending on the INRG clinical and biological variables. Variables in grey mean no significant statistical relationship. Colored variables show significant statistical relationship (**table 32**). The median values are shown.

- Reticulin fibers shape variables

In general, favorable tumors present a higher aspect, a lower roundness (except for ploidy), a higher perimeter ratio (except for

ploidy), a lower fractal dimension (except for age) and a higher branching (except for ploidy) (figure 54).

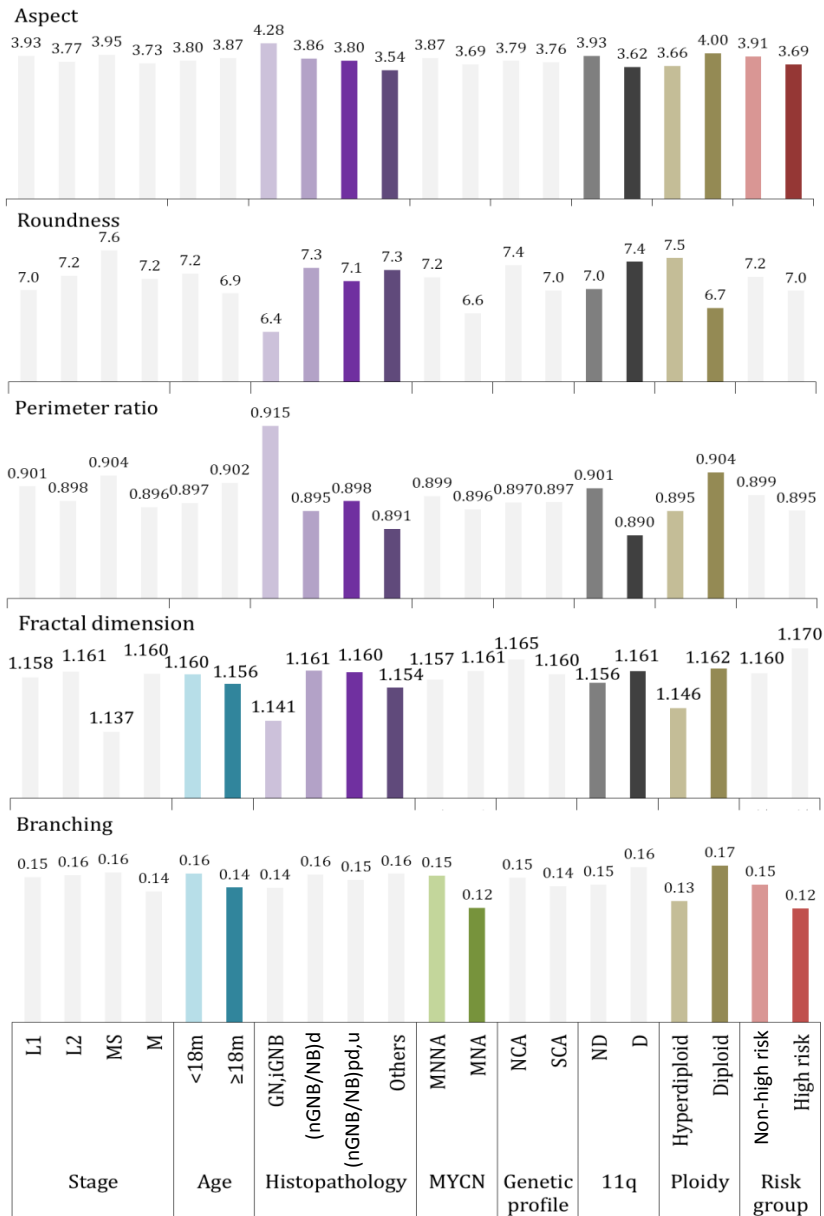


Figure 54: Distribution of the shape variables depending on the INRG clinical and biological variables. Variables in grey mean no significant statistical relationship. Colored variables show significant statistical relationship (table 32). The median values are shown.

A summary of the previous results is provided as an integrative image (figure 55).

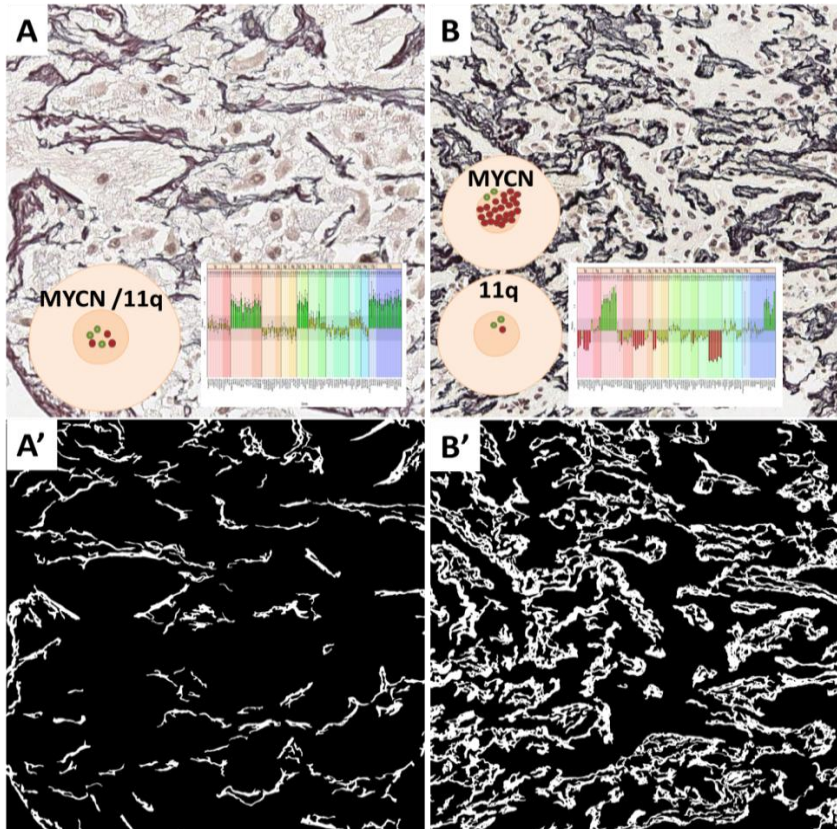


Figure 55: Simplified summary of the major associations between the INRG parameters and the reticulin fibers. **A)** Tumors with differentiated histopathology (iGNB), no segmental aberrations and triploid DNA content are related to less area of smaller reticulin fibers with more regular outlines. **A')** Binary image to better distinguish the fibers properties in A. **B)** Tumors with unfavorable histopathology (uNB) with segmental aberrations including 11qD and MNA and diploid DNA content are related to a higher area covered by bigger and more irregular reticulin fibers. **B')** Binarized image to better distinguish the reticulin fiber networks properties in B. The age variable appears to be inversely related to the fractality and branching of the reticulin fibers.

4.1.5. Survival analysis

A. Multivariate analysis

When testing the reticulin fibers variables on their own or in combination with the INRG variables, none of them influenced survival, whether including or excluding stage. A table showing HR and p-values is therefore not provided.

B. Study of the high risk group

The dichotomized morphometric variables showed statistically significant differences regarding survival (OS, EFS). A table with the morphometric parameters and the cut points is provided (**table 33**). The Kaplan-Meier graphs are shown (**figure 56 to 60**).

Table 33: Morphometric variables and cut points used to dichoromize them.

Parameter	EFS		OS	
	Cut point	p-value	Cut point	p-value
Density	-	-	-	-
% of stained area	Q2: 5.8	0.03	Q2: 5.8	0.000
Area	-	-	Q2: 77.7	0.013
Length	-	-	Q2: 20.8	0.013
Width	-	-	Q2: 8.5	0.013
Aspect	-	-	-	-
Roundness	Q2: 6.9	0.007	Q2: 6.9	0.002
Perimeter ratio	-	-	-	-
Fractal dimension	-	-	Q1: 1.15	0.046
Branching	Q1: 0.08	0.014	Q2: 0.12	0.003

Q1: first quartile, Q2: median, Q3: third quartile, -: not statistically significant.

- Reticulin fibers quantity variables

The % of area covered by networks of reticulin fibers defined two risk groups within the high risk patients. When the % of stained

area was over the median (high stained area), the patients had a $16.6 \pm 7.3\%$ 5-year EFS and a $11.3 \pm 6.3\%$ 5-year OS (**figure 56**).

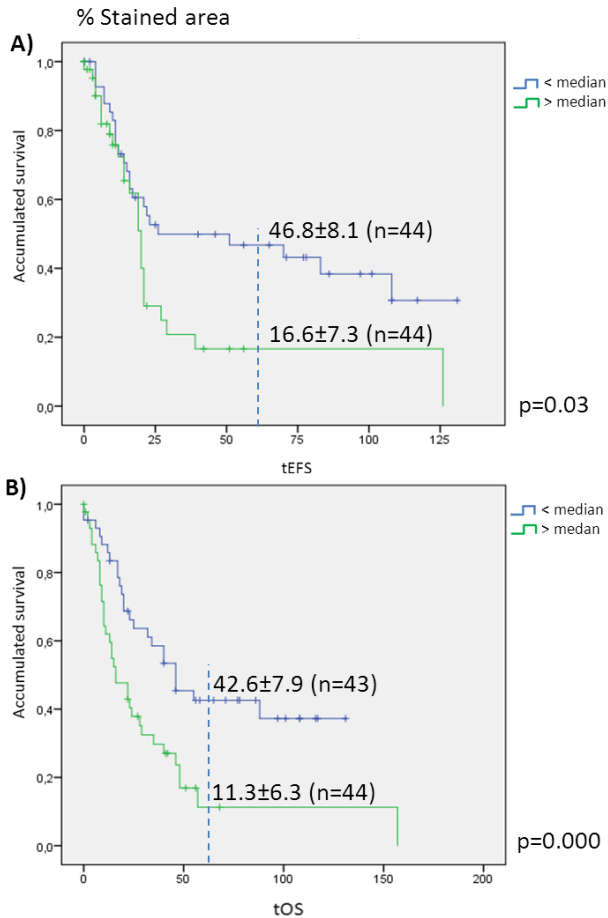


Figure 56: Kaplan-meier graph showing the different accumulated survival depending on the % of stained area. **A)** EFS and **B)** OS.

- Reticulin fibers size variables

An area, length and width over the median value defined a very poor survival group with $<17\%$ 5-year OS, within the high risk patients group (**figure 57**).

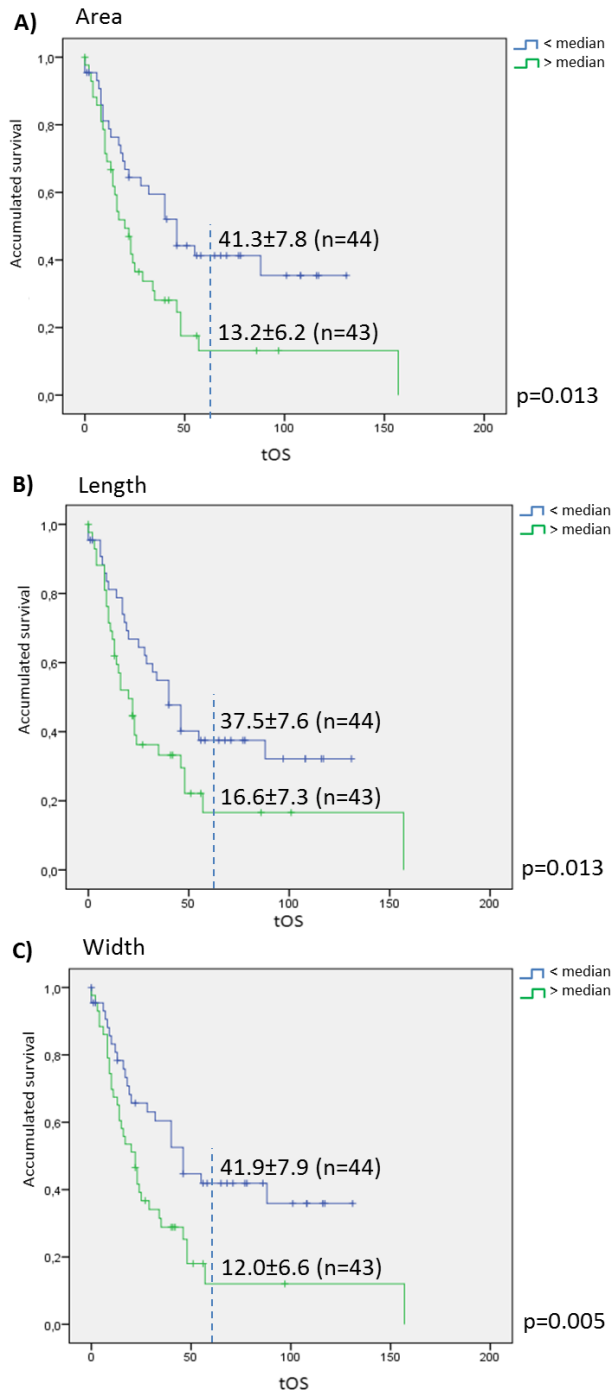


Figure 57: Kaplan-meier graph showing the different accumulated OS depending on the size variables. **A) Area**, **B) width** and **C) length**.

- Reticulin fibers shape variables

A roundness over the median value defined a very poor prognostic group with <16% 5-year EFS and 5-year OS (**figure 58**). A branching degree over the 1st quartile for EFS and over the median value for OS defined a group with 21.8±6.6% 5-year EFS and 10.9±6.1% 5-year OS (**figure 59**). Finally, a fractal dimension over the median defined a 13.4±7.7% 5-year OS (**figure 60**).

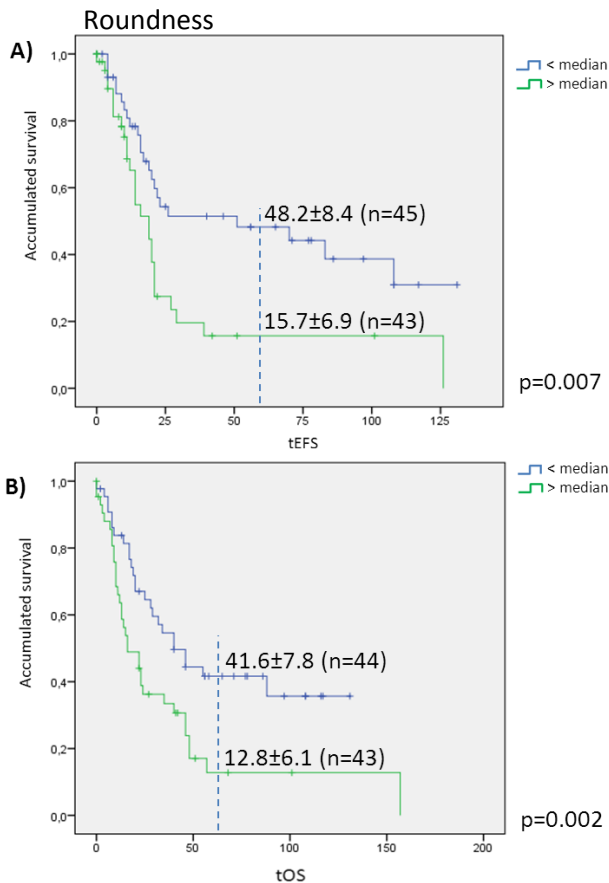


Figure 58: Kaplan-meier graph showing the different accumulated survival depending on the roundness. **A)** EFS and **B)** OS.

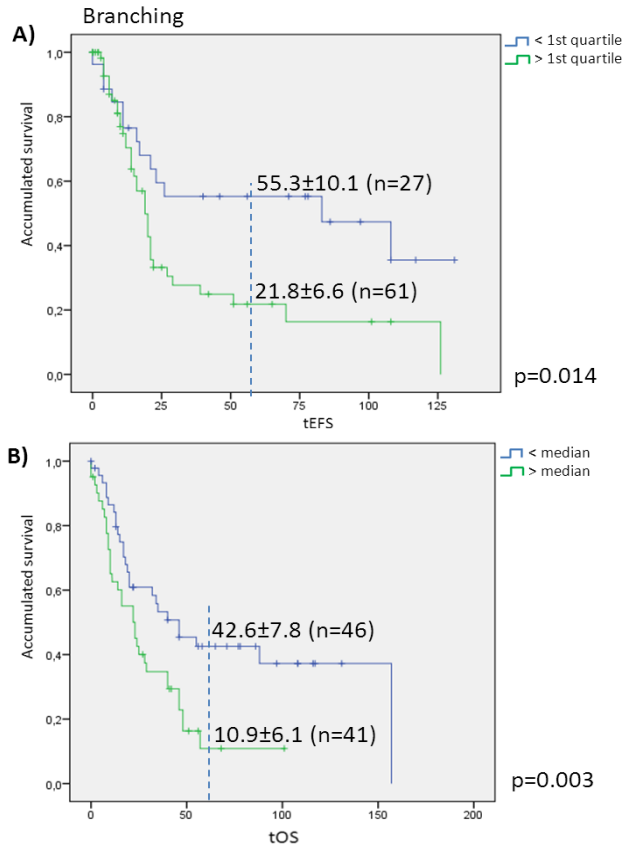


Figure 59: Kaplan-meier graph showing the different accumulated survival depending on the branching. **A)** EFS and **B)** OS.

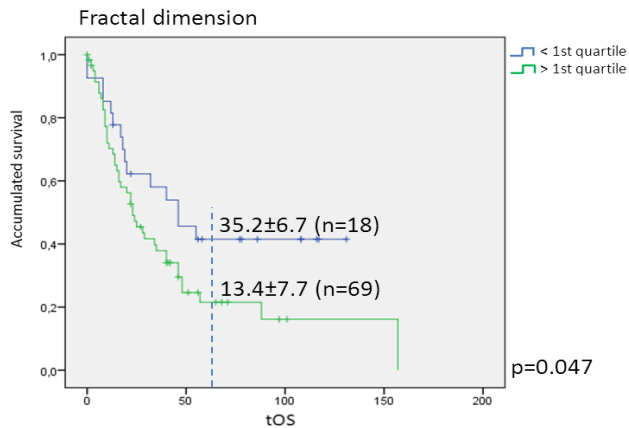


Figure 60: Kaplan-meier graph showing the different accumulated OS depending on the fractal dimension.

4.1.6. Reticulin fibers after treatment and in other samples

The stained area of reticulin fibers corresponding to the different samples of primary NB, non-primary NB, peritumoral tissue, other tumors tissue and non-tumoral tissue is shown in **table 34**. The statistical analysis comparing the different groups of samples is presented in **table 35**.

Both primary and non-primary NB samples presented an amount of reticulin fibers around 8%, equal to the amount found in sympathetic ganglia and paraganglia and fat. Primary NB accounted for a lower amount of reticulin fibers compared to peritumor areas and non-tumoral areas and, specifically, they had a lower amount of fibers than the adrenal gland and similar to the liver. We also observed that non-primary NB presented a decreased amount of fibers compared to peritumoral tissue, other tumors tissue and non-tumoral tissue. Indeed, a disruption of the organization of the reticulin fibers is observed when passing from peritumoral tissue to tumoral tissue, which is mainly observable at the tumor-host margin (**figure 61**). Pancreas was the sample with the highest reticulin fiber amount, followed by lymphoma, peritumoral liver and lymph node (>17%).

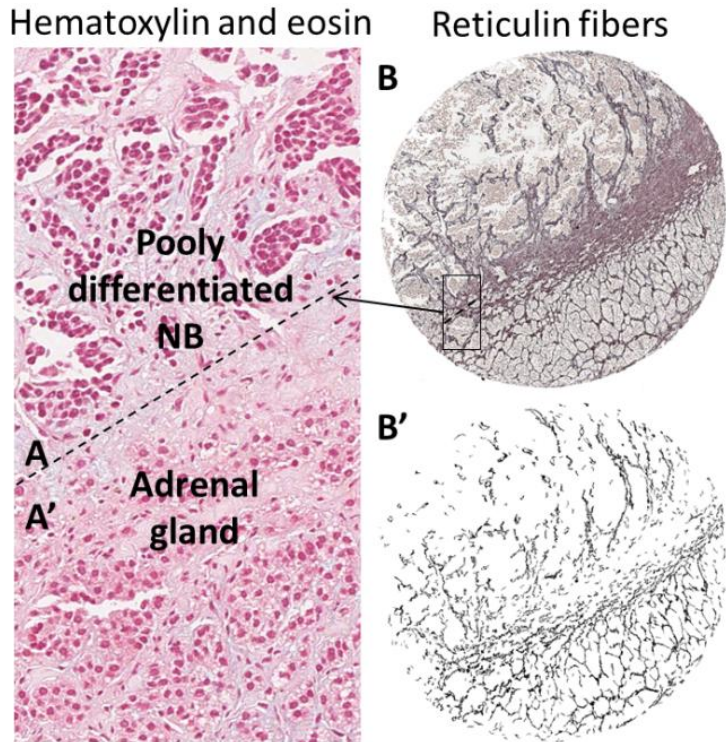


Figure 61: TMA cylinder containing **A)** a poorly differentiated neuroblastic tumor and **A')** the host tissue, being the adrenal gland. **B)** The reticulin fibers have been selected and the binarized images are shown in **B'**. A disruption of the organization of the fibrous scaffolding is observable in general and mainly at the tumor-host boundaries.

Table 34: % of stained area occupied by reticulin fibers in the different control tissues studied.

Samples	Reticulin fibers	
	Mean	Median
Primary NB (n=393)	8.4±7.2	6.5
Non-primary NB (n=76)	8.7±6.9	7.0
Peritumoral tissue (n=24):	12.7±7.6	12.2
• Lymph node (n=1)	17.2	17.2
• Adrenal gland (n=8)	11.9±6.3	12.2
• Liver (n=2)	17.7±5.6	17.7
• Striated muscle (n=1)	31.5	31.5
• Pancreas (n=2)	18.9±6.8	18.9
• Simpathetic ganglia and paraganglia, fat (n=10)	8.6±5.9	9.0
Other tumors tissue (not NB) (n=4):	12.9±4.4	10.7
• Lymphoma (n=1)	18.0	18.0
• Olfactory estesioNB (n=1)	9.9	9.9
• CC. sarcoma of the kidney (n=1)	-	-
• Adrenocortical carcinoma (n=1)	10.7	10.7
Non-tumoral tissue/organs (n=27):	12.4±4.8	11.7
• Kidney (n=14)	14.7±3.7	15.2
• Liver (n=2)	8.2±9.7	8.2
• Striated / Smooth muscle (n=5)	10.8±7.1	11.6
• Spleen (n=1)	6.02	6.02
• Placenta (n=4)	10.2±2.3	10.5
• Salivary gland (n=1)	11.3	11.3

CC.: Clear cell, -: data not available (artefactual staining).

Table 35: p-values arising from the comparison of ECM non-cellular parameters in different tissues.

Parameter	Reticulin fibers
Prim. NB vs non-prim. NB	-
Prim. NB vs per. tissue	0.002
Prim. NB vs other tumors	-
Prim. NB vs non-tumoral	0.000
Non-prim. NB vs per. tissue	0.007
Non-prim. NB vs other tumors	0.015
Non-prim. NB vs non-tumoral	0.000
Per. Tissue vs other tumors	-
Per. Tissue vs non-tumoral	-
Other tumors vs non-tumoral	-

Prim. NB: primary NB, not-prim NB: non-primary NB, per.tissue: peritumoral tissue.

4.2. Collagen fibers

4.2.1. Histological observation

In general, collagen type I fibers distribution is restricted to stromal fibrous areas or large trabecules (**figure 62**). Masson's trichrome staining shows that these fibers are also located in the perineurium of nerve bundles (**figure 63**). Collagen type I fibers are also found in the *adventitia* of large blood vessels (**figure 64**).

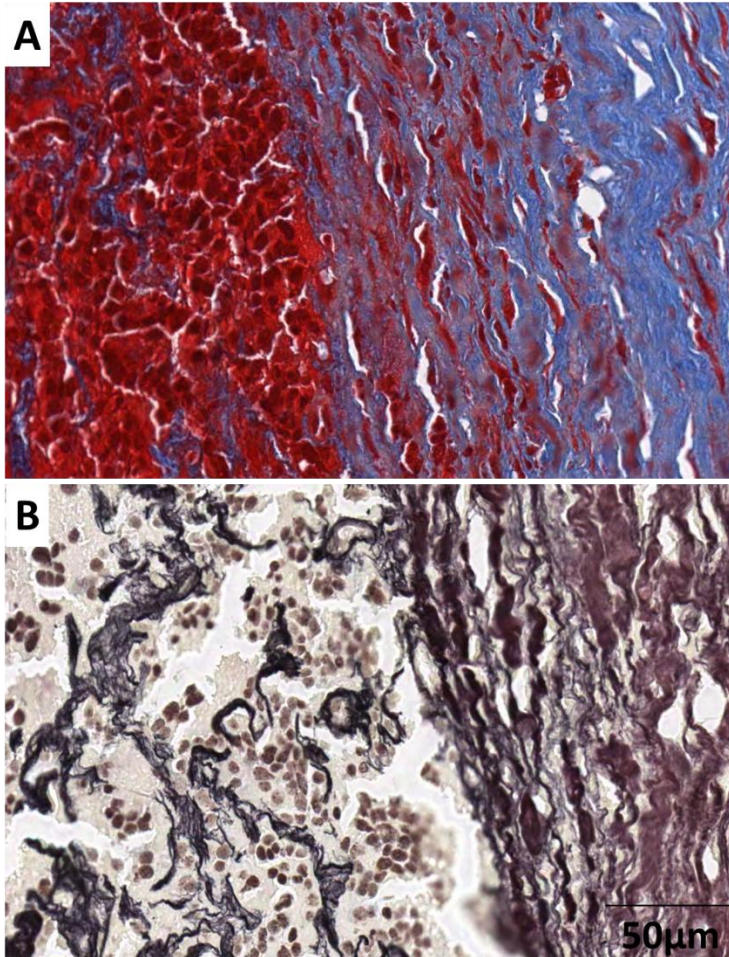


Figure 62: Neuroblastic tumor tissue showing a cellular area and a large trabecule. **A)** Masson's trichrome showing large collagen type I fibers in the trabecule and thinner fibers within neuroblasts. **B)** Gomori staining revealing black argentic staining of the reticulin fibers within the neuroblasts and wavy purple fibers in the trabecule, corresponding to collagen type I fibers.

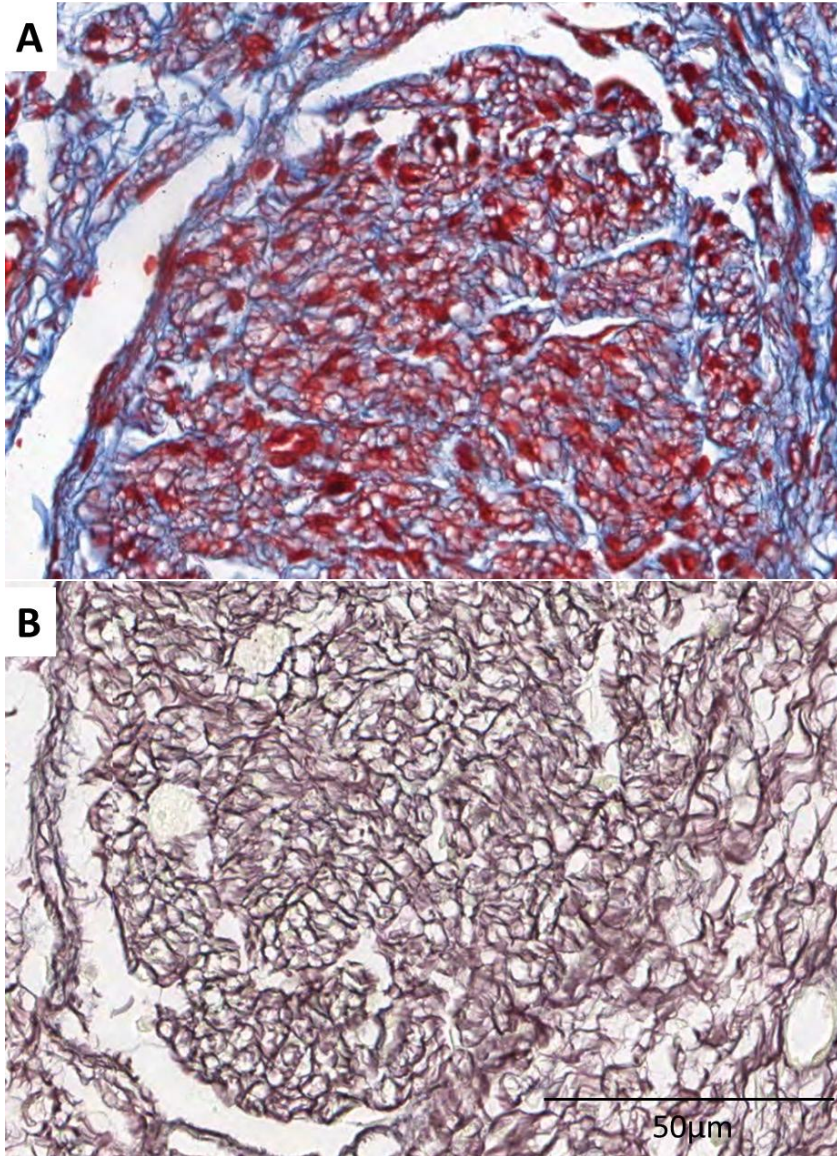


Figure 63: Nerve bundle. **A)** Masson's trichrome revealing fine collagen fibers in the endoneurium and wavy bundles in the perineurium. **B)** Gomori staining revealing black argentic staining of the reticulin fibers in the endoneurium and wavy purple fibers in the perineurium, corresponding to collagen type I fibers.

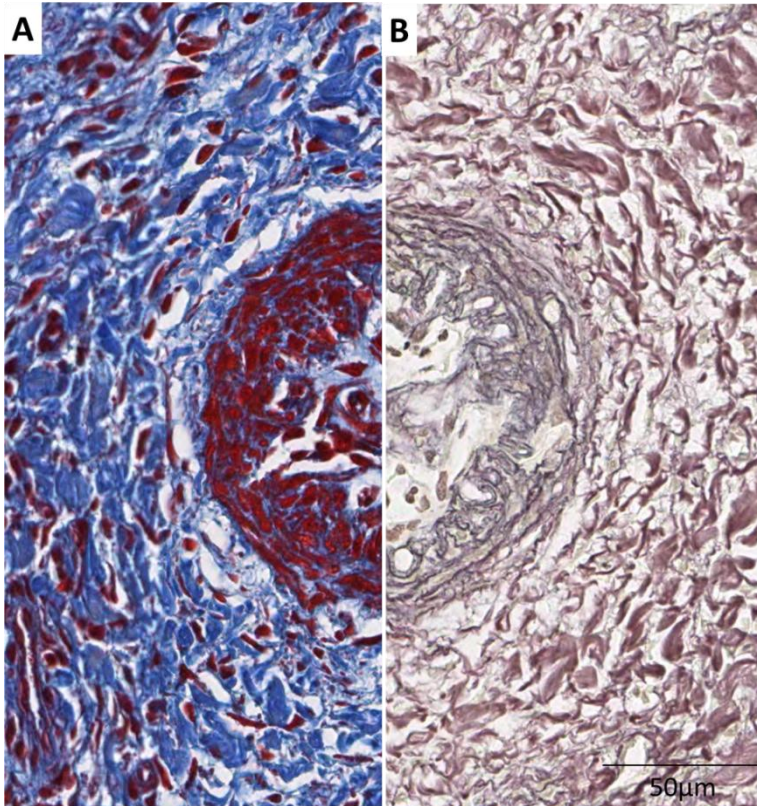


Figure 64: Large blood vessel with a huge adventicia composed by collagen type I fibers. **A)** Masson's trichrome revealing fine collagen fibers in the *adventitia*. **B)** Gomori staining revealing black argentic staining of the reticulin fibers in the *tunica intima* and wavy purple fibers in the *adventitia*, corresponding to collagen type I fibers.

4.2.2. Description of the variables

Given the restrictive parameters used to design a specific algorithm to detect only thick bundles of collagen type I fibers, only the variable % of stained area was calculated. Although all collagen fibers were observable as blue-stained fibers, only those fibers forming bundles were measured by restricting the thickness of the elements recognized, and the data reported corresponds only to them. 393 biopsies (84%) were eligible for collagen type I bundles analysis. Among

them, the average % of stained area was $2.25 \pm 4.35\%$ and the median value was of 0.24. This difference was explained by the fact that a very high proportion of the biopsies showed no collagen type I fibers in their ECM. Specifically, 104 biopsies (26%) had 0% of stained area detected and 50 samples had $<1\%$ of stained area. The positive biopsies presented a collagen type I fibers amount ranging from 0.1% to 31.2% (**figure 65**, **table 36**). The number samples out of study was of 65, being 47 of them lost cylinders and 18 of them not representative.

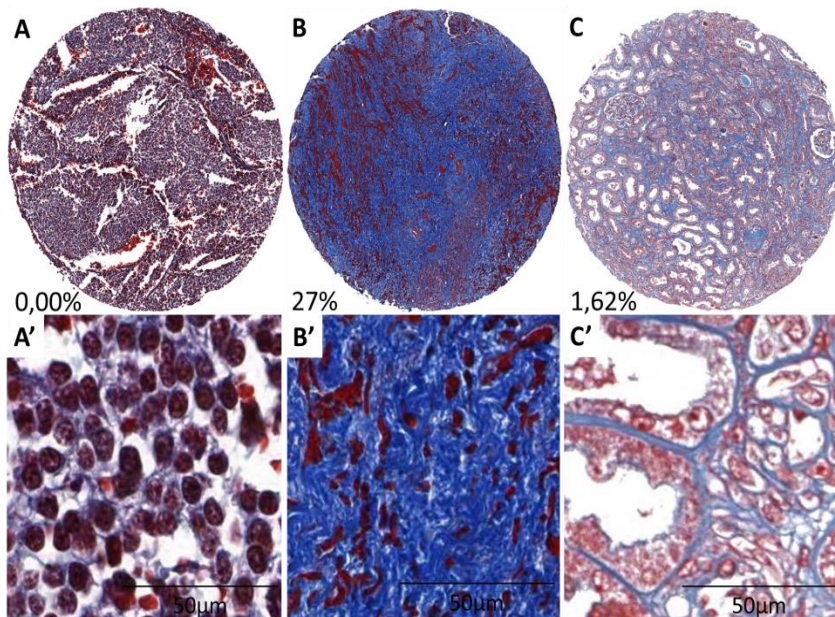


Figure 65: Examples of cylinders with different amounts of collagen fibers in the ECM. **A)** Neuroblastic tumor presenting no collagen type I fibers in the ECM but presenting reticulin fibers instead. **A')** Detail of the ECM of image A where it can be observed that blue stain does not correspond to collagen type I fibers. **B)** Neuroblastic tumor with a very high content (27%) of collagen type I fibers in its stroma. **B')** Detail of image B. Large collagen type I bundles are shown. Reticulin fibres are also stained. **C)** Control cylinder corresponding to a kidney with 1.62% of area covered by collagen type I fibers. **C')** Detail of image C. The majority of fibers correspond to type III collagen (reticulin fibers).

Table 36: Description of the morphometric measurements of the collagen type I fibers in a subset of 393 samples.

Parameter	Mean	Median	SD	Min.	Max.
% stained area	2.25	0.24	4.35	0.00	31.2

4.2.3. Favorable and unfavorable collagen type I histological patterns

The results of the univariate non-parametric analyses comparing the collagen fibers amount with the INRG variables with prognostic value are shown in **table 37**. The abundance of collagen type I fibers in neuroblastic tumors was related to the age of the patient, to the tumor histopathology, genetic aberrations in general and, specifically, *MYCN* status, and, therefore, to the risk group.

Table 37 p-values resulting from the relation of the morphometric characterization of the collagen type I fibers and the clinical and genetic INRG variables.

INRG variable	% stained area
Stage	-
Age	0.006
Histopathology	0.000
<i>MYCN</i>	0.005
Genetic profile	0.014
11q	-
Ploidy	-
Risk group	0.011

-: not statistically significant

How these parameters were distributed in the subcategories of the clinical and biological INRG variables is shown in **figure 66**. Tumors of patients younger than 18 months of age with favorable histopathology, MNNA, NCA alterations and non-high risk had a higher content of collagen type I.

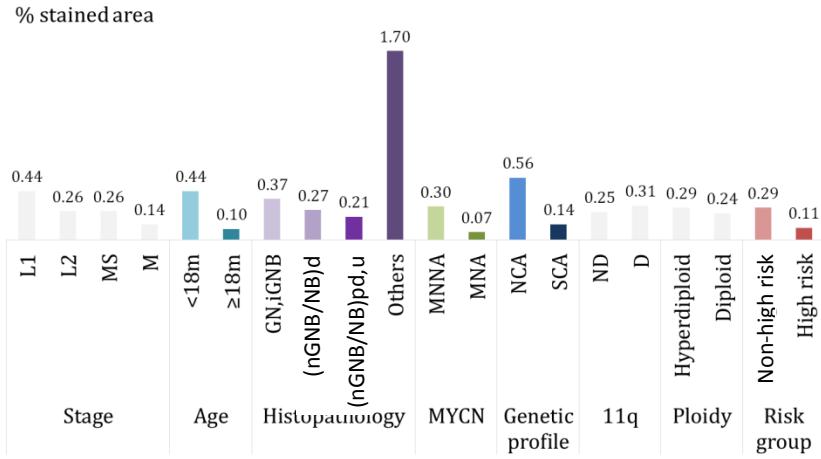


Figure 66: Distribution of the % of collagen type I stained area depending on the INRG clinical and biological variables. Variables in grey mean no significant statistical relationship. Colored variables show significant statistical relationship (**table X**). The median values are shown.

How the INRG parameters were associated with the abundance of collagen type I fibers is summarized in **figure 67**.

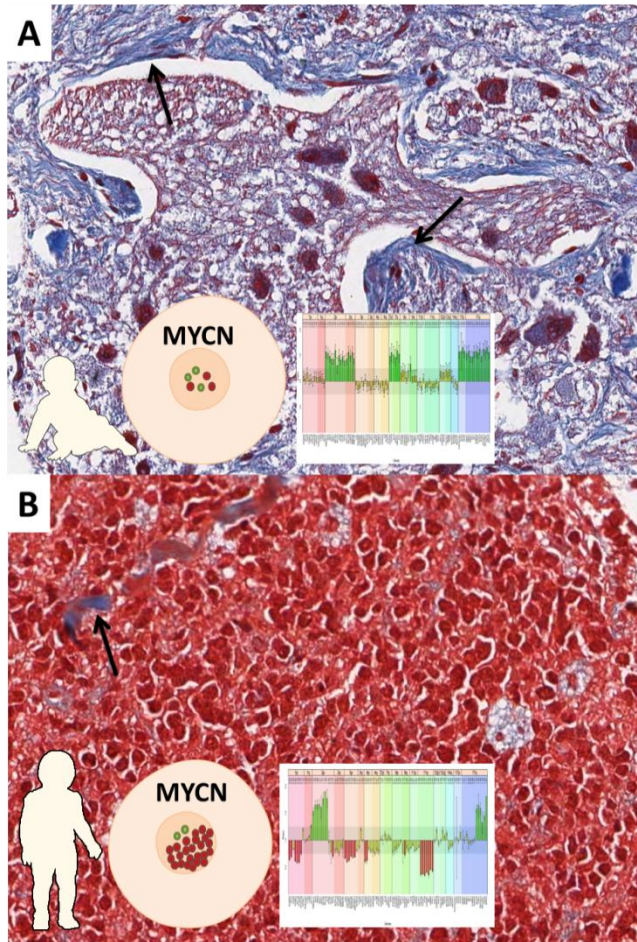


Figure 67: Representation of the associations between the INRG parameters and the collagen type I fibers. **A)** Tumors of children less than 18 months of age with differentiated histopathology (iGNB), MNNA and numerical aberrations are associated with a higher collagen type I fibers content (although minimal) (arrow). **B)** Tumors from patients over 18 months of age with unfavorable histopathology (uNB) with segmental aberrations including MNA are related to a lower area covered by collagen type I fibers bundles (arrow).

4.2.4. Survival analysis

A. Multivariate analysis

A smaller area covered of collagen type I fibers, alone, triggered a poor OS with a HR of 0.876 (0.7-0.9) (**table 38**).

Nevertheless, this factor did not influence EFS. Moreover, when combining the amount of collagen type I fibers with the INRG variables, no influence was found on survival, whether including or excluding stage.

Table 38: Results of the Cox regression showing the influence of collagen type I fibers amount on survival.

Variable	Wald	HR (95% CI)	p-value
EFS			
a,b,c	-		
OS			
a % stained area	4.4	0.876 (0.7-0.9) [^]	0.035
b, c	-		

a: morphometric variable on its own, b: morphometric variables + all INRG variables, c: morphometric variables + INRG variables except stage, HR: Hazard ratio, CI: Confidence interval, -: no statistically significant morphometric variable. [^]Inverse correlation.

B. Study of the high risk group

The dichotomized variable corresponding to the amount of collagen type I fibers in the ECM of high risk neuroblastic tumors did not influence survival. A table with the morphometric parameters and the cut points is thus not provided.

4.1.5. Collagen type I fibers after treatment and in other samples

The stained area collagen type I fibers corresponding to the different samples of primary NB, non-primary NB, peritumoral tissue, other tumors tissue and non-tumoral tissue is shown in **table 39**. The statistical analysis comparing the different groups of samples is presented in **table 40**.

Primary NB accounted for a lower amount of collagen type I fibers compared to non-primary NB and to peritumor areas. Besides of the adrenocortical carcinoma sample, the highest abundance of collagen type I fibers corresponded to simpathetic ganglia and paraganglia and fat samples and to the salivary gland.

Table 39: % of stained area occupied by collagen type I fibers in the different control tissues studied.

Samples	Collagen type I	
	Mean	Median
Primary NB (n=393)	2.2±4.3	0.24
Non-primary NB (n=76)	4.5±8.0	1.1
Peritumoral tissue (n=24):	5.3±10.4	1.5
• Lymph node (n=1)	5.8	5.8
• Adrenal gland (n=7/8/8)	2.6±5.4	0.25
• Liver (n=2)	0.29±0.4	0.29
• Striated muscle (n=1)	7.8	7.8
• Pancreas (n=2)	1.5±0.4	1.5
• Simpathetic ganglia and paraganglia, fat (n=10)	9.0±14.9	1.99
Other tumors tissue (not NB) (n=4):	5.6±6.09	4.7
• Lymphoma (n=1)	0.0	0.0
• Olfactory estesioNB (n=1)	1.3	1.32
• CC. sarcoma of the kidney (n=1)	8.1	8.1
• Adrenocortical carcinoma (n=1)	13.0	13.0
Non-tumoral tissue/organs (n=25):	2.1±2.29	1.7
• Kidney (n=12)	2.0±1.7	1.9
• Liver (n=2)	0.02±0.03	0.02
• Striated / Smooth muscle (n=5)	4.48±2.1	1.9
• Spleen (n=1)	0.0	0.0
• Placenta (n=5)	1.5±1.8	0.9
• Salivary gland (n=1)	6.1	6.1

CC.: Clear cell.

Table 40: p-values arising from the comparison of ECM non-cellular parameters in different tissues.

Parameter	Collagen type I F
Prim. NB vs Non-prim. NB	0.015
Prim. NB vs per. tissue	0.015
Prim. NB vs other tumors	-
Prim. NB vs non-tumoral	-
Non-prim. NB vs per. tissue	-
Non-prim. NB vs other tumors	-
Non-prim. NB vs non-tumoral	-
Per. Tissue vs other tumors	-
Per. Tissue vs non-tumoral	-
Other tumors vs non-tumoral	-

Prim. NB: primary NB, not-prim NB: non-primary NB, per.tissue: peritumoral tissue.

4.3. Elastic fibers

Elastic fibers appear restricted to vascular contours and, in few cases, to fibrous trabecules. In every case, the amount of elastic fibers in tumor parenchymatous areas was negligible (**figure 68**). 100% of the evaluable cylinders are scored negative: no expression is detected or <5% of stained area.

This ECM element is therefore not specially distributed within different subsets of neuroblastic tumors not can be used as prognostic factor for neuroblastoma patients.

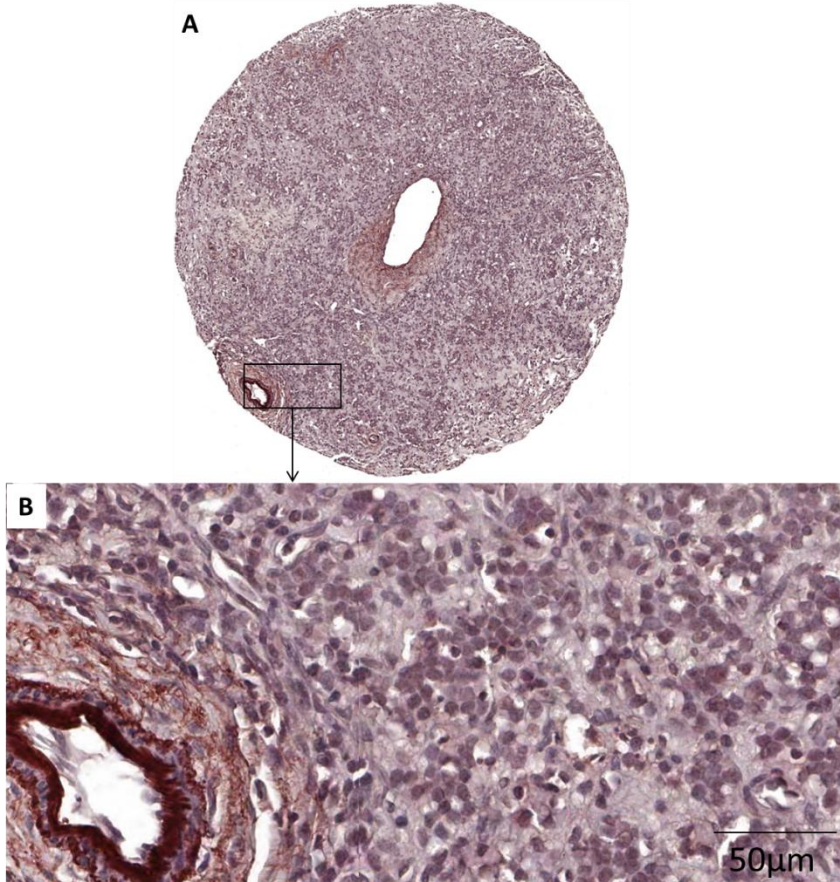


Figure 68: Example of a cylinder stained with Orcein to detect elastic fibers. **A)** The whole cylinder is shown. **B)** Detail where it can be observed that no elastic fibers exist within the tumor cells and that these fibers are restricted to blood vessels.

5. Study of the blood vessels.

5.1. Generalities of vascularization

Among the 458 primary tumors studied, 85 samples could not be analyzed for technical reasons (not representative area and mostly lost cylinder). Among the 373 samples left, 48 did not show any positivity for blood vessels. These cases were counted as samples with zero vessels/mm² and 0% of stained area for quantity variables and therefore were not taken into account for size and shape variables, which were calculated for a subset of 325 samples (**figure 69**).

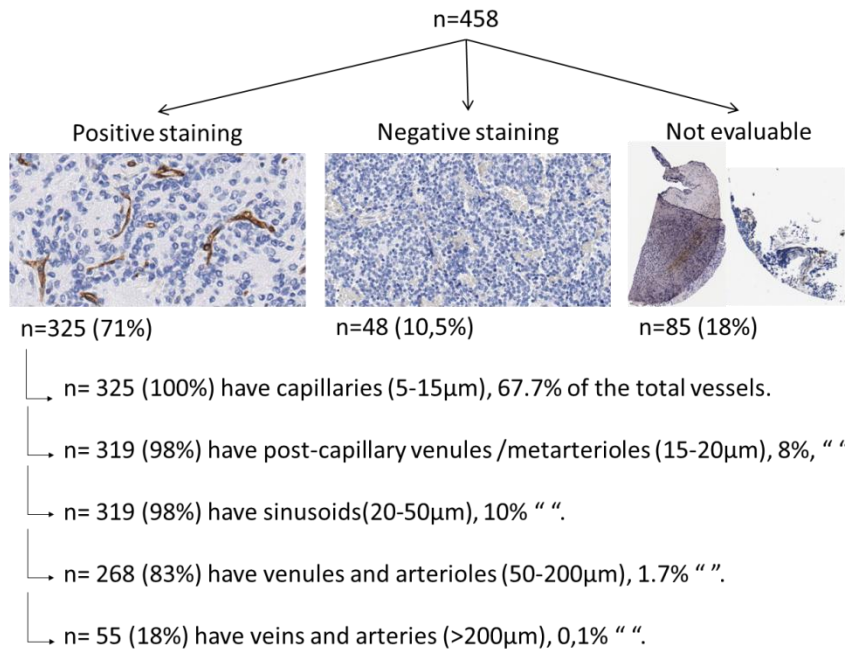


Figure 69: Distribution of the positive samples for CD31 immunohistochemistry, depending on the type of blood vessels studied, according to their maximum diameter or length.

5.2. Histological observation

Some vessels had an incomplete outline of epithelial cells expressing CD31 (**figure70**). The outline lacking epithelial cells was covered by round or polygonal cells which could be neuroblastic cells, immune cells or stem cells. Occasionally, other more fusiform cells occupied these spaces. This could correspond to angiogenic mimicry.

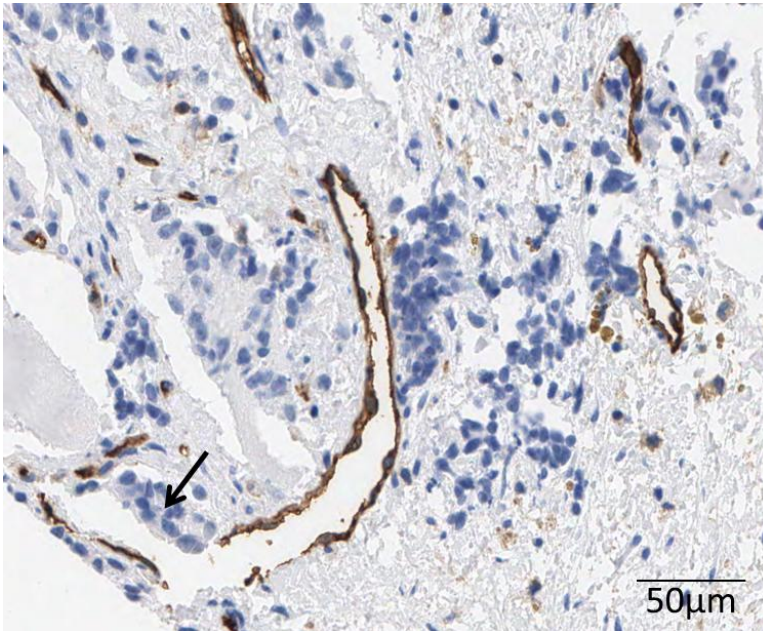


Figure 70: Example of a blood vessel with incomplete outline. Note the neuroblastic-like cells occupying the area without epithelial cells (arrow).

In a few samples most of the tissue area lacked CD31 expression, but however presented one or two vessels with CD31 positive endothelial cells. One example is shown in **figure 71**. In it, we can observe how the cylinder is mainly negative but shows, in the lower part of the cylinder two stained vessels, therefore indicating that the technique is working properly. Different hypotheses to explain this finding will be discussed.

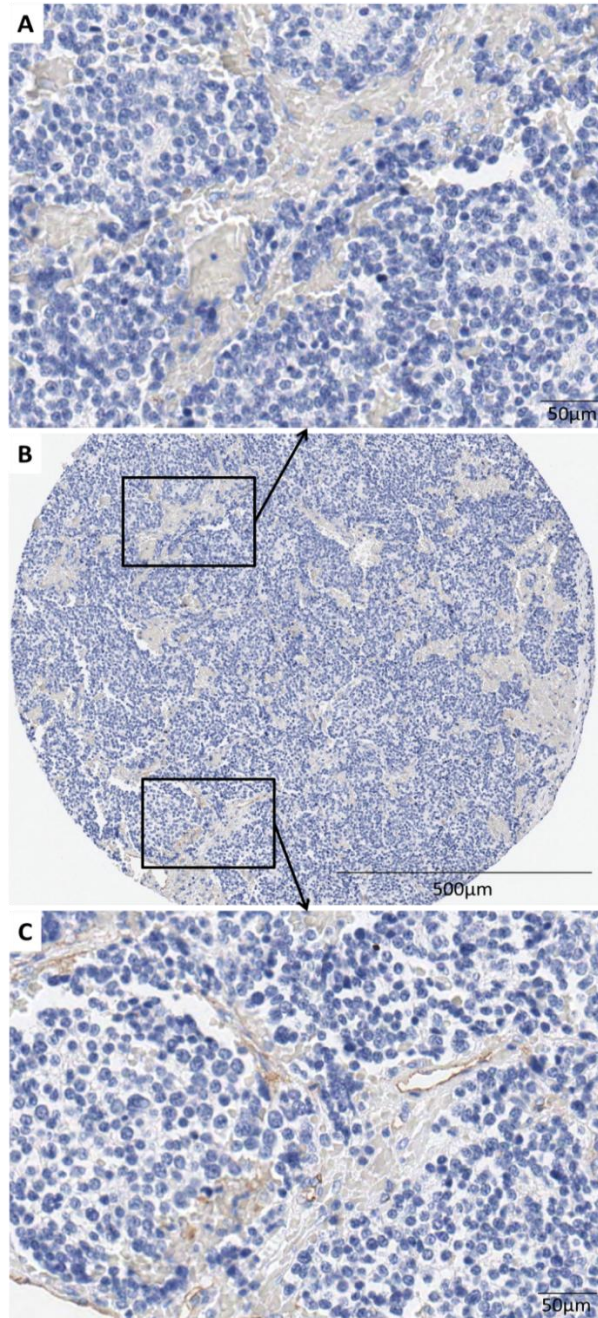


Figure 71: Cylinder with no expression for CD31 antibody except for two stained blood vessels. **A)** Detail of a negative area filled with erythrocytes. **B)** Image showing the whole cylinder with several areas such as the one presented in A. **C)** Detail of an area with two CD31 positive blood vessels.

In some cases, high endothelial venules (HEV) were found associated to tertiary lymph nodes or to non-grouped leukocytes (**figure 72**). Different antibodies were used to characterize the leukocytic cells. Moreover, some special organizations of the blood vessels with regard to neuroblastic and stromal cells are shown in **figure 73**. Blood vessels could be embolized by tumor cells therefore fostering the spreading of the disease, but some observed characteristics made difficult to distinguish whether this corresponded to a blood vessel embolization or the presence of tumor cell bundles isolated and surrounded by several blood vessels which were also present inside the clusters. In other cases, blood vessels were found collapsed (**figure 74**).

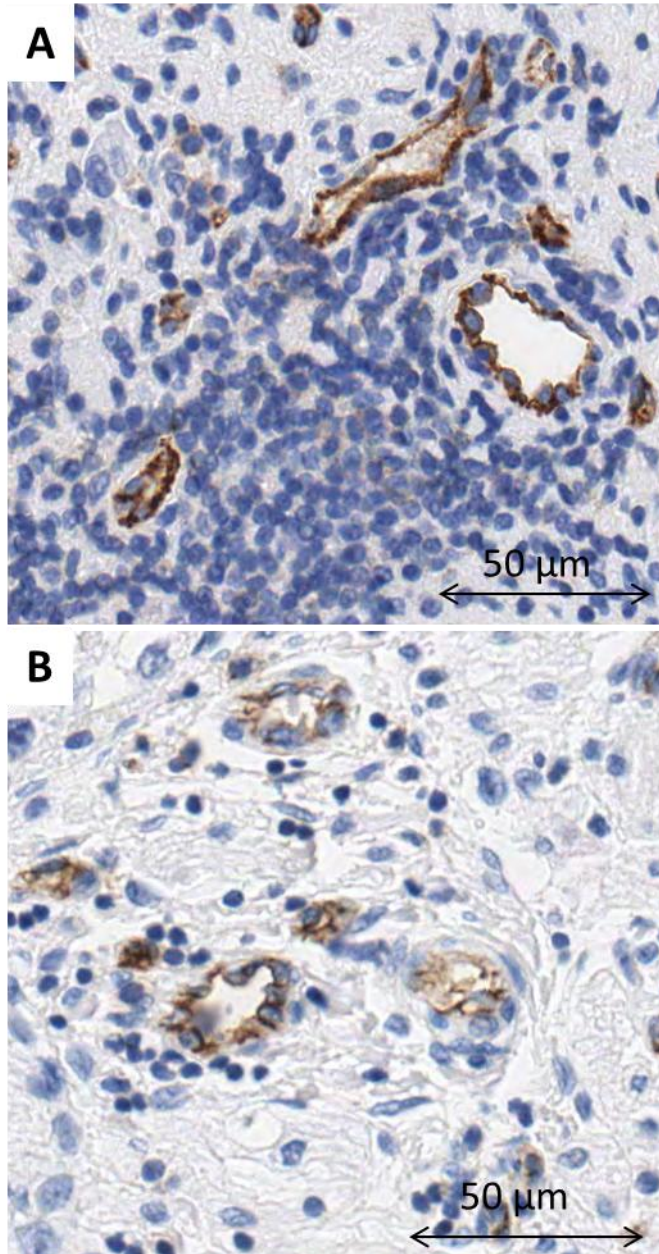


Figure 72: Special blood vessels in a subset of NBs, detected with CD31 antibody. A) HEV within a tertiary lymph node. B) HEV in close relationship with individual leukocytes within the tumor stroma.

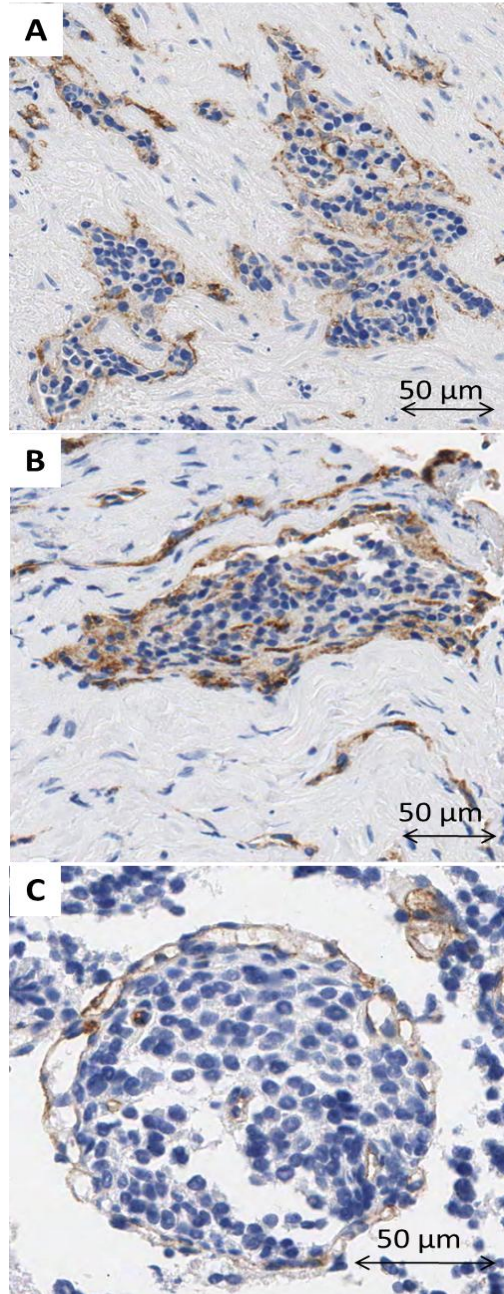


Figure 73: Spatial relationship between blood vessels and neuroblastic cells clusters. **A)** The vessels are embolized by tumor cells. **B)** Tumor cells are inside a blood vessel or many intermingled vessels surround the tumor cells. Some small vessels can be noticed inside the tumor cell cluster. **C)** In this case we can appreciate how many blood vessels with visible lumen are surrounding a tumor cell cluster with some microvessels inside.

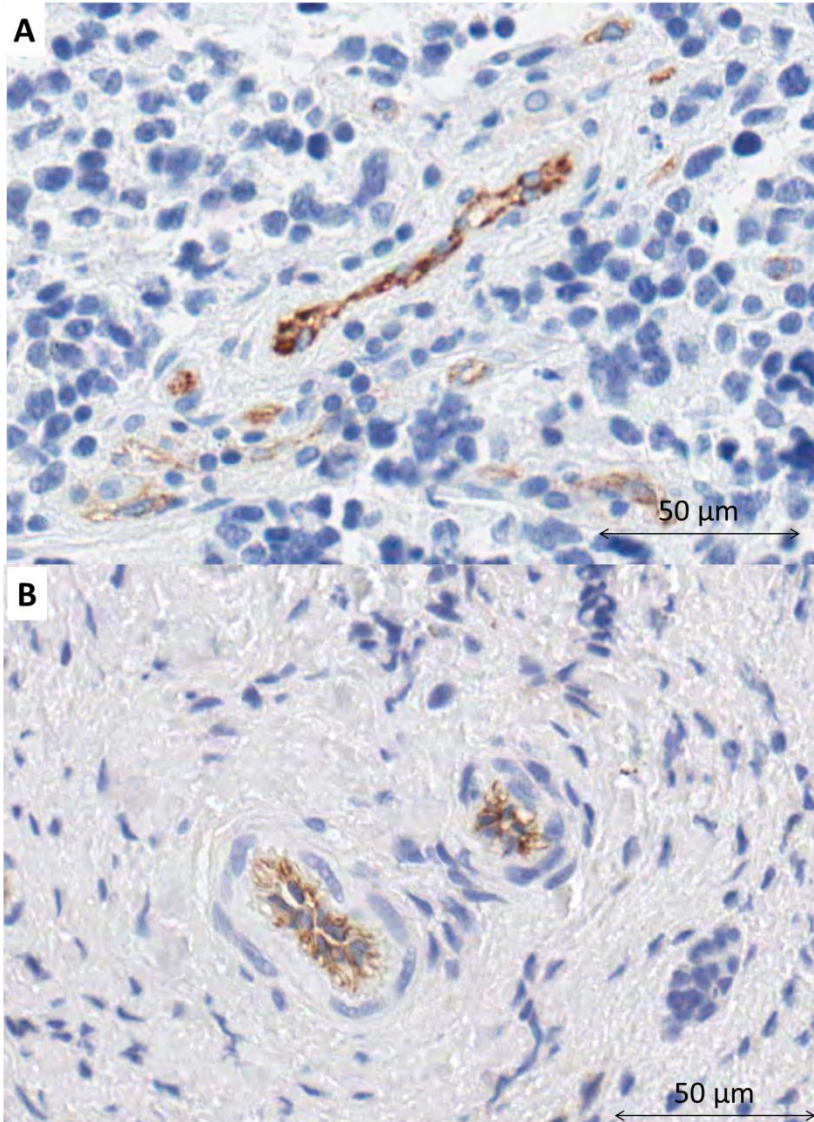


Figure 74: Two examples of blood vessels with collapsed *lumen*.

5.3. Total blood vascularization

5.3.1. Description of the variables

The description of the quantity, size and shape is shown in **table 41**. Neuroblastic tumors had an average of 161 ± 177 vessels/ mm^2

(figure 75) occupying an area of $1.7 \pm 1.2\%$ of the tissue. The mean blood vessel was $14 \mu\text{m}$ long and $7 \mu\text{m}$ wide and had a perimeter of $42 \mu\text{m}$ with an average area of $101 \mu\text{m}^2$. Regarding the average of the shape parameters, neuroblastic tumors blood vessels describe round, regular and smooth shapes with low degree of deformity and branching.

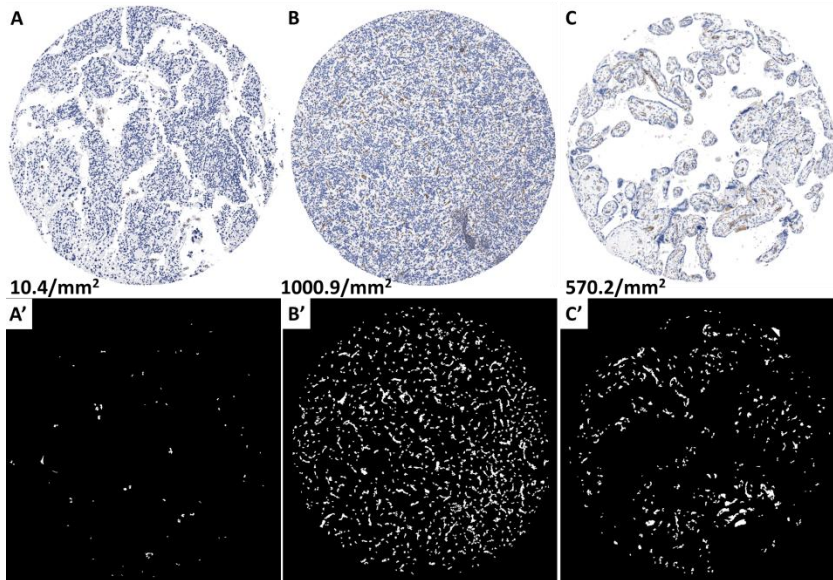


Figure 75: Different degrees of presence of blood vessels. The number of vessels per mm^2 is shown. **A)** NB with scarce blood vessels in its ECM. **B)** NB with high amount of blood vessels. **C)** Placenta as positive control, with a high amount of blood vessels (mainly capillaries). **A', B', C':** The binarized image of A, B, C is shown to better distinguish the blood vessels (in white on a black background)

Table 41: Description of the morphometric measurements of the blood vessels in a subset of 373 samples for quantity variables and 325 for size and shape variables.

	Parameter	Mean	Median	SD	Min.	Max.
Quantity	Density	161.1	102.4	177.7	0	1105
	% stained area	1.7	1.2	1.9	0	15
Size	Average area	100.9	69.6	278.9	22	4801
	Length	13.9	12.5	13.1	8	239
	Width	6.8	6.6	1.7	4	21
	Perimeter	42.4	40	14.4	21	187
Shape	Aspect	2.2	2.1	0.2	2	4
	Roundness	2.4	2.3	0.3	2	4
	Perimeter ratio	0.84	0.85	0.01	0.79	0.90
	Deformity	600.6	427.2	652.8	42	6198
	Shape factor	2.2	0.4	21.5	0.1	373
	Branching	2.7	2.7	0.2	2	4

5.3.2. Favorable and unfavorable blood vessel histological patterns

Most of the morphometric variables related to blood vessels were associated to the risk group. Blood vessels quantity was related to histopathology, size was related to *MYCN* status, shape was related to stage (aspect and vertices), histopathology (aspect and shape factor), *MYCN* status (all variables except roundness and perimeter ratio) and 11q status (aspect). Stage was very close from being significantly related to the blood vessels width ($p= 0.058$) and age was very close from being related to the blood vessels roundness ($p= 0.051$) (**table 42**).

Table42: Results of the relation of the morphometric characterization of total blood vessels and the clinical and genetic INRG variables.

Parameter	Stage	Age	Histopathology	MYCN	Genetic profile	11q	Ploidy	Risk group
Quantity	Density	-	0.008	-	-	-	-	-
	% stained area	-	0.033	-	-	-	-	-
Size	Average area	-	-	0.000	-	-	-	0.006
	Length	-	-	0.001	-	-	-	0.006
	Width	0.058*	-	0.000	-	-	-	0.000
	Perimeter	-	-	0.000	-	-	-	0.006
Shape	Aspect	0.036	0.000	0.001	-	0.043	-	0.002
	Roundness	-	0.051*	-	-	-	-	-
	Perimeter ratio	-	-	-	-	-	-	-
	Deformity	-	-	-	0.001	-	-	0.026
	Shape factor	-	-	0.014	0.046	-	-	-
	Branching	0.045	-	-	0.000	-	-	-

-: not statistically significant, *Tendency.

How these variables behaved depending on the INRG features is shown in **figures 76 to 798** Only variables with significant relationship with at least one INRG variable are shown.

A. Quantity variables

Tumors with a differentiated histology had a smaller amount of blood vessels which covered a smaller area, than tumors with undifferentiated histology (**figure 76**).

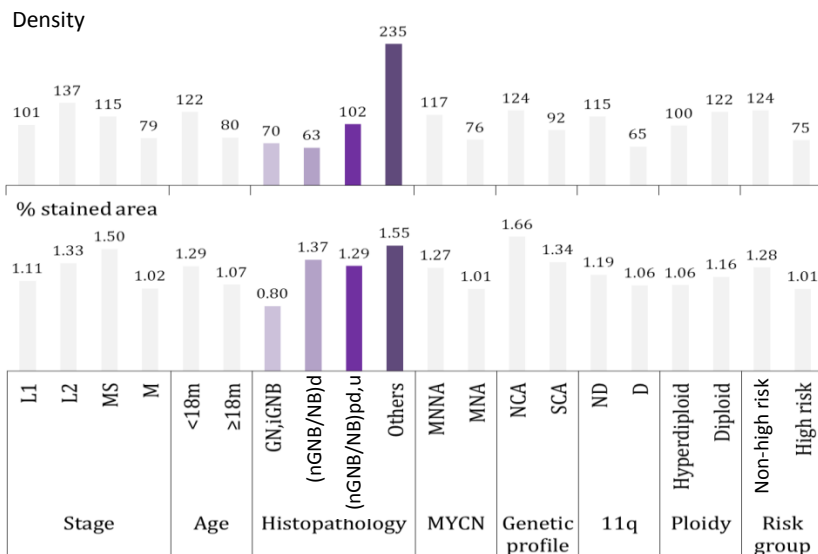


Figure 76: Distribution of the total number of vessels/mm² depending on the INRG clinical and biological variables. Variables in grey mean no significant statistical relationship. Colored variables show significant statistical relationship (**table 42**). The median values are shown.

B. Size variables

The blood vessels of MNNA tumors and of those from non-high risk patients were smaller than the vessels of MNA tumors and from high risk patients. Although not completely significant, localized stages also had vessels with lower width than advances stages (**figure 77**).

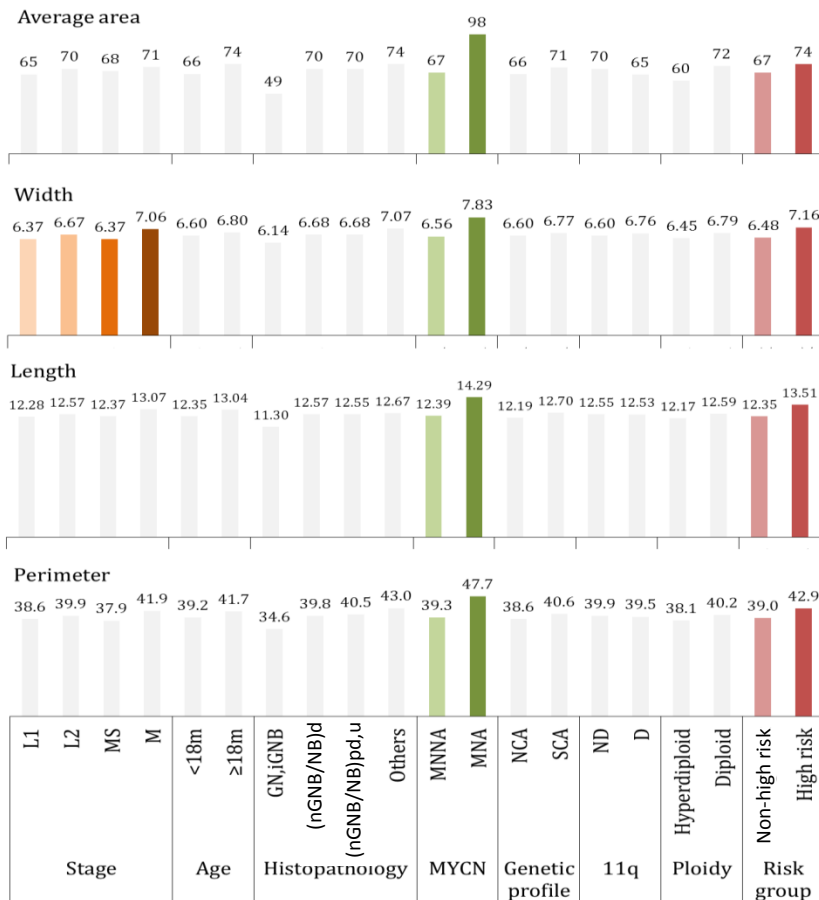


Figure 77: Distribution of the average area of total vascularization depending on the INRG clinical and biological variables. Variables in grey mean no significant statistical relationship. Colored variables show significant statistical relationship (**table 42**). The median values are shown.

C. Shape variables

Aspect was higher and, therefore, blood vessels were more ovoid for all better-prognosis INRG categories of stage, histopathology, MYCN status, 11q status and risk group. On the contrary, tumors from patients younger than 18 months of age tended to have a smaller roundness which is associated with a more round (less ovoid) shape. Neuroblastic tumors blood vessels had a smaller deformity for MNNA

tumors and those from non-high risk patients and a more regular shape for MNA and differentiated tumors. Fewer branching was found in MNNA tumors with localized disease and from non-high risk patients (figure 78).

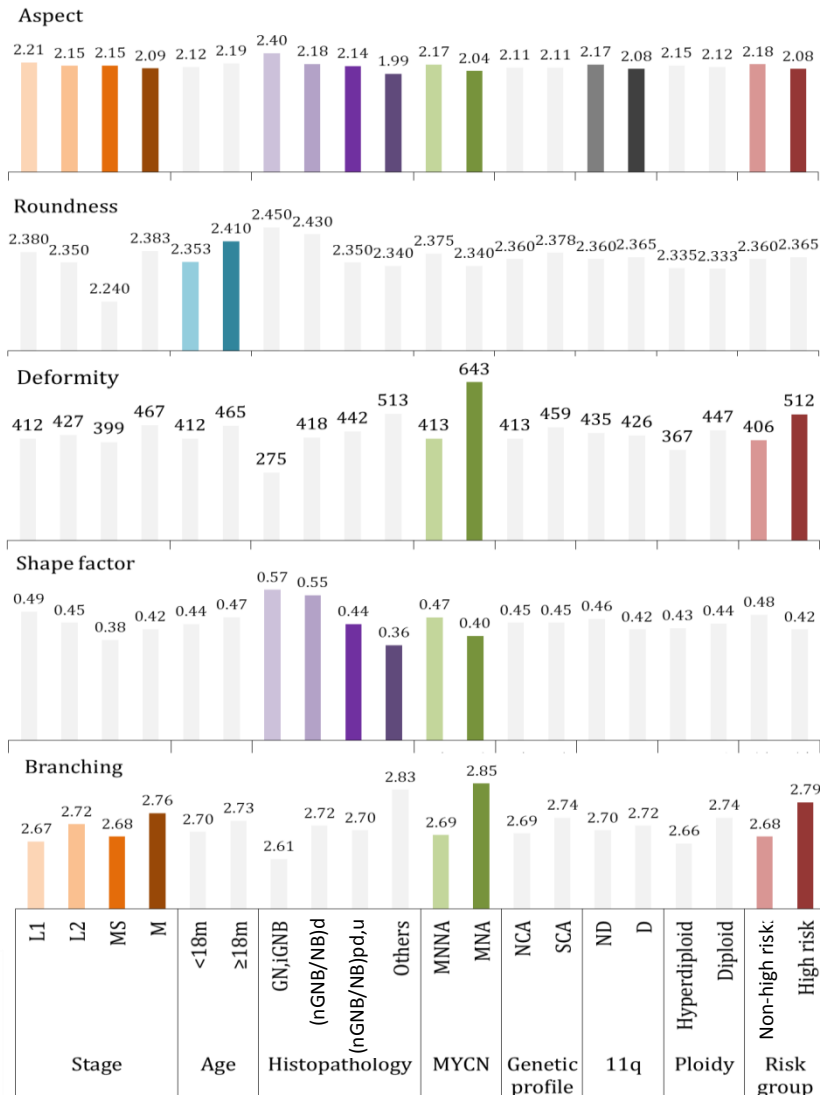


Figure 78: Distribution of the aspect of total vascularization depending on the INRG clinical and biological variables. Variables in grey mean no significant statistical relationship. Colored variables show significant statistical relationship (table 42). The median values are shown.

5.3.3. Survival analysis

A. Multivariate analysis

The results of the analysis of the relationship between the total blood vessels morphometric measurements and the EFS and OS variables on the 325 samples presenting blood vessels are shown in **table 43**.

Regarding EFS, we can observe that a larger length and a lower roundness were related with a higher risk of relapse with HR of 9.7 (1.01-1.08) and 4.2 (0.1-0.9), respectively. Regarding OS, we could observe that a higher branching degree, with a HR of 12.3 (2.0-12.8), and a lower amount of vessels, with a HR of 4.2 (0.9-1.0), influenced poor OS. Nevertheless, in both cases, the influence was lost when including the INRG variables, whether considering or not the stage variable.

Table 43: Results of the Cox regression showing the influence of total blood vessels morphometric measurements on their own and in combination with the INRG variables on 5 and 10-year EFS%.

	Variable	HR (95% CI)	p-value
EFS			
a	BV length	9.7 (1.01-1.08)	0.002
	BV roundness	4.2 (0.1-0.9)^	0.036
b, c		-	
OS			
a	BV branching	12.3 (2.0-12.8)	0.000
	BV density	4.2 (0.9-1.0)^	0.000
b, c		-	

a: morphometric variables on their own, b: morphometric variables + all INRG variables, c: morphometric variables + INRG variables except stage, BV: blood vessels, n^o: number of blood vessels, HR: Hazard ratio, CI: Confidence interval, -: no statistically significant morphometric variable. ^Inverse correlation.

B. Study of the high risk group

The dichotomized morphometric variables showed statistically significant differences regarding survival (OS, EFS). A table with the morphometric parameters and the cut points is provided (**table 44**). The Kaplan-Meier graphs are shown (**figure 79 to 80**).

Table 44: Morphometric variables and cut points used to dichoromize them.

Parameter	EFS		OS	
	Cut point	p-value	Cut point	p-value
Density	-	-	-	-
% stained area	-	-	Q3: 2.27	0.020
Average area	-	-	-	-
Length	-	-	-	-
Width	-	-	-	-
Perimeter	-	-	-	-
Aspect	-	-	-	-
Roundness	-	-	-	-
Perimeter ratio	-	-	-	-
Deformity	-	-	-	-
Shape factor	Q1: 0.28	0.047	Q1: 0.28	0.033
Branching	-	-	-	-

Q1: first quartile, Q2: median, Q3: third quartile, -: not statistically significant.

- Blood vessels quantity variables

The % of area covered by blood vessels defined two risk groups within the high risk patients. When the % of stained area was over the 3rd quartile, the patients had a 23.7±7.0% 5-year OS (**figure 79**).

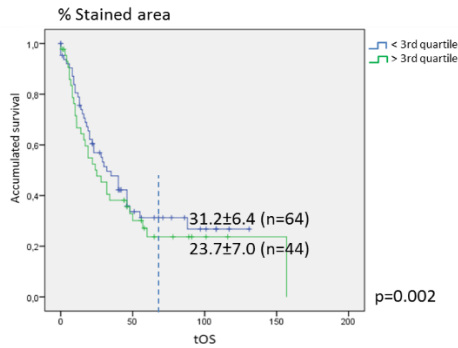


Figure 79: Kaplan-meier graph showing the different accumulated survival depending on the % of stained area.

- Blood vessels shape variables

A shape factor over the first quartile value defined a high risk group with 30% 5-year EFS and 24% 5-year OS, within our high risk cohort (**figure 80**).

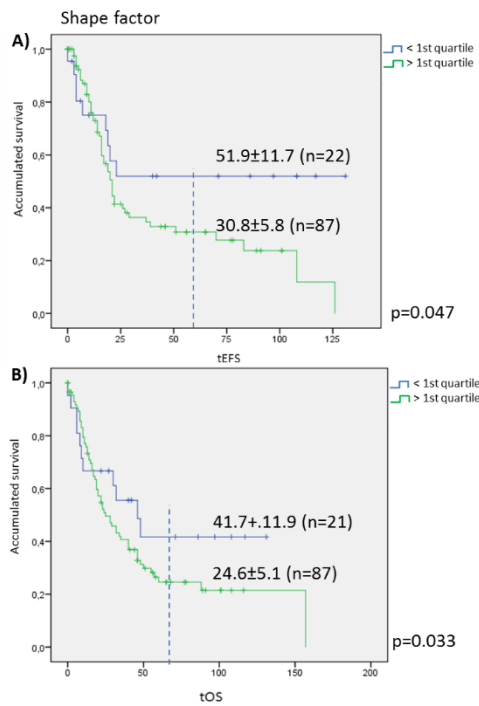


Figure 80: Kaplan-meier graph showing the different accumulated survival depending on the shape factor. **A)** EFS and **B)** OS.

5.3.4. Blood vessels after treatment and in other samples

The number of blood vessels of the different subtypes corresponding to the different samples of primary NB, non-primary NB, peritumoral tissue, tissue from other tumors and non-tumoral tissue is shown in **table 45**. The statistical analysis comparing the different groups of samples is presented in **table 46**.

No statistically significant changes were found between the amount of blood vessels in primary tumors and non-primary tumors. Both primary and non-primary NB blood vascularization differed from peritumoral tissue and non-tumoral tissue blood vessels. In general, total and all subtypes of blood vessels are increased in number in neuroblastic tumors (primary and non-primary) with respect to the major host tissue, the adrenal gland. This rise was more important for venules and arterioles.

Table 45: Density of blood vessels in the different control tissues studied.

Samples	TOTAL	Cap	PC/MA	S	Vu/Ao	V/A
Primary NB (n=373)	161±177	121±130	18±19	24±26	13±27	2.9±20
Non-primary NB (n=75)	165±187	123±138	18±17	26±26	15±24	3±21
Peritumoral tissue (n=22):	176±265	140±226	14±21	18±27	3±6	0.3±1.4
• Lymph node (n=1)	85.9	83.4	2.5	0.00	0.00	0.00
• Adrenal gland (n=8)	108±199	80±136	11±23	14±33	2±6	0.9±2
• Liver (n=2)	763±735	686±660	44±47	30±26	1.1±1.6	0.2±0.3
• Striated muscle (n=0)	-	-	-	-	-	-
• Pancreas (n=1)	392.8	338.1	21.6	30.5	2.5	0.00
• Sympathetic ganglia and paraganglia, fat (n=10)	104±113	75±88	8.8±8.9	15±19	3±6	0.1±0.3
Other tumors tissue (not NB) (n=3):	264±350	162±196	36±53	56±87	9±14	0.2±0.5
• Lymphoma (n=1)	131.9	107.4	11.1	11.8	1.4	0.00
• Olfactory estesioNB (n=1)	0.00	0.00	0.00	0.00	0.00	0.00
• CC. sarcoma of the kidney (n=0)	-	-	-	-	-	-
• Adrenocortical carcinoma (n=1)	662.3	380.3	97.3	157.0	26.6	0.89
Non-tumoral tissue/organs (n=24):	208±250	163±186	19±27	21±32	3±7	0.1±0.5
• Kidney (n=12)	147±241	113±174	15±28	16±32	2±7	0.6±0.2
• Liver (n=1)	0.00	0.00	0.00	0.00	0.00	0.00
• Striated / Smooth muscle (n=5)	142.8±126	140.2±112	10.8±7	11.4±6	0.6±7	0.1±0.5
• Spleen (n=1)	21.11	21.11	0.00	0.00	0.00	0.00
• Placenta (n=4)	571±147	431±123	56±14	69±18	13±6	0.6±1.2
• Salivary gland (n=1)	194.9	174.9	13.5	6.3	0.00	0.00

Cap: capillaries, PC/MA: post-capillary venules and metarterioles, S: sinusoid-like blood vessels, Vu/Ao: venules and arterioles, V/A: veins and arteries, CC: clear cell. -: no data available (lost cylinder). Because of space requirements, only the mean values are shown.

Table 46: p-values arising from the comparison of the blood vessels amount in different tissues.

Parameter	TOTAL	Cap	PC/MA	S	Vu/Ao	V/A
Prim. NB vs Non-prim. NB	-	-	-	-	-	-
Prim. NB vs per. tissue	-	-	0.019	0.026	0.008	-
Prim. NB vs other tumors	-	-	-	-	-	-
Prim. NB vs non-tumoral	-	-	-	0.033	0.002	-
Non-prim. NB vs per. tissue	-	-	0.009	0.016	0.002	-
Non-prim. NB vs other tumors	-	-	-	-	-	-
Non-prim. NB vs non-tumoral	-	-	-	0.025	0.001	-
Per. Tissue vs other tumors	-	-	-	-	-	-
Per. Tissue vs non-tumoral	-	-	-	-	-	-
Other tumors vs non-tumoral	-	-	-	-	-	-

Cap: capillaries, PC/MA: post-capillary venules and metarterioles, S: sinusoid-like blood vessels, collecting-venules and end-arterioles, Vu/Ao: venules and arterioles, V/A: veins and arteries, Prim. NB: primary NB, not-prim NB: non-primary NB, per.tissue: peritumoral tissue, -: not statistically significant.

5.4. Capillaries (5-15 μ m)

5.4.1. Description of the variables

The majority of the vessels (67.6%) found in neuroblastic tumors belonged to this class of small vessels with 5 to 15 μ m of maximum diameter. These are the vessels enabling nutrient and oxygen exchange. Neuroblastic tumors had an average of 121 of this type of blood vessels per mm² and a tumor area occupied by vessels of 0.5%. The features related to these vessels are shown in **table 47**.

Table 47: Description of the morphometric measurements of the blood vessels within 5 and 15µm of length, in a subset of 373 samples for quantity and 325 for size and shape variables.

	Parameter	Mean	Median	SD	Min.	Max.
Quantity	Density	121.1	84.1	130.9	0	735
	% stained area	0.5	0.4	0.4	0	3
	Relative density	67.6	76.1	27.4	0	100
	Relative area	32.3	30.8	21.1	0	100
Size	Average area	30.8	31.5	5.6	18	50
	Length	8.6	8.6	0.4	7	10
	Width	5	6.2	0.6	4	7
	Perimeter	25.7	26	1.9	20	33
Shape	Aspect	2.1	2	0.3	2	4
	Roundness	1.9	1.9	0.2	2	3
	Perimeter ratio	0.87	0.87	0.008	0.84	0.91
	Deformity	93.6	93.5	15.1	42	155
	Shape factor	0.5	0.2	1.5	0.1	26
	Branching	2.4	2.4	0.1	2	3

5.4.2. Favorable and unfavorable capillaries histological patterns

Histopathology and *MYCN* status were related with almost all variables of quantity, size and shape. Stage was related to the shape of the capillaries and very near to be related with width and aspect. Age was related to the % of stained area, relative area and deformity, and tended to be related to perimeter. Exactly the same variables of size and shape that are related to *MYCN* status (area, width, aspect, roundness and shape factor) area also related to the risk group (**table 48**).

Table 48: p-values resulting from the relation of the morphometric characterization of the blood vessels with 5-15µm length and the clinical and genetic INRG variables.

Parameter	Stage	Age	Histopathology	MYCN	Genetic profile	11q	Ploidy	Risk group
Density	-	-	0.008	-	-	-	-	-
% stained area	-	0.040	0.028	0.021	-	-	-	-
Relative density	-	-	-	0.018	-	-	-	-
Relative area	-	0.039	-	0.032	-	-	-	-
Average area	-	-	0.001	0.001	-	-	-	0.006
Length	-	-	0.010	-	-	-	-	-
Width	0.055*	-	0.001	0.001	-	-	-	0.003
Perimeter	-	0.055*	0.001	-	-	-	-	-
Aspect	0.051*	-	0.001	0.000	-	-	-	0.001
Roundness	-	-	0.001	0.000	-	-	-	0.002
Perimeter ratio	-	-	-	-	-	-	-	-
Deformity	-	0.046	0.015	-	-	-	-	-
Shape factor	0.026	-	0.000	0.000	-	-	-	0.000
Branching	-	-	0.007	-	-	-	-	-

-: not statistically significant, *Tendency.

How these variables were related is shown in **figure 81 to 83**. Only variables with significant relationship with at least one INRG variable are shown.

A. Quantity variables

The number of capillaries and the stained area were lower in the differentiated tumors. This last parameter was higher in tumors with MNNA and in tumors from patients younger than 18 months of age. Moreover, the tumors with MNNA had a higher amount of their vessels corresponding to this group and a higher amount of stained area corresponding to capillaries was found in tumors from patients younger than 18 months of age (**figure 81**).

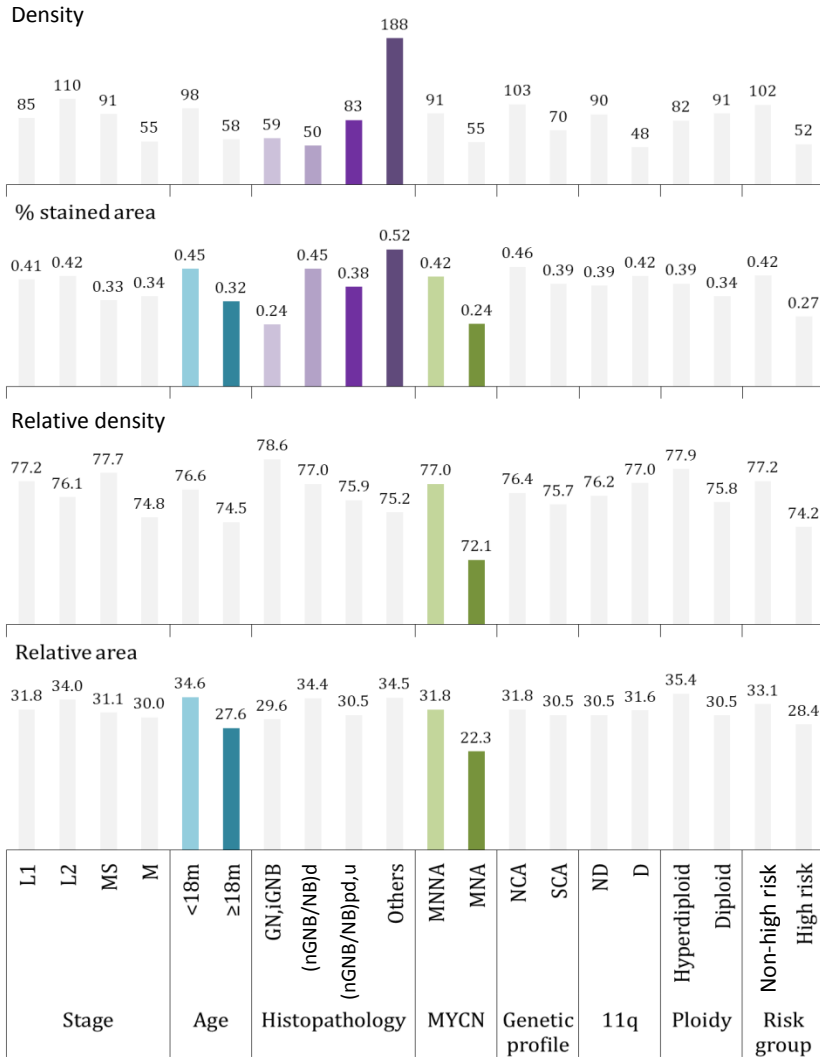


Figure 81: Distribution of the number of capillaries/mm² depending on the INRG clinical and biological variables. Variables in grey mean no significant statistical relationship. Colored variables show significant statistical relationship (**table 48**). The median values are shown.

B. Size variables

In general, the capillaries from tumors with favorable features (non-high risk patients, differentiated histology and/or MNNA) were smaller (area, length, width, perimeter) than their counterparts. The same happens with localized tumors for the width variable. Patients

older than 18 months of age have tumor capillaries with small perimeter (**figure 82**).

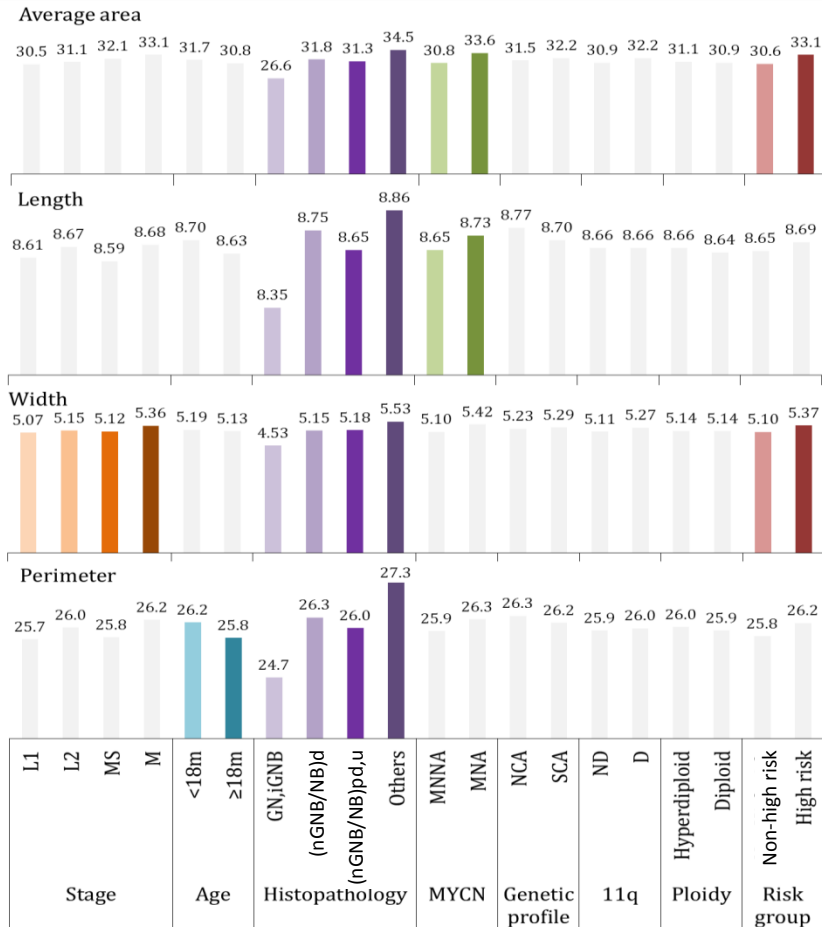


Figure 82: Distribution of the average area occupied by capillaries depending on the INRG clinical and biological variables. Variables in grey mean no significant statistical relationship. Colored variables show significant statistical relationship (**table 48**). The median values are shown.

C. Shape variables

Non-high risk patients with tumors with localized disease, favorable histology, MNNA and 11ND had capillaries with a higher aspect or more ovoid and therefore less round with less deformity,

higher shape factor and lower branching than their counterparts. Tumors from patients <18 months have a more deformed capillaries than those from patients >18 months (**figure 83**).

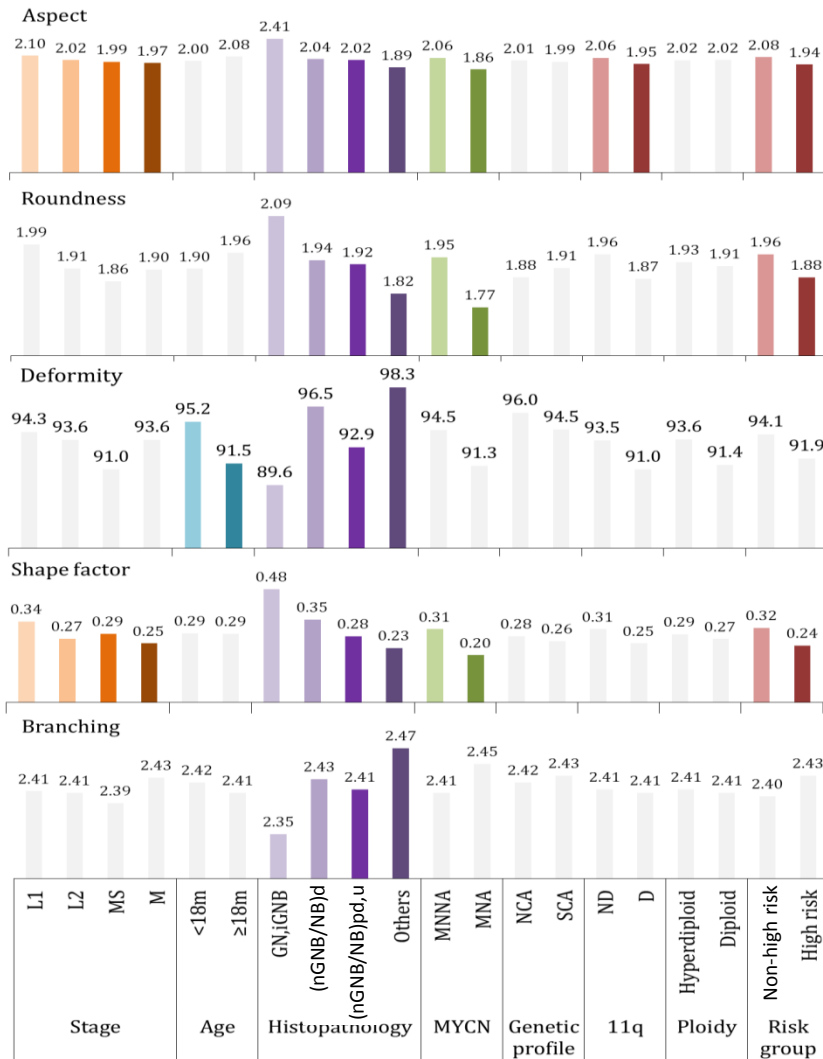


Figure 48: Distribution of the aspect of the capillaries depending on the INRG clinical and biological variables. Variables in grey mean no significant statistical relationship. Colored variables show significant statistical relationship (**table 32**). The median values are shown.

5.4.3. Survival analysis

A. Multivariate analysis

The results of the analysis of the relationship between the morphometric measurements of capillaries and the EFS and OS variables on 325 samples (those presenting capillaries) are shown in **table 49**.

This table indicates that a lower amount of capillaries affected EFS although the influence was not strong enough to be found in combination with the INRG variables, with and without including the stage variable. Regarding OS, we could observe that, again a lower amount of capillaries, together with a lower relative amount of vessels corresponding to this subgroup affected survival.

Table 49: Results of the Cox regression showing the influence of capillary morphometric measurements on their own and in combination with the INRG variables on EFS and OS.

	Variable	Wald	HR (95% CI)	p-value
EFS				
a	C density	5.5	0.99 (0.9-1.0)^	0.019
b, c		-		
OS				
a	C density	6.0	0.99 (0.94-0.99)^	0.014
	C rel. density	5.7	0.96 (0.94-0.99)^	0.017
b	MYCN	25.0	4.97 (2.6-9.3)	0.000
	Stage	19.46		0.000
c	MYCN	28.8	5.36 (2.9-9.9)	0.000
	Age	6.5	2.40 (1.2-4.7)	0.010

a: morphometric variables on their own, b: morphometric variables + all INRG variables, c: morphometric variables + INRG variables except stage, C: capillary, rel. density: relative number of vessels corresponding to this subgroup, HR: Hazard ratio, CI: Confidence interval, -: no statistically significant morphometric variable. ^Inverse correlation.

B. Study of the high risk group

The dichotomized morphometric variables showed statistically significant differences regarding survival (OS, EFS). A table with the morphometric parameters and the cut points is provided (**table 50**). The Kaplan-Meier graphs are shown in **figure 84**.

Table 50: Morphometric variables and cut points used to dichoromize them.

Parameter	EFS		OS	
	Cut point	p-value	Cut point	p-value
Density	-	-	-	-
% stained area	-	-	-	-
Relative density	-	-	-	-
Relative area	-	-	-	-
Average area	-	-	-	-
Length	-	-	-	-
Width	-	-	-	-
Perimeter	-	-	-	-
Aspect	-	-	-	-
Roundness	Q1: 1.71	0.026	-	-
Perimeter ratio	-	-	-	-
Deformity	-	-	-	-
Shape factor	Q2: 0.24	0.006	-	-
Branching	-	-	-	-

Q1: first quartile, Q2: median, Q3: third quartile, -: not statistically significant.

- Capillaries shape variables

A roundness over the first quartile defined an ultra-high risk subgroup with 30 ± 5 % of 5-year EFS. Moreover, a shape factor over the median value was associated with an ultra-high risk group with 12% 5-year EFS, within the high risk patients group (**figure 84**).

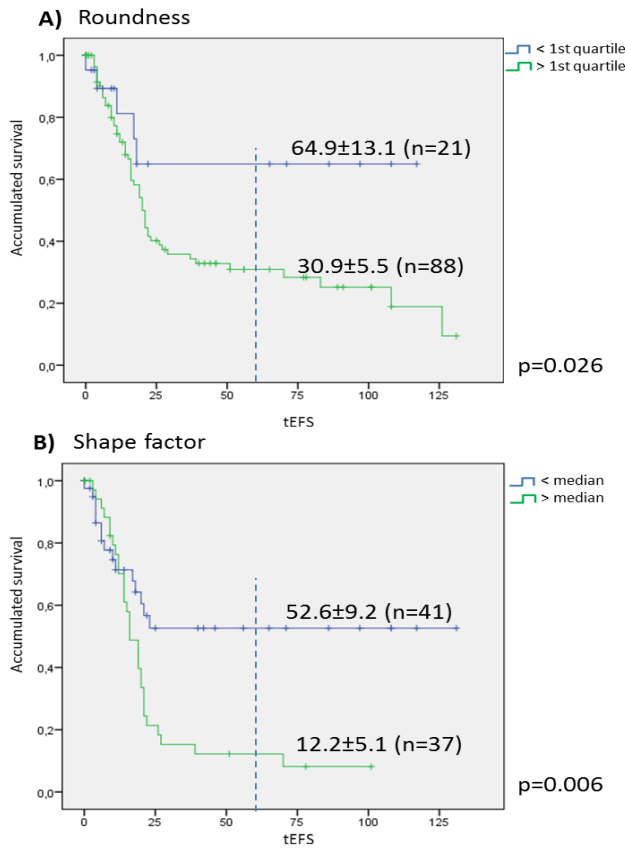


Figure 84: Kaplan-meier graph showing the different accumulated survival depending on the shape parameters. **A)** roundness and **B)** shape factor.

5.5. Post-capillary venules and metarterioles (15-20µm)

5.5.1. Description of the variables

Almost 8% of the vessels belonged to this class of small vessels with 15 to 20µm of length. Neuroblastic tumors showed an average of 18.5 of this type of blood vessels per mm² and a tumor area occupied by vessels of 0.18%. The features related to these vessels were shown in **table 51**. Among the 325 samples with positivity for CD31, 6 cases did not present any vessel between 15 and 20µm of length.

Table 51: Description of the morphometric measurements of the blood vessels within 15 and 20 μ m of length, in a subset of 373 samples for quantity and 319 for size and shape variables.

	Parameter	Mean	Median	SD	Min.	Max.
Quantity	Density	18.5	14.7	19	0	143
	% stained area	0.18	0.12	0.19	0	1
	Relative density	7.8	8.5	4.1	0	23
	Relative area	9.8	10.8	5.7	0	37
Size	Average area	88	88.1	14.6	34	145
	Length	17.1	17.2	0.8	16	19
	Width	8.92	8.98	1.2	4	13
	Perimeter	54.5	54.8	4.6	19	71
Shape	Aspect	2.3	2.2	0.4	1	6
	Roundness	2.9	2.8	0.4	1	4
	Perimeter ratio	0.79	0.79	0.04	0.41	0.90
	Deformity	467	168.2	93	109	1004
	Shape factor	0.74	0.44	1.2	0.1	13
	Branching	3.26	3.29	0.3	1	4

5.5.2. Favorable and unfavorable post-capillaries venules and metarterioles histological patterns

Stage, *MYCN* status and risk group were the variables most related with the morphometric variables. Stage was related to the size (area, length, width), the aspect and the shape index of the vessels within 15 and 20 μ m. *MYCN* status was related to the relative amount of vessels corresponding to this subgroup, to the area and width, and to the aspect, roundness, shape factor and branching. The risk group was related to the same size and shape parameters than *MYCN*. The age was related to the number of vessels. Finally, histopathology was related to the shape parameters aspect and shape factor (**table 52**).

Table 52: p-values resulting from the relation of the morphometric characterization of the blood vessels with 15-20µm length and the clinical and genetic INRG variables.

Parameter	Stage	Age	Histopathology	MYCN	Genetic profile	11q	Ploidy	Risk group
Quantity	Density	-	0.034	-	-	-	-	-
	% stained area	-	-	-	-	-	-	-
	Relative density	-	-	0.023	-	-	-	-
	Relative area	-	-	-	-	-	-	-
Size	Average area	0.018	-	0.000	-	-	-	0.000
	Length	0.033	-	-	-	-	-	-
	Width	0.039	-	0.003	-	-	-	0.000
	Perimeter	-	-	-	-	-	-	-
Shape	Aspect	0.044	-	0.013	0.005	-	-	0.000
	Roundness	-	-	-	0.000	-	-	0.000
	Perimeter ratio	-	-	-	-	-	-	-
	Deformity	-	-	-	-	-	-	-
	Shape factor	0.012	-	0.039	0.000	-	-	0.000
	Branching	-	-	-	0.005	-	-	0.000

-: not statistically significant.

How these variables were related is shown in **figures 85 to 87**. Only variables with significant relationship with at least one INRG variable are shown.

A. Quantity variables

Tumors from patients under 18 months of age had a higher amount of post-capillary venules and metarterioles. On the contrary, although not statistically significant, the rest of parameters related to better prognosis presented a lower amount of blood vessels of this type. Moreover, tumors with MNNA had a lower relative number of blood vessels corresponding to this subgroup than tumors with MNA (**figure 85**).

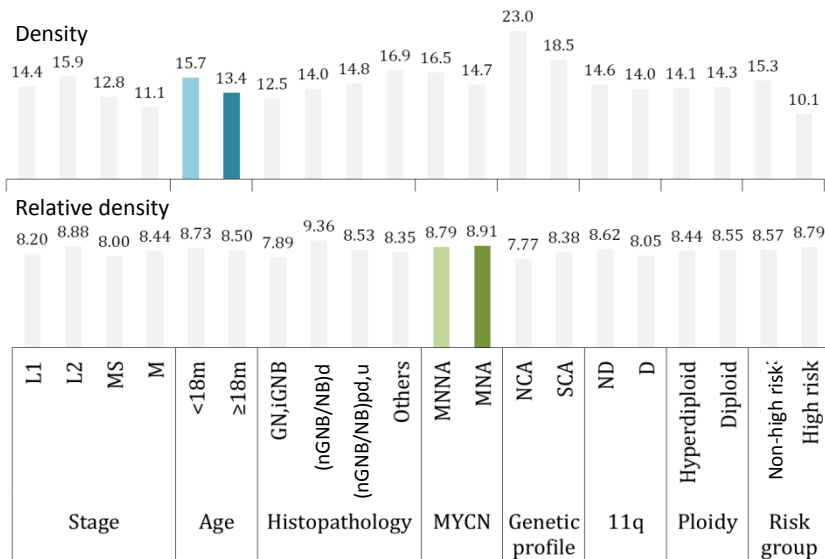


Figure 85: Distribution of the number of post-capillary venules and metarterioles/mm² depending on the INRG clinical and biological variables. Variables in grey mean no significant statistical relationship. Colored variables show significant statistical relationship (**table 52**). The median values are shown.

B. Size variables

Post-capillary venules and metarterioles with the lower size were related to localized stages (average area, length and width), non-high risk patients (width) and MNNA tumors (average area and width) (figure 86).

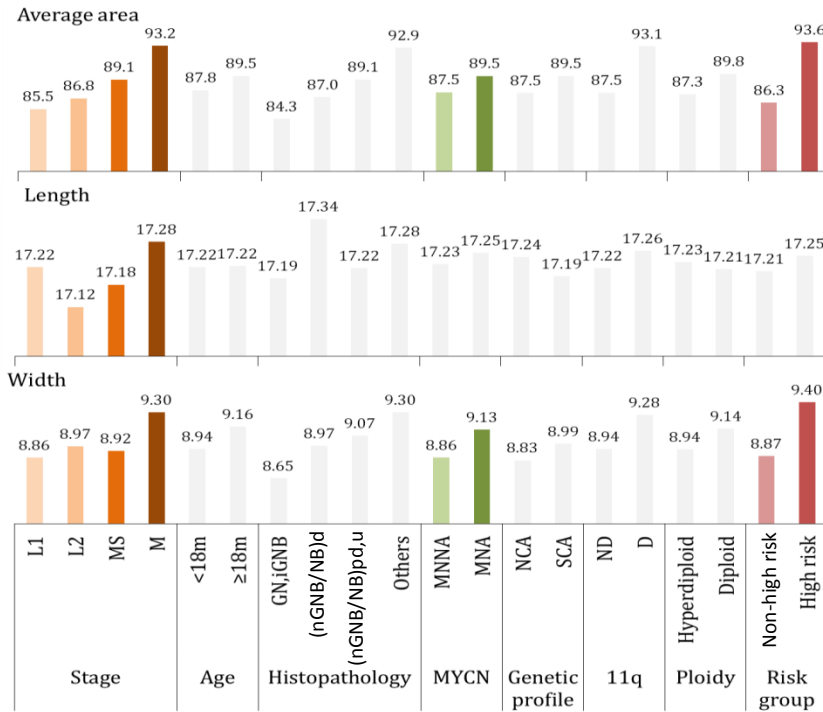


Figure 86: Distribution of the average area of post-capillary venules and metarterioles depending on the INRG clinical and biological variables. Variables in grey mean no significant statistical relationship. Colored variables show significant statistical relationship (table 52). The median values are shown.

C. Shape variables

Tumors corresponding to localized stage disease, with differentiated histopathology, MNNA and from non-high risk patients had more ovoid vessels in this subgroup and a lower shape factor. Roundness is lower for MNA tumors but higher for tumors from non-

high risk patients than for their counterparts. A lower branching was detected in MNNA tumors and those from non-high risk patients compared to MNA tumors and from high risk patients (**figure 87**).

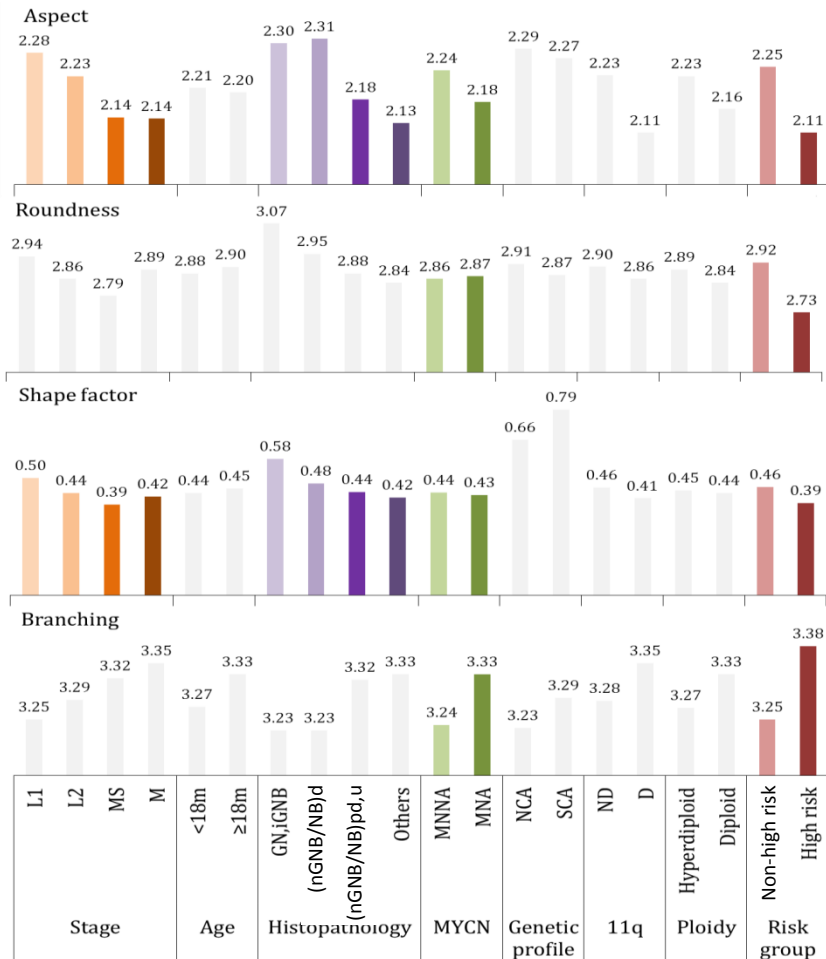


Figure 87: Distribution of the aspect of post-capillary venules and metarterioles depending on the INRG clinical and biological variables. Variables in grey mean no significant statistical relationship. Colored variables show significant statistical relationship (**table 52**). The median values are shown.

5.5.3. Survival analysis

A. Multivariate analysis

The results of the analysis of the relationship between the capillaries morphometric measurements and the EFS and OS variables on 325 samples (those presenting post-capillary venules and metarterioles) are shown in **table 53**.

Both for EFS and for OS, the size variables larger area and shorter length were influencing survival when including in the analysis only the morphometric variables. For EFS, a higher shape factor was also related with poor survival after a larger area and a shorter length. When including all INRG variables, the shorter length remained significantly related to EFS, with a HR of 0.625 (0.4-0.8), after stage, histopathology, thicker width, with a HR of 1.4 (1.1-1.7), and genomic profile. Regarding OS, the stage variable was so strong that the influence of the size morphometric variables disappeared. When considering all INRG variables except the stage, some size variables appeared as significantly related to survival. Specifically, a larger area was related to EFS with a HR of 1.02 (1.0-1.03) and thicker and shorter vessels were related to OS with HRs of 1.4 (1.1-1.8) and 0.7 (0.5-0.9), respectively. Moreover, a higher shape index and a lower perimeter ratio were found related to EFS after *MYCN* status, with a HR of 0.0 (0.0-0.03).

Table 53: Results of the Cox regression showing the influence of post-capillary venules and metarterioles morphometric measurements on survival.

	Variable	Wald	HR (95% CI)	P-value
EFS				
a	PC/MA shape factor	4.3	1.1 (1.0-1.3)	0.036
	PC/MA area	19.2	1.0(1.02-1.05)	0.000
	PC/MA length	11.5	0.6 (0.4-0.8)^	0.001
b	Stage	22.04		0.000
	Histopathology	6.9		0.072
	PC/MA width	7.7	1.4 (1.1-1.7)	0.005
	Genomic profile	4.9	2.5 (1.1-5.7)	0.027
	PC/MA length	4.4	0.7 (0.5-0.9)^	0.035
c	<i>MYCN</i>	13.3	2.8 (1.6-5.0)	0.000
	PC/MA per. ratio	10.6	0.0 (0.0-0.03)^	0.001
	11q	9.1	2.2 (1.3-3.8)	0.003
	Age	5.8	2.0 (1.1-3.5)	0.016
	PC/MA area	5.5	1.02 (1.0-1.03)	0.018
OS				
a	PC/MA area	17.7	1.03 (1.02-1.05)	0.000
	PC/MA length	10.0	0.6 (0.4-0.8)^	0.002
b		-		
c	<i>MYCN</i>	18.4	4.0 (2.1-7.7)	0.000
	Age	7.3	2.6 (1.3-5.4)	0.007
	PC/MA width	7.2	1.4 (1.1-1.8)	0.007
	11q	6.4	2.2 (1.2-4.0)	0.011
	PC/MA length	4.3	0.7 (0.5-0.9)^	0.037

a: morphometric variables on their own, b: morphometric variables + all INRG variables, c: morphometric variables + INRG variables except stage, PC/MA: post-capillary venules and metarterioles, per. ratio: perimeter ratio, HR: Hazard ratio, CI: Confidence interval, -: not statistically significant morphometric variable. ^Inverse correlation.

B. Study of the high risk group

No differences were found in EFS and OS for high risk patients regarding the post-capillaries/metarterioles morphometric variables. Kaplan-Meier curves are therefore not shown.

5.6. Sinusoid-like blood vessels (20-50 μ m)

5.6.1. Description of the variables

An average of almost 10% of the vessels belonged to this class of small vessels with 20 to 50 μ m of length. These were the second most frequent type of vessels in NB, which had an average of 24,8 of this type of blood vessels per mm^2 and an area occupied by vessels of 0,5% of the tumor area. The features related to these vessels are shown in **table 54**. Among the 325 samples with positivity for CD31, 6 cases did not present any vessel between 20 and 50 μ m of length.

Table 54: Description of the morphometric measurements of the blood vessels within 20 and 50 μ m of length, in a subset of 373 samples for quantity and 319 for size and shape variables.

	Parameter	Mean	Median	SD	Min.	Max.
Quantity	Density	24.8	19.7	27	0	200
	% stained area	0.52	0.31	0.61	0	4
	Relative density	9.87	10.4	6.3	0	28
	Relative area	24.7	27.6	13.7	0	60
Size	Average area	196.3	191.3	57.7	84	768
	Length	28.4	28.4	2.7	20	50
	Width	12.8	12.8	2	7	27
	Perimeter	95	94.6	13.7	64	210
Shape	Aspect	2.6	2.5	0.3	1	4
	Roundness	4.1	4	0.76	2	14
	Perimeter ratio	0.75	0.75	0.37	0.58	0.88
	Deformity	1478.3	1456.2	398	356	3699
	Shape factor	1.1	0.7	2	0.7	26
	Branching	3.8	3.8	0.3	3	6

5.6.2. Favorable and unfavorable sinusoid-like blood vessels histological patterns

Stage was related to the amount of vessels and the relative number of vessels of to this type, to width, aspect, roundness, shape factor and branching. Histopathology was related to all variables except relative number, length, roundness and deformity. *MYCN* was related to relative number, all size variables except perimeter and all shape variables except deformity. Age was related to the branching degree of sinusoid-like blood vessels. Genetic profile, 11q status and ploidy did not show any statistically significant relationship with the morphometric variables regarding this subgroup of vessels. Again, risk group was related to exactly the same variables than *MYCN* (except for length and perimeter ratio) (**table 55**).

Table 55: p-values resulting from the relation of the morphometric characterization of the blood vessels with 20-50µm length and the clinical and genetic INRG variables.

Parameter	Stage	Age	Histopathology	MYCN	Genetic profile	11q	Ploidy	Risk group
Density	0.050	-	0.041	-	-	-	-	-
% stained area	-	-	0.024	-	-	-	-	-
Relative density	0.043	-	-	0.004	-	-	-	0.034
Relative area	-	-	0.052*	-	-	-	-	-
Average area	-	-	0.035	0.000	-	-	-	0.001
Length	-	-	-	0.015	-	-	-	-
Width	0.024	-	0.018	0.004	-	-	-	0.001
Perimeter	-	-	0.051*	-	-	-	-	-
Aspect	0.001	-	0.005	0.017	-	-	-	0.001
Roundness	0.018	-	-	0.000	-	-	-	0.000
Perimeter ratio	-	-	0.016	0.022	-	-	-	-
Deformity	-	-	-	-	-	-	-	-
Shape factor	0.000	-	0.001	0.000	-	-	-	0.000
Branching	0.017	0.033	0.056*	0.043	-	-	-	0.000

-: not statistically significant, *Tendency.

How these variables were related is shown in **figures 88 to 90**. Only variables with significant relationship with at least one INRG variable are shown.

A. Quantity variables

Tumors with the lower amount of sinusoid-like blood vessels corresponded to differentiated neuroblastic tumors with localized stage disease. Differentiated tumors also had a lower stained area, and a lower amount of vessels belonging to this subgroup (relative area). Non-high risk patients with localized disease and tumors MNNA had a lower relative number of vessels corresponding to sinusoid-like blood vessels (**figure 88**).

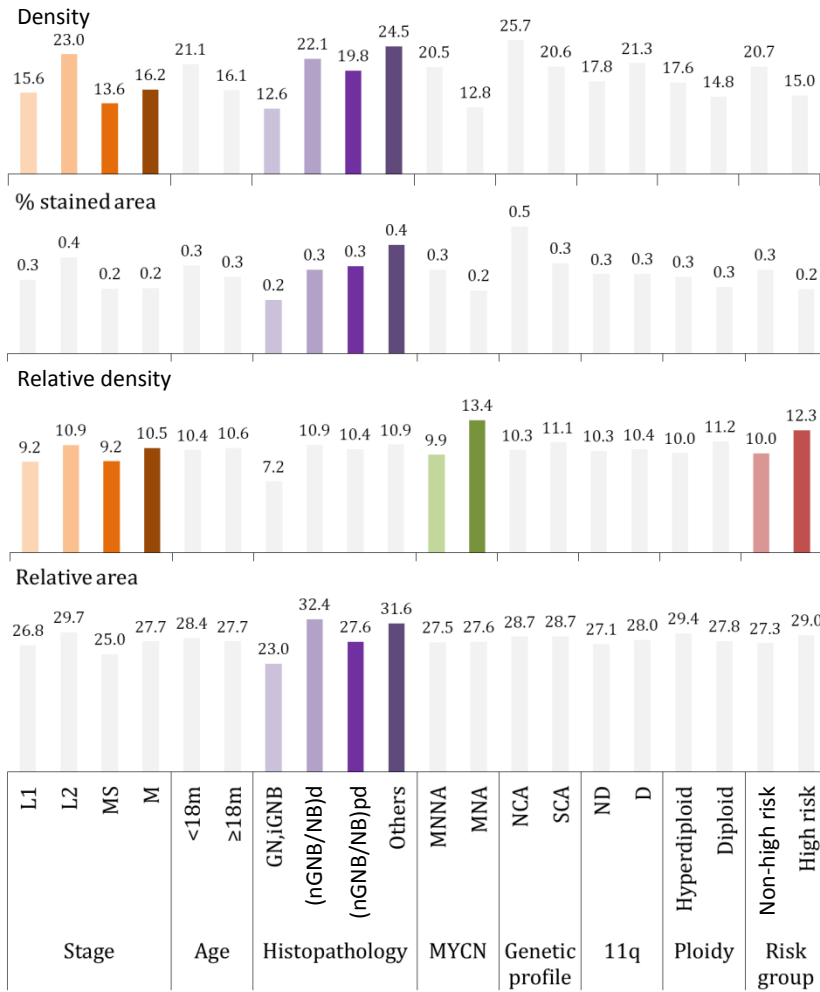


Figure 88: Distribution of the number of sinusoid-like blood vessels/mm² depending on the INRG clinical and biological variables. Variables in grey mean no significant statistical relationship. Colored variables show significant statistical relationship (table 55). The median values are shown.

B. Size variables

Tumors from non-high risk patients (for area and width) with differentiated histology, MNNA (except for perimeter) and from patients with localized disease (for width) had smaller blood vessels in this subgroup (figure 89).

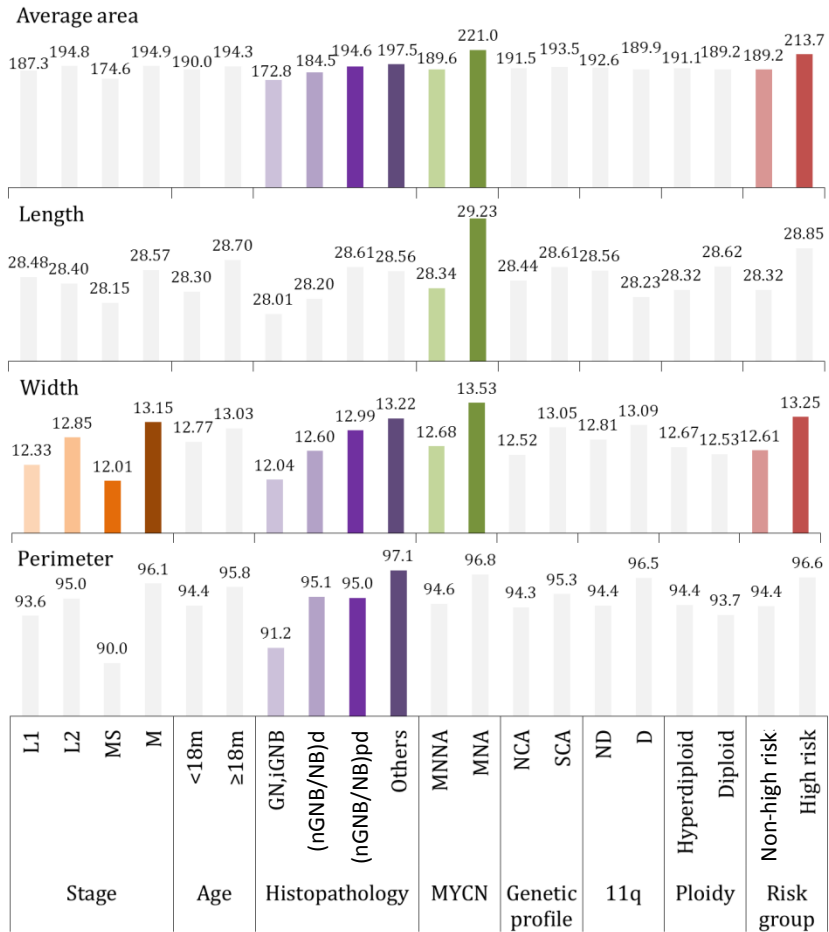


Figure 89: Distribution of the average area of sinusoid-like blood vessels depending on the INRG clinical and biological variables. Variables in grey mean no significant statistical relationship. Colored variables show significant statistical relationship (**table 55**). The median values are shown.

C. Shape variables

High risk patients with localized disease and MNNA tumors had sinusoid-like blood vessels with a higher aspect, a higher roundness, a higher shape and a lower branching degree than their counterparts. MNNA tumors were also associated with a lower perimeter ratio (more irregular outline), contrarily from tumors with differentiated

histopathology. The later also had sinusoid-like blood vessels with a higher aspect, shape factor and branching than undifferentiated tumors. Finally, age under 28 months was related to a lower branching degree (figure 90).

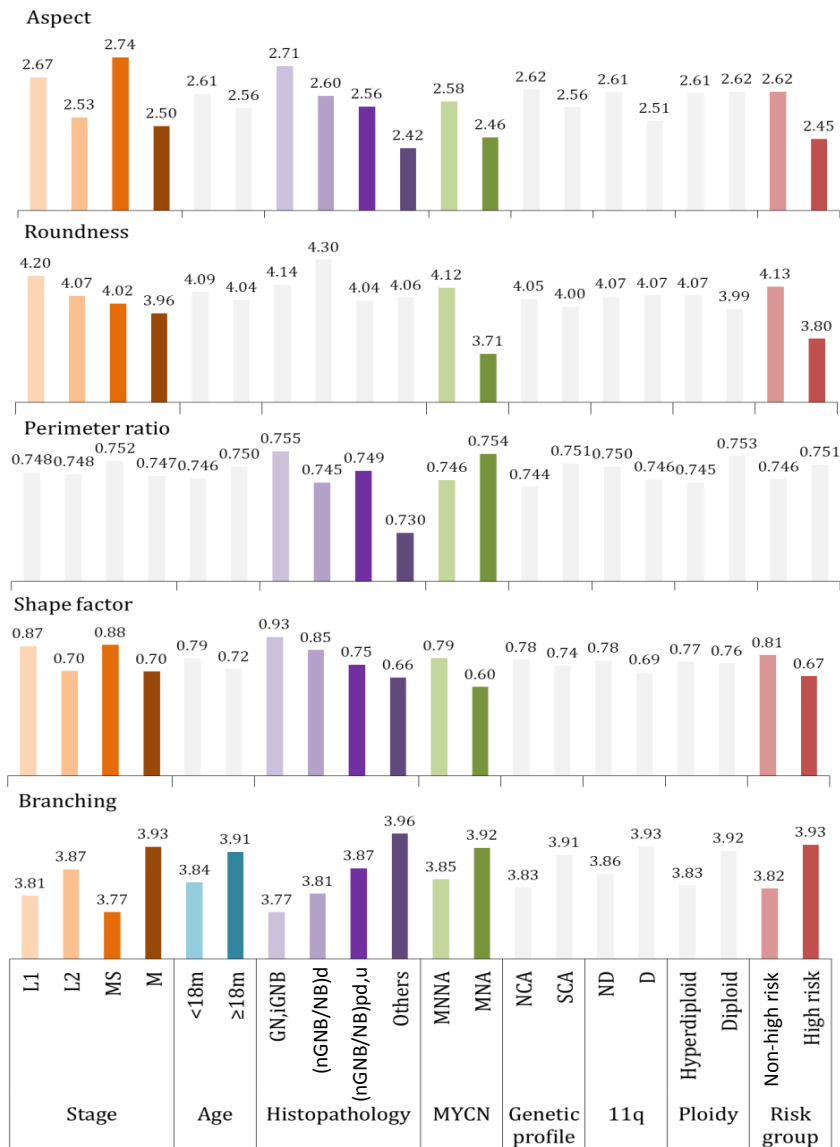


Figure 90: Distribution of the aspect of sinusoid-like blood vessels depending on the INRG clinical and biological variables. Variables in grey mean no significant statistical relationship. Colored variables show significant statistical relationship (table 55). The median values are shown.

5.6.3. Survival analysis

A. Multivariate analysis

The results of the analysis of the relationship between the sinusoid-like blood vessels measurements and the EFS and OS variables on the 319 samples are shown in **table 56**.

A lower roundness and aspect were related to EFS with HRs of 0.5 (0.3-0.8) and 0.3 (0.1-0.8), respectively, when testing the morphometric variables on their own. A lower aspect was also related to OS with a HR of 0.1 (0.3-0.2), together with a higher perimeter ratio, with a HR of 8.2e5 (175-3.8e9) and a higher relative number of blood vessels corresponding to sinusoid-like blood vessels, with a HR of 1.0 (1.0-1.1). When including all INRG variables, short sinusoid-like blood vessels were significantly related to a higher risk of relapse whether including or not the stage (0.8 (0.7-0.9)). Regarding OS, we could observe that shorter sinusoid-like blood vessels were also related to poor prognosis in combination with a higher relative number of vessels corresponding to this subgroup, when considering all INRG variables with or without the stage.

Table 56: Results of the Cox regression showing the influence of sinusoid-like blood vessels morphometric measurements in combination with the INRG variables on 5 and 10-year OS%.

	Variable	Wald	HR (95% CI)	p-value
EFS				
a	S roundness	7.8	0.5 (0.3-0.8)^	0.05
	S aspect	6.0	0.3 (0.1-0.8)^	0.014
b	Stage	20.1		0.000
	MYCN	16.4	3.2 (1.8-5.8)	0.000
	S length	8.6	0.8 (0.7-0.9)^	0.003
	11q	8.1	2.2 (1.2-3.9)	0.004
c	MYCN	24.1	4.3 (2.4-7.7)	0.000
	11q	17.1	3.0 (1.8-5.1)	0.000
	S length	8.0	0.8 (0.7-0.9)^	0.004
	Age	5.3	1.9 (1.1-3.2)	0.021
OS				
a	S aspect	20.1	0.1 (0.3-0.2)^	0.000
	S per. ratio	9.9	8.2e5 (175-3.8e9)	0.002
	S rel. density	8.6	1.0 (1.0-1.1)	0.003
b	MYCN	24.1	5.0 (2.6-9.5)	0.000
	Stage	19.9		0.000
	S length	9.8	0.8 (0.7-0.9)^	0.002
	S rel. density	6.6	1.0 (1.0-1.1)	0.002
	11q	5.6	2.1 (1.1-4.0)	0.017
c	MYCN	27.3	5.9 (3.0-11.5)	0.001
	S length	10.2	0.8 (0.7-0.9)^	0.001
	11q	10.1	2.6 (1.4-4.9)	0.001
	Age	8.8	2.8 (1.4-5.5)	0.003
	S rel. density	4.5	1.0 (1.0-1.1)	0.033

a: morphometric variables on their own, b: morphometric variables + all INRG variables, c: morphometric variables + INRG variables except stage, S: Sinusoid-like blood vessels, per. ratio: perimeter ratio, rel. density: relative number of vessels corresponding to this subgroup, HR: Hazard ratio, CI: Confidence interval. ^Inverse correlation.

B. Study of the high risk group

No differences were found in EFS and OS for high risk patients regarding the sinusoid-like blood vessels morphometric variables. Kaplan-Meier curves are therefore not shown.

5.7. Venules and arterioles (50-200 μ m)

5.7.1. Description of the variables

Only 1.7% of the vessels belonged to this class of vessels with 20 to 50 μ m of length. Neuroblastic tumors had an average of 13 blood vessels this type of per mm^2 and an area occupied by vessels of 0.4% of the tumor area. The features related to these vessels are shown in **table 57**. Among the 325 samples with positivity for CD31, 57 cases did not present any vessel between 50 and 200 μ m of length.

Table 57: Description of the morphometric measurements of the blood vessels within 50 and 200 μ m of length, in a subset of 373 samples for quantity and 268 for size and shape variables.

	Parameter	Mean	Median	SD	Min.	Max.
Quantity	Density	13.2	2.6	27.4	0.0	271.2
	% stained area	0.4	0.2	0.7	0.0	4.6
	Relative density	1.7	1.1	2.1	0.0	15.2
	Relative area	16.2	13.9	15.7	0.0	81.4
Size	Average area	992.0	836.8	748.3	168.7	8168.3
	Length	74.0	72.0	14.9	50.1	150.0
	Width	27.1	26.2	9.8	9.1	100.4
	Perimeter	280.1	271.1	97.6	134.8	1124.6
Shape	Aspect	3.37	3.27	0.94	1.44	7.74
	Roundness	7.73	7.63	2.31	1.93	16.28
	Perimeter ratio	0.66	0.66	0.08	0.40	0.93
	Deformity	10649	9358	6924	993	79615
	Shape factor	5.96	2.04	14.47	0.05	127.05
	Branching	5.30	5.33	0.72	3.00	9.00

5.7.2. Favorable and unfavorable venules and arterioles histological patterns

Histopathology, *MYCN* status, ploidy and the risk group showed statistically significant relationships with few morphometric variables regarding venules and arterioles. Histopathology was related to roundness, *MYCN* status, the relative density and the relative area; and ploidy was related to all size variables (area, length, width and perimeter) (**table 58**).

Table 58: p-values resulting from the relation of the morphometric characterization of the blood vessels with 50-200µm length and genetic INRG variables.

Parameter	Stage	Age	Histopathology	MYCN	Genetic profile	11q	Ploidy	Risk group
Density	-	-	-	-	-	-	-	-
% stained area	-	-	-	-	-	-	-	-
Relative density	-	-	-	0.000	-	-	-	0.018
Relative area	-	-	-	0.002	-	-	-	-
Average area	-	-	-	-	-	-	0.006	-
Length	-	-	-	-	-	-	0.001	-
Width	-	-	-	-	-	-	0.041	-
Perimeter	-	-	-	-	-	-	0.032	-
Aspect	-	-	-	-	-	-	-	-
Roundness	-	-	0.032	-	-	-	-	-
Perimeter ratio	-	-	-	-	-	-	-	-
Deformity	-	-	-	-	-	-	-	-
Shape factor	-	-	-	-	-	-	-	-
Branching	-	-	-	-	-	-	-	-

-: not statistically significant.

How that these variables were related is shown in **figures 91 to 93**. Only variables with significant relationship with at least one INRG variable are shown.

A. Quantity variables

MNNA tumors presented a lower relative number of venules and arterioles that occupied a lower relative area with respect to total blood vasculature, compared to MNA tumors. Tumors from low risk patients also presented a lower relative number of vessels corresponding to venules and arterioles than tumors from high risk patients (**figure 91**). Although not statistically significant, all INRG variables related with good-prognosis were also associated to a lower relative amount and area corresponding to venules and arterioles.

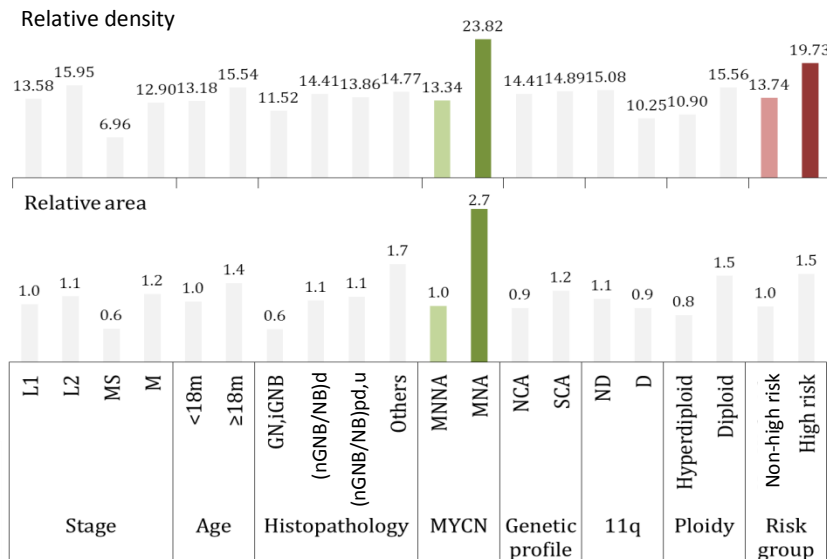


Figure 91: Distribution of the number of venules and arterioles/mm² depending on the INRG clinical and biological variables. Variables in grey mean no significant statistical relationship. Colored variables show significant statistical relationship (**table 58**). The median values are shown.

B. Size variables

Only ploidy was related to all size variables. Hyperdiploid tumors had smaller venules and arteries in area, length and width and perimeter than diploid tumors (**figure 92**).

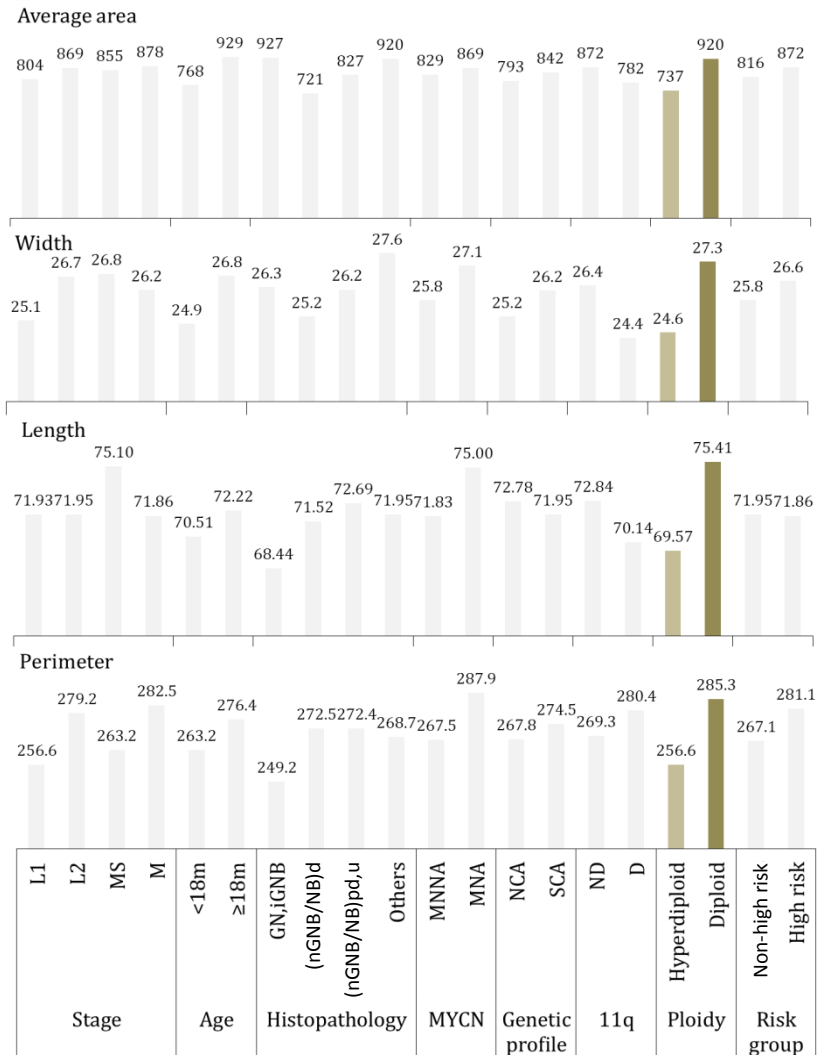


Figure 92: Distribution of the average area of venules and arterioles depending on the INRG clinical and biological variables. Variables in grey mean no significant statistical relationship. Colored variables show significant statistical relationship (**table 58**). The median values are shown.

C. Shape variables

Tumors with the better prognosis-related histopathology showed venules and arteries with a rounder shape (lower roundness value) than tumors with undifferentiated or poorly differentiated histopathology (**figure 93**).

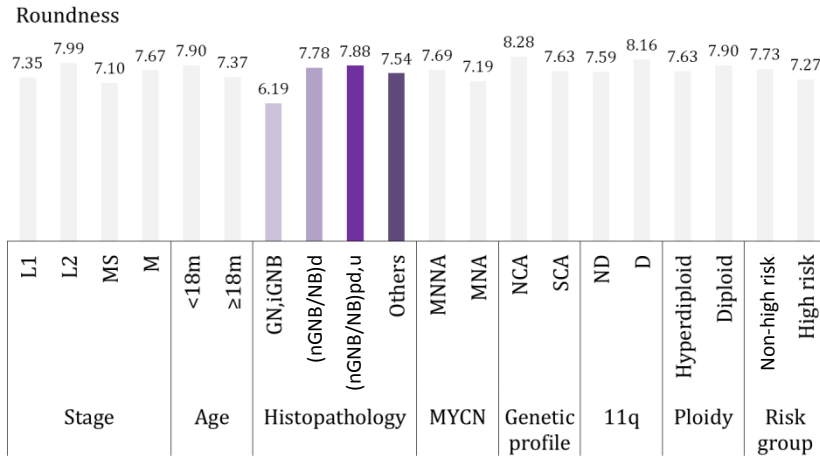


Figure 93: Distribution of the roundness of venules and arterioles depending on the INRG clinical and biological variables. Variables in grey mean no significant statistical relationship. Colored variables show significant statistical relationship (**table 58**). The mean values are shown.

5.7.3. Survival analysis

A. Multivariate analysis

The results of the analysis of the relationship between the venules and arterioles measurements and the EFS and OS variables on the 268 samples are shown in **table 59**.

Regarding EFS, we could observe that a higher shape factor of the venules and arterioles affected survival with a HR of 1.01 (1.00-1.02). When including all INRG variables in the analysis, a lower relative area occupied by venules and arterioles appeared to be associated with

poor survival after stage, *MYCN* and 11q status, whether including or excluding the stage variable with HRs of 0.97 (0.95-0.99) and 0.96 (0.94-0.98), respectively, and, when excluding the stage variable, longer vessels also influenced EFS with a HR of 1.02 (1.00-1.04) after *MYCN* status, 11q status, relative area and age.

Regarding OS, a higher shape factor, a higher relative number or a lower relative area covered by venules and arterioles appeared as related with survival in the three cases. When considering all morphometric variables together with the INRG variables, a higher percentage of stained area was also significantly related to prognosis, whether including or not the stage variable.

Table 59: Results of the Cox regression showing the influence of venules and arterioles morphometric measurements on their own and in combination with the INRG variables on survival.

	Variable	Wald	HR (95% CI)	p-value
EFS				
a	Vu/Ao shape factor	6.8	1.0 (1.00-1.02)	0.009
b	Stage	20		0.000
	<i>MYCN</i>	17.4	3.9 (2.0-7.5)	0.000
	11q	6.36	2.1 (1.1-3.8)	0.012
	Vu/Ao rel. area	6.35	0.9 (0.95-0.99) [^]	0.012
c	<i>MYCN</i>	24.0	4.9 (2.6-9.4)	0.009
	11q	16.0	3.2 (1.8-5.8)	0.000
	Vu/Ao rel. area	8.9	0.9 (0.94-0.98) [^]	0.037
	Age	6.8	2.2 (1.2-4.1)	0.009
	Vu/Ao length	4.3	1.0 (1.00-1.04)	0.037
OS				
a	Vu/Ao shape factor	10.9	1.01 (1.00-1.03)	0.001
	Vu/Ao rel density	5.3	1.1 (1.0-1.3)	0.021
b	<i>MYCN</i>	28.1	7.9 (3.6-17.1)	0.000
	Stage	9.9		
	11q	7.1	2.6 (1.3-5.3)	0.007
	Vu/Ao rel. area	6.7	0.96 (0.94-0.99) [^]	0.010
	Vu/Ao shape factor	3.9	1.0 (1.00-1.02)	0.048
	Vu/Ao % stained area	3.7	1.4 (0.9-2.1)	0.053*
c	<i>MYCN</i>	32.6	8.5 (4.0-17.8)	0.000
	11q	9.7	3.0 (1.5-5.9)	0.002
	Vu/Ao rel. area	7.1	0.96 (0.93-0.99) [^]	0.007
	Vu/Ao shape factor	6.3	1.0 (1.00-1.02)	0.012
	Age	5.2	2.3 (1.1-4.9)	0.022
	Vu/Ao % stained area	4.5	1.5 (1.0-2.3)	0.032

a: morphometric variables on their own, b: morphometric variables + all INRG variables, c: morphometric variables + INRG variables except stage, Vu/Ao: Venules/arterioles, rel. density: relative number of vessels corresponding to this subgroup, rel. area: relative area covered by vessels corresponding to this subgroup, HR: Hazard ratio, CI: Confidence interval, *: not statistically significant. [^]Inverse correlation.

B. Study of the high risk group

The dichotomized morphometric variables showed statistically significant differences regarding survival (OS, EFS). A table with the

morphometric parameters and the cut points is provided (**table 60**). The Kaplan-Meier graphs are shown (**figure 94 to 95**).

Table 60: Morphometric variables and cut points used to dichoromize them.

Parameter	EFS		OS	
	Cut point	p-value	Cut point	p-value
Density	-	-	-	-
% stained area	-	-	-	-
Relative density	-	-	-	-
Relative area	-	-	-	-
Average area	-	-	Q2: 872.3	0.013
Length	-	-	-	-
Width	-	-	-	-
Perimeter	-	-	-	-
Aspect	-	-	-	-
Roundness	-	-	Q1: 5.86	0.047
Perimeter ratio	-	-	-	-
Deformity	-	-	-	-
Shape factor	-	-	-	-
Branching	-	-	-	-

Q1: first quartile, Q2: median, Q3: third quartile, -: not statistically significant.

- Venules and arterioles size variables

The area of venules and arterioles defined two risk groups within the high risk patients. When the area was over the median, the patients had a $10\pm 6\%$ 5-year OS (**figure 94**).

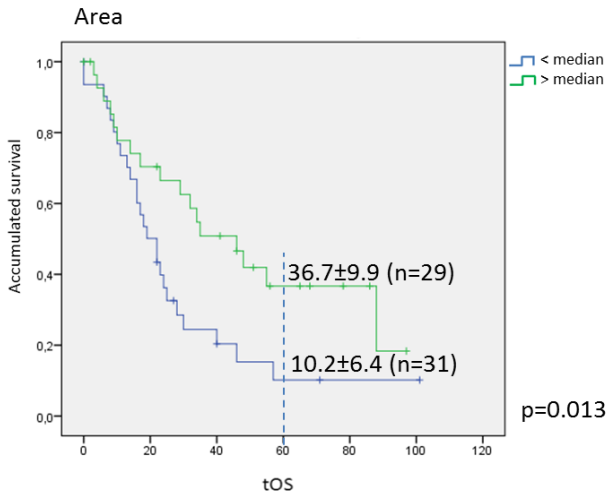


Figure 94: Kaplan-meier graph showing the different accumulated survival depending on the area.

- Venules and arterioles shape variables

A roundness over the first quartile defined an ultra-high risk subgroup with 26 ± 5 % of 5-year OS (**figure 95**).

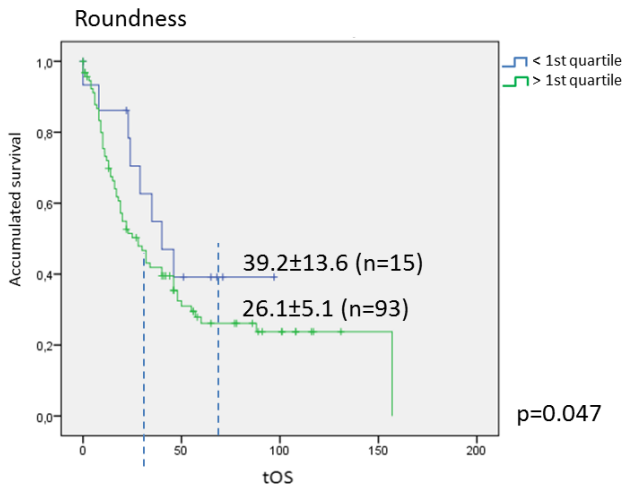


Figure 95: Kaplan-meier graph showing the different accumulated survival depending on the roundness parameter.

5.8. Veins and arteries (>200µm)

5.8.1. Description of the variables

0,1% of the vessels belonged to this class of vessels with 20 to 50 µm of length. Neuroblastic tumors had an average of 2,8 blood vessels of this type per mm² and a tumor area occupied by vessels of 0,1%. The features related to these vessels are shown in **table 61**. Among the 325 samples with positivity for CD31, only 55 presented vessels > 200µm of length.

Table 61: Description of the morphometric measurements of the blood vessels with more than 200µm of length, in a subset of 373 samples for quantity and 55 for size and shape variables.

	Parameter	Mean	Median	SD	Min.	Max.
Quantity	Density	2.9	0.0	20.6	0.0	271.6
	% stained area	0.1	0.0	0.6	0.0	7.4
	Relative density	0.1	0.0	0.9	0.0	16.7
	Relative area	4.0	0.0	13.3	0.0	99.7
Size	Average area	14917.2	8677.7	17685.5	1274.3	105384.4
	Length	327.9	274.6	183.2	202.5	1260.0
	Width	90.8	80.3	50.5	24.6	291.4
	Perimeter	1340.7	1017.4	1086.6	622.1	6966.3
	Aspect	5.06	3.70	7.20	1.63	55.56
Shape	Roundness	15.84	11.60	14.25	2.67	71.19
	Perimeter ratio	0.61	0.61	0.17	0.18	0.96
	Deformity	136230	87337	157030	18844	888036
	Shape factor	11.68	1.95	26.87	0.01	164.26
	Branching	8.26	8.00	1.83	4.00	12.00

5.8.2. Favorable and unfavorable veins and arteries histological patterns

Stage and age were related to the area and width of the veins and arteries. Roundness and shape factor for stage and shape factor and branching for age were also statistically related. Histopathology and the risk group were related to the width of this subgroup of blood vessels. Finally, ploidy was related to the % of stained area corresponding to veins and arteries (**table 62**).

Table 62: p-values resulting from the relation of the morphometric characterization of the blood vessels with >200µm length and the clinical and genetic INRG variables.

Parameter	Stage	Age	Histopathology	MYCN	Genetic profile	11q	Ploidy	Risk group
Density	-	-	-	-	-	-	-	-
Quantity								
% stained area	-	-	-	-	-	-	0.44	-
Relative density	-	-	-	-	-	-	-	-
Relative area	-	-	-	-	-	-	-	-
Average area	0.011	0.010	-	-	-	-	-	-
Size								
Length	-	-	-	-	-	-	-	-
Width	0.035	0.016	0.023	-	-	-	-	0.033
Perimeter	-	-	-	-	-	-	-	-
Shape								
Aspect	-	-	-	-	-	-	-	-
Roundness	0.029	-	-	-	-	-	-	-
Perimeter ratio	-	-	-	-	-	-	-	-
Deformity	-	-	-	-	-	-	-	-
Shape factor	0.019	0.024	-	-	-	-	-	-
Branching	-	0.044	-	-	-	-	-	-

-: not statistically significant.

How that these variables were related is shown in **figures 96 to 98**. Only variables with significant relationship with at least one INRG variable are shown.

A. Quantity variables

Hyperdiploid tumors had a higher relative stained area corresponding to veins and arteries, compared to diploid tumors (**figure 96**).

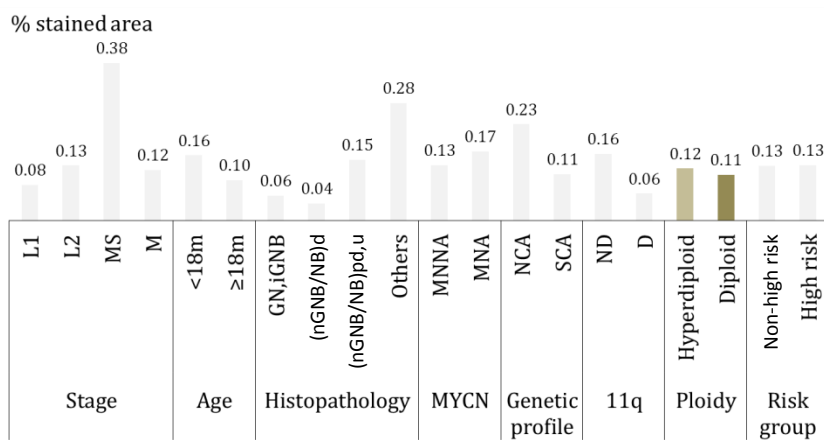


Figure 96: Distribution of the % of stained area corresponding to of veins and arteries depending on the ploidy. Variables in grey mean no significant statistical relationship. Colored variables show significant statistical relationship (**table 62**). The median values are shown.

B. Size variables

Tumors from localized disease (L1, L2) had smaller area and width for blood vessels corresponding to veins and arteries than the metastatic tumors (M). Veins and arteries were thicker in advanced stages, unfavorable histopathologies and high risk patients than their counterparts. On the contrary, tumors from patients younger than 18

months of age had larger veins and arteries in total area and width (figure 97).

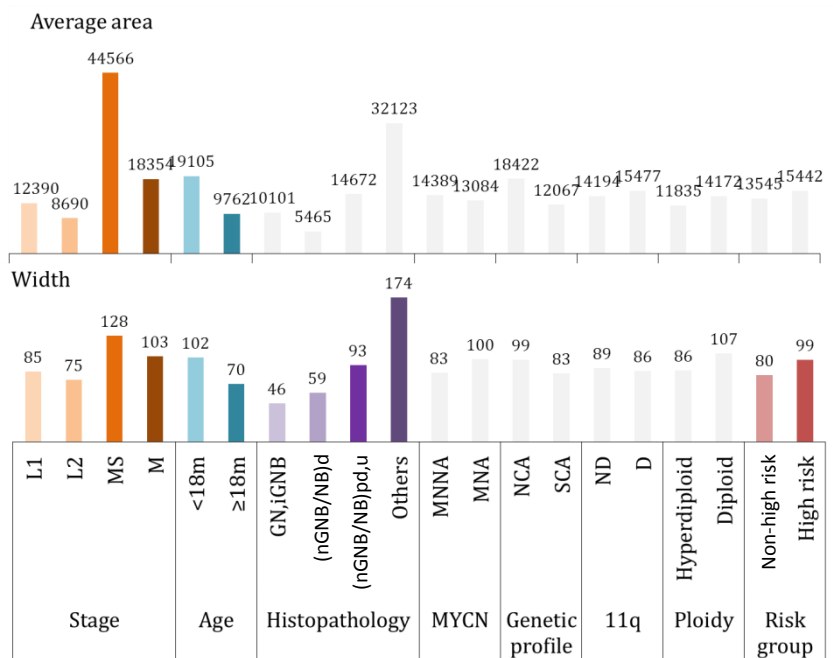


Figure 97: Distribution of the average area of veins and arteries depending on the INRG clinical and biological variables. Variables in grey mean no significant statistical relationship. Colored variables show significant statistical relationship (table 62). The median values are shown.

C. Shape variables

Tumors from patients with stage Ms of the disease had rounder blood vessels corresponding to veins and arteries (lower roundness value) and with a higher shape factor. Tumors from patients under 18 months of age also had a higher shape factor and a higher branching degree than those from older patients (figure 98).

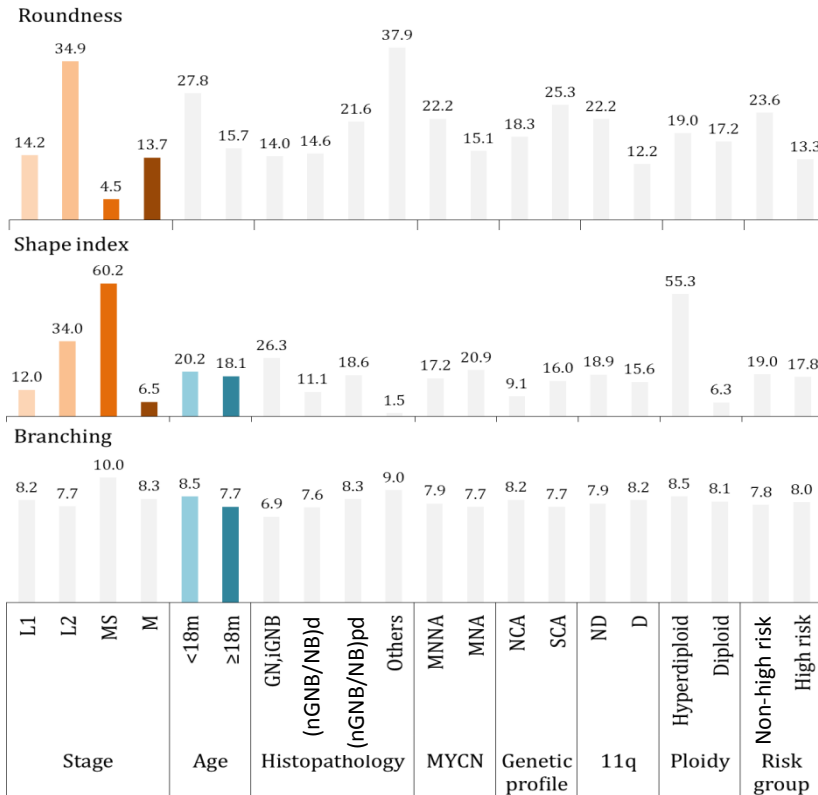


Figure 98: Distribution of the roundness of veins and arteries depending on the INRG clinical and biological variables. Variables in grey mean no significant statistical relationship. Colored variables show significant statistical relationship (**table 62**). The median values are shown.

5.8.3. Survival analysis

A. Multivariate analysis

The statistically significant relationships between veins and arteries morphometric measurements and the survival variables on 55 samples (those presenting veins and arteries) are shown in **table 63**.

Regarding EFS, we could observe that a higher relative area corresponding to veins and arteries was affecting survival when considering the morphometric variables on their own, with a HR of 1.0

(1.00-1.03), and also when considering the INRG variables except stage, with a HR of 1.03 (1.01-1.05). In the later case, a higher aspect of veins and arteries also affected survival with a HR of 1.3 (1.0-1.7). A higher aspect was only related to OS when considering the morphometric variables on their own, with a HR of 1.3 (1.0-1.7). Given the low number of valid cases for this section, the results should be taken with care.

Table 63: Results of the Cox regression showing the influence of veins and arteries morphometric measurements on their own on 5 and 10-year OS%.

	Variable	Wald	HR (95% CI)	p-value
EFS				
a	V/A rel. area	4.2	1.0 (1.00-1.03)	0.040
b		-		
c	V/A rel. area	8.3	1.03 (1.01-1.05)	0.004
	<i>MYCN</i>	6.8	6.4 (1.5-25.7)	0.009
	V/A aspect	4.0	1.3 (1.0-1.7)	0.044
OS				
a	V/A aspect	4.2	1.3 (1.0-1.7)	0.038
b, c		-		

a: morphometric variables on their own, b: morphometric variables + all INRG variables, c: morphometric variables + INRG variables except stage, V/A: veins and arteries, rel. area: relative area covered by vessels corresponding to this subgroup, HR: Hazard ratio, CI: Confidence interval, -: no statistically significant morphometric parameter.

B. Study of the high risk group

No differences were found in EFS and OS for high risk patients regarding the veins and arterioles morphometric variables. Kaplan-Meier curves are therefore not shown.

6. Topological integration of reticulin fibers and blood vessels regarding neuroblastic cells

This procedure has shown some hints of discrimination regarding the organization and co-location of these elements. On the one hand, we found that this method could differentiate between samples from high risk and non-high risk patients except for some high risk cases which are found within the non-high risk samples (**figure 99**). On the other hand, when focusing on the misclassified samples, we found that they correlated with the topology of MNNA samples, well differentiated thanks to the network characteristics of these two ECM elements with respect to the neuroblastic cells (**figure 100**). Taken together, this means that the topological organization of the ECM markers is different depending on the clinical and genetic features of the samples and that MNA carries a detectable topological change within the high risk patients group.

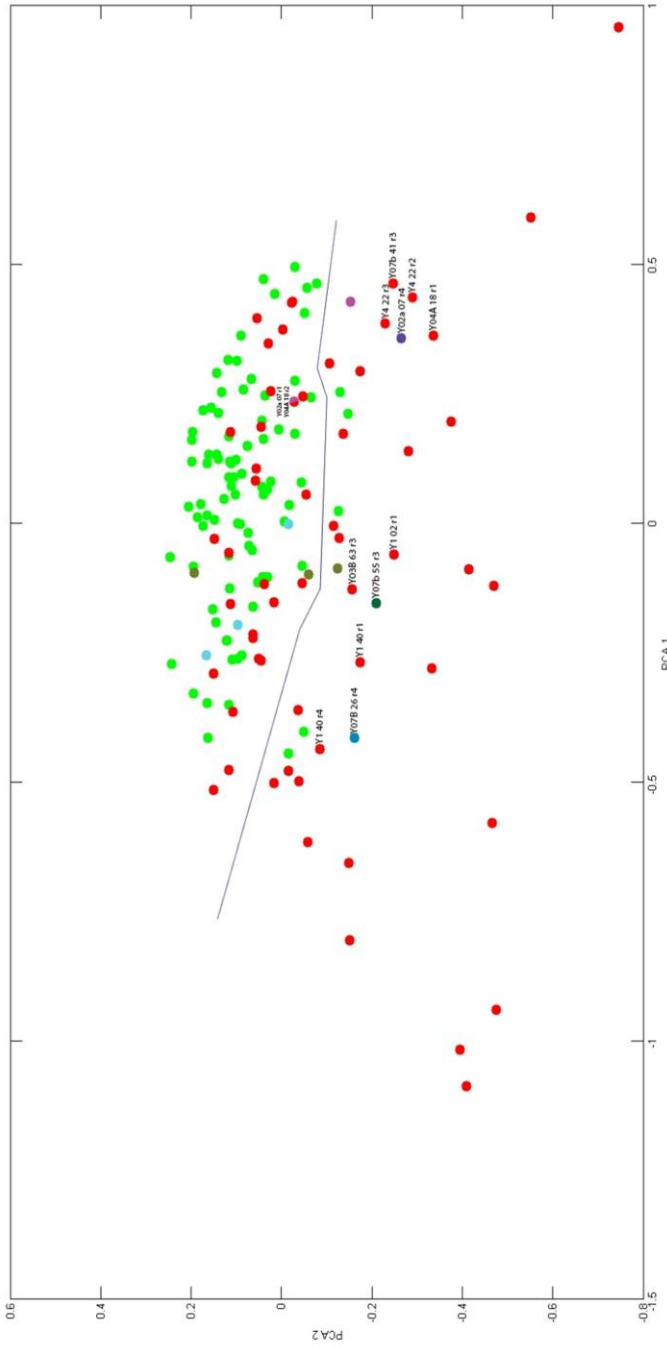


Figure 99: Principal component analysis (PCA) of high risk (red) and non-high risk (green) patients defining the topological relationship between blood vessels, reticulin fibers and neuroblastic cells. Each point represents a region of interest corresponding to different samples. Blue, green and purple points are samples corresponding to non-high risk patients but with topological relationships associated with high risk samples.

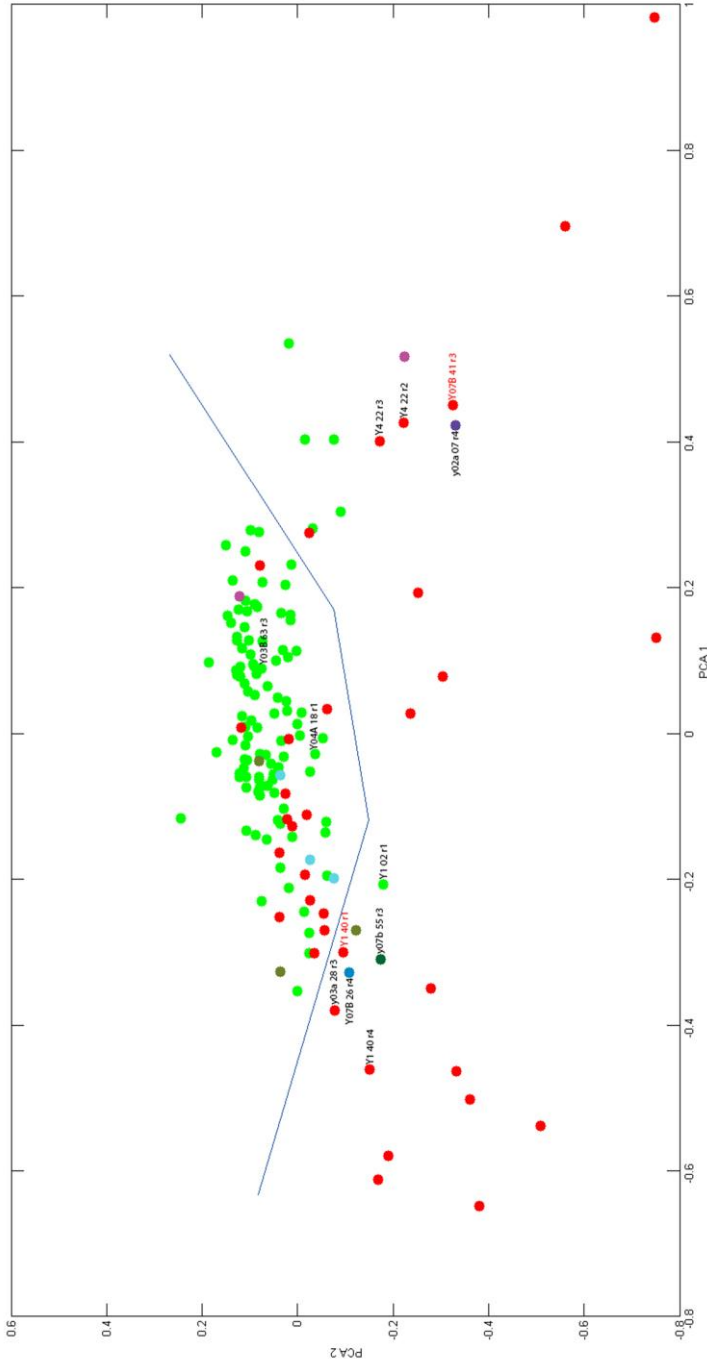


Figure 100: Principal component analysis (PCA) of MNA (red) and MNNA (green) tumors features defining the topological relationship between blood vessels, reticulin fibers and neuroblastic cells. Each point represents a region of interest corresponding to different samples. Blue, green and purple points are samples corresponding to non-high risk patients but with topological relationships associated with high risk samples.

V. DISCUSSION

1. Morphometric techniques

The digitization of the samples is required to perform morphometric analysis. As described in the **material and methods section**, the method available in most laboratories is the capture of several images per sample with a photomicroscope. This is a process that requires too much time when analyzing more than 500 samples. The use of a slide scanner is the only method that permits the digitization of a high number of cases in a reasonable time when developing a routine image biobank (187, 188) or a research project as ours. Additionally, the use of slide scanners provides the possibility to standardize the image quality using preserved light conditions. Three different scanners were tested (Aperio Scanscope from Aperio technologies, Panoramic Midi from 3D Histech and the Ventana iScann Coreo Au from Roche) (187, 189). Aperio Scanscope XT was chosen because of its time sparing and quality properties.

As a consequence of this study, an image database including 5,725 images was obtained and a total of 107,630 data were generated. This number of images of whole tissue cylinders (at 40x magnification) would be extremely hard to obtain without the use of a slide scanner and the data would be really difficult to obtain or analyze subjectively or with methods other than morphometry and statistics. Additionally, we decided to store the working images in JPEG format. The slight loss in the image quality carried by JPEG compression does not compromise the quality of the image analysis and the storage and the analysis of this amount of images would have been very slow otherwise (180-182). Only the images corresponding to blood vessels

were stored in TIFF, because of the need to detect the stained pixels very restrictively and specifically.

The proper software for each ECM element has been selected from the available systems (Image Pro-plus, providing shape and size measurements for fibers) or, when not available, it has been used from other laboratories (Positive Pixel Count, Aperio, in Ciudad Real for GAGs) or even designed (Angiopath, in collaboration with VISILAB, for blood vessels (183, 185)). The innovative algorithms configured in the present work for reticulin fibers, collagen type I fibers, GAGs and blood vessels made possible the quantification of these elements in neuroblastic tumors and, in the case of reticulin fibers and blood vessels, not only they have been quantified, but also their shape and size have been evaluated.

Several studies have focused on glycosaminoglycans in tumors. Nevertheless, the vast majority of them detect the presence of specific glycosaminoglycans or sulfation patterns or quantify them by means of molecular techniques (124, 190) or even by analyzing the infrared spectra (191). Few studies have described the presence of glycosaminoglycans by histochemistry on histological sections or have quantified them subjectively by pathologists in tumors (192-195). To the best of our knowledge, this is the first time that acid glycosaminoglycans have been automatically and objectively quantified in tumor tissue sections and in neuroblastic tumors with histological methods. As there were no specific requirements to distinguish alcian blue staining from the background and the cell staining, the commercial Aperio ImageScope software with the positive pixel count algorithm was used.

The grading of fibrosis in general and namely of reticulin fibers is of main interest in bone marrow pathologies (196) and pathologies of the liver (197). For this reason, different methods for the quantification of reticular fibrosis have been developed, some of them consisting in automated morphometry (198-204). However, these methods quantify the percentage of stained area and we considered that not only the amount of fibers but also the morphometric features were relevant for neuroblastoma prognosis, given that in other pathologies these are subjectively assessed (133, 170). Algorithms to quantify collagen fibers based on Masson's trichrome staining have also been described but (198, 205), as we wanted to differentially detect collagen type I fibers with respect to other collagens stained blue, by means of the restriction of color hues and size features, we had to customize our own algorithm with Image Pro-plus (170).

A common feature of tumor vessels studies is that the researchers focus on microvessel density overlooking other parameters that might be significant, such as the size and shape of the microvessels (206). Studies have revealed the importance of the size and shape of blood vessels in, for instance, laryngeal tumors (207). To our knowledge, there are only two applications providing vessel closing when the whole perimeter of the vessels is not completely stained, which could be a basic feature in translational research. Aperio's application for angiogenesis analysis is an excellent tool for managing microvessels analysis (208). This software allows performing many measurements on whole slide images but the closing algorithm is not automatic. For closing vessels, the user must draw manually the lost segment on the image. The second algorithm is free and available at

<http://www.caiman.org.uk/> (209). This algorithm cannot process image files larger than 2MB. Both softwares measure shape parameters but the measurements are global; the properties of each microvessel are not calculated individually. Other softwares have also been developed in order to calculate morphometric measurements in microvessels (186, 207, 210-213). Most of them are semiautomatic and require manual interaction. Some extract morphometric measurements like area, perimeter, convex perimeter, or circularity in microvessels but when the vessels are not closed a manual correction is performed (212, 213). The division of the process into two tasks, microvessel selection and measurements, has also been proposed through the use of filters and image segmentation techniques for selecting microvessels (186). Other studies are based on the selection of each microvessel manually and work with the grayscale image (210). Then, measurements of these vessels are calculated using other image analysis software, i. e., VIDAS release 2.5 (Kontron Elektronik, Eching, Germany) and ImageJ software (National Institute of Health, USA). These processes do not consider open vessels. Our aim was to develop a morphometric tool able to perform a segmentation of blood and lymphatic vessels to study vascularization following the hypothesis that tumor prognosis may not only be influenced by microvascular density but also by the shape and size of the vessels. A robust morphometric tool providing microvessel closing and shape measurements can only be achieved through an integrating effort from informatics/engineers and scientists. Thus, the tool we have used is able to deal with closed and open vessels and provides morphometric measurements for each detected vessel. Besides, the tool provides two kinds of executions, an automatic execution without user interaction and another where the user can

select the vessels to be analyzed. To this end, a segmentation algorithm based on two complementary methodologies has been developed to segment closed and open vessels. The design of this software has been published (183, 214) and the copyright has been requested.

We believe that the systematic quantification of such digitized cohort of neuroblastic tumors provides useful information in the following critical areas:

- Ensure consistency of results with less intra- and inter-observer variability
- Compare the tumor ECM markers obtained by immunohistochemistry and genetic techniques
- Relate the biomarker expression and the genotypic signatures of tumor cells

Indeed, the tests performed in our study indicate that the algorithms are standardized, correlate with subjective assessment, are reproducible and robust enough to be applied in samples obtained from different image capture methods and different subjective parameters considered when customizing the algorithm. Nevertheless, we recommend maintaining the same configurations to compare the results between different samples for a good morphometric study.

2. Our clinical and biological data (INRG)

We could confirm that our data behave as previously described in bibliography in that stage, age, *MYCN*, 11q and genomic profile are related to survival as expected (2, 4, 7, 9, 11-13). Nevertheless, histopathology does not completely respond to the published patterns

in our cohort. This difference may be due to the fact that, in the INRG classification, 96% of the cases (n=3889) were uNB, pdNB+nGNB and only 4% of the cases (n=182) were dNB + GN + iGNB. Furthermore, according to the INRG classification, histological category and grade of tumor differentiation only shows an influence on the risk of relapse in the localized tumors (stages L1 and L2). International collaborative studies are needed to increase the number of studied cases and therefore confirm and extrapolate our results. Regarding the potential implication of our results on the clinical practice, the study of our cohort has revealed that some of the morphometric measurements of the ECM elements studied could be used to improve the INRG pre-treatment risk stratification. Moreover, some of them may help to define a neuroblastic tumor patient's subgroup with ultra-high risk of relapse or death, within the high risk patients group, as will be discussed next.

3. ECM elements patterns, potential use as prognostic markers and treatment strategies

3.1. GAGs

Given that the histological category of neuroblastic tumors (GN, GNB and NB) is related to the amount of Schwannian stroma (12), and that GAGs are components of this stroma, it could be expected that the amount of GAGs were proportional to the amount of stroma. In the same way that tumor GAGs amount is driven by the abundance of stroma, the degree of differentiation has reciprocally been shown to be regulated by some EMC GAGs. Recent studies have demonstrated that ECM GAGs enhance differentiation of some cell types (215) and

specifically HS participates in the neuroblastic differentiation to suppress neuroblastoma growth. When ECM GAGs increase, neuroblastic cells can bind to the matrix and settle in a substrate where they differentiate (216). In fact, in our cohort, the poorest amount of GAGs (2.3% of stained tissue area) is related with NBpd/u, which are stroma-poor neuroblastomas (12). An intermediate percentage of GAGs (2.9%) are related to nGNB tumors (a mix of stroma-rich/dominant for GNB and stroma-poor for the nodular area) and dNB (stroma-poor tumors). Finally, the category related to the highest percentage of GAGs (4.8%) was the GN and iGNB group which is composed of stroma-dominant and stroma-rich tumor, respectively (12). The quantity of GAGs per tumor is thus found dependent of the abundance of tumor schwannian stroma (histological category of neuroblastoma) and grade of tumor differentiation (**appendix 2**).

An ECM without or with scant amount of GAGs may arise from the destruction of local GAGs by different enzymes (heparanases or hyaluronidases, for example), from an inhibited synthesis of GAGs or from a combination of both. It could also be due to an increased presence of fibers or cell components which limit the physical space available for GAGs. The expression of heparanase is significantly higher in the NB patients with age >12 months and/or NBpd, and/or high MKI (217). In other malignancies such as sarcomas and carcinomas, heparanase is upregulated and is a potent modulator of tumor behavior due to its protumorigenic, proangiogenic and prometastatic activities (218, 219). The expression of elevated hyaluronidase levels correlates with tumor aggressiveness and poor patient survival in bladder and prostate cancer (123, 220-222). Hyaluronidases on the

surfaces of cancer cells may produce HA oligosaccharides which induce cleavage of the HA receptor involved in cell-cell and cell-matrix interactions, CD44, promoting motility and invasion (223).

As HS chains of proteoglycans are involved in the organization of the ECM through binding with other ECM molecules, such as collagens, it has been shown that the presence of HS chains in ECM proteoglycans promotes cell adhesion, whereas their absence promotes invasion and migration in malignant cells (224). The amount of HA has been contradictorily associated with prognosis in adenocarcinomas (breast, lung and ovarian cancer) compared to squamous cell carcinoma and melanoma. In the two later, the low content of HA is directly correlated with the metastatic potential, whereas the opposite effect occurs in adenocarcinomas (225-227). The presence of HS and CS has also been related with neuronal morphogenesis and neuroprotection (228-230). A common proteoglycan is lumican, whose overexpression has been shown to negatively affect the migration of human colon cancer cells through filamentous actin reorganization, or to inhibit melanoma cell migration dependent on the binding with integrins (231, 232). The effects of ECM GAGs on the capacity of tumor cells to spread and metastasize in some malignancies are examples helping to better understand our results. Neuroblastomas with the highest amount of GAGs correspond to localized stages (L1 and L2), whereas the neuroblastic tumors with the lowest amount of GAGs are stage M (**appendix 2**). Indeed, some malignancies, including prostate carcinomas, osteosarcomas and neuroblastomas carrying MNA have the capacity to downregulate the receptor of HA, CD44 (125, 233-237). The binding with HA regulates

several processes such as cell migration and mechanosensing (125, 236, 238). Our data showed that a lower percentage of GAGs is found in tumors presenting MNA compared to MNNA samples. The suppression of the expression of functional CD44 receptor by MNA could entail the downregulation of HA synthesis or the destruction of existing HA and would explain our findings related to GAGs in neuroblastoma.

The scant amount of GAGs in the ECM does not affect survival in our cohort but, because of the strong correlation with some of the variables determining the risk of relapse, it can be considered as an actor contributing to malignancy. Neuroblastic cells may modify ECM GAGs to escape cell-matrix binding and ECM GAGs may contribute to neuroblastic differentiation. Therefore, GAGs and interacting elements can be used to revert the agresiveness of neuroblastoma. Indeed, current treatment approaches in patients with neuroblastoma, simultaneously result in a small, although statistically significant, rise in the amount of ECM GAGs (from 4.1% to 5.3% stained area) which correlates with a slight increase of the proportion of GN, GNB and NBd found in our cohort.

GAGs are related to tumor cells and to the fibrous scaffolding, and also to tumor vascularization. For example, HS proteoglycans have long been implicated in the control of angiogenesis and have evolved as important receptors for several molecules with angiogenic activity (239, 240). Therefore, a first therapeutic approach would be the manipulation of this GAG to affect angiogenic functions. The use of GAGs and, more frequently, HS and CS, in cancer treatment has long been investigated given their known biological roles and even some

clinical trials are being developed (241-243). Most of the studies focus on the inhibition of the synthesis (244-246) and the function of GAGs by impeding cell-ECM interactions (245, 246). Other studies use GAGs as vectors for the release of therapeutic agents, because of their ability to deliver chemicals (247, 248). Nevertheless, in neuroblastoma, a scant amount of GAGs is related to poor prognosis and, therefore, therapeutic strategies focusing in GAGs and GAGs-receptors synthesis, injection or the inhibition of degrading enzymes may be considered.

3.2. Fibrous scaffolding

Tumor tissue stiffness is mostly produced by the fibrous scaffold and, specially, by collagen fibers, and it influences the tumor progression (249). Increased tissue stiffness has been correlated with liver, pancreatic or prostate cancer where it contributes to cancer progression (250-252), evidencing that cells are highly responsive to the mechanical properties of their surroundings and viceversa (253). In this sense, the North American Division Health Ministries have recently introduced the requirement to inform about the mammographic density (254), understood as the ratio between the ECM collagen to adipose cell volume, given that a high mammographic density predicts a two- to sixfold higher risk of developing breast cancer (255, 256). Regarding neuroblastoma, neuroblastic cells are highly sensitive to the biomechanical properties of their microenvironment and exhibit changes in differentiation behavior in response to 3-D culture matrices (61, 63). It has been published that an increasing ECM stiffness carried by collagen type I scaffoldings enhances neuritogenesis, suppresses cell proliferation and also reduces the expression of *MYCN* (61). In our samples, a slightly higher area covered by collagen type I fibers,

implying a stiffer and less porous collagen type I ECM, was associated with differentiated histology and favorable genetic features and clinical presentations. However, neuroblastic tumors ECM is composed by networks of reticulin fibers in a notably higher amount (mean of 8.4% and median of 6.6% of stained area) than by thick bundles of collagen type I fibers, which are mainly rare as interneuroblastic scaffolding (mean of 2.5% and median of 0.24% of stained area) and, moreover, elastic fibers were found only restricted to vessels contours and are negligible in interneuroblastic cells stroma in our cohort. Consequently, the reticulin fibers features are those better determining the behavior of ECM in neuroblastic tumors (**appendix 2**). Neuroblastic tumors seem to have different reticulin fibers amounts in relationship with malignancy defined by the INRG parameters. A higher area occupied by reticulin fibers correlates with undifferentiated histopathology and 11q deletion whereas a lower stained area correlates with age over 18 months and diploid tumors. 11q deletion includes the 11q22.3 region where the MMP-1 gene is found (257). A deletion of this region will trigger the incapacity of secreting collagenases to the ECM and could explain why collagens type I and III are found in a higher amount in 11q deleted than in 11q non-deleted tumors. Other factors of poor prognosis are related, although not statistically significant, with a low area covered by reticulin fibers. However, not only an increase in tumor fibers content triggers stiffness, but matrix reorganization and alignment, which is mainly observable at the tumor-host margin (**figure 61, page 143**), can also result in a stiffer matrix (135, 258).

Tumor cells utilize contractility events to reorganize the ECM to provide contact guidance that facilitates 3D migration and invasion

along oriented collagen fibers (135, 259). This fiber alignment, in turn, correlates with increased tumor invasion. It has been described that tumor-associated collagens (type I and III) are often linearized and crosslinked, reflecting elevated deposition and significant post-translational modification (133). This fact restructures and progressively stiffens the ECM which thereafter elicits diverse effects on cellular differentiation, gene expression, proliferation, survival and migration, which can in turn significantly modify tumor progression and influence treatment response (100, 133). In breast cancer, it has been shown that tumorigenesis is accompanied by collagen crosslinking, ECM stiffening and increased focal adhesion and that stiff crosslinked collagen can modulate tissue fibrosis to force focal adhesions, growth factor signaling and predicts poor survival (100, 260). It has also been found that physical compaction of human glioblastoma cell lines induces expression of some collagen types and collagen crosslinking by the enzyme lysyl oxidase which is involved in creating a growth permissive fibrotic microenvironment capable of supporting metastatic growth (261, 262). In our cohort, we found that tumors with undifferentiated histopathology, 11q deletion and/or diploid DNA content have mostly reticulin fibers forming large networks (large size, low aspect), crosslinking (high roundness), with a tortuous outline (low perimeter ratio) and reorganized with high spatial complexity (high fractal dimension). Although undifferentiated tumors and tumors with 11q deletion present a higher branching, the age of the patient over 18 months, together with MNA, are related to a low presence of transverse anastomosis (low branching), associated with the linearized fibers described in other tumors (133). In general, the ECM reticulin fibers scaffold of tumors with unfavorable characteristics is stiff and

with low porosity. Therefore, our data correlate with the reported behavior of ECM collagens.

Some of the pathways by which tumor stiffening promotes tumor spread have been described and are related to biotensegrity (258, 263). ECM collagen-generated tensile forces regulate a signaling circuit that activates microRNA expression to drive tumor progression. Increased ECM stiffness transcriptionally activates *MYC* and miR-18a, leading to reduced expression of the tumor suppressor phosphatase and tensin homolog (PTEN) and therefore, inducing invasion and metastasis in mice (264). Other pathways described include the promotion of integrin clustering by ECM stiffness, which enhances ERK activity and increased Rho/ROCK-generated cell contractility that can disrupt tissue organization and promote tumorigenesis (265). Finally, a rigid extracellular matrix promotes invasiveness of tumor cells via increased activity of invadopodia (266), which enable tumor cells to migrate along stiff collagen fibers, now turned into highways for migration into the adjacent stroma (133, 249, 267). This relationship between the fibrous scaffold and cells was observed in our cohort as is reflected in **figures 46 and 47 (results section, page 141 and 142)**, where we could observe special arrangements around tumor and stromal cells. Tumor and stromal cells may be using reticulin fibers as pathways along which to migrate. Indeed, evidence has been provided supporting the reticular network as a pathway for lymphocyte migration (268). However, collagen in tissues can also represent a physical barrier against invasion and the proteolysis of types I and IV collagen by MMP and cathepsins, among others, is essential for migration through the ECM (269-271). In this sense, we also observed

this phenomenon in several analyzed tumors. **Figure 46 B** represents this idea by showing differentiated neuroblastic cells apparently trapped within a network of reticulin and collagen type I fibers and, as we can see in **figure 46 C**, reticulin fibers surround a huge cell cluster while being scant within the cells and may be isolating tumor cells. In this case, an initiating necrosis can be observed in the center of the tumor cell cluster, which may be a consequence of the fibrous scaffold barrier. In fact, it has been described that the distribution of collagens in the stroma is not uniform in human breast and prostate cancer. Dense collagen type I was detected in normoxic regions while it was excluded from hypoxic regions of the tumor, which would in turn correlate with the scant amount found in unfavorable tumors ECM (272). In this sense, the detected reticulin fibers patterns in the cohort analyzed must play a role in necrosis and therefore in prognosis. Nevertheless, more approaches must be done to properly assess the spatial distribution of the ECM elements automatically and objectively.

Neuroblastic tumors ECM fibrous scaffolding does not have prognostic value in our cohort in combination with the INRG variables. Nevertheless, the study of survival within the high risk group shows that some morphometric features defining ECM stiffness, carried by reticulin fibers, define a new group within the high risk patients with very high risk of relapse or death (mostly under 15% of 5-year EFS or OS). This subgroup is composed by tumors whose ECMs presents reticulin fibers occupying a huge stained area and forming large networks with high crosslinking, high branching and disorganized within the tumor tissue space (**appendix 3**). Therefore, these parameters could be used to enhance the pre-treatment risk

stratification through the definition of an ultra-high risk group of patients who could benefit from more accurate and targeted treatments against the ECM fibrous scaffolding.

We have described that the increased deposition or crosslinking of fibers in the ECM contributes to a stiffer and thickened ECM which is associated to malignancy in neuroblastoma. The accumulation of non-fluid elements in the tumor ECM carries the establishment of a solid pressure within the tumor tissue, which, together with other pressure sources, leads to an elevated tumor interstitial pressure (273). Elevated tumor pressure alters gene expression, cancer cell proliferation, apoptosis and invasiveness, stromal cell function and extracellular matrix synthesis and organization (274-276). Additionally, it has a negative impact on cancer treatment and is known to reduce the efficacy of cancer therapy through a reduced uptake and heterogeneous distribution of drugs (277, 278). The understanding of the fact that biomechanical forces affect cell-cell and cell-matrix crosstalk and alter tumor cells fate, suggests the possibility of developing new therapies that can target the behaviors that arise from these complex interactions (258). Regarding ECM fibers, therapies that attack some of the major physical changes themselves, such as inhibiting matrix crosslinking, could be developed to revert pressure within the tumor tissue (279). Most of the therapeutic strategies under study are based on altering the fibroblastic pathways of collagen synthesis and inhibiting fibroblast growth factor (280-283). Fibroblasts are rather scant in neuroblastic tumors ECM, being replaced by Schwann cells. Indeed, fibroblasts are inversely correlated with the presence of Schwann cells, suggesting

that these could prevent the activation of fibroblasts (284). Schwann cells synthesize distinct types of collagen and express collagen receptors belonging or not to the integrin family, which enable them to adhere and migrate on collagen substrates (285). Maybe the same strategies regulating collagens biosynthesis pathways in fibroblasts can be applied to these supportive cells. Otherwise, strategies focusing on the destruction of existing fibrosis should be developed. In this sense, collagenase has been shown to reduce tumor interstitial pressure by cleaving collagen and consequently destroying the collagen crosslinked networks in tumors in human osteosarcoma xenografts (286). Moreover, this enzyme could indirectly affect tumor ECM by degrading the reticulin fibers associated with blood vessels. Another therapeutic approach not affecting the amount of fibers but the morphology consists in impeding an increased crosslinking. The reduction of lysyl-oxylase-like-2, catalyzing the production of a crosslinked collagenous matrix, by the monoclonal antibody AB0023, was efficacious in reducing disease in different models of cancer and fibrosis (279). Incorporating biomechanical forces into our current picture of the tumor microenvironment fundamentally changes the context in which we study the basic cell and molecular biology of cancer. If there is one core message from the last two decades of research into the tumor ECM, it is that context matters (258).

Finally, the fibrous scaffold is not only important as a support for tumor and stromal cells migration. It has also been found to play a key role in tumor angiogenesis development which is, at least in part, regulated by the mechanical interactions between neovessel sprouts and the ECM (287). Additionally, the crosslinking of collagen scaffolds

promotes vascular stability. In fact, **figure 48 (results section, page 141)** showed how reticulin fibers were arranged around blood vessels to support and stabilize them and, some times, extended inwards and outwards the vessels, probably allowing stromal or tumor cell migration and perhaps the establishment of perivascular tumor niches.

3.3. Blood vascularization

Several studies have revealed the relationship between vascular density and prognosis. High microvascular density was associated with poor differentiation and advanced stage and correlated with poor survival in invasive pulmonary adenocarcinoma (288). Increased vascularization has also been related to unfavourable outcome in endometrial carcinomas (289) or with higher stages in prostate cancer (290). The opposite was found for other malignancies such as pancreatic ductal adenocarcinoma where well differentiated samples contained higher microvascular density than poorly differentiated carcinomas (291). A recent study points out the clinical importance of low microvascular density at the tumor center as an independent prognostic factor of distant metastasis development in breast cancer (292). In neuroblastic tumors, different studies have related vascularization with prognosis, showing sometimes contradictory results, probably because of the different techniques used (149-154, 293). Our data show that, in our cohort, total blood vessels density is significantly increased in undifferentiated tumors although it is decreased for the rest of unfavorable clinical and biological features albeit these results are not statistically significant (**appendix 2**). In our cohort, a percentage of stained area over the 3rd quartile can be used to define a very poor prognosis group (23% of 5-

year OS) within the high risk patients (**appendix 3**). When we focus on the different microvasculature and macrovasculature subgroups, we can observe that capillaries and post-capillaries/metarterioles densities decrease in tumors with poor prognosis whereas the amount of sinusoid-like blood vessels, venules/arterioles and veins and arteries are increased in density and occupied tissue area. Moreover, in the poor-prognosis group, the relative amount of blood vessels corresponding to capillaries, regarding total vascularization, is lessened and the relative amount of blood vessels corresponding to sinusoid-like blood vessels, venules/arterioles and veins/arteries is increased. In addition, the total vascular density is increased in both primary and non-primary NB, corresponding to a significant rise in post-capillaries/metarterioles, sinusoid-like blood vessels, venules/arterioles and veins/arteries with respect to normal tissue and to peritumoral tissue, while the capillaries amount is decreased (**appendix 2**). Translated to biological significance, this would mean that tumors with unfavorable characteristics present mostly sinusoid-like blood vessels and a minority of capillaries in their ECM, together with increased venules and veins which would be a consequence of the high number of pathological sinusoid-like blood vessels and, therefore, the need to drain such amount of blood. The fact that sinusoid-like blood vessels have thin vessel walls could explain the occurrence of intratumoral hemorrhages associated to poor prognosis in neuroblastoma. These tumors would therefore be more hypoxic than those with favorable features, with much more capillary density and thus oxygenation. Hypoxia enhances mutational rate, metastatic spread, and resistance to radiation and chemotherapy and promotes dedifferentiation of neuroblastoma and breast carcinoma cells as well as the development

of stem cell-like features (294). In both tumor forms there is a correlation between low differentiation stage and poor outcome, and we conclude that the dedifferentiating effect of lowered oxygen adds to the aggressive phenotype induced by hypoxia (295).

In general, tumor vessels are highly disorganized, tortuous and dilated, with uneven diameter, excessive branching and shunts (145, 146, 296). For instance, a study of angiogenesis in laryngeal tumor material revealed that vessel structure, size and shape were related to the tumor growth pattern and behavior, small regular vessels predominating in benign conditions and large and irregular vessels in malignant neoplasms (207). In the same sense, our results show that, in general, blood vessels of neuroblastic tumors associated with unfavorable features have a bigger size, are more deformed and have an increased branching, compared to those from tumors with favorable clinical and biological characteristics (**appendix 2**). Additionally, a shape factor over the 1st quartile is related to very high risk of relapse or death within the high risk cohort (30% and 24% 5-year EFS, respectively) (**appendix 3**). Focussing in the different blood vessels subtypes we could observe that, with few exceptions related to the length parameter, all blood vessel types are present with larger sizes (area, width and length) in tumors with unfavorable biological features and/or from patients with unfavorable clinical characteristics (**appendix 2**). Solid stresses affect tumor pathophysiology directly by compressing cancer and stromal cells but also indirectly by deforming blood and lymphatic vessels as described in pancreatic cancer, where compressed vessels are observable at the histological level (277). The compression of tumor vasculature also leads to a reduction in tumor

blood flow and subsequently reduces the anticancer agent transport to tumor cells (297). We could observe that neuroblastic tumors vessels are frequently found compressed, with scant or undistinguished lumen, as shown in **figure 74 (results section, page 181)**. However, this compression, although frequent, is not a rule within neuroblastic tumors and is variable from one tumor to the next and potentially from the primary site to the metastatic site, like in breast cancers (277) and therefore, the shape parameters are more irregularly distributed within the different blood vessels subgroups.

The capillaries of unfavorable tumors are larger (area, width and length) and rounder compared to the favorable tumors capillaries, which are smaller and more ovoid or bevel-cut, presumably correlating with terminal (such as brain and kidney) and plexiform (such as dermis) network configurations, respectively (**appendix 2**). The anastomotic plexiform or network configuration would avoid hypoxia in case of occlusion of vascular networks by tumor embolisms. Nevertheless, when we focus on the high risk cohort, we can observe that more irregular shapes (roundness value and shape index value over the 1st quartile and the median, respectively) with a higher branching (found related to the unfavorable INRG variables) define a subgroup of patients with very poor 5-year EFS (30% and 12%, respectively), correlating with a plexiform pattern, such as for favorable tumors (**appendix 3**). Our hypothesis is that a good plexiform capillary network would be required to maintain tissue homeostasis, but in combination with a sinuoid-enriched ECM, it could contribute to an increase of intratumoral pressure and chaos within the tumor tissue.

Larger post-capillaries/metarterioles with a more regular shape (less protrudings) and more irregular outline are found in unfavorable neuroblastomas. Thicker and with larger area but shorter length and more irregularly shaped and outlined post-capillaries/metarterioles are related with poor prognosis and these parameters could be used to improve the INRG risk stratification. A more irregular shape and outline, together with shorter lengths could be explained by refolded vessels with an atypical internal layer detected as an alternation of outlines corresponding to endothelial cells and segments filled by the morphometric tool in response to frequent lacks of endothelial cells in the blood vessel wall. This would correspond to discontinuous and permeable post-capillaries/metarterioles. During the angiogenic switch, a process by which cancerous tissue acquire angiogenic capacity in response of various signals including metabolic stress, mechanical stress, immune/inflammatory response and genetic mutations (298, 299) tumor vessels develop by sprouting or intussusception from pre-existing vessels (300, 301) and the vessel wall is not always formed by a homogeneous layer of endothelial cells. Instead, it may be lined with only cancer cells or a mosaic of cancer and endothelial cells, where cancer cells would be mimicking endothelial cells in what is known as vasculogenic mimicry. An example in neuroblastic tumors is shown in **figure 70 (results section, page 176)**. Cancer cells invading the vessel lumen, co-opted vessels or the apoptosis of endothelial cells which exposes underlying cancer cells would be alternative hypothesis for vessel wall mosaicism (146). All these angiogenic changes result in structurally and functionally abnormal tumor vessels. Therapeutic chemicals are normally transported through the interstitial space by convection, a transport

process that is dependent on pressure gradients, but increased tumor vessel permeability creates a less steep gradient along the vessels. This leads to a reduction in convective transport across the vessels in tumor bulk (301). Additionally, an increase in vessels permeability enables the extravasation of stem and immune cells, among others, and the entrance of malignant cells into the bloodstream to promote metastasis (305).

Sinusoid-like vessels which are larger in area and width, with poor protrusion and more regular vessel outline are associated with poor prognosis. A shorter length is related to poor prognosis and would correlate, together with the shape parameters, with sinusoid-like vessels forming swollen areas or cisterns in contrast with complex sinusoidal networks, which would form longer vessels. The consideration of this feature could enhance the stratification of the patients, complementary to the INRG variables (**appendix 2**). The abnormal morphology of tumor blood vessels causes a fluid pressure which, together with solid pressure, defines the total interstitial pressure, which has been identified as one of the culprits that impedes effective cancer treatment (302). Moreover, abnormal and tortuous tumor vasculature causes blood stasis, which leads to the reduction of oxygen and blood flow in tumors causing hypoxia and subsequently ischemia and necrosis (297). This effect increases anabolic metabolism which produce an acid ECM that degrades or deactivates some therapeutic drugs and renders them ineffective (303). Hypoxia also can cause resistance to radiotherapy and can help tumor cells to escape immunosurveillance (304).

In general, unfavorable neuroblastomas present larger and irregularly-shaped venules and arterioles. The irregular shape and the larger size of venules and arteries are also related to poor prognosis in combination with the INRG prognostic factors and could be used to enhance the stratification of the patients (**appendix 2**). Additionally, a roundness over the 1st quartile (irregularly-shaped vessels), but an area under the median, enable the discrimination of a group of high risk patients with very poor 5-year OS (26% and 10%, respectively) (**appendix 3**). This could be explained by the fact that venules and arterioles from high risk patients with very poor prognosis present more invaginations in their vessel walls and are smaller. Given that intravascular pressure increases as the luminal diameter of these vessels decreases (305), this subgroup of very high risk patients would present more altered biotensegrity. This phenomenon results in a hostile tumor microenvironment (hypoxia, low pH and high interstitial fluid pressure) that facilitates the selection of malignant tumor clones and the escape of tumor cells through leaky vessels, as well as it impedes the function of immune cells and the distribution of chemotherapeutics and oxygen, thereby entering a self-reinforcing loop (305-307).

Given the intrinsic design of the TMAs, areas with huge veins and arteries were avoided and the number of samples presenting veins and arteries in their ECM is reduced (only 0.1%). The results cannot therefore be discussed.

Our data show that the blood vascularization, together with the fibrous scaffold and the fundamental substance, plays a central role in the determination of the fate of the neuroblastic tumors. Because of

its importance to the tumor, it also represents an “Achilles’ heel” that can be used for cancer therapy (110). Given the central relevance of angiogenesis in tumor development, multiple antiangiogenic therapeutic strategies have been developed in the last decades for many different malignancies (146). Several direct angiogenic inhibitors (angiostatin, endostatin and thrombospondin) targeting endothelial cells and indirect anti-angiogenic agents blocking the production or activity of pro-angiogenic molecules, such as VEGF, have been developed (293). Recent studies have focused on the value of normalizing tumor vasculature to improve responses to conventional anticancer therapies rather than destroying tumor vessels to starve primary tumors from oxygen and induce tumor shrinkage (306). Vessel normalization results in reduced vessel diameter, increased pericyte coverage and normalized basement membrane, accompanied by normalization of its function. This normalized tumor vasculature becomes less permeable and tortuous and leads to reduced fluid and protein extravasation into the interstitium, resulting in the decrease tumor interstitial pressure (308, 309). For example, various preclinical studies have shown that the high levels of VEGF observed in tumors induce vessel abnormalities (310, 311). Therefore, targeting VEGF using anti-VEGF antibodies and inhibitors such as bevacizumab has been shown to reduce tumor interstitial pressure (312, 313). Another protein playing an important role in tumor angiogenesis is PDGF. Imatinib, a PDGFR-inhibitor has been shown to reduce tumor interstitial pressure and enhance therapeutic efficacy (314). Other drugs such as hydralazine and cachectin are vasodilators that cause a decrease in vascular resistance followed by an increase in tumor blood flow, which can potentially improve intratumoral transport of macromolecules and

that have been shown to reduce intratumoral pressure (315, 316). In addition to these therapeutic drugs, some physical approaches have been tested to decrease tumor ECM pressure, that can be summarized as follows: irradiation reduces the vascular wall permeability to fluid and leads to a reduction of intratumoral pressure (317); induced hyperthermia or hypothermia have shown similar results regarding the reduction of intratumoral pressure as for irradiation (318); ultrasounds due to mechanical (cavitation) and thermal pressure cause damage to tumor cells and ECM, which increase the interstitial hydraulic conductivity, reduces matrix tension and enhances tumor blood flow (319); hyperbaric oxygen increases oxygen tension and delivery to tissues (320); finally, photodynamic therapy impaired microcirculation in tumors (321). All these strategies are possible by the knowledge of the physiopathology of vascularity in tumors ECM. Most of them are in the initial phases and others are already in clinical trials with patients. Neuroblastic tumors present differential vascular densities depending on the blood vessel type, specifically focused on capillaries and sinusoid-like vessels density. Additionally, not only the vessels density but also the shape and size morphologic parameters are differentially found in the neuroblastic histologic categories. These parameters can potentially be useful to predict survival, as well. These findings, together with the vascular normalization approaches, offer a new spectrum of therapeutic opportunities whose application in neuroblastoma should be considered and studied.

3.4. Topological, genetic and clinical integration

Hanahan and Weinberg have proposed that eight hallmarks of cancer together constitute an organizing principle that provides a logical framework for understanding the remarkable diversity of neoplastic diseases, including sustained proliferative signalling, evading growth suppressors, activating invasion and metastasis or genetic changes, among others (322, 323). To study the hallmarks, several concepts have been proposed and considered at different scales of complexity, such as protein interactions, biochemical pathways, cellular functions or whole organism studies (324, 325). A novel ninth hallmark which includes the aspect of physics and mechanotransduction has recently been emphasized (326). The subjective assessment of the latter by the observer by analyzing the structural variations in tumor tissues, at diagnosis as well as during tumor progression and after treatment, using TMAs, is a challenging process (327). However, the difficulty can be overcome by forming mathematical descriptors to represent the histological texture and classify the structural changes via sophisticated computational methods (328-330). The results of our research suggests that genetic information and Schwannian stroma are not the only important factors in the molecular and histopathologic analysis of neuroblastic tumors but that, in fact, tensegrity and mechanotransduction changes carried by some characteristics of glycosaminoglycans, reticulin fibers, collagen fibers, blood vessels are also relevant to tumor progression and outcome, together with immune response stromal cells (lymphocytes B and T) (89).

During the last decade, cell-matrix contacts based on the transmembrane adhesion receptors from the integrin family (focal adhesions) have emerged as the major mechanosensitive structural elements that connect, collect, process and integrate the information of the ECM. Recent proteomic studies have not only found many more components, but have also revealed that many of these elements are recruited to focal adhesions in a force-dependent manner, supporting the view that focal adhesions harbor a network of mechanosensitive processes (331). Specifically, the $\alpha8\beta1$ integrin or tensegrin can bind to several ECM molecules and has been shown to be associated with focal adhesion points, where it participates in the regulation of spreading, adhesion, growth and survival in different neuronal and mesenchymal-derived cell types (332, 333). Indeed, we have shown that the topology of reticulin fibers, blood vessels and neuroblastic cells is associated with the risk of relapse and death. The topological network analysis and the graph theory in combination with Voronoi tessellations, that intend to capture relevant information about the organization of different tissue markers, have recently been found to be useful in the diagnosis of muscular dystrophies and neurogenic atrophies, in the classification of neuromuscular disease or to model the progression of dementia (159-161, 334). In neuroblastoma, the topological analysis of a subset of samples enables the differentiation between high risk and non-high risk samples and between MNA and MNNA samples, meaning that clinical and biological changes are reflected in ECM topology. Moreover, our preliminary results show that MNA triggers a detectable topological change within the high risk samples. This topological change, in turn, is translated into changes in

mechanotransduction (263). Nevertheless, more studies must be done in an increased cohort to confirm our preliminary findings.

Patients with neuroblastic tumors, specifically those still subject to therapeutic failure despite current knowledge, could benefit from novel therapeutic strategies which could arise from the study of the ECM biotensegrity. It is known that neuroblastic cells are committed to a complex interaction with the surrounding tumor microenvironment. Together, our data strongly support the notion that ECM rigidity modulates neuroblastoma cell differentiation and that the mechanical signals from the cellular microenvironment influence neuroblastoma differentiation and behavior. These observations support further research on the role of microenvironmental mechanical signals in neuroblastoma proliferation and differentiation and suggest that pharmacological agents that modulate the underlying mechanotransductive signaling pathways may have a role in neuroblastoma therapy.

V. CONCLUSIONS/ CONCLUSIONES

The purpose of this work was to demonstrate the importance of the extracellular matrix of neuroblastic tumors as a set of elements with prognostic and therapeutic value, through their morphometric study and the correlation with tumoral aggressiveness.

Specifically, we have analyzed morphometric parameters of glycosaminoglycans, the three types of fibers constituting the tumoral scaffolding, and the vascular spectrum and configuration. The obtained results were related with the clinical and biological factors with known prognostic value in neuroblastoma and with the clinical evolution of the patients. Putting all this together, we conclude:

1. The studied cohort, including more than 500 tumoral samples, meets the criteria of International Neuroblastoma Risk Group (INRG), regarding the clinical parameters such as the age and the stage, and the biological parameters such as the status of the *MYCN* oncogene, the integrity of the 11q region and the category defined by the genomic profile.
2. Tissue micro array (TMA) slide scanning is required for the histological analysis the extracellular matrix elements in large amounts of tumor samples, due to the huge morphological heterogeneity of neuroblastic tumors.
3. Novel and accurate image analysis tools are needed for the quantification, without inter- and intra-observer, of the fundamental substance and the characterization of the fibrous scaffolding and the vascular system of neuroblastic tumors.
4. A decreased amount of glycosaminoglycans, detected in tumors associated with poor prognostic factors, could enable neuroblastic cells to escape cell-matrix binding and may inhibit neuroblastic

differentiation. We propose the research on therapeutic approaches attempting to increase extracellular matrix glycosaminoglycans *in vitro*.

5. Collagen type I bundles are scarce as intercellular scaffolding, being less abundant in unfavorable neuroblastomas than in favorable neuroblastomas. This extracellular matrix element does not seem to influence survival. It would be suitable to perform studies on whole histological sections of more than one tumoral sample per case to confirm these findings.
6. After the study of an initial sample subset, we can infer that elastic fibers are not specific features in neuroblastic tumors stroma.
7. Reticulin fibers are the main components of the fibrous scaffolding in neuroblastic tumors. Not only the amount but also the shape and the size have been found different within the risk groups. Specifically, we define, by integrating all the analyzed parameters, the presence of a stiff and poorly porous extracellular matrix in unfavorable neuroblastomas, compared with a loose and permeable matrix found in favorable neuroblastomas.
8. In general, blood vessels are larger, more abundant and more irregularly-shaped in unfavorable neuroblastomas than in favorable neuroblastomas.
9. Specifically, capillaries are less abundant and sinusoid-like blood vessels are more abundant in unfavorable neuroblastoma. This fact suggests that this type of microvascularization, found in aggressive neuroblastomas, triggers a hypoxic microenvironment and a high intratumoral pressure. Therefore, we consider it reasonable to perform basic research on treatments based on vascular normalization in neuroblastic tumors.

10. An atypical and discontinuous endothelial layer of post-capillaries and metarterioles, together with sinusoid-like vessels forming cisterns, and arterioles and venules with irregularly-shaped lumens, are related with poor prognosis. These features could be used, after multicentric validation, to improve the INRG risk stratification.
11. The subgroup of the high risk cohort with very unfavorable prognosis can be defined by morphometric variables regarding reticulin fibers and blood vessels. Specifically, those samples with a high stained area occupied by reticulin fibers forming large, crosslinking, branching and disorganized networks present a very short survival. The samples corresponding to this subgroup of patients with ultra-high risk, also present a similar density of blood vessels, although these occupy a larger area. Additionally, they have capillaries with protrusions, and dilated venules and arterioles.
12. The integration of the topological information of reticulin fibers, blood vessels and neuroblastic cells by means of the Graph Theory and tessellations enables the identification of different dispositions regarding genetic and clinical features. Moreover, our preliminary results show how *MYCN* amplification triggers a topological change within the high risk patients group.
13. The overall results obtained from the morphometric analysis of extracellular matrix elements enable, for the first time, the comparison with clinical indicators, biomarkers expression and genotypic signatures of tumor cells, and reveal a prognostic value and a mechanotherapeutic viability in neuroblastoma.

El propósito de este trabajo es demostrar la importancia de la matriz extracelular en los tumores neuroblásticos como un conjunto de elementos con valor pronóstico y terapéutico, a través de su estudio morfométrico y de la correlación con la agresividad tumoral.

Concretamente, hemos analizado parámetros morfométricos de glicosaminoglicanos, los tres tipos de fibras que constituyen el andamiaje tumoral, y del espectro y configuración vascular. Los resultados obtenidos fueron relacionados con los factores clínicos y biológicos con valor pronóstico conocido en el neuroblastoma y con la evolución de los pacientes. Con todo esto, concluimos:

1. La cohorte estudiada, que incluye más de 500 muestras tumorales, cumple los criterios de predicción de riesgo de la Clasificación Internacional (INRG), en relación a los parámetros clínicos como la edad y el estadio y los parámetros biológicos como el estatus del oncogen MYCN, la integridad de la region cromosómica 11q y la categoría definida por el perfil genómico.
2. La digitalización de micromatrices de tejidos (TMAs) es necesaria para el análisis histológico de los elementos de la matriz extracelular en gran número de muestras tumorales, debido a la gran heterogeneidad morfológica de los tumores neuroblásticos.
3. Son necesarias herramientas de análisis de imagen novedosas y precisas para realizar la cuantificación sin variabilidad intra- e inter-observador, de la sustancia fundamental y la

caracterización del andamiaje fibroso y del sistema vascular de los tumores neuroblásticos.

4. Una baja cantidad de glicosaminoglicanos detectada en tumores asociados a factores de mal pronóstico, podría permitir a las células neuroblásticas escapar de la union célula-matriz e inhibir su diferenciación. Proponemos la investigación en aproximaciones terapéuticas centradas en el aumento de los glicosaminoglicanos en la matriz extracelular *in vitro*.
5. Los haces de colágeno tipo I son escasos como andamiaje intercelular, siendo menos abundantes en neuroblastomas desfavorables que en neuroblastomas favorables. Este elemento de la matriz extracelular no parece influir en la supervivencia. Para confirmar estos resultados sería adecuado realizar estudios con secciones histológicas completas de más de una muestra tumoral por caso.
6. Podemos inferir, por los resultados obtenidos en un subgrupo muestral inicial, que las fibras elásticas no son elementos característicos del estroma de los tumores neuroblásticos.
7. Las fibras de reticulina son el componente principal del andamiaje fibroso de los tumores neuroblásticos. No sólo la cantidad sino también la forma y el tamaño son distintos entre los diferentes grupos de riesgo. Específicamente, definimos, integrando todos los parámetros analizados, la presencia de una matriz rígida y pobremente porosa en neuroblastomas desfavorables, frente a una matriz laxa y permeable presente en los neuroblastomas favorables.

8. En general, los vasos sanguíneos son más grandes, más abundantes y tienen una forma más irregular en los neuroblastomas desfavorables, con respecto a los neuroblastomas favorables.
9. Concretamente, los capilares son menos abundantes y los vasos tipo sinusoide son más abundantes en neuroblastomas desfavorables. Esta situación sugiere que este tipo de microvascularización, existente en neuroblastomas agresivos, genera un microambiente hipóxico y una alta presión intratumoral. Así, consideramos razonable realizar investigación básica sobre tratamientos centrados en la normalización vascular en los tumores neuroblásticos.
10. Una capa endotelial atípica y discontinua en los vasos post-capilares y metarteriolas, junto con vasos tipo sinusoide que forman cisternas, y arteriolas y venulas con luces de conformación irregular, se relacionan con un pronóstico pobre. Éstas características podrían ser utilizadas, tras la validación multicéntrica, para mejorar la estratificación de riesgo de la INRG.
11. El subgrupo de la cohorte de alto riesgo con pronóstico muy desfavorable puede ser definido gracias a variables morfométricas de fibras de reticulina y de vasos sanguíneos. Concretamente, aquellas muestras tumorales con una gran área ocupada por grandes redes entrecruzadas, ramificadas y con compleja organización de fibras de reticulina, pertenecen a pacientes con muy corta supervivencia. Este subgrupo de pacientes con riesgo ultra alto, también presenta en sus biopsias un número similar de vasos sanguíneos, aunque

ocupando un área mayor. Además, tienen capilares con mayor número de protrusiones, y vénulas y arteriolas dilatadas.

12. La integración de la información topológica de las fibras de reticulina, vasos sanguíneos y células neuroblásticas por medio de la Teoría de Grafos y teselaciones, permite la identificación de distintas configuraciones relacionadas con características genéticas y clínicas. Además, nuestros resultados preliminares muestran cómo la amplificación de *MYCN* conlleva un cambio topológico en el grupo de pacientes de alto riesgo.
13. Los resultados globales obtenidos del análisis morfométrico de los elementos de la matriz extracelular estudiados permiten, por primera vez, la comparación con los indicadores clínicos, la expresión de biomarcadores y las firmas genotípicas de las células tumorales, y revelan un valor pronóstico y una viabilidad mecanoterapéutica en neuroblastoma.

VI. REFERENCES

1. Ambros PF, Ambros IM, Brodeur GM, et al. International consensus for neuroblastoma molecular diagnostics: Report from the international neuroblastoma risk group (inrg) biology committee. *Br J Cancer* 2009;100:1471-82.
2. Cohn SL, Pearson AD, London WB, et al. The international neuroblastoma risk group (inrg) classification system: An inrg task force report. *J Clin Oncol* 2009;27:289-97.
3. Maris JM, Hogarty MD, Bagatell R, Cohn SL. Neuroblastoma. *Lancet* 2007;369:2106-20.
4. Brodeur GM. Neuroblastoma: Biological insights into a clinical enigma. *Nat Rev Cancer* 2003;3:203-16.
5. Peris-Bonet R, Felipe S, Fuentes G, Navarro R, Pardo E, Tamarit C. Cáncer infantil en españa. Estadísticas 1980-2009. Registro Nacional de Tumores Infantiles (RNTI-SEHOP). Valencia, Spain: Universitat de València. 2010;Preliminar edition.
6. Peris-Bonet R, Salmeron D, Martinez-Beneito MA, et al. Childhood cancer incidence and survival in spain. *Ann Oncol* 2010;21 Suppl 3:iii103-10.
7. Monclair T, Brodeur GM, Ambros PF, et al. The international neuroblastoma risk group (inrg) staging system: An inrg task force report. *J Clin Oncol* 2009;27:298-303.
8. Simon T, Hero B, Benz-Bohm G, von Schweinitz D, Berthold F. Review of image defined risk factors in localized neuroblastoma patients: Results of the gpoh nb97 trial. *Pediatr Blood Cancer* 2008;50:965-9.
9. London WB, Boni L, Simon T, et al. The role of age in neuroblastoma risk stratification: The german, italian, and children's oncology group perspectives. *Cancer Lett* 2005;228:257-66.
10. Berbegall AP, Villamon E, Tadeo I, et al. Neuroblastoma after childhood: Prognostic relevance of segmental chromosome aberrations, atrx protein status, and immune cell infiltration. *Neoplasia* 2014;16:471-80.
11. Shimada H, Ambros IM, Dehner LP, Hata J, Joshi VV, Roald B. Terminology and morphologic criteria of neuroblastic tumors: Recommendations by the international neuroblastoma pathology committee. *Cancer* 1999;86:349-63.
12. Shimada H, Ambros IM, Dehner LP, et al. The international neuroblastoma pathology classification (the shimada system). *Cancer* 1999;86:364-72.
13. Navarro S, Piqueras M, Villamon E, et al. New prognostic markers in neuroblastoma. *Expert Opin Med Diagn* 2012;6:555-67.
14. Guo C, White PS, Hogarty MD, et al. Deletion of 11q23 is a frequent event in the evolution of mycn single-copy high-risk neuroblastomas. *Med Pediatr Oncol* 2000;35:544-6.
15. Attiyeh EF, London WB, Mosse YP, et al. Chromosome 1p and 11q deletions and outcome in neuroblastoma. *N Engl J Med* 2005;353:2243-53.
16. Caren H, Kryh H, Nethander M, et al. High-risk neuroblastoma tumors with 11q-deletion display a poor prognostic, chromosome instability phenotype with later onset. *Proc Natl Acad Sci U S A* 107:4323-8.
17. Villamon E, Berbegall AP, Piqueras M, et al. Genetic instability and intratumoral heterogeneity in neuroblastoma with mycn amplification plus 11q deletion. *PLoS One* 2013;8:e53740.
18. Ladenstein R, Ambros IM, Potschger U, et al. Prognostic significance of DNA di-tetraploidy in neuroblastoma. *Med Pediatr Oncol* 2001;36:83-92.

19. Look AT, Hayes FA, Shuster JJ, et al. Clinical relevance of tumor cell ploidy and n-myc gene amplification in childhood neuroblastoma: A pediatric oncology group study. *J Clin Oncol* 1991;9:581-91.
20. George RE, London WB, Cohn SL, et al. Hyperdiploidy plus nonamplified mycn confers a favorable prognosis in children 12 to 18 months old with disseminated neuroblastoma: A pediatric oncology group study. *J Clin Oncol* 2005;23:6466-73.
21. Schneiderman J, London WB, Brodeur GM, Castleberry RP, Look AT, Cohn SL. Clinical significance of mycn amplification and ploidy in favorable-stage neuroblastoma: A report from the children's oncology group. *J Clin Oncol* 2008;26:913-8.
22. White PS, Thompson PM, Gotoh T, et al. Definition and characterization of a region of 1p36.3 consistently deleted in neuroblastoma. *Oncogene* 2005;24:2684-94.
23. Henrich KO, Bauer T, Schulte J, et al. Camta1, a 1p36 tumor suppressor candidate, inhibits growth and activates differentiation programs in neuroblastoma cells. *Cancer Res* 71:3142-51.
24. Liu Z, Yang X, Li Z, et al. Casz1, a candidate tumor-suppressor gene, suppresses neuroblastoma tumor growth through reprogramming gene expression. *Cell Death Differ* 18:1174-83.
25. Fujita T, Igarashi J, Okawa ER, et al. Chd5, a tumor suppressor gene deleted from 1p36.31 in neuroblastomas. *J Natl Cancer Inst* 2008;100:940-9.
26. Bown N, Cotterill S, Lastowska M, et al. Gain of chromosome arm 17q and adverse outcome in patients with neuroblastoma. *N Engl J Med* 1999;340:1954-61.
27. Janoueix-Lerosey I, Penther D, Thioux M, et al. Molecular analysis of chromosome arm 17q gain in neuroblastoma. *Genes Chromosomes Cancer* 2000;28:276-84.
28. Janoueix-Lerosey I, Lequin D, Brugieres L, et al. Somatic and germline activating mutations of the alk kinase receptor in neuroblastoma. *Nature* 2008;455:967-70.
29. Mosse YP, Laudenslager M, Longo L, et al. Identification of alk as a major familial neuroblastoma predisposition gene. *Nature* 2008;455:930-5.
30. Reiff T, Tsarovina K, Majdazari A, Schmidt M, del Pino I, Rohrer H. Neuroblastoma phox2b variants stimulate proliferation and dedifferentiation of immature sympathetic neurons. *J Neurosci* 30:905-15.
31. Bachetti T, Di Paolo D, Di Lascio S, et al. Phox2b-mediated regulation of alk expression: In vitro identification of a functional relationship between two genes involved in neuroblastoma. *PLoS One* 2010; 5(10). pii: e13108.
32. Berthier A, Piqueras M, Villamon E, et al. Anaplastic lymphoma kinase expression in neuroblastomas and its relationship with genetic, prognostic, and predictive factors. *Hum Pathol* 2011;42(2):301-2.
33. Schleiermacher G, Janoueix-Lerosey I, Ribeiro A, et al. Accumulation of segmental alterations determines progression in neuroblastoma. *J Clin Oncol* 2010;28:3122-30.
34. Schleiermacher G, Michon J, Ribeiro A, et al. Segmental chromosomal alterations lead to a higher risk of relapse in infants with mycn-non-amplified localised unresectable/disseminated neuroblastoma (a siopen collaborative study). *Br J Cancer* 2011;105:1940-8.

35. Schleiermacher G, Mosseri V, London WB, et al. Segmental chromosomal alterations have prognostic impact in neuroblastoma: A report from the inrg project. *Br J Cancer* 2012;107:1418-22.
36. Coco S, Theissen J, Scaruffi P, et al. Age-dependent accumulation of genomic aberrations and deregulation of cell cycle and telomerase genes in metastatic neuroblastoma. *Int J Cancer* 2012;131:1591-600.
37. Janoueix-Lerosey I, Schleiermacher G, Michels E, et al. Overall genomic pattern is a predictor of outcome in neuroblastoma. *J Clin Oncol* 2009;27:1026-33.
38. Villamon E, Piqueras M, Berbegall AP, et al. Comparative study of mlpa-fish to determine DNA copy number alterations in neuroblastic tumors. *Histol Histopathol* 2011;26:343-50.
39. Schleiermacher G, Michon J, Ribeiro A, et al. Segmental chromosomal alterations lead to a higher risk of relapse in infants with mycn-non-amplified localised unresectable/disseminated neuroblastoma (a siopen collaborative study). *Br J Cancer* 2011;105(12):1940-8105:1940-8.
40. Molenaar JJ, Koster J, Zwijnenburg DA, et al. Sequencing of neuroblastoma identifies chromothripsis and defects in neuritogenesis genes. *Nature* 2012;483:589-93.
41. Kryh H, Caren H, Erichsen J, et al. Comprehensive snp array study of frequently used neuroblastoma cell lines; copy neutral loss of heterozygosity is common in the cell lines but uncommon in primary tumors. *BMC Genomics* 2011;12:443.
42. Pers TH, Dworzynski P, Thomas CE, Lage K, Brunak S. Metaranker 2.0: A web server for prioritization of genetic variation data. *Nucleic Acids Res* 2013; 41(Web Server issue):W104-8.
43. Do R, Kathiresan S, Abecasis GR. Exome sequencing and complex disease: Practical aspects of rare variant association studies. *Hum Mol Genet* 2012;21:R1-9.
44. Hirschhorn JN, Daly MJ. Genome-wide association studies for common diseases and complex traits. *Nat Rev Genet* 2005;6:95-108.
45. Huyghe JR, Jackson AU, Fogarty MP, et al. Exome array analysis identifies new loci and low-frequency variants influencing insulin processing and secretion. *Nat Genet* 2013;45:197-201.
46. Jensen MK, Pers TH, Dworzynski P, Girman CJ, Brunak S, Rimm EB. Protein interaction-based genome-wide analysis of incident coronary heart disease. *Circ Cardiovasc Genet* 2011;4:549-56.
47. Zou F, Chai HS, Younkin CS, et al. Brain expression genome-wide association study (egwas) identifies human disease-associated variants. *PLoS Genet* 2012;8:e1002707.
48. Wei JS, Johansson P, Chen QR, et al. Microrna profiling identifies cancer-specific and prognostic signatures in pediatric malignancies. *Clin Cancer Res* 2009;15:5560-8.
49. Guo J, Dong Q, Fang Z, et al. Identification of mirnas that are associated with tumor metastasis in neuroblastoma. *Cancer Biol Ther* 2010;9(6):446-52.
50. Stallings RL. Microrna involvement in the pathogenesis of neuroblastoma: Potential for microrna mediated therapeutics. *Curr Pharm Des* 2009;15:456-62.
51. Schulte JH, Schowe B, Mestdagh P, et al. Accurate prediction of neuroblastoma outcome based on mirna expression profiles. *Int J Cancer* 2010;127:2374-85.

52. Buckley PG, Alcock L, Bryan K, et al. Chromosomal and microRNA expression patterns reveal biologically distinct subgroups of 11q- neuroblastoma. *Clin Cancer Res* 2010; 16:2971-8.
53. Lin RJ, Lin YC, Chen J, et al. MicroRNA signature and expression of dicer and drosha can predict prognosis and delineate risk groups in neuroblastoma. *Cancer Res* 2010;70:7841-50.
54. De Preter K, Mestdagh P, Vermeulen J, et al. Mirna expression profiling enables risk stratification in archived and fresh neuroblastoma tumor samples. *Clin Cancer Res* 2011;17:7684-92.
55. Alaminos M, Davalos V, Cheung NK, Gerald WL, Esteller M. Clustering of gene hypermethylation associated with clinical risk groups in neuroblastoma. *J Natl Cancer Inst* 2004;96:1208-19.
56. Abe M, Watanabe N, McDonnell N, et al. Identification of genes targeted by CpG island methylator phenotype in neuroblastomas, and their possible integrative involvement in poor prognosis. *Oncology* 2008;74:50-60.
57. Grau E, Martinez F, Orellana C, et al. Hypermethylation of apoptotic genes as independent prognostic factor in neuroblastoma disease. *Mol Carcinog* 2011; 50:153-62.
58. Michalowski MB, de Fraipont F, Plantaz D, Michelland S, Combaret V, Favrot MC. Methylation of tumor-suppressor genes in neuroblastoma: The *rassf1a* gene is almost always methylated in primary tumors. *Pediatr Blood Cancer* 2008;50:29-32.
59. Yang Q, Kiernan CM, Tian Y, et al. Methylation of *casp8*, *dcr2*, and *hin-1* in neuroblastoma is associated with poor outcome. *Clin Cancer Res* 2007;13:3191-7.
60. Misawa A, Tanaka S, Yagyu S, et al. *Rassf1a* hypermethylation in pre-treatment serum DNA of neuroblastoma patients: A prognostic marker. *Br J Cancer* 2009;100:399-404.
61. Lam WA, Cao L, Umesh V, Keung AJ, Sen S, Kumar S. Extracellular matrix rigidity modulates neuroblastoma cell differentiation and *n-myc* expression. *Mol Cancer* 2010;9:35.
62. Liu S, Tian Y, Chlenski A, Yang Q, Salwen HR, Cohn SL. 'cross-talk' between schwannian stroma and neuroblasts promotes neuroblastoma tumor differentiation and inhibits angiogenesis. *Cancer Lett* 2005;228:125-31.
63. Li GN, Livi LL, Gourd CM, Deweerd ES, Hoffman-Kim D. Genomic and morphological changes of neuroblastoma cells in response to three-dimensional matrices. *Tissue Eng* 2007;13:1035-47.
64. Noguera R, Nieto OA, Tadeo I, Farinas F, Alvaro T. Extracellular matrix, biotensegrity and tumor microenvironment. An update and overview. *Histol Histopathol* 2012;27:693-705.
65. Kim SH, Turnbull J, Guimond S. Extracellular matrix and cell signalling: The dynamic cooperation of integrin, proteoglycan and growth factor receptor. *J Endocrinol* 2011;209:139-51.
66. Fuller RB. Tensegrity. *Portfolio Art News Ann* 1961;4:112-27.
67. Fuller RB 1962 Tensile-integrity structures. US patent, p 521.
68. Galli C, Guizzardi S, Passeri G, Macaluso GM, Scandroglio R. Life on the wire: On tensegrity and force balance in cells. *Acta Biomed* 2005;76:5-12.
69. Ingber DE. The architecture of life. *Sci Am* 1998;278:48-57.
70. Ingber DE. Tensegrity-based mechanosensing from macro to micro. *Prog Biophys Mol Biol* 2008;97:163-79.

71. Hu S, Chen J, Wang N. Cell spreading controls balance of prestress by microtubules and extracellular matrix. *Front Biosci* 2004;9:2177-82.
72. Ingber DE. Tensegrity ii. How structural networks influence cellular information processing networks. *J Cell Sci* 2003;116:1397-408.
73. Ingber DE. Tensegrity i. Cell structure and hierarchical systems biology. *J Cell Sci* 2003;116:1157-73.
74. Laurent VM, Canadas P, Fodil R, et al. Tensegrity behaviour of cortical and cytosolic cytoskeletal components in twisted living adherent cells. *Acta Biotheor* 2002;50:331-56.
75. Stamenovic D, Mijailovich SM, Tolic-Norrelykke IM, Chen J, Wang N. Cell prestress. ii. Contribution of microtubules. *Am J Physiol Cell Physiol* 2002;282:C617-24.
76. Stamenovic D, Mijailovich SM, Tolic-Norrelykke IM, Wang N. Experimental tests of the cellular tensegrity hypothesis. *Biorheology* 2003;40:221-5.
77. Volokh KY, Vilnay O, Belsky M. Tensegrity architecture explains linear stiffening and predicts softening of living cells. *J Biomech* 2000;33:1543-9.
78. Wang N, Naruse K, Stamenovic D, et al. Mechanical behavior in living cells consistent with the tensegrity model. *Proc Natl Acad Sci U S A* 2001;98:7765-70.
79. Wang N, Tolic-Norrelykke IM, Chen J, et al. Cell prestress. I. Stiffness and prestress are closely associated in adherent contractile cells. *Am J Physiol Cell Physiol* 2002;282:C606-16.
80. Ross TD, Coon BG, Yun S, et al. Integrins in mechanotransduction. *Curr Opin Cell Biol* 2013;25:613-8.
81. Mustata T, Rusu V. [mechanotransduction and tensegrity (i)]. *Rev Med Chir Soc Med Nat Iasi* 1998;102:25-35.
82. Huang C, Miyazaki K, Akaishi S, Watanabe A, Hyakusoku H, Ogawa R. Biological effects of cellular stretch on human dermal fibroblasts. *J Plast Reconstr Aesthet Surg* 2013; 66(12):e351-61
83. Lovett DB, Shekhar N, Nickerson JA, Roux KJ, Lele TP. Modulation of nuclear shape by substrate rigidity. *Cell Mol Bioeng* 2013;6:230-8.
84. Engler AJ, Sen S, Sweeney HL, Discher DE. Matrix elasticity directs stem cell lineage specification. *Cell* 2006;126:677-89.
85. Lo CM, Wang HB, Dembo M, Wang YL. Cell movement is guided by the rigidity of the substrate. *Biophys J* 2000;79:144-52.
86. Ingber DE. Cancer as a disease of epithelial-mesenchymal interactions and extracellular matrix regulation. *Differentiation* 2002;70:547-60.
87. Hu M, Polyak K. Microenvironmental regulation of cancer development. *Curr Opin Genet Dev* 2008;18:27-34.
88. Huang S, Ingber DE. A non-genetic basis for cancer progression and metastasis: Self-organizing attractors in cell regulatory networks. *Breast Dis* 2006;26:27-54.
89. Tlsty TD, Coussens LM. Tumor stroma and regulation of cancer development. *Annu Rev Pathol* 2006;1:119-50.
90. Stasinopoulos I, Penet MF, Chen Z, Kakkad S, Glunde K, Bhujwala ZM. Exploiting the tumor microenvironment for theranostic imaging. *NMR Biomed* 2011;24:636-47.
91. Aguilar-Cuenca R, Juanes-Garcia A, Vicente-Manzanares M. Myosin ii in mechanotransduction: Master and commander of cell migration, morphogenesis, and cancer. *Cell Mol Life Sci* 2014;71(3):479-92

92. DuFort CC, Paszek MJ, Weaver VM. Balancing forces: Architectural control of mechanotransduction. *Nat Rev Mol Cell Biol* 2010;12:308-19.
93. Chandler EM, Seo BR, Califano JP, et al. Implanted adipose progenitor cells as physicochemical regulators of breast cancer. *Proc Natl Acad Sci U S A* 2012;109:9786-91.
94. Kalluri R, Zeisberg M. Fibroblasts in cancer. *Nat Rev Cancer* 2006;6:392-401.
95. Otranto M, Sarrazay V, Bonte F, Hinz B, Gabbiani G, Desmouliere A. The role of the myofibroblast in tumor stroma remodeling. *Cell Adh Migr* 2012;6:203-19.
96. Delnero P, Song YH, Fischbach C. Microengineered tumor models: Insights & opportunities from a physical sciences-oncology perspective. *Biomed Microdevices* 2013;15(4):583-93
97. Netti PA, Berk DA, Swartz MA, Grodzinsky AJ, Jain RK. Role of extracellular matrix assembly in interstitial transport in solid tumors. *Cancer Res* 2000;60:2497-503.
98. Chandler EM, Saunders MP, Yoon CJ, Gourdon D, Fischbach C. Adipose progenitor cells increase fibronectin matrix strain and unfolding in breast tumors. *Phys Biol* 2011;8:015008.
99. Hinz B. Tissue stiffness, latent *tgf-beta1* activation, and mechanical signal transduction: Implications for the pathogenesis and treatment of fibrosis. *Curr Rheumatol Rep* 2009;11:120-6.
100. Levental KR, Yu H, Kass L, et al. Matrix crosslinking forces tumor progression by enhancing integrin signaling. *Cell* 2009;139:891-906.
101. Mammoto A, Connor KM, Mammoto T, et al. A mechanosensitive transcriptional mechanism that controls angiogenesis. *Nature* 2009;457:1103-8.
102. Willis AL, Sabeh F, Li XY, Weiss SJ. Extracellular matrix determinants and the regulation of cancer cell invasion stratagems. *J Microsc* 2013;251:250-60.
103. Pathak A, Kumar S. From molecular signal activation to locomotion: An integrated, multiscale analysis of cell motility on defined matrices. *PLoS One* 2011;6:e18423.
104. Zaman MH, Trapani LM, Sieminski AL, et al. Migration of tumor cells in 3d matrices is governed by matrix stiffness along with cell-matrix adhesion and proteolysis. *Proc Natl Acad Sci U S A* 2006;103:10889-94.
105. Carey SP, Kraning-Rush CM, Williams RM, Reinhart-King CA. Biophysical control of invasive tumor cell behavior by extracellular matrix microarchitecture. *Biomaterials* 2012;33:4157-65.
106. Delnero P, Song YH, Fischbach C. Microengineered tumor models: Insights & opportunities from a physical sciences-oncology perspective. *Biomed Microdevices* 2013;15(4):583-93
107. Pathak A, Kumar S. Independent regulation of tumor cell migration by matrix stiffness and confinement. *Proc Natl Acad Sci U S A* 2012;109:10334-9.
108. Cross SE, Jin YS, Rao J, Gimzewski JK. Nanomechanical analysis of cells from cancer patients. *Nat Nanotechnol* 2007;2:780-3.
109. Lekka M, Laidler P, Gil D, Lekki J, Stachura Z, Hryniewicz AZ. Elasticity of normal and cancerous human bladder cells studied by scanning force microscopy. *Eur Biophys J* 1999;28:312-6.
110. Choi IK, Strauss R, Richter M, Yun CO, Lieber A. Strategies to increase drug penetration in solid tumors. *Front Oncol* 2013;3:193.
111. Sun Y, Nelson PS. Molecular pathways: Involving microenvironment damage responses in cancer therapy resistance. *Clin Cancer Res* 2012;18:4019-25.

112. Johnson LM, Price DK, Figg WD. Treatment-induced secretion of wnt16b promotes tumor growth and acquired resistance to chemotherapy: Implications for potential use of inhibitors in cancer treatment. *Cancer Biol Ther* 2013;14:90-1.
113. Sun Y, Campisi J, Higano C, et al. Treatment-induced damage to the tumor microenvironment promotes prostate cancer therapy resistance through wnt16b. *Nat Med* 2012;18:1359-68.
114. Triulzi T, Ratti M, Tortoreto M, et al. Maspin influences response to doxorubicin by changing the tumor microenvironment organization. *Int J Cancer* 2014;134(12):2789-97.
115. Gao C, Kozłowska A, Nechaev S, et al. Tlr9 signaling in the tumor microenvironment initiates cancer recurrence after radiation therapy. *Cancer Res* 2013;73(24):7211-21.
116. Karamanos NK, Tzanakakis GN. Glycosaminoglycans: From "Cellular glue" To novel therapeutical agents. *Curr Opin Pharmacol* 2012;12(2):220-2.
117. Afratis N, Gialeli C, Nikitovic D, et al. Glycosaminoglycans: Key players in cancer cell biology and treatment. *FEBS J* 2012;279(7):1177-97.
118. Bai X, Zhou D, Brown JR, Crawford BE, Hennes T, Esko JD. Biosynthesis of the linkage region of glycosaminoglycans: Cloning and activity of galactosyltransferase ii, the sixth member of the beta 1,3-galactosyltransferase family (beta 3galt6). *J Biol Chem* 2001;276:48189-95.
119. Zhang L. Glycosaminoglycan (gag) biosynthesis and gag-binding proteins. *Prog Mol Biol Transl Sci* 2010;93:1-17.
120. Victor XV, Nguyen TK, Ethirajan M, Tran VM, Nguyen KV, Kuberan B. Investigating the elusive mechanism of glycosaminoglycan biosynthesis. *J Biol Chem* 2009;284:25842-53.
121. Theocharis AD, Skandalis SS, Tzanakakis GN, Karamanos NK. Proteoglycans in health and disease: Novel roles for proteoglycans in malignancy and their pharmacological targeting. *FEBS J* 2010;277:3904-23.
122. Edwards IJ. Proteoglycans in prostate cancer. *Nat Rev Urol* 2012;9:196-206.
123. Sironen RK, Tammi M, Tammi R, Auvinen PK, Anttila M, Kosma VM. Hyaluronan in human malignancies. *Exp Cell Res* 2011;317:383-91.
124. Weyers A, Yang B, Yoon DS, et al. A structural analysis of glycosaminoglycans from lethal and nonlethal breast cancer tissues: Toward a novel class of theragnostics for personalized medicine in oncology? *OMICS* 2012;16:79-89.
125. Gross N, Balmas Bourlout K, Brognara CB. Mycn-related suppression of functional cd44 expression enhances tumorigenic properties of human neuroblastoma cells. *Exp Cell Res* 2000;260:396-403.
126. Lowery JL, Datta N, Rutledge GC. Effect of fiber diameter, pore size and seeding method on growth of human dermal fibroblasts in electrospun poly(epsilon-caprolactone) fibrous mats. *Biomaterials* 2010;31:491-504.
127. Ushiki T. Collagen fibers, reticular fibers and elastic fibers. A comprehensive understanding from a morphological viewpoint. *Arch Histol Cytol* 2002;65:109-26.
128. Alberts B, Johnson A, Lewis J, Raff M, Roberts K, Walter P 2008 *Molecular biology of the cell*. Garland Science, New York.
129. Ren YJ, Zhang S, Mi R, et al. Enhanced differentiation of human neural crest stem cells towards the schwann cell lineage by aligned electrospun fiber matrix. *Acta Biomater* 2013;9:7727-36.
130. Ng MR, Brugge JS. A stiff blow from the stroma: Collagen crosslinking drives tumor progression. *Cancer Cell* 2009;16:455-7.

131. Fukuda T, Tsuneyoshi M. Adhesion proteins, cellular morphology and fibrous components around the cell/extracellular-matrix interface in myxoid liposarcomas. *J Cancer Res Clin Oncol* 2000;126:320-4.
132. Yu E, Lee I. Reticular network of the human thymus. *J Korean Med Sci* 1993;8:431-6.
133. Egeblad M, Rasch MG, Weaver VM. Dynamic interplay between the collagen scaffold and tumor evolution. *Curr Opin Cell Biol* 2010;22:697-706.
134. Cheon DJ, Tong Y, Sim MS, et al. A collagen-remodeling gene signature regulated by tgfbeta signaling is associated with metastasis and poor survival in serous ovarian cancer. *Clin Cancer Res* 2014;20(3):711-23.
135. Provenzano PP, Eliceiri KW, Campbell JM, Inman DR, White JG, Keely PJ. Collagen reorganization at the tumor-stromal interface facilitates local invasion. *BMC Med* 2006;4:38.
136. Urban Z, Boyd CD. Elastic-fiber pathologies: Primary defects in assembly-and secondary disorders in transport and delivery. *Am J Hum Genet* 2000;67:4-7.
137. Agrawal U, Rai H, Jain AK. Morphological and ultrastructural characteristics of extracellular matrix changes in oral squamous cell carcinoma. *Indian J Dent Res* 2011;22:16-21.
138. Toupance S, Brassart B, Rabenoelina F, et al. Elastin-derived peptides increase invasive capacities of lung cancer cells by post-transcriptional regulation of mmp-2 and upa. *Clin Exp Metastasis* 2012;29:511-22.
139. Devy J, Duca L, Cantarelli B, et al. Elastin-derived peptides enhance melanoma growth in vivo by upregulating the activation of mcol-a (mmp-1) collagenase. *Br J Cancer* 2012;103:1562-70.
140. Folkman J, Merler E, Abernathy C, Williams G. Isolation of a tumor factor responsible for angiogenesis. *J Exp Med* 1971;133:275-88.
141. Maiese K. The many facets of cell injury: Angiogenesis to autophagy. *Curr Neurovasc Res* 2012;9:83-4.
142. Chang YS, di Tomaso E, McDonald DM, Jones R, Jain RK, Munn LL. Mosaic blood vessels in tumors: Frequency of cancer cells in contact with flowing blood. *Proc Natl Acad Sci U S A* 2000;97:14608-13.
143. Hillen F, Griffioen AW. Tumour vascularization: Sprouting angiogenesis and beyond. *Cancer Metastasis Rev* 2007;26:489-502.
144. Styp-Rekowska B, Hlushchuk R, Pries AR, Djonov V. Intussusceptive angiogenesis: Pillars against the blood flow. *Acta Physiol (Oxf)* 2011;202:213-23.
145. Bergers G, Benjamin LE. Tumorigenesis and the angiogenic switch. *Nat Rev Cancer* 2003;3:401-10.
146. Carmeliet P, Jain RK. Angiogenesis in cancer and other diseases. *Nature* 2000;407:249-57.
147. Ichihara E, Kiura K, Tanimoto M. Targeting angiogenesis in cancer therapy. *Acta Med Okayama* 2011;65:353-62.
148. Weis SM, Cheresh DA. Tumor angiogenesis: Molecular pathways and therapeutic targets. *Nat Med* 2011;17:1359-70.
149. Canete A, Navarro S, Bermudez J, Pellin A, Castel V, Llombart-Bosch A. Angiogenesis in neuroblastoma: Relationship to survival and other prognostic factors in a cohort of neuroblastoma patients. *J Clin Oncol* 2000;18:27-34.
150. Jakovljevic G, Culic S, Stepan J, Kosuta I, Seiwerth S. Relationship between tumor vascularity and vascular endothelial growth factor as prognostic factors for patients with neuroblastoma. *Coll Antropol* 2011;35:1071-9.

151. Meitar D, Crawford SE, Rademaker AW, Cohn SL. Tumor angiogenesis correlates with metastatic disease, n-myc amplification, and poor outcome in human neuroblastoma. *J Clin Oncol* 1996;14:405-14.
152. Ozer E, Altungoz O, Unlu M, Aygun N, Tumer S, Olgun N. Association of mycn amplification and 1p deletion in neuroblastomas with high tumor vascularity. *Appl Immunohistochem Mol Morphol* 2007;15:181-6.
153. Peddinti R, Zeine R, Luca D, et al. Prominent microvascular proliferation in clinically aggressive neuroblastoma. *Clin Cancer Res* 2007;13:3499-506.
154. Ribatti D, Surico G, Vacca A, et al. Angiogenesis extent and expression of matrix metalloproteinase-2 and -9 correlate with progression in human neuroblastoma. *Life Sci* 2001;68:1161-8.
155. Cornelis F, Saut O, Cumsille P, et al. In vivo mathematical modeling of tumor growth from imaging data: Soon to come in the future? *Diagn Interv Imaging* 2013;94:593-600.
156. Pham DL, Xu C, Prince JL. Current methods in medical image segmentation. *Annu Rev Biomed Eng* 2000;2:315-37.
157. Michor F, Liphardt J, Ferrari M, Widom J. What does physics have to do with cancer? *Nat Rev Cancer* 2011;11:657-70.
158. Voronoi GF. Nouvelles applications des paramètres continus à la théorie de formes quadratiques. *Journal für die reine und angewandte Mathematik* 1908;134:198-287.
159. Raj A, Kuceyeski A, Weiner M. A network diffusion model of disease progression in dementia. *Neuron* 2012;73:1204-15.
160. Saez A, Acha B, Montero-Sanchez A, Rivas E, Escudero LM, Serrano C. Neuromuscular disease classification system. *J Biomed Opt* 2013;18:066017.
161. Saez A, Rivas E, Montero-Sanchez A, et al. Quantifiable diagnosis of muscular dystrophies and neurogenic atrophies through network analysis. *BMC Med* 2013;11:77.
162. Ganeshan B, Miles KA. Quantifying tumour heterogeneity with ct. *Cancer Imaging* 2013;13:140-9.
163. Kalinli A, Sarikoc F, Akgun H, Ozturk F. Performance comparison of machine learning methods for prognosis of hormone receptor status in breast cancer tissue samples. *Comput Methods Programs Biomed* 2013;110:298-307.
164. Kowal M, Filipczuk P, Obuchowicz A, Korbicz J, Monczak R. Computer-aided diagnosis of breast cancer based on fine needle biopsy microscopic images. *Comput Biol Med* 2013;43:1563-72.
165. Ninos K, Kostopoulos S, Sidiropoulos K, et al. Computer-based image analysis system designed to differentiate between low-grade and high-grade laryngeal cancer cases. *Anal Quant Cytol Histol* 2013;35:261-72.
166. Gurcan MN, Boucheron LE, Can A, Madabhushi A, Rajpoot NM, Yener B. Histopathological image analysis: A review. *IEEE Rev Biomed Eng* 2009;2:147-71.
167. Kong J, Sertel O, Boyer KL, Saltz JH, Gurcan MN, Shimada H. Computer-assisted grading of neuroblastic differentiation. *Arch Pathol Lab Med* 2008;132:903-4; author reply 4.
168. Sertel O, Kong J, Shimada H, Catalyurek UV, Saltz JH, Gurcan MN. Computer-aided prognosis of neuroblastoma on whole-slide images: Classification of stromal development. *Pattern Recognit* 2009;42:1093-103.
169. Garcia-Bonafe M, Moragas A. Nuclear texture in poorly differentiated small round cell tumors. Image analysis study of fine needle aspiration material. *Anal Quant Cytol Histol* 1995;17:189-96.

170. Tadeo I, Piqueras M, Montaner D, et al. Quantitative modeling of clinical, cellular and extracellular matrix variables suggest prognostic indicators in cancer. A model in neuroblastoma. *Pediatric Research* 2014;75(2):302-14.
171. Villamon E, Piqueras M, Meseguer J, et al. Neupat: An intranet database supporting translational research in neuroblastic tumors. *Comput Biol Med* 2013;43:219-28.
172. Ambros IM, Benard J, Boavida M, et al. Quality assessment of genetic markers used for therapy stratification. *J Clin Oncol* 2003;21:2077-84.
173. Piqueras M, Navarro S, Canete A, Castel V, Noguera R. How to minimise the effect of tumour cell content in detection of aberrant genetic markers in neuroblastoma. *Br J Cancer* 2011;105:89-92.
174. Piqueras M, Subramaniam MM, Navarro S, Gale N, Noguera R 2011 Chapter 34: Fluorescence in situ hybridization (fish) on formalin-fixed paraffin-embedded (ffpe) tissue sections. In Stanta G (ed) *Guidelines for molecular analysis in archive tissues*. Springer, Trieste, Italy, pp 225-30.
175. Brown LA, Huntsman D. Fluorescent in situ hybridization on tissue microarrays: Challenges and solutions. *J Mol Histol* 2007;38:151-7.
176. Ambros IM, Brunner B, Aigner G, et al. A multilocus technique for risk evaluation of patients with neuroblastoma. *Clin Cancer Res* 2011;17:792-804.
177. Berbegall AP, Villamón E, Navarro S, Noguera R 2011 Chapter 33: Multiplex ligation-dependent probe amplification (mlpa). In G. S (ed) *Guidelines for molecular analysis in archive tissues*. Springer, Trieste, Italy, pp 215-24.
178. Yamamoto G, Nannya Y, Kato M, et al. Highly sensitive method for genomewide detection of allelic composition in nonpaired, primary tumor specimens by use of affymetrix single-nucleotide-polymorphism genotyping microarrays. *Am J Hum Genet* 2007;81:114-26.
179. Melegh Z, Csernak E, Toth E, et al. DNA content heterogeneity in neuroblastoma analyzed by means of image cytometry and its potential significance. *Virchows Arch* 2005;446:517-24.
180. Lejeune M, Lopez C, Bosch R, et al. Jpeg2000 for automated quantification of immunohistochemically stained cell nuclei: A comparative study with standard jpeg format. *Virchows Arch* 2011;458:237-45.
181. Lopez C, Jaen Martinez J, Lejeune M, et al. Roundness variation in jpeg images affects the automated process of nuclear immunohistochemical quantification: Correction with a linear regression model. *Histochem Cell Biol* 2009;132:469-77.
182. Lopez C, Lejeune M, Escriva P, et al. Effects of image compression on automatic count of immunohistochemically stained nuclei in digital images. *J Am Med Inform Assoc* 2008;15:794-8.
183. Fernández-Carrobles MM, Tadeo I, Bueno G, et al. TMA vessel segmentation based on color and morphological features. Application to angiogenesis research. *Journal of Biomedicine and Biotechnology* 2013 ;2013:263190.
184. Tadeo I, Piqueras M, Montaner D, et al. Quantitative modeling of clinical, cellular and extracellular matrix variables suggest prognostic indicators in cancer. A model in neuroblastoma. *Pediatr Res* 2014;75(2):302-14.
185. Fernández-Carrobles MM, Tadeo I, Noguera R, et al. A morphometric tool applied to angiogenesis research based on vessel segmentation. *Diagn Pathol* 2013;8:5.
186. Virgintino D, Monaghan P, Robertson D, et al. An immunohistochemical and morphometric study on astrocytes and microvasculature in the human cerebral cortex. *Histochem J* 1997;29:655-60.

187. Peces C, Garcia-Rojo M, Sacristan J, Gallardo AJ, Rodriguez A. Serendipia: Castilla-la mancha telepathology network. *Diagn Pathol* 2008;3 Suppl 1:55.
188. Slodkowska J, Garcia-Rojo M. Digital pathology in personalized cancer therapy. *Stud Health Technol Inform* 2012;179:143-54.
189. Rojo MG, Bueno G, Slodkowska J. Review of imaging solutions for integrated quantitative immunohistochemistry in the pathology daily practice. *Folia Histochem Cytobiol* 2009;47:349-54.
190. Frazier SB, Roodhouse KA, Hourcade DE, Zhang L. The quantification of glycosaminoglycans: A comparison of hplc, carbazole, and alcian blue methods. *Open Glycosci* 2008;1:31-9.
191. Brezillon S, Untereiner V, Lovergne L, et al. Glycosaminoglycan profiling in different cell types using infrared spectroscopy and imaging. *Anal Bioanal Chem* 2014;406(24):5795-803.
192. Seiz V, Sames K, Schmiegelow P. [histotopochemical quantification of glycosaminoglycans in melanomas and the surrounding epidermis]. *Dermatol Monatsschr* 1990;176:745-55.
193. Engelhardt A. Detection of acid mucopolysaccharides in human brain tumors by histochemical methods. *Acta Neuropathol* 1980;49:199-203.
194. George J, Narang RS, Rao NN. Stromal response in different histological grades of oral squamous cell carcinoma: A histochemical study. *Indian J Dent Res* 2012;23:842.
195. Skalova A, Vaneczek T, Majewska H, et al. Mammary analogue secretory carcinoma of salivary glands with high-grade transformation: Report of 3 cases with the *etv6-ntrk3* gene fusion and analysis of *tp53*, *beta-catenin*, *egfr*, and *ccnd1* genes. *Am J Surg Pathol* 2014;38:23-33.
196. Thiele J, Kvasnicka HM, Facchetti F, Franco V, van der Walt J, Orazi A. European consensus on grading bone marrow fibrosis and assessment of cellularity. *Haematologica* 2005;90:1128-32.
197. Chen LB, Huang HH, Shu X, et al. [pathological study of liver biopsy from 156 patients clinically diagnosed with mild chronic hepatitis b based on current guideline]. *Zhonghua Shi Yan He Lin Chuang Bing Du Xue Za Zhi* 2009;23:138-40.
198. Krajewska M, Smith LH, Rong J, et al. Image analysis algorithms for immunohistochemical assessment of cell death events and fibrosis in tissue sections. *J Histochem Cytochem* 2009;57:649-63.
199. Caballero T, Perez-Milena A, Masseroli M, et al. Liver fibrosis assessment with semiquantitative indexes and image analysis quantification in sustained-responder and non-responder interferon-treated patients with chronic hepatitis c. *J Hepatol* 2001;34:740-7.
200. Duregon E, Fassina A, Volante M, et al. The reticulin algorithm for adrenocortical tumor diagnosis: A multicentric validation study on 245 unpublished cases. *Am J Surg Pathol* 2013;37:1433-40.
201. Huss S, Schmitz J, Goltz D, Fischer HP, Buttner R, Weiskirchen R. Development and evaluation of an open source delphi-based software for morphometric quantification of liver fibrosis. *Fibrogenesis Tissue Repair* 2010;3:10.
202. Vertemati M, Moscheni C, Petrella D, et al. Morphometric analysis of hepatocellular nodular lesions in hcv cirrhosis. *Pathol Res Pract* 2012;208:240-4.
203. Vertemati M, Vizzotto L, Moscheni C, Dhillon A, Quaglia A. A morphometric model to minimize subjectivity in the histological assessment of

- hepatocellular carcinoma and its precursors in cirrhosis. *Microsc Res Tech* 2008;71:606-13.
204. Teman CJ, Wilson AR, Perkins SL, Hickman K, Prchal JT, Salama ME. Quantification of fibrosis and osteosclerosis in myeloproliferative neoplasms: A computer-assisted image study. *Leuk Res* 2010;34:871-6.
205. Dahab GM, Kheriza MM, El-Beltagi HM, Fouda AM, El-Din OA. Digital quantification of fibrosis in liver biopsy sections: Description of a new method by photoshop software. *J Gastroenterol Hepatol* 2004;19:78-85.
206. Korkolopoulou P, Patsouris E, Kavantzias N, et al. Prognostic implications of microvessel morphometry in diffuse astrocytic neoplasms. *Neuropathol Appl Neurobiol* 2002;28:57-66.
207. Laitakari J, Nayha V, Stenback F. Size, shape, structure, and direction of angiogenesis in laryngeal tumour development. *J Clin Pathol* 2004;57:394-401.
208. Aperio technologies. Microvessel analysis algorithm, user's guide. @ONLINE 2008.
209. Reyes-Aldasoro CC, Williams LJ, Akerman S, Kanthou C, Tozer GM. An automatic algorithm for the segmentation and morphological analysis of microvessels in immunostained histological tumour sections. *J Microsc* 2011;242:262-78.
210. Dagnon K, Heudes D, Bernaudin JF, Callard P. Computerized morphometric analysis of microvasculature in non-small cell lung carcinoma. *Microvasc Res* 2008;75:112-8.
211. Luukka H, Laitakari J, Vahlberg T, Klemi P, Stenback F, Grenman R. Morphometric analysis of cd34-positive vessels in salivary gland adenoid cystic and mucoepidermoid carcinomas. *J Oral Pathol Med* 2009;38:695-700.
212. Tsuji T, Sasaki Y, Tanaka M, Hanabata N, Hada R, Munakata A. Microvessel morphology and vascular endothelial growth factor expression in human colonic carcinoma with or without metastasis. *Lab Invest* 2002;82:555-62.
213. van der Laak JA, Westphal JR, Schalkwijk LJ, et al. An improved procedure to quantify tumour vascularity using true colour image analysis. Comparison with the manual hot-spot procedure in a human melanoma xenograft model. *J Pathol* 1998;184:136-43.
214. Fernández-Carrobles MM, Tadeo I, Noguera R, et al. A morphometric tool applied to angiogenesis research based on vessel segmentation. *Diagnostic Pathology* 2013; 8(Suppl 1): S20. Proceedings of the 11th European Congress on Telepathology and 5th International Congress on Virtual Microscopy.
215. Akita K, Toda M, Hosoki Y, et al. Heparan sulphate proteoglycans interact with neurocan and promote neurite outgrowth from cerebellar granule cells. *Biochem J* 2004;383:129-38.
216. Knelson EH, Gaviglio AL, Nee JC, et al. Stromal heparan sulfate differentiates neuroblasts to suppress neuroblastoma growth. *J Clin Invest* 2014;124:3016-31.
217. Zheng LD, Tong QS, Tang ST, et al. Expression and clinical significance of heparanase in neuroblastoma. *World J Pediatr* 2009;5:206-10.
218. Gomes AM, Stelling MP, Pavao MS. Heparan sulfate and heparanase as modulators of breast cancer progression. *Biomed Res Int* 2013;2013:852093.
219. Vlodavsky I, Elkin M, Ilan N. Impact of heparanase and the tumor microenvironment on cancer metastasis and angiogenesis: Basic aspects and clinical applications. *Rambam Maimonides Med J* 2011;2:e0019.

220. Lokeshwar VB, Cerwinka WH, Isoyama T, Lokeshwar BL. Hyal1 hyaluronidase in prostate cancer: A tumor promoter and suppressor. *Cancer Res* 2005;65:7782-9.
221. Lokeshwar VB, Cerwinka WH, Lokeshwar BL. Hyal1 hyaluronidase: A molecular determinant of bladder tumor growth and invasion. *Cancer Res* 2005;65:2243-50.
222. Stern R. Hyaluronidases in cancer biology. *Semin Cancer Biol* 2008;18:275-80.
223. Sugahara KN, Hirata T, Hayasaka H, Stern R, Murai T, Miyasaka M. Tumor cells enhance their own cd44 cleavage and motility by generating hyaluronan fragments. *J Biol Chem* 2006;281:5861-8.
224. Sanderson RD. Heparan sulfate proteoglycans in invasion and metastasis. *Semin Cell Dev Biol* 2001;12:89-98.
225. Anttila MA, Tammi RH, Tammi MI, Syrjänen KJ, Saarikoski SV, Kosma VM. High levels of stromal hyaluronan predict poor disease outcome in epithelial ovarian cancer. *Cancer Res* 2000;60:150-5.
226. Karjalainen JM, Tammi RH, Tammi MI, et al. Reduced level of cd44 and hyaluronan associated with unfavorable prognosis in clinical stage i cutaneous melanoma. *Am J Pathol* 2000;157:957-65.
227. Kosunen A, Ropponen K, Kellokoski J, et al. Reduced expression of hyaluronan is a strong indicator of poor survival in oral squamous cell carcinoma. *Oral Oncol* 2004;40:257-63.
228. Egea J, Garcia AG, Verges J, Montell E, Lopez MG. Antioxidant, antiinflammatory and neuroprotective actions of chondroitin sulfate and proteoglycans. *Osteoarthritis Cartilage* 2010;18 Suppl 1:S24-7.
229. Colombres M, Henriquez JP, Reig GF, et al. Heparin activates wnt signaling for neuronal morphogenesis. *J Cell Physiol* 2008;216:805-15.
230. Dudas B, Semenik K. Glycosaminoglycans and neuroprotection. *Handb Exp Pharmacol* 2012:325-43.
231. Pietraszek K, Brezillon S, Perreau C, Malicka-Blaszkiwicz M, Maquart FX, Wegrowski Y. Lumican - derived peptides inhibit melanoma cell growth and migration. *PLoS One* 2013;8:e76232.
232. Radwanska A, Litwin M, Nowak D, et al. Overexpression of lumican affects the migration of human colon cancer cells through up-regulation of gelsolin and filamentous actin reorganization. *Exp Cell Res* 2012;318:2312-23.
233. Gvozdenovic A, Arlt MJ, Campanile C, et al. Silencing of cd44 gene expression in human 143-b osteosarcoma cells promotes metastasis of intratibial tumors in scid mice. *PLoS One* 2013;8:e60329.
234. Combaret V, Gross N, Lasset C, et al. Clinical relevance of cd44 cell-surface expression and n-myc gene amplification in a multicentric analysis of 121 pediatric neuroblastomas. *J Clin Oncol* 1996;14:25-34.
235. Gao AC, Lou W, Dong JT, Isaacs JT. Cd44 is a metastasis suppressor gene for prostatic cancer located on human chromosome 11p13. *Cancer Res* 1997;57:846-9.
236. Gross N, Balmas K, Beretta Brognara C. Role of cd44h carbohydrate structure in neuroblastoma adhesive properties. *Med Pediatr Oncol* 2001;36:139-41.
237. Gross N, Beretta C, Peruisseau G, Jackson D, Simmons D, Beck D. Cd44h expression by human neuroblastoma cells: Relation to mycn amplification and lineage differentiation. *Cancer Res* 1994;54:4238-42.
238. Kim Y, Kumar S. Cd44-mediated adhesion to hyaluronic acid contributes to mechanosensing and invasive motility. *Mol Cancer Res* 2014; pii: molcanres.0629.2013.

239. Folkman J, Langer R, Linhardt RJ, Haudenschild C, Taylor S. Angiogenesis inhibition and tumor regression caused by heparin or a heparin fragment in the presence of cortisone. *Science* 1983;221:719-25.
240. Kasza Z, Fredlund Fuchs P, Tamm C, et al. MicroRNA-24 suppression of n-deacetylase/n-sulfotransferase-1 (ndst1) reduces endothelial cell responsiveness to vascular endothelial growth factor a (vegfa). *J Biol Chem* 2013;288:25956-63.
241. Afratis N, Gialeli C, Nikitovic D, et al. Glycosaminoglycans: Key players in cancer cell biology and treatment. *FEBS J* 2012;279:1177-97.
242. Belting M. Glycosaminoglycans in cancer treatment. *Thromb Res* 2014;133 Suppl 2:S95-101.
243. Karamanos NK, Tzanakakis GN. Glycosaminoglycans: From "Cellular glue" To novel therapeutical agents. *Curr Opin Pharmacol* 2012;12:220-2.
244. Dredge K, Hammond E, Davis K, et al. The pg500 series: Novel heparan sulfate mimetics as potent angiogenesis and heparanase inhibitors for cancer therapy. *Invest New Drugs* 2010;28:276-83.
245. Lai E, Singh R, Teng B, et al. Inhibition of hyaluronan synthase-3 decreases subcutaneous colon cancer growth in mice. *Dis Colon Rectum* 2010;53:475-82.
246. Teng BP, Heffler MD, Lai EC, et al. Inhibition of hyaluronan synthase-3 decreases subcutaneous colon cancer growth by increasing apoptosis. *Anticancer Agents Med Chem* 2011;11:620-8.
247. Arpicco S, Milla P, Stella B, Dosio F. Hyaluronic acid conjugates as vectors for the active targeting of drugs, genes and nanocomposites in cancer treatment. *Molecules* 2014;19:3193-230.
248. Saravanakumar G, Deepagan VG, Jayakumar R, Park JH. Hyaluronic acid-based conjugates for tumor-targeted drug delivery and imaging. *J Biomed Nanotechnol* 2014;10:17-31.
249. Seewaldt V. Ecm stiffness paves the way for tumor cells. *Nat Med* 2014;20:332-3.
250. Hoyt K, Castaneda B, Zhang M, et al. Tissue elasticity properties as biomarkers for prostate cancer. *Cancer Biomark* 2008;4:213-25.
251. Iglesias-Garcia J, Dominguez-Munoz JE, Castineira-Alvarino M, Luaces-Regueira M, Larino-Noia J. Quantitative elastography associated with endoscopic ultrasound for the diagnosis of chronic pancreatitis. *Endoscopy* 2010;45:781-8.
252. Nahon P, Kettaneh A, Lemoine M, et al. Liver stiffness measurement in patients with cirrhosis and hepatocellular carcinoma: A case-control study. *Eur J Gastroenterol Hepatol* 2009;21:214-9.
253. Discher DE, Janmey P, Wang YL. Tissue cells feel and respond to the stiffness of their substrate. *Science* 2005;310:1139-43.
254. Grady D .2012 New laws add a divisive component to breast screening. *The new york times*, New York.
255. Boyd NF, Lockwood GA, Martin LJ, et al. Mammographic densities and breast cancer risk. *Breast Dis* 1998;10:113-26.
256. Boyd NF, Martin LJ, Stone J, Greenberg C, Minkin S, Yaffe MJ. Mammographic densities as a marker of human breast cancer risk and their use in chemoprevention. *Curr Oncol Rep* 2001;3:314-21.
257. NCBI. Gene database (<http://www.Ncbi.Nlm.Nih.Gov/gene/>).
258. Shieh AC. Biomechanical forces shape the tumor microenvironment. *Ann Biomed Eng* 2011;39:1379-89.

259. Provenzano PP, Inman DR, Eliceiri KW, Trier SM, Keely PJ. Contact guidance mediated three-dimensional cell migration is regulated by rho/rock-dependent matrix reorganization. *Biophys J* 2008;95:5374-84.
260. Conklin MW, Eickhoff JC, Riching KM, et al. Aligned collagen is a prognostic signature for survival in human breast carcinoma. *Am J Pathol* 2011;178:1221-32.
261. Cox TR, Bird D, Baker AM, et al. Lox-mediated collagen crosslinking is responsible for fibrosis-enhanced metastasis. *Cancer Res* 2013;73:1721-32.
262. Mammoto T, Jiang A, Jiang E, Panigrahy D, Kieran MW, Mammoto A. Role of collagen matrix in tumor angiogenesis and glioblastoma multiforme progression. *Am J Pathol* 2013;183:1293-305.
263. Tadeo I, Berbegall AP, Escudero LM, Alvaro T, Noguera R. Biotensegrity of the extracellular matrix: Physiology, dynamic mechanical balance, and implications in oncology and mechanotherapy. *Front Oncol* 2014;4:39.
264. Mouw JK, Yui Y, Damiano L, et al. Tissue mechanics modulate microRNA-dependent pten expression to regulate malignant progression. *Nat Med* 2014;20:360-7.
265. Paszek MJ, Zahir N, Johnson KR, et al. Tensional homeostasis and the malignant phenotype. *Cancer Cell* 2005;8:241-54.
266. Parekh A, Weaver AM. Regulation of cancer invasiveness by the physical extracellular matrix environment. *Cell Adh Migr* 2009;3:288-92.
267. Liotta LA. Tumor invasion and metastases--role of the extracellular matrix: Rhoads memorial award lecture. *Cancer Res* 1986;46:1-7.
268. Sobocinski GP, Toy K, Bobrowski WF, Shaw S, Anderson AO, Kaldjian EP. Ultrastructural localization of extracellular matrix proteins of the lymph node cortex: Evidence supporting the reticular network as a pathway for lymphocyte migration. *BMC Immunol* 2010;11:42.
269. Lu C, Li XY, Hu Y, Rowe RG, Weiss SJ. Mt1-mmp controls human mesenchymal stem cell trafficking and differentiation. *Blood* 2010;115:221-9.
270. Pilcher BK, Dumin JA, Sudbeck BD, Krane SM, Welgus HG, Parks WC. The activity of collagenase-1 is required for keratinocyte migration on a type I collagen matrix. *J Cell Biol* 1997;137:1445-57.
271. Rowe RG, Weiss SJ. Breaching the basement membrane: Who, when and how? *Trends Cell Biol* 2008;18:560-74.
272. Kakkad SM, Solaiyappan M, O'Rourke B, et al. Hypoxic tumor microenvironments reduce collagen I fiber density. *Neoplasia* 2010;12:608-17.
273. Stylianopoulos T, Martin JD, Snuderl M, Mpekris F, Jain SR, Jain RK. Coevolution of solid stress and interstitial fluid pressure in tumors during progression: Implications for vascular collapse. *Cancer Res* 2013;73:3833-41.
274. Demou ZN. Gene expression profiles in 3d tumor analogs indicate compressive strain differentially enhances metastatic potential. *Ann Biomed Eng* 2010;38:3509-20.
275. Paszek MJ, Weaver VM. The tension mounts: Mechanics meets morphogenesis and malignancy. *J Mammary Gland Biol Neoplasia* 2004;9:325-42.
276. Tse JM, Cheng G, Tyrrell JA, et al. Mechanical compression drives cancer cells toward invasive phenotype. *Proc Natl Acad Sci U S A* 2012;109:911-6.
277. Jain RK, Baxter LT. Mechanisms of heterogeneous distribution of monoclonal antibodies and other macromolecules in tumors: Significance of elevated interstitial pressure. *Cancer Res* 1988;48:7022-32.

278. Salmon H, Franciszkiewicz K, Damotte D, et al. Matrix architecture defines the preferential localization and migration of t cells into the stroma of human lung tumors. *J Clin Invest* 2012;122:899-910.
279. Barry-Hamilton V, Spangler R, Marshall D, et al. Allosteric inhibition of lysyl oxidase-like-2 impedes the development of a pathologic microenvironment. *Nat Med* 2010;16:1009-17.
280. Loeffler M, Kruger JA, Niethammer AG, Reisfeld RA. Targeting tumor-associated fibroblasts improves cancer chemotherapy by increasing intratumoral drug uptake. *J Clin Invest* 2006;116:1955-62.
281. Kendall RT, Feghali-Bostwick CA. Fibroblasts in fibrosis: Novel roles and mediators. *Front Pharmacol* 2014;5:123.
282. Ko SY, Naora H. Therapeutic strategies for targeting the ovarian tumor stroma. *World J Clin Cases* 2014;2:194-200.
283. Ostapoff KT, Kutluk Cenik B, Wang M, et al. Neutralizing murine tgfbeta2 promotes a differentiated tumor cell phenotype and inhibits pancreatic cancer metastasis. *Cancer Res* 2014. In press.
284. Zeine R, Salwen HR, Peddinti R, et al. Presence of cancer-associated fibroblasts inversely correlates with schwannian stroma in neuroblastoma tumors. *Mod Pathol* 2009;22:950-8.
285. Parkinson DB, Dong Z, Bunting H, et al. Transforming growth factor beta (tgfbeta) mediates schwann cell death in vitro and in vivo: Examination of c-jun activation, interactions with survival signals, and the relationship of tgfbeta-mediated death to schwann cell differentiation. *J Neurosci* 2001;21:8572-85.
286. Eikenes L, Bruland OS, Brekken C, Davies Cde L. Collagenase increases the transcapillary pressure gradient and improves the uptake and distribution of monoclonal antibodies in human osteosarcoma xenografts. *Cancer Res* 2004;64:4768-73.
287. Edgar LT, Underwood CJ, Guilkey JE, Hoying JB, Weiss JA. Extracellular matrix density regulates the rate of neovessel growth and branching in sprouting angiogenesis. *PLoS One* 2014;9:e85178.
288. Ullah E, Nagi AH, Lail RA. Angiogenesis and mast cell density in invasive pulmonary adenocarcinoma. *J Cancer Res Ther* 2012;8:537-41.
289. Haldorsen IS, Stefansson I, Gruner R, et al. Increased microvascular proliferation is negatively correlated to tumour blood flow and is associated with unfavourable outcome in endometrial carcinomas. *Br J Cancer* 2014;110:107-14.
290. Ozerdem U, Wojcik EM, Duan X, Ersahin C, Barkan GA. Prognostic utility of quantitative image analysis of microvascular density in prostate cancer. *Pathol Int* 2013;63:277-82.
291. Barau A, Ruiz-Sauri A, Valencia G, et al. High microvessel density in pancreatic ductal adenocarcinoma is associated with high grade. *Virchows Arch* 2013;462:541-6.
292. Fernandez-Guinea O, Alvarez-Cofino A, Eiro N, et al. Low microvascular density at the tumor center is related to the expression of metalloproteases and their inhibitors and with the occurrence of distant metastasis in breast carcinomas. *Int J Clin Oncol* 2013;18:629-40.
293. Rossler J, Taylor M, Geoerger B, et al. Angiogenesis as a target in neuroblastoma. *Eur J Cancer* 2008;44:1645-56.

294. Pietras A, Johnsson AS, Pahlman S. The hif-2alpha-driven pseudo-hypoxic phenotype in tumor aggressiveness, differentiation, and vascularization. *Curr Top Microbiol Immunol* 2010;345:1-20.
295. Holmquist L, Lofstedt T, Pahlman S. Effect of hypoxia on the tumor phenotype: The neuroblastoma and breast cancer models. *Adv Exp Med Biol* 2006;587:179-93.
296. Sozio F, Rossi A, Weber E, et al. Morphometric analysis of intralobular, interlobular and pleural lymphatics in normal human lung. *J Anat* 2012;220:396-404.
297. Padera TP, Stoll BR, Tooredman JB, Capen D, di Tomaso E, Jain RK. Pathology: Cancer cells compress intratumour vessels. *Nature* 2004;427:695.
298. Gullino PM. Angiogenesis and oncogenesis. *J Natl Cancer Inst* 1978;61:639-43.
299. Kerbel RS. Tumor angiogenesis: Past, present and the near future. *Carcinogenesis* 2000;21:505-15.
300. Patan S, Haenni B, Burri PH. Implementation of intussusceptive microvascular growth in the chicken chorioallantoic membrane (cam): 1. Pillar formation by folding of the capillary wall. *Microvasc Res* 1996;51:80-98.
301. Patan S, Munn LL, Jain RK. Intussusceptive microvascular growth in a human colon adenocarcinoma xenograft: A novel mechanism of tumor angiogenesis. *Microvasc Res* 1996;51:260-72.
302. Heldin CH, Rubin K, Pietras K, Ostman A. High interstitial fluid pressure - an obstacle in cancer therapy. *Nat Rev Cancer* 2004;4:806-13.
303. Vaupel P, Kallinowski F, Okunieff P. Blood flow, oxygen and nutrient supply, and metabolic microenvironment of human tumors: A review. *Cancer Res* 1989;49:6449-65.
304. Sitkovsky MV, Kjaergaard J, Lukashev D, Ohta A. Hypoxia-adenosinergic immunosuppression: Tumor protection by t regulatory cells and cancerous tissue hypoxia. *Clin Cancer Res* 2008;14:5947-52.
305. Ariffin AB, Forde PF, Jahangeer S, Soden DM, Hinchion J. Releasing pressure in tumors: What do we know so far and where do we go from here? A review. *Cancer Res* 2014;74:2655-62.
306. Carmeliet P, Jain RK. Principles and mechanisms of vessel normalization for cancer and other angiogenic diseases. *Nat Rev Drug Discov* 2011;10:417-27.
307. Nagy JA, Chang SH, Shih SC, Dvorak AM, Dvorak HF. Heterogeneity of the tumor vasculature. *Semin Thromb Hemost* 2010;36:321-31.
308. Goel S, Wong AH, Jain RK. Vascular normalization as a therapeutic strategy for malignant and nonmalignant disease. *Cold Spring Harb Perspect Med* 2012;2:a006486.
309. Jain RK, Tong RT, Munn LL. Effect of vascular normalization by antiangiogenic therapy on interstitial hypertension, peritumor edema, and lymphatic metastasis: Insights from a mathematical model. *Cancer Res* 2007;67:2729-35.
310. Baffert F, Le T, Sennino B, et al. Cellular changes in normal blood capillaries undergoing regression after inhibition of vegf signaling. *Am J Physiol Heart Circ Physiol* 2006;290:H547-59.
311. Jain RK. Normalization of tumor vasculature: An emerging concept in antiangiogenic therapy. *Science* 2005;307:58-62.
312. Salnikov AV, Heldin NE, Stuhr LB, et al. Inhibition of carcinoma cell-derived vegf reduces inflammatory characteristics in xenograft carcinoma. *Int J Cancer* 2006;119:2795-802.

313. Tong RT, Boucher Y, Kozin SV, Winkler F, Hicklin DJ, Jain RK. Vascular normalization by vascular endothelial growth factor receptor 2 blockade induces a pressure gradient across the vasculature and improves drug penetration in tumors. *Cancer Res* 2004;64:3731-6.
314. Fan Y, Du W, He B, et al. The reduction of tumor interstitial fluid pressure by liposomal imatinib and its effect on combination therapy with liposomal doxorubicin. *Biomaterials* 2013;34:2277-88.
315. Jarm T, Podobnik B, Sersa G, Miklavcic D. Effect of hydralazine on blood flow, oxygenation, and interstitial fluid pressure in subcutaneous tumors. *Adv Exp Med Biol* 2003;510:25-9.
316. Kristensen CA, Nozue M, Boucher Y, Jain RK. Reduction of interstitial fluid pressure after tnf-alpha treatment of three human melanoma xenografts. *Br J Cancer* 1996;74:533-6.
317. Multhoff G, Vaupel P. Radiation-induced changes in microcirculation and interstitial fluid pressure affecting the delivery of macromolecules and nanotherapeutics to tumors. *Front Oncol* 2012;2:165.
318. Sen A, Capitano ML, Sperryak JA, et al. Mild elevation of body temperature reduces tumor interstitial fluid pressure and hypoxia and enhances efficacy of radiotherapy in murine tumor models. *Cancer Res* 2011;71:3872-80.
319. Watson KD, Lai CY, Qin S, et al. Ultrasound increases nanoparticle delivery by reducing intratumoral pressure and increasing transport in epithelial and epithelial-mesenchymal transition tumors. *Cancer Res* 2012;72:1485-93.
320. Stuhr LE, Raa A, Oyan AM, et al. Hyperoxia retards growth and induces apoptosis, changes in vascular density and gene expression in transplanted gliomas in nude rats. *J Neurooncol* 2007;85:191-202.
321. Kleemann B, Loos B, Scriba TJ, Lang D, Davids LM. St john's wort (hypericum perforatum L.) photomedicine: Hypericin-photodynamic therapy induces metastatic melanoma cell death. *PLoS One* 2014;9:e103762.
322. Hanahan D, Weinberg RA. The hallmarks of cancer. *Cell* 2000;100:57-70.
323. Hanahan D, Weinberg RA. Hallmarks of cancer: The next generation. *Cell* 2011;144:646-74.
324. Sanga S, Frieboes HB, Zheng X, Gatenby R, Bearer EL, Cristini V. Predictive oncology: A review of multidisciplinary, multiscale in silico modeling linking phenotype, morphology and growth. *Neuroimage* 2007;37 Suppl 1:S120-34.
325. Rejniak KA, McCawley LJ. Current trends in mathematical modeling of tumor-microenvironment interactions: A survey of tools and applications. *Exp Biol Med (Maywood)* 2010;235:411-23.
326. Mierke CT. Physical break-down of the classical view on cancer cell invasion and metastasis. *Eur J Cell Biol* 2013.
327. Garcia Rojo M. State of the art and trends for digital pathology. *Stud Health Technol Inform* 2012;179:15-28.
328. Braun M, Kirsten R, Rupp NJ, et al. Quantification of protein expression in cells and cellular subcompartments on immunohistochemical sections using a computer supported image analysis system. *Histol Histopathol* 2013;28:605-10.
329. Gabril MY, Yousef GM. Informatics for practicing anatomical pathologists: Marking a new era in pathology practice. *Mod Pathol* 2010;23:349-58.
330. Laurinavicius A, Raslavicus P. Consequences of "Going digital" For pathology professionals - entering the cloud. *Stud Health Technol Inform* 2012;179:62-7.

331. Schwarz US. Catch me because you can: A mathematical model for mechanosensing. *Biophys J* 2013;105:1289-91.
332. Benoit YD, Lussier C, Ducharme PA, et al. Integrin alpha8beta1 regulates adhesion, migration and proliferation of human intestinal crypt cells via a predominant rhoa/rock-dependent mechanism. *Biol Cell* 2009;101:695-708.
333. Zargham R. Tensegrin in context: Dual role of alpha8 integrin in the migration of different cell types. *Cell Adh Migr* 2010;4:485-90.
334. Voronoi GF. Nouvelles applications des paramètres continus à la théorie de formes quadratiques. *Journal für die reine und angewandte Mathematik* 1908;134.

VII. APPENDIX

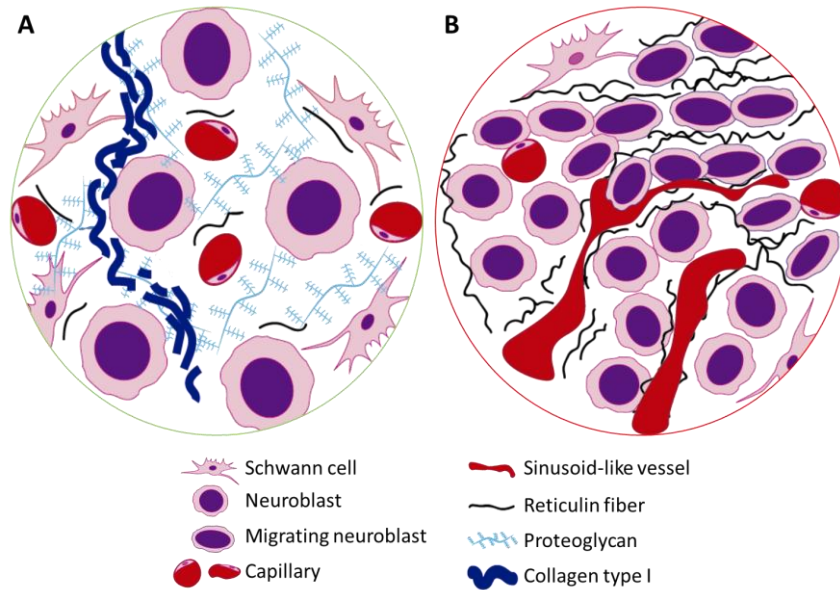
Appendix: Summary of the results

ECM element	Morphometric parameter	Poor prognosis					HR cohort
		Histological patterns		Cox	Contrary results	HR cohort	
		Majoritary results	Minoritary results				
Glycosaminoglycans	↓ % stained area	p<0.05 M, NBu, HR	p>0.05 >18m, MNA	p<0.05	p>0.05 SCA, D, 2n		
Collagen type fibers	↓ % stained area	>18, NBu, MNA, SCA, HR	M, 2n		D	= OS ^a	
	↓ density	NBu, MNA, HR	M, >18, SCA, 2n		D		
	↑ % stained area	NBu, D		>18, 2n	MNA, SCA, HR	= EFS, OS	
	↑ size	NBu	M, MNA, D, HR	2n	>18, SCA	= OS	
	↓ aspect	NBu, D, HR	M, MNA, SCA	2n	>18		
Reticulin fibers	↑ crosslinking	NBu, D	M	2n	>18, MNA, SCA, HR	= EFS, OS	
	↑ wavy	NBu, D	M, MNA, HR	2n	>18	= OS	
	↑ messy	NBu, D	HR, MNA,	>18, 2n	SCA	# EFS, OS	
	↓ branching	>18, MNA, HR	M, SCA	2n	D, NBu		
	↑ density	NBu	2n		M, >18, MNA, SCA, D, HR	# OS ^a	
	↑ % stained area	NBu	2n		M, >18, MNA, SCA, D, HR	= OS	
	↑ size	MNA, HR, M	M, >18, NBu, SCA, D, 2n		D (area, length, per).		
Total Blood Vessels	↓ aspect	M, NBu, MNA, D, HR	2n		>18		
	↑ roundness	>18	M, SCA, D, HR		NBu, MNA, 2n	# EFS ^a	
	↑ deformity	MNA, HR	M, >18, NBu, SCA, 2n		D		
	↓ shape factor	NBu, MNA	M, D, HR		2n, >18	# EFS, OS	
	↑ branching	M, MNA, HR	>18, NBu, SCA, D, 2n			= OS ^a	

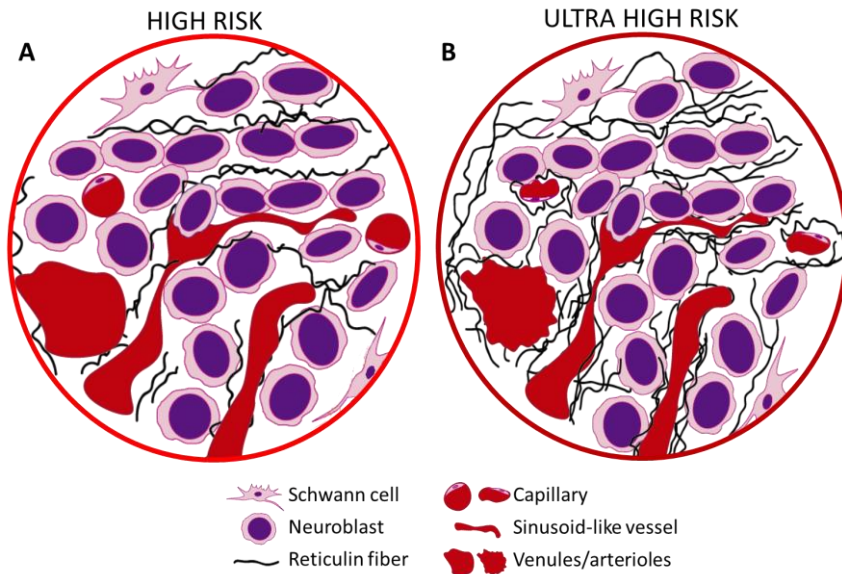
ECM element	Morphometric parameter	Poor prognosis						HR cohort
		Histological patterns			Cox			
		Majoritary results		Contrary results		Cox		
		p<0.05	p>0.05	p<0.05	p>0.05			
Capillaries	↑ density	NBu	2n		M, >18, MNA, SCA, D, HR		≠ EFS, OS ^a	
	↓ % stained area	>18, MNA	M, SCA, 2n, HR	NBu	D			
	↓ relative density	MNA	M, >18, NBu, SCA, 2n, HR		D		= OS ^a	
	↓ relative stained area	>18, MNA	M, SCA, 2n, HR		D			
	↑ size	NBu, MNA, HR	M, MNA, SCA, D		2n, >18, SCA			
	↓ aspect	M, NBu, MNA, D, HR	SCA		>18			
	↓ roundness	NBu, MNA, HR	M, D, 2n		>18, SCA		≠ EFS	
	↓ deformity	>18	M, MNA, SCA, D, 2n, HR	NBu				
	↓ shape factor	M, NBu, MNA, HR	SCA, D, 2n				≠ EFS	
	↑ branch	NBu	M, MNA, SCA, HR		>18, D, 2n			
Post-capillaries/ metarterioles	↓ density	>18	M, MNA, SCA, D, HR		NBu, 2n			
	↑ relative density	MNA	NBu, SCA, 2n, HR		>18, D		= EFS ^{a,b,c} , OS ^{a,c} (≠ length EFS ^a ; OS ^c)	
	↑ size	M, MNA, HR	>18, NBu, SCA, D, 2n		SCA, 2n for length			
	↓ aspect	M, NBu, MNA, HR	>18, SCA, D, 2n					
	↓ roundness	HR	NBu, SCA, D, 2n	MNA	>18, D			
	↓ shape factor	M, NBu, MNA, HR	D, 2n		>18, SCA		≠ EFS ^a	
	↑ branching	MNA, HR	M, >18, NBu, SCA, D, 2n					
	↓ perimeter ratio						= EFS ^c	

ECM element	Morphometric parameter	Poor prognosis						HR cohort
		Histological patterns			Cox	HR cohort	HR cohort	
		Majoritary results	Contrary results	Cox				
p<0.05	p>0.05	p<0.05	p>0.05					
Sinusoid-like vessels	↑ density	NBu	D					
	↑ % stained area	NBu						
	↑ relative density	M, MNA, HR	>18, NBu, SCA, D, 2n		M, >18, MNA, SCA, 2n, HR			
	↑ relative stained area	NBu	MNA, SCA, D, HR		>18, 2n		= OS ^{a,b,c}	
	↑ size	M, NBu, MNA, HR	M, >18, SCA, HR, MNA		D, 2n		≠ length EFS, OS ^{b,c}	
	↓ aspect	M, NBu, MNA, HR	>18, SCA, D		2n		= EFS, OS ^a	
	↓ Roundness	M, MNA, HR	>18, NBu, SCA, 2n				= EFS ^a	
	↓ shape	M, NBu, MNA, HR	>18, SCA, D, 2n				= OS ^{b,c}	
	↑ branching	M, >18, NBu, MNA, HR	SCA, D, 2n				= EFS ^a	
	↑ Perimeter ratio	MNA	>18, SCA, 2n, HR	NBu		M, D		= EFS ^a
Venules/Arterioles	↑ % stained area							
	↑ relative density	MNA, HR	>18, NBu, SCA, 2n					
	↑ relative area	MNA	M, >18, NBu, SCA, 2n, HR					
	↑ size	2n	M, >18, NBu, MNA, SCA, HR,		HR length, M width, length, D		≠ length EFS ^c	
	↑ roundness	NBu	M, D, 2n		>18, MNA, SCA, HR		= EFS ^a , OS ^{a,b,c}	
	↑ shape factor							
	↓ % stained area	2n	>18, SCA, D			M, NBu, MNA		= EFS ^{a,c}
	↑ size	M, NBu, HR	MNA, 2n, D	>18		SCA		
	↓ roundness	M	>18, MNA, D, 2n, HR			NBu, SCA		
	↓ shape factor	>18	NBu, D, 2n, HR	M		MNA, SCA		
Veins/Arteries	↓ branching	>18	MNA, SCA, 2n					
	↑ aspect							

M: advanced stages, NBu: undifferentiated neuroblastomas including poorly differentiated, HR: high risk, >18m: age over 18 months, MNA: MYCN amplification, SCA: segmental chromosome aberrations, D: 11q deletion, 2d: diploid and tetraploid tumors, Cox: results of the multivariate analysis, EFS: event-free survival, OS: overall survival, ^a: multivariate analysis with morphometric variables on their own, ^b: multivariate analysis including morphometric variables and all INRG variables, ^c: multivariate analysis including morphometric variables and all INRG variables except stage, ≠: the opposite results are found, =: the same results are found.



Appendix 2: Illustration summarizing the results regarding favorable and unfavorable neuroblastic tumors. Only the ECM elements showing differences are shown. **A)** Favorable neuroblastoma: neuroblastic cells differentiate in a microenvironment well irrigated by capillaries, rich in fundamental substance to which they can bind and with a very loose meshwork of reticulin fibers. **B)** Unfavorable neuroblastoma present an ECM with low porosity due to the reticulin fibers scaffolding which also could serve as migratory pathways and creates a stiff microenvironment subject to tension. This ECM also presents a poor amount of capillaries and an increased presence of sinusoid-like vessels, which could promote cell extra- and intra-vasation.



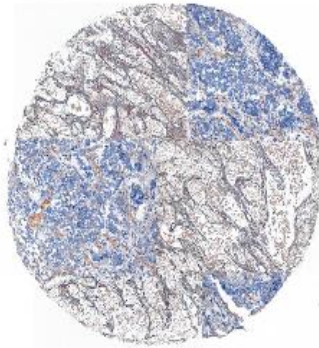
Appendix 3: Illustration summarizing the results regarding the high risk cohort. Only the ECM elements showing differences are shown. The dilated sinusoid-like vessels associated to the unfavorable subgroup are also represented. **A)** High risk tumor. **B)** Ultra-high risk tumor example. The reticulin fibers occupy an increased area and could enable neuroblastic cells to further migrate, as well as could contribute to worsen the pathological tension within the ECM and the neuroblastic cells. In addition to the dilated sinusoids, irregularly-shaped capillaries and venules/arterioles could also contribute to the promotion of aggressiveness.

IX. COMUNICACIONES TO
CONGRESSES AND
PUBLICATIONS

Diploma de Estudios Avanzados. *Introducción al estudio de la matriz extracelular del neuroblastoma: caracterización de las fibras de reticulina y de la vascularización*. Presentado el 22 de noviembre de 2010. Calificación: sobresaliente.

Trabajo de Investigación
Departamento de Patología
Facultad de Medicina y Odontología
Universidad de Valencia

**INTRODUCCIÓN AL ESTUDIO DE LA MATRIZ
EXTRACELULAR DEL NEUROBLASTOMA:
CARACTERIZACIÓN DE LAS FIBRAS DE RETICULINA
Y DE LA VASCULARIZACIÓN**



Irene Tadeo Cervera

Tutora: Dra. Rosa Noguera Salvá

Curso 26438, 2009-2010 (12 créditos)

Convocatoria de junio.

Financiación: Fundación AECC (369/2009) y

Red Temática de Investigación Cooperativa en Cáncer (RTICC),

Ministerio Español de Ciencia e Innovación (RD06/0020/0102)

Congress 1: II Encuentro Científico de Jóvenes Investigadores RTICC 2010. 14 a 15 de octubre de 2010, Madrid. Introducción al estudio de la matriz extracelular del neuroblastoma. Fibras de reticulina y vascularización. Tadeo I, Berbegall A, Piqueras M, Navarro S, Noguera R.

P-12 INTRODUCCIÓN AL ESTUDIO DE LA MATRIZ EXTRACELULAR DEL NEUROBLASTOMA. FIBRAS DE RETICULINA Y VASCULARIZACIÓN. Tadeo I, Berbegall A, Piqueras M, Navarro S, Noguera S. Departamento de Patología, Facultad de Medicina y Odontología, Universidad de Valencia.

INTRODUCCIÓN. TUMOR → tejido funcional conectado y dependiente de un microambiente que le envía señales y que recoge las señales por el propio parénquima tumoral. OBJETIVOS: Estudiar diferencias: Arquitectura vascular, Fibras de reticulina, factores clínico-biológicos pronósticos. CONCRETAMENTE: Cuantificamos y caracterizamos las fibras de reticulina en neuroblastomas con distintas características morfológicas mediante técnicas de imagen, a partir de una tinción de Gomori.

MATERIAL Y MÉTODOS. Material disponible: Estadio, Edad, Grado de diferenciación genética, Supervivencia global (OS). Selección de los casos: Clasificación de riesgo del INRG, Clasificación de riesgo de la SIOP. Proceso de las imágenes: SEGMENTACIÓN (Rango 0-117, Umbral 0-175, Anal. 05-209). Tinción para fibras de reticulina: tinción de Gomori, CD 34 (ED Bioscience 150). Inmunohistoquímica frente a CD 34 (ED Bioscience 150).

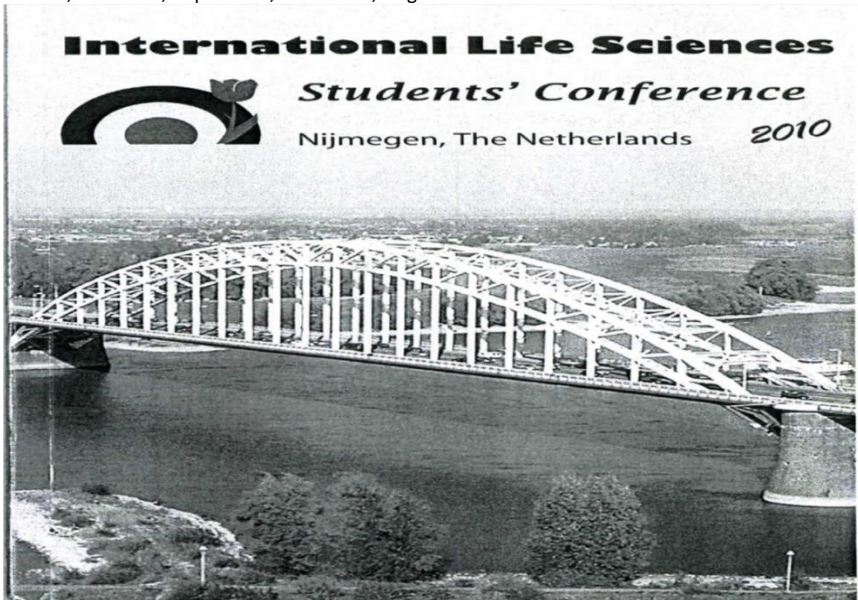
RESULTADOS. CARACTERIZACIÓN DE LOS VASOS SANGUÍNEOS. VARIABLES DICOTÓMICAS. Según estos resultados: 1. < 18 meses -> vasos cortos, regulares y redondos. 2. Alteraciones numéricas -> vasos cortos, regulares, redondos y diámetro anchura y área media pequeñas. 3. Tumores diferenciados -> vasos irregulares y alargados.

RESULTADOS. CARACTERIZACIÓN DE LA RETICULINA. Según estos resultados: 1. Estadios localizados -> haces de reticulina pequeños, estrechos y regulares. 2. Bajo riesgo -> mismas características. 3. Tumores diferenciados -> haces de reticulina regulares.

RESULTADOS. CARACTERIZACIÓN DE LA RETICULINA. Según estos resultados: 1. Riesgo más bajo -> vasos más largos e irregulares que riesgo bajo. 2. Tumores diferenciados: Mayor % de área teñida y vaso más estrechos que los ND indiferenciados. Vasos más estrechos, más irregulares y más diámetro anchura y área media que los ND pobremente diferenciados.

CONCLUSIONES. Existen diferencias en la vascularización y la distribución de las fibras de reticulina con respecto a los distintos factores clínico-biológicos que determinan el pronóstico de los enfermos de neuroblastoma. Fibras de reticulina: Los tumores con características clínico-biológicas favorables (estadios localizados, tumores con mayor grado de diferenciación neuroblástica y clasificados en riesgo bajo según la SIOP) presentan agregados de fibras reticulínicas más pequeños, más estrechos y más regulares, es decir, que tienen un estroma estructurado con haces de fibras de reticulina más regulares y compactos por un menor número de fibras que los tumores con estadios avanzados, con grado de diferenciación neuroblástica indiferenciado o pobremente diferenciado y englobados en riesgo intermedio o alto según la SIOP. Morfología vascular: Los tumores pertenecientes a niños menores de 18 meses y con alteraciones cromosómicas numéricas presentan vasos más redondos y regulares que los de pacientes mayores de 18 meses y con alteraciones cromosómicas numéricas. Los tumores con mayor grado de diferenciación neuroblástica presentan más área vascularizada, siendo sus vasos más anchos e irregulares que los que se observan en los tumores indiferenciados o pobremente diferenciados.

Congress 2: 4th International Life Sciences Students' Conference (ILSSC'10). 10 a 14 de noviembre de 2010, Nijmegen. *Study of Extracellular Matrix compounds in Neuroblastoma.* Tadeo I, Navarro S, Piqueras M, Villamón E, Noguera R. Presentación oral.



relationship analysis. In case of stable transfectants where protein expression is moderate and difficult to detect using conventional methods, using a screening strategy allows to see significant difference in transported dye accumulation compared to negative control.

Discussion: In conclusion, this recently developed HCS method, taking advantage of newly available bright fluorescent markers and novel technology, permits rapid and reliable ABCB1 efflux activity assay. We hope that it can speed up and ease further P-glycoprotein structure modification studies when ABCB1 transport activity can possibly be modulated.

Study of extracellular matrix compounds in neuroblastoma

Irene Tadeo, Samuel Navarro, Marta Piqueras, Eva Villamón, Rosa Noguera*

*Department of Pathology, Medical school, University of Valencia, Spain

Contact: irene.tadeo@uv.es

Background: To understand the influence of the genome, transcriptome, proteome and interactome in the behaviour of neuroblastoma, the study of large activity-based structures, in which a variety of types of cells and molecules are brought together to perform a function, is relevant.

Aim: To study the biological neuroblastoma complexity via construction of a morphometry model based on the collection of extracellular matrix (ECM) structures and data and the correlation with the clinical presentation, prognostic impact and treatment stratification.

Material and Methods: We analyze some ECM compounds in 24 neuroblastomas included in a tissue microarray and belonging, equally, to differentiated, undifferentiated and poorly differentiated neuroblastic tumors. Clinical and other biological data available are: age, stage, genetic profile and risk classification. Immunohistochemistry, using the following stainings: Masson's trichrome, Gomori, alcian blue and anti-CD34, was used to characterize and quantify ECM. Collagen bundles, reticulin fibers, as well as mucopolysaccharids aggregations (MPS) and angiogenic patterns have been quantified and measured by semiautomatic image morphometry with Image-Pro Plus 5.1. Statistic analysis has been performed with SPSS 17.0.


Results: Tumors of patients with favourable clinical and biological features (younger than 18 months, localized stages, with differentiated and MYCN not amplified tumors) have an ECM with more MPS, small and regular fibers areas and blood vessels. Tumors of patients older than 18 months, with disseminated disease present neuroblastic cells with segmental chromosomal aberration profiles and undifferentiated histopathology and an ECM composed of a low number of MPS aggregations, and irregular fiber and vascularisation areas.

Conclusion: This study reveals the necessity to further investigate ECM of neuroblastomas, studying other compounds as well as the stromal cells. Grants: Fundación AECG (369/2009), RTICC-ISCIII- (RD06/0020/0102).

Congress 3: XXIX Congreso Centroamericano de Patología. 29 de noviembre a 1 de diciembre 2010, Panamá. *Caracterización de la arquitectura vascular en neuroblastoma por técnicas morfológicas y estudio de su relación con parámetros clínico-biológicos determinantes del pronóstico y con otros marcadores del microambiente angiogénico.* Tadeo I, Piqueras M, Villamón E, Berbegall A, Machado I, Navarro S, Noguera R, Villamón E, Berbegall A, Machado I, Navarro S, Noguera R. Premio al mejor poster.

UNIVERSITAT DE VALÈNCIA

Facultat de Medicina i Odontologia



CARACTERIZACIÓN DE LA ARQUITECTURA VASCULAR EN NEUROBLASTOMA POR TÉCNICAS MORFOMÉTRICAS Y ESTUDIO DE SU RELACIÓN CON PARÁMETROS CLÍNICO-BIOLÓGICOS DETERMINANTES DEL PRONÓSTICO Y CON OTROS MARCADORES DEL MICROAMBIENTE ANGIOGÉNICO

Tadeo I, Piqueras M, Villamón E, Berbegall A, Machado I, Navarro S, Noguera R.
Departamento de Patología, Facultad de Medicina y Odontología, Universidad de Valencia.

INTRODUCCIÓN

TUMOR = ÚNICAMENTE UN DESORDEN EN LA PROLIFERACIÓN CELULAR

TUMOR → tejido funcional conectado y dependiente de un microambiente que le envía señales y que recoge las emitidas por el propio parénquima tumoral.

MICROAMBIENTE TUMORAL:

- FUNCIÓNES:**
 - Filtro biofísico tridimensional.
 - Soporte para:
 - Células delimitadas
 - Células de conexión
 - Capilares
 - Terminaciones nerviosas libres
- COMPOSICIÓN:**
 - Fibras:
 - Elasticas
 - Colágenas
 - RETÍCULINA
 - Sustancia fundamental
 - Proteoglicanos / GAG y Glicoproteínas
 - Moléculas de transmisión de señales

NEUROBLASTOMA: 10% de tumores por cáncer, 18 meses, 18 meses, 18 meses

El aumento del conocimiento sobre trayectorias del cáncer: células tumorales y extracelular e hiperestructuras permitirá una mejor delimitación de los subgrupos pronósticos del neuroblastoma.

OBJETIVOS

Estudiar diferencias:

ARQUITECTURA VASCULAR ↔ MICROAMBIENTE ANGIOGÉNICO: HIF1-α, HIF2-α, VEGF

PARÁMETROS CLÍNICO-BIOLÓGICOS PRONÓSTICOS

Concretamente:

- Realizamos un análisis semi-cuantitativo objetivo de la arquitectura vascular a partir de la tinción inmunohistoquímica frente a CD34, mediante un programa informático de análisis de imagen.
- Comparamos los datos obtenidos con datos sobre el microambiente angiogénico, estudiados a partir de tinciones inmunohistoquímicas frente a HIF1-α, HIF2-α y VEGF con análisis semi-cuantitativo subjetivo llevado a cabo por 3 investigadores.
- Comparamos ambos tipos de datos con las variables clínico-biológicas que determinan el pronóstico y la evolución de los pacientes.

RESULTADOS

ARQUITECTURA VASCULAR Y MICROAMBIENTE ANGIOGÉNICO

CD34: Morfología

IRREGULAR ↔ REGULAR

VEGF

HIF1-α

HIF2-α

Según estos resultados:

- Perímetro-ratio, Aspecto y Redondez más lejanos al 1-indicativos de irregularidad → marcaje intenso de HIF1-α y de VEGF; patrón homogéneo de HIF1-α.

RELACIÓN DE LOS PARÁMETROS DEL MICROAMBIENTE ANGIOGÉNICO ENTRE SÍ

- HIF1-α y VEGF → Correlación en rango (p<0.021).
- VEGF y HIF2-α → Tendencia a la correlación en rango y patrón (p=0.074). Podría ser significativa al aumentar el número de datos.

ARQUITECTURA VASCULAR Y PARÁMETROS CLÍNICO-BIOLÓGICOS PRONÓSTICOS

VARIABLES DICOTÓMICAS

Tabla: valores resultantes de los contrastes no paramétricos.

Según estos resultados:

- < 18 meses → vasos cortos, regulares y redondos.
- Tumores diferenciados → vasos irregulares y alargados.
- Alteraciones numéricas → vasos cortos, regulares, redondos y diámetro, anchura y área media pequeñas.

VARIABLES NO DICOTÓMICAS:

- Grado de diferenciación en 3 grupos:

Según estos resultados:

- Tumores diferenciados:
 - Mayor % de área teñida y vasos más elipsoides que los NB indiferenciados.
 - Vasos más estrechos, más irregulares y más elipsoides que los NB pobremente diferenciados.
- Riesgo muy bajo → vasos más largos e irregulares que riesgo bajo.

MATERIAL Y MÉTODOS

Material disponible

- MICROMATRIZ DE TEJIDO: Años 1998/99
- DATOS CLÍNICO-BIOLÓGICOS:
 - Edad
 - Estadio
 - Grado de diferenciación
 - Alteraciones genéticas
 - Supervivencia global (OS)
 - Supervivencia libre de eventos (EFS)
 - Clasificación de riesgo del INRG

Inmunohistoquímica

CD34 (BD Biotécnicas 1:50) HIF1-α (Novus 1:100) HIF2-α (Novus 1:400) VEGF (Santa Cruz 1:100)

Elección de los casos

8 Tumores diferenciados (NB)

8 Tumores pobremente diferenciados (NBpd)

ANÁLISIS SEMI-CUANTITATIVO objetivo

***SEGMENTACIÓN*:** CD 34

Rango: 0-138 (Rojo), 0-196 (Verde), 0-148 (Azul)

SOFTWARE de análisis de imagen: Image ProPlus v. 5

MEDIDAS:

- Área
- Área del core
- Longitud
- Diámetro
- FORMA, IRREGULARIDAD (Cuanto más cercanos a 1, más regular es la forma.)
- TAMAÑO

ANÁLISIS SEMI-CUANTITATIVO subjetivo

RANGO: 0-25%, 26-75%, >75%

LIGERA + MODERADA ++ INTENSA +++

INTENSIDAD

HOMOGÉNEO (Focal y/o difuso) HETEROGÉNEO

REDONDEZ

ASPECTO

PERÍMETRO-RATIO (p-ratio)

PATRÓN

CONCLUSIONES

Arquitectura vascular y microambiente angiogénico:

- Los tumores que muestran vasos sanguíneos de morfología vascular irregular muestran expresión de HIF1-α y de VEGF intenso, asociado a hipoxia.
- El patrón de expresión de HIF1-α y de VEGF están correlacionados.
- Existe una tendencia a la correlación en rango y patrón entre VEGF y HIF2-α que podría ser significativa si aumenta el número de casos.

Arquitectura vascular y factores clínico-biológicos pronósticos:

- Los tumores de niños menores de 18 meses y con alteraciones cromosómicas numéricas presentan vasos más redondos y regulares que los de pacientes mayores de 18 meses y con alteraciones cromosómicas segmentarias.
- Los tumores con mayor grado de diferenciación neuroblastica presentan más área vascularizada, siendo sus vasos más anchos e irregulares que los que se observan en los tumores indiferenciados o pobremente diferenciados.

Este estudio muestra la necesidad de seguir investigando la vascularización y otros componentes de la matriz extracelular del neuroblastoma.

XXIX CONGRESO CENTROAMERICANO DE PATOLOGÍA DE YUCAJUTÓN, YUCATÁN, MÉXICO

Congress 4: Tissue Engineering and Regenerative Medicine International Society (TERMIS-EU). 7 a 10 de Junio 2011, Granada. Characterization of the reticulin fibres bundles in neuroblastoma by means of integrated quantitative image analysis. Tadeo Cervera I., Piqueras Franco M., Berbegall Beltrán A., Villamón Ribate E., García Rojo M., Navarro Fos, Noguera Salvá R.

Facultat de Medicina i Odontologia

20.P7

CHARACTERIZATION OF THE RETICULIN FIBERS BUNDLES IN NEUROBLASTOMA BY MEANS OF INTEGRATED QUANTITATIVE IMAGE ANALYSIS

Tadeo I¹, Piqueras M¹, Berbegall A¹, Villamón E¹, Rojo M², Navarro S¹, Noguera S¹.

¹Molecular Pathology laboratory, Department of Pathology, Medical School, University of Valencia, Valencia, Spain.
²Department of Pathology, Hospital General de Ciudad Real, Ciudad Real, Spain

INTRODUCTION

NEUROBLASTOMA The most frequent solid extracranial malignancy in childhood

Age Genetic profile

NEUROBLASTOMA PROGNOSIS

- Neuroblastoma (NB)
- Ganglioneuroblastoma (intermed, nodular)
- Ganglioneuroma (GANG)

Stage Histological category

Degree of differentiation (NB)

- NB: Undifferentiated, poorly differentiated, differentiating
- GANG: Mature / maturing

RETICULIN FIBERS Prognostic factor in several bone marrow diseases → poor prognosis when increased.

OBJECTIVES

General:

Characterize the **RETICULIN fibers bundles (RFB)** in Neuroblastoma with **automated IMAGE ANALYSIS**.

Specific:

- Compare the measurements obtained after applying the two algorithms to measure the RFB for the respective intake method.
- Compare the results of the quantitative image analysis with the clinical-biological data with prognostic value.

MATERIAL AND METHODS

***Tissue microarray**

Years 1998-1999

***Gomori stain**

CASE SELECTION n=24

- 8 differentiated tumors:
 - Differentiating NB
 - Intermed gangliob
 - Maturing ganglioneuroma
- 8 undifferentiated NB.
- 8 poorly differentiated NB.

***Clinical-biological data**

- Age
- Stage
- Histopathology
- Genetic profile
- SIOP risk stratification
- Overall survival(OS)
- Event-free survival(EFS)

RESULTS

1. K values of the Kappa correlation test between the data related to number, size and shape obtained after applying the algorithms for automated and manual image intake.

AUTOMATED / MANUAL	Number of RFB	% stained area	Average area	Length	Width	Roundness	Aspect	Perimeter ratio
Number of RFB	0,796							
% stained area		0,825						
Average area (µm²)			0,875					
Length (µm)				0,938				
Width (µm)					0,750			
Roundness						0,571		
Aspect							0,625	
Perimeter ratio								0,438

K VALUE CONCORDANCE STRENGTH

<-0,20 Poor

0,21-0,40 Weak

0,41-0,60 Mild

0,61-0,80 Good

0,81-1,00 Very good

2) Image Intake

MANUAL Photomicroscope Leica DMD 108

AUTOMATED Scanner ScanScope XT, Aperio

Jointed with Adobe Photoshop

Extracted with ImageScope, Aperio

20x

40x

3) Algorithm design

SEGMENTATION: Image-Pro Plus 5.1

Red: 0-117

Green: 0-175

Blue: 65-209

Red: 0-119

Green: 0-115

Blue: 0-126

CONCLUSIONS

1. A large amount of samples stained for reticulin fibers need to be screened in NB. This requires fast and reliable:
 - Image Acquisition Systems.
 - Algorithms for automated image analysis.
2. The scanning of the whole TMA with the ScanScope XT, Aperio, is the fastest system available and provides the best image quality.
3. Quantitative image analysis with specifically designed algorithms with ImagePro Plus 5.1 is a solid and reliable technique.

4) Image data

Data related to **NUMBER**, **SIZE** and **SHAPE** of the stained areas:

- Number of RFB
- % of stained area
- Average area
- Length
- Width
- Aspect
- Perimeter-ratio
- Roundness

The data are grouped in 3 groups with 1/3 of the data in each one, following the values shown in the table. Roundness has been grouped in 2 groups.

NUMBER	MANUAL IMAGE INTAKE			AUTOMATED IMAGE INTAKE		
	Score	Min	High	Score	Min	High
Number of RFB	95-690	708-1283	1340-2238	143-685	738-1254	1277-2578
% stained area	0,155-0,37	0,651-0,99	1,305-2,27	0,262-0,48	1,194-1,68	1,698-3,68
SIZE	Small	Intermediate	Big	Small	Intermediate	Big
Average area (µm²)	51,0-24,3	28,7-46,4	56,3-134,1	15,8-23,6	26,6-40,6	42,93-115,0
Length (µm)	9,3-24,8	13,5-19,8	22,5-24,1	19,0-22,9	33,0-55,2	55,4-76,4
Width (µm)	2,6-4,4	4,2-6,0	6,1-8,5	2,8-4,3	4,8-5,5	5,2-8,5
SHAPE (roundness)	Low	Intermediate	High	Low	Intermediate	High
Aspect	1,49-1,27	3,79-3,97	3,89-5,21	3,60-3,24	3,79-4,09	4,30-5,88
Perimeter ratio	0,177-0,421	0,423-0,492	0,502-0,729	0,162-0,393	0,318-0,418	0,421-0,761
Roundness	Transversal	Longitudinal	Transversal	Longitudinal	Transversal	Longitudinal
	<5	5-15,8	<5	5-15,2		

SATELLITE MEETING

XVI CONGRESO DE LA SOCIEDAD ESPAÑOLA DE HISTOLOGÍA E INGENIERÍA TISULAR

Congress 5: 11th European Congress on Telepathology and 5th International Congress on Virtual Microscopy. 6 a 9 de Junio 2012, Venecia. *A morphometric tool applied to angiogenesis research based on vessel segmentation.* M Milagro Fernández, Irene Tadeo, Rosa Noguera, Samuel Navarro, Marcial García-Rojo, Oscar Déniz, Jesús Salido, Gloria Bueno. Publicado en *Diagnostic Pathology: A morphometric tool applied to angiogenesis research based on vessel segmentation.*



11th European Congress on Telepathology and 5th International Congress on Virtual Microscopy

C5 IMAGE ANALYSIS 2

A morphometric tool applied to angiogenesis research based on vessel segmentation

M Milagro Fernández, Irene Tadeo, Rosa Noguera, Samuel Navarro, Marcial García-Rojo, Oscar Déniz, Jesús Salido, Gloria Bueno

Spain

Background

Given that angiogenesis and lymphangiogenesis are strongly related to prognosis in neoplastic and other pathologies, and that some existing methods for their study provide different results, we aim to construct a morphometric tool to allow complete and accurate quantification and measurement of different aspects of the shape and size of vascular vessels.

Findings

The developed tool herein presented is based on vessel closing which is an essential property to properly count the number and characterize the size and the shape of blood and lymphatic vessels.

Conclusions

The method is fast and accurate improving existing tools for angiogenesis and lymphangiogenesis analysis. The tool also improves the accuracy of vascular density measurements, since unconnected endothelial parts are joined and considered as a single object forming a vessel.

Congress 6: Advances in Neuroblastoma Research (ANR). 18 a 21 de Junio 2012, Toronto. *Can a given presence of acid mucopolysaccharides explain the different prognosis for neuroblastoma patients younger and older than 18 months?* Tadeo I, Piqueras M, Berbegall A, Villamón E, Navarro S, Montaner D, Cañete A, Rojo M, Noguera R.

UNIVERSITAT VALÈNCIA  Facultat de Medicina i Odontologia

POT 111

Can a given presence of acid mucopolysaccharides explain the different prognosis for neuroblastoma patients younger and older than 18 months?

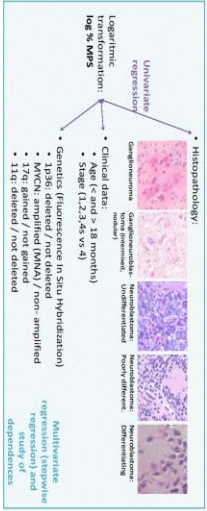
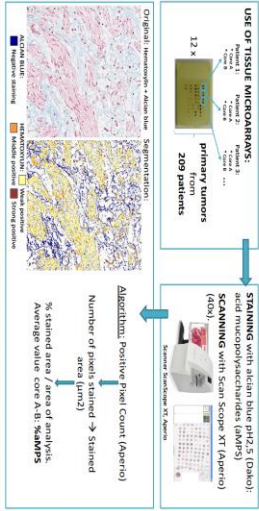


Tadeo I¹, Piqueras M², Berbegall A², Villamón E², Navarro S², Montaner D³, Cañete A⁴, Rojo M⁵, Noguera R⁶
 1 Fundacion Investigación Reserach Clínica de Valencia - IICIV (part of radiology, Medical School, Universidad de Valencia - IISUM) and Geriatrics research group, Centro de Investigación Superior de Geriátrica (CISG) 2 Instituto Oncológico Superior de Valencia (IOSV) 3 Instituto de Diagnóstico y Referencia Epidemiológica (IDRE) 4 Instituto de Diagnóstico y Referencia Epidemiológica (IDRE) 5 Instituto de Diagnóstico y Referencia Epidemiológica (IDRE) 6 Instituto de Diagnóstico y Referencia Epidemiológica (IDRE)

BACKGROUND

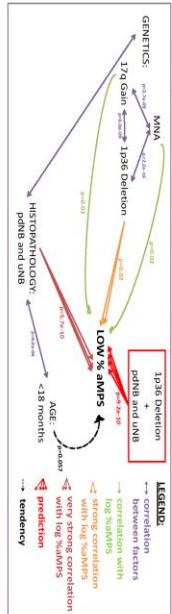
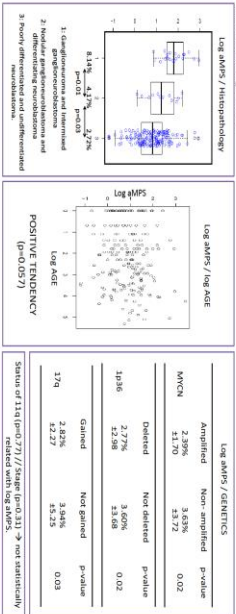
- The quantity of acid mucopolysaccharides (AMPS) has been contradictorily related to prognosis in different malignancies.
- MPS carry certain biofiling, scaffolding and cell anchoring properties and their quantity decreases with aging in normal tissue.
- AIM: to determine if AMPS percentage can help to explain the different evolution observed depending on patient age in neuroblastoma (NB).

MATERIALS AND METHODS



- ### CONCLUSIONS
- In our cohort, the absence/scarcity presence of AMPS is related to clinical biological features.
 - Specifically, it is strongly related to a regional chromosome alterations tumor profile and to unfavorable histopathology.
 - A larger and specific study would explain the different prognosis between both age groups, which would arise due to a change in the percentage and/or to the different filtering properties and the structural and/or cell anchoring characteristics.

RESULTS



Congress 7: XXX Congreso Centroamericano de Patología. 24-27 de octubre de 2012, La Romana, República Dominicana. Diseño del modelo de patrones de organización de las fibras de reticulina en los tumores neuroblásticos. Tadeo I., Fuster E., Piqueras M., Villamón E., Berbegall A.P., Navarro S., Noguera R.

Facultat de Medicina i Odontologia

DISEÑO DEL MODELO DE PATRONES DE ORGANIZACIÓN DE LAS FIBRAS DE RETICULINA EN LOS TUMORES NEUROBLÁSTICOS.

Tadeo I.¹, Fuster E.², Piqueras M.², Villamón E.², Berbegall A.P.³, Navarro S.², Noguera R.²

¹ Fundación para la Investigación del Hospital Clínico de Valencia (FICLUV-INCLIVA).

² Departamento de Patología, Facultad de Medicina, Universidad de Valencia

³ Grupo de Informática Biomédica (IBIME-ITACA) de la Universitat Politècnica de Valencia

* Misma contribución



Table with 2 columns: INTRODUCCIÓN and OBJETIVOS. The introduction describes the study's goal to study reticulin fiber organization in neuroblastomas. The objectives list 5 steps: 1. Experiment with classification, 2. Define patterns, 3. Compare clusters, 4. Statistical analysis of 11 variables, 5. Statistical analysis of 3 clusters.

MATERIALES Y MÉTODOS

Methodology diagram showing the process from tissue staining (Gomori) and segmentation (ImagePro-Plus) to the creation of 1135 cylinders and 120 patterns. It includes a list of parameters like Area, Aspecto, and Perímetro ratio, and a dendrogram showing hierarchical clustering of the cylinders.

RESULTADOS

Results section showing three clusters of patterns (ORGANOIDE, LOBULAR, RETICULAR) with corresponding histological images and a table of relative parameters. The table lists parameters like 'Los MIPs y MIPs' and 'Los MIPs con los que las fibras...' for each cluster.

CONCLUSIONES

- La pertenencia a un cluster implica la determinación de patrones de organización objetivos de fibras de reticulina.
• La histopatología se relaciona significativamente con los parámetros objetivos del análisis de imagen y con los patrones objetivos.
• Es necesario comprobar la implicación de la presencia de un determinado patrón en la evolución clínica.
• La influencia en la evolución clínica conllevará el diseño de un software de uso general para determinar tanto las variables implicadas en el pronóstico como los patrones.

UNIVERSITAT DE VALÈNCIA



Congress 8: XVII Congreso de la Sociedad Española de Histología e Ingeniería tisular (SEHIT). 12-14 de septiembre de 2013, Logroño. *Automatic classification of reticulin fibers patterns based on a dictionary learning strategy.* José Enrique Romero*, Irene Tadeo*, Elies Fuster, Ana P. Berbegall, Samuel Navarro, Montserrat Robles, José Vicente Manjón, Rosa Noguera. Publicación en *Histology and Histopathology*, Vol 28 (1): 118. 2013.

F7



AUTOMATIC CLASSIFICATION OF RETICULIN FIBERS PATTERNS BASED ON A DICTIONARY LEARNING STRATEGY

José Enrique Romero^{1*}, Irene Tadeo^{2*}, Elies Fuster¹, Ana P. Berbegall³, Samuel Navarro³, Montserrat Robles¹, José Vicente Manjón¹, Rosa Noguera³.

¹ Instituto de Aplicaciones de las Tecnologías de la Información y de las Comunicaciones Avanzadas (ITACA), Universitat Politècnica de València, Valencia, Spain.
² Fundación para la Investigación del Hospital Clínico de Valencia (INCLIVA) Dpto. Patología, Fac. de Medicina y Odontología, Universidad de Valencia, Valencia, Spain.
³ Dpto. Patología, Fac. de Medicina y Odontología, Universidad de Valencia, Valencia, Spain.
 * Both authors contributed equally.



FACULTAT DE Medicina i Odontologia

Background	Hypothesis
<ul style="list-style-type: none"> The analysis and classification of reticulin-fiber patterns is a useful tool in some neoplasms. We have noticed that reticulin fibers in digitized microscopy images of neuroblastic tumors are arranged in some repeating distributions similar to those found in different digitized histologic tissues/organs. 	<ul style="list-style-type: none"> The pattern analysis of the reticulin fibers may provide valuable information to enhance neuroblastoma patients prognosis.
Objectives	
<ul style="list-style-type: none"> To create a computer tool to automatically characterize and classify reticulin fiber-stained images into the different groups identified. 	

Materials and methods

Dataset

- 80 tumor/ 10 non-tumor control images
- Coming from digitized TMAs
- Stained with Gomori
- Previously classified subjectively by two researchers in two types of patterns (classes):

(A) LOBULAR / TRABECULAR

(B) ORGANOID / RETICULAR

Neuroblastic examples

Normal examples

- Fibers around huge sets (lobules) of cells and mostly scarce within them.
- Around the tumor cell areas they form strong trabeculae.
- Similar to our TMA non-tumor control muscular tissue.
- Fibers around small sets of cells and present within them.
- forming thin lines around the tumor cell areas looking like a complex network.
- Similar to our TMA non-tumor control kidney (organoid) and liver (reticular) tissue.

Dictionary learning

- In order to extract the information relative to each pattern we use a novel strategy.
- Step 1:** First we train a global dictionary from the whole dataset.
- Step 2:** Then we train a local dictionary for every single image. Both are trained using the KSVD algorithm.
- Step 3:** Finally we obtain a signature for each image comparing both dictionaries, associated to its subjective pattern. This signatures are reduced using the Relief algorithm to increase its discriminative power.
- Step 4:** We obtain a reduced signature set with each signature associated to a reticulin fiber class.

Classification method

- Similar to the training process.
- We perform steps 1-4 to obtain the image signature.
- Step 5:** This signature is compared with the signatures from the "reduced signature set" calculating the euclidean distance giving rise to set of distances associated to a potential class.
- Step 6:** We choose the 3 most similar reduced signatures (smaller euclidean distances) with their corresponding class.
- Step 7:** The major class is assigned to the input image, using the K nearest neighbor algorithm.

Performance test

The performance of the model was tested by a leave-one-out cross validation strategy.

Results	Conclusions and Future work
<p>The method showed an accuracy of 64.56% and a balanced accuracy rate of 55% comparing the assigned class to the subjectively described.</p>	<ul style="list-style-type: none"> This work shows promising results about the usefulness of automated classification of image-based reticulin fiber patterns, which may be useful in detecting and delineating tumor and stromal cell interactions. We are now going to develop complex classifiers to be able to classify the images depending on clinico-biological and prognosis neuroblastic features.

Congress 9: Advances in Neuroblastoma Research (ANR). 13 a 16 de Mayo 2014, Cologne. *Prognostic significance of non-cellular extracellular matrix elements in neuroblastic tumors.* Tadeo I., Berbegall A.P., Piqueras M., Zúñiga V., Santonja F. J., Navarro S., Castel V., Noguera R.

POT 099 **PROGNOSTIC SIGNIFICANCE OF NON-CELLULAR EXTRACELLULAR MATRIX ELEMENTS IN NEUROBLASTIC TUMORS**

Facultat de Medicina i Odontologia
UNIVERSITAT DE VALÈNCIA



Tadeo I.¹, Berbegall A.P.¹, Piqueras M.², Zúñiga V.¹, Santonja F. J.³, Navarro S.⁴, Castel V.³, Noguera R.¹

¹Department of Pathology, Medical School, University of Valencia;
²Medical Research Foundation INCLIVA, Valencia, Spain
³Dpt. of Statistics and Operational Research, University of Valencia, Spain
⁴Pediatric Oncology Unit, University and Polytechnic Hospital La Fe, Valencia, Spain



HYPOTHESIS	AIMS
The influence of non-cellular extracellular matrix (ECM) elements in neuroblastoma (NB) homeostasis, dynamics and growth can enhance patient stratification, provide novel therapeutic targets or may be useful to provide new cancer pathological models for biomedical engineering.	<ul style="list-style-type: none"> To study ECM elements in NB through the objective morphometric analysis of histochemistry stained histologic sections: reticulin fibers (Ret F), collagen type I fibers (Col I F) and glycosaminoglycans (GAGs) To relate the generated data with current stratification factors (stage, age, histopathology, MYCN status, 11q status, genomic profile) and prognosis (EFS, OS)

MATERIALS AND METHODS
<p>TMA construction: Staining: 19 TMAs, 499 patients, 544 samples, 458 primary NB. Staining: Ret F (Gomori), Col I F (Masson's trichrome), GAGs (Alcian blue, pH2.5).</p> <p>Digitation: Aperio ScanScope XT (Aperio technologies).</p> <p>Image analysis: Image Pro-plus (Media Cybernetics), Image Pro-plus (Media Cybernetics), Aperio ImageScope (Aperio technologies).</p> <p>Extraction of data*: <ul style="list-style-type: none"> Size (only Ret F): area, length, width Shape (only Ret F): aspect, roundness, perimeter ratio, fractal dimension, branching, angle Amount: % of stained area (all markers), number of elements (Ret F) </p> <p>Statistics: INRG prognostic factors, Survival. Cox regression.</p>

Relationship with the INRG prognostic factors												
Parameter		Ret F		Col I F	GAGs							
INRG variable	N° elements	% stained area	Average length	Width	Aspect	Roundness	Perimeter ratio	Fractal dimension	branching	Angle	% stained area	% stained area
Age	-	0.044	-	-	-	-	-	0.047	0.048	-	-	0.041
Histopathology	0.003	0.011	0.000	0.001	0.000	0.000	0.017	0.000	0.000	0.011	0.000	0.000
Genetic profile	0.002	-	-	-	-	-	-	-	0.001	-	0.005	0.000
11q	-	0.010	-	0.008	0.040	-	0.013	-	-	-	0.014	-
Phenyl	-	0.020	0.005	0.016	0.001	0.018	0.002	0.003	0.001	0.000	-	-

Relationship with survival										
Variable	5-year		10-year		p-value	5-year		10-year		
	HR (95% CI)	p-value	HR (95% CI)	p-value		HR (95% CI)	p-value	HR (95% CI)	p-value	
Stage III	17.3 (5.6-125.2)	0.002	17.9 (5.6-110.1)	0.001	0.000	MNA	13.8 (5.124-33)	0.000	14.2 (5.124-33)	0.000
Stage L2	10.2 (2.8-48.1)	0.002	11.4 (2.8-48.2)	0.002	0.000	SCA	8.1 (3.120-20)	0.002	8.4 (3.120-20)	0.002
SCA	8.1 (3.08-21.9)	0.004	7.0 (3.0-16.0)	0.001	0.000	Ret F	2.12 (1.1-3.7)	0.020	3.31 (1.1-10)	0.001
MNA	2.12 (1.1-3.7)	0.020	3.31 (1.1-10)	0.001	0.000	Col I F	1.29 (0.93-1.89)	0.001	1.42 (1.11-1.82)	0.001
Ret F branching	4.26 (3.01-5.99)	0.000*	4.02 (2.11-7.45)	0.000	0.000	Ret F angle	4.26 (3.01-5.99)	0.000*	4.47 (1.64-12.38)	0.004
Stage M1	3.92 (1.6-9.1)	0.001	4.24 (1.0-45.0)	0.000	0.000	Stage L1	4.01 (1.6-10.7)	0.004	4.18 (1.6-10.8)	0.001

HR: Hazard ratio, CI: Confidence Interval, *cor. statistically significant, †inverse correlation.

High risk of relapse: stage M, stage L2, SCA and MNA, Ret F low angle and high branching (ECM with low porosity).

Poor prognosis: MNA, stage M, nGNB/NB pdu, thick Ret F networks.

Col I F									
Variable	5-year	10-year	Poor prognosis: Scarce Col I F bundles (stiff ECM). This effect is lost in combination with the INRG variables.						
	HR (95% CI)	p-value	HR (95% CI)	p-value					
% stained area	4.7 (0.7-0.9)	0.030*	4.5 (0.7-0.9)	0.034*					

In the presented study, the quantity of GAGs in neuroblastic tumors ECM does not seem to affect survival.

CONCLUSIONS									
<p>Ret F</p> <p>A. <18, GN+IGNB, MNNA, NCA: accumulation of Col I F bundles.</p> <p>B. >18, pd,uNB, MNA, SCA: scarce Col I F bundles.</p>					<ul style="list-style-type: none"> Tumors from patients with clinical features associated with favorable outcome and/or presenting benign biological features have an ECM with little area occupied by small networks of Ret F presenting little crosslinking and branching and homogeneously aligned, together with Col I F trabeculae and an accumulation of GAGs. A low angle and high branching degree of Ret F, together with the presence of thick Ret F networks and scarce Col I F are related to poor prognosis, indicating the potentiality of these ECM features as independent prognostic factors in the INRG stratification. A European collaboration is needed to further investigate the potential value of NB ECM as prognostic factors. 				
<p>GAGs</p> <p>A. Stage L1 and L2, GN+IGNB, (MNNA): accumulation of GAGs.</p> <p>B. Stage M, pduNB, (MNA): scarce GAGs.</p>									

Congress 10: SIOPEN Translational Biology meeting. 16-17 Junio 2014, Institut Curie, Paris. *Study of extracellular matrix elements in high risk neuroblastoma patients.* Irene Tadeo, Luis M^a Escudero, Daniel Sánchez, Rosa Noguera.

Study of extracellular matrix elements in high risk neuroblastoma patients

Irene Tadeo¹, Luis M^a Escudero², Daniel Sánchez, Rosa Noguera¹

¹Department of Pathology, Medical School, University of Valencia, INCLIVA, Valencia, Spain.

²Institute of Biomedicine, Hospital Virgen del Rocío-CSIC- of the University of Seville (Department of Cellular Biology), Seville, Spain.

Background: New predictors for a more specific pre-treatment stratification are required to improve the clinical management of ultra-high risk patients.

Objective: We aim to focus on the value of glycosaminoglycans (GAGs), reticulin fibers (RetF) and collagen type I fibers (Col-1F) extracellular elements (ECM) morphometric measurements as potential risk markers or therapeutic targets within the high risk tumors.

Materials and methods: 19 tissue microarrays were constructed including at least two cylinders per sample of 458 primary tumors including tumors from 110 high risk patients, to properly represent tissue histology. Serial sections of the TMAs were cut and stained with alcian blue pH2.5 for glycosaminoglycans, Gomori for reticulin fibers and Masson's trichrome for collagen type I. Image analysis algorithms were set up or designed with Aperio ImageScope (Aperio technologies) for GAGs and Image Pro-plus (Media cybernetics) for RetF and Col-1F to specifically detect the ECM elements studied and extract morphometric measurements. For GAGs and Col-1F, the percentage area covered by the ECM element was calculated. For RetF, amount (number of fibers and percentage of stained area), size (area, length and width), shape (aspect, roundness or crosslinking, fractal dimension, perimeter ratio and branching) and orientation (angle) variables were calculated for each tumor sample. All morphometric variables were dichotomized using the median values or quartiles and survival analysis were performed in the high risk cohort with the log-rank test and Kaplan-Meier curves. Moreover, we carried out a preliminary study of the topology, relating blood vessels, RetF and neuroblastic cells by means of graph theory and performing Voronoi tessellations.

Results: The median 5-year event-free survival (EFS) was 35.4±5.3 and the median 5-year overall survival (OS) was 28.1±4.8. The amount of GAGs did not influence survival in the high risk cohort. Regarding RetF, we found that a high percentage of stained area, together with large, highly crosslinking and branching networks organized in a messy manner (high fractal dimension) defined a subgroup with very poor prognosis within the high risk cohort with 5-year EFS and/or OS mostly <15% (ranging from 11.3±6.3% to 21.8±6.6%). A high percentage of Col-1F stained area also defined a subgroup with 16.6±7.3% of 5-year EFS. Two different topological organizations were distinguished between high risk and non-high risk and between MNA and MNNA samples. Some high risk samples were mixed with non-high risk samples and correlated with MNNA samples. MNA therefore carries topological changes within the high risk group samples, with respect to the relative organization of neuroblastic cells, blood vessels and RetF.

Conclusions: The quantitative and topological analysis of RetF and Col-1F enables the discrimination of a very poor prognostic group within the HR patients. We advocate their use as new biomarkers and their potential use as therapeutic targets.

Future work: We will analyze larger high risk cohorts and ultra-high risk patients (when defined) to validate our findings and improve the stratification. This would potentially provide new targets for the development of more accurate therapies related to ECM elements in the ultra-high risk subgroup.

Grants: This study was supported by grants from FIS (PI10/15) and RTICC (RD06/0020/102; RD12/0036/0020).

1. *Extracellular matrix, biotensegrity and tumor microenvironment.* Rosa Noguera, Olga Alicia Nieto, Irene Tadeo, Fernando Fariñas, Tomás Álvaro. *Histology and Histopathology.* 2012 Jun; 27(6):693-705.
2. *Quantitative modeling of clinical, cellular and extracellular matrix variables suggest prognostic indicators in cancer. A model in neuroblastoma.* Tadeo I*, Piqueras M*, Montaner D, Villamón E, Berbegall AP, Cañete A, Navarro S, Noguera R. *Pediatr Res.* 2014 Feb;75(2):302-14
3. *TMA Vessel Segmentation Based on Color and Morphological Features: Application to Angiogenesis Research.* M. Milagro Fernández-Carrobles, Irene Tadeo, Gloria Bueno, Rosa Noguera, Oscar Déniz, Jesús Salido, and Marcial García-Rojo. Hindawi Publishing Corporation. *The ScientificWorld Journal.* 2013 Dec 5;2013:263190.
4. *Biotensegrity of the extracellular matrix: physiology, dynamic mechanical balance and implications in oncology and mechanotherapy.* Tadeo I, Berbegall AP, Escudero LM, Álvaro T, Noguera R. *Frontiers in Oncology.* 2014 Mar 4;4:39
5. *Glycosaminoglycans profiling in different cell types using infrared spectroscopy and imaging.* Brezillon S, Untereiner V, Lovergne L, Tadeo I, Noguera R, Maquart FX, Wegrowski Y, Sockalingum G. *Analytical and bioanalytical chemistry.* 2014 Sep;406(24):5795-803

Review

Extracellular matrix, biotensegrity and tumor microenvironment. An update and overview

Rosa Noguera¹, Olga Alicia Nieto², Irene Tadeo¹, Fernando Fariñas³ and Tomás Álvaro⁴

¹Pathology Department, Medical School, University of Valencia, Valencia, Spain, ²University of Quindío, Quindío, Colombia,

³Pathology and Infectious Diseases Institute, Málaga, Spain and ⁴Pathology Service, Verge de la Cinta Hospital, Tortosa, Tarragona, Spain

Summary. The extracellular matrix (ECM) constitutes a three-dimensional network that surrounds all cells, organs and tissues in the body. It forms a biophysical filter for protection, nutrition and cell innervation, as well as the medium for facilitating immune response, angiogenesis, fibrosis and tissue regeneration. It is the mechanism by which mechanical forces are transmitted to the basement membrane which, through the integrins, supports the tensegrity system and activates the epigenetic mechanisms of the cell. A review and update on current knowledge on this topic reveals how disturbance of the ECM leads to a loss of efficient filtering, nutrition, elimination, and cell denervation functions, in addition to loss of regeneration capacity and disorders in mechanotransduction. Furthermore, such disturbance results in a loss of substrate, and with it the ability to provide a proper immune response against tumor, toxic and infectious agents. Reciprocal communication between ECM stromal and parenchymatous cells directs gene expression. The oncogenic capacity of the stroma derives from the associated cells as well as from the tumor cells, the angiogenic microenvironment and from an alteration in *tensegrity*; all of which are dependent on the ECM. It has been shown that the malignant phenotype is reversible by correction of the altered cues of the ECM.

Key words: Extracellular matrix, Pischinger basic system, *Tensegrity*, Desmoplasia, Cancer

Introduction

Body tissues communicate within themselves at a higher speed to that provided by the nervous system. At histological level, these support and communication functions reside in the extracellular matrix (ECM), which is also responsible for the supply of oxygen and nutrients, as well as the elimination of CO₂, toxins and other waste materials. The toxins accumulated in the ECM are drained through the lymphatic system. When such drainage is insufficient, a response is produced, resulting in inflammation, acidosis and pain. The ECM is innervated through the vegetative nerve fibers; the correct function of which determines the predisposition of the matrix to respond with an inflammatory process to any nonphysiologic stimulus. Moreover, the ECM acts as a reservoir for numerous molecules, including growth factors, cytokines and proteases (Alvaro et al., 2009b, 2010).

The ECM accounts for 20% of our whole body weight and as such is the largest organ in our system. It is composed fundamentally of collagen, and constitutes the main structural support element in multicellular animals, performing a central role in tissue organization and orientation, as well as in cell adhesion, migration, differentiation, proliferation and apoptosis (Huxley-Jones et al., 2007, 2009). The ECM consists of a complex mixture of proteins, proteoglycans (PGs) and glycoproteins (GPs) that confer the structural properties of cells and tissues. Each cell presents its own receptor profile, creating a communication interface with the surrounding microenvironment. The ECM acts through these receptors to influence cell growth, death, adhesion, invasion, gene expression and differentiation processes. All these cellular events are present in the physiologic processes of embryonic development, tissue morphogenesis or angiogenesis. When the correct

information is lost, these events result in pathologic, autoimmune, inflammatory, degenerative and neoplastic processes as well.

Since Virchow first propounded the model of cellular pathology, it has been considered that the minimum unit of life in the organism is the cell. Nevertheless, a single cell cannot survive alone in isolation from its environment. In recent years, Alfred Pischinger has suggested the names ‘the third system’, ‘the basic system’, or ‘the basal regulation system’ to denote the entire structure surrounding the cell, defining it as a homeostatic system, and proposing the capillary-ECM-cell triad as the minimum unit of life in vertebrates (Fig. 1) (Pischinger, 2006). Several scientists have laid the foundations for knowledge of the ECM and have each contributed with essential features to the concept of the third system (Noble, 2008; Saks et al., 2009). Modern investigation does not understand the ECM as an inert material or a passive support tissue, but as a dynamic living component, possessing multiple functions, “a living matrix” (Oschman, 2009).

Study techniques and ECM histology

The techniques used for the morphologic study of

the ECM, such as immunohistochemistry, immunofluorescence or electronic microscopy, require the fixation, processing and cutting of tissue, thus limiting the study of these structures and making dynamic observation *in vivo* impossible. The fine structure of the ECM is poorly preserved by histologic fixatives, usually appearing as a granular material between the cells and fibers. When using frozen tissue, the ECM is stained metachromatically with Periodic Acid Schiff’s reaction (PAS).

Other techniques, such as *in vivo* confocal microscopy or multi-photon microscopy (MPM), facilitate the dynamic study of the ECM. MPM is able to utilize the properties of the collagen fibers of the matrix to generate a harmonic signal known as second harmonic generation or frequency doubling, allowing these fibers to be observed without the need to process the tissue (Friedl et al., 2007; Schenke-Layland et al., 2008). The elastic fibers of the ECM can also be studied with this method (Konig et al., 2005).

The ECM is the structural framework within which the support cells, the free nerve endings, the capillaries and the cells of the immune response system reside. It is constituted by fibers and by the ground substance, a viscous gel made of highly hydrated macromolecules

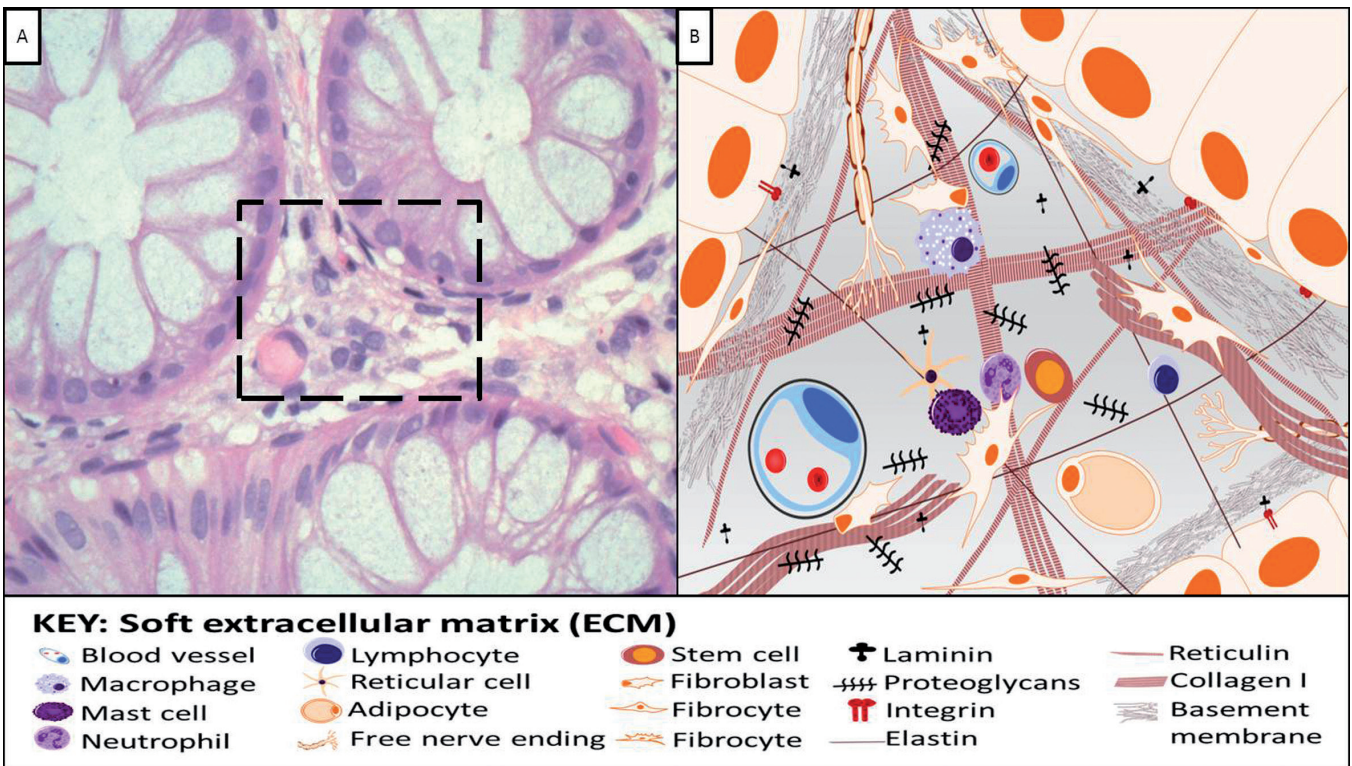


Fig. 1. A. Intestinal mucosae: Lieberkühn’s glands and lamina propria. Hematoxylin and eosin stain. x 100. **B.** Schematic representation of the selected area in A. The capillary-ECM-cell triad is the minimum unit of life. It provides the structural support of *tensegrity*, a matrix through which the stimulus of innervation is transmitted and a capillary network to provide nutrition and to discard waste materials from the parenchymatous cells. It is also the framework for monitoring and action by immune system, as well as an energy flow network for high-speed local and distant communication.

Tissular hyperstructure

(Geneser, 2000; Stevens and Lowe, 2006). The fibers confer tensile resistance and elasticity, and form a scaffold upon which the cells are arranged. The fine structure of PGs and GPs lies between a thick structure of collagen and elastin fibers, covered by interstitial or tissular fluid (Fig. 2).

The collagen system consists of different types of collagen fibers, each having their own structural and support function; reticular fibers, which are bundles of collagen fibrils smaller than 50 nm; collagens associated to fibrils, which bind the reticular fibers both together and to other ECM components; and anchorage collagens, which bind the type I collagen fibers to the basement membranes and laminas, among others.

Within the elastic system, thinner fibers branch out and bind together, forming a very irregular network.

PG monomers are formed by sulfated glycosaminoglycans (GAGs), previously known as mucopolysaccharides, linked to central proteins by covalent bonds. In form they resemble a laboratory brush, with a proteic central structure and the GAGs simulating the bristles. The GAGs are long, non-branched polymers of several disaccharides (up to 200 repeated saccharides), consisting of one uronic acid (almost always glucuronic acid) and one hexosamine (glucosamine or galactosamine).

The main GAGs are composed of hyaluronic acid, dermatan sulfate, keratan sulfate, chondroitin sulfate and heparan sulfate. The PG aggregates are structures formed by a molecule of hyaluronic acid to which the PG monomers bind transversely. The hydrophilic property of the ECM arises from the high overall presence of GAGs, consisting of very negatively charged polyanions linked by electrovalent bonds to a high number of cations, principally sodium, which, in turn, attract and retain a large quantity of water molecules. Any change in these electric charges would modify the hydrophilic properties of the ECM. The PG macromolecules occupy a large proportion of the ECM, forming domains or pores with a large, open helical configuration. The spatial organization and the negative charge of the PGs, together with an intrinsic turgor, facilitate the selective diffusion of the various molecules, creating a tridimensional network which acts as a biophysical filter opposing compression forces and counteracting deformation. The PG aggregates are found not only in the ECM, but also in the basement membrane (perlecan) or on cell surfaces (syndecan, betaglycan). PGs and GAGs synthesize rapidly, the fibroblasts are able to generate these structures in only 1 to 2 minutes, and their half-life is 2 to 120 days.

Glycoproteins contain oligosaccharide chains (glycans) covalently attached to polypeptide side-chains. Structural GP, which occur in connective tissue, help bind the fibers, cells and ground substance together. They may also help components of the tissue bind to inorganic substances, such as calcium in bone. Fibronectin, with binding sites for cells, collagen and

GAGs, binds to the integrin cell receptors and links the cell to its extracellular environment. Laminin participates in this linking of cells and influences the filtration of molecules through the basement laminae. Nidogen, tenascin and vitronectin are others of the many existing structural GPs of the connective tissue.

The interstitial fluid is essential to maintaining the homeostasis between intracellular and extracellular areas. It is composed of a water vector containing mainly fatty acids, amino acids, sugars, coenzymes, chemical messengers such as cytokines, hormones, neurotransmitters, mineral salts and discard products.

The ECM has various structural patterns and a number of different biochemical compositions; one of these elements is the basement membrane, a highly complex and specialized structure. Epithelial cells adhere to the basement membrane through which they receive the controlling signals originating from the ECM. The basement membrane consists of a lamina lucida and a lamina densa, as well as GPs which vary depending on the tissue type: laminin, type IV collagen, nidogen and heparan sulfate-like PGs (Fig. 3). Among its functions we can highlight cell adhesion, regulation of proliferation and its role as a selective filter for molecular diffusion.

Biological and functional aspects of the third system

The living cell literally vibrates in permanent interaction with its surrounding environment. The formation of tissues and organs is based upon environment recognition, the distribution of cytoplasmic compounds, changes in shape, mobilization and directed displacement of cells; and the establishment of contacts and associations with other cells and / or extracellular materials which are scant in epithelial tissue and highly abundant in connective tissue.

The plasma membrane consists of a double lipid

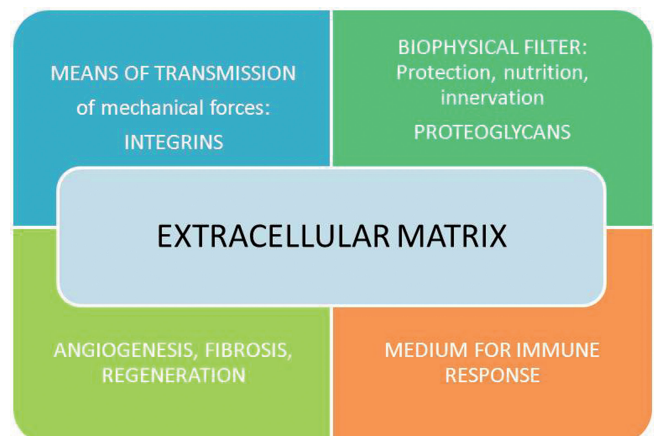


Fig. 2. Functional aspects of the third system.

layer and integrated proteins that traverse the membrane totally or partially. These components are able to make molecular movements such as turning, tilting from the outer to the inner surface and moving across the membrane. This explains cellular functions such as membrane flow, receptor function, cell recognition, surface enzyme activity, cell-cell and cell-substrate adhesion, cell motility in a liquid or over substrates, endocytosis and exocytosis, changes in cell shape, interactions and recruitment of ligands, and immune and histocompatibility phenomena.

The cytoskeleton is also a dynamic structure, made up of polymers comprising microfilaments, microtubules and intermediate filaments (Fig. 3). The cytoskeleton can be modified by extracellular changes in electric potential.

The main support cells are constituted by fibroblasts/fibrocytes, chondroblasts/chondrocytes, osteoblasts/osteocytes, myofibroblasts, adipocytes and gliocytes, which are essential for the synthesis of the extracellular fiber structures, as well as the PGs and the GPs. The quality of the biophysical filter formed by the PGs and the GAGs of the ECM depends on these support cells. Healthy support cells facilitate the rapid

repair of the ECM after injury. The macrophages, neutrophils, mastocytes and other phagocytes remove the majority of unwanted substances, while the cytotoxic T lymphocytes and NK cells remove the poisoned or injured aberrant cells (Fig. 2).

The niches or biochemical and mechanical microenvironments are defined by coordinated competitive interactions between soluble factors, cells and the ECM. These niches are variable in both function and number, and can be created or altered under specific conditions, with a complex and dynamic regulation that influences stem cell transit, survival, self-renewal, proliferation and differentiation (Scadden, 2006; Discher et al., 2009).

Lymphoid cells are the main users of the communication highways of the ECM along which the lymphocytes flow easily at high speed (Korpos et al., 2009). When migrating they exhibit amoeboid movements which allow the cell body to align with the collagen fibers, using them as a physical scaffold to guide migration. This lymphocyte migratory movement is facilitated principally by Integrins which play a central role in this process (Lammermann et al., 2008; Sabeh et al., 2009).

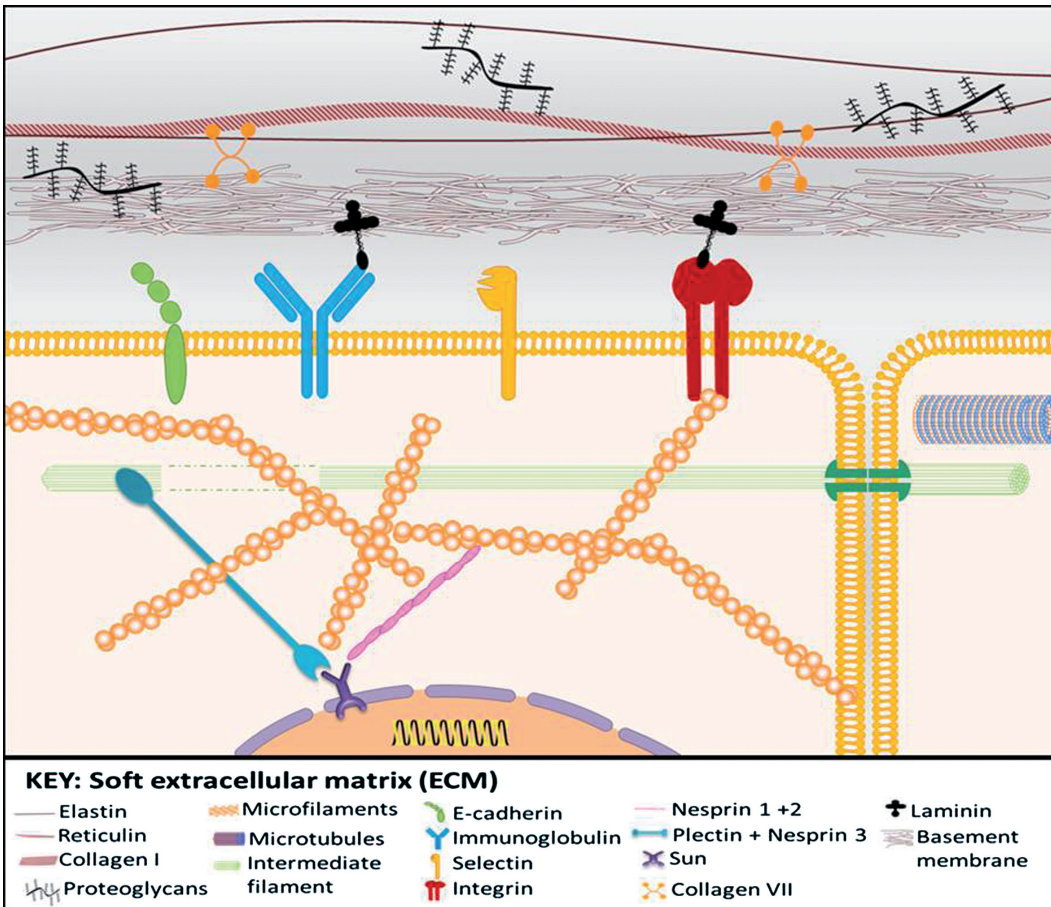


Fig. 3. The basement membrane. It provides structural support for epithelial cellularity. The cytoplasmic framework establishes connecting links between the nuclear matrix and the ECM through focal adhesions and integrins. The *tensegrity* and mechanotransduction forces are transmitted through the cytoskeleton; these forces give shape and movement to the cell, translate the biochemical stimuli and activate the epigenetic mechanisms of the cell.

CAMs (cell adhesion molecules) and Integrins

CAMs are a group of membrane GPs involved in biological processes entailing cell-cell or cell-matrix contact, such as proliferation, migration, differentiation and cell death. They recognize specific receptors, usually other CAM molecules located in other cells or in the cell matrix (Hynes, 1999). CAMs are grouped into families such as cadherins, immunoglobulins, selectins, integrins and ECM GPs. They can bind to molecules of a similar (homophilic interaction) or different nature (heterophilic interaction).

Cadherins are found on the surface of the majority of animal cells, and recognize other cadherins in adjacent cells. Immunoglobulin-type molecules establish homophilic bonds with immunoglobulins in the adjacent cells, whereas the selectins form heterophilic bonds, i.e., they bind to glucids present in the neighboring cell, and are important in the binding of leukocytes to the walls of the endothelium when they leave the bloodstream to enter the tissues.

Signals from the ECM molecules are transmitted to the surrounding cells through integrins which act as specialized mechanoreceptors. Integrins are able to translate and transmit a mechanical signal from the cell surface through a specific molecular pathway and convert it into intracellular biochemical changes, stimulate other receptors or induce gene expression. In addition, macromolecular complexes constitute adhesion points between the ECM and the cell, forming true mechanosensitive organelles or focal adhesions able to promote cell survival, the physiologic process of anoikis (apoptosis in response to an inappropriate relationship cell/ECM) and the proper replacement of tissue (Fig. 3) (Gilmore, 2005).

Integrins constitute the most important molecules involved in binding cells to the ECM. These molecules comprise a large family of transmembrane proteins that are expressed according to the type and physiologic needs of the tissues and cells, and possess an intracellular domain which is in contact with the cytoskeleton and an extracellular globular domain able

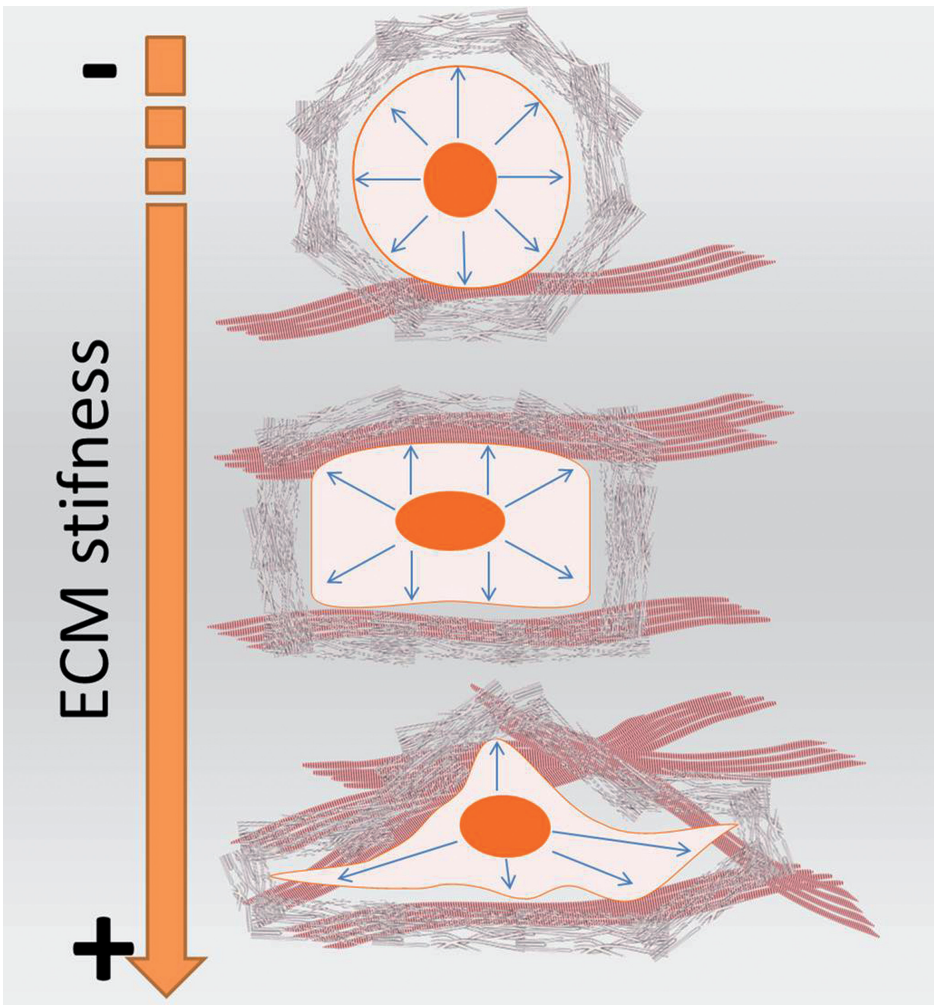


Fig. 4. Biotensegrity. The flattened or rounded morphology of the cellular elements and the three-dimensional structure of the tissue patterns, forming glands, alveoli, ducts and papillae, depend on the stiffness or flexibility of the basement membrane, as well as on its coordinated movement.

to bind to collagen, integrins and laminins (Akiyama, 1996).

The ECM provides a direct structural link between the nuclear matrix and the cell matrix (Getzenberg et al., 1991; Haque et al., 2006). The cytoskeleton (consisting of actin microfilaments, tubulin microtubules and intermediate filaments, specific for each cell type) is anchored to the nucleus through nesprins 1 and 2, which bind to actin filaments, whereas nesprin-3 can associate with intermediate filaments through plectin. Finally, the nuclear lamina forms a stable structure together with the nuclear structures, thus completing the mechano-transduction pathway between the ECM and the interior of the nucleus (Fig. 3) (Jaalouk and Lammerding, 2009).

Mechanotransduction and *biotensegrity*

Through the mechanotransduction process (Alenghat and Ingber, 2002), cells are able to convert mechanical changes into chemical or genetic changes. This process has been comprehensively studied in different cell types (Lin et al., 2009; Mammoto et al., 2009). In the body, bones constitute the basic compression support structure, forming part of a more complex framework in which all muscle, cartilage, ligament and tendons combine to form a tension structure. The fine balance between the forces that bind this framework together, through critical points

such as joints, both holds the body together and enables it to move. Living organisms are holographic structures, systems within systems which repeat their properties at different levels. In fact the cell maintains its morphology and function through an integrated tension system, denominated *tensegrity*. Within the cell, microtubules constitute the compression structures, and the actin filaments, closely related to myosin filaments, the tension structures (Ingber, 2008). Mechanical tension generated by movement is transmitted by pressure to the ECM which in turn transfers the movement into the cell through the integrins. The cytoskeleton translates these forces into chemical signals and mechanical stimuli which are transferred into the nucleus through the intermediate filaments that connect with nesprins and Sun proteins. These in turn communicate with the nuclear lamina, and the nuclear lamina communicates with the DNA (Jaalouk and Lammerding, 2009). The nucleus itself also has its own *tensegrity* system, and activates proliferation, cell metabolism, differentiation or apoptosis through mechanical stimuli.

A system has evolved through which it is possible to activate different genetic cell programs by modifying the shape of a cell (Ingber, 1998). *Tensegrity* may offer a scientific explanation for the effect of massage and qigong (Manzaneque et al., 2004), or for the genetic modification of the cell as a response to relaxation

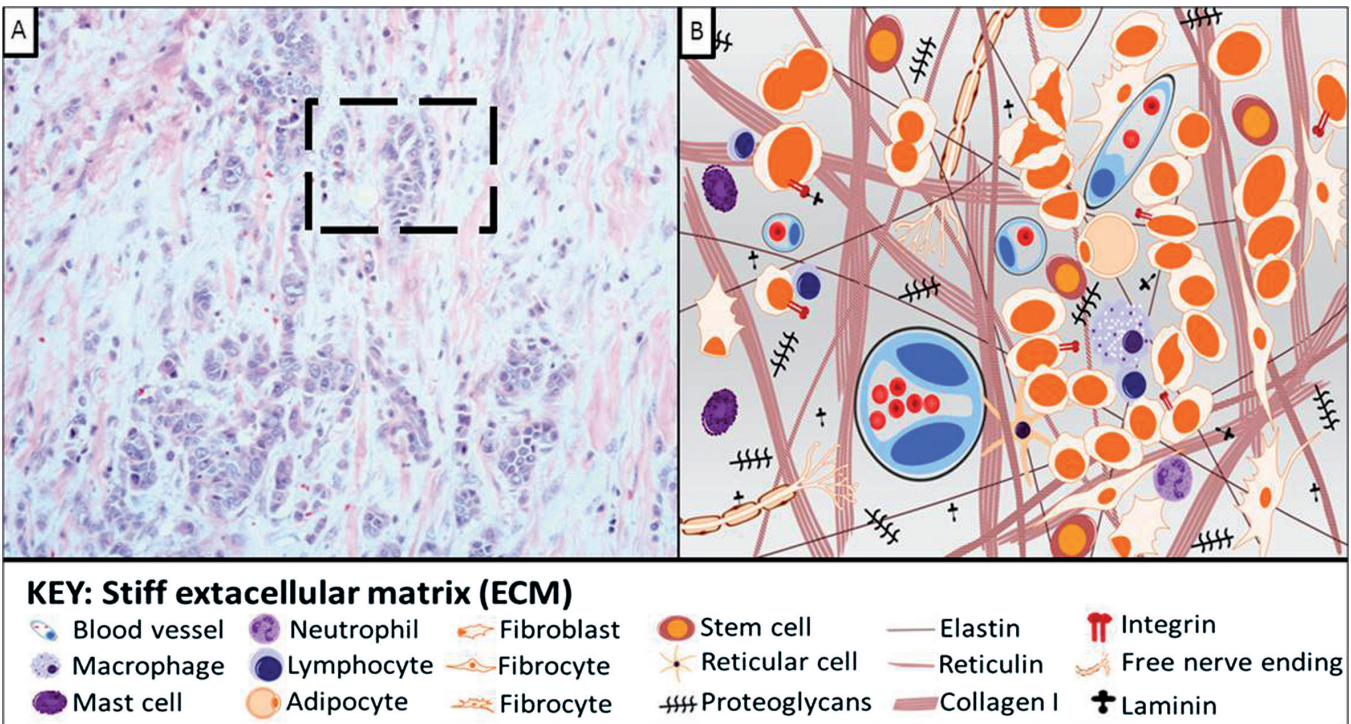


Fig. 5. A. Breast carcinoma. Hematoxylin and eosin stain. x 10. **B.** Schematic representation of the selected area in A. In this tumor, the oncogenic capacity of the stroma derives from the effect of its own cells, the lymphoid cells, and from the mechanical stimulation of *tensegrity* of the ECM. The loss of the tissue architecture causes a lesion to become a malignant tumor. ECM stiffness, the new-angiogenesis and desmoplasia cause an increased consistency that enables clinical detection of the tumor.

(Dusek et al., 2008). When a cell is flattened, the tension generated indicates that more cells are needed and the division process is activated. If the shape becomes rounded, the opposite process occurs and the apoptosis or anoikis program is activated. To establish equilibrium, the cell seeks the optimal conditions for differentiation and function according to the microenvironment in which it resides. All cells in the body are subject to this *tensegrity* mechanism based on the inner structure of the nuclear matrix and the cytoskeleton. Thus, every cell senses its environment and reacts to it according to its own needs (Fig. 4) (Ingber, 2003a,b, 2006; Discher et al., 2005).

Variations in the rigidity of the ECM allow it to produce a differentiated phenotype in the mesenchymal stem cells. A soft ECM with a pressure or 1kPa (kilopascal) would produce neurogenic differentiation; a stiff ECM of 10kPa would induce muscle differentiation (Engler et al., 2006). Such isometric tension is vital to life and explains why cells, organs and tissues take on a given shape, or why a hollow organ collapses when opened; this tension is found at the tissular, cellular, organic and molecular level, including the DNA structure itself (Getzenberg et al., 1991). A mechanical force applied to a living organ is transmitted down through a structural hierarchy that spans multiple size scales until becoming biochemical cellular stimulus through specific transduction molecules (Ingber, 2006).

The mechanotransduction process converts mechanical stimuli into chemical signals and allows the cell to adapt to its microenvironment (Jaalouk and Lammerding, 2009). This mechanism includes steps that pass from the ECM to the cytoplasmic membrane, the cytoskeleton and the nuclear membrane, and therefore involves an enormous amount of proteins and molecules. These elements have therefore been classified into three groups, comprising those of the extracellular microenvironment, those affecting the cell structure and organization, and finally, those related to cell signaling. All these proteins and molecules will eventually affect the nuclear chromatin at a genetic and epigenetic level (Wang et al., 2009).

Energy flow and physiopathology of the ECM

The electric and magnetic fields generated by tissues and organs possess an important biologic function. This function is altered in the pathologic processes of inflammation, degeneration or the appearance of new tissue within an organ. The electromagnetic activity of an organ is not only restricted to the boundaries of the capsule, but extends outwards involving the fields of neighboring organs, interrelating and communicating with adjacent and sometimes distant structures, similar to the electromagnetic wave sent by the heart throughout the body via the bloodstream. The essential unit of the ECM, the matrisome, hosts the function of maintaining the osmotic, ionic, electromagnetic and protonic

homeostasis, both at local and systemic level.

Biological electricity is an ionic phenomenon linked to the polarity of the cell membrane, it occurs in nerve transmission, muscle contractility and in all living cells. These potential differences are easily measurable, although electrons and protons produce much smaller flows. Thus we have a system based on interaction of energy, which, together with the chemical system constitutes a language essential to the integrity of the body; an integrated network that links genes and nuclear matrix to the ECM and to its collagen fibers through integrins and focal adhesions. Knowledge of this structure provides histology with a clue to its function, allowing the visualization within tissues of the circuits of energy that support life and its relationships, integrated through the *tensegrity* and mechanotransduction mechanisms. Thus, the nuclear matrix, the cytoplasmic matrix and the ECM form an interconnected network linking all molecules in the body (Fig. 5) (Wang et al., 2009).

Energy pathways and information circuits are routed principally in the ECM, whose composition and structure not only provides a supportive element, but also precise circuits for mechanical, ionic, electrical, protonic and chemical transmission. The electric fields produced by movement provide the information that directs cell activity and the pattern of tissue remodeling (Bassett, 1993). The ECM is able to provide the means for high speed communication thanks to its hydrophilicity, which depends on the intense negative charges of its GAGs components. All diseases are accompanied by changes in ions and water content, and in pH levels of the extracellular fluids, thus affecting the cell membranes and their electric micropotentials (Goller et al., 1986; Kim et al., 2007).

ECM components are semiconductors able to transfer the electricity of the electrons and the proticity of the protons, which is another function of the ECM studied by quantum chemistry (Alvaro et al., 2009a). The ECM is a pool of negative charges able to donate or absorb electrons, used in the neutralization of free radicals released by oxidative processes, as in the case of inflammation.

The ECM determines tissue specificity and takes an active part in the development and maturation of the central nervous system, its remodeling, axonal guidance, regeneration after injury and the capacity for neural plasticity (Zimmermann and Dours-Zimmermann, 2008) (Huang et al., 2009). Furthermore, it can act as a stimulus for cell survival, as well as affecting its viability. The molecules of the ECM are related to the processes of cell life and death through the balance between metalloproteinases (MMP) and its inhibitors (MMPI), and can play an important role in tumor progression, inducing or suppressing apoptosis (Marastoni et al., 2008). The balance between MMP and MMPI affect different physiologic and pathologic processes, including embryonic implantation,

angiogenesis and carcinogenesis (Huang et al., 2009), thus constituting new potential therapeutic targets in inflammatory (Korpos et al., 2009) and tumor (Denys et al., 2009) processes. In prostate cancer the metastatic process is associated with changes in the ECM (Stewart et al., 2004); and in melanoma the degradation of the basement membrane and remodeling of the ECM are produced by MMP and its inhibitors (Hofmann et al., 2005).

The evidence available suggests that one of the mechanisms by which a lesion is converted into a malignant tumor is through the loss of tissue architecture (Fig. 6). The parenchymatous cells are anchored three-dimensionally through interactions with the ECM. This contact is essential for cell survival, to the point that anoikis occurs when a cell becomes detached from the network and is left with no locational reference (Gilmore, 2005); only metastatic tumor cells escape this law. The majority of malignant tumors show an increase in consistency due to the stiffness of their ECM. Mechanical changes to the matrix activate integrins, which not only promote cell proliferation through the Ras and Erk pathways, but also affect cell contractility through the Rho pathway (Huang and Ingber, 2005) whereby the greater the rigidity, the greater the stimulation of the integrins, which in turn increases stiffness, a fact that is reflected in the malignant phenotype of the epithelial tumors (Fig. 7).

The ECM, furnishing the tumor microenvironment

The concept of genetic determinism is currently under review given the evidence that tumors are heterogeneous cellular entities whose growth depends on the interaction between the genetically altered cells and the tumor microenvironment in which they develop (Ingber, 2008). This microenvironment consists of ECM, stroma cells and immune response, determining not only the morphology and the classification of the tumor, but also the clinical aggressiveness, prognosis and response to treatment (Alvaro et al., 2009a; Lejeune and Alvaro, 2009). A tumor could therefore be considered as a functional tissue, connected and dependent on the microenvironment which sends and receives signals to and from the tumor tissue itself. Thus, cancer may be a disease of neoplastic cell development, whose abnormal growth could be normalized through embryonic tissues or the ECM itself (Kenny and Bissell, 2003), changes in the ECM and in normal tissue architecture being as oncogenic as radiation or viruses (Ingber, 2008). The oncogenic capacity of the stroma derives from the effect of its own cells, the lymphoid cells, and from the mechanical stimulation of *tensegrity* of the ECM (Li et al., 2007).

Tumor stromal cells derive from bone marrow progenitors which are mobilized through the bloodstream until entering the tumor microenvironment (Roorda et al., 2009) where they differentiate following different cell pathways in endothelia, fibroblasts and

histiocyte-macrophages, which control tumor cell growth, the metastatic potential of the tumor and also determine the response to treatment (Li et al., 2007). The collaboration of one of these cell types in particular, the macrophages, is essential in the processes of migration, invasion and tumor metastasis (Condeelis and Pollard, 2006); however it is the mesenchymal stem cells of the tumor stroma that drive the tumor cells to metastasize (Karnoub et al., 2007). Stem cells in the bone marrow are the precursors of metastasis to distant organs, and ensure the activation of an optimal microenvironment or niche to receive and host the tumor cells which arrive later (Kaplan et al., 2005; Hu and Polyak, 2008). Fibroblasts are the chief fabricators of ECM and are able to change their phenotype and function both in physiologic and pathologic contexts. In the tumor context we can find myofibroblasts, peritumoral fibroblasts, reactive stromal cells and carcinoma-associated fibroblasts (CAF) (Fig. 5) (Olumi et al., 1999) acting on tumor cells, as well as on the rest of the tumor microenvironment (Fig. 8) (Tlsty and Coussens, 2006).

The stromal cells and their products are able to produce cellular oncogenic transformation (Pupa et al., 2002), which acts through alteration in the homeostatic regulation of the tissue. Under normal conditions this regulation is responsible for maintaining architecture, adhesion, and programmed cell death or cell proliferation signals; so if the cells cease to receive this information from the ECM, firstly their function will be altered, followed by their structure and, finally, the oncogenic change will occur (Alvaro et al., 2009a). Remodeling of the tumor microenvironment will determine both the response to cytotoxic treatment and tumor prognosis.

The number of inflammation-derived mediators with the potential to promote cell proliferation, genomic instability and metastasis is virtually endless. Some examples are the release of cytokines and chemokines, the release of cytotoxic mediators including reactive

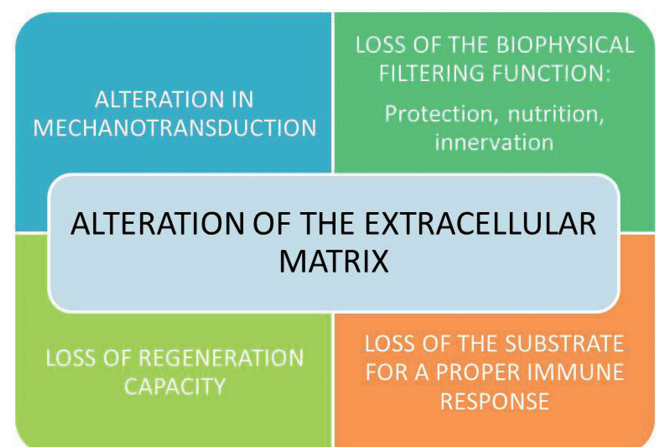


Fig. 6. Physiopathology of the ECM.

Tissular hyperstructure

oxygen species, the secretion of proteases (especially MMP), soluble mediators of cell death and cell proliferation as TNF, interleukins, interferons and so on. These mediators are so abundant and have so many functions that the individual study of any one of these agents has so far produced little information. This circumstance calls for a reading at a higher level, that of the so-called hyperstructures, in an attempt to interrelate the data coming from the different fields of genomics, proteomics and all cellular physiology (Amar et al., 2002). The concept of hyperstructures considers the interaction of thousands of molecules, genes, ions, lipids etc. in carrying out a single tissue or cellular function. This interaction is influenced by extracellular regulatory signals proceeding from the microenvironment and the non-neoplastic cells of the tumor stroma, constituting the epigenetic framework for tumor progression (Huang and Ingber, 2006).

Transformation from a benign proliferative cell into a malignant cell can be produced by a peculiar phenotypic change, known as epithelial-mesenchymal transition (Guarino et al., 2007). This transformation involves breaking contact with sister cells and increasing motility, as the result of a change in the epithelial cytoskeleton, with its corresponding proprieties for a pseudomesenchymal phenotype, which enables migration, invasion and dissemination (Lee et al., 2006).

While normal cells adhere to their environment through integrins, and their body has a proper consistency, tumor cells lose that consistency and *tensegrity*, becoming easily deformable elements (causing pleomorphism), with high elasticity (enhancing infiltration) and with an increased degree of mobility (enabling metastasis) (Suresh, 2007).

In lymphomas, the ECM regulators, especially MMP-9, influence angiogenic activity both at local and distant level (Negaard et al., 2009). Abnormal vasculature in the stroma, as well as fibrosis and increased interstitial pressure, confer the firmness of the tumor on palpation. Under homeostatic conditions, collagen fibrils are subject to a scant turnover. However, this turnover is accelerated during tissue remodeling and tumor development, as evidenced by the serum levels of its degradation products. A desmoplastic reaction is frequent in many solid tumors, such as breast, prostate, colon or lung, in which high levels of TGF- β and PDGF are found. These growth factors are produced by the mesenchymal cells of the tumor stroma and induce immunophenotypic changes. These changes are observable by studying actin- α , myosin, vimentin, desmin and the altered production of several ECM proteins, such as collagen, laminin, tenascin, MMP and MMPI, and several growth factors (Pupa et al., 2002).

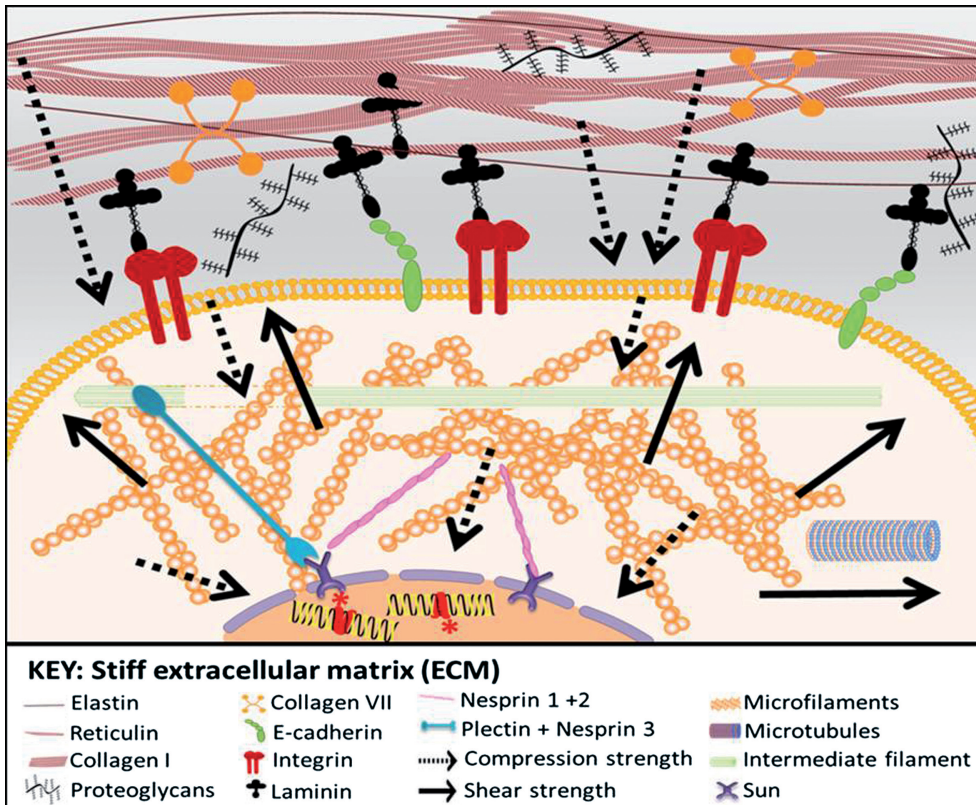


Fig. 7. The reciprocal communication between the stromal cells and the tissue parenchyma directs gene expression. E-cadherin is involved in the processes of tissue differentiation and morphogenesis and plays an important role in modulating the invasiveness of tumor cells in breast cancer and other epithelial tumors.

Studies of the ECM have revealed that the components of the tumor microenvironment are fundamental, not only for the regulation of tumor progression (Tlsty, 2001; Tlsty and Coussens, 2006), but are also essential even before the tumor appears. The stromal cells are able to produce the transformation of the adjacent cells through an alteration in the homeostatic regulation of the tissue, including the control of architecture, adhesion, cell death and proliferation (Pupa et al., 2002).

An overexpression of the ECM molecules themselves can increase tumor proliferation and confer resistance to chemotherapy, as in small cell lung carcinoma.

Molecular mechanics and therapeutic consequences of the regulation of the third system

Malignant transformation is accompanied by a progressive loss of local homeostasis and an alteration in tissue architecture. This culminates in tumor cell invasion and the production of distant metastasis. Throughout this entire process, a series of changes related to cell and tissue *tensegrity* are produced and result in a mechanical phenotypic change in both the

tumor cell and its microenvironment (Figs. 7, 8). Micromechanical alterations of the ECM, together with remodeling of the stroma by the tumor cell, are linked to the phenomena of dysplasia, infiltration and metastasis (Kumar and Weaver, 2009). Knowledge of the molecular mechanisms by which a cell receives, processes and responds to mechanical stimuli is opening up new perspectives on the biology of cancer and its treatment. Alterations in the mechanical interaction between cells and their microenvironment contribute to cellular dysplasia. Conversely, the homeostatic regulation of the tensional force within the cell is able to reverse the malignant phenotype (Paszek et al., 2005; Johnson et al., 2007).

The emission of filopodia-like projections with a higher actin density, known as invadopodia, are used by the tumor cells to help digestion and invasion of the ECM, remodeling the existing matrix and establishing new pathways in the ECM which will be used for tumor invasion (Yamaguchi et al., 2005). During this action, the tumor cell will suffer significant cytoplasmic and nuclear deformations, with corresponding changes in organization of the cytoskeleton on traversing a rigid stroma. In turn, the expanding tumor compresses the adjacent ECM, with the consequent reduction of flow in

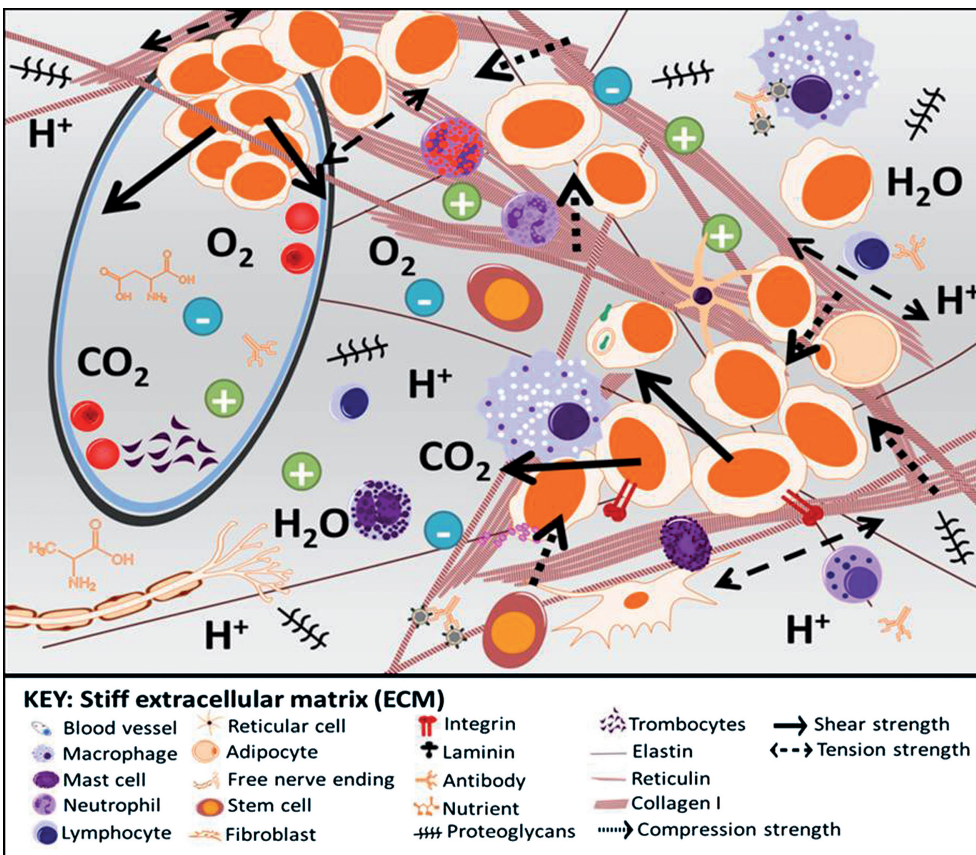


Fig. 8. Cancer cells, represented as the largest ovoid cells, often metastasize to different organs with very different microenvironmental and mechanical properties. The mechanics of remote tissues and the cancer cells could regulate cell dormancy, proliferation and differentiation in these organs.

the vascular and lymph vessels and of the interstitial space. Tumor growth is associated, first, to an increased matrix deposition and the adjacent ECM densification, and second, to a massive secretion of MMP and peritumoral matrix digestion.

Currently, two humanized monoclonal antibodies that act on the integrin interactions have been approved. Efalizumab interacts with the integrin lymphocyte function-associated antigen 1 (LFA-1) and is used in the treatment of patients with chronic plaque psoriasis, whereas natalizumab interacts with VLA-4 and is used in the treatment of multiple sclerosis.

With respect to the CAMs, a large number of investigations consider them to play a relevant role in pathology, and several projects to investigate new therapies with CAMs as the therapeutic target, usually by means of antibodies to modulate their action, are underway.

The perspective of the epithelial-mesenchymal transition in epithelial tumors has opened the door to a new line of treatment which considers the genetic and epigenetic mechanisms associated with resistance to chemotherapy (Sabbah et al., 2008). In breast cancer, treatment with doxorubicin results in an increase in fibuline-1, an ECM protein, and its binding proteins, fibronectin and laminin-1, which constitute a source of chemoresistance (Pupa et al., 2007). Monoclonal antibodies against fibulin-1 are able to reverse such chemoresistance, and the inhibition of MMP seems to have a therapeutic effect (Jodele et al., 2006).

Chemotherapeutic agents often base their cytotoxic action on the modification of cell membranes and the cytoskeleton. For example, doxorubicin produces peroxidation of the cell membranes, Taxol increases polymerization of tubulin, and vincristine impedes the addition of monomers to the microtubules, thus eliminating the possibility of mitosis (Suresh, 2007). In follicular lymphoma and diffuse large cell lymphoma, treatment with lenalidomide affects the immune synapses of intracellular T lymphocytes (Ramsay et al., 2009). Similarly, chemotherapeutic agents alter cell mechanics which increases the risk of vascular complications, as occurs in the treatment of leukemia. In leukemias, the treatment of tumor lymphocytes increases their rigidity due to the reorganization of the actin filaments, which in turn leads to a decrease in cell deformability with the consequent leukostasis, microcirculation obstruction and vascular complications (Lam et al., 2007).

Conclusion

Continued advances in cancer treatment require new and innovative approaches. The discovery that the malignant phenotype can be reversed through the correction of cues from the tumor microenvironment (Kenny and Bissell, 2003), paves the way for a new focus on experimentation and derived knowledge.

Experimental evidence suggests that the cancerigenic effect of hormones on an epithelium occurs through an alteration in the stromal-epithelial interaction, and it has been shown that inducing changes in the ECM, *in vivo* or *in vitro*, is enough to influence the tumor phenotype. Nevertheless the opposite is also true, and some tumors may undergo regression by restoring an ECM which enables the proper interaction between the epithelium and the stroma (Ingber, 2008). The discovery that several cell behaviors are controlled by purely physical interactions has brought about a new era in which it will be possible to integrate current knowledge on the ECM and its function, together with the mechanisms of *biotensegrity*, mechanotransduction, energy flow, immune response and epithelium-mesenchymal transition. These advances will provide a truly comprehensive view of the neoplastic process, allowing a more specific and sensitive therapeutic management of the body and its diseases.

Acknowledgements. We would like to thank Lucía Álvaro for her excellent collaboration in the electronic edition of the text, and to David Harrison for English language support. This study was performed with grants from Instituto de Salud Carlos III: FIS (PI10/00015) and RTICC (RD06/0020/0120).

References

- Akiyama S.K. (1996). Integrins in cell adhesion and signaling. *Hum. Cell* 9, 181-186.
- Alenghat F.J. and Ingber D.E. (2002). Mechanotransduction: all signals point to cytoskeleton, matrix, and integrins. *Sci STKE*. 2002, pe6.
- Alvaro T., Lejeune M., Escriva P., Pons L.E., Bosch R., Jaen J., Lopez C., Salvado M.T. and de Sanjose S. (2009a). Appraisal of immune response in lymphoproliferative syndromes: a systematic review. *Crit. Rev. Oncol. Hematol.* 70, 103-113.
- Alvaro T., Noguera-Salvá R. and Fariñas F. (2009b). Matriz extracelular: morfología, función y biotensegridad (parte I). *Rev. Esp. Patol.* 42, 249-261.
- Alvaro T., Noguera-Salvá R. and Fariñas F. (2010). Matriz extracelular: de la mecánica molecular al microambiente tumoral (parte II). *Rev. Esp. Patol.* 43, 24-32.
- Amar P., Ballet P., Barlovatz-Meimon G., Benecke A., Bernot G., Bouligand Y., Bourguine P., Delaplace F., Delosme J.M., Demarty M., Fishov I., Fourmentin-Guilbert J., Fralick J., Giavitto J.L., Gleyse B., Godin C., Incitti R., Kepes F., Lange C., Le Sceller L., Loutellier C., Michel O., Molina F., Monnier C., Natowicz R., Norris V., Orange N., Pollard H., Raine D., Ripoll C., Rouviere-Yaniv J., Saier M. Jr, Soler P., Tambourin P., Thellier M., Tracqui P., Ussery D., Vincent J.C., Vannier J.P., Wiggins P. and Zemirline A. (2002). Hyperstructures, genome analysis and I-cells. *Acta Biotheor.* 50, 357-373.
- Basset C.A. (1993). Beneficial effects of electromagnetic fields. *J. Cell Biochem.* 51, 387-393.
- Condeelis J. and Pollard J.W. (2006). Macrophages: obligate partners for tumor cell migration, invasion, and metastasis. *Cell* 124, 263-266.
- Denys H., Braems G., Lambein K., Pauwels P., Hendrix A., De Boeck A., Mathieu V., Bracke M. and De Wever O. (2009). The

- extracellular matrix regulates cancer progression and therapy response: implications for prognosis and treatment. *Curr. Pharm. Des.* 15, 1373-1384.
- Discher D.E., Janmey P. and Wang Y.L. (2005). Tissue cells feel and respond to the stiffness of their substrate. *Science*. 310, 1139-1143.
- Discher D.E., Mooney D.J. and Zandstra P.W. (2009). Growth factors, matrices, and forces combine and control stem cells. *Science* 324, 1673-1677.
- Dusek J.A., Otu H.H., Wohlhueter A.L., Bhasin M., Zerbini L.F., Joseph M.G., Benson H. and Libermann T.A. (2008). Genomic counter-stress changes induced by the relaxation response. *PLoS One* 3, e2576.
- Engler A.J., Sen S., Sweeney H.L. and Discher D.E. (2006). Matrix elasticity directs stem cell lineage specification. *Cell* 126, 677-689.
- Friedl P., Wolf K., von Andrian U.H. and Harms G. (2007). Biological second and third harmonic generation microscopy. *Curr. Protoc. Cell Biol.* Chapter 4, Unit 4 15.
- Geneser F. (2000). Tejido conectivo. In: Geneser F. *Histología*. 3^o ed. Editorial Médica Panamericana. Madrid. pp 197-126.
- Getzenberg R.H., Pienta K.J., Ward W.S. and Coffey D.S. (1991). Nuclear structure and the three-dimensional organization of DNA. *J. Cell Biochem.* 47, 289-299.
- Gilmore A.P. (2005). Anoikis. *Cell Death Differ.* 12 Suppl 2, 1473-1477.
- Goller D.A., Weidema W.F. and Davies R.J. (1986). Transmural electrical potential difference as an early marker in colon cancer. *Arch. Surg.* 121, 345-350.
- Guarino M., Rubino B. and Ballabio G. (2007). The role of epithelial-mesenchymal transition in cancer pathology. *Pathology* 39, 305-318.
- Haque F., Lloyd D.J., Smallwood D.T., Dent C.L., Shanahan C.M., Fry A.M., Trembath R.C. and Shackleton S. (2006). SUN1 interacts with nuclear lamin A and cytoplasmic nesprins to provide a physical connection between the nuclear lamina and the cytoskeleton. *Mol. Cell Biol.* 26, 3738-3751.
- Hofmann U.B., Houben R., Brocker E.B. and Becker J.C. (2005). Role of matrix metalloproteinases in melanoma cell invasion. *Biochimie* 87, 307-314.
- Hu M. and Polyak K. (2008). Microenvironmental regulation of cancer development. *Curr. Opin. Genet. Dev.* 18, 27-34.
- Huang S. and Ingber D.E. (2005). Cell tension, matrix mechanics, and cancer development. *Cancer Cell* 8, 175-176.
- Huang S. and Ingber D.E. (2006). A non-genetic basis for cancer progression and metastasis: self-organizing attractors in cell regulatory networks. *Breast Dis.* 26, 27-54.
- Huang S.C., Sheu B.C., Chang W.C., Cheng C.Y., Wang P.H. and Lin S. (2009). Extracellular matrix proteases - cytokine regulation role in cancer and pregnancy. *Front. Biosci.* 14, 1571-1588.
- Huxley-Jones J., Robertson D.L. and Boot-Handford R.P. (2007). On the origins of the extracellular matrix in vertebrates. *Matrix Biol.* 26, 2-11.
- Huxley-Jones J., Pinney J.W., Archer J., Robertson D.L. and Boot-Handford R.P. (2009). Back to basics--how the evolution of the extracellular matrix underpinned vertebrate evolution. *Int. J. Exp. Pathol.* 90, 95-100.
- Hynes R.O. (1999). Cell adhesion: old and new questions. *Trends Cell Biol.* 9, M33-37.
- Ingber D.E. (1998). The architecture of life. *Sci. Am.* 278, 48-57.
- Ingber D.E. (2003a). Tensegrity I. Cell structure and hierarchical systems biology. *J. Cell. Sci.* 116, 1157-1173.
- Ingber D.E. (2003b). Tensegrity II. How structural networks influence cellular information processing networks. *J. Cell. Sci.* 116, 1397-1408.
- Ingber D.E. (2006). Cellular mechanotransduction: putting all the pieces together again. *FASEB J.* 20, 811-827.
- Ingber D.E. (2008). Tensegrity-based mechanosensing from macro to micro. *Prog. Biophys. Mol. Biol.* 97, 163-179.
- Jaalouk D.E. and Lammerding J. (2009). Mechanotransduction gone awry. *Nat. Rev. Mol. Cell Biol.* 10, 63-73.
- Jodele S., Blavier L., Yoon J.M. and DeClerck Y.A. (2006). Modifying the soil to affect the seed: role of stromal-derived matrix metalloproteinases in cancer progression. *Cancer Metastasis Rev.* 25, 35-43.
- Johnson K.R., Leight J.L. and Weaver V.M. (2007). Demystifying the effects of a three-dimensional microenvironment in tissue morphogenesis. *Methods Cell Biol.* 83, 547-583.
- Kaplan R.N., Riba R.D., Zacharoulis S., Bramley A.H., Vincent L., Costa C., MacDonald D.D., Jin D.K., Shido K., Kerns S.A., Zhu Z., Hicklin D., Wu Y., Port J.L., Altorki N., Port E.R., Ruggero D., Shmelkov S.V., Jensen K.K., Rafii S. and Lyden D. (2005). VEGFR1-positive haematopoietic bone marrow progenitors initiate the pre-metastatic niche. *Nature* 438, 820-827.
- Karnoub A.E., Dash A.B., Vo A.P., Sullivan A., Brooks M.W., Bell G.W., Richardson A.L., Polyak K., Tubo R. and Weinberg R.A. (2007). Mesenchymal stem cells within tumour stroma promote breast cancer metastasis. *Nature* 449, 557-563.
- Kenny P.A. and Bissell M.J. (2003). Tumor reversion: correction of malignant behavior by microenvironmental cues. *Int. J. Cancer* 107, 688-695.
- Kim B.S., Isaacson D., Xia H., Kao T.J., Newell J.C. and Saulnier G.J. (2007). A method for analyzing electrical impedance spectroscopy data from breast cancer patients. *Physiol. Meas.* 28, S237-246.
- Konig K., Schenke-Layland K., Riemann I. and Stock U.A. (2005). Multiphoton autofluorescence imaging of intratissue elastic fibers. *Biomaterials* 26, 495-500.
- Korpos E., Wu C., Song J., Hallmann R. and Sorokin L. (2009). Role of the extracellular matrix in lymphocyte migration. *Cell Tissue Res.* 339, 47-57.
- Kumar S. and Weaver V.M. (2009). Mechanics, malignancy, and metastasis: the force journey of a tumor cell. *Cancer Metastasis Rev.* 28, 113-127.
- Lam W.A., Rosenbluth M.J. and Fletcher D.A. (2007). Chemotherapy exposure increases leukemia cell stiffness. *Blood* 109, 3505-3508.
- Lammermann T., Bader B.L., Monkley S.J., Worbs T., Wedlich-Soldner R., Hirsch K., Keller M., Forster R., Critchley D.R., Fassler R. and Sixt M. (2008). Rapid leukocyte migration by integrin-independent flowing and squeezing. *Nature* 453, 51-55.
- Lee J.M., Dedhar S., Kalluri R. and Thompson E.W. (2006). The epithelial-mesenchymal transition: new insights in signaling, development, and disease. *J. Cell Biol.* 172, 973-981.
- Lejeune M. and Alvaro T. (2009). Clinicobiological, prognostic and therapeutic implications of the tumor microenvironment in follicular lymphoma. *Haematologica* 94, 16-21.
- Li H., Fan X. and Houghton J. (2007). Tumor microenvironment: the role of the tumor stroma in cancer. *J. Cell. Biochem.* 101, 805-815.
- Lin Y.W., Cheng C.M., Leduc P.R. and Chen C.C. (2009). Understanding sensory nerve mechanotransduction through localized elastomeric matrix control. *PLoS One* 4, e4293.
- Mammoto A., Connor K.M., Mammoto T., Yung C.W., Huh D., Aderman

Tissular hyperstructure

- C.M., Mostoslavsky G., Smith L.E. and Ingber D.E. (2009). A mechanosensitive transcriptional mechanism that controls angiogenesis. *Nature* 457, 1103-1108.
- Manzaneque J.M., Vera F.M., Maldonado E.F., Carranque G., Cubero V.M., Morell M. and Blanca M.J. (2004). Assessment of immunological parameters following a qigong training program. *Med. Sci. Monit.* 10, CR264-270.
- Marastoni S., Ligresti G., Lorenzon E., Colombatti A. and Mongiat M. (2008). Extracellular matrix: a matter of life and death. *Connect. Tissue Res.* 49, 203-206.
- Negaard H.F., Svennevig K., Kolset S.O., Iversen N., Lothe I.M., Ostenstad B., Sandset P.M. and Iversen P.O. (2009). Alterations in regulators of the extracellular matrix in non-Hodgkin lymphomas. *Leuk. Lymphoma* 50, 998-1004.
- Noble D. (2008). Claude Bernard, the first systems biologist, and the future of physiology. *Exp. Physiol.* 93, 16-26.
- Olumi A.F., Grossfeld G.D., Hayward S.W., Carroll P.R., Tlsty T.D. and Cunha G.R. (1999). Carcinoma-associated fibroblasts direct tumor progression of initiated human prostatic epithelium. *Cancer Res.* 59, 5002-5011.
- Oschman J.L. (2009). Charge transfer in the living matrix. *J. Bodyw Mov Ther.* 13, 215-228.
- Paszek M.J., Zahir N., Johnson K.R., Lakins J.N., Rozenberg G.I., Gefen A., Reinhart-King C.A., Margulies S.S., Dembo M., Boettiger D., Hammer D.A. and Weaver V.M. (2005). Tensional homeostasis and the malignant phenotype. *Cancer Cell* 8, 241-254.
- Pischinger A. (2006). The extracellular matrix and ground regulation. In: *Basis for a holistic medicine*. Heine H. (ed). North Atlantic books. Berkeley (CA).
- Pupa S.M., Menard S., Forti S. and Tagliabue E. (2002). New insights into the role of extracellular matrix during tumor onset and progression. *J. Cell Physiol.* 192, 259-267.
- Pupa S.M., Giuffrè S., Castiglioni F., Bertola L., Cantu M., Bongarzone I., Baldassari P., Mortarini R., Argraves W.S., Anichini A., Menard S. and Tagliabue E. (2007). Regulation of breast cancer response to chemotherapy by fibulin-1. *Cancer Res.* 67, 4271-4277.
- Ramsay A.G., Clear A.J., Kelly G., Fatah R., Matthews J., Macdougall F., Lister T.A., Lee A.M., Calaminici M. and Gribben J.G. (2009). Follicular lymphoma cells induce T-cell immunologic synapse dysfunction that can be repaired with lenalidomide: implications for the tumor microenvironment and immunotherapy. *Blood* 114, 4713-4720.
- Roorda B.D., ter Elst A., Kamps W.A. and de Bont E.S. (2009). Bone marrow-derived cells and tumor growth: contribution of bone marrow-derived cells to tumor micro-environments with special focus on mesenchymal stem cells. *Crit. Rev. Oncol. Hematol.* 69, 187-198.
- Sabbah M., Emami S., Redeuilh G., Julien S., Prevost G., Zimmer A., Ouelaa R., Bracke M., De Wever O. and Gespach C. (2008). Molecular signature and therapeutic perspective of the epithelial-to-mesenchymal transitions in epithelial cancers. *Drug Resist. Updat.* 11, 123-151.
- Sabeh F., Shimizu-Hirota R. and Weiss S.J. (2009). Protease-dependent versus -independent cancer cell invasion programs: three-dimensional amoeboid movement revisited. *J. Cell Biol.* 185, 11-19.
- Saks V., Monge C. and Guzun R. (2009). Philosophical basis and some historical aspects of systems biology: from Hegel to Noble - applications for bioenergetic research. *Int. J. Mol. Sci.* 10, 1161-1192.
- Scadden D.T. (2006). The stem-cell niche as an entity of action. *Nature* 441, 1075-1079.
- Schenke-Layland K., Xie J., Angelis E., Starcher B., Wu K., Riemann I., MacLellan W.R. and Hamm-Alvarez S.F. (2008). Increased degradation of extracellular matrix structures of lacrimal glands implicated in the pathogenesis of Sjogren's syndrome. *Matrix Biol.* 27, 53-66.
- Stevens A. and Lowe J. (2006). Células de sostén y la matriz extracelular. In: *Histología Humana*, 3^o ed. Stevens A. and Lowe J. (eds). Elsevier Mosby. Madrid. pp 46-64.
- Stewart D.A., Cooper C.R. and Sikes R.A. (2004). Changes in extracellular matrix (ECM) and ECM-associated proteins in the metastatic progression of prostate cancer. *Reprod. Biol. Endocrinol.* 2, 2.
- Suresh S. (2007). Biomechanics and biophysics of cancer cells. *Acta Biomater.* 3, 413-438.
- Tlsty T.D. (2001). Stromal cells can contribute oncogenic signals. *Semin Cancer Biol.* 11, 97-104.
- Tlsty T.D. and Coussens L.M. (2006). Tumor stroma and regulation of cancer development. *Annu. Rev. Pathol.* 1, 119-150.
- Wang N., Tytell J.D. and Ingber D.E. (2009). Mechanotransduction at a distance: mechanically coupling the extracellular matrix with the nucleus. *Nat. Rev. Mol. Cell Biol.* 10, 75-82.
- Yamaguchi H., Lorenz M., Kempiak S., Sarmiento C., Coniglio S., Symons M., Segall J., Eddy R., Miki H., Takenawa T. and Condeelis J. (2005). Molecular mechanisms of invadopodium formation: the role of the N-WASP-Arp2/3 complex pathway and cofilin. *J. Cell Biol.* 168, 441-452.
- Zimmermann D.R. and Dours-Zimmermann M.T. (2008). Extracellular matrix of the central nervous system: from neglect to challenge. *Histochem. Cell Biol.* 130, 635-653.

Accepted January 11, 2011

Research Article

TMA Vessel Segmentation Based on Color and Morphological Features: Application to Angiogenesis Research

M. Milagro Fernández-Carrobles,¹ Irene Tadeo,² Gloria Bueno,¹ Rosa Noguera,³ Oscar Déniz,¹ Jesús Salido,¹ and Marcial García-Rojo⁴

¹ VISILAB, E.T.S.I. Industriales, Universidad de Castilla-La Mancha, 13071 Ciudad Real, Spain

² Fundación Investigación Clínico de Valencia, Instituto de Investigación Sanitaria, INCLIVA, 46010 Valencia, Spain

³ Laboratorio de Patología Molecular, Departamento de Patología, Facultad de Medicina y Odontología, Universidad de Valencia, 46010 Valencia, Spain

⁴ Departamento de Anatomía Patológica, Hospital General Universitario de Ciudad Real, 13005 Ciudad Real, Spain

Correspondence should be addressed to M. Milagro Fernández-Carrobles; mmilagro.fernandez@uclm.es and Gloria Bueno; gloria.bueno@uclm.es

Received 31 August 2013; Accepted 17 September 2013

Academic Editors: B. Jasani and A. Matsukawa

Copyright © 2013 M. Milagro Fernández-Carrobles et al. This is an open access article distributed under the Creative Commons Attribution License, which permits unrestricted use, distribution, and reproduction in any medium, provided the original work is properly cited.

Given that angiogenesis and lymphangiogenesis are strongly related to prognosis in neoplastic and other pathologies and that many methods exist that provide different results, we aim to construct a morphometric tool allowing us to measure different aspects of the shape and size of vascular vessels in a complete and accurate way. The developed tool presented is based on vessel closing which is an essential property to properly characterize the size and the shape of vascular and lymphatic vessels. The method is fast and accurate improving existing tools for angiogenesis analysis. The tool also improves the accuracy of vascular density measurements, since the set of endothelial cells forming a vessel is considered as a single object.

1. Background

Angiogenesis is present during development as well as during embryogenesis and during reparative processes for wound healing. It also has a significant role during organ transplantation since new vessel formation can be crucial to successfully prevent allograft rejection. The role of angiogenesis in the pathogenesis of chronic inflammatory diseases is of considerable interest. A positive feedback has been found in which inflammatory state promotes angiogenesis and the angiogenesis in turn facilitates chronic inflammation [1, 2]. There is increasing evidence that chronic inflammation is tightly linked to diseases associated with endothelial dysfunction and plays a role in the induction of aberrant angiogenesis [3]. Lymphatic vasculature is a prerequisite for the maintenance of tissue fluid balance and immunity in the body [4].

It is now widely accepted that tumor growth and metastasis are angiogenesis and lymphangiogenesis dependent providing novel therapeutic targets in malignant disease [5–7].

A common feature of tumor vessels studies is that the investigators focus on microvessel density overlooking other parameters that might be significant, such as the size and shape of the microvessels [8]. In many aspects, tumor vessels are different from normal vessels [9, 10]. Studies have revealed the importance of the size and shape of blood vessels in, for example, laryngeal tumors [11].

To our knowledge, there are only two applications providing vessel closing when the whole perimeter of the vessels is not completely stained, which could be a basic feature in translational research. Aperio's application for angiogenesis analysis [12] is an excellent tool for managing microvessels. This software allows to perform many operations in whole slide images but the closing algorithm is not automatic. For closing vessels the user must draw manually the lost segment on the image. The second algorithm is free and available at <http://www.caiman.org.uk/> [13]. The algorithm cannot process image files larger than 2 MB. Both of them measure shape

parameters but are global measurements; the properties of each microvessel are not calculated individually.

Other works such as van der Laak et al. [14], Tsuji et al. [15], Laitakari et al. [11], Luukka et al. [16], Virgintino et al. [17], and Dagnon et al. [18] have been also developed in order to calculate morphometric measurements in microvessels. Most of them are semiautomatic and require manual interaction. Van der Laak extracts morphometric measurements like area, perimeter, convex perimeter, or circularity in microvessels but when the vessels are not closed a manual correction is performed. Selecting regions of interest and vessels is necessary in Tsuji's work. Virgintino and Dagnon divide the process into two tasks, microvessel selection and measure calculation. Virgintino applies filters and image segmentation techniques for selecting microvessels. Dagnon selects each microvessel manually and works with the grayscale image. Then, measurements of these vessels are calculated using other image analysis software, that is, VIDAS release 2.5 (Kontron Elektronik, Eching, Germany) and ImageJ software (National Institute of Health, USA). These processes do not consider open vessels.

Our aim is to develop a morphometric tool able to perform a segmentation of blood and lymphatic vessels to study vascularization following the hypothesis that tumor prognosis may not only be influenced by microvascular density but also by the shape and size of the vessels. Thus, the tool is able to deal with closed and open vessels and provide morphometric measurements for each detected vessel. Besides, the tool provides two kinds of executions, an automatic execution without user interaction and another where the user can select the vessels to be analyzed. To this end a segmentation algorithm based on two complementary methodologies has been developed to segment closed and open vessels. A description of the materials used for this work can be found in Section 2. Section 2.1 presents the algorithm implementation and how the application works. Section 3 shows the results for the implemented tool, called *AngioPath*, with a comparison of *CAIMAN* tool. Finally, conclusions are drawn in Section 4.

2. Materials and Methods

A dataset of 700 cores extracted from 10 TMA scanned slides was considered. TMA images were formed by several vessels, from 2 to 600 vessels of different sizes and stains. The images have been stained with IHQ technique against D2-40 (lymphatic vessels) and from a previously stained TMA with anti-CD34 antibody (blood vessels). This dataset was prepared with an automatic tissue arrayer composed of 70 cores/TMA and digitized with Aperio ScanScope T2 at 40x. The resolution of Aperio ScanScope T2 at 40x objective is $0.23 \mu\text{m}/\text{pixel}$. Thus, these cores are images at 40x magnification and their size varies between 6200 and 7300 pixels.

Experiments were performed on an Intel Core i7 950 3.07 Ghz and 12 GB RAM. The method has been implemented using C/C++ and the IPP libraries for image processing. Also, the Intel TBB library has been used for parallelization of the algorithms.

TABLE 1: Morphometric measurements.

Measurements	Meaning	Units
Localization	x - y coordinates	Pixels
Area	Vessel contour area	Physical units (μm^2)
Size	Vessel width and height	Physical units (μm)
Perimeter	Perimeter	Physical units (μm)
Angle	Angle between the horizontal axis and the first side (i.e., length)	Radians
Vascular density	$\frac{\text{Number of vessels}}{\text{core}}$	Physical units (vessel number/ μm^2)
Aspect	$\frac{\text{Major axis}^*}{\text{minor axis}}$	
Roundness	$\frac{\text{Perimeter}^2}{4 * \pi * \text{area}}$	
Perimeter ratio	$\frac{\text{Convex perimeter}}{\text{perimeter}}$	
Deformity	Convex area – area	Physical units (μm)
Shape	$\max_{i=1,2} \frac{ m_i^A - m_i^B }{ m_i^A }$	
Vertices	Calculates the approximate contour polygon vessel with less distance between vertices using the Douglas-Peucker algorithm [19]	

$m_i^A = \text{sign}(h_i^A) \cdot \log(h_i^A)$ and $m_i^B = \text{sign}(h_i^B) \cdot \log(h_i^B)h_i^A$. h_i^B are the Hu moments of the normal and convex contour area (A , B), respectively, and i represents the seven Hu invariant moments.

*These axes correspond to the best-fitting ellipsoid of the vessel contour.

2.1. Algorithm Implementation. Histologic sections comprise two types of vessels: vessels with unquestionable endothelial cells completely stained in their perimeter (closed vessels) and vessels whose endothelial cells do not show a completely staining reaction (open vessels). Closed vessels can present vascular lumen or not. However, open vessels must always present a vascular lumen. The database used in this study is composed of both types of vessels. In the case of closed vessels, their morphometric measurements can be easily calculated. The challenge appears when the stain is weak or the vessels are not closed. In the first case, color analysis is needed; in the second case a radial algorithm is also used.

The system developed for vessels segmentation, called *AngioPath*, consists of two parts: (a) color-based segmentation and (b) radial distribution of the vessel contour pixels. The algorithm is illustrated in Figure 1.

Eleven morphometric measurements are calculated for each vessel detected. The measurements describe the shape and geometrical properties of the vessels. They are briefly explained in Table 1. In addition, a summary of the measurements is also provided. The vessels are grouped by their height

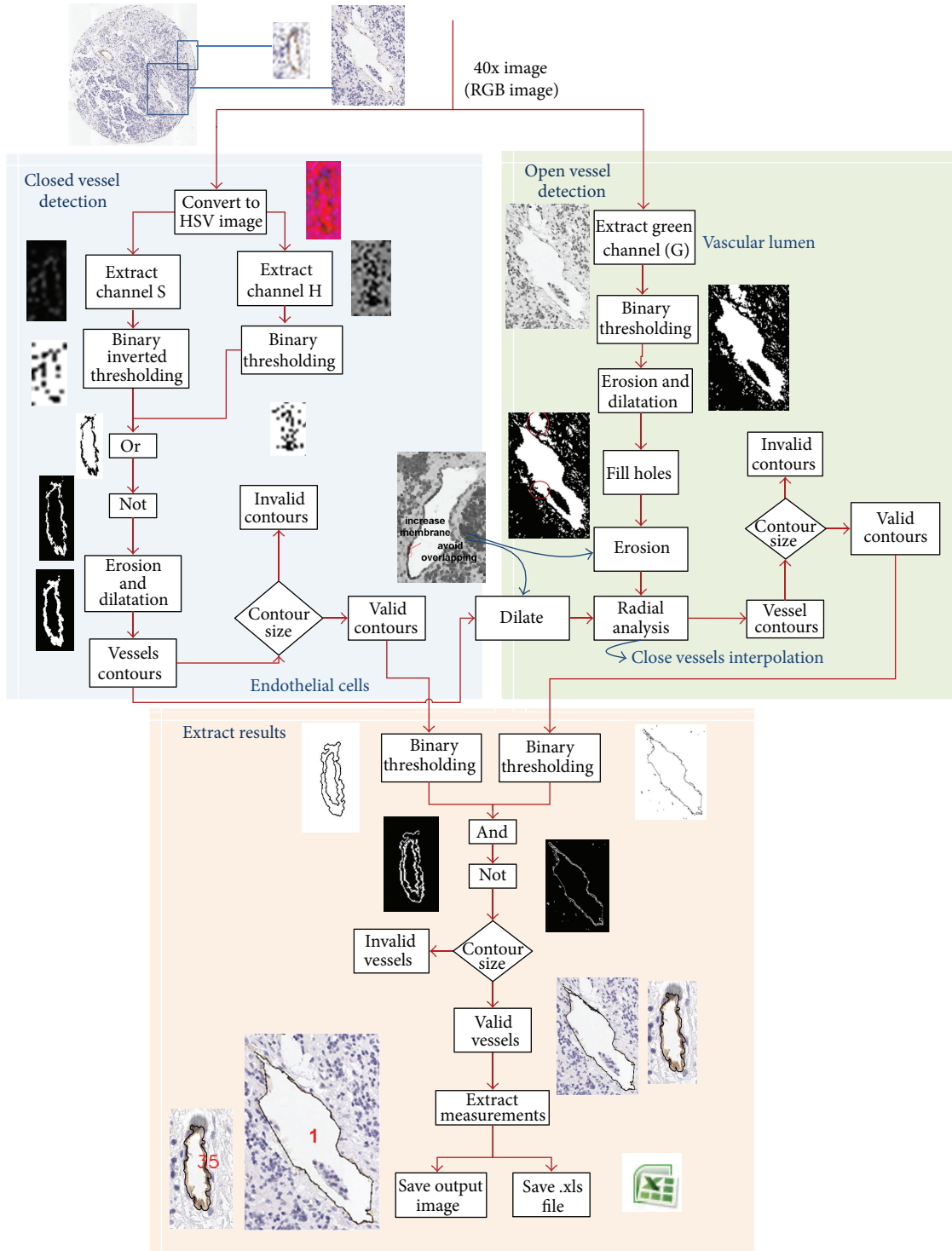


FIGURE 1: TMA blood vessel segmentation process. Division of the algorithm in two steps: first the segmentation based on HSV color model (right) and then the radial algorithm for joining open vessels.

and the measurements are calculated for each group. There are 5 height groups: between [5 and 15 μm), [15 and 20 μm), [20 and 59 μm), [50 and 200 μm), and more than 200 μm . Also, the total area, a percentage of area, and the total number of vessels are calculated for groups. Finally, an average of the

eleven measurements for all vessels is calculated; thus a total of 24 morphometric measurements are provided for all the segmented vessels (see Table 2).

The methods applied for the development of AngioPath are described as follows.

TABLE 2: Summary of measurements.

Height (μm)	Ratio measurements	Total	Percentage	Vessels
[5-15), [15-20), [20-50), [50-200), ≥ 200	$\frac{\sum \text{area of group}_i}{\text{total vessels of group}_i}, \frac{\sum \text{width of this group}}{\text{total vessels of this group}},$ $\frac{\sum \text{height of group}_i}{\text{total vessels of group}_i}, \frac{\sum \text{angle of group}_i}{\text{total vessels of group}_i},$ $\frac{\sum \text{roundness of group}_i}{\text{total vessels of group}_i}, \dots$ <p style="text-align: center;">$(i = 1, \dots, 5)$</p>	Total feature _j in group _i	$\frac{\sum \text{area of group}_i}{\text{total area}} * 100$ <p style="text-align: center;">$(j = 1, \dots, 12)$</p>	Total vessels group _i
Average	$\frac{\sum \text{areas}}{\text{total vessels}}, \frac{\sum \text{width}}{\sum \text{feature}_j}, \frac{\sum \text{height}}{\text{total vessels}}, \dots$	Total area	Total percentage of areas	Total vessels

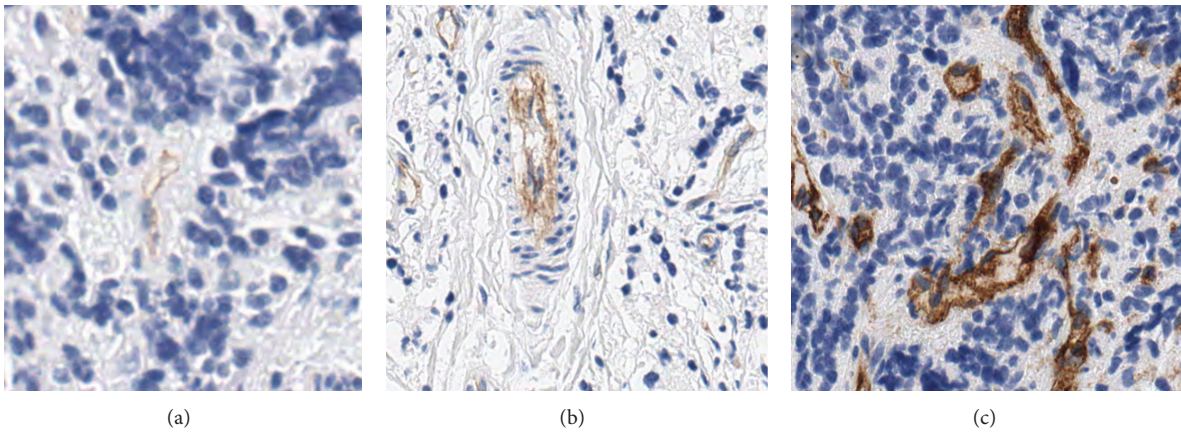


FIGURE 2: Vessels in TMA samples with different degrees of staining. (a) Weak stain, (b) normal stain, and (c) strong stain.

2.1.1. Segmentation Based on HSV Color Model. The objective of this part is brown color segmentation through HSV color model to detect the endothelial cells. Most of the closed vessels can be detected through their brown color. Open vessels undergo a radial analysis after segmentation of their endothelial cells. This algorithm proceeds as follows.

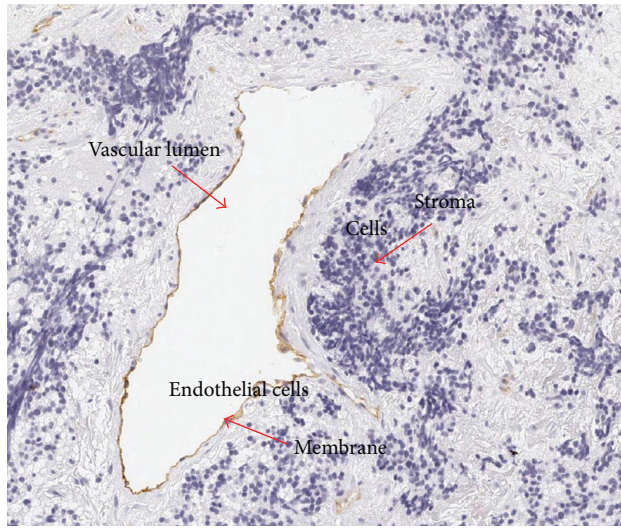
- (1) *Conversion of the RGB TMA Image to the HSV Color Model.* This conversion is useful for segmentation of brown color; in other words, it allows extracting the vascular vessels membrane for both closed and open vessels.
- (2) *Extraction of the S and H Channels from HSV Image.* The S channel contains most of the shades and brown stains, but it is not enough. Therefore, the H channel is also used.
- (3) *Application of a Binary Thresholding to the H Channel Image and a Binary Inverted Thresholding to the S Channel Image.* The thresholding operation makes a comparison between the values of the image pixels and one threshold value. In case of binary thresholding (see (1)) when the value of the pixel, $I(x, y)$, is larger than the established threshold value, T_H , the new pixel, $I'(x, y)$, will take the maximum value M

(with M equal to 255). On the contrary, if the value of $I(x, y)$ is lower than T_H , then $I'(x, y)$ will take value 0:

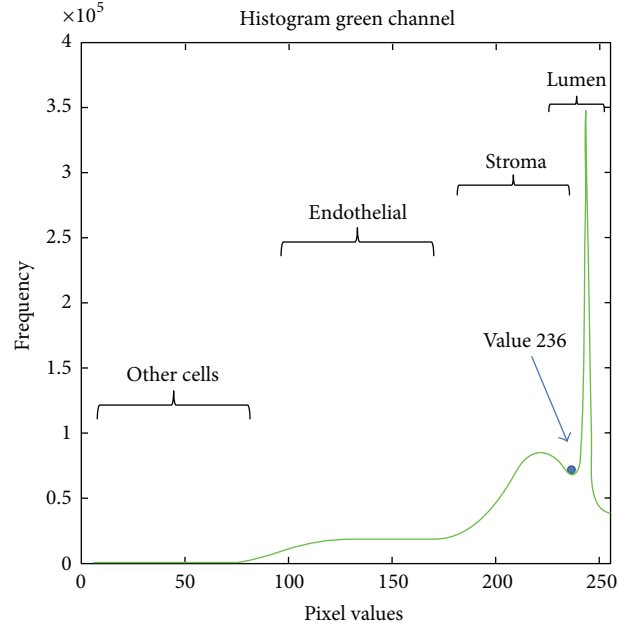
$$I'(x, y) = \begin{cases} M & I(x, y) > T_H, \\ 0 & \text{otherwise.} \end{cases} \quad (1)$$

In the binary inverted thresholding the new pixel values, $I'(x, y)$, are inverted. When the value of $I(x, y)$ in the S color image is larger than the established threshold value, T_S , $I'(x, y)$ will be equal to 0. The pixel values lower than the threshold T_S will take value 255. Threshold values depend on the stain selected. The threshold T_H applied to the H channel is always 20 but the inverted threshold T_S applied to S channel is 10 for weak stains, 20 for normal stains, and 30 for strong stains. Figure 2 shows samples of TMAs with different degrees of stain. Moreover, the user can select manually other values for the T_H and T_S .

- (4) *Application of a Logical OR Operator to Both Binary Images.* This operation segments brown color and erases the rest of the colors.



(a)



(b)

FIGURE 3: Statistical analysis of the TMA structures based on the image histogram. (a) Original TMA sample with the main structures, (b) histogram of the green channel image.

- (5) *Application of a Logical NOT Operator in Order to Invert the Image.* This operation is needed to highlight the contour vessels.
- (6) *Elimination of Small Artifacts of the Input Image and Joining Nearby Structures.* Erosion and dilation operations of 2 and 4 iterations, respectively, are performed in the image. Erosion, $E(x, y)$ (see (2)), is done by means of a convolution where the minimum value of the neighborhood pixels are selected. The erosion allows eliminating small artifacts in the image and therefore reducing false positives. Then, the dual operation to erosion, that is, a dilation, $D(x, y)$ (see (3)), is performed to join nearby structures:

$$E(x, y) = \min_{x', y' \in \text{kernel}} I(x + x', y + y'), \quad (2)$$

$$D(x, y) = \max_{x', y' \in \text{kernel}} I(x + x', y + y'). \quad (3)$$

- (7) *Application of a Contour Finding Operator.* Finally, a contour finding operator is applied to find the core contours. This algorithm computes contours from binary images like images created by a Canny operator, which have edges pixel in them, or images created by a binary thresholding, in which the edges are implicit as boundaries between positive and negative regions. Then, the algorithm retrieves contours from the binary image using the algorithm of Suzuki and Abe [20]. The algorithm allows storing the vessel contour pixels through sequences and manipulating them individually.

- (8) *Discarding Small Artifacts.* Contours whose length is lower than 6 pixels ($1.38 \mu\text{m}$) or their width and height are higher than 20 pixels ($4.6 \mu\text{m}$) are discarded. The remaining contour pixels are the valid vessels.

2.1.2. Radial Distribution of the Vessel Contour Pixels. This algorithm finds the vascular lumen, which is always present in open vessels, and their brown endothelial surrounding cells. Then the unconnected parts of the vessel are joined together. Once the open vessels are closed, the morphometric measurements are calculated. The algorithm proceeds as follows.

- (1) Extraction of the green channel from RGB image, Green channel, I_G , helps to distinguish the different vascular lumens at the TMA core. Besides the use of a single channel can reduce the computational time and also reduce the RAM memory used to process images.
- (2) A binary thresholding is applied for extracting vascular lumens at the I_G image. The threshold value was established at 236. This was done after statistical analysis of the image histogram, where it was found that the vascular lumens have a gray level larger or equal to 236; see Figure 3.
- (3) To join large structures and remove the smaller ones from the previous binary image, a combination of morphological transformations was applied. These transforms were erosion with 3 iterations and dilation with 2 iterations.
- (4) Those closed contours that have internal holes smaller than a minimum size of about $92 \mu\text{m}$ (400 pixels) are filled.

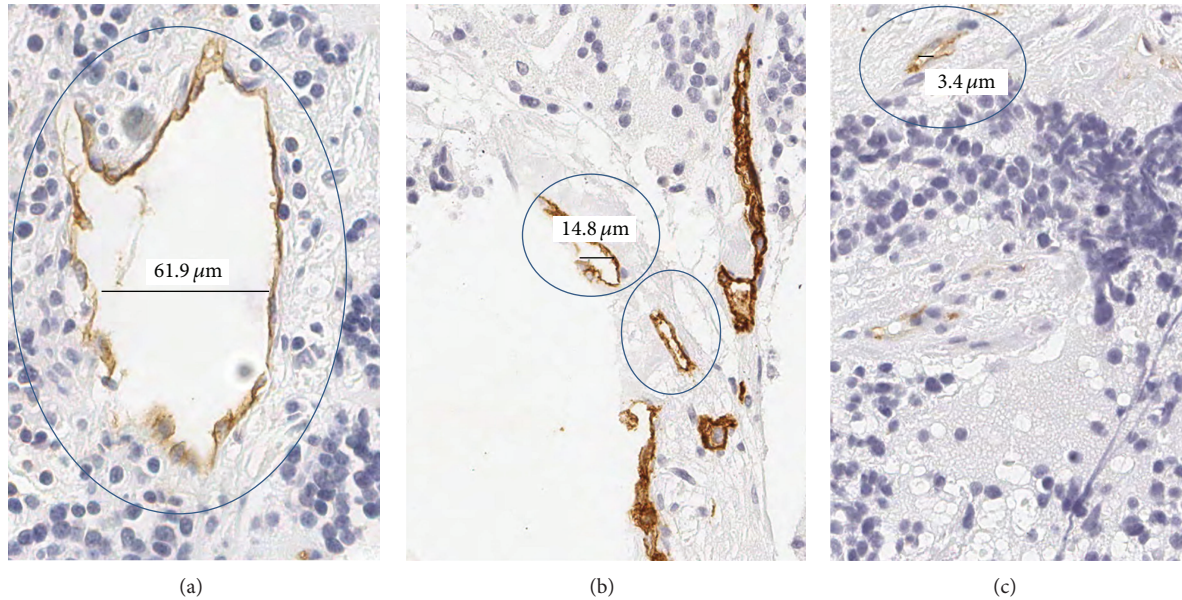


FIGURE 4: Different size of vessels to calculate the radial distribution.

- (5) Again, an erosion of 1 iteration is performed in the image. This erosion allows creating space between the vascular lumen and the vessel membrane.
- (6) Radial analysis consists of computing the normal direction for each vascular lumen point on the border with a possible vessel point. Then, the radial direction is used to check if there is any part of the membrane vessel nearby within a radio of $3 \mu\text{m}$. To this end the endothelial cells detected in the previous algorithm are also used. Notice that a dilatation of 2 iterations is performed to the endothelial cells to avoid overlapping with the vascular lumen.
A vessel is considered valid depending on the ratio of checked pixels that actually belong to the membrane vessel. The ratio is adjusted depending on the length of the vascular lumen contour, being equal to 60%, 50%, and 40% for small, medium, and big vessels, respectively. Small vessels are those with a vascular lumen contour length lower than $12.42 \mu\text{m}$, medium vessels between $12.42 \mu\text{m}$ and $31.05 \mu\text{m}$, and large vessels greater than $31.05 \mu\text{m}$. Figure 4 shows different vessels classified by size. Once a pixel is considered as a valid vessel a linear interpolation is done to close the open vessels.
- (7) Contours finding is a transformation is applied to find the vessel contours obtained in the radial analysis. This procedure is similar to point (7) of the color-based segmentation algorithm.
- (8) The small artifacts are removed. This procedure is similar to point (8) of the color-based segmentation algorithm.

2.1.3. Extraction of Results. At this point, the algorithm provides two images composed of closed and open vessels. In the

following steps both images are joined together and the morphometric measurements are calculated.

- (9) A binary thresholding is applied on the previous two images. This thresholding is performed in order to obtain a binary image with only the vessel contours; therefore the threshold value is 0.
- (10) Application of a logical AND operator to both images combines into the same image those vessels segmented by the HSV color model and those obtained by the radial distribution analysis.
- (11) Application of a logical NOT operator is done in order to invert the image and highlight the contour vessels.
- (12) A contour finding algorithm is applied to find the vessel contours of the final image. This procedure is similar to point (7) of the color-based segmentation algorithm and the radial analysis.
- (13) For each valid vessel, its position by means of its center pixel and twelve morphometric measurements are given. Morphometric measurements are also provided for each group of vessels according to their height.
- (14) The algorithm provides 2 outputs: (a) all morphometric measurements that are saved in an Excel format file and (b) the final image with the vessel segmented and labeled. The final image is stored in a tiff format file.

2.2. How Does the Application Work? AngioPath has an intuitive interface through which the user selects the execution parameters (see Figure 5). These parameters are the following.

- (1) *Type of Execution: Automatic or Manual.* The system provides automatically an output with all vessels

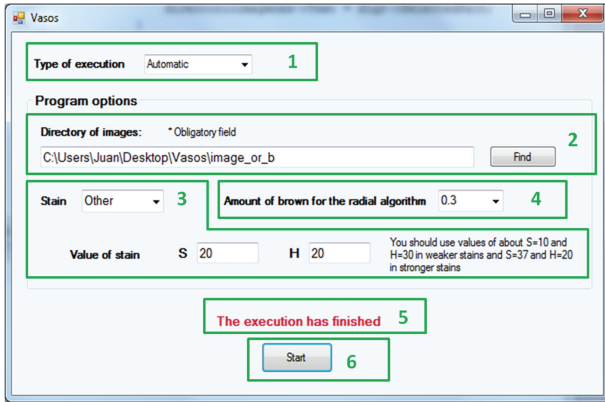


FIGURE 5: AngioPath graphical user interface. Interface parameters that can be selected or modified by the user.

and their morphometric measurements. However, in order to reduce false positives which may occur in the radial analysis, the algorithm allows a manual mode. In manual mode, the user selects the undesired vessels just after the AND operation, see Figure 1. During the execution, a window with the vessels found is displayed. At that time, the undesired vessels are selected. This selection is made with mouse clicks on the center point of the vessel and immediately the selected vessel is marked. When all undesired vessels have been selected the user must press the enter key or close the window and the selected vessels will be removed. Figure 6 illustrates the manual mode with a TMA sample where 5 vessels have been selected as undesired.

- (2) *Directory of Images*. It is compulsory to indicate the directory where the images are stored. To this end, the *Find* option allows browsing through the file system. The path selected is displayed in the corresponding text box.
- (3) *Type of Stain*. The user can make use of default values for the H and S thresholds or rather define them. Default values depend on three different stain options for weak (WS), medium (MS), and strong (SS) stain. The threshold values can also be selected by the user with *Other* option. The interface shows the variables S and H to enter their value when *Other* option is selected. Then, the new threshold values, T_S and T_H , can be entered.
- (4) *Percentage of Stained Vessels*. This option is a list of percentages between 0.1 and 0.9. The user can specify the minimum and maximum amount of endothelial cells needed to close the vessels. Thus, the minimum amount of brown pixels is 0.1 and the maximum amount is 0.9. This percentage is related to the intensity of the stain (see Figure 2).

The system also provides warning labels. There are three types of warnings: (a) if the *Start* option is selected and the directory of images has not been previously selected, (b) if the *Other* option of stain is selected but the threshold values for S

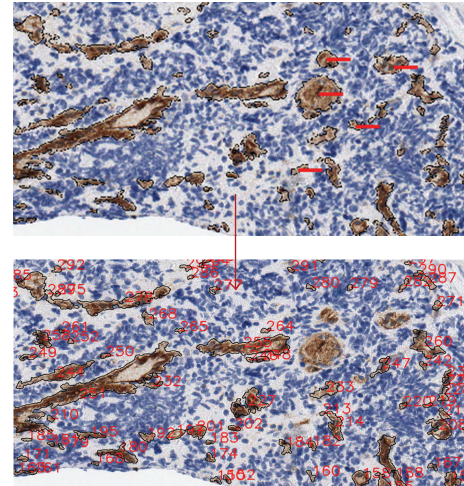


FIGURE 6: Working session with AngioPath in manual mode. Selection of undesired vessels to be eliminated in the TMA image.

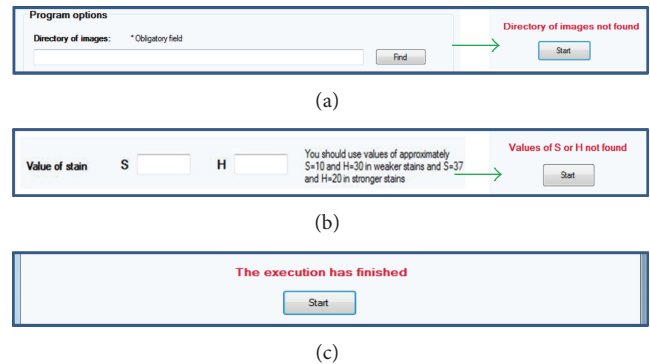


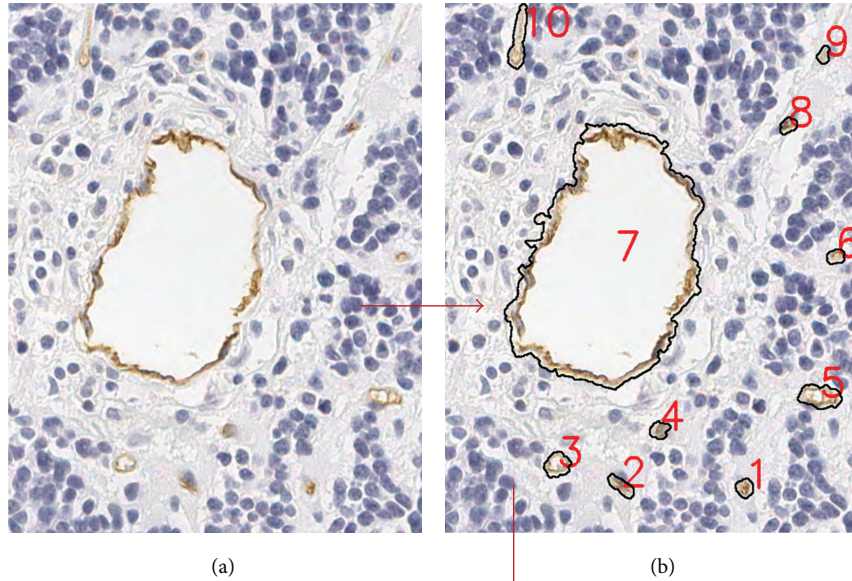
FIGURE 7: Warning labels. (a) *Directory of images not found* is displayed when the *Start* option is selected and the directory of images has not been previously selected. (b) *Values of S or H not found* is displayed when the *Other* option of stain is selected but the threshold values for S or H have not been set and (c) *the execution has finished* is displayed when all the images have been processed.

or H have not been set, and (c) if the process has finished, that is all vessels for all TMA images have been detected and measured. Figure 7 shows the warning labels.

When all the options have been set, the *Start* button initiates the execution. An example of the final result obtained with AngioPath is illustrated in Figure 8. Figure 8 shows a TMA sample with 10 vessels and their morphometric measurements.

3. Results

AngioPath has been compared with the free available algorithm CAIMAN in terms of speed, accuracy, morphometric measurements, and other properties such as the maximum allowed image size and the modes of execution. A summary of the results of this comparison is shown in Table 3. The comparison was done with a subset of 40 TMA subsamples composed of 23 samples from our database and 17 from the CAIMAN database.



Vessel	Pixel_x	Pixel_y	Area	Width	Height	Angle	Roundness	Aspect	Perimeter ratio	Perimeter	Deformity	Shape	Vertices	Group (height size)
1	495	755	36.69	6.54	6.89	-45	1.14	1.06	0.842843	22.94	14.5	0.05	3	1
2	304	752	46.31	4.81	11.91	-53.62	1.58	2.66	0.876089	30.3	47	0.11	2	1
3	206	722	71.03	9.19	10.08	-45	1.3	1.15	0.915282	34.07	69.5	0.01	4	1
4	363	668	36.69	6.93	7.16	-63.43	1.35	1.22	0.911399	24.94	56	0.2	2	1
5	611	618	111.78	9.15	17.03	-87.4	1.54	1.98	0.895175	46.52	167.5	0.08	4	2
6	635	409	30	5.5	6.75	0	1.21	1.36	0.833875	21.4	19	0.06	2	1
7	295	414	5134.69	69.55	97.19	-65.96	2.07	1.55	0.758274	365.75	7312	0.07	8	4
8	562	213	29.09	5.3	7.25	-45	1.27	1.4	0.872457	21.58	24	0.09	2	1
9	618	107	22.63	5.13	6.19	-45	1.34	1.53	0.934005	19.52	27	0.13	2	1
10	148	78	102.34	6.52	24.61	-78.69	2.64	4.63	0.820745	58.31	245	0.25	3	3
Height size	Area	Width	Height	Angle	Roundness	Aspect	Perimeter ratio	Perimeter	Deformity	Shape	Vertices	Total area	% Group area/ total area	Total vessels
5-15	38.92	6.2	8.03	-42.44	1.31	1.48	0.883707	24.96	36.71	0.09	2.43	272.44	4.85	7
15-20	111.78	9.15	17.03	-87.4	1.54	1.98	0.895175	46.52	167.5	0.08	4	111.78	1.99	1
20-50	102.34	6.52	24.61	-78.69	2.64	4.63	0.820745	58.31	245	0.25	3	102.34	1.82	1
50-200	5134.69	69.55	97.19	-65.96	2.07	1.55	0.758274	365.75	7312	0.07	8	5134.69	91.34	1
	562.13	12.86	19.5	-52.91	1.55	1.85	0.866015	64.53	798.15	0.11	3.2	5621.25	100	10

(c)

FIGURE 8: Results provided by AngioPath. (a) Original image. TMA sample with 10 vessels, (b) segmented vessels and labeled and (c) morphometric measurements for each vessel and for each group of vessels according to their height.

Our method takes between 10 and 180 seconds for images with 2 and 600 vessels, respectively. The algorithm accepts images of any size. The average image size of our dataset is 6300×6300 pixels, that is, 120 MB. CAIMAN takes an average of 230 seconds for a 1.5 MB image, that is, about 1200×960 pixels. CAIMAN could not handle the image size of our dataset since the maximum size allowed is 2 MB.

Among the parameters measured, the shape factors roundness and aspect are calculated in both algorithms. Moreover, AngioPath includes perimeter-ratio which represents the regularity of the contour of the vessels and which we found to be related to clinical-biological features in, at least, neuroblastic tumors. AngioPath provides in total 24 morphometric measurements and CAIMAN provides

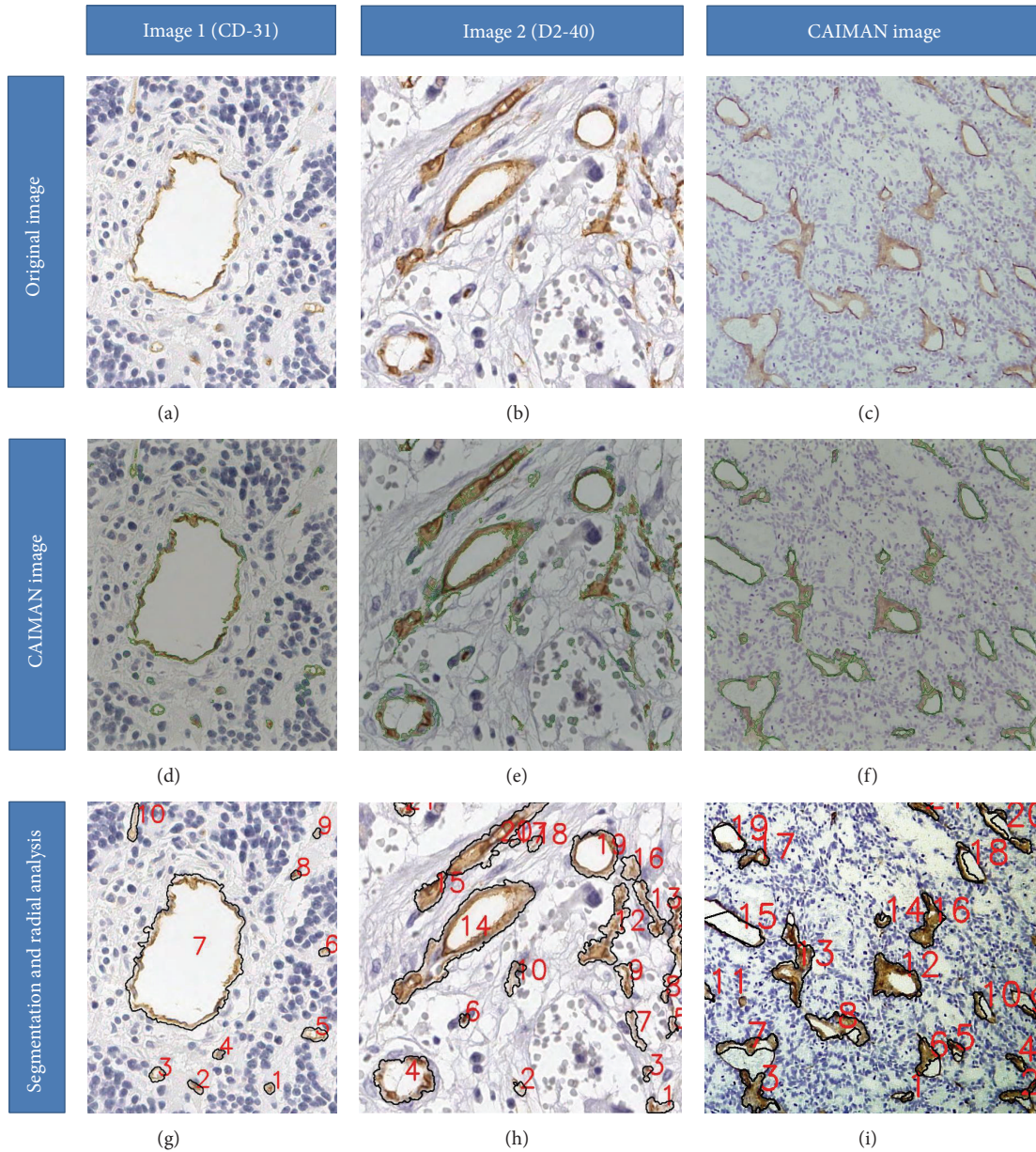


FIGURE 9: CAIMAN application. (1st row) original images: (a) and (b) are images from our database and (c) is an example image provided by CAIMAN with a less-lighted caption. (2nd row) segmentation performed by CAIMAN (green line) which does not detect small or too large vessels (d) and sometimes divide large vessels in small ones or segment blue areas as vessels (e). Their image is well segmented (f). (3rd row) results provided by AngioPath with the color-based segmentation and the radial analysis.

5 morphometric measurements and 2 related to density, that is, the average stained area (lumen excluded) and the average vessel area (lumen included).

Our algorithm runs in manual mode which allows to correlating a measurement with a given vessel and eliminating it. This solves the problem of false positives when segmenting undesired vessels. Both CAIMAN and the tool developed herein show a similar percentage of contour pixels correctly detected in automatic mode, 95.92% and 96.82%, respectively. However, CAIMAN has a larger number of false positives; the

specificity of CAIMAN is 80% against 98.75% of AngioPath. CAIMAN does not detect small or too large vessels and sometimes takes blue areas as vessels. An example of the results obtained with both systems is shown in Figure 9 with 3 TMA subsamples, 2 from our database and 1 from CAIMAN database. CAIMAN provided better results when segmenting images from their own database. The discrepancies could probably be related to a specific and differently designed brown color spectrum given by the stain or the digital image quality. Nevertheless, the morphometric tool described

TABLE 3: Comparison of AngioPath versus CAIMAN.

	AngioPath	CAIMAN
Speed	0.27 s/MB	124 s/MB
Measurements	24 features	7 features
Mode	Automatic & Manual	Automatic
Maximum size	No limit	2 MB
Sensitivity	96.82%	95.92%
Specificity	98.75%	80.00%
Accuracy	97.78%	87.96%

herein has shown better results in speed and accuracy. An average value of 97.78% accuracy was obtained for AngioPath against 87.96% for CAIMAN.

Finally, AngioPath has been validated with 700 cores obtained from whole slide TMA images [21] by means of a ROC analysis. An average of 97% sensitivity and 99% specificity was obtained.

4. Conclusions

This paper has described a morphometric tool implemented to measure different aspects of the shape and size of vascular vessels in a complete and accurate way. The developed tool takes into account both closed and open vessels. Vessel closing is an essential property to properly quantify and characterize the shape and size of vascular and lymphatic vessels. In the same way, the set of endothelial cells forming a vessel are considered together as a single object, making vascular density measurement more accurate. The tool, called AngioPath, is able to detect vessels in whole slide TMA images with an average accuracy of 97.89%. Moreover, AngioPath provides 24 morphometric measurements of the detected vessels.

Although AngioPath has shown encouraging results in the database tested, it may be improved by applying invariant color analysis techniques to properly segment vessels with different stain. By applying this tool it is expected that further studies can be carried out to test whether shape and size measurements are as important for prognosis as literature suggests.

Conflict of Interests

The authors declare that there is no conflict of interests associated with the tools and datasets used in this paper.

Acknowledgments

The authors would like to thank the Pathology services of Hospital Clínico de Valencia and of Hospital General Universitario de Ciudad Real. This work has been carried out with the support of the research projects ISCIII (FIS PI10/15), DPI2008-06071, and ISCIII (RD 06/0020/0102) of the Spanish Research Ministry.

References

- [1] N. Mittal, G. S. M. Shankari, and S. Palaskar, "Role of angiogenesis in the pathogenesis of oral lichen planus," *Journal of Oral and Maxillofacial Pathology*, vol. 16, no. 1, pp. 45–48, 2012.
- [2] X. Tao, Y. Huang, and R. Li, "Assessment of local angiogenesis and vascular endothelial growth factor in the patients with atrophic-erosive and reticular oral lichen planus," *Oral Surgery, Oral Medicine, Oral Pathology, Oral Radiology, and Endodontics*, vol. 103, pp. 661–670, 2007.
- [3] G. Rajashekhar, A. Willuweit, C. E. Patterson et al., "Continuous endothelial cell activation increases angiogenesis: evidence for the direct role of endothelium linking angiogenesis and inflammation," *Journal of Vascular Research*, vol. 43, no. 2, pp. 193–204, 2006.
- [4] S. Nakao, A. Hafezi-Moghadam, and T. Ishibashi, "Lymphatics and lymphangiogenesis in the eye," *Journal of Ophthalmology*, vol. 2012, Article ID 783163, 11 pages, 2012.
- [5] J. Folkman, E. Merler, C. Abernathy, and G. Williams, "Isolation of a tumor factor responsible for angiogenesis," *The Journal of Experimental Medicine*, vol. 133, no. 2, pp. 275–288, 1971.
- [6] E. Ichihara, K. Kiura, and M. Tanimoto, "Targeting angiogenesis in cancer therapy," *Acta Medica Okayama*, vol. 65, no. 6, pp. 353–362, 2011.
- [7] J. D. McAllister and M. S. Cohen, "Role of the lymphatics in cancer metastasis and chemotherapy applications," *Advanced Drug Delivery Reviews*, vol. 63, no. 10–11, pp. 867–875, 2011.
- [8] P. Korokolopoulou, E. Patsouris, N. Kavantzias et al., "Prognostic implications of microvessel morphometry in diffuse astrocytic neoplasms," *Neuropathology and Applied Neurobiology*, vol. 28, no. 1, pp. 57–66, 2002.
- [9] G. Bergers and L. E. Benjamin, "Tumorigenesis and the angiogenic switch," *Nature Reviews Cancer*, vol. 3, no. 6, pp. 410–420, 2003.
- [10] P. Carmeliet and R. K. Jain, "Angiogenesis in cancer and other diseases," *Nature*, vol. 407, no. 6801, pp. 249–257, 2000.
- [11] J. Laitakari, V. Näyhä, and F. Stenbäck, "Size, shape, structure, and direction of angiogenesis in laryngeal tumour development," *Journal of Clinical Pathology*, vol. 57, no. 4, pp. 394–401, 2004.
- [12] I. Aperio Technologies, *Microvessel Analysis Algorithm, User'S Guide @ONLINE*, 2008.
- [13] C. C. Reyes-Aldasoro, L. J. Williams, S. Akerman, C. Kanthou, and G. M. Tozer, "An automatic algorithm for the segmentation and morphological analysis of microvessels in immunostained histological tumour sections," *Journal of Microscopy*, vol. 242, no. 3, pp. 262–278, 2011.
- [14] J. A. van der Laak, J. R. Westphal, L. J. Schalkwijk et al., "An improved procedure to quantify tumour vascularity using true colour image analysis. comparison with the manual hot-spot procedure in a human melanoma xenograftmodel," *The Journal of Pathology*, vol. 184, no. 2, pp. 136–143, 1998.
- [15] T. Tsuji, Y. Sasaki, M. Tanaka, N. Hanabata, R. Hada, and A. Munakata, "Microvessel morphology and vascular endothelial growth factor expression in human colonic carcinoma with or without metastasis," *Laboratory Investigation*, vol. 82, no. 5, pp. 555–562, 2002.
- [16] H. Luukkkaa, J. Laitakari, T. Vahlberg, P. Klemi, F. Stenbäck, and R. Grénman, "Morphometric analysis of Cd34-positive vessels in salivary gland adenoid cystic and mucoepidermoid carcinomas," *Journal of Oral Pathology and Medicine*, vol. 38, no. 9, pp. 695–700, 2009.
- [17] D. Virgintino, P. Monaghan, D. Robertson et al., "An immunohistochemical and morphometric study on astrocytes and microvasculature in the human cerebral cortex," *The Histochemical Journal*, vol. 29, no. 9, pp. 655–660, 1997.

- [18] K. Dagnon, D. Heudes, J. F. Bernaudin, and P. Callard, "Computerized morphometric analysis of microvasculature in non-small cell lung carcinoma," *Microvascular Research*, vol. 75, no. 1, pp. 112–118, 2008.
- [19] D. Douglas and T. Peucker, "Algorithms for the reduction of the number of points required to represent a digitized line or its caricature," *Cartographica*, vol. 10, no. 2, pp. 112–122, 1973.
- [20] S. Suzuki and K. Abe, "Topological structural analysis of digitized binary images by border following," *Computer Vision, Graphics and Image Processing*, vol. 30, no. 1, pp. 32–46, 1985.
- [21] M. Fernández-Carrobles, G. Bueno, O. Déniz, J. Salido, and M. García-Rojo, "Automatic handling of tissue microarray cores in high-dimensional microscopy images," *IEEE Journal of Biomedical and Health Informatics*, 2013.

Quantitative modeling of clinical, cellular, and extracellular matrix variables suggest prognostic indicators in cancer: a model in neuroblastoma

Irene Tadeo¹, Marta Piqueras², David Montaner³, Eva Villamón², Ana P. Berbegall², Adela Cañete⁴, Samuel Navarro² and Rosa Noguera²

BACKGROUND: Risk classification and treatment stratification for cancer patients is restricted by our incomplete picture of the complex and unknown interactions between the patient's organism and tumor tissues (transformed cells supported by tumor stroma). Moreover, all clinical factors and laboratory studies used to indicate treatment effectiveness and outcomes are by their nature a simplification of the biological system of cancer, and cannot yet incorporate all possible prognostic indicators.

METHODS: A multiparametric analysis on 184 tumor cylinders was performed. To highlight the benefit of integrating digitized medical imaging into this field, we present the results of computational studies carried out on quantitative measurements, taken from stromal and cancer cells and various extracellular matrix fibers interpenetrated by glycosaminoglycans, and eight current approaches to risk stratification systems in patients with primary and nonprimary neuroblastoma.

RESULTS: New tumor tissue indicators from both fields, the cellular and the extracellular elements, emerge as reliable prognostic markers for risk stratification and could be used as molecular targets of specific therapies.

CONCLUSION: The key to dealing with personalized therapy lies in the mathematical modeling. The use of bioinformatics in patient-tumor-microenvironment data management allows a predictive model in neuroblastoma.

To clearly distinguish the heterogeneous spectrum of clinical, histological, and molecular markers of cancer, and thereafter determine the markers essential to diagnosing the degree of malignancy and predicting response to therapy, remains a difficult challenge. These essential markers may be elucidated by considering the patient's organism and transformed tissues as holistically interconnected and dependent on microenvironment interactions via biochemical and biophysical signals (1). Mathematical models enable us to integrate measures made at different levels and generate from relatively simple to highly complex computational descriptors

of the disease process of human tumors (2). Digitization of clinical data is necessary to deal with the complex hallmarks of cancer (3). To achieve personalized therapy, wellness and image-defined risk factors must be quantified (4). Hanahan and Weinberg have proposed that eight hallmarks of cancer together constitute an organizing principle that provides a logical framework for understanding the remarkable diversity of neoplastic diseases (5,6). A novel ninth hallmark which includes the aspect of physics has recently been emphasized (7). The identification of these hallmarks by quantifying the structural variations in tumor tissues, at diagnosis as well as during tumor progression and after treatment, using whole histological sections or tissue microarrays with the human eye is a challenging process (8). However, the difficulty can be overcome by forming morphometric data to represent the histological texture and classify the structural changes via sophisticated computational methods (9–11). Cancer cell behavior is altered due to an accumulation of both genetic and epigenetic changes that influence a variety of cellular functions. At the same time, the transformed cells are committed in a complex interaction with the surrounding tumor microenvironment. The tumor microenvironment is comprised of a variety of cell types, lying among a dense network of various extracellular matrix (ECM) fibers merged within the interstitial fluid and gradients of several chemical species, which constantly interplay with malignant cells (12). The stromal cells provide a rich source of growth factors and cytokines, and play a crucial role in modifying the existing connective tissue and depositing new matrix. Tissue scaffolds regulate cell behavior and influence tumor progression (5–7,12,13). Biomathematical analysis of promising biomarker candidates, such as genomic, transcriptomic, proteomic, and epigenomic changes, at the tumor tissue level will play an important role in developing a more powerful mathematical modeling of tumor–microenvironment interactions (14,15). The information obtained can then be linked to tumor progression in patients either refractory to current therapy, or who relapse or who might benefit from novel therapies

The first two authors contributed equally to this work.

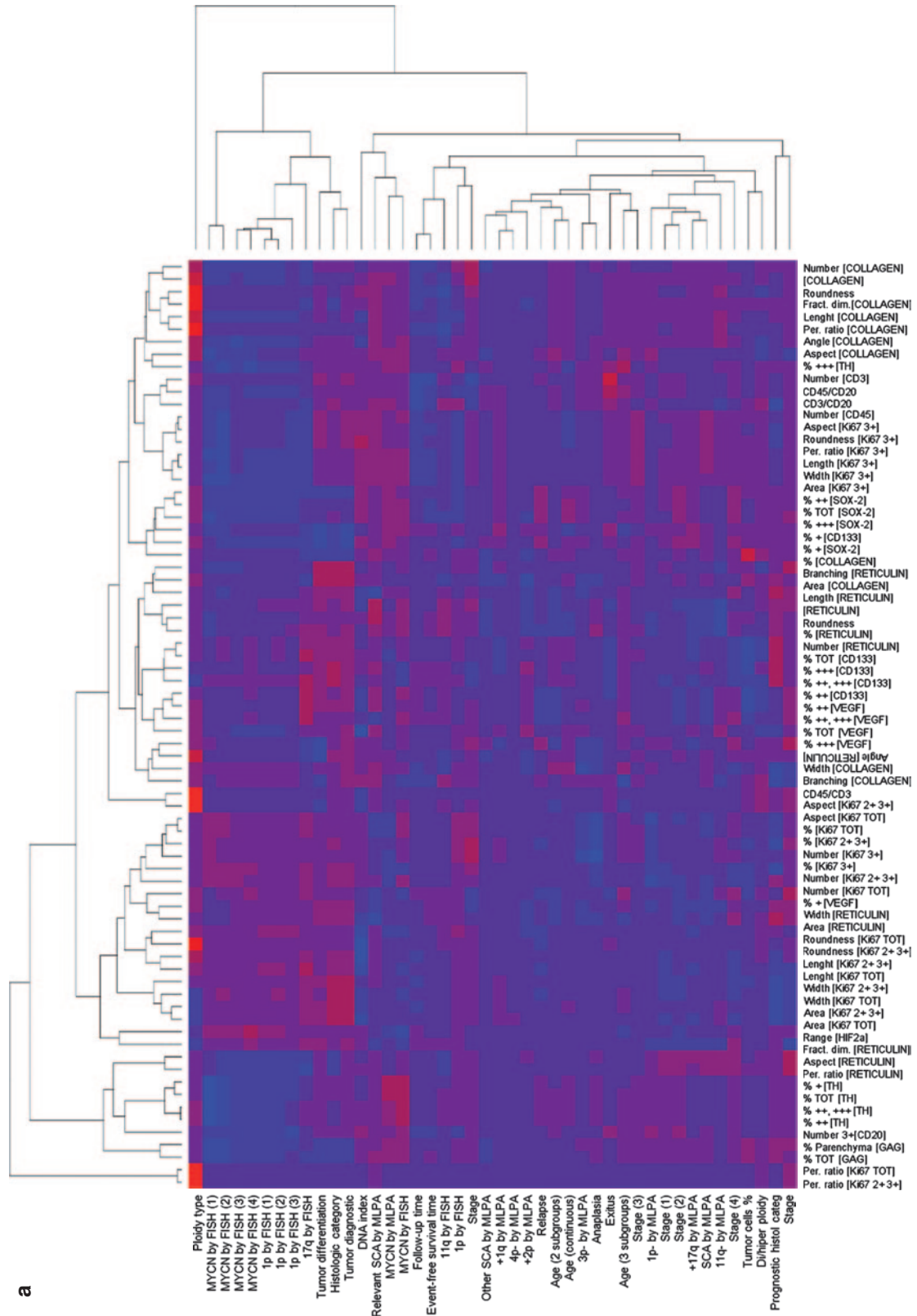
¹Medical Research Foundation INCLIVA, Hospital Clínico, Valencia, Spain; ²Pathology Department, Medical School, University of Valencia, Valencia, Spain; ³Department of Bioinformatics and Genomics, Príncipe Felipe Research Center (CIPF), Valencia, Spain; ⁴Pediatric Oncology Unit, Hospital Universitario y Policlínico La Fe, Valencia, Spain.

Correspondence: Rosa Noguera (rosa.noguera@uv.es)

Received 13 March 2013; accepted 9 June 2013; advance online publication 22 January 2014. doi:10.1038/pr.2013.217

at an earlier stage, in addition to, or instead of, current strategies (16,17). Nevertheless, the mathematical integration of information acquired from clinical and tumor microenvironment interactions into a common description is as difficult to achieve as it is to understand the underlying complexities of

the tumor biology itself, and requires translational researchers, experimentalists and biomathematicians (18,19). Due to the diverse behavior exhibited by neuroblastoma tumors, an algorithm of clinical, histopathological and genetic factors to stratify risk assessment and delineate therapeutic decisions has



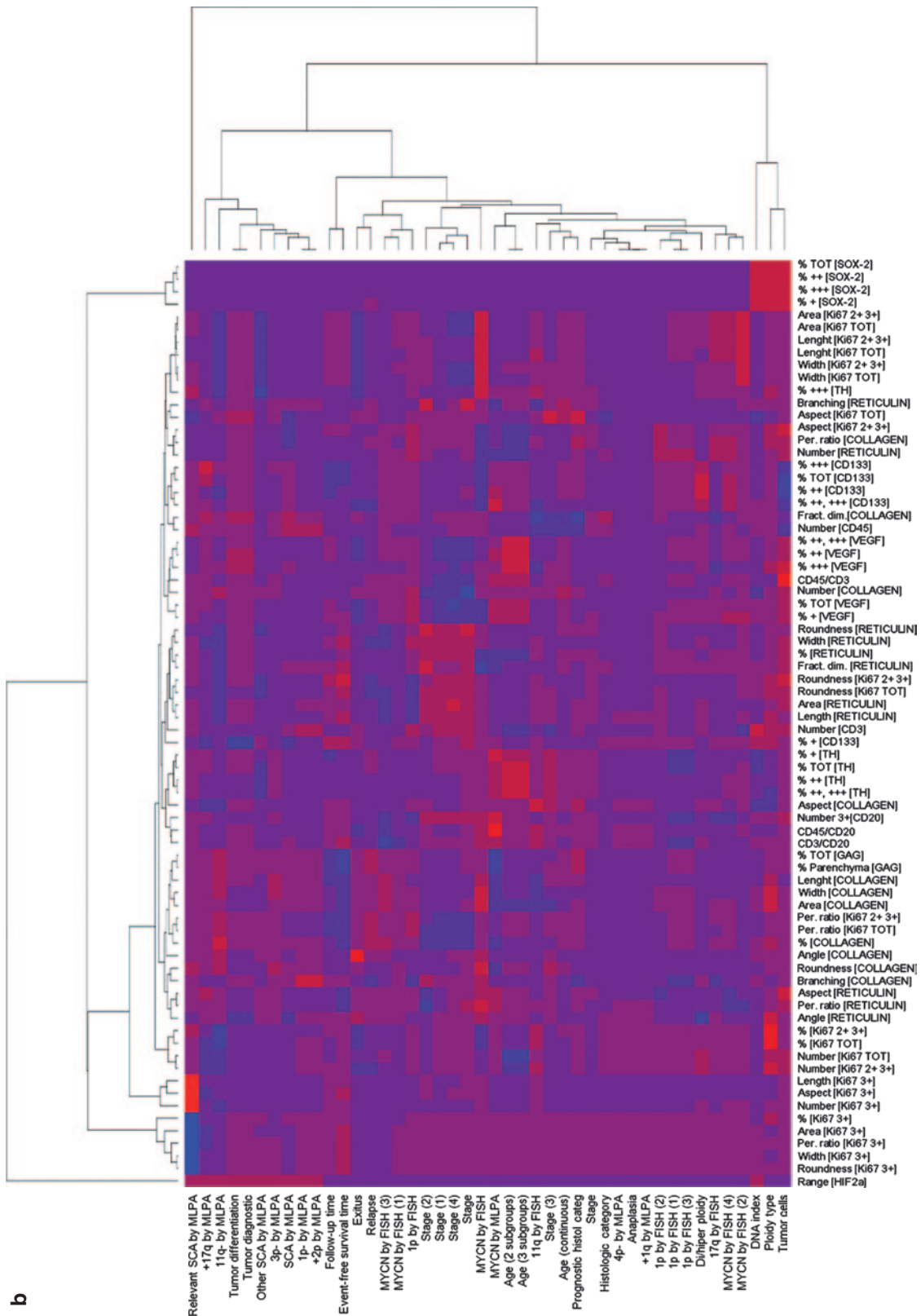


Figure 1. Heatmap clustering indicating the statistical relationship between established prognostic markers and the tumor tissue markers analyzed in (a) primary and (b) nonprimary neuroblastomas. Standard hierarchical clustering showing the correlation in two colors: red (negative) and blue (positive). Statistically significant levels are indicated by the gradient between these two colors; brighter colors represent higher significance. Differences were considered statistically significant for P values <0.05 .

Table 1. Summary of statistically significant relationships between factors used for current risk stratification and several of the tumor tissue markers analyzed in primary tumors

	Clinical			Histopathological			Genetics					
	Alive patients	Localized tumors ^a	Disease-free patients	Few neuroblasts	Not anaplastic	GN and iGNB ^a	Absent or scarce SCA ^a	MYCN nonamplified ^a	17q not gained	1p36 not deleted	11q not deleted ^a	Aneuploidy ^a
ECM												
Fibers	—	—	—	—	—	—	High (P = 0.038)	—	—	—	—	—
Nets	—	—	—	—	—	—	—	—	—	—	—	—
% Reticulin	—	—	—	—	—	—	—	—	—	—	—	—
Aspect reticulin	—	Ovoid (P = 0.049)	—	—	—	—	—	—	—	—	—	—
Fractal dimension reticulin	—	Regular (P = 0.038)	—	—	—	—	—	Regular (P = 0.043)	—	—	—	—
Perimeter-ratio reticulin	—	Regular (P = 0.038)	—	—	—	—	—	Regular (P = 0.038)	—	Regular (P = 0.038)	—	—
% Collagen	—	—	—	High (P = 0.020)	—	—	—	—	—	—	—	—
Thick bundles	—	—	High (P = 0.038)	—	—	—	—	—	—	—	—	—
No./mm ² collagen	—	—	—	—	—	—	—	—	—	—	—	—
% GAG	—	High (P = 0.048)	—	High (P = 0.019)	—	High (P = 0.013)	High (P = 0.048)	High (P = 0.038)	—	High (P = 0.034)	—	—
% Ki-67 ⁺ (3+)	—	—	—	—	Low (P = 0.019)	—	—	—	—	—	—	—
Ground substance	—	—	—	—	—	—	—	—	—	—	—	—
Nuclear size	—	—	—	—	—	Small (P = 0.038)	—	—	—	—	—	—
Ki-67 ⁺ (total+ and 2+ plus 3+)	—	—	—	—	—	—	—	—	—	—	—	—
perimeter-ratio Ki-67 ⁺ (total+ and 2+ plus 3+)	—	—	—	—	—	—	—	—	—	—	—	Irregular (P = 0.019)
Differentiation %TH ⁺	—	—	—	—	—	—	—	High (P = 0.016)	—	—	—	—
Hypoxia No. HIF-2 α ⁺	—	—	—	—	—	—	—	Low (P = 0.013)	—	—	—	—
Immune Subgroup lymphocytes	High (P = 0.045)	—	—	—	—	—	—	—	—	—	—	—
CD45 ⁺ /CD20 ⁺	—	—	—	—	—	—	—	—	—	—	—	—
B lymphocytes No. CD20 ⁺	High (P = 0.038)	—	—	—	—	—	—	High (P = 0.038)	High (P = 0.038)	High (P = 0.038)	—	—

—: Not statistically significant.

ECM, extracellular matrix; GAG, glycosaminoglycan; GN, ganglioneuroma; HIF-2 α , hypoxia-inducible factor-2 α ; iGNB, intermixed ganglioneuroblastoma.

^aFactors used for current risk stratification.

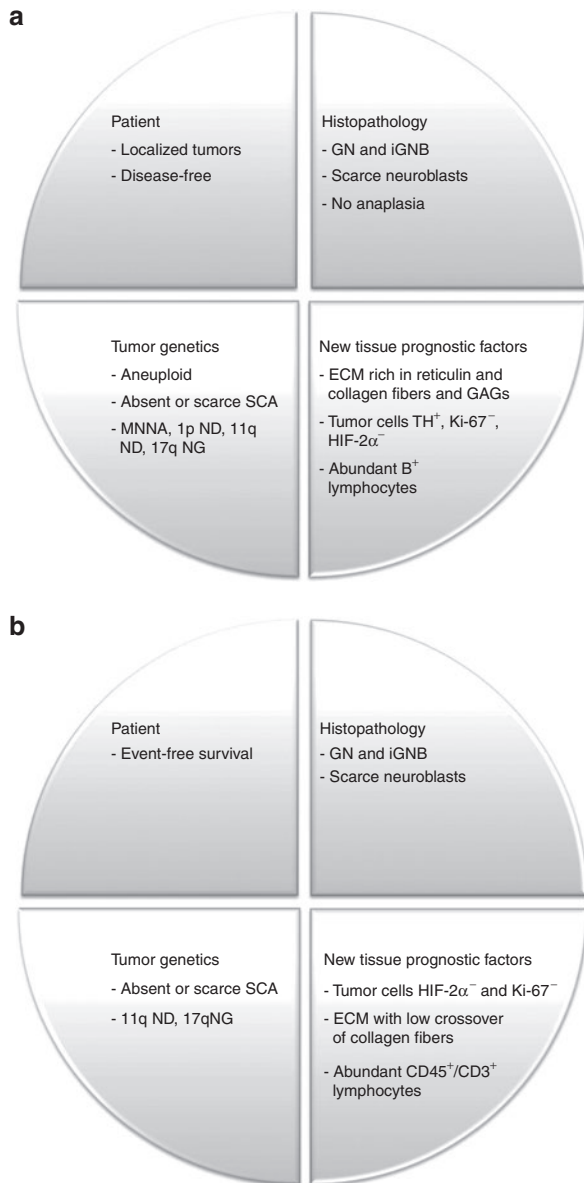


Figure 2. Mathematical modeling of (a) primary and (b) nonprimary neuroblastomas. Synopsis of patient characteristics with better outcome, considering histopathology, tumor genetics, and tumor tissue prognostic factors. ECM, extracellular matrix; GAGs, glycosaminoglycans; GN, ganglioneuroma; iGNB, intermixed ganglioneuroblastoma; SCA, segmental chromosomal aberrations.

been devised. Prognostic systems are based on a combination of patient age at diagnosis (age cut-off 18 mo); disease stage defined by the International Neuroblastoma Risk Grouping Staging System or the International Neuroblastoma Staging System (20); on histopathological information; *MYCN* copy number and segmental chromosomal aberrations (SCA) such as 1p deletion (D) 11q aberrations or 17q gain (G) (21); and sometimes DNA ploidy. Accordingly, treatment protocols can vary widely (22). The use of precise quantification by imaging technology of pathology specimens to analyze the structural variations emerging from interactions between cells and ECM elements is a sensitive, objective, and reproducible method that can provide important information for inclusion

in computational formulations for risk stratification systems. To illustrate some of these principles, we present the mathematical integration of multimodal data, combining imaging and nonimaging clinical and tumor tissue data, acquired in the context of neuroblastoma studies, suggesting testable hypotheses for making prognostic predictions. Harnessing the synergy of the various forms of data, including clinical variables and biomarker profiles, will allow mathematical predictive models to form part of the holistic approach to medicine in the 21st century.

RESULTS

Combined multiparametric analysis gives us an idea about the relationship between the objectively and subjectively quantified histological features and the clinical and genetics data. In **Figure 1** the bright colors show some tumor tissue indicators from transformed neuroblastic cells and the cellular and the extracellular compartment, emerging statistically as reliable prognostic markers in primary (PT) and nonprimary tumors (N-PT) (**Figure 1a,b** respectively).

These results represent an assessment of prognostic criteria based on classical clinical, histological, and growth patterns (age and stage, amount of Schwannian stroma, neuroblastic cell differentiation, and mitosis-karyorrhexis index) and established genetics (*MYCN* status).

Primary Tumors

A summary of statistically significant relationships between the established prognostic markers (clinical, histopathological, and genetic parameters) and tumor tissue markers (ECM elements and tumor and immune cells) with good prognostic impact in PT is presented in **Table 1**. With respect to established prognostic markers and ECM, a high percentage of reticulin fibers were associated with neuroblastomas with absent or scarce SCA, ovoid reticulin nets were related to localized tumors indicating their crosswise arrangement, and regular reticulin nets were present in localized tumors, tumors without 17q gain (NG) and 11q nondeleted (ND). In addition, tumors with scant neuroblasts, as well as PT from disease-free patients, were surrounded by a large amount of collagen fibers. A high quantity of glycosaminoglycans was also associated with localized tumors, ganglioneuroma (GN) and intermixed ganglioneuroblastoma or tumors with very few neuroblasts, absent or scarce SCAs, *MYCN* nonamplified (MNNA) nor 1p36 deletion (D). Biomathematical analyses also revealed that Ki-67⁺ cells from GN and intermixed ganglioneuroblastoma had small nuclei, whereas tumors without anaplasia presented low expression of Ki-67 and aneuploid tumors showed irregular Ki-67⁺ cell nuclei. In addition, MNNA tumors expressed a high amount of TH and low amount of hypoxia-inducible factor-2 α (HIF-2 α ⁺). Regarding immune cells, a higher quantity of CD20⁺ cells was observed in tumors MNNA, without 1p36 deletion, and PT from alive patients when compared with *MYCN* amplification (A), 1p36 D and PT from deceased patients. **Figure 2a** outlines the characteristics of neuroblastoma patients having a better outcome, considering new and established prognostic markers.

Table 2. Summary of statistically significant relationships between the established hallmarks for current risk stratification and a few of the tumor tissue markers analyzed in nonprimary tumors

				Clinical		Histopathological		Genetics			
				Alive patients	Event-free survival	Few neuroblasts	GN and iGNB ^a	Absent or scarce SCA ^a	17q not gained	11q not deleted ^a	
ECM	Fibers	Thick bundles	Angle collagen	Low (<i>P</i> = 0.012)	—	—	—	—	—	—	
Cells	Tumor	Proliferation	% Ki-67 3 ⁺	—	—	—	—	Low (<i>P</i> = 0.000)	—	Low (<i>P</i> = 0.027)	
			No. mm ² Ki-67 3 ⁺	—	—	—	—	High (<i>P</i> = 0.000)	—	—	
			Nuclear size Ki-67 3 ⁺	—	Small (<i>P</i> = 0.003)	—	—	Small (<i>P</i> = 0.000)	Small (<i>P</i> = 0.019)	—	—
			Aspect Ki-67 3 ⁺	—	Ovoid (<i>P</i> = 0.004)	—	—	—	Ovoid (<i>P</i> = 0.002)	—	—
			Perimeter-ratio Ki-67 3 ⁺	—	Irregular (<i>P</i> = 0.004)	—	—	Irregular (<i>P</i> = 0.000)	Irregular (<i>P</i> = 0.000)	—	—
			Roundness Ki-67 3 ⁺	—	Round (<i>P</i> = 0.004)	—	—	Round (<i>P</i> = 0.000)	Round (<i>P</i> = 0.007)	—	—
			Hypoxia	No. HIF-2 α ⁺	—	—	—	Low (<i>P</i> = 0.000)	—	—	—
Immune	Subgroup lymphocytes	CD45 ⁺ /CD3 ⁺	—	—	High (<i>P</i> = 0.026)	—	—	—	—		

GN, ganglioneuroma; HIF-2 α , hypoxia-inducible factor-2 α ; iGNB, intermixed ganglioneuroblastoma; SCA, segmental chromosomal aberrations.

^aFactors used for current risk stratification.

Nonprimary Tumors

A summary of the statistically significant relationships between the data in N-PT is presented in **Table 2**. The integration of digitized multimodal data showed that tumors from alive patients presented low crossover of the thick bundles of collagen. In addition, tumors without 11q D and with absent or scarce SCA showed a low amount of Ki-67 positive cells. The Ki-67⁺ cells had small, round and irregular nuclei in tumors with 17q NG, absent or scarce SCA, as well as tumors from patients with long event-free survival. Moreover, GN and intermixed ganglioneuroblastoma had a low amount of HIF-2 α ⁺ cells, whereas tumors with scant neuroblasts presented a high CD45⁺/CD3⁺ cell ratio (*P* = 0.026). **Figure 2b** represents the predictive guide for N-PT in neuroblastoma patients with better outcome.

DISCUSSION

We outline the benefit to clinical practice of combining established prognostic clinic-biological markers, and medical imaging technology of tumor tissue elements, in a digitized form, using primary and nonprimary neuroblastoma as an example. The hallmarks of cancer constitute an organizing principle for rationalizing the complexities of neoplastic disease. They include sustaining proliferate signaling, evading growth suppressors, avoiding immune destruction, resisting cell death, enabling replicate immortality, inducing angiogenesis, deregulating cellular energetics, activating invasion and metastasis, and physical interactions of cancer cells with their microenvironments (5–7). To study

the hallmarks, several concepts have been proposed and considered at different scales of complexity, such as protein interactions, biochemical pathways, cellular functions, or whole organism studies (2,18). The mathematical model in which the whole organism is the principal modeling unit is most intricate and implies the intercorrelation of data from patients, tumor and stromal cells, and extracellular tumor matrix. Clinical data used to construct classifiers in cancer can be transformed into mathematical descriptors, based, at least in part, on medical images for inclusion in whole organism modeling (1,23,24). In fact, in neuroblastoma it has become crucial to evaluate the clinical significance of imaging in detecting PT stage and residual disease in quality-controlled prospective clinical trials. The International Neuroblastoma Risk Grouping has developed a staging system based on preoperative features, since diagnostic images provide more robust and reproducible data than those based on operative findings and approaches (20). This new staging system is not intended to be a substitute for the International Neuroblastoma Staging System, and currently, it is recommended that both systems be used in parallel during a transitional period. We utilized the widely used International Neuroblastoma Staging System to define the tumor stage of our retrospective cohort, based on the age of the patient at diagnosis, local and distant extent of the disease, and the resectability of the tumor. Recognition of the widespread applicability of image-defined risk factors (25) as well as other computational clinical data will increasingly affect the development of mathematical models with

Table 3. Summary of cases with relevant clinical, histopathological, and genetic prognostic factors

Clinical data	Histopathological data ^a	Genetic data ^b
PT/N-PT	PT/N-PT	PT/N-PT
Age at diagnosis (months) ≤18 ^c	Histologic category (INPC)	FISH (INRG) ^d
28.0 ± 34.3/41.8 ± 44.4	Neuroblastoma (NB): 70/13	Status MYCN gene ^e :
≤18: 37/4; >18: 40/8	Nodular ganglioneuroblastoma (nGNB): 1/0	MNNA: 33/5;
≤12: 29/4; 13–18: 8/0; >18: 40/8	Intermixed ganglioneuroblastoma (iGNB): 4/0	G: 8/3;
Stage (INSS) 1; 2; 3; 4: 4s ^c	Ganglioneuroma (GN): 2/1	hetA: 5/1;
1: 18/1; 2: 3/0; 3: 15/5; 4: 35/5; 4s: 6/2	Grade of tumor differentiation ^c	homA: 31/5
1 + 2: 21/1; 3 + 4: 50/10; 4s: 6/2	Undifferentiated (u): 22/1	11q deletion ^c :
Relapse	Poorly differentiated (pd): 44/11	ND: 57/8; D: 15/4
N: 52/6; Y: 26/7	Differentiating (d): 4/1	1p deletion:
Event-free survival time (months)	Not otherwise specified (NOS): 1/1	ND: 32/5; I: 1/1; D: 39/8; I + D: 2/0
40.3 ± 36.4/54.3 ± 48.8	Diagnostic	17q gain:
Exitus	uNB: 22/1	NG: 30/2; G: 44/11
N: 48/9; Y: 30/4	pdNB: 44/11	MLPA/aSNP (INRG) ^d
Follow-up time (months)	dNB: 2/0	MYCN amplification
46.2 ± 36.1/68.3 ± 44.2	NOS NB: 1/1	N: 31/3; Y: 21/2
	nGNB: 1/0	SCA
	iGNB: 4/0	N: 19/2; Y: 33/3
	Prognostic histologic category (INRG) ^c	Number of SCA
	GN + iGNB: 6/1	1.7 ± 1.7/1.2 ± 1.3
	nGNB + dNB: 6/0	Deletion
	pdNB + uNB: 66/12	1p: 26/2; 3p: 4/1; 11q: 12/2
	Tumor cells (%)	Gain
	60.3 ± 21.5/54.6 ± 23.8	1q: 3/0; 2p: 16/2; 17q: 29/3
	Anaplasia	Other SCA
	N: 75/14; Y: 2/0	N: 46/5; Y: 4/1
		DNA index ^e D; T; Te; P; O ^c
		1.6 ± 0.4/1.3 ± 0.4
		D: 19/3; T: 16/4; Te: 3/2; P: 2/0; O: 7/3
		D + Te: 22/5; T + P: 18/4; O: 7/3

D, diploid; GN, ganglioneuroma; hetA, heterogeneous amplification; homA, homogeneous amplification; I, imbalance; INRG, International Neuroblastoma Risk Group; INPC, International Neuroblastoma Pathology Classification; INSS, International Neuroblastoma Staging System; N, no; N-PT, nonprimary tumors; O, other; P, pentaploid; PT, primary tumors; SCA, segmental chromosomal aberrations; T, triploid; Te, tetraploid; Y, yes.

^aThe histology category was determined according INPC (37) and the INRG (22). ^bGenetic results were interpreted following INRG Biology Committee guidelines (21,34,35); mean ± standard deviations results from quantitative variables. ^cFactors used for current risk-adapted therapy. ^dFluorescence *in situ* hybridization (FISH), multiplex ligation–dependent probe amplification (MLPA), and single-nucleotide polymorphisms arrays (aSNP) were performed to detect genetic aberrations in tumor cells, as previously described (36,38,39). ^eDNA index was measured using image cytometry.

the whole organism as the modeling unit, and not limited to neuroblastoma alone, but applicable also to other neoplastic diseases.

Technologies for digitizing pathology specimens have advanced significantly in the last decade (8,11,26). Slide scanners are capable of producing high-magnification high-resolution images from whole slides and tissue microarrays within a few minutes. Hence, it is becoming increasingly feasible for basic, clinical and translational research studies to produce thousands of slide images (27). It is fundamental to have a reliable and objective method for precise and quantitative

comparison (28,29). We used fast and accurate methods for digitization and objective quantification. Computer-aided evaluation of pathology image analysis to generate risk stratification have been developed for lymphoma (30), glioblastoma (14), breast and prostate cancers (4). A computer-based grading system to support diagnosis for neuroblastoma that uses grades of differentiation and stromal development was published (29,31). Discrimination of stroma-poor and stroma-rich regions has also been reported using a mathematical model performed on digitized hematoxylin-eosin stained whole-sections with extraction of textural features (32). Genome

Table 4. Tissue markers with possible prognostic impact for novel treatment schemes

Antibody	Function	HC ^d and IHC ^c : dilution (source)	Algorithm
Reticulin fibers ^a	Delicate support net	Gomori ^d	IPP
Collagen fibers ^a	Thick support bundles	Masson's trichrome ^d	IPP
GAGs ^b	Diffusion, barrier–matrix interactions	Alcian blue ^d	PPC
Ki-67 ^a	Nuclear protein for cellular proliferation	1/50 (Dako) ^e	IPP
TH ^b	Enzyme catalyzing the conversion of L-tyrosine to L-DOPA	1/30 (Novus) ^e	PPC
VEGF ^{b,c}	Signal protein stimulating vasculogenesis and angiogenesis	1/100 (Santa Cruz Biotechnology) ^e	PPC
HIF-2 α ^c	Transcription factor responding to changes in available oxygen in ECM	1/1000 (Novus) ^e	—
CD133 ^{b,c}	Cancer stem cell marker	CD133 (Abcam) ^e	NQ
SOX-2 ^{b,c}	Transcription factor: embryonic and neural stem cells	1/50 (Abcam) ^e	NQ
CD3 ^b	Receptor T lymphocytes	1/100 (Dako) ^e	MQ
CD20 ^b	Receptor to enable optimal B-cell immune response	1/100 (Dako) ^e	MQ
CD45 ^b	Receptor playing a crucial role in the function of all leucocytes	1/100 (Dako) ^e	MQ
CD31 ^c	Protein that marks endothelial cell intercellular junctions	1/100 (Dako) ^e	—

—: Not applied.

CD, cluster of differentiation; CD133, CD133 glycoprotein; CD31, platelet endothelial cell adhesion molecule; GAGs, glycosaminoglycans; HC, histochemistry; HIF-2 α , hypoxia-inducible factor-2 α ; IHC, immunohistochemistry; Ki-67, Ki-67 protein; MQ, Membrane Quantification; NQ, Nuclear Quantification; PPC, Positive Pixel Count; TH, tyrosine hydroxylase; VEGF, vascular endothelial growth factor.

^{a,b}Objective quantification: ^aImage Pro-Plus (IPP) software. ^bAperio ImageScope software. ^cSubjective quantification. ^dHistochemistry. ^eImmunohistochemistry; Dako Headquarters, Denmark; Novus Biologicals, Littleton, CO; Santa Cruz Biotechnology, Santa Cruz, CA; Abcam, Cambridge, UK.

instability, inflammation, and physical interactions are recently recognized as characteristics crucial to the acquisition of the cancer hallmarks. It is also clear that much biology is executed by virtue of cells of different types interacting with one another or by interactions with environmental signals from tissue scaffolds or other cells generating phenotypic/genotypic changes (5–7,12,13). The linkage of pathology images with genomics presents an opportunity to study morphology in the context of genetics and patient outcome. For this reason, we consider it important to include not only quantification of grade of tumor differentiation, percentage of tumor cells, protein expression of cancer stem cells and differentiated cancer cells, various immune system cell markers, and amount of vascular structures but also quantification of features of the two major components of the ECM (fibrillar proteins and glycosaminoglycan). The predictive model of these characteristics measured by image analysis techniques with current digitization approaches used for risk stratification system has revealed that the clinical, histopathological, and genetic descriptors that define clinically relevant groups are reflected in the essential characteristics of the cellular morphology and ECM architecture. The mechanical properties of ECM play an important role in governing the behavior of neuroblastic, Schwann, and lymphocyte cells. Our results suggest that Schwannian stroma is not the only important factor in the histopathologic analysis of neuroblastic tumors. Multiparametric analysis of other tumor stroma components (reticulin, collagen fibers, glycosaminoglycan, and immune cells) detected by classic histochemistry (HC) and immunohistochemistry (IHC) techniques and incorporated into a quantitative morphological analysis would improve the International Neuroblastoma Pathology

Classification value. The systematic quantification of a larger digitized cohort of neuroblastoma tumors will resolve difficulties in the following critical areas: consistency of results with less intra- and interobserver variability; assessment of intratumoral histological and genetic heterogeneity; comparative analysis of biomarker expression and genotypic signatures of tumor cells; evaluation of the tumor cell markers obtained by IHC and genetic techniques; and tumor tissue analysis throughout tumor progression. We present a new approach for whole organism modeling of neuroblastoma patients, combining the computational processing of clinicobiological markers used for prognostic stratification and digitized tissue measurements. Advanced high-resolution and high-content imaging technology and computational studies are being developed to integrate knowledge into medical decision support systems (33). We consider that a contribution to the overall goal in cancer would be to construct high-quality bioinformatics strategies to fuse clinical, histologic, and molecular imaging and nonimaging markers for prognosis, response to therapy, and prediction of recurrence in patients, as well as for identifying patient subgroups for inclusion in future clinical trials for new therapeutic compounds. Routine use of digital medical image and computational technologies will allow extraction of parametric information or new hallmarks that could be used as targets of specific therapies in cancer.

METHODS

Subjects and Prognostic Factors

Ninety-two tumors from 90 patients (78 original and 14 relapse/posttreatment) and 4 control tissues included by duplication in two tissue microarrays were used for the study; producing a total of 184 tumor cores and 8 control cores. This study was approved by the

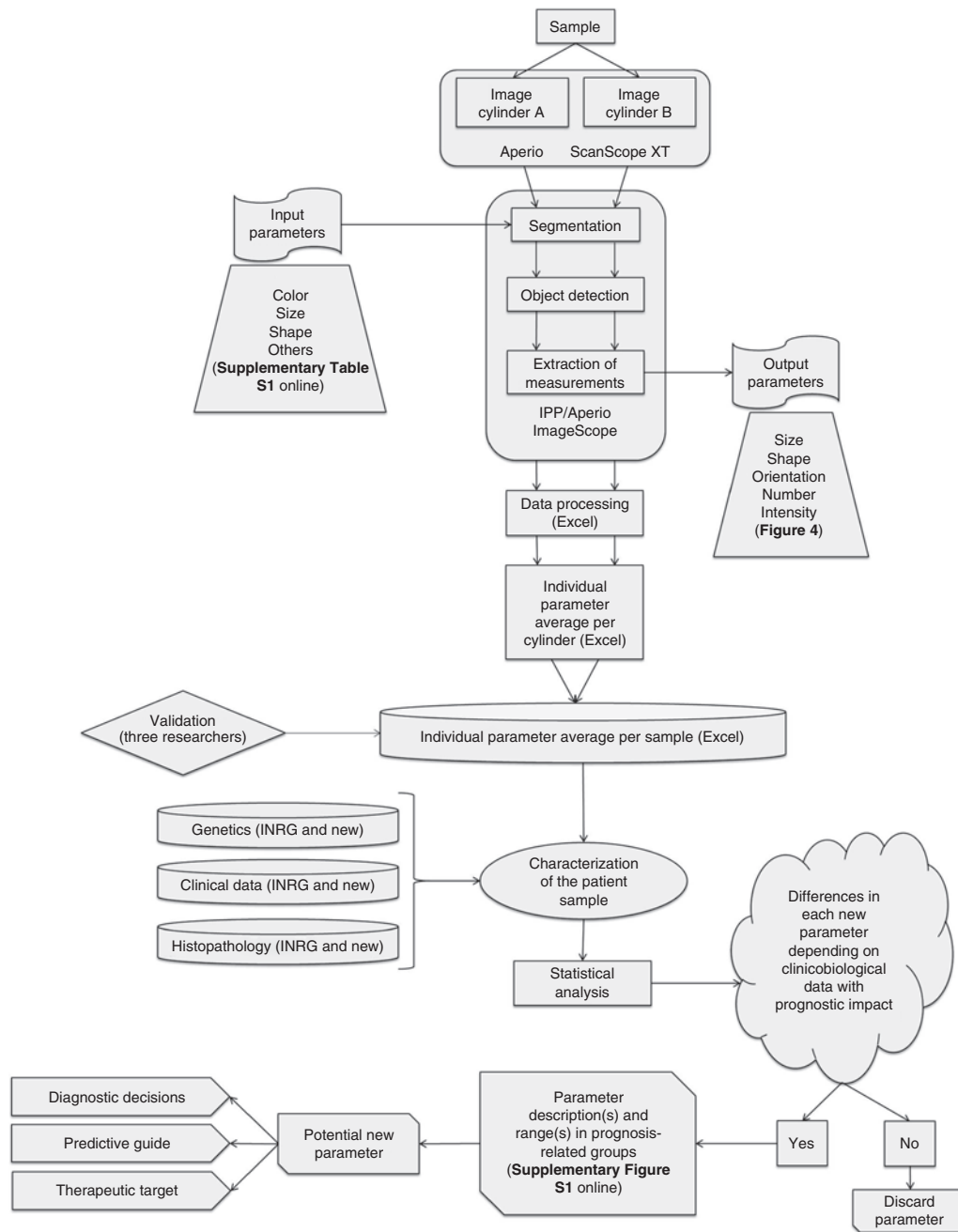








Figure 3. Flowchart showing the multiresolution neuroblastoma image analysis system. Images belonging to different samples stained with different markers have been quantified by image analysis following a common process including segmentation (differential recognition of the staining) with specific input parameters for each marker and method (**Supplementary Table S1** online) and extraction of some given parameters (output parameters in **Figure 4**). The data obtained have been correlated with clinicobiological prognostic data to obtain potential new parameters and ranges for predictive guide, therapeutic decisions, and/or therapeutic target (**Supplementary Figure S1** online). IPP, Image Pro-Plus.

Experimental Research Ethics Committee of the Spanish Society of Pediatric Hematology and Oncology (File number: 59C18ABR2002; EC number: 2010-021396-81). Participants or their family members/informants signed written informed consent forms. **Table 3** summarizes the cases with respect to the eight markers currently used for risk-adapted therapy (indicated as^c) (21,22,34–39). In addition, we created new variables related to age, stage, histopathology and genetics. In total, 8 clinical, 6 histopathological, and 17 genetic variables were considered. The hypothetical prognostic factors detected by HC and IHC, as well as the function of the markers, staining conditions, and quantitative algorithms used, are shown in **Table 4**.

Image Analysis Measurements

All the slides were digitized at 40× magnification using a ScanScope XT scanner (Aperio Technologies, Vista, CA). The image analysis flowchart is showed in **Figure 3**. Considering the 3 HC and the 10 IHC stains in each tumor core, a total of 2,576 tumor core images were obtained. Two objective methods (1 and 2), and one subjective method (3) were used to quantify the expression of the markers in the digitized images (**Figure 4**). For objective quantification, different algorithms from image analysis software were applied (**Table 4** and **Supplementary Table S1** online). Method 1 used self-designed algorithms with the Image Pro-Plus (IPP) software (MediaCybernetics, Warrendale, PA) for noncellular components, such as reticulin and

Techniques and tissue markers	Variables
	Parameter (definition; unit)/schema
	Quantity
	Percentage of stained area ((sum of all areas × 100) ÷ area core; percentage)
	Number of fibers (number of fibers × 1 mm ² ÷ area core; number/square millimeter)
	Size
	Width (diameter along minor axis of object; micrometers)
	Length (diameter along major axis of object; micrometers)
	Area (area of object; square micrometer)
	Shape
	Aspect (ratio between major axis and minor axis of ellipse equivalent to object)
	Roundness ((perimeter ²) ÷ [4 × π × area])
	Perimeter ratio (ratio of convex perimeter ^c to perimeter)
	Fractal dimension (fractal dimension of the object's outline)
	Branching (number of one-pixel-thick open branches)
	Orientation
	Angle (angle between the major axis of the object and the vertical; degrees)
	Quantity
	Percentage of stained area or cells ((sum of positive areas or cells × 100) ÷ area core or total cells; percentage)
	Number of cells (number of cells × 1 mm ² ÷ area core; number/square millimeter)
	Intensity
	Intensity of the staining (0; 1+; 2+; 3+) ^d
	Nuclear: 
	Membrane: 
	Cytoplasm: 
	Pattern
	Distribution pattern of the positive cells (0: negative; 1: focal; 2: heterogeneous; 3: homogeneous)
	1  2  3 
	Quantity
	Range (percentage of stained cells; 0+: <10%; 1+: 10–25%; 2+: 26–75%; 3+: >75%)
	Intensity
	Intensity of the staining (0: negative; 1+: weak; 2+: moderate; 3+: intense)
	Vasculature*
	Type (1: microvasculature; 2: micro- and macrovasculature)

^aDigitalization by ScanScope XT scanner at 40x magnification. ^bIn all different intensities of staining, the parameters were measured. ^cPerimeter of the convex outline of the object. ^dIntensity options of the markers. *Measured by CD31 marker.

Figure 4. Description of the parameters measured on the tissue markers related to objective (methods 1 and 2) and subjective (method 3) quantification.

collagen fibers, and for cellular proliferation, such as Ki-67 protein expression. This method measured several parameters to describe the quantity (percentage of stained area; number of objects/mm²), the size (width, length, and area), the shape (aspect or how oval the object is; roundness; perimeter ratio or how regular is the surface of the object; fractal dimension or space-filling capacity of a pattern; branching or how many bifurcations has the object), and the orientation (angle) of stained objects. Method 2 applied previously designed algorithms from the Aperio ImageScope software (Aperio Technologies, Vista, CA): a Positive Pixel Count algorithm for total staining area, Membrane Quantification algorithm for membrane staining, and Nuclear Quantification algorithm for nuclear staining. Parameters measured with method 2 estimated the quantity (percentage of stained areas/cells; number of stained cells), and the staining intensity. Finally, the subjective method (method 3) established the pattern (distribution of positive cells), the range (percentage of stained cells), and the staining intensity, as previously described (40), as well as the presence of vascular structures. A summary of objective and subjective measurements, including mean and

standard deviation, distinguishing PT and N-PT tumors is shown in **Tables 5 and 6** respectively. In total, 23 HC parameters (with objective quantification) plus 28 IHC parameters (15 with objective and 13 subjective quantification) were determined in each tumor core analyzed. Four possible options for staining intensity (indicated in **Figure 3d**) of the IHC markers were considered for each of the 15 objectively quantified parameters. In total, 97 parametric measures from each core were obtained. Given that the 92 analyzed tumors had duplicated cores in tissue microarrays, 17,848 tumor parametric measures were obtained overall.

Statistical Analysis

For a more complete statistical analysis, in addition to the 23 HC and 28 IHC parameters already defined, seven new variables were created. For IHC immune cell markers, the three ratios CD45⁺/CD3⁺, CD45⁺/CD20⁺, and CD20⁺/CD3⁺ were also calculated. With regard to subjectively quantified IHC staining parameters, the sum of staining intensity, range, and pattern was created for each analyzed marker, except CD31. Moreover, in the objectively quantified IHC staining

Table 5. Summary of results from objective quantifications of new tumor tissue markers with possible prognostic impact distinguishing primary and nonprimary tumors

Parameters	Reticulin fibers ^a	Collagen fibers ^a	Glycosaminoglycans ^a	Ki-67 ^b	TH ^b	VEGF ^b	CD133 ^b	SOX-2 ^b	CD3 ^b	CD20 ^b	CD45 ^b
Percentage of positive objects or cells											
PT	4.5±4.4	8.9±8.4	4.6±5.1	5.3±8.4	11.9±18.8	24.8±16.1	44.9±26.9	24.6±16.7	—	—	—
N-PT	7.2±6.1	18.3±17.5	6.8±5.9	6.3±13.2	7.3±12.3	20.4±14.9	40.6±23.6	23.9±4.1	—	—	—
No./mm ²											
PT	643.5±455.8	210.2±129.7	—	448.3±800.5	—	—	—	—	1,136.2±1,718.0	29.3±95.9	3,431.1±5,417.1
N-PT	910.4±633.9	183.9±145.4	—	472.1±1,074.5	—	—	—	—	816.7±1,163.8	12.1±16.8	2,659.6±2,280.5
Width											
PT	7.0±2.0	19.4±6.7	—	5.9±0.7	—	—	—	—	—	—	—
N-PT	7.5±2.9	23.1±6.9	—	5.2±0.8	—	—	—	—	—	—	—
Length											
PT	19.6±4.5	40.5±9.3	—	8.0±0.9	—	—	—	—	—	—	—
N-PT	19.6±4.9	45.9±7.3	—	7.6±1.1	—	—	—	—	—	—	—
Nuclear or object mean area											
PT	60.57±37.05	735.94±2,418.59	—	34.9±7.3	—	—	—	—	—	—	—
N-PT	75.08±62.48	1,963.07±3,714.43	—	31.1±7.9	—	—	—	—	—	—	—
Aspect											
PT	4.3±0.8	3.2±0.7	—	1.4±0.1	—	—	—	—	—	—	—
N-PT	4.3±0.9	3.1±0.4	—	1.4±0.1	—	—	—	—	—	—	—
Roundness											
PT	6.6±1.6	21.1±4.9	—	1.3±0.1	—	—	—	—	—	—	—
N-PT	7.0±1.9	21.4±4.5	—	1.3±0.1	—	—	—	—	—	—	—
Perimeter ratio											
PT	0.91±0.02	0.8±0.1	—	0.96±0.03	—	—	—	—	—	—	—
N-PT	0.91±0.02	0.8±0.02	—	0.96±0.01	—	—	—	—	—	—	—
Fractal dimension											
PT	1.1±0.02	1.3±0.2	—	—	—	—	—	—	—	—	—
N-PT	1.1±0.03	1.3±0.02	—	—	—	—	—	—	—	—	—
Dendrites											
PT	0.1±0.1	3.3±1.1	—	—	—	—	—	—	—	—	—
N-PT	0.1±0.1	2.9±1.0	—	—	—	—	—	—	—	—	—
Angle											
PT	91.5±9.9	87.8±14.3	—	—	—	—	—	—	—	—	—
N-PT	95.3±14.8	90.0±12.6	—	—	—	—	—	—	—	—	—

Mean and SD results from sum of all positive cells/objects in each parameter analyzed.

N-PT, nonprimary tumors; PT, primary tumors; VEGF, vascular endothelial growth factor.

^aHistochemistry. ^bImmunohistochemistry.

Table 6. Summary of results from subjective quantifications of new tumor tissue markers with possible prognostic impact distinguishing primary and nonprimary tumors

Parameters	Number of cases				
	VEGF	HIF-2 α	CD133	SOX-2	CD31
Range (0/1/2/3)					
PT	13/25/22/11	32/18/5/6	18/2/14/39	28/10/17	—
N-PT	5/4/1/2	9/1/0/0	4/1/1/8	5/3/3/3	—
Pattern (n/het/hom/f)					
PT	13/0/53/5	32/16/5/2	18/2/12/41	28/3/25/17	—
N-PT	5/0/6/1	9/1/0/0	4/1/1/8	5/2/4/3	—
Intensity (n/w/m/h)					
PT	13/28/12/18	32/13/2/13	18/3/8/44	28/6/17/22	—
N-PT	5/4/1/2	9/0/0/1	4/1/1/8	5/2/3/4	—
Type of vasculature (mi/b)					
PT	—	—	—	—	62/8
N-PT	—	—	—	—	11/2

(0) <10%, (1) 10–25%, (2) 26–75%, (3) >75%; (n) negative, (f) focal, (w) weak, (m) moderate, (h) high; (mi) micro, (b) both macro/micro.

HIF-2 α , hypoxia-inducible factor-2 α ; N-PT, nonprimary tumors; PT, primary tumors; VEGF, vascular endothelial growth factor.

parameters, in addition to the four intensity categories distinguished, two new categories were created: the sum of all positive cells (1+, 2+, and 3+), and the sum of 2+ and 3+ positive cells. Subsequently, these 58 tissue marker variables (Tables 4–6) plus the 31 variables derived from the patient's clinical history, the histopathology and the tumor genetic information (Table 3) were analyzed. Linear regression models were used to assess the dependence of the clinical variables upon genetic and histopathologic markers. All continuous variables were log transformed where necessary to achieve a more normal or symmetric distribution. A regression model was constructed for each analyzed pair of variables. The Wald statistic was used to derive *P* values accounting for the significance of the slope in the model, being different from zero. Thus, for continuous variables, linear regression models provide the same information as the Pearson correlation. Linear models also have the advantage of being applicable when the independent variable, the marker in our case, is binary or discrete. Thus, we can explore the relationship of our clinical variables with each of our markers, independently of whether the marker is a continuous or a discrete variable. This paradigm is appropriate to our study as half our variables, the genetic ones, are discrete while those derived from imaging are generally continuous. Separate analyses were carried out for PT and N-PT. All *P* values were corrected for multiple testing to control the false discovery rate. The standard procedure described in Benjamini–Hochberg was used for this study (41). All analyses were done using R statistical software (42). A sample classification would be possible after processing a whole set of data for a single patient (Supplementary Figure S1 online)

SUPPLEMENTARY MATERIAL

Supplementary material is linked to the online version of the paper at <http://www.nature.com/pr>

ACKNOWLEDGMENTS

We thank Marcial García-Rojo (Pathology Unit, General Hospital, Ciudad Real, Spain) and Javier Chaves (Genetic Diagnosis and Genotyping Unit, Medical Research Foundation INCLIVA, Hospital Clínico Universitario, Valencia, Spain) for excellent technical assistance, SEHOP (Spanish Society of Hematology and Pediatric Oncology) and Désirée Ramal (Paediatric Oncology Unit, University Hospital La Fe, Valencia, Spain) for patient data management, and David Harrison for English language assistance.

STATEMENT OF FINANCIAL SUPPORT

This study was supported by grants from the Fundación Asociación Española contra el Cáncer; FIS (contract PI10/15) and RTICC (Red Temática de Investi-

gación Cooperativa en Cáncer, contracts RD06/0020/0102; RD12/0036/0020), Instituto Carlos III Madrid & ERDF (European Regional Development Fund), Spain.

Disclosure: The authors declare no conflict of interest.

REFERENCES

- Hood L, Balling R, Auffray C. Revolutionizing medicine in the 21st century through systems approaches. *Biotechnol J* 2012;7:992–1001.
- Sanga S, Frieboes HB, Zheng X, Gatenby R, Bearer EL, Cristini V. Predictive oncology: a review of multidisciplinary, multiscale in silico modeling linking phenotype, morphology and growth. *Neuroimage* 2007;37:Suppl 1:S120–34.
- Smarr L. Quantifying your body: a how-to guide from a systems biology perspective. *Biotechnol J* 2012;7:980–91.
- Madabhushi A, Agner S, Basavanahally A, Doyle S, Lee G. Computer-aided prognosis: predicting patient and disease outcome via quantitative fusion of multi-scale, multi-modal data. *Comput Med Imaging Graph* 2011;35:506–14.
- Hanahan D, Weinberg RA. The hallmarks of cancer. *Cell* 2000;100:57–70.
- Hanahan D, Weinberg RA. Hallmarks of cancer: the next generation. *Cell* 2011;144:646–74.
- Mierke CT. Physical break-down of the classical view on cancer cell invasion and metastasis. *Eur J Cell Biol* 2013;92:89–104.
- García Rojo M. State of the art and trends for digital pathology. *Stud Health Technol Inform* 2012;179:15–28.
- Braun M, Kirsten R, Rupp NJ, et al. Quantification of protein expression in cells and cellular subcompartments on immunohistochemical sections using a computer supported image analysis system. *Histol Histopathol* 2013;28:605–10.
- Gabril MY, Yousef GM. Informatics for practicing anatomical pathologists: marking a new era in pathology practice. *Mod Pathol* 2010;23:349–58.
- Laurinavicius A, Raslavicus P. Consequences of “going digital” for pathology professionals - entering the cloud. *Stud Health Technol Inform* 2012;179:62–7.
- Noguera R, Nieto OA, Tadeo I, Fariñas F, Alvaro T. Extracellular matrix, biotensegrity and tumor microenvironment. An update and overview. *Histol Histopathol* 2012;27:693–705.
- Brábek J, Mierke CT, Rösel D, Veselý P, Fabry B. The role of the tissue microenvironment in the regulation of cancer cell motility and invasion. *Cell Commun Signal* 2010;8:22.

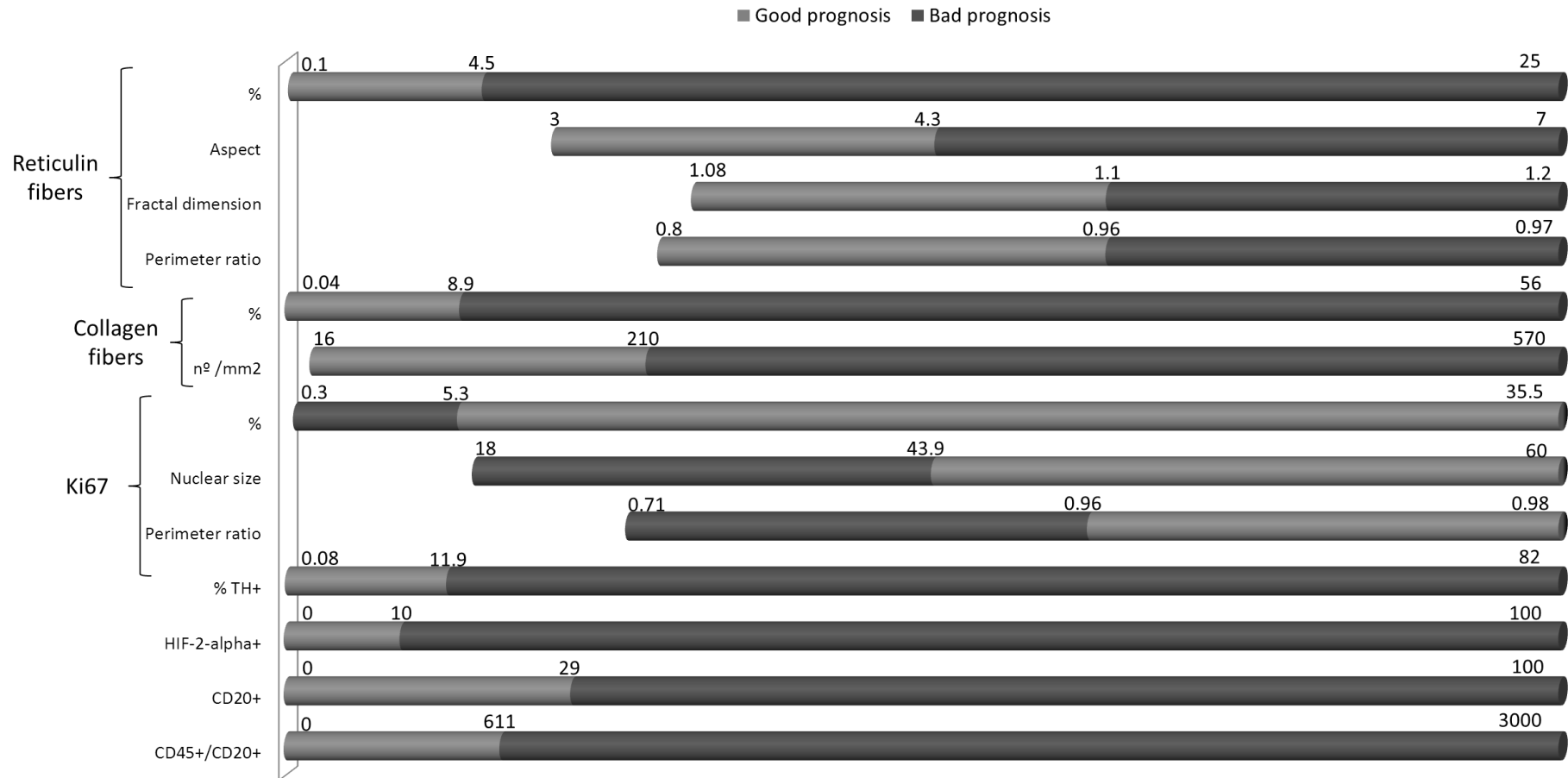
14. Cooper LA, Kong J, Gutman DA, et al. Integrated morphologic analysis for the identification and characterization of disease subtypes. *J Am Med Inform Assoc* 2012;19:317–23.
15. Martínez-González A, Calvo GF, Pérez Romasanta LA, Pérez-García VM. Hypoxic cell waves around necrotic cores in glioblastoma: a bio-mathematical model and its therapeutic implications. *Bull Math Biol* 2012;74:2875–96.
16. Cohen JE. Mathematics is biology's next microscope, only better; biology is mathematics' next physics, only better. *PLoS Biol* 2004;2:e439.
17. Moghaddasi FL, Bezak E, Marcu L. In silico modelling of tumour margin diffusion and infiltration: review of current status. *Comput Math Methods Med* 2012;2012:672895.
18. Rejniak KA, McCawley LJ. Current trends in mathematical modeling of tumor-microenvironment interactions: a survey of tools and applications. *Exp Biol Med (Maywood)* 2010;235:411–23.
19. Trisilowati T, Mallet DG. In silico experimental modeling of cancer treatment. *ISRN Oncol* 2012;2012:828701.
20. Monclair T, Brodeur GM, Ambros PF, et al.; INRG Task Force. The International Neuroblastoma Risk Group (INRG) staging system: an INRG Task Force report. *J Clin Oncol* 2009;27:298–303.
21. Schleiermacher G, Mosseri V, London WB, et al. Segmental chromosomal alterations have prognostic impact in neuroblastoma: a report from the INRG project. *Br J Cancer* 2012;107:1418–22.
22. Cohn SL, Pearson AD, London WB, et al.; INRG Task Force. The International Neuroblastoma Risk Group (INRG) classification system: an INRG Task Force report. *J Clin Oncol* 2009;27:289–97.
23. Frieboes HB, Zheng X, Sun CH, Tromberg B, Gatenby R, Cristini V. An integrated computational/experimental model of tumor invasion. *Cancer Res* 2006;66:1597–604.
24. Wolkenhauer O, Auffray C, Jaster R, Steinhoff G, Dammann O. The road from systems biology to systems medicine. *Pediatr Res* 2013;73(4 Pt 2):502–7.
25. Brisse HJ, McCarville MB, Granata C, et al.; International Neuroblastoma Risk Group Project. Guidelines for imaging and staging of neuroblastic tumors: consensus report from the International Neuroblastoma Risk Group Project. *Radiology* 2011;261:243–57.
26. Prasad K, Prabhu GK. Image analysis tools for evaluation of microscopic views of immunohistochemically stained specimen in medical research—a review. *J Med Syst* 2012;36:2621–31.
27. Garcia Rojo M, Punys V, Slodkowska J, Schrader T, Daniel C, Blobel B. Digital pathology in Europe: coordinating patient care and research efforts. *Stud Health Technol Inform* 2009;150:997–1001.
28. Al-Janabi S, Huisman A, Van Diest PJ. Digital pathology: current status and future perspectives. *Histopathology* 2012;61:1–9.
29. Gurcan MN, Boucheron LE, Can A, Madabhushi A, Rajpoot NM, Yener B. Histopathological image analysis: a review. *IEEE Rev Biomed Eng* 2009;2:147–71.
30. Sertel O, Lozanski G, Shana'ah A, Gurcan MN. Computer-aided detection of centroblasts for follicular lymphoma grading using adaptive likelihood-based cell segmentation. *IEEE Trans Biomed Eng* 2010;57:2613–6.
31. Kong J, Sertel O, Boyer KL, Saltz JH, Gurcan MN, Shimada H. Computer-assisted grading of neuroblastic differentiation. *Arch Pathol Lab Med* 2008;132:903–4; author reply 904.
32. Sertel O, Kong J, Shimada H, Catalyurek UV, Saltz JH, Gurcan MN. Computer-aided Prognosis of Neuroblastoma on Whole-slide Images: Classification of Stromal Development. *Pattern Recognit* 2009;42:1093–103.
33. Bernsen MR, Ruggiero A, van Straten M, et al. Computed tomography and magnetic resonance imaging. *Recent Results Cancer Res* 2013;187:3–63.
34. Ambros IM, Benard J, Boavida M, et al. Quality assessment of genetic markers used for therapy stratification. *J Clin Oncol* 2003;21:2077–84.
35. Ambros PF, Ambros IM, Brodeur GM, et al. International consensus for neuroblastoma molecular diagnostics: report from the International Neuroblastoma Risk Group (INRG) Biology Committee. *Br J Cancer* 2009;100:1471–82.
36. Piqueras M, Navarro S, Castel V, Cañete A, Llombart-Bosch A, Noguera R. Analysis of biological prognostic factors using tissue microarrays in neuroblastic tumors. *Pediatr Blood Cancer* 2009;52:209–14.
37. Shimada H, Umehara S, Monobe Y, et al. International neuroblastoma pathology classification for prognostic evaluation of patients with peripheral neuroblastic tumors: a report from the Children's Cancer Group. *Cancer* 2001;92:2451–61.
38. Villamón E, Berbegall AP, Piqueras M, et al. Genetic instability and intratumoral heterogeneity in neuroblastoma with MYCN amplification plus 11q deletion. *PLoS ONE* 2013;8:e53740.
39. Villamón E, Piqueras M, Berbegall AP, et al. Comparative study of MLPA-FISH to determine DNA copy number alterations in neuroblastic tumors. *Histol Histopathol* 2011;26:343–50.
40. Gómez-Mateo Mdel C, Piqueras M, Pählman S, Noguera R, Navarro S. Prognostic value of SOX2 expression in neuroblastoma. *Genes Chromosomes Cancer* 2011;50:374–7.
41. Benjamini Y, Hochberg Y. Controlling the false discovery rate: A practical and powerful approach to multiple testing. *J R Stat Soc Ser B Stat Methodol* 1995;57:289–300.
42. R Core Team. R: A language and environment for statistical computing. R Foundation for Statistical Computing, 2013. (<http://r-project.org/>)

Supplemental Table S1. List of softwares, algorithms and input parameters used.

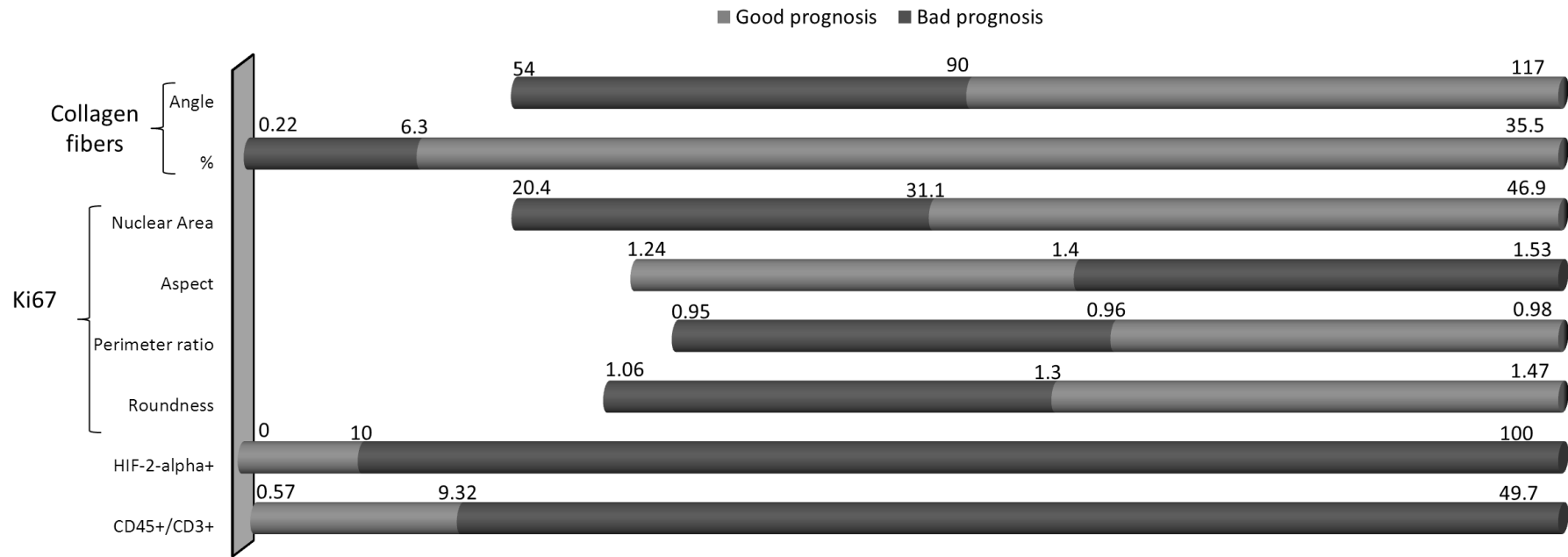
Method	Software	Algorithms	Markers	Input parameters							
				Image pre-treatment	Range of colour			Values of morphometric parameters	Other parameters		
					Staining	Counterstaining	Background				
1	Image Pro Plus	Self-designed	Reticulin fibers	None		<120			Roundness >3 Area >7.5 Length, Width >8, >1.5	Smoothing: 3 Others: off	
			Collagen fibers	Brightness: 68 Contrast: 81 Gamma: 1	R,G,B	<17,90,all			>2 Density blue: (1+) 0.22-0.24 (2+) 0.24-0.37 (3+) >0,.37	Smoothing: 3 Others: off	
			Ki67	None						Smoothing: 3 Others: off	
2	Aperio Image Scope	Positive Pixel Count	GAGs			>221				Default	
			VEGF			210,180,140 Hue width 0.5 Hue Value 0.3				Color saturation threshold: 0.06 Others: default	
			TH			220,187,120				Default	
		Membrane Quantification	CD3			255,255,195				Nuclear size cell size radius 5-125	
			CD20			250,1,140	255	255		5-125 4	Default
			CD45			255,1,226				Completeness threshold 78	
Nuclear Quantification	SOX-2	None	Average R+G+B (1+,2+,3+)		193,188,175 Positive stain Blue: 0.82	Blue: 0.31		Nuclear size 20-10000	Segmentation type: 0 Threshold type: 1 Edge trimming: 1		
	CD133				200,180,162	Default	Remove light object: 0 Cytoplasm intensity threshold: 200 Clear area intensity: 230 Lower/upper threshold: 0/230	Nuclear size 5-125 Roundness 0.1 Compactness 0.1 Elongation 0.1 Average radius 0.1 Curvature 1.37 Completeness threshold 1.2	Segmentation type: 1 Threshold type: 1 Edge trimming: 1		

Supplemental Figure S1. Prognosis prediction depending on values for each new histomorphometric marker to be used as a classification guide.

A) Primary tumors



B) Non-primary tumors





Biotensegrity of the extracellular matrix: physiology, dynamic mechanical balance, and implications in oncology and mechanotherapy

Irene Tadeo¹, Ana P. Berbegall^{1,2}, Luis M. Escudero³, Tomás Álvaro⁴ and Rosa Noguera^{2*}

¹ Foundation INCLIVA, Hospital Clínico de Valencia, Valencia, Spain

² Department of Pathology, Medical School, University of Valencia, Valencia, Spain

³ Instituto de Biomedicina de Sevilla, Hospital Universitario Virgen del Rocío/CSIC/Departamento de Biología Celular de la Universidad de Sevilla, Seville, Spain

⁴ Department of Pathology, Hospital de Tortosa, Verge de la Cinta, IISPV, URV, Tortosa, Spain

Edited by:

Jozsef Dudas, Medical University
Innsbruck, Austria

Reviewed by:

Xose S. Puente, Universidad de
Oviedo, Spain

Christian Oliver Pritz, Medical
University Innsbruck, Austria

*Correspondence:

Rosa Noguera, Department of
Pathology, Medical School, University
of Valencia, Avda. Blasco Ibañez 15,
Valencia 46015, Spain
e-mail: rnoquera@uv.es

Cells have the capacity to convert mechanical stimuli into chemical changes. This process is based on the tensegrity principle, a mechanism of tensional integrity. To date, this principle has been demonstrated to act in physiological processes such as mechanotransduction and mechanosensing at different scales (from cell sensing through integrins to molecular mechanical interventions or even localized massage). The process involves intra- and extracellular components, including the participation of extracellular matrix (ECM) and microtubules that act as compression structures, and actin filaments which act as tension structures. The nucleus itself has its own tensegrity system which is implicated in cell proliferation, differentiation, and apoptosis. Despite present advances, only the tip of the iceberg has so far been uncovered regarding the role of ECM compounds in influencing biotensegrity in pathological processes. Groups of cells, together with the surrounding ground substance, are subject to different and specific forces that certainly influence biological processes. In this paper, we review the current knowledge on the role of ECM elements in determining biotensegrity in malignant processes and describe their implication in therapeutic response, resistance to chemo- and radiotherapy, and subsequent tumor progression. Original data based on the study of neuroblastic tumors will be provided.

Keywords: biotensegrity, cancer, extracellular matrix, mechanotherapy, neuroblastoma

INTRODUCTION

The study of spatial and temporal responses to mechanical forces of tissue structures of biological organisms is a growing field in health sciences. Such responses can be modified by mechanotherapeutic interventions, ranging from the molecular level to whole body systems, and involving a broad spectrum of target molecules belonging to the microenvironment. In order to carry out mechanotherapy effectively, we should consider the stabilizing elements of tension and compression, or biotensegrity systems, existing at all structural levels in the body. Tensegrity is an architectural principle put forth by Buckminster Fuller in the 1960s (1, 2). According to the tensegrity principle, structures or tensegrity systems are stabilized by continuous tension with discontinuous compression (3). Coming under the term biotensegrity, the tensegrity principle applies to essentially all detectable scales in the body, from the musculoskeletal system to proteins or DNA (4, 5).

In this review, we highlight the current challenges and on-going issues for dissecting the mechanisms of tumor extracellular matrix (ECM) biotensegrity and discuss how these concepts may be translated into treatment and prognosis of cancer. To illustrate the biotensegrity principle, we present some preliminary results on the mathematical integration of multimodal data, combining imaging and non-imaging tumor tissue data, acquired in the context of neuroblastoma (NB) studies, suggesting testable hypotheses for

making prognostic predictions and therapeutic response related with this principle.

CELL AND TISSUE BIOTENSEGRAL PHYSIOLOGY

Several studies have demonstrated that cells can function as independent pre-stressed tensegrity structures through their cytoskeleton architecture. Ingber defined the pre-stressed tensegrity model as a structural support on biological systems. It is constituted by a number of continuous elements of tension and a number of discontinuous elements resistant to compression providing a stabilized structure (6–14). As a tensegrity network, a single cell presents such continuous tension (mediated by cytoskeleton elements such as microfilaments and intermediate filaments) and local discontinuous compression (mediated by ECM and other cytoskeleton elements such as microtubules). The individual pre-stressed cells are poised and ready to receive mechanical signals and convert them into biochemical changes (15). Therefore, cell membrane, nucleus, and all the organelles are hard-wired by the cytoskeletal scaffold. When the mechanical cue is received, sensed mainly by focal adhesion complexes induced by integrins, the signal modifies the cytoskeletal scaffold. Thus, the local mechanical signal is amplified and propagated through a series of force-dependent biochemical reactions, whereby intra-cellular signaling pathways become sequentially activated through mechanotransduction (16). At the

molecular level, several elements resist compression, such as all structures containing alpha-helix, beta-sheet, or even DNA backbone structures, while others, such as attraction and repulsion forces of molecular, atomic, and ionic bonds (such as Van der Waals forces, covalent bonds, etc.), resist continuous tension. Many molecules display such structures and are subject to these two forces at different stages along the mechanical intra-cellular signal pathways. Among these abundant and intermingled pathways, many remain unknown. We believe that knowledge on how we could potentially interfere with these signaling pathways or cascades may provide new therapeutic targets. Nevertheless, as many molecules play multiple roles in different pathways, molecular therapy based on mechanotransduction, should be carried out on specific targets to avoid adverse effects.

The tensegrity architecture of the cytoskeleton and signal pathways is linked to the tensegrity elements of the outer and inner nuclear membrane through KASH–SUN bridges, where KASH proteins are located in the outer nuclear membrane (Nesprin-1 and Nesprin-2 link nuclei with actin filaments, Nesprin-3 interacts with intermediate filaments, and Nesprin-4 binds to microtubules) (17–19) and SUN proteins in the inner nuclear membrane (Samp1 and lamin). This connection is critical for intra-cellular force transmission in physiological homeostasis (20–22) and might ensure that chromatin organization is not perturbed when tissues experience stress, and may be fundamental for normal development (23).

The self-balanced mechanical stability of the cytoskeleton enables the macro-mechanical forces to be converted into molecular changes. Since cells are connected to each other through cell junctions, mediated mainly by cadherins, these changes not only affect the cell that receives the signal, but are also transferred to the neighboring cells. Indeed, recent biophysical studies have revealed that the size of cell–cell contacts can be regulated in response to the mechanical forces exerted on those junctions and that cells are also able to regulate the forces exerted on their junctions (24–26). It is known that cell–cell junctions are anchored to neighboring cells and focal adhesions to ECM, and all are connected to the intra-cellular cytoskeletal network, therefore the forces that cross these structures fluctuate strongly when tissue is remodeled. It is becoming apparent that these structures do not just transmit forces while maintaining tissue cohesion, but also respond to fluctuations in force by actively influencing cell morphology and behavior (27). The biological significance of this mechanotransduction is to promote coordinated cytoskeletal reorganizations that can define changes in shape across the whole tissue. The basal lamina plays a central role in this process. It provides physical support to epithelial cells, surrounds muscle cells, fat cells, and Schwann cells, and is the environment where cells and ECM bind through focal adhesions and integrins. Accordingly, the shape of tissue cells (round or flattened) and the three-dimensional structure of the tissue patterns that constitute glands, alveoli, ducts, and papillae (among others), depend on the stiffness and flexibility and on the coordinated movement of the basal lamina (28).

ROLE OF ECM IN BIOTENSEGRITY

During the last decade, cell-matrix contacts based on the transmembrane adhesion receptors from the integrin family or focal

adhesions have emerged as the major mechanosensitive structural elements that connect, collect, process, and integrate the information of the ECM. Recent proteomic studies have not only found many more components, but also have revealed that many of these elements are recruited to focal adhesions in a force-dependent manner, supporting the view that focal adhesions harbor a network of mechanosensitive processes (29). Integrins are transmembrane $\alpha\beta$ heterodimer receptors that function as structural and functional bridges between the cytoskeleton and ECM molecules. Specifically, $\alpha8\beta1$ or tensegrin can bind to several ECM molecules and has been shown to be associated with focal adhesion points, where it participates in the regulation of spreading, adhesion, growth, and survival in different neuronal and mesenchymal-derived cell types (30, 31).

Various interconnected cells bind to their microenvironment, forming a mechanical tensegral system, which implies the existence of a mechanical balance between compression (ECM) and tension (cell) forces. The ECM is made up of a mixture of ground substance [glycosaminoglycans (GAGs) – mostly hyaluronan, proteoglycans, and glycoproteins] situated in close relationship with a fibrous scaffold [reticulin (Ret F) – elastin and collagen fibers (Col F)], and supplies much of the structural support available to parenchymal cells in tissues, by adding tensile strength and flexibility (32). The ECM is a dynamic and multifunctional regulator and has its own biotensegrity with Ret F and elastin fibers acting as tensional elements, and ground substance and Col F as compression-resistance elements. This tensegral network is considered to be a solid-state regulatory system of all cell functions, responsible for changes in genes and proteins, as well as alterations in cell shape and movement (33–35). One result of cell–ECM biotensegrity is substrate rigidity, which can control nuclear function and hence cell function (36). Cells can use this substrate rigidity to exert traction forces, thus altering the ECM. Indeed, in a state of reciprocal isometric mechanical tension, a dynamic balance exists between cell traction forces and points of resistance within the ECM. This dynamic biotensegral system with its mechanotransduction phases (**Figure 1**) enables our cells to mechanosense, modifying their microenvironment, thus promoting ECM remodeling in homeostasis and in tissue disorders (37). Manipulation of this mechanical balance could be used to promote tissue regeneration. In fact, various studies have demonstrated that different elasticities of the ECM drive mesenchymal stem cell differentiation in a very specific way. Neurogenic, myogenic, or osteogenic differentiations are induced under identical matrix serum conditions, with variations in ECM softness, strength, and stiffness (38). Furthermore, ECM stiffness guides cell migration. It has been shown that fibroblasts prefer rigid substrates and when placed on flexible sheets of polyacrylamide, they migrate from the soft to the stiff areas (39). Under homeostatic conditions, collagen fibrils have a minimal turnover. However, this turnover is accelerated during tissue remodeling and tumor development, as evidenced by the serum levels of its degradation products (40). Studies of the ECM have revealed that the components of the tumor microenvironment are fundamental, not only for the regulation of tumor progression (41, 42), but also are essential even before the tumor appears. The stromal cells are able to transform the adjacent cells through an alteration in the homeostatic regulation of the tissue,

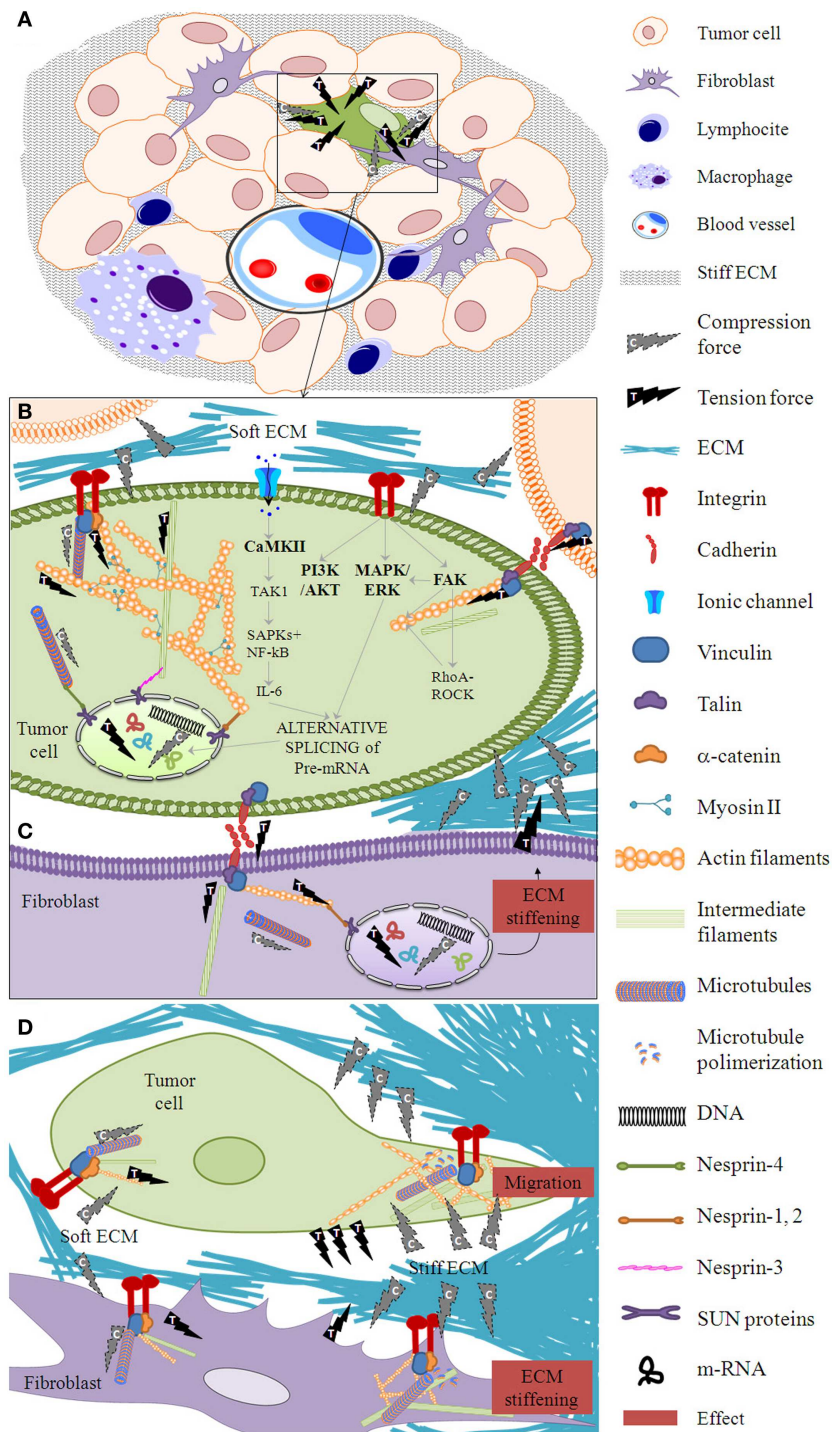


FIGURE 1 | Mechanotransduction phases. (A) When forces are exerted on a tissue after proliferation of tumor and stroma cells, a cell within the cell mass (for example, the one marked in green) is subject to mechanical deformation in a phase called mechanocoupling. Following the principle of tensegrity at the tissue level, ECM elements apply compression forces to the tissue cells and tissue cells exert tension forces between themselves and to the ECM. Biotensegral elements of the boxed area are detailed in (B–D).

(B) This particular tumor cell activates a biochemical coupling phase in which the mechanical signal is transformed into intra-cellular biochemical signals through the integrin–cytoskeleton–nuclear matrix structure or stretch-activated cation channels within the cell membrane, among other

mechanisms. Some essential players in mechanosensing are shown (44–47).

(C) The biochemical signal is transmitted to neighbor cells (marked in purple) through cell–cell junctions. Following the principle of tensegrity at the cell level, the compression elements are the microtubules, whereas the tension elements are the intermediate filaments and the actin filaments.

(D) A fibroblast neighbor cell can produce a stiff ECM which in turn enables the first cell to flatten and migrate through this stiffened ECM. The effector cell response phase arises from the biotensegrity principle: a simple cytoskeleton when the ECM compression is low switches to a complex cytoskeleton when the ECM exerts high compression on the cells and the cells exert high tension on the ECM.

including the control of architecture, adhesion, cell death, and proliferation (43).

CELL AND TISSUE BIOTENSEGRITY IN CANCER

Cancer can be understood as a disease of the developmental processes that govern how cells organize into tissues (48). The tumor microenvironment is comprised of a variety of cell types lying among a network of various ECM fibers merged within the interstitial fluid and gradients of several chemical compounds, which constantly interplay with malignant cells (34). Therefore, we can infer that the previously described biotensegral systems also exist within tumor tissue. In fact, the dynamic mechanical balance achieved through mechanosensors, cytoskeletal tensegrity, molecular biotensegral intra-cellular pathways, ECM with compressive and resistant elements, supportive cells (such as fibroblasts and multiple tumor-associated immune cells), and vascular and lymphatic vessels tensional structures, can be as important as the genetic instability of tumor cells in the pathogenesis and evolution of the malignant process (42, 49). In this regard, various studies have demonstrated the importance of cell–ECM biotensegrity in cancer (34, 48, 50). Indeed, a desmoplastic reaction is frequent in many solid tumors, such as breast, prostate, colon, or lung, in which high levels of TGF- β and PDGF are found. These growth factors are produced by the mesenchymal cells of the tumor stroma and induce immunophenotypic changes. These changes are observable by studying actin- α , myosin, vimentin, desmin, and the altered production of several ECM proteins, such as collagens, laminin, tenascin, ECM metalloproteinases (MMP), and MMP-inhibitors (43). Additionally, ECM stiffness modulates cancer progression; cancer cells promote stiffening of their environment, which in turn feeds back to increase malignant behaviors such as loss of tissue architecture and invasion (51). For instance, the speed of malignant cells *in vitro* is affected by the geometry of the ECM. Human glioma cells move faster through narrow channels than through wide channels or in non-stretched 2D surfaces. This is thought to be triggered by an increase in the polarity of the traction forces between cell and ECM (52). Indeed, recent publications describe that not only neoplastic ECM stiffness, but also the firmness of tumor cells play a significant role in tumor progression. The firmness of tumor cells, especially the metastatic cells, has been found to be lower than that of the normal cells of the same sample, and is caused by the loss of actin filaments and/or microtubules and the subsequent lower density of scaffold (53, 54). In this regard, it has been shown that the transformation from a benign proliferative cell into a malignant cell can be produced by a peculiar phenotypic change, known as epithelial–mesenchymal transition (55). This transformation involves breaking contact with sister cells and increasing motility, as a result of a change in the epithelial cytoskeleton, with its corresponding properties for a pseudomesenchymal phenotype, which enables migration, invasion, and dissemination (56). While normal cells adhere to their environment through integrins, and their body has a proper consistency, tumor cells lose that consistency and tensegrity, becoming easily deformable elements (causing pleomorphism), with high elasticity (enhancing infiltration) and with an increased degree of mobility (enabling metastasis) (57). In breast cancer, the genomic profile expressing mainly mesenchymal features is actually found

in the most invasive cell lines (58). Moreover, it has been published that chronic growth stimulation, ECM remodeling, alteration of cell mechanics, and disruption of tissue architecture are non-genetic influences on cancer progression (42, 49). These ideas not only agree with basic predictions of cellular tensegrity, but also support the idea that therapy based on the manipulation of the biotensegrity principle cues should be considered as a way to revert the malignant phenotype (59, 60).

In cancer research, the hallmark which includes the physical aspects of tissue has been less investigated, but it is known that this hallmark is one of the most basic mechanisms in enhancing tumor proliferation and creating resistance to cancer treatment, among other processes (61). A previous study by our group takes into account some structural elements of ECM that have the capacity to influence physical conditions and suggests that Schwannian stroma cells are not the only important factor in the histopathologic analysis of neuroblastic tumors (50). Specifically, multi-parametric analysis of other tumor stroma components (Ret F, Col F, GAG, and immune cells) detected by classic histochemistry (HC) and immunohistochemistry (IHC) techniques and incorporated into a quantitative morphological analysis would improve the value of the International NB Pathology Classification (62). As we will show later, chemotherapy and radiotherapy are known to act on tumor cells as well as on stromal cells and ECM elements (63, 64). As a consequence, injury to the ECM can contribute directly to treatment resistance, creating niches of resistant tumor cells (64, 65). Furthermore, damage to DNA induces the production of cytokines and growth factors by stromal cells, this triggers inflammation, cell survival, and tumor progression, thus the effect of therapy on ECM may be to promote relapse or chemoresistance (66, 67). We hypothesize that studying the different elements of the ECM, as one of the main contributors to biotensegrity, through objective morphometric analysis and the creation of mathematical networks of histologic sections stained with HC and IHC, can shed light on how biotensegrity influences tumor microenvironment and could provide clues to its action mechanism.

EVIDENCES OF ECM BIOTENSEGRITY CHANGES IN MALIGNANT TISSUE

It is known that tumor cells alter the mechanical properties of the microenvironment in order to create favorable conditions for their proliferation and/or dissemination (68). In addition, adhesion molecules such as E-cadherin are involved in the processes of tissue differentiation and morphogenesis and play an important role in modulating the invasiveness of tumor cells in breast cancer and other epithelial tumors (69). For instance, the reciprocal communication between the stromal cells and the tissue parenchyma directs gene expression, and in prostate carcinoma and breast carcinoma, the oncogenic potentiality arises from stroma-associated fibroblasts, immune response, and the alterations of biotensegrity (49, 70). Deregulation and disorganization of the composition, structure, and stiffness of the ECM elements progressively increase interstitial fluid pressure, leading to limited penetration and dissemination of therapeutic agents within solid tumors, thus enabling the creation of niches within tissues and organs that offer sanctuary to tumors and activate therapy resistance programs

(11–13, 64, 65). Tumor cells are not the only cells that change the mechanical properties of the microenvironment. Despite all the efforts of tumor cells to make ECM elements work for their survival and proliferation, tumor stromal cells, specifically, immune system cells, try to reverse the pathological condition. Indeed, two lymphoproliferative syndromes (follicular lymphoma and Hodgkin lymphoma) are good examples of the fact that a tumor can be considered as functional tissue, connected and dependent on the microenvironment, which sends and receives signals to and from the tumor tissue itself. In such syndromes, tumor microenvironment stromal cells, including immune response, determine the morphology, clinical stratification, aggressiveness, prognosis, and response to treatment of the tumor (71).

In the next two sub-sections, we describe the methods developed for the study of biotensegrity in neuroblastic tumors.

MORPHOMETRIC ANALYSIS OF ECM ELEMENTS – AN EXAMPLE IN NB

Accurate quantification of pathology specimens using imaging technology to analyze the variations in structural tissue that arise from interactions between tumor and stroma cells and ECM elements is providing important information. This approach would allow biotensegral patterns to be included in computational formulations for risk stratification systems and aid in designing better anti-cancer treatment strategies (29). However, the validity of the model depends on the quality of the data. This quantification depends on the staining, scanning, image analysis, and statistical evaluation. For that purpose, automatic stained sections must be digitized using microscopic preparation scanners such as Aperio Scanscope XT (Aperio technologies) or Panoramic Midi (3Dhistech) or with a photomicroscope if a scanner is not available. Different image analysis systems can be used, such as Image Pro-plus software (Media cybernetics), ImageScope (Aperio technologies), Panoramic viewer (3D Histech), free software (ImageJ of the NIH), or self-designed software to obtain customized *macros* or algorithms (informatic protocols) to detect and characterize the quantity (number of objects and area occupied), size (area, width, length), shape (aspect, roundness, perimeter ratio, fractal dimension), and orientation (angle), among other parameters, of the ECM elements of interest. All systems provide mark-up images or masks, which represent the recognized and measured element in white upon a black background. The use of tissue microarrays is advised for standardization purpose of background subtraction and color segmentation, given that these techniques tend to be dependent of the intensity of the staining and algorithms must be recalibrated with every change of intensity/ground noise/contrast staining, thus losing objectiveness. Further details regarding objective quantification of different cell and ECM elements and a flowchart of the analysis used by our group, are described elsewhere (50).

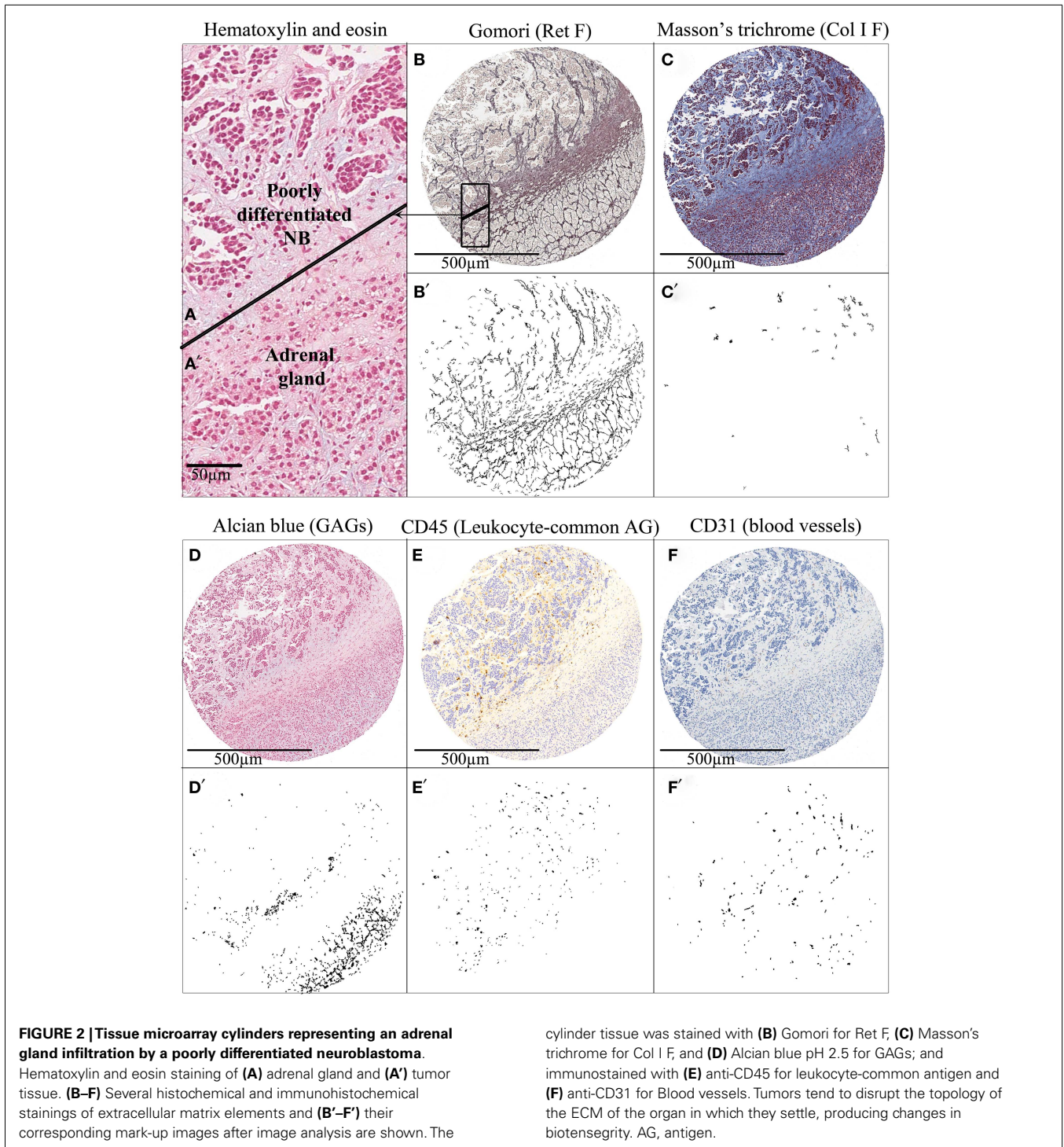
Neuroblastic cells are known to be committed in a complex interaction with the surrounding tumor microenvironment and we believe that patients with neuroblastic tumors, specifically those still subject to therapeutic failure despite current knowledge, could benefit from novel therapeutic strategies which could originate from the study of ECM biotensegrity. To investigate such new therapeutic targets, we have objectively quantified Ret F, Col I F, GAGs (Gomori, Masson's trichrome, and Alcian blue pH 2.5

HC, respectively), blood vessels (CD31 IHC, Dako), lymph vessels (D2-40 IHC, Dako), and cell markers, including leukocyte lineage (CD45/LC IHC, Dako) and NB cells, in primary NB. A first approach to the evaluation of the role of ECM biotensegrity in neuroblastic tumors is the observation of the mark-up images of tissue microarrays cylinders comprising a mixture of tumor and normal tissue either in the primary and/or metastatic location. In the particular case presented in **Figure 2**, included for illustrative purpose, a clear disruption in the organization of the ECM elements can be observed when passing from the normal tissue area to the neoplastic tissue. In the tumor area, Ret F becomes disorganized, Col I F is slightly increased (although minimal), GAGs almost disappear, CD45 reactive cells accumulate, and blood vessels vary in size and characteristics.

Statistical analysis of the quantitative data of fibers, GAGs, tumor cells, and immune system markers compared with the current parameters used to predict risk of relapse (stage, age, histopathology, state of *MYCN* oncogene, state of 11q region, overall genomic profile, and ploidy) (72–74) and other genetic markers of prognostic interest in a subset of 78 primary neuroblastic tumors has already been published by our group, and highlights the interest of studying ECM in neuroblastic tumors (50). The fact that ECM elements differ depending on the characteristics of the tumors and, more interestingly, the fact that the characteristics of ECM elements are related to prognosis (relapse or overall survival) advocates on behalf of the regulatory role of ECM biotensegrity in tumor progression.

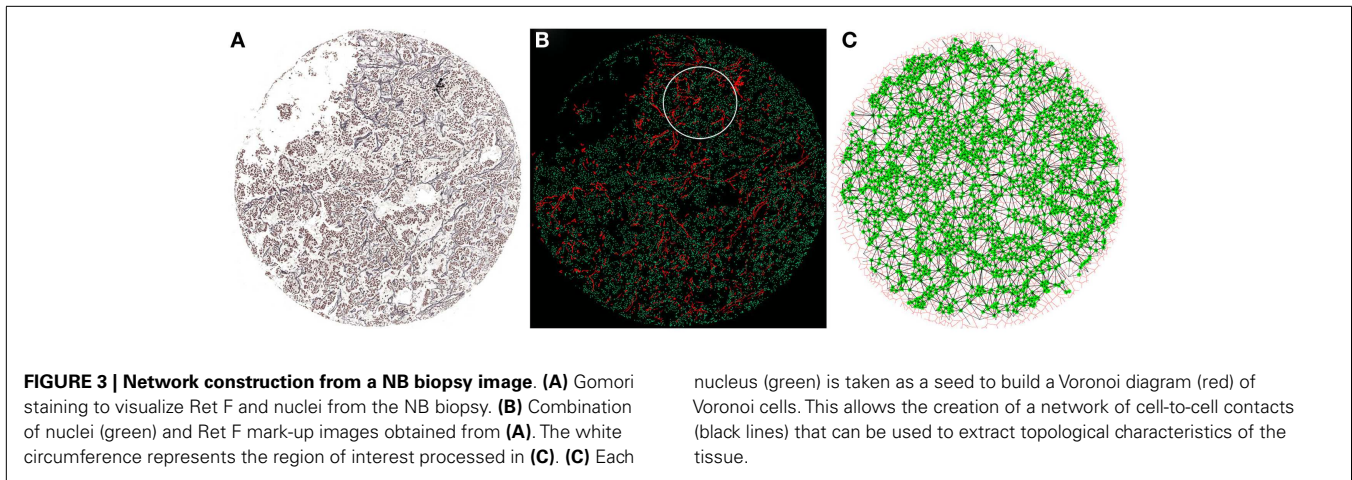
DEVELOPMENT OF MATHEMATICAL TOPOLOGY OF ECM ELEMENTS – AN EXAMPLE IN NB

The combination of multidisciplinary efforts by clinicians, biologists, pathologist, bioengineers, and biostatisticians could elucidate how ECM elements interact with tumor and stromal cells. In this respect, a new and interesting approach is to analyze biopsies by converting the tissue into a mathematical network of cell-to-cell contacts (75–78). Using graph theory concepts, these networks can provide organizational information that seems relevant in embryologic development and disease. For example, this method has been applied to the analysis of neuromuscular diseases, serving as a diagnostic tool able to quantify the severity of the pathology in a muscle biopsy (77). We propose that this technology can be adapted to the analysis of tumor biopsies. It is already possible to compare different mark-up images obtained from the analysis of several markers which have been assessed on serial thin sections with preserved histology. These overlapping images enable several markers to be considered at the same time and allow the co-location and study of the interaction between continuous tensional elements and discontinuous compression elements. In this regard, we have analyzed the relationship between different biopsy components taking the cell nuclei as a reference. The procedure is based in the identification of the cell nuclei and the calculation of their respective centroids. These centroids serve as seeds to perform a Voronoi diagram of Voronoi cells (79, 80). A new partitioned image is produced in which each nuclei is associated with its corresponding Voronoi cell. In this way, it is possible to construct a network based on the neighboring Voronoi cells. Topological approaches and the use of Voronoi cells need to be able



to capture the presence and relative disposition of tissue heterogeneities derived from, for example, the luminal space of glands, blood and lymph vessels, or larger extracellular spaces. They will be reflected through different characteristics and will be taken into account for the study, testing if they can be part of the relevant features that define a specific condition. The selection of regions of interest in each biopsy will allow studying only tumor tissue areas

without artifacts that could bias the study, leading to wrong conclusions. The combination of graph-related parameters with the morphometric information will enable a comprehensive analysis of the changes arising from different compression forces in relation to the different types of ECM (stiff/soft, organized/chaotic) in combination with the tumor stroma cells such as immune cell infiltrates. We have performed preliminary comparisons based



on the genetic features of NB using Ret F and blood vessels (in addition to the nuclei) as the reference features for providing the biological clues. This procedure has shown some hints of discrimination regarding the organization and co-location of these elements (**Figure 3**). We found that some network characteristics were relevant to perform this initial separation. This suggests that diverse backgrounds can respond differently to the pathological process depending on the organization of the tumor. Following the same approach, we will use other mark-up images of the positive cells stained with the different monoclonal antibodies against the different cells of the leukocyte lineage. We hope that this combination of mathematical and statistical methods will answer the question on the relationships between ECM biotensegrity and the changes mediated by the cell infiltrate.

EFFECT OF TREATMENT ON TUMOR MICROENVIRONMENT AND CONSEQUENCES

There is much evidence that the lack of total specificity of cancer therapeutic agents (chemotherapy and radiotherapy) causes collateral damage to the mechanical properties of the tumor ECM and benign stromal cells (which were previously fighting the tumor), creating resistance to therapy and favoring relapse and metastasis. This fact becomes evident while analyzing post-treatment biopsies, which contain a high degree of fibrosis and calcification. Some studies have shown that cancer therapy can sometimes damage tumor DNA and stromal cells, which results in the secretion of a spectrum of proteins, including the Wnt family members. For example, in prostate cancer, the expression of this proteins in the tumor microenvironment, regulated by lymph B cells, attenuates the effects of cytotoxic chemotherapy *in vivo*, promoting tumor cell survival and disease progression (63, 81). It has also been reported that in follicular lymphoma and diffuse large cell lymphoma, treatment with lenalidomide affects the immune synapses of intra-tumoral T lymphocytes (82). In breast cancer, treatment with doxorubicin results in an increase in fibulin-1, an ECM protein, and its binding proteins, fibronectin and laminin-1, which constitute a source of chemoresistance (83) and triggers overexpression of maspin protein, which induces the accumulation of collagen fibers, thus causing disease progression (84). A novel Toll receptor-9-dependent mechanism that initiates

tumor regrowth after local radiotherapy has also been reported (85). Monoclonal antibodies against fibulin-1 are able to reverse such chemoresistance, and the inhibition of MMP seems to have a therapeutic effect (86).

An example of the effect of treatment in NB is shown in **Figure 4**. When comparing a primary NB with its non-primary sample, we can appreciate that Ret F, GAGs, and Col I F accumulate in the ECM of the post-treatment sample. The amount of blood macrovasculature is slightly decreased. All these findings describe a stiffer ECM after multimodal treatment.

POTENTIALITY OF MECHANOTHERAPY

The changes exerted on ECM by therapeutic agents and the perspective of the epithelial–mesenchymal transition in epithelial tumors have opened the door to a new line of treatment, which considers the genetic and epigenetic mechanisms associated with resistance to chemotherapy (59, 87). There is a need to personalize therapeutics taking into account not only the features known to have prognosis impact, but also new markers, such as the mechanical stress of the tumor ECM elements. Indeed, because of its importance to the tumor, the ECM represents an “Achilles heel” that can be exploited in designing cancer therapy. The bionetwork between the ECM and tumor cells is dynamic, and for every action, such as exposure to genotoxic stress, there are reactions and consequences throughout the micro and macrosystem (65). Removal of ECM barriers will either have a direct negative effect on tumor cells or facilitate anti-tumor immune responses and drug treatment, through better intra-tumoral penetration and accessibility to target cells. In this regard, a number of experimental approaches are aimed toward the transient degradation or down regulation of ECM proteins using injection of ECM-degrading enzymes into the tumor or their intra-tumoral expression after viral- or stem cell-based gene transfer (65). Other approaches attempt to indirectly decrease tumor-associated ECM by killing tumor stromal cells that produce ECM proteins (64) or aim at enhancing the host immune response (88). The potentiality of therapeutic agents to modify ECM can be turned around in such a way that new chemicals can be applied to modify a given ECM stiffness or composition into one shown to trigger a better prognosis.

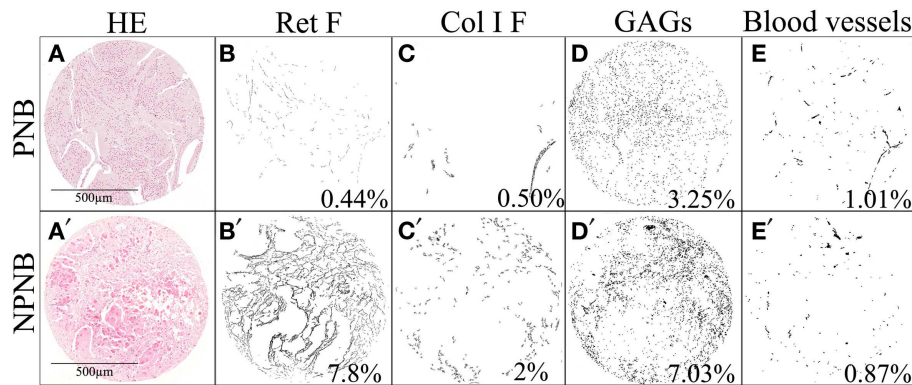


FIGURE 4 | Changes in the ECM after treatment in one neuroblastic tumor. Several stainings (HC and IHC) of (A–E) a primary neuroblastoma and (A'–E') its post-treatment biopsy are shown. The presented mark-up images of (B,B') Ret F, (C,C') Col I F, and (D,D') GAGs show that these ECM elements are increased in NPNB. Regarding blood vessels (E,E'), the amount of does not seem to change after treatment but the type of vessels has changed in

such a way that they are smaller in NPNB. The remodeling characteristics of the ECM components, with different mechanical properties, are differentially related to prognostically significant clinical and biological features in NB. The percentages of stained area are indicated. PNB, primary neuroblastoma; NPNB, non-primary neuroblastoma (after treatment); HE, hematoxylin and eosin.

CONCLUDING REMARKS

Biotensegrity is the structural principle of mechanotherapy. Cells are linked both to each other and to the ECM forming a mechanical biotensegral system in homeostasis. Cell–cell junctions are anchored to neighboring cells and focal adhesions to ECM, allowing forces to cross via intra-cellular cytoskeletal and nuclear networks. These structures fluctuate, and the multiple responses appear to strongly affect tissue remodeling and cell transformation. As described, normal organs tissue, primary NB, and post-treatment NB have a different amount and topography of biotensegral ECM elements. Conventional approaches have traditionally focused on the neoplastic cell. Moreover, an arsenal of mechanotherapeutic approaches to enhance the efficacy of more classical cancer therapeutics and overcome treatment resistance has already been discovered. To achieve more effective personalized strategies, further studies should consider to improve the definition of the interactions between tumor and stromal cells and the ECM elements and vascular constituents of the tumor, as well as their influence on treatment. We propose that integrating the tumor topo-functional networks of the ECM elements with the clinical, histopathology, and genetic information could provide new information about the impact of biotensegrity on patient care. Understanding the mechanical properties of tumor ECM components, related to variations in quantity, degree of interference, and types of organization, is key to defining new potential mechanotherapeutic targets and agents.

ACKNOWLEDGMENTS

This study was supported by grants from the FIS (contract PI10/15) and RTICC (Red Tematica de Investigacion Cooperativa en Cancer, contracts RD06/0020/0102; RD12/0036/0020), Instituto Carlos III Madrid, and ERDF (European Regional Development Fund). Luis María Escudero was supported by the Miguel Servet program (Instituto Carlos III). We would like to thank Marcial Garcia-Rojo (Pathology Unit, General Hospital, Ciudad Real,

Spain) for excellent technical assistance; SEHOP (Spanish Society of Hematology and Pediatric Oncology) and Desiree Ramal, Victoria Castel, and Adela Cañete (Pediatric Oncology Unit, University Hospital La Fe, Valencia, Spain) for patient clinical data management; and David Harrison for English language assistance.

REFERENCES

- Fuller RB. Tensegrity. *Portfolio Art News Annu* (1961) 4:112–27.
- Fuller RB. *Tensile-Integrity Structures*. United States patent 3063521 (1962).
- Galli C, Guizzardi S, Passeri G, Macaluso GM, Scandroglio R. Life on the wire: on tensegrity and force balance in cells. *Acta Biomed* (2005) 76(1):5–12.
- Ingber DE. The architecture of life. *Sci Am* (1998) 278(1):48–57. doi:10.1038/scientificamerican0198-48
- Ingber DE. Tensegrity-based mechanosensing from macro to micro. *Prog Biophys Mol Biol* (2008) 97(2–3):163–79. doi:10.1016/j.pbiomolbio.2008.02.005
- Hu S, Chen J, Wang N. Cell spreading controls balance of prestress by microtubules and extracellular matrix. *Front Biosci* (2004) 9:2177–82. doi:10.2741/1352
- Ingber DE. Tensegrity II. How structural networks influence cellular information processing networks. *J Cell Sci* (2003) 116(Pt 8):1397–408. doi:10.1242/jcs.00360
- Ingber DE. Tensegrity I. Cell structure and hierarchical systems biology. *J Cell Sci* (2003) 116(Pt 7):1157–73. doi:10.1242/jcs.00359
- Laurent VM, Canadas P, Fodil R, Planus E, Asnacios A, Wendling S, et al. Tensegrity behaviour of cortical and cytosolic cytoskeletal components in twisted living adherent cells. *Acta Biotheor* (2002) 50(4):331–56. doi:10.1023/A:1022676903680
- Stamenovic D, Mijailovich SM, Tolic-Norrelykke IM, Chen J, Wang N. Cell prestress. II. Contribution of microtubules. *Am J Physiol Cell Physiol* (2002) 282(3):C617–24. doi:10.1152/ajpcell.00271.2001
- Stamenovic D, Mijailovich SM, Tolic-Norrelykke IM, Wang N. Experimental tests of the cellular tensegrity hypothesis. *Biorheology* (2003) 40(1–3):221–5.
- Volokh KY, Vilnay O, Belsky M. Tensegrity architecture explains linear stiffening and predicts softening of living cells. *J Biomech* (2000) 33(12):1543–9. doi:10.1016/S0021-9290(00)00157-3
- Wang N, Naruse K, Stamenovic D, Fredberg JJ, Mijailovich SM, Tolic-Norrelykke IM, et al. Mechanical behavior in living cells consistent with the tensegrity model. *Proc Natl Acad Sci U S A* (2001) 98(14):7765–70. doi:10.1073/pnas.141199598
- Wang N, Tolic-Norrelykke IM, Chen J, Mijailovich SM, Butler JP, Fredberg JJ, et al. Cell prestress. I. Stiffness and prestress are closely associated in

- adherent contractile cells. *Am J Physiol Cell Physiol* (2002) **282**(3):C606–16. doi:10.1152/ajpcell.00269.2001
15. Ross TD, Coon BG, Yun S, Baeyens N, Tanaka K, Ouyang M, et al. Integrins in mechanotransduction. *Curr Opin Cell Biol* (2013) **25**(5):613–8. doi:10.1016/j.ceb.2013.05.006
 16. Chen CS. Mechanotransduction – a field pulling together? *J Cell Sci* (2008) **121**(Pt 20):3285–92. doi:10.1242/jcs.023507
 17. Luxton GW, Gomes ER, Folker ES, Vintinner E, Gundersen GG. Linear arrays of nuclear envelope proteins harness retrograde actin flow for nuclear movement. *Science* (2010) **329**(5994):956–9. doi:10.1126/science.1189072
 18. Morgan JT, Pfeiffer ER, Thirkill TL, Kumar P, Peng G, Fridolfsson HN, et al. Nesprin-3 regulates endothelial cell morphology, perinuclear cytoskeletal architecture, and flow-induced polarization. *Mol Biol Cell* (2011) **22**(22):4324–34. doi:10.1091/mbc.E11-04-0287
 19. Ketema M, Sonnenberg A. Nesprin-3: a versatile connector between the nucleus and the cytoskeleton. *Biochem Soc Trans* (2011) **39**(6):1719–24. doi:10.1042/BST20110669
 20. Tapley EC, Starr DA. Connecting the nucleus to the cytoskeleton by SUN-KASH bridges across the nuclear envelope. *Curr Opin Cell Biol* (2013) **25**(1):57–62. doi:10.1016/j.ceb.2012.10.014
 21. Lombardi ML, Jaalouk DE, Shanahan CM, Burke B, Roux KJ, Lammerding J. The interaction between nesprins and sun proteins at the nuclear envelope is critical for force transmission between the nucleus and cytoskeleton. *J Biol Chem* (2011) **286**(30):26743–53. doi:10.1074/jbc.M111.233700
 22. Roux KJ, Crisp ML, Liu Q, Kim D, Kozlov S, Stewart CL, et al. Nesprin 4 is an outer nuclear membrane protein that can induce kinesin-mediated cell polarization. *Proc Natl Acad Sci U S A* (2009) **106**(7):2194–9. doi:10.1073/pnas.0808602106
 23. Swift J, Ivanovska IL, Buxboim A, Harada T, Dingal PC, Pinter J, et al. Nuclear lamin-A scales with tissue stiffness and enhances matrix-directed differentiation. *Science* (2013) **341**(6149):1240104. doi:10.1126/science.1240104
 24. Liu Z, Tan JL, Cohen DM, Yang MT, Sniadecki NJ, Ruiz SA, et al. Mechanical tugging force regulates the size of cell-cell junctions. *Proc Natl Acad Sci U S A* (2010) **107**(22):9944–9. doi:10.1073/pnas.0914547107
 25. Maruthamuthu V, Sabass B, Schwarz US, Gardel ML. Cell-ECM traction force modulates endogenous tension at cell-cell contacts. *Proc Natl Acad Sci U S A* (2011) **108**(12):4708–13. doi:10.1073/pnas.1011123108
 26. le Duc Q, Shi Q, Blonk I, Sonnenberg A, Wang N, Leckband D, et al. Vinculin potentiates E-cadherin mechanosensing and is recruited to actin-anchored sites within adherens junctions in a myosin II-dependent manner. *J Cell Biol* (2010) **189**(7):1107–15. doi:10.1083/jcb.201001149
 27. Twiss F, de Rooij J. Cadherin mechanotransduction in tissue remodeling. *Cell Mol Life Sci* (2013) **70**(21):4101–16. doi:10.1007/s00018-013-1329-x
 28. Huang S, Ingber DE. The structural and mechanical complexity of cell-growth control. *Nat Cell Biol* (1999) **1**(5):E131–8. doi:10.1038/13043
 29. Schwarz US. Catch me because you can: a mathematical model for mechanosensing. *Biophys J* (2013) **105**(6):1289–91. doi:10.1016/j.bpj.2013.08.016
 30. Benoit YD, Lussier C, Ducharme PA, Sivret S, Schnapp LM, Basora N, et al. Integrin alpha8beta1 regulates adhesion, migration and proliferation of human intestinal crypt cells via a predominant RhoA/ROCK-dependent mechanism. *Biol Cell* (2009) **101**(12):695–708. doi:10.1042/BC20090060
 31. Zargham R. Tensegrin in context: dual role of alpha8 integrin in the migration of different cell types. *Cell Adh Migr* (2010) **4**(4):485–90. doi:10.4161/cam.4.4.12403
 32. Kim SH, Turnbull J, Guimond S. Extracellular matrix and cell signalling: the dynamic cooperation of integrin, proteoglycan and growth factor receptor. *J Endocrinol* (2011) **209**(2):139–51. doi:10.1530/JOE-10-0377
 33. Mustata T, Rusu V. Mechanotransduction and tensegrity (I). *Rev Med Chir Soc Med Nat Iasi* (1998) **102**(3-4):25–35.
 34. Noguera R, Nieto OA, Tadeo I, Farinas F, Alvaro T. Extracellular matrix, biotensegrity and tumor microenvironment. An update and overview. *Histol Histopathol* (2012) **27**(6):693–705.
 35. Huang C, Miyazaki K, Akaishi S, Watanabe A, Hyakusoku H, Ogawa R. Biological effects of cellular stretch on human dermal fibroblasts. *J Plast Reconstr Aesthet Surg* (2013) **66**(12):e351–61. doi:10.1016/j.jbjs.2013.08.002
 36. Lovett DB, Shekhar N, Nickerson JA, Roux KJ, Lele TP. Modulation of nuclear shape by substrate rigidity. *Cell Mol Bioeng* (2013) **6**(2):230–8. doi:10.1007/s12195-013-0270-2
 37. Duncan RL, Turner CH. Mechanotransduction and the functional response of bone to mechanical strain. *Calcif Tissue Int* (1995) **57**(5):344–58. doi:10.1007/BF00302070
 38. Engler AJ, Sen S, Sweeney HL, Discher DE. Matrix elasticity directs stem cell lineage specification. *Cell* (2006) **126**(4):677–89. doi:10.1016/j.cell.2006.06.044
 39. Lo CM, Wang HB, Dembo M, Wang YL. Cell movement is guided by the rigidity of the substrate. *Biophys J* (2000) **79**(1):144–52. doi:10.1016/S0006-3495(00)76279-5
 40. Zou X, Feng B, Dong T, Yan G, Tan B, Shen H, et al. Up-regulation of type I collagen during tumorigenesis of colorectal cancer revealed by quantitative proteomic analysis. *J Proteomics* (2013) **94**:473–85. doi:10.1016/j.jpro.2013.10.020
 41. Tlsty TD. Stromal cells can contribute oncogenic signals. *Semin Cancer Biol* (2001) **11**(2):97–104. doi:10.1006/scbi.2000.0361
 42. Tlsty TD, Coussens LM. Tumor stroma and regulation of cancer development. *Annu Rev Pathol* (2006) **1**:119–50. doi:10.1146/annurev.pathol.1.110304.100224
 43. Pupa SM, Menard S, Forti S, Tagliabue E. New insights into the role of extracellular matrix during tumor onset and progression. *J Cell Physiol* (2002) **192**(3):259–67. doi:10.1002/jcp.10142
 44. Dityatev A, Schachner M, Sonderegger P. The dual role of the extracellular matrix in synaptic plasticity and homeostasis. *Nat Rev Neurosci* (2010) **11**(11):735–46. doi:10.1038/nrn2898
 45. Liu H, Tang L. Mechano-regulation of alternative splicing. *Curr Genomics* (2013) **14**(1):49–55. doi:10.2174/138920213804999156
 46. Plotnikov SV, Waterman CM. Guiding cell migration by tugging. *Curr Opin Cell Biol* (2013) **25**(5):619–26. doi:10.1016/j.ceb.2013.06.003
 47. Smith HW, Marshall CJ. Regulation of cell signalling by uPAR. *Nat Rev Mol Cell Biol* (2010) **11**(1):23–36. doi:10.1038/nrm2821
 48. Ingber DE. Cancer as a disease of epithelial-mesenchymal interactions and extracellular matrix regulation. *Differentiation* (2002) **70**(9–10):547–60. doi:10.1046/j.1432-0436.2002.700908.x
 49. Huang S, Ingber DE. A non-genetic basis for cancer progression and metastasis: self-organizing attractors in cell regulatory networks. *Breast Dis* (2006) **26**:27–54.
 50. Tadeo I, Piqueras M, Montaner D, Villamon E, Berbegall AP, Canete A, et al. Quantitative modeling of clinical, cellular and extracellular matrix variables suggest prognostic indicators in cancer. A model in neuroblastoma. *Pediatr Res* (2013) **75**(2):302–14. doi:10.1038/pr.2013.217
 51. DuFort CC, Paszek MJ, Weaver VM. Balancing forces: architectural control of mechanotransduction. *Nat Rev Mol Cell Biol* (2010) **12**(5):308–19. doi:10.1038/nrm3112
 52. Pathak A, Kumar S. Independent regulation of tumor cell migration by matrix stiffness and confinement. *Proc Natl Acad Sci U S A* (2012) **109**(26):10334–9. doi:10.1073/pnas.1118073109
 53. Cross SE, Jin YS, Rao J, Gimzewski JK. Nanomechanical analysis of cells from cancer patients. *Nat Nanotechnol* (2007) **2**(12):780–3. doi:10.1038/nnano.2007.388
 54. Lekka M, Laidler P, Gil D, Lekki J, Stachura Z, Hryniewicz AZ. Elasticity of normal and cancerous human bladder cells studied by scanning force microscopy. *Eur Biophys J* (1999) **28**(4):312–6. doi:10.1007/s002490050213
 55. Guarino M, Rubino B, Ballabio G. The role of epithelial-mesenchymal transition in cancer pathology. *Pathology* (2007) **39**(3):305–18. doi:10.1080/00313020701329914
 56. Lee JM, Dedhar S, Kalluri R, Thompson EW. The epithelial-mesenchymal transition: new insights in signaling, development, and disease. *J Cell Biol* (2006) **172**(7):973–81. doi:10.1083/jcb.200601018
 57. Suresh S. Biomechanics and biophysics of cancer cells. *Acta Biomater* (2007) **3**(4):413–38. doi:10.1016/j.actbio.2007.04.002
 58. Blick T, Widodo E, Hugo H, Waltham M, Lenburg ME, Neve RM, et al. Epithelial mesenchymal transition traits in human breast cancer cell lines. *Clin Exp Metastasis* (2008) **25**(6):629–42. doi:10.1007/s10585-008-9170-6
 59. Kenny PA, Bissell MJ. Tumor reversion: correction of malignant behavior by microenvironmental cues. *Int J Cancer* (2003) **107**(5):688–95. doi:10.1002/ijc.11491
 60. Vassy J, Portet S, Beil M, Millot G, Fauvel-Lafeve F, Gasset G, et al. Weightlessness acts on human breast cancer cell line MCF-7. *Adv Space Res* (2003) **32**(8):1595–603. doi:10.1016/S0273-1177(03)90400-5
 61. Mierke CT. Physical break-down of the classical view on cancer cell invasion and metastasis. *Eur J Cell Biol* (2013) **92**(3):89–104. doi:10.1016/j.ejcb.2012.12.002

62. Shimada H, Ambros IM, Dehner LP, Hata J, Joshi VV, Roald B, et al. The International Neuroblastoma Pathology Classification (the Shimada system). *Cancer* (1999) **86**(2):364–72. doi:10.1002/(SICI)1097-0142(19990715)86:2<364::AID-CNCR21>3.0.CO;2-7
63. Sun Y, Campisi J, Higano C, Beer TM, Porter P, Coleman I, et al. Treatment-induced damage to the tumor microenvironment promotes prostate cancer therapy resistance through WNT16B. *Nat Med* (2012) **18**(9):1359–68. doi:10.1038/nm.2890
64. Sun Y, Nelson PS. Molecular pathways: involving microenvironment damage responses in cancer therapy resistance. *Clin Cancer Res* (2012) **18**(15):4019–25. doi:10.1158/1078-0432.CCR-11-0768
65. Choi IK, Strauss R, Richter M, Yun CO, Lieber A. Strategies to increase drug penetration in solid tumors. *Front Oncol* (2013) **3**:193. doi:10.3389/fonc.2013.00193
66. Cukierman E, Bassi DE. The mesenchymal tumor microenvironment: a drug-resistant niche. *Cell Adh Migr* (2012) **6**(3):285–96. doi:10.4161/cam.20210
67. Pritchard JR, Gilbert LA, Meacham CE, Ricks JL, Jiang H, Lauffenburger DA, et al. Bcl-2 family genetic profiling reveals microenvironment-specific determinants of chemotherapeutic response. *Cancer Res* (2011) **71**(17):5850–8. doi:10.1158/0008-5472.CAN-11-1014
68. Aguilar-Cuenca R, Juanes-García A, Vicente-Manzanares M. Myosin II in mechanotransduction: master and commander of cell migration, morphogenesis, and cancer. *Cell Mol Life Sci* (2013) **71**(3):479–92. doi:10.1007/s00018-013-1439-5
69. Álvaro Naranjo T, Noguera Salvá R, Fariñas Guerrero F. Extracellular matrix: morphology, function and biotensegrity (part I). *Rev Esp Patol* (2009) **42**(4):249–61.
70. Álvaro Naranjo T, Noguera Salvá R, Fariñas Guerrero F. The extracellular matrix: from the molecular mechanics to the tumoral microenvironment (part II). *Rev Esp Patol* (2010) **43**(1):24–32.
71. Negaard HF, Svennevig K, Kolset SO, Iversen N, Lothe IM, Ostensstad B, et al. Alterations in regulators of the extracellular matrix in non-Hodgkin lymphomas. *Leuk Lymphoma* (2009) **50**(6):998–1004. doi:10.1080/10428190902889270
72. Cohn SL, Pearson AD, London WB, Monclair T, Ambros PF, Brodeur GM, et al. The International Neuroblastoma Risk Group (INRG) classification system: an INRG Task Force report. *J Clin Oncol* (2009) **27**(2):289–97. doi:10.1200/JCO.2008.16.6785
73. Schleiermacher G, Janoueix-Lerosey I, Ribeiro A, Klijanienko J, Couturier J, Pierron G, et al. Accumulation of segmental alterations determines progression in neuroblastoma. *J Clin Oncol* (2010) **28**(19):3122–30. doi:10.1200/JCO.2009.26.7955
74. Schleiermacher G, Mosseri V, London WB, Maris JM, Brodeur GM, Attiyeh E, et al. Segmental chromosomal alterations have prognostic impact in neuroblastoma: a report from the INRG project. *Br J Cancer* (2012) **107**(8):1418–22. doi:10.1038/bjc.2012.375
75. Escudero LM, Costa Lda F, Kicheva A, Briscoe J, Freeman M, Babu MM. Epithelial organization revealed by a network of cellular contacts. *Nat Commun* (2011) **2**:526. doi:10.1038/ncomms1536
76. Saez A, Acha B, Montero-Sanchez A, Rivas E, Escudero LM, Serrano C. Neuromuscular disease classification system. *J Biomed Opt* (2013) **18**(6):066017. doi:10.1117/1.JBO.18.6.066017
77. Saez A, Rivas E, Montero-Sanchez A, Paradas C, Acha B, Pascual A, et al. Quantifiable diagnosis of muscular dystrophies and neurogenic atrophies through network analysis. *BMC Med* (2013) **11**:77. doi:10.1186/1741-7015-11-77
78. Sanchez-Gutierrez D, Saez A, Pascual A, Escudero LM. Topological progression in proliferating epithelia is driven by a unique variation in polygon distribution. *PLoS One* (2013) **8**(11):e79227. doi:10.1371/journal.pone.0079227
79. Csikasz-Nagy A, Escudero LM, Guillaud M, Sedwards S, Baum B, Cavaliere M. Cooperation and competition in the dynamics of tissue architecture during homeostasis and tumorigenesis. *Semin Cancer Biol* (2013) **23**(4):293–8. doi:10.1016/j.semcancer.2013.05.009
80. Guillaud M, Clem C, Macaulay C. An in silico platform for the study of epithelial pre-invasive neoplastic development. *Biosystems* (2010) **102**(1):22–31. doi:10.1016/j.biosystems.2010.07.008
81. Johnson LM, Price DK, Figg WD. Treatment-induced secretion of WNT16B promotes tumor growth and acquired resistance to chemotherapy: implications for potential use of inhibitors in cancer treatment. *Cancer Biol Ther* (2013) **14**(2):90–1. doi:10.4161/cbt.22636
82. Ramsay AG, Clear AJ, Kelly G, Fatah R, Matthews J, Macdougall F, et al. Follicular lymphoma cells induce T-cell immunologic synapse dysfunction that can be repaired with lenalidomide: implications for the tumor microenvironment and immunotherapy. *Blood* (2009) **114**(21):4713–20. doi:10.1182/blood-2009-04-217687
83. Pupa SM, Giuffrè S, Castiglioni F, Bertola L, Cantu M, Bongarzone I, et al. Regulation of breast cancer response to chemotherapy by fibulin-1. *Cancer Res* (2007) **67**(9):4271–7. doi:10.1158/0008-5472.CAN-06-4162
84. Triulzi T, Ratti M, Tortoreto M, Ghirelli C, Aiello P, Regondi V, et al. Maspain influences response to doxorubicin by changing the tumor microenvironment organization. *Int J Cancer* (2013). doi:10.1002/ijc.28608
85. Gao C, Kozłowska A, Nechaev S, Li H, Zhang Q, Hossain DM, et al. TLR9 signaling in the tumor microenvironment initiates cancer recurrence after radiation therapy. *Cancer Res* (2013) **73**(24):7211–21. doi:10.1158/0008-5472.CAN-13-1314
86. Jodele S, Blavier L, Yoon JM, DeClerck YA. Modifying the soil to affect the seed: role of stromal-derived matrix metalloproteinases in cancer progression. *Cancer Metastasis Rev* (2006) **25**(1):35–43. doi:10.1007/s10555-006-7887-8
87. Sabbah M, Emami S, Redeuilh G, Julien S, Prevost G, Zimmer A, et al. Molecular signature and therapeutic perspective of the epithelial-to-mesenchymal transitions in epithelial cancers. *Drug Resist Updat* (2008) **11**(4–5):123–51. doi:10.1016/j.drug.2008.07.001
88. Raymond E, Dalgleish A, Damber JE, Smith M, Pili R. Mechanisms of action of tasquinimod on the tumour microenvironment. *Cancer Chemother Pharmacol* (2013) **73**(1):1–8. doi:10.1007/s00280-013-2321-8

Conflict of Interest Statement: The authors declare that the research was conducted in the absence of any commercial or financial relationships that could be construed as a potential conflict of interest.

Received: 31 December 2013; paper pending published: 20 January 2014; accepted: 15 February 2014; published online: 04 March 2014.

Citation: Tadeo I, Berbegall AP, Escudero LM, Álvaro T and Noguera R (2014) Biotensegrity of the extracellular matrix: physiology, dynamic mechanical balance, and implications in oncology and mechanotherapy. *Front. Oncol.* **4**:39. doi: 10.3389/fonc.2014.00039

This article was submitted to *Molecular and Cellular Oncology*, a section of the journal *Frontiers in Oncology*.

Copyright © 2014 Tadeo, Berbegall, Escudero, Álvaro and Noguera. This is an open-access article distributed under the terms of the Creative Commons Attribution License (CC BY). The use, distribution or reproduction in other forums is permitted, provided the original author(s) or licensor are credited and that the original publication in this journal is cited, in accordance with accepted academic practice. No use, distribution or reproduction is permitted which does not comply with these terms.

Glycosaminoglycan profiling in different cell types using infrared spectroscopy and imaging

Stéphane Brézillon · Valérie Untereiner · Lila Lovergne · Irene Tadeo · Rosa Noguera · François-Xavier Maquart · Yanusz Wegrowski · Ganesh D. Sockalingum

Received: 2 April 2014 / Revised: 30 May 2014 / Accepted: 24 June 2014
© Springer-Verlag Berlin Heidelberg 2014

Abstract We recently identified vibrational spectroscopic markers characteristic of standard glycosaminoglycan (GAG) molecules. The aims of the present work were to further this investigation to more complex biological systems and to characterize, via their spectral profiles, cell types with different capacities for GAG synthesis. After recording spectral information from individual GAG standards (hyaluronic acid, chondroitin sulfate, dermatan sulfate, heparan sulfate) and GAG-GAG mixtures, GAG-defective mutant Chinese hamster ovary (CHO)-745 cells, wild-type CHO cells, and chondrocytes were analyzed as suspensions by high-

throughput infrared spectroscopy and as single isolated cells by infrared imaging. Spectral data were processed and interpreted by exploratory unsupervised chemometric methods based on hierarchical cluster analysis and principal component analysis. Our results showed that the spectral information obtained was discriminant enough to clearly delineate between the different cell types both at the cell suspension and single-cell levels. The abilities of the technique are to perform spectral profiling and to identify single cells with different potentials to synthesize GAGs. Infrared microspectroscopy/imaging could therefore be developed for cell screening purposes and further for identifying GAG molecules in normal tissues during physiological conditions (aging, healing process) and numerous pathological states (arthritis, cancer).

Electronic supplementary material The online version of this article (doi:10.1007/s00216-014-7994-2) contains supplementary material, which is available to authorized users.

S. Brézillon · L. Lovergne · I. Tadeo · F.-X. Maquart · Y. Wegrowski
Laboratoire de Biochimie médicale et de Biologie Moléculaire, UFR de Médecine, Université de Reims Champagne-Ardenne, 51 rue Cognacq-Jay, 51095 Reims Cedex, France

S. Brézillon · V. Untereiner · F.-X. Maquart · Y. Wegrowski · G. D. Sockalingum (✉)
CNRS UMR7369, Matrice Extracellulaire et Dynamique Cellulaire, MEDyC, 51095 Reims, France
e-mail: ganesh.sockalingum@univ-reims.fr

V. Untereiner · L. Lovergne · G. D. Sockalingum
MÉDIAN-Biophotonique et Technologies pour la Santé, UFR de Pharmacie, Université de Reims Champagne-Ardenne, 51 rue Cognacq-Jay, 51096 Reims Cedex, France

F.-X. Maquart
Laboratoire Central de Biochimie, CHU de Reims, 51092 Reims Cedex, France

I. Tadeo · R. Noguera
Laboratorio de Patología Molecular, Departamento de Patología, Facultad de Medicina y Odontología, INCLIVA (Universidad de Valencia; Fundación Investigación Hospital Clínico de Valencia), Avda. Blasco Ibañez 15, Valencia 46010, Spain

Keywords Glycosaminoglycans · Chondrocytes · Chinese hamster ovary cells · Infrared spectroscopy · Image analysis · Data analysis

Abbreviations

CHO	Chinese hamster ovary
CS	Chondroitin sulfate
DPBS	Dulbecco's phosphate buffer saline
DS	Dermatan sulfate
FTIR	Fourier transform infrared
GAG	Glycosaminoglycan
HA	Hyaluronic acid
HCA	Hierarchical cluster analysis
HEP	Heparin
HS	Heparan sulfate
KS	Keratan sulfate
PC	Principal component
PCA	Principal component analysis

PFA	Paraformaldehyde
PG	Proteoglycan

Introduction

Proteoglycans (PGs) are ubiquitous major macromolecules of extracellular matrices, cell surfaces, and some intracellular granules [1]. They exhibit an architectural role and maintain the integrity of the tissue. PGs are composed of a glycoprotein core to which one or several sulfated glycosaminoglycan (GAG) chains are attached by covalent linkage. GAGs are expressed in a spatially and temporally regulated manner [2]. The structure and abundance of GAG chains vary according to the tissue, cell types, developmental states, and regulatory signals received from soluble factors [3].

Physicochemical analysis of GAGs from tissue sections was first reported for hyaluronic acid (HA) and chondroitin sulfate (CS) [4, 5], for CS/dermatan sulfate (DS) [6], and for keratan sulfate (KS) [7, 8]. These studies involved ion pairing chromatography and mass spectrometry applied to enzyme digest solutions. The chemical analysis of such preparations is therefore a tedious task accomplished by enzymatic depolymerization of the chain with specific bacterial enzymes followed by disaccharide analysis by high-performance liquid chromatography, capillary electrophoresis, or fluorophore-assisted carbohydrate electrophoresis [9, 10].

Methods were developed to analyze GAGs from small tissue quantities. Considering the heterogeneity of normal tissue and the cell microenvironment, a profiling method for GAG applicable to the histological scale was recently developed [11]. To better understand the roles of GAGs in physiology and pathophysiology, it is important to be able to determine the structures of GAGs from a small quantity of tissue but even better at the cell scale according to the cell phenotype.

We previously showed that infrared (IR) and Raman microspectroscopies are sensitive enough to characterize, differentiate, and classify types and subtypes of GAGs despite their close molecular structures [12, 13]. The first IR spectra of GAGs were published more than 50 years ago [14]. IR physicochemical characterization of isolated GAGs was described [15–24]. In terms of structural and compositional analysis, IR spectroscopy is able to give a complete “molecular fingerprint” of the studied sample. It is highly sensitive to the structure, composition, and environment of the molecules constituting the studied specimen. Furthermore, this biophotonic method is rapid, non-destructive, and non-contact and does not require external markers. The association of spectroscopy with powerful data analytical methods gives more insight into the interpretation of the spectral information and molecular-level phenomena. When coupled with a

microscope, vibrational microspectroscopies become highly sensitive methods capable of probing at the micron level, thus necessitating only small amounts of sample.

With the use of chemometric methods, such as hierarchical cluster analysis (HCA) and principal component analysis (PCA), some characteristic spectral regions and bands were identified, which could be used to well characterize standard GAGs by vibrational microspectroscopy [12, 13]. These results could be extremely useful for performing quality tests on GAG samples. Moreover, vibrational microspectroscopy was shown to be both qualitative and quantitative. Therefore, the aim of this study was to apply infrared spectroscopy and imaging to get in a first step the spectroscopic signatures of molecular mixtures of different GAGs and in a second step those of cells expressing different levels of GAG molecules, both in suspensions and in isolated single cells.

Cartilage chondrocytes are the cells with the highest capacity for GAG synthesis. Cartilage plays an important role as a shock absorber and space holder in living organisms [25]. These physical properties are closely connected with its molecular structure and intermolecular interactions between polymeric components, such as GAGs. The swelling of cartilage is based on the binding of water to polar groups of GAGs (carboxylate, sulfate), on the electrostatic repulsion between GAG molecules and entropic contributions resulting from the mixing of water and counterions [14]. HA and CS belong to the most important GAG molecules present in cartilage. The CHO-745 cell line, lacking xylosyl transferase, is the only known mutant deficient in the synthesis of CS and heparan sulfate (HS) [26] which results in a decreased amount of GAGs in these cells, compared to the wild-type CHO (CHO-WT). In the present work, we first report IR spectroscopy of major types of GAGs, i.e., HA, heparin (HEP), HS, C4S, C6S, and DS. We next determined the mean IR spectra of CHO-745, CHO-WT, and chondrocyte cells in suspension and performed IR imaging of single cells. Spectral data were analyzed by HCA and PCA chemometric methods in order to characterize these cell types exhibiting from low to high levels of GAG synthesis.

Materials and methods

GAG samples

Six standard glycosaminoglycans (Table 1) were analyzed. In our previous study, the range of the concentrations of these standard GAG solutions was defined [13]. Each GAG was solubilized in sterilized water at 1 mg/mL concentration. For infrared imaging, one drop of 3 μ L for each GAG (or their mixtures) was deposited in three replicates on a calcium fluoride substrate, transparent to infrared radiation, and dried at room temperature.

Table 1 Description of the standard GAG molecules used

Glycosaminoglycans	Abbreviation	Species	Tissue	Supplier
Hyaluronic acid	HA	Undefined	Undefined	MP Biomedicals
Chondroitin-4-sulfate	C4S	Whale	Cartilage	Sigma
Chondroitin-6-sulfate	C6S	Shark	Cartilage	Sigma
Dermatan sulfate	DS	Undefined	Undefined	Celsus
Heparan sulfate	HS	Undefined	Undefined	Celsus
Heparin	HEP	Undefined	Undefined	US Biomedical

Cell culture

In this study, three cell cultures were carried out: two cell lines, CHO-WT (CHO-K1, ATCC[®] CCL-61[™]) and CHO mutated cells lacking xylosyl transferase (CHO-745, ATCC[®] CRL-2242[™]), and one primary culture of human chondrocytes. Chondrocytes and CHO cells were grown in DMEM/F-12 medium (Dulbecco's Modified Eagle Medium: Nutrient Mixture F-12, Gibco, Invitrogen, France) supplemented with an antifungal agent (Amphotericin B, Gibco, Invitrogen, France). Cultures were maintained at 37 °C in a humidified atmosphere containing 5 % (v/v) CO₂. Cells were detached at 80 % of confluency with 0.5 % trypsin/EDTA (Invitrogen). Cells in suspension were centrifuged at 420g for 3 min, then pellets were resuspended. Cell viability was assessed by trypan blue exclusion assay. For infrared high-throughput analysis, 5 µL of cell suspension (1 × 10⁵ cells/5 µL) was deposited in five replicates on a silicon 384-well optical substrate and air-dried at room temperature. For infrared imaging, the three different cell types were plated on a calcium fluoride substrate at 1.5 × 10⁴ cells/mL and allowed to adhere. After 24 to 48 h, CaF₂ substrates were removed from the culture medium and washed three times with Dulbecco's phosphate buffer saline (DPBS). Cell fixation was performed using 4 % paraformaldehyde for 30 min at room temperature. Cells were rinsed with DPBS and distilled water to remove PFA, then air-dried.

High-throughput infrared analysis of cells in suspension

Cells in suspension were deposited on the silicon sample plate, dried, and placed in the high-throughput screening HTS-XT extension (Bruker Optics GmbH, Ettlingen, Germany) which was coupled to a Tensor 27 (Bruker Optics GmbH) spectrometer (see Electronic Supplementary Material (ESM) Fig. S1a). Fourier transform infrared (FTIR) measurements were performed in transmission mode and were recorded at a spectral resolution of 4 cm⁻¹ using 64 scans in the spectral range 4,000–400 cm⁻¹ (OPUS v6.5 software, Bruker Optics GmbH, Ettlingen, Germany). Before each sample measurement, a background was taken in the same conditions and subsequently subtracted automatically.

Infrared imaging of GAG dried drops and single cells

IR images were acquired in transmission mode using the PerkinElmer Spectrum Spotlight 400 imaging system (Courtaboeuf, France) at a spatial resolution of 25 µm/pixel for GAG drops and 6.25 µm/pixel for cells (see ESM, Fig. S1b). The spectral range 4,000–800 cm⁻¹ was used at a spectral resolution of 4 cm⁻¹. Sixteen and 128 scans were averaged for GAG drops and for single cells, respectively. The raw spectra were subjected to atmospheric correction algorithm to compensate for water vapor and CO₂ contributions (Spectrum-Image, version 1.6, PerkinElmer).

Spectral images of GAG samples were taken across the diameter of each drop, and all spectra were averaged. For fixed cells, spectral images were taken of the whole single cell and all spectra were averaged after removing spectral contribution from the CaF₂ substrate.

Data analysis

Spectra were preprocessed with the OPUS 6.5 software (Bruker Optics GmbH, Ettlingen, Germany). The following procedures were used: baseline correction, spectral averaging, second derivative, and vector normalization. Preprocessed spectral data sets were analyzed by two unsupervised exploratory methods: HCA and PCA. HCA is a method of cluster analysis that seeks to construct a hierarchy of clusters. It gives the heterogeneity between spectra by calculating the distance between them. This constitutes the linkage criterion, and the most common distance measured is the Euclidean distance or the squared Euclidean distance. Another criterion is the method used for cluster combination. The agglomerative method based on the closest neighbor principle (Ward's algorithm) was used for FTIR data. Therefore, HCA groups spectra according to their similarities and the final representation is a dendrogram. HCA was performed using the OPUS 6.5 software (Bruker Optics GmbH).

PCA is a statistical procedure which, via an orthogonal transformation, converts a set of observations of possibly correlated variables into a set of values of linearly uncorrelated variables called principal components (PCs). In this case, the first principal component carries the largest possible variance

in the data and each succeeding component in turn has the highest variance possible. PCA reveals the internal structure of the data in a way that best explains the variance in the data. It is a common algorithm used to reduce high-dimensional data such as spectroscopic data and to represent them in the new space composed of the principal components. The discrimination between spectral data can be observed using the scores of the PCs and represented via 2D or 3D scatterplots. PCA was performed using an in-house routine built in the MATLAB software (MathWorks, Natick, MA, USA).

Results and discussion

Infrared microspectroscopy of GAG mixtures

Each GAG molecule (HA, HS, HEP, DS, C4S, C6S) was analyzed independently in the form of a dried drop using infrared microspectroscopy. The representative spectrum of each GAG was calculated by averaging all spectra across the drop diameter (see ESM, Fig. S2). The spectral window 1,800–900 cm^{-1} was used because this range was found to be most specific for individual GAG molecules in our previous studies [13]. The bands near 1,610 and 1,410 cm^{-1} were

assigned, respectively, to the presence of the planar $-\text{COO}^-$ group antisymmetric and symmetric vibrations in the C_6 position of the disaccharide unit of uronic acid. The band around 1,250 cm^{-1} corresponded to the sulfate group (SO_3^-) antisymmetric vibration present in GAG except for hyaluronic acid which is a non-sulfated GAG. For this vibration, the most intense band was attributed to HEP and the least one to HS. The region covering the range 1,100–1,000 cm^{-1} was associated to the vibrations of saccharide molecular links corresponding to C–O–C, C–C–C, and C–C–O stretchings of the pyranose ring structures of the GAG molecules [27].

The arithmetic mean spectrum was computed using the six representative spectra. Then, the six solubilized GAG molecules were mixed and the resulting solution was analyzed in the form of dried drops. When the mean spectrum of the mixture was compared to the arithmetic mean spectrum (see Fig. 1), there was no discernable difference between the two mean spectra, indicating an absence of interactions between the GAG molecules.

Characterization of GAGs in cells in suspension by high-throughput FTIR spectroscopy

Taking into account the characteristic spectral information obtained with individual GAG molecules and GAG mixtures,

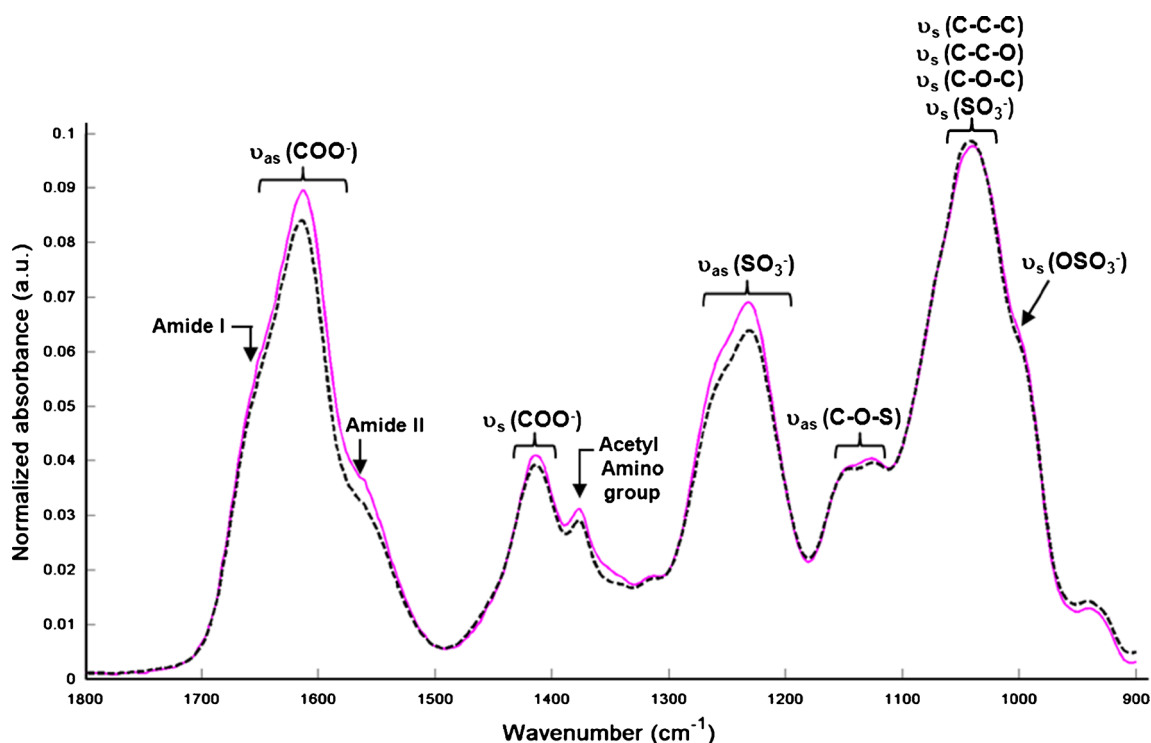


Fig. 1 FTIR spectroscopy of GAG mixtures. Comparison between the mean spectrum of a mixture of six glycosaminoglycan standards (pink curve) and the arithmetic sum of the spectra of the six GAGs (black dotted curve) in the spectral range 1,800–900 cm^{-1} . The six GAG standards used

were hyaluronic acid, heparan sulfate, heparin, dermatan sulfate, chondroitin-6-sulfate, and chondroitin-4-sulfate. Bands are tentatively assigned to their corresponding chemical group vibration. ν stretching, a_s antisymmetric, s symmetric vibrations

we have undertaken measurements to characterize cells capable of synthesizing GAGs from very low to high levels, i.e., CHO-745, CHO-WT, and chondrocytes. In Fig. 2a, we compared the normalized mean FTIR spectrum of these cell types obtained from cells in suspension. Visually, the spectral profiles of CHO-745, CHO-WT, and chondrocytes were quite similar in the 1,800–900-cm⁻¹ spectral range, with, however, some very minor modifications for chondrocytes in the 1,200–900-cm⁻¹ spectral range (saccharide absorption region).

The cell suspension spectra of CHO-745, CHO-WT, and chondrocytes were analyzed by the HCA multivariate

statistical analysis. This method was performed on all second derivative spectra ($n=5$) for each cell suspension in the 1,200–900-cm⁻¹ spectral range. The five spectra of each cell suspension were grouped in the same cluster and exhibited a low degree of heterogeneity, indicating a good reproducibility of the measurements and, therefore, a low intra-group variability. The inter-group variability was sufficiently high to distinguish the three cell types (Fig. 2b). The dendrogram also revealed that the variability between CHO-745 and CHO-WT was lower than the variability between the two CHO types and the chondrocytes. The clear-cut classification using the second

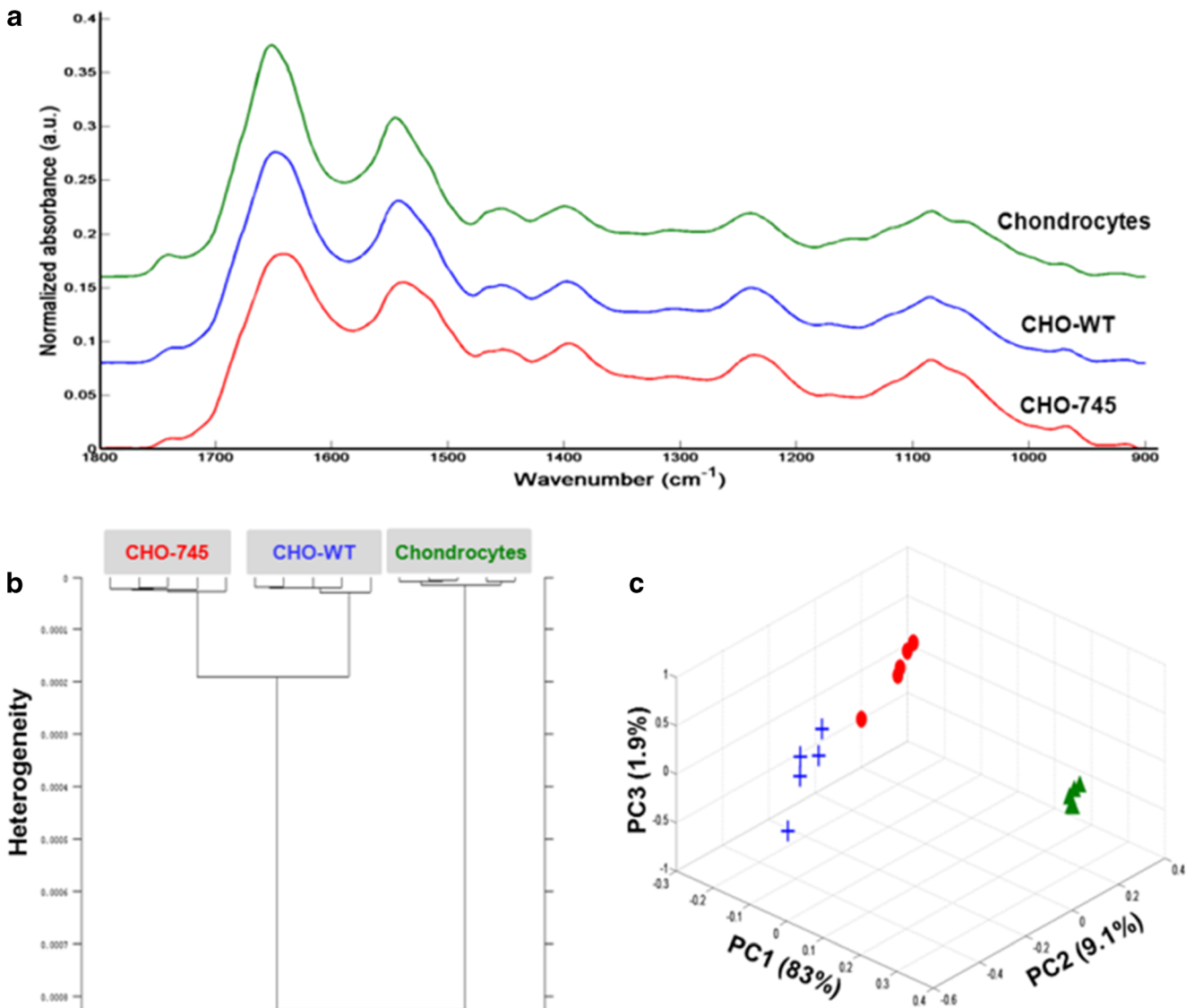


Fig. 2 Data processing of infrared spectra from high-throughput analysis of cells in suspension. **a** Comparison between the mean spectra of CHO-745 (red curve), CHO-WT (blue curve), and chondrocytes (green curve) in suspension in the spectral range 1,800–900 cm⁻¹. Each mean spectrum is an average of five replicate spectra. **b** Hierarchical cluster analysis (HCA) of CHO-745, CHO-WT cell lines, and chondrocyte spectra. HCA was calculated on second derivative spectra in the spectral range 1,200–

900 cm⁻¹. All replicates of each cell type are well clustered together, and each cell type is well discriminated. **c** 3D PCA score plot of different cell suspension spectra CHO-745 (red circles), CHO-WT (blue crosses), and chondrocytes (green triangles). PCA was calculated on derivative spectra in the spectral range 1,200–900 cm⁻¹. All cell replicates are well grouped together. Each cell type is well discriminated

derivative spectra in the 1,200–900-cm⁻¹ spectral range indicated that chondrocytes differed from CHO types by their spectral differences in the saccharide absorption region.

FTIR spectra were then analyzed by PCA to validate these results. Figure 2c shows the PCA score plot of the three cell types using the three first principal components carrying the highest explained variance. The first principal component (PC1) carried 83 % of the total variance and allowed clear

separation of CHO-745 and CHO-WT from chondrocytes. These results also demonstrated that PC2, representing 9.1 % of the total variance, was discriminant enough to separate between CHO-745 and CHO-WT.

When PCA was applied to the CHO-745 and CHO-WT datasets only, only the first two PCs were enough to give a good separation between the two cell types (see ESM, Fig. S3a). PC1 carried the maximum explained variance

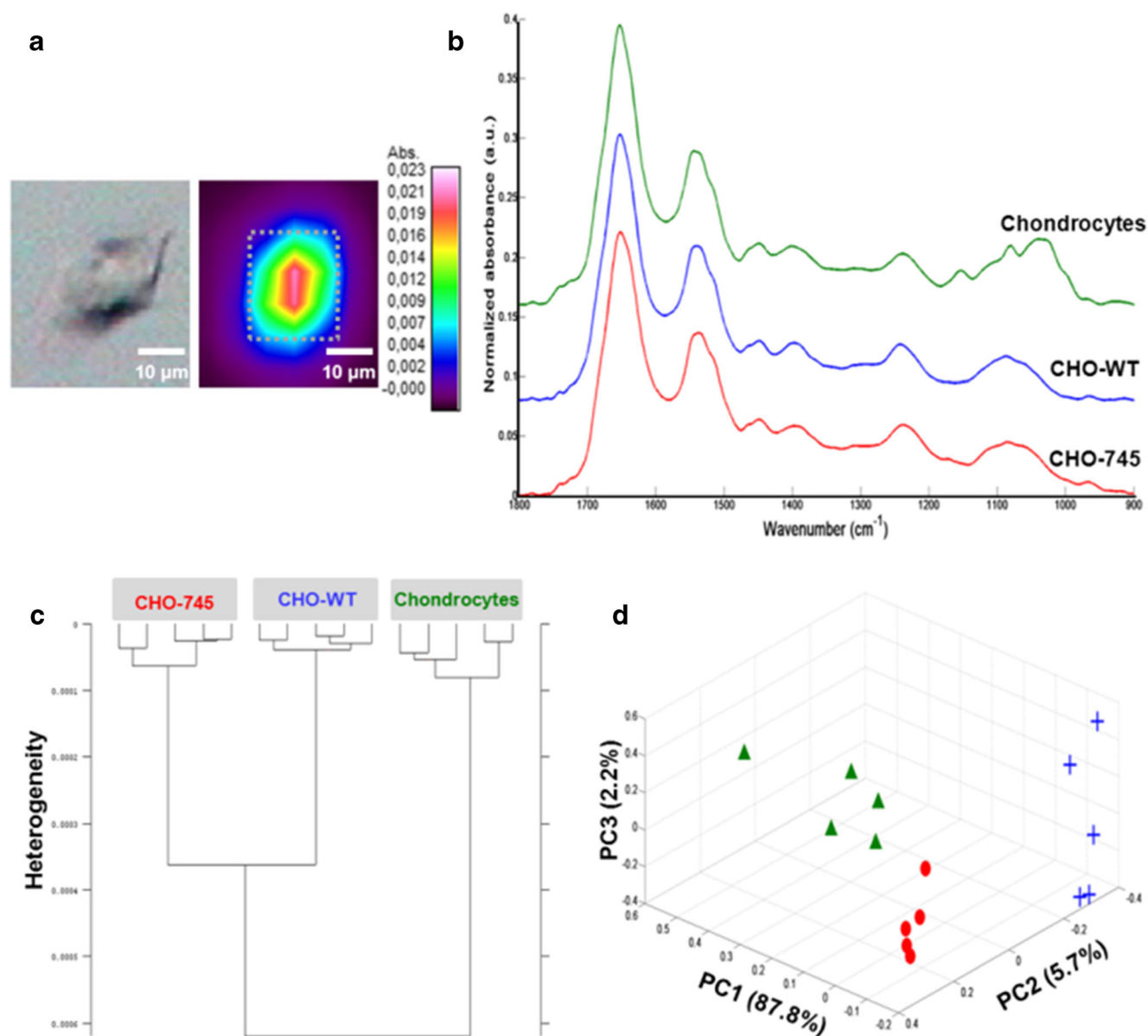


Fig. 3 Data processing of infrared spectra from a single-cell image. **a** White light image (left) and corresponding spectral image built on the total absorbance (right) of the same chondrocyte. A spectrum of the whole single cell can be averaged from the spectral image (cf. dotted rectangle). **b** Comparison between mean single-cell spectra of CHO-745 (red curve), CHO-WT (blue curve), and chondrocytes (green curve) in the spectral range 1,800–900 cm⁻¹. Each mean spectrum is an average calculated from five single-cell images. **c** HCA analysis of single-cell

spectra of CHO-745, CHO-WT, and chondrocytes. HCA was calculated on second derivative spectra in the spectral range 1,200–900 cm⁻¹. All replicate spectra of each single cell are well clustered together, and each cell type is well discriminated. **d** 3D PCA score plot of different single-cell spectra of CHO-745 (red circles), CHO-WT (blue crosses), and chondrocytes (green triangles). PCA was calculated on derivative spectra in the spectral range 1,200–900 cm⁻¹. All replicate spectra are well grouped together. Each cell type is well discriminated

(71.8 %) between these two cell types. PCA therefore confirmed the results obtained with HCA, i.e., cells with different capacity for GAG synthesis can be clearly delineated. In the same way, Fig. S3b shows a good discrimination between CHO-WT and chondrocytes. PC1, explaining the maximum of the explained variance (92.3 %), was discriminant enough to differentiate the two cell types. Thus, PCA can discriminate cell types with low and high ability to synthesize GAGs.

Characterization of GAGs in single cells by FTIR imaging

After the evidence obtained above with cells in suspension, we wanted to transpose the experiments to the single-cell level and verify our working hypothesis that the cell types can be distinguished. FTIR micro-imaging of single cells was carried out on the individual cells grown on specific substrates, fixed, and then dried before analysis. First, a white light image of the cell was taken to localize it on the substrate and to determine the acquisition zone for imaging (Fig. 3a, left panel). After acquisition, a pseudo-color spectral image of the cell (Fig. 3a, right panel) was obtained based on the total absorbance, with a color coding going from black (lowest absorption) to white (highest absorption). In this spectral image, each pixel element of $6.25 \mu\text{m}$ contained a spectrum and the dotted line indicated

the area selected to calculate an average spectrum of the imaged cell.

For each cell type, five individual cells were imaged and their corresponding average spectra, computed as explained earlier, were compared (Fig. 3b). It can be noticed that the mean spectra of CHO-745 and CHO-WT were very similar. On the other hand, for chondrocytes, the spectral changes depicted mainly in the $1,200\text{--}900\text{-cm}^{-1}$ range (saccharide absorbing region) were more marked than those of cells in suspension. Further analysis by HCA was performed on average spectra of each cell type using the $1,200\text{--}900\text{-cm}^{-1}$ spectral range. It can be observed that, as for cells in suspension, the mean spectra of the same cell type were grouped in the same cluster, indicating the low level of heterogeneity between the micro-FTIR spectra of the same cell type. The inter-group variability allowed separating the different cell types (Fig. 3c). The classification showed a slightly higher intra-group variability and a lower inter-group distance between CHO-745, CHO-WT, and chondrocytes as compared to data from cells in suspension.

The cell-typing potential of FTIR at the single-cell level was confirmed by the PCA on the three cell types (Fig. 3d). The PCA score plot was built using the three PCs with the highest explained variance. The outcome of the score plot showed that the average spectra of each cell type were

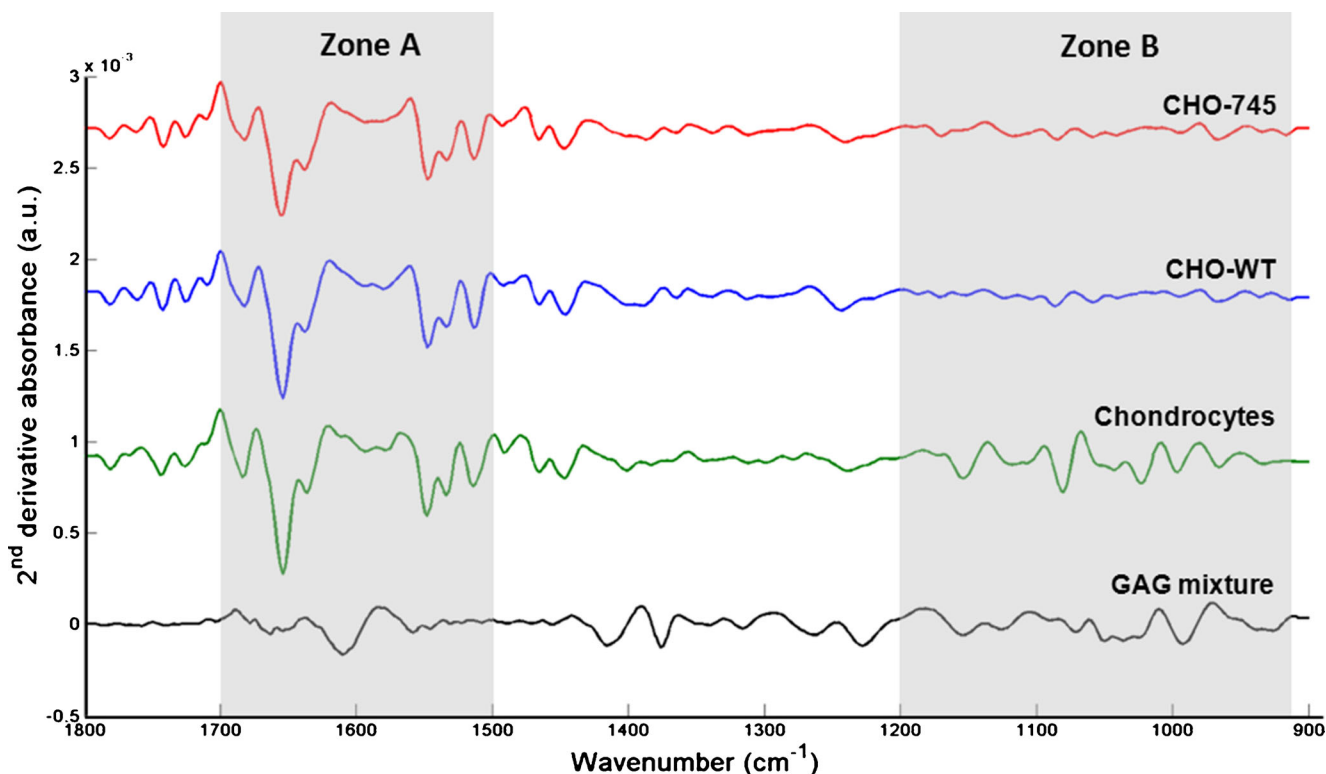


Fig. 4 Identification of GAG spectral profiles from single cells. Comparison between mean second derivative spectra of the mixture of six GAG standards and CHO-745 (red curve), CHO-WT (blue curve), and chondrocytes (green curve) in the spectral range $1,800\text{--}900 \text{ cm}^{-1}$. The six

GAG standards (black curve) used were hyaluronic acid, heparan sulfate, heparin, dermatan sulfate, chondroitin-6-sulfate, and chondroitin-4-sulfate. Each mean spectrum was the average of five cells

grouped together. The first PC carrying 87.8 % of the total variance allowed separating CHO-745 and CHO-WT from chondrocytes. CHO-745 and CHO-WT could be well distinguished with the variance carried by principal component 2 (5.7 %).

PCA computation of the CHO-745 and CHO-WT data sets gave a good separation between these two cell types, with PC1 carrying the maximum explained variance (82.6 %) between the two groups (see ESM, Fig. S3c). Further, CHO-WT and chondrocytes were well separated (see ESM, Fig. S3d), with a maximum of explained variance for PC1 (93 %). PCA results confirmed that FTIR spectroscopy could apparently discriminate, at the single-cell level, different cell types with varying potentials for GAG synthesis. This clustering between CHO-745 versus CHO-WT and CHO-WT versus chondrocytes confirmed the findings obtained with the cells in suspension.

In an attempt to find the spectral signature of GAG molecules at the individual cell level, we compared the mean spectra of CHO-745, CHO-WT, and chondrocytes with that of the GAG mixture. For this, all mean spectra underwent a second derivative to increase the spectral differences. The comparison between the three cell types with different capacities for GAG synthesis should allow the removal of the cellular contribution in the FTIR spectrum and to possibly identify the spectral information originating from GAGs.

Figure 4 shows the spectral comparison, at the single-cell level, between the different cell types, CHO-745, CHO-WT, chondrocytes, and the mixture of the six GAGs. Two zones can be highlighted: zone A and zone B for protein and saccharide absorption regions, respectively. In zone A, mean derivative spectra of three cell types show many distinct bands. The three profiles looked very similar and are attributed to the cellular profile. In zone B, spectra of CHO-745 and CHO-WT exhibited very similar profiles and very small bands while the chondrocyte spectrum showed some bands that seem to correspond with those of the GAG mixture in the same spectral zone.

These results tend to point out that by using the saccharide absorbing region as a marker region, FTIR imaging could help to identify, via the spectral profile of single cells, those that exhibit the potential to synthesize GAG molecules.

Indeed, our previous studies on GAG standards by infrared and Raman microspectroscopies allowed the identification of characteristic bands specific to their conformation [12, 13]. However, it is difficult to determine the GAG conformation in a complex biological system like a cell compared to GAG standards. Most conformational studies on GAG standards showed that these molecules exhibit a high flexibility [28, 29]. Further works are required to analyze the secreted GAGs in the cell medium in order to identify them, but again, the conformation will be different from that adopted in the cell. Raman microspectroscopy is foreseen as a promising approach for characterizing these cells in live conditions and

with higher spatial resolution. In addition, the development of the nanoparticle-based SERS approach using antibody-directed techniques could be a specific tool in particular for probing cell surface GAGs [30].

Conclusions

In this study, we have applied high-throughput FTIR spectroscopy and FTIR imaging to investigate cell suspensions and single cells, respectively, with the aim of verifying whether it was possible to identify, at both levels, cells with different capacities of synthesizing GAGs. Based on the spectral profiles obtained from cell suspensions and cell images, there was a clear-cut difference between the different cell types. Thus, it was possible, via the use of two different chemometric clustering approaches, to distinguish between the CHO-WT cell line and its mutant counterpart, CHO-745, lacking xylosyl transferase. The inter-group differences were more marked when the latter two cell lines were compared to the primary culture from human chondrocytes. Our findings suggest that FTIR methodology can be a useful approach for screening and identifying cells that exhibit the capacity for GAG synthesis. Furthermore, the method is rapid, non-destructive, non-contact, and label-free. Taking into account the importance of GAGs in the biomedical field, it will be challenging and further work is needed to transpose the methodology to tissue analysis in order to identify GAG molecules in normal tissues and during pathophysiological conditions (aging, healing, and numerous pathological states).

Acknowledgments The authors thank the Reims PICT-IBiSA Platform and the Service de Chirurgie Orthopédique, CHU de Reims. The financial support of the Ligue Nationale contre le Cancer (Comité de la Mame et Comité de Haute-Marne, Conférence de Coordination InterRégionale du Grand Est (CCIR-GE)), the FEDER and the Région Champagne-Ardenne (CPER 2007–2013), FIS (contract PII0/15), and RTICC (Red Temática de Investigación Cooperativa en Cáncer, contracts RD06/0020/0102; RD12/0036/0020), Instituto Carlos III Madrid & ERDF (European Regional Development Fund), Spain, is gratefully acknowledged.

References

1. Stevens R, Wong G, Humphries D (2000) Serglycin proteoglycans: the family of proteoglycans stored in the secretory granules of certain effector cells of the immune system. Dekker, New York
2. Kreuger J, Spillmann D, Li J-p, Lindahl U (2006) Interactions between heparan sulfate and proteins: the concept of specificity. *J Cell Biol* 174:323–327
3. Maccarana M, Sakura Y, Tawada A, Yoshida K, Lindahl U (1996) Domain structure of heparan sulfates from bovine organs. *J Biol Chem* 271:17804–17810

4. Koshiishi I, Horikoshi E, Imanari T (1999) Quantification of hyaluronan and chondroitin/dermatan sulfates in the tissue sections on glass slides. *Anal Biochem* 267:222–226
5. Koshiishi I, Takenouchi M, Hasegawa T, Imanari T (1998) Enzymatic method for the simultaneous determination of hyaluronan and chondroitin sulfates using high-performance liquid chromatography. *Anal Biochem* 265:49–54
6. Oguma T, Toyoda H, Toida T, Imanari T (2001) Analytical method of chondroitin/dermatan sulfates using high performance liquid chromatography/turbo ion spray ionization mass spectrometry: application to analyses of the tumor tissue sections on glass slides. *Biomed Chromatogr* 15:356–362
7. Conrad AH, Zhang Y, Walker AR, Olberding LA, Hanzlick A, Zimmer AJ, Morffi R, Conrad GW (2006) Thyroxine affects expression of KSPG-related genes, the carbonic anhydrase II gene, and KS sulfation in the embryonic chicken cornea. *Invest Ophthalmol Vis Sci* 47:120–132
8. Zhang Y, Conrad AH, Tasheva ES, An K, Corpuz LM, Kariya Y, Suzuki K, Conrad GW (2005) Detection and quantification of sulfated disaccharides from keratan sulfate and chondroitin/dermatan sulfate during chick corneal development by ESI-MS/MS. *Invest Ophthalmol Vis Sci* 46:1604–1614
9. Lamari F, Militopoulou M, Mitropoulou T, Hjerpe A, Karamanos N (2002) Analysis of glycosaminoglycan-derived disaccharides in biologic samples by capillary electrophoresis and protocol for sequencing glycosaminoglycans. *Biomed Chromatogr* 16:95–102
10. Plaas AH, West L, Midura RJ, Hascall VC (2001) Disaccharide composition of hyaluronan and chondroitin/dermatan sulfate: analysis with fluorophore-assisted carbohydrate electrophoresis. *Methods Mol Biol* 171:117–128
11. Shao C, Shi X, Phillips JJ, Zaia J (2013) Mass spectral profiling of glycosaminoglycans from histological tissue surfaces. *Anal Chem* 85:10984–10991
12. Mainreck N, Brézillon S, Sockalingum GD, Maquart FX, Manfait M, Wegrowski Y (2011) Rapid characterization of glycosaminoglycans using a combined approach by infrared and Raman microspectroscopies. *J Pharm Sci* 100:441–450
13. Mainreck N, Brézillon S, Sockalingum GD, Maquart F-X, Manfait M, Wegrowski Y (2012) In: Rédini F (ed) Characterization of glycosaminoglycans by tandem vibrational microspectroscopy and multivariate data analysis. Springer, London
14. Orr S (1954) Infra-red spectroscopic studies of some polysaccharides. *Biochim Biophys Acta* 14:173–181
15. Bychkov S, Bogatov V, Kuz'mina S (1981) Comparative study of the IR-spectra of glycosaminoglycans and their monomers. *Biull Eksp Biol Med* 91:442–445
16. Cabassi F, Casu B, Perlin AS (1978) Infrared absorption and Raman scattering of sulfate groups of heparin and related glycosaminoglycans in aqueous solution. *Carbohydr Res* 63:1–11
17. Foot M, Mulholland M (2005) Classification of chondroitin sulfate A, chondroitin sulfate C, glucosamine hydrochloride and glucosamine 6 sulfate using chemometric techniques. *J Pharm Biomed Anal* 38:397–407
18. Grant D, Long WF, Moffat CF, Williamson FB (1991) Infrared spectroscopy of heparins suggests that the region 750–950 cm^{-1} is sensitive to changes in iduronate residue ring conformation. *Biochem J* 275:193–197
19. Haxaire K, Marechal Y, Milas M, Rinaudo M (2003) Hydration of polysaccharide hyaluronan observed by IR spectrometry. I. Preliminary experiments and band assignments. *Biopolymers* 72:10–20
20. Haxaire K, Marechal Y, Milas M, Rinaudo M (2003) Hydration of hyaluronan polysaccharide observed by IR spectrometry. II. Definition and quantitative analysis of elementary hydration spectra and water uptake. *Biopolymers* 72:149–161
21. Longas MO, Breitweiser KO (1991) Sulfate composition of glycosaminoglycans determined by infrared spectroscopy. *Anal Biochem* 192:193–196
22. Maréchal Y, Milas M, Rinaudo M (2003) Hydration of hyaluronan polysaccharide observed by IR spectrometry. III. Structure and mechanism of hydration. *Biopolymers* 72:162–173
23. Servaty R, Schiller J, Binder H, Arnold K (2001) Hydration of polymeric components of cartilage an infrared spectroscopic study on hyaluronic acid and chondroitin sulfate. *Int J Biol Macromol* 28:121–127
24. Terho T, Hartiala K, Hakkinen I (1966) Infrared spectroscopic investigations of a new acid mucopolysaccharide isolated from human gastric juice. *Nature* 211:198–199
25. Maroudas A, Kuettner KE (1990) *Methods in cartilage research*. London: Academic Press edn. Academic Press, London
26. Franco CR, Rocha HA, Trindade ES, Santos IA, Leite EL, Veiga SS, Nader HB, Dietrich CP (2001) Heparan sulfate and control of cell division: adhesion and proliferation of mutant CHO-745 cells lacking xylosyl transferase. *Braz J Med Biol Res* 34:971–975
27. Parker FS (1983) In: Parker FS (ed) *Carbohydrates*. Plenum Press edn. Springer, New York
28. Casu B, Choay J, Ferro D, Gatti G, Jacquinet J, Petitou M, Provasoli A, Ragazzi M, Sinay P, Torri G (1986) Controversial glycosaminoglycan conformations. *Nature* 322:215–216
29. Casu B, Petitou M, Provasoli M, Sinay P (1988) Conformational flexibility: a new concept for explaining binding and biological properties of iduronic acid-containing glycosaminoglycans. *Trends Biochem Sci* 13:221–225
30. Hodges MD, Kelly JG, Bentley AJ, Fogarty S, Patel II, Martin FL, Fullwood NJ (2011) Combining immunolabeling and surface-enhanced Raman spectroscopy on cell membranes. *ACS Nano* 5:9535–9541

